UNIVERSITY OF CALIFORNIA, SAN DIEGO

Horizontal Load Resisting Mechanisms of External Shear Keys in Bridge Abutments

A dissertation submitted in partial satisfaction of the requirements for the degree

Doctor of Philosophy

in

Structural Engineering

by

Alexandra Kottari

Committee in charge:

Professor P. Benson Shing, Chair
Professor Yuri Bazilevs
Professor Thomas Bewley
Professor Francesco Lanza Di Scalea
Professor Jose I. Restrepo

2016

The dissertation of Alexandra Kottari is approved and it is acceptable in quality and form for publication on microfilm and electronically:

_____

_____

_____

_____

_____

Chair

University of California, San Diego

2016

TABLE OF CONTENTS

LIST OF ABBREVIATIONS

AASHTO	American Society of State Highway and Transportation Officials
ACI	American Concrete Institute
ASTM	American Society for Testing and Materials
Caltrans	California Department of Transportation
LRFD	Load and Resistance Factor Design
RC	Reinforced Concrete
RM	Reinforced Masonry
SDC	Seismic Design Criteria

LIST OF SYMBOLS

Chapter 2

a	distance of applied horizontal load measured from the top of the stem wall
a_{cl}	parameter for shear key design target capacity evaluation
A_{cv}	area of concrete engaged in interface shear transfer
A_{sh}	horizontal reinforcement area
A_{sk}	vertical reinforcement area
A_{sk}^{iso}	area of vertical reinforcement in isolated shear keys
$A_{sk}^{Non\text{-}iso}$	area of vertical reinforcement in non-isolated shear keys
b	width of stem wall
d	horizontal distance of the first row of steel bar from the toe of the stem wall
f_c'	compressive strength of concrete
f_{ce}'	confined compressive strength of concrete
f_{ye}	expected yield strength of steel
f_{su}	tensile strength of steel
F_p	prestressing force of stem wall
F_{sk}	design target capacity of shear keys
h	height of stem wall
h_p	distance of prestressing force from the toe of the stem wall

n_n	numbers of side faces with horizontal side reinforcement
n_v	numbers of side faces with vertical side reinforcement
P_{dl}	superstructure dead load plus the weight of abutment and footing
P_{dl}^{sup}	superstructure dead load
s	center to center distance of the vertical and horizontal side reinforcement
T_1	yield force of the horizontal reinforcement of stem wall
$T_{1,h}$	yield force of horizontal side reinforcement
$T_{1,v}$	yield force of vertical side reinforcement
T_2	yield force of first row of steel bar crossing the shear key interface
V_c	resistance of concrete
V_n	total shear resistance of the stem wall
V_{piles}	lateral capacity of the abutment pile group
V_s	resistance of steel
V_{ww}	shear capacity of one wing wall
α	angle of kink
β	angle of the inclined face of the shear key
μ_f	friction coefficient of shear key construction joint

Chapter 3

a	parameter for the calculation of bearing strength of concrete
b	parameter for the calculation of bearing stiffness
B	parameter for the calculation of dowel strength
c	parameter for the calculation of bearing stiffness
c_1	coefficient for the calculation of the bearing stiffness of concrete
C	parameter for the solution of beam on elastic foundation
C_r	constant for dowel strength calculation
d_b	reinforcing bar diameter
D	parameter for the solution of beam on elastic foundation
e	eccentricity of the dowel force
E	Young's modulus of steel
f	parameter for the calculation of bearing stiffness
f_c'	concrete cylinder compressive strength
f_{cb}	bearing strength of concrete for simplified calculation of dowel strength
f_{ck}	concrete cube compressive strength
f_y	bar yield strength
F	dowel force
F_d	dowel strength
I	moment of inertia of bar
k	modified bearing stiffness of concrete

k_c	bearing stiffness of concrete
K	modulus of elastic foundation
l_c	inactive zone length
l_y	effective length
M_o	moment due to the eccentricity of dowel force
M_{pl}	plastic moment capacity of a reinforcing bar
n	coefficient for local confinement of concrete
N	tension force
N_y	tensile yield force
w	displacement of dowel bar in the beam of elastic foundation method
α	parameter for the calculation of bearing stiffness
α_f	parameter for the calculation of dowel force
β	parameter for the solution of beam on elastic foundation
γ	parameter for the calculation of dowel force
δ	dowel displacement
ε	parameter for dowel strength calculation
ρ	parameter for the calculation of dowel force
σ_s	tensile stress in bar
φ	inclination angle
ω	modification factor for bearing stiffness calculation

Chapter 4

a	parameter for the calculation of bearing strength
$\mathbf{b}$	shape factor vector
b	parameter for the calculation of bearing strength
c	parameter for the calculation of bearing strength
d	parameter for the calculation of bearing strength
d_b	bar diameter
d_{n1}	internal variable used in the normal unloading-reloading law for the cohesive crack interface
d_{n2}	internal variable used in the normal unloading-reloading law for the cohesive crack interface
J	Jacobian for bond-slip and dowel action interface
f_c'	concrete cylinder compressive strength
f_m'	compressive strength of masonry
$\boldsymbol{f}_x$	interface force in x direction
$\boldsymbol{f}_y$	interface force in y direction
k_0	bearing strength initial value
K_{un}	unloading stiffness of bearing strength
K_{in}	initial loading stiffness of bearing strength
L_{12}	distance between point 1 and point 2 of interface

L_{14} distance between point 1 and point 4 of interface

L_{23} distance between point 2 and point 3 of interface

L_{34} distance between point 3 and point 4 of interface

s_{peak} slip at peak bond stress

s_R slip at residual bond stress

$\boldsymbol{u}$ vector of nodal tangential displacements

u_c displacement in tangential direction of concrete side

u_s displacement in tangential direction of steel side

$\tilde{u}$ relative displacement in tangential direction

$\boldsymbol{v}$ vector of nodal normal displacements

v_c displacement in normal direction of concrete side

v_s displacement in normal direction of steel side

$\tilde{v}$ relative displacement in normal direction

$\dot{\tilde{v}}$ rate of change of relative displacement in normal direction

α parameter connecting natural coordinate of steel and concrete sides

β parameter connecting natural coordinate of steel and concrete sides

γ multiplication factor

δ_{cur} displacement at reloading

δ_g gap length

δ_r final value of displacement at unloading

δ_u displacement when unloading starts

$\delta \boldsymbol{u}$ vector of virtual nodal tangential displacement

$\delta \tilde{u}$ virtual relative tangential displacement

$\delta \boldsymbol{v}$ vector of virtual nodal displacement in *y* direction

$\delta \tilde{v}$ virtual relative normal displacement in *y* direction

δW_E external virtual work

δW_I internal virtual work

η_c natural coordinate of concrete side

η_s natural coordinate of steel side

$\rho_{b,c}$ degradation factor of bearing resistance due to cyclic slip reversals

$\rho_{b,s}$ reduction factor of the bearing resistance due to tensile yielding of bar

$\rho_{f,c}$ degradation factor of frictional resistance due to cyclic slip reversals

$\rho_{f,s}$ reduction factor of the frictional resistance due to tensile yielding of bar

σ normal stress

$\dot{\sigma}$ rate of change of normal stress

σ_u normal stress when unloading starts

τ shear stress

τ_b bearing resistance

τ_f frictional resistance

τ_{max} maximum bond strength for monotonic loading

τ_{res} residual bond strength for monotonic loading

ω value of modification factor for bearing stiffness calculation

ω_{in} initial value of modification factor for bearing stiffness calculation

Chapter 5

a parameter for the calculation of bearing strength

a_k angle of kink

$A_{i,h}$ area of horizontal reinforcing bar *i* of the stem wall

$A_{j,v}$ area of vertical reinforcing bar *j* of the stem wall

$A_{t,s}$ area of horizontal shear reinforcing bar *t* of the stem wall

A_{vs} total area of vertical dowel bars

C_c vertical force in the compression region

d width of stem wall

d_b bar diameter

f_c' concrete cylinder compressive strength

f_{cb} bearing strength of concrete for simplified calculation of dowel strength

f_{su} tensile strength of reinforcing bars

f_y yield strength of reinforcing bars

F_d dowel strength

$F_{i,h}$ axial force of horizontal reinforcing bar *i* of the stem wall

$F_{j,v}$ axial force of vertical reinforcing bar *j* of the stem wall

F_s total axial force of vertical dowel bars

F_{s1} vertical component of total axial force of vertical dowel bars

F_{s2} horizontal component of total axial force of vertical dowel bars

$F_{t,s}$ axial force of horizontal reinforcing bar *t* of the stem wall

h vertical distance of externally applied horizontal force from point *A*

$l_{i,h}$ vertical distance of horizontal bar *i* from point *A*

$l_{j,v}$ horizontal distance of vertical bar *j* from point *A*

$l_{t,s}$ vertical distance of horizontal shear reinforcing bar *t* of stem wall from point *A*

L horizontal distance of externally applied vertical force from point *A*

M_{pl} plastic moment capacity of a reinforcing bar

P_{slid} first sliding vertical resistance

P_w diagonal shear failure vertical resistance

P_u ultimate failure vertical resistance

T cohesive strength

V_c horizontal force in the compression region

V_{slid} first sliding horizontal resistance

V_w diagonal shear failure horizontal resistance

V_u ultimate failure horizontal resistance

α_c compression zone length

β	angle of inclined face of shear key with respect to a vertical plane
μ_f	coefficient of friction of construction joint surface

Chapter 6

c	cohesive strength
d	width of shear key
d_a	maximum aggregate size
f_c'	concrete cylinder compressive strength
f_{su}	tensile strength of reinforcing bars
f_y	yield strength of reinforcing bars
F_s	total axial force of vertical dowel bars
l	length of shear key
$l_{i,h}$	vertical distance of horizontal bar *i* from point *A*
$l_{j,v}$	horizontal distance of vertical bar *j* from point *A*
$l_{t,s}$	vertical distance of horizontal shear reinforcing bar *t* of stem wall from point *A*
P_{slid}	first sliding vertical resistance
T	cohesive force
V_{slid}	first sliding horizontal resistance
X	parameter for the calculation of cohesive strength
V_u	ultimate failure horizontal resistance

α_c compression zone length

β angle of inclined face of shear key with respect to a vertical plane

μ_f coefficient of friction

Chapter 7

A_b total area of vertical reinforcing bars

E modulus of elasticity of prestressing bars

f_{pu} ultimate strength of prestressing bars

f_{su} tensile strength of reinforcing bars

f_y yield strength of reinforcing bars

F_{ch} horizontal contact force

F_{cv} vertical contact force

F_h horizontal component of external load applied to the shear key

F_p resultant prestressing force

F_t force of vertical tie

F_v vertical component of external load applied to the shear key

h_p vertical distance of resultant prestressing force from point *O*

l length of prestressing bars

l_{cv} vertical distance of horizontal contact force from point *O*

l_h horizontal distance from point of load application to point *O*

l_v vertical distance from point of load application to point *O*

T_{ch} frictional force due to horizontal force

T_{cv} frictional force due to vertical contact force

α shear key block rotation

δ horizontal displacement at the point of load application

Δl_p elongation of prestressing bars

μ coefficient of friction

Chapter 8

f_{su} tensile strength of reinforcing bars

f_y yield strength of reinforcing bars

Chapter 9

Section 9.1 – Section 9.2

$\boldsymbol{B}$ matrix relating relative displacements to nodal displacements

$\boldsymbol{d}$ vector of relative shear displacements

$\boldsymbol{d}^e$ vector of relative elastic shear displacements

$\boldsymbol{d}^g$ vector of relative geometric shear displacements

$\boldsymbol{d}^p$ vector of relative plastic shear displacements

$\dot{\boldsymbol{d}}^p$ rate of vector of relative plastic shear displacements

d_n relative normal displacement

$d_{n,m}$ relative normal displacement in step m

$d_{n,m+1}$ relative normal displacement in step m+1

d_n^e relative elastic normal displacement

d_n^p relative plastic normal displacement

$\dot{d}_n^p$ rate of relative plastic normal displacement

d_n^g relative geometric normal displacement

d_{n1} internal variable used in the normal unloading-reloading law for interface

$d_{n1,m}$ internal variable used in the normal unloading-reloading law for interface in step m

d_{n2} internal variable used in the normal unloading-reloading law for interface

$d_{n2,m}$ internal variable used in the normal unloading-reloading law for interface in step m

d_o material parameter for the calculation of the dilatation parameter

d_{res}^p resultant plastic shear displacement

d_s relative shear displacement in s displacement

d_s^e relative elastic shear displacement in s displacement

d_s^p relative plastic shear displacement in s displacement

$\dot{d}_s^p$ rate of relative plastic shear displacement in s displacement

d_t relative shear displacement in t displacement

d_t^e relative elastic shear displacement in t displacement

$d_t^{\,p}$	relative plastic shear displacement in *t* displacement
$\dot{d}_t^{\,p}$	relative plastic shear displacement in *t* displacement
D_{nn}	elastic stiffness for normal displacement
D_{ss}	elastic stiffness for shear displacement in *s* direction
D_{tt}	elastic stiffness for shear displacement in *t* direction
$\boldsymbol{F}$	yield criterion function
G_f^I	total Mode-I fracture energy
G_f^{II}	total Mode-II fracture energy
$\boldsymbol{L}$	matrix relating bottom and top surface displacements to relative displacements
$\boldsymbol{m}$	vector defining direction of rate of plastic strain vector
m_1	normal component of vector defining direction of rate of plastic strain vector
$m_{1,m+1}$	normal component of vector defining direction of rate of plastic strain vector in step m+1
m_2	tangential component of vector defining direction of rate of plastic strain vector
$m_{2,m+1}$	tangential component of vector defining direction of rate of plastic strain vector in step m+1
m_3	tangential component of vector defining direction of rate of plastic strain vector
$m_{3,m+1}$	tangential component of vector defining direction of rate of plastic strain vector in step m+1
$\boldsymbol{M}$	matrix relating bottom and top surface displacements to nodal displacements

$\boldsymbol{N}$	matrix relating spatial to natural coordinates
$\boldsymbol{N}_s$	matrix containing the linear shape functions defined in the natural coordinates
$\boldsymbol{q}$	vector of internal variables
$\boldsymbol{q}_m$	vector of internal variables in step m
$\boldsymbol{q}_{m+1}$	vector of internal variables in step m+1
$\boldsymbol{Q}$	plastic potential
r	radius of curvature at the apex of the yield surface
r_m	radius of curvature at the apex of the yield surface in step m
r_{m+1}	radius of curvature at the apex of the yield surface in step m+1
r_o	initial value of radius of curvature at the apex of the yield surface
r_r	residual value of radius of curvature at the apex of the yield surface
s	value of tensile strength
s_m	value of tensile strength in step m
s_{m+1}	value of tensile strength in step m+1
s_o	initial value of tensile strength
u_b	displacement in t direction of bottom surface
u_i	displacement in t direction of node i
u_t	displacement in t direction of top surface
$\boldsymbol{u}$	vector of nodal displacements
$\bar{\boldsymbol{u}}$	vector containing displacements of top and bottom surfaces

v_b displacement in *s* direction of bottom surface

v_i displacement in *s* direction of node *i*

v_t displacement in *s* direction of top surface

w_b displacement in *n* direction of n bottom surface

w_i displacement in *n* direction of node *i*

w_t displacement in *n* direction of top surface

α parameter controlling the degradation of the slope of the asymptotes of the hyperboloid

β parameter controlling the degradation of the radius of the curvature at the apex of the hyperboloid

γ angle to calculate projection of stress in global axes

δ displacement in interface example

Δd_n discrete increment of normal displacement

$\Delta d_n^{\ g}$ discrete increment of normal geometric displacement

$\Delta d_n^{\ p}$ discrete increment of normal plastic displacement

Δd_{n1} discrete increment of internal variable used in the normal unloading-reloading law for interface

Δd_s discrete increment of shear displacement in *s* direction

$\Delta d_s^{\ p}$ discrete increment of plastic shear displacement in *s* direction

Δd_t discrete increment of shear displacement in *t* direction

$\Delta d_t^{\,p}$	discrete increment of plastic shear displacement in *t* direction
$\Delta\lambda$	discrete increment of plastic multiplier
ζ_{dil}	dilatation coefficient
$\zeta_{dil,o}$	initial value of dilatation coefficient
$\zeta_{dil,r}$	residual value of dilatation coefficient
η	parameter controlling plastic compaction due to damage
$\dot{\boldsymbol{\kappa}}$	vector containing the rates of plastic work
κ_1	plastic work associated with Mode-I fracture
κ_2	plastic work associated with Mode-II fracture
κ_3	plastic work associated with the smoothening of the sliding surface
$\dot{\lambda}$	plastic multiplier
$\boldsymbol{\Lambda}(\boldsymbol{\sigma})$	matrix associating the rate of plastic displacements to the plastic work
μ	slope of the asymptotes of the hyperboloid
μ_m	slope of the asymptotes of the hyperboloid in step *m*
μ_{m+1}	slope of the asymptotes of the hyperboloid in step *m*+1
μ_o	initial value of the slope of the asymptotes of the hyperboloid
μ_r	residual value of the slope of the asymptotes of the hyperboloid
$\boldsymbol{\sigma}$	stress vector
$\boldsymbol{\sigma}_m$	stress vector in step *m*
$\boldsymbol{\sigma}_{m+1}$	stress vector in step *m*+1

σ	normal stress
σ^{el}	elastic predictor of normal stress
σ_m	normal stress in step m
σ_{m+1}	normal stress in step m+1
σ_{m+1}^{el}	elastic predictor of normal stress in step m+1
τ_{r1}	shear strength under a normal stress when the tensile strength is zero
$\tau_{r1,m+1}$	shear strength under a normal stress when the tensile strength is zero in step m+1
τ_{r2}	shear strength under a normal stress when the tensile strength is zero and the material parameters have residual values
$\tau_{r2,m+1}$	shear strength under a normal stress when the tensile strength is zero and the material parameters have residual values in step m+1
τ_s	shear stress in s direction
τ_s^{el}	elastic predictor of shear stress in s direction
$\tau_{s,m}$	shear stress in s direction in step m
$\tau_{s,m+1}$	shear stress in s direction in step m+1
$\tau_{s,m+1}^{el}$	elastic predictor of shear stress in s direction in step m+1
τ_t	shear stress in t direction
τ_t^{el}	elastic predictor of shear stress in t direction
$\tau_{t,m}$	shear stress in t direction in step m

$\tau_{t,m+1}$ shear stress in t direction in step m+1

$\tau_{t,m+1}^{el}$ elastic predictor of shear stress in t direction in step m+1

Section 9.3

a parameter for the calculation of bearing strength

$\boldsymbol{b}$ shape factor vector

b parameter for the calculation of bearing strength

c parameter for the calculation of bearing strength

d parameter for the calculation of bearing strength

d_b bar diameter

$\boldsymbol{f}_x$ interface force in x direction

$\boldsymbol{f}_y$ interface force in y direction

$\boldsymbol{f}_z$ interface force in z direction

k_0 bearing strength initial value

K_{un} unloading stiffness of bearing strength

K_{in} initial loading stiffness of bearing strength

L_{12} distance between point 1 and point 2 of interface

L_{14} distance between point 1 and point 4 of interface

L_{23} distance between point 2 and point 3 of interface

L_{34} distance between point 3 and point 4 of interface

$\tilde{s}$	resultant normal displacement in radial direction
$\dot{\tilde{s}}$	rate of change of relative normal displacement in radial direction
$\boldsymbol{u}$	vector of nodal tangential displacements
u_c	displacement in tangential direction of concrete side
u_i	tangential displacement of node *i*
u_s	displacement in tangential direction of steel side
$\tilde{u}$	relative displacement in tangential direction
$\boldsymbol{v}$	vector of nodal normal displacements in *y* direction
v_c	displacement in normal *y* direction of concrete side
v_i	normal displacement of node *i* in *y* direction
v_s	displacement in normal *y* direction of steel side
$\tilde{v}$	relative displacement in normal *y* direction
$\boldsymbol{w}$	vector of nodal normal displacements in *z* direction
w_c	displacement in normal *z* direction of concrete side
w_i	normal displacement of node *i* in *z* direction
w_s	displacement in normal *z* direction of steel side
$\tilde{w}$	relative displacement in normal *z* direction
α_f	parameter connecting natural coordinate of steel and concrete sides
β_f	parameter connecting natural coordinate of steel and concrete sides
γ	multiplication factor

γ_d angle of resultant normal displacement with respect to *y* axis

δ imposed displacement in example

δ_{cur} displacement at reloading

δ_g gap length

δ_r final value of displacement at unloading

δ_u displacement when unloading starts

$\delta\boldsymbol{u}$ vector of virtual nodal tangential displacement

$\delta\tilde{u}$ virtual relative tangential displacement

$\delta\boldsymbol{v}$ vector of virtual nodal displacement in *y* direction

$\delta\tilde{v}$ virtual relative normal displacement in *y* direction

$\delta\boldsymbol{w}$ vector of virtual nodal displacement in *z* direction

$\delta\tilde{w}$ virtual relative normal displacement in *z* direction

δW_E external virtual work

δW_I internal virtual work

η_c natural coordinate of concrete side

η natural coordinate of steel side

σ normal stress

σ_y normal stress in *y* direction

σ_z normal stress in *z* direction

$\dot{\sigma}$ rate of change of normal stress

σ_u normal stress when unloading starts

τ shear stress

ω value of modification factor for bearing stiffness calculation

ω_{in} initial value of modification factor for bearing stiffness calculation

Chapter 10

d parameter for the calibration of the post-peak behavior of concrete model

d_o material parameter for the calculation of the dilatation parameter

D_{nn} elastic stiffness for normal displacement

D_{tt} elastic stiffness for shear displacement

E Young's modulus for steel

g_c parameter of concrete model

G_f^I total Mode-I fracture energy

G_f^{II} total Mode-II fracture energy

f_c' concrete cylinder compressive strength

f_{su} tensile strength of reinforcing bars

f_y yield strength of reinforcing bars

r_o initial value of radius of curvature at the apex of the yield surface

r_r residual value of radius of curvature at the apex of the yield surface

s_o initial value of tensile strength

α parameter controlling the degradation of the slope of the asymptotes of the hyperboloid

α_c material constant of concrete model

α_p dilatancy parameter of concrete model

β parameter controlling the degradation of the radius of the curvature at the apex of the hyperboloid

ε_f strain at fracture of steel

$\zeta_{dil,o}$ initial value of dilatation coefficient

$\zeta_{dil,r}$ residual value of dilatation coefficient

η parameter controlling plastic compaction due to damage

μ_o initial value of the slope of the asymptotes of the hyperboloid

μ_r residual value of the slope of the asymptotes of the hyperboloid

Chapter 11

a parameter for the calculation of bearing strength

a_k angle of kink

$A_{i,h}$ area of horizontal reinforcing bar *i* of the stem wall

$A_{j,v}$ area of vertical reinforcing bar *j* of the stem wall

$A_{t,s}$ area of horizontal shear reinforcing bar *t* of the stem wall

A_{vs} total area of vertical dowel bars

c cohesive strength

C_c vertical force in the compression region

d width of stem wall

d_a maximum aggregate size

d_b reinforcing bar diameter

f_c' concrete cylinder compressive strength

f_{cb} bearing strength of concrete for simplified calculation of dowel strength

f_{su} tensile strength of reinforcing bars

f_y yield strength of reinforcing bars

F_d dowel strength

$F_{i,h}$ axial force of horizontal reinforcing bar *i* of the stem wall

$F_{j,v}$ axial force of vertical reinforcing bar *j* of the stem wall

F_s total axial force of vertical dowel bars

F_{sx} horizontal component of total axial force of vertical dowel bars

F_{sy} vertical component of total axial force of vertical dowel bars

$F_{t,s}$ axial force of horizontal reinforcing bar *t* of the stem wall

h vertical distance of externally applied horizontal force from point *A*

l length of shear key

$l_{i,h}$ vertical distance of horizontal bar *i* from point *A*

$l_{j,v}$ horizontal distance of vertical bar *j* from point *A*

$l_{t,s}$ vertical distance of horizontal shear reinforcing bar *t* of stem wall from point *A*

L	horizontal distance of externally applied vertical force from point *A*
M_{pl}	plastic moment capacity of a reinforcing bar
P_{slid}	first sliding vertical resistance
P_w	diagonal shear failure vertical resistance
P_u	ultimate failure vertical resistance
T	cohesive force
V_c	horizontal force in the compression region
V_{slid}	first sliding horizontal resistance
V_w	diagonal shear failure horizontal resistance
V_u	ultimate failure horizontal resistance
X	parameter for the calculation of cohesive strength
α_c	compression zone length
β	angle of inclined face of shear key with respect to a vertical plane
λ_t	parameter controlling the tensile softening behavior of the cracked concrete material
μ_f	coefficient of friction of construction joint surface

LIST OF FIGURES

LIST OF TABLES

ACKNOWLEDGEMENTS

This research study was conducted under the supervision of Professor Benson Shing at the University of California San Diego (UC San Diego). I would like to express my gratitude to the California Department of Transportation for funding the experimental work conducted in this research project and for partially supporting my studies. I would also like to thank the Structural Engineering Department for awarding me the graduate fellowship in the first year of my studies and the Alexander Onassis Foundation for financially supporting part of my studies.

I would like to thank the members of my dissertation committee, Professors Y. Bazilevs, T. Bewley, F. Lanza di Scalea and J. Restrepo for their feedback on my research. Professor J. Restrepo provided valuable advice for the experimental work.

The experimental work presented in this dissertation was conducted at the Powell Lab Structural Research Laboratories at UC San Diego. I am grateful to all the lab staff members for their cooperation and help in conducting the tests.

I would also like to thank Mr. Ron Bromenschenkel and Dr. Charles Sikorsky of the California Department of Transportation for their technical input and continuous support throughout this project.

My advisor, Professor Benson Shing, has had a great impact on my engineering thinking and I am grateful for his guidance during my studies.

I would like to acknowledge the help of Professor I. Koutromanos and his graduate student M. Moharrami who provided their concrete model, and Dr. M. Mavros

for sharing the bond-slip interface element formulation. I would also like to thank them for their interest on my research and their constructive comments.

Finally, I would like to express my gratitude to my parents, Kyriakos and Eleni, and my siblings, Yannis and Renata, for always being on my side, for their support and understanding.

Part of Chapters 1 through 12 are a reprint of the material that will appear in a technical report, which will be submitted to the California Department of Transportation in 2016, Kottari, A., P. B. Shing, J. I. Restrepo, under the title "Design and Capacity Assessment of External Shear Keys in Bridge Abutments". The dissertation author will be the primary investigator and author of this report.

VITA

July 2009	Diploma in Civil Eng., National Technical University of Athens
December 2011	M.S., Structural Eng., University of California, San Diego
March 2016	Ph. D., Structural Eng., University of California, San Diego

ABSTRACT OF THE DISSERTATION

Horizontal Load Resisting Mechanisms of External Shear Keys

in Bridge Abutments

by

Alexandra Kottari

Doctor of Philosophy in Structrual Engineering

University of California, San Diego, 2016

Professor P. Benson Shing, Chair

Shear keys in bridge abutments are intended to provide lateral restraints to the bridge superstructure in the event of a moderate earthquake and to serve as fuses to

prevent the transmission of large lateral forces to the abutment piles when a severe earthquake occurs.

This study is to acquire a comprehensive understanding of the behavior and resistance mechanisms of external shear keys in bridge abutments and to develop reliable analytical methods for the evaluation of the capacity of shear keys with different material properties, construction methods, reinforcing details, geometries, and degrees of skew. Six shear key-stem wall assemblies were tested. The tests on isolated shear keys have provided useful information on the influence of the construction joint preparation on the shear key behavior and have been used to validate simplified strength assessment methods. The study has shown that non-isolated shear keys can be so reinforced that their failure mechanism is governed by horizontal sliding rather than diagonal cracking of the stem wall, which is costly to repair. A reliable analytical method has been proposed to calculate the resistance of non-isolated shear keys based on the shear key geometry, the concrete strength, and the amount of the vertical dowel reinforcement. An innovative design concept using post-tensioned rocking shear keys has been explored and proven to be feasible. Finally, the test data have shown that a shear key with a 60-degree skew can be significantly weaker than a shear key with zero-degree skew and the same amount of vertical dowel reinforcement.

Nonlinear finite element analysis can be an accurate means to understand the failure mechanism and predict the resistance of shear keys. For such analysis, a 3-D cohesive crack interface model has been developed to represent concrete fracture in a realistic manner, and an interface material law has been proposed to simulate the dowel action of steel reinforcing bars crossing cracks and construction joints.

Based on the experimental and numerical studies, general recommendations are provided for the design of shear keys. The simplified analytical methods proposed here can be used to design shear keys and stem walls to achieve the desired performance.

CHAPTER 1

INTRODUCTION

1.1 Background

External shear keys in bridge abutments are intended to resist lateral forces generated by small to moderate earthquakes and service loads so that the bridge superstructure will not displace with respect to its abutments under these load conditions. However, they are designed to act as structural fuses to protect the abutment piles from damage in the event of a major earthquake.

In the past, limited experimental studies (Borzogzadeh et al., 2006, Megally et al., 2002) have been conducted to evaluate the behavior of two types of shear key types, which have been used by the California Department of Transportation (Caltrans). They are isolated shear keys and non-isolated shear keys. An isolated shear key is separated from the stem wall with a construction joint, and has vertical reinforcing bars connecting it to the stem wall. Non-isolated shear keys are cast monolithically with the stem wall. The latter are more economical to construct.

In the event of a major earthquake, the desired failure mode of a shear key functioning as a structural fuse to protect the abutment piles from damage is the sliding of the shear key on top of the stem wall. This type of failure is easier and more economical to repair as compared to the diagonal shear failure of the stem wall. Hence, the design of

shear keys and stem walls requires accurate calculations of their respective strengths to avoid undesired failure mechanisms. Borzogzadeh et al. (2006) have proposed a formula to calculate the shear sliding resistance of an isolated shear key. The formula has been validated by some experimental data and has been adopted by Caltrans in the Seismic Design Criteria (2010). Nevertheless, the general validity of the formula for different amounts and sizes of vertical reinforcing bars connecting the shear key to the stem wall has not been proven by any experimental data. In addition, the formula is only applicable to smooth construction joints with bond breaker. The ability to reliably predict the shear sliding resistance of a non-isolated shear key and the diagonal shear strength of a stem wall is still lacking. Non-isolated shear keys and even some isolated shear keys tested by Borzogzadeh et al. (2006) and Megally et al. (2002) had failures governed by diagonal shear cracks developed in the stem walls.

All the past studies were focused on shear keys in non-skewed bridges. However, it is expected that the angle of skew of a bridge abutment should affect the resistance of a shear key under lateral loading.

1.2 Research Objectives and Scope

The research reported here is intended to close the aforementioned knowledge gaps and to develop comprehensive design recommendations for external shear keys in bridge abutments. To this end, six shear key-stem wall assemblies were tested. These tests were to investigate the performance and resistance of shear keys with and without construction joints, and with different amounts of vertical reinforcement connecting the

shear keys to the stem walls, different amounts of horizontal shear reinforcement in the stem walls, different concrete strengths, and different surface preparations for the construction joints. Five of the specimens had a zero skew angle and one had a 60-degree skew, which was the maximum expected. One specimen was designed with an innovative concept of post-tensioned shear keys that were allowed to rock without causing damage.

Nonlinear finite element models of shear key-stem wall assemblies have been developed in this study. For these models, a 3-D cohesive crack interface model has been developed to represent concrete facture and the behavior of construction joints, and an interface material law has been proposed to simulate the dowel action of steel reinforcing bars crossing cracks and construction joints. The models have been implemented in a finite element program FEAP (Taylor, 2014) and validated by experimental results. Finite element analyses have been conducted to acquire a better understanding of the behavior of shear keys. The modeling method developed here provides a tool to predict the strength and performance of shear keys of different designs.

Simplified analytical methods that can be used in design have been developed in this study to calculate the shear sliding resistance of isolated and non-isolated shear keys as well as the diagonal shear strength of stem walls. General design recommendations for shear keys are also provided.

1.3 Outline of Dissertation

This dissertation can be divided into three main parts. The first part focuses on the mechanics of the dowel action of reinforcing bars crossing cracks or construction joints,

and the development of a modeling scheme to simulate the dowel action of reinforcing bars. The second part, Chapters 5 through 8, presents the results of the experimental study on shear keys carried out in this project. The third and the last part focuses on the finite element modeling of shear keys and final design recommendations.

Chapter 2 presents a summary of the experimental and analytical studies conducted in the past to evaluate the behavior and resistance of shear keys in bridge abutments. Current Caltrans design specifications for shear keys in bridge abutments are also briefly summarized.

Chapter 3 focuses on the mechanics of the dowel action of steel reinforcing bars. Past experimental studies and existing analytical models are summarized, and a new analytical method is proposed for the calculation of the dowel resistance. This model has been calibrated and validated by existing experimental data. A study has been conducted with a simplified beam element model to confirm the validity of the analytical method.

Chapter 4 presents a constitutive model for the simulation of dowel action in finite element analysis. The model describes the bearing resistance developed in concrete in the vicinity of a bar during dowel action. For the bearing stress-vs.-displacement relation, an existing phenomenological model has been adopted and extended to account for cyclic loading. This material law has been implemented in an interface model. Examples of single steel reinforcing bars subjected to monotonic and cyclic loading have been presented to demonstrate the accuracy of the model. The model has also been validated by analyses conducted on reinforced masonry shear walls.

Chapter 5 presents the results of the experimental study of two isolated shear keys. The objective of these tests was to validate the existing and new analytical methods

for calculating the diagonal shear strength of stem walls and the sliding shear resistance of isolated shear keys. Additional data regarding the dowel behavior of steel reinforcing bars were also obtained.

Chapter 6 presents the results of the experimental study on non-isolated shear keys. Three specimens with two shear keys each were tested. The main objective of this study was to investigate if the stem wall and shear key could be appropriately reinforced such that the diagonal shear failure of the stem wall could be prevented and a horizontal failure plane could develop between the shear key and the stem wall, similar to the behavior of isolated shear keys. Non-isolated shear keys with different concrete strengths and amounts of vertical reinforcing bars were tested.

Chapter 7 presents the experimental results of the test of a specimen that had two rocking shear keys connected to the stem wall with horizontal, unbonded, post-tensioned bars. Design details that allowed large shear key displacements without damaging the stem wall are presented.

Chapter 8 presents the experimental results from a specimen that had two non-isolated shear keys with an angle of skew of 60 degrees. This test provided valuable information regarding the influence of the angle of skew on the behavior of shear keys.

Chapter 9 presents the formulation of the planar cohesive crack interface model. The model is suitable for three-dimensional analyses of concrete structures. It can account for mixed-mode fracture, reversible shear dilatation, irreversible compaction, and crack opening and closing. The model for the simulation of dowel action for three-dimensional analyses is also presented. This model is an extension of the model presented in Chapter 4.

Chapter 10 presents the verification analyses conducted with nonlinear finite element models for a number of shear keys which exhibited different failure mechanisms in the tests. The meshing schemes and the calibration of the material models are presented.

Chapter 11 presents the simplified analytical methods proposed for the calculation of the resistance of shear keys and stem walls to lateral loading. These methods are developed and validated with the experimental and finite element analysis results.

Chapter 12 presents the summary of conclusions of this study.

1.4 Acknowledgement of Publication

Part of this chapter is a reprint of the material that will appear in a technical report which will be submitted to the California Department of Transportation in 2016, Kottari, A., P. B. Shing, J. I. Restrepo, under the title "Design and Capacity Assessment of External Shear Keys in Bridge Abutments". The dissertation author will be the primary investigator and author of this report.

CHAPTER 2

LITERATURE REVIEW OF PAST STUDIES OF SHEAR KEYS IN BRIDGE ABUTMENTS

2.1 Introduction

The study of the performance of shear keys in bridge abutments has been limited. Experimental study was carried out by Megally et al. (2002) to evaluate the load capacities of internal and external shear keys in bridge abutments. Later, Borzogzadeh et al. (2006) and Bauer (2006) continued the study with additional experimental testing and analytical investigation of the resistance of shear keys. Some of their research findings were incorporated in the Caltrans Seismic Design Criteria in 2010 (Version 1.6).

In this chapter, a summary of the past research studies of shear keys is presented. Current design specifications for shear keys provided in the Caltrans Seismic Design Criteria (2013, SDC v1.7) are also discussed.

2.2 Past Experimental Investigation of Shear Keys

Megally et al. (2002) tested three shear key-abutment stem wall specimens, identified as Specimens 1, 2 and 3. The specimens represented a 40%-scale model of the abutment stem wall in the South Ave OC (Caltrans Br. #39-0146). Each specimen consisted of one stem wall and two shear keys. The objective of the first test was to examine the Caltrans as-built design details. The two shear keys, termed 1A and 1B, had

the same amount and arrangement of reinforcement. Each shear key had 24 No. 3 vertical dowel bars that continued into the stem wall. Additional shrinkage and temperature reinforcement consisting of No. 3 horizontal and vertical bars was placed near the two side faces of shear keys and the stem wall. The vertical side reinforcement also continued into the stem wall. Five No. 3 bars were placed near the top surface of the stem wall as horizontal shear reinforcement. The difference between the two shear keys is that shear key 1B was constructed together with the back wall and the wing wall, while shear key 1A was only connected to the stem wall. The design details of the specimens are shown in Figure 2.2. In the tests, the shear keys were loaded horizontally one at a time. Both sides had a diagonal shear failure in the stem wall and the maximum load resistances reached were 222 kips and 285 kips, respectively, occurring at horizontal displacements between 1.20 and 1.50 in., measured at the top of each shear key. Figure 2.2 shows the damage developed in the specimen at the end of the tests and Figure 2.3 shows the load-vs.-displacement curves.

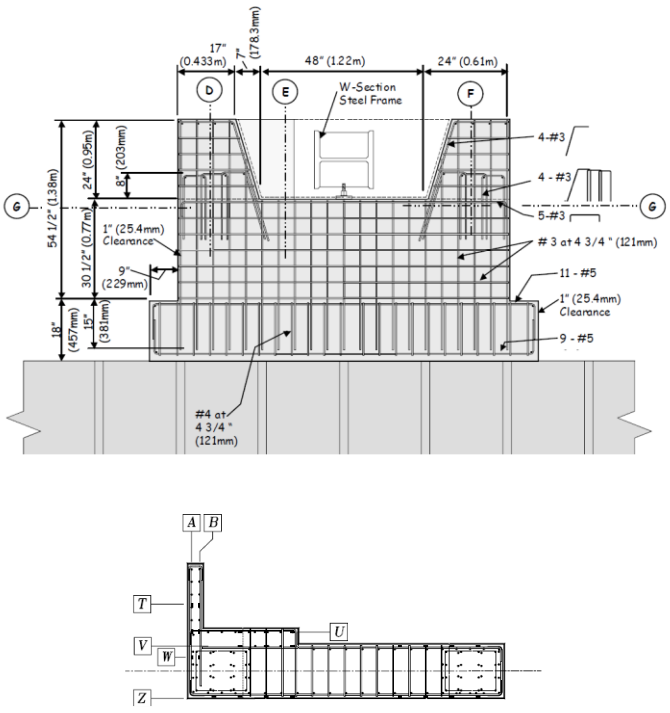

Figure 2.1 Elevation view (up) (top) and plan view (bottom) of design details for Specimen 1 (from Megally et al., 2002)

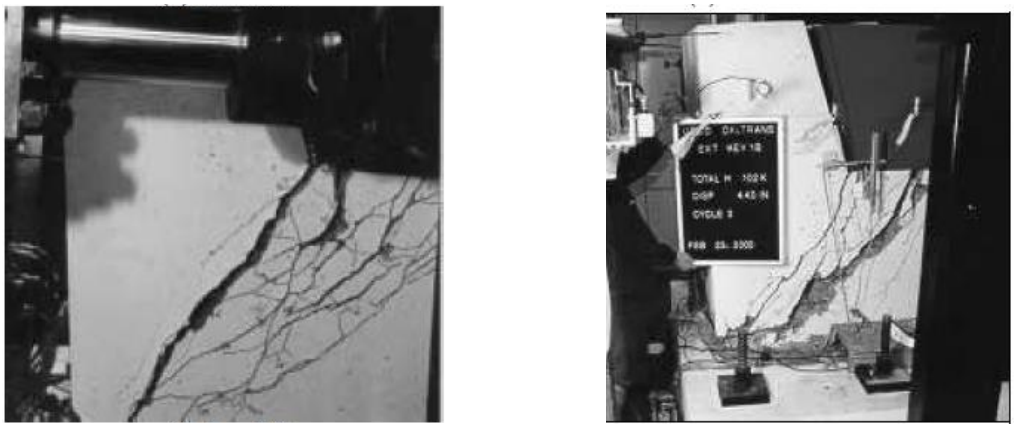

a) b)

Figure 2.2 Condition of Specimen 1 at the end of the tests: a) shear key 1A; b) shear key 1B (from Megally et al., 2002)

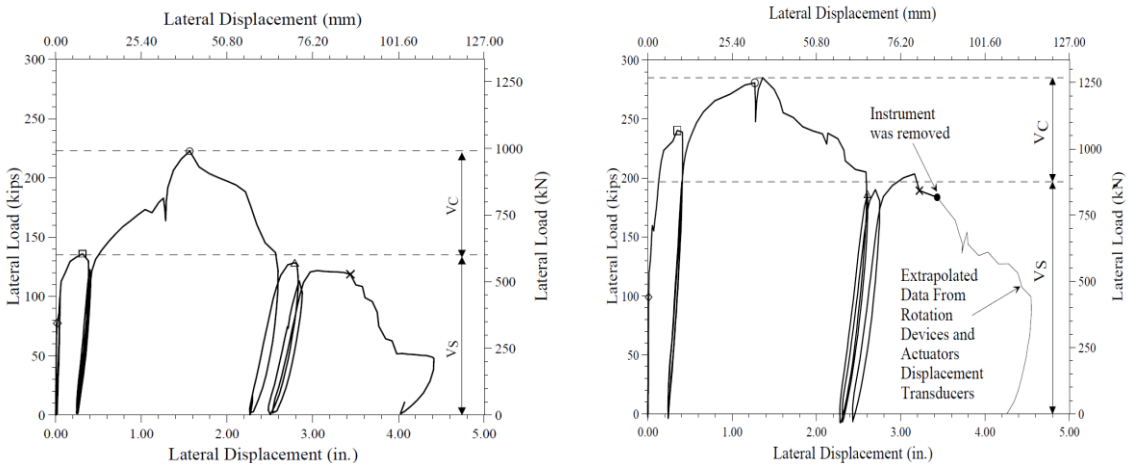

a) b)

Figure 2.3 Lateral load-vs.-lateral displacement curves for Specimen 1: a) shear key 1A; b) shear key 1B (from Megally et al., 2002)

Specimen 2 was designed to prevent diagonal shear cracks in the stem wall. The amount of the vertical and horizontal reinforcement of the stem wall and the shear keys was identical to that of Specimen 1. Shear key 2A had a construction joint with the stem wall, as compared to shear key 1A which was monolithic with the stem wall. It had the same amount of vertical dowel bars as shear key 1A. Hydraulic oil was applied as bond breaker to the construction joint, which was a smooth finished surface on top of the stem wall, to have the failure of the shear key governed by horizontal sliding. Shear key 2B was designed to have a flexural-shear behavior, which would increase the displacement capacity of the shear key. To this end, the length of the shear key was reduced to one third of that of shear key 2A, but the height was not changed. There was no back wall or wing wall. The vertical dowels consisted of 18 No. 5 bars, and No. 3 closed stirrups were used for the transverse reinforcement. The design details of Specimen 2 are shown in Figure 2.4.

Nevertheless, in spite of the construction joint, shear key 2A did not develop horizontal sliding and failure was governed by the opening of a diagonal shear crack in the stem wall, as shown in Figure 2.5. The peak resistance developed was 159 kips occurring at a displacement of 1.50 in. Shear key 2B was subjected to fully reversed displacement cycles. It also formed a diagonal crack with the stem wall. However, the crack was more localized at the base of the shear key as compared to 2A, as shown in Figure 2.5. The maximum load resistance reached was 69 kips and a displacement ductility of 8 was reached. The load-vs.-displacement curves for shear keys 2A and 2B are shown in Figure 2.6.

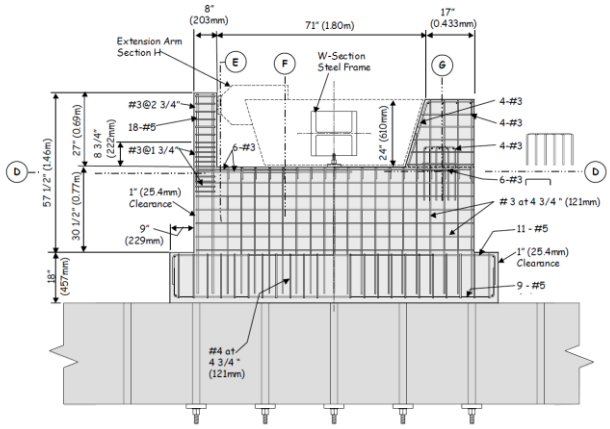

Figure 2.4 Elevation view of design details for Specimen 2 (from Megally et al., 2002)

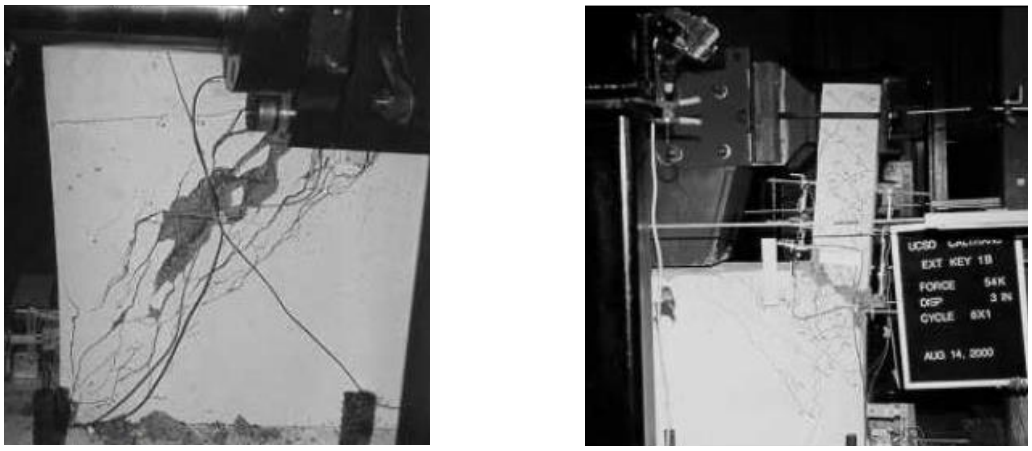

a) b)

Figure 2.5 Condition of Specimen 2 at the end of the test: a) shear key 2A; b) shear key 2B (from Megally et al., 2002)

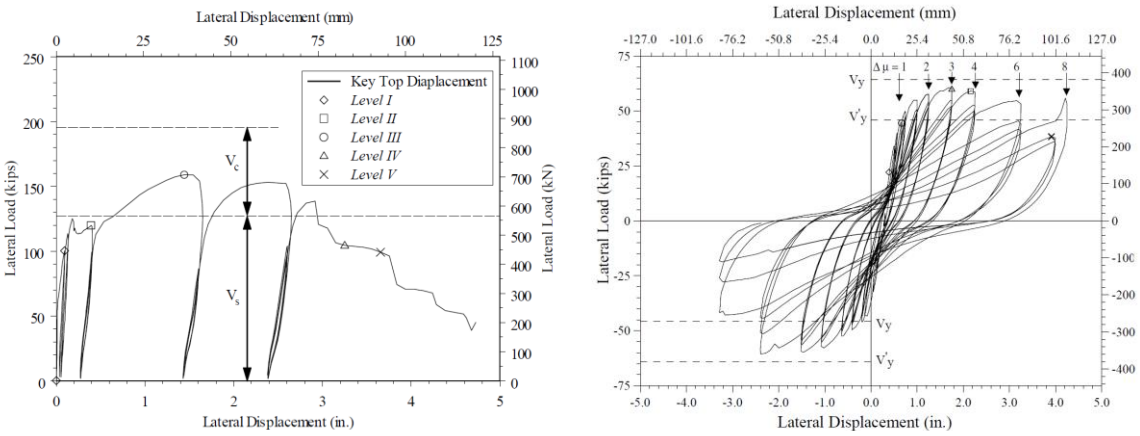

a) b)

Figure 2.6 Lateral load-vs.-lateral displacement curves for Specimen 2: a) shear key 2A; b) shear key 2B (from Megally et al., 2002)

To strengthen the stem wall and prevent diagonal cracking, Megally et al. post-tensioned the abutment wall right below the shear key in Specimen 3. Two 1 ⅜ in. high-strength bars were post-tensioned to a total force of 320 kips. Horizontal construction joints were also used for shear keys 3A and 3B. For shear key 3B, the construction joint was placed 3 in. higher than the top surface of the stem wall. The horizontal shear

reinforcement in the stem wall consisted of 8 No. 5 and 2 No. 3 bars. In each of the shear keys, the vertical dowels were 8 No. 5 headed bars. For shear key 3B, couplers were placed on the vertical No. 5 bars right below the construction joint to allow the replacement of the bars in a retrofit scenario. Also, a portion of 3B was separated from the stem wall with foam. Eight No. 5 vertical bars were placed in the stem wall below the foam to control cracking in this region. The design details are shown in Figure 2.7.

During the tests, shear keys 3A and 3B slid on the construction joint surface. Figure 2.8 shows cracking and concrete spalling occurring in the shear key and the region of the stem wall below the construction joint. No diagonal cracking was observed in the stem wall. The peak horizontal loads registered for 3A and 3B were 267 kips and 239 kips, respectively. The tests stopped at displacements of 8.50 in. and 6 in. respectively, measured at the top of the shear key, as shown in the load-vs.-displacement curves in Figure 2.9.

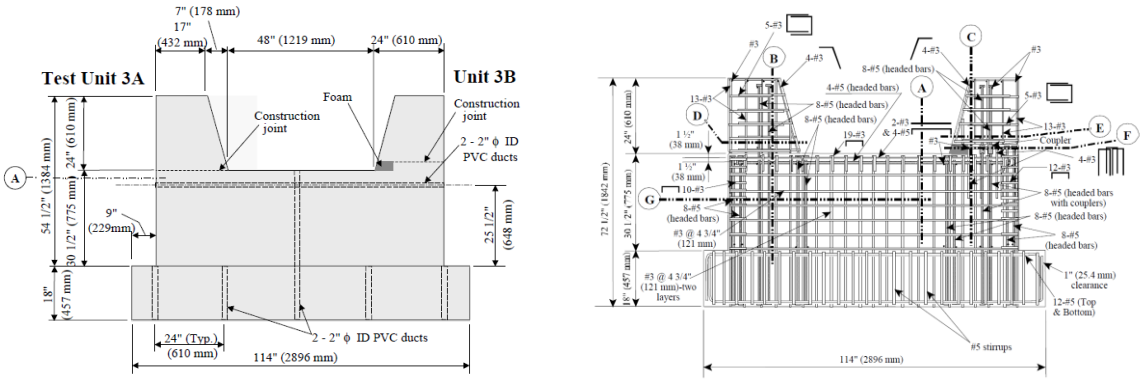

a) b)

Figure 2.7 Design of Specimen 3: a) post-tensioning and construction joint location; b) elevation view of design details (from Megally et al., 2002)

a) b)

Figure 2.8 Condition of shear keys at the end of the test: a) shear key 3A; b) shear key 3B (from Megally et al., 2002)

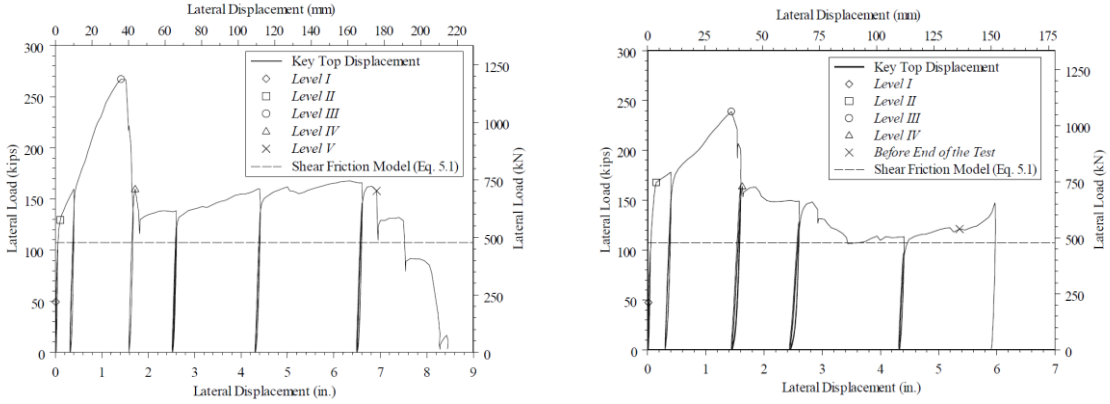

a) b)

Figure 2.9 Lateral load-vs.-lateral displacement curves for Specimen 3: a) shear key 3A; b) shear key 3B (from Megally et al., 2002)

Specimen 4, consisting of shear keys 4A and 4B, was tested by Borzogzadeh et al. (2006). Shear key 4A was designed according to Caltrans Bridge Design Specifications (Caltrans 1993) and was cast together with the stem wall, while shear key 4B was cast over a rough joint. The preparation of the construction joint was not reported. In each shear key, the vertical dowel bars consisted of 24 No. 3 bars, placed in four rows each containing 3 No. 3 U-shaped bars, as shown in Figure 2.10. Additional No. 3 vertical bars

were used for temperature and shrinkage near the side faces of the shear keys. For shear key 4A, all the vertical side bars continued from the shear key into the stem wall, while in shear key 4B they stopped at the base of the shear key. The horizontal shear reinforcement of the stem wall consisted of 8 No. 4 bars.

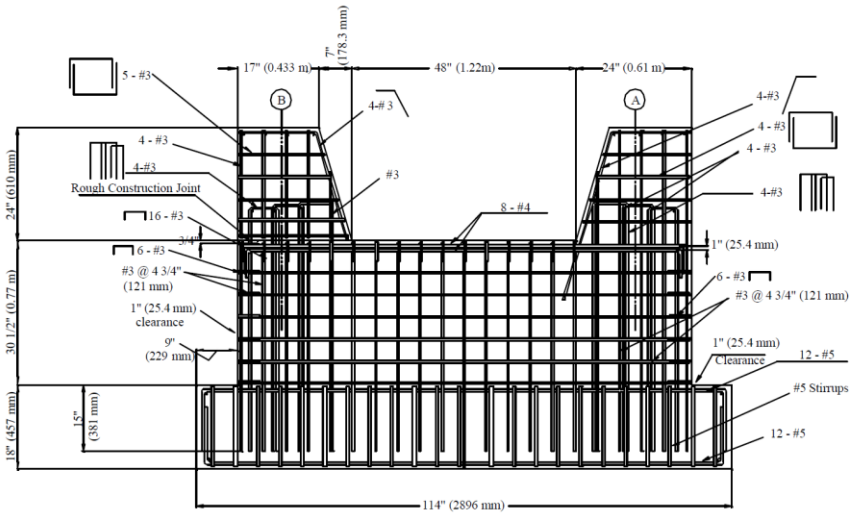

Figure 2.10 Elevation view of design details for Specimen 4
(from Borzogzadeh et al., 2006)

In spite of the construction joint used in shear key 4B, both shear keys failed in a similar manner. In each test, a diagonal shear crack started at the toe of the shear key and propagated towards the toe of the stem wall. This crack led to a diagonal shear failure of the stem wall, as shown in Figure 2.11. The diagonal shear failure was a result of insufficient horizontal shear reinforcement in the stem wall. The load resistances measured for shear keys 4A and 4B were 329 and 299 kips, respectively. The horizontal load applied to each shear key is plotted against the horizontal displacement of the shear key measured at the top of the shear key, as shown in Figure 2.12.

a) b)

Figure 2.11 Condition of shear keys at the end of the test: a) shear key 4A; b) shear key 4B (from Borzogzadeh et al., 2006)

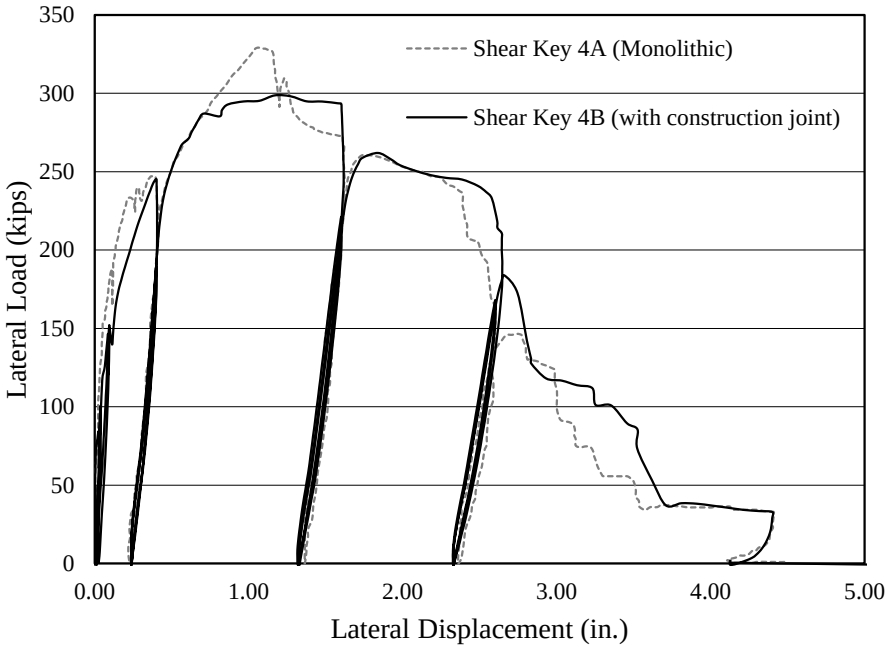

Figure 2.12 Lateral load-vs.-lateral displacement curves for shear keys 4A and 4B (from Borzogzadeh et al., 2006)

Specimen 5 was designed with a goal that a behavior similar to that of Specimen 3 would be achieved without applying a prestressing force to the stem wall. The stem

wall was strengthened with additional horizontal shear reinforcement. In total, 14 No. 4 horizontal bars were placed in two rows near the top of the stem wall, as shown in Figure 2.13. The two shear keys, 5A and 5B, were each isolated from the stem wall with a construction joint.

Shear key 5A was constructed with a rough construction joint. First, the stem wall was cast, and a thick layer of foam was used to separate the shear key from the stem wall so that the construction joint between the two was reduced to an 8 in. x 8 in. area at the center. This construction joint had a rough surface, but the preparation of the surface was not described in detail. Four No. 4 vertical dowel bars were placed in the joint region. The bars were placed in a single row as shown in Figure 2.13. The vertical reinforcement for shrinkage and temperature in the shear key consisted of No. 3 bars. This reinforcement stopped at the base of the shear key and did not continue into the stem wall.

For shear key 5B, the construction joint had a smooth finish. Hydraulic oil was applied to the joint to eliminate the cohesive force. Four No. 4 bars were used as dowel bars. As in shear key 5A, the side reinforcement for shrinkage and temperature did not continue from the shear key into the stem wall.

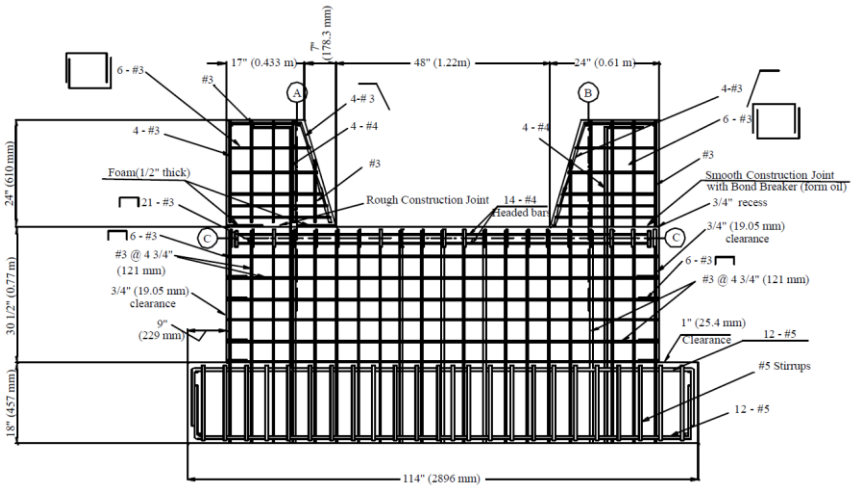

Figure 2.13 Elevation view of design details for Specimen 5 (from Borzogzadeh et al., 2006)

The two shear keys had a sliding shear failure. Prior to sliding, shear key 5A also developed a cohesive force due to the roughness of the construction joint and the absence of bond breaker. Shear key 5A developed a maximum load capacity of 163 kips. After that, a significant load drop was observed and the shear key started to slide. Shear key 5B started to slide on the construction joint from the beginning of the test. During sliding, the vertical dowel bars were bent. After the maximum load resistance of 75 kips was reached, some of the vertical bars fractured, leading to a significant drop of the load resistance. The force-vs.-displacement curves are shown in Figure 2.15. After the end of the test, a dowel bar was extracted from shear key 5B. The bar was severely bent, and the angle of kink was measured to be 37 degrees. This bar is shown in Figure 2.16.

Figure 2.14 Displaced positions of shear key 5A (left) and 5B (right) at the end of the tests (from Borzogzadeh et al., 2006)

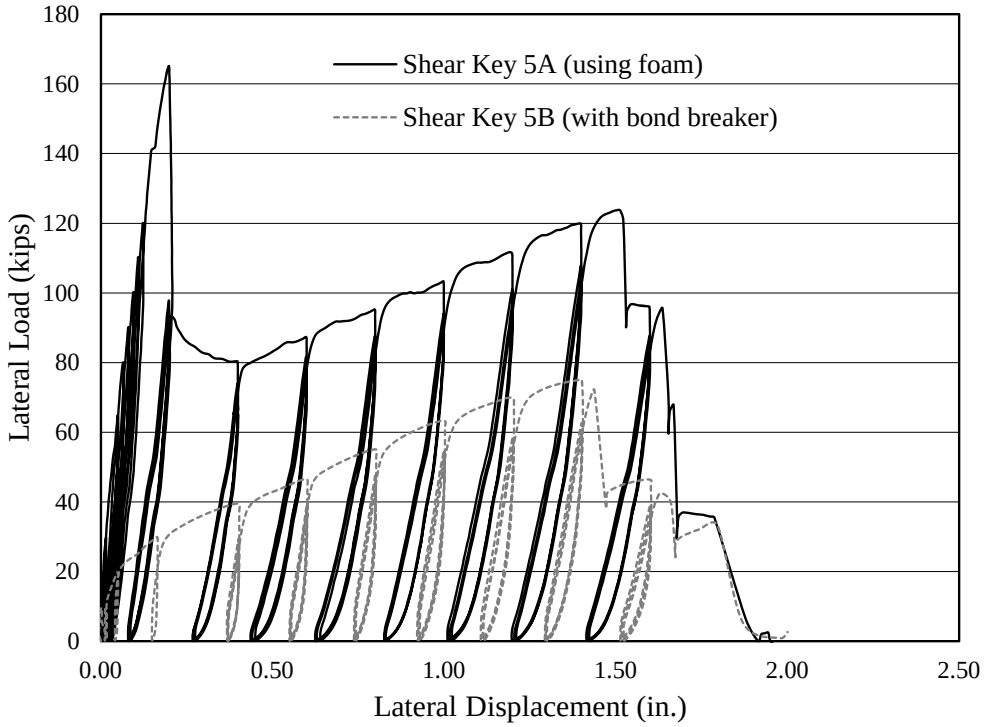

Figure 2.15 Lateral load-vs.-lateral displacement curve for shear keys 5A and 5B (from Borzogzadeh et al., 2006)

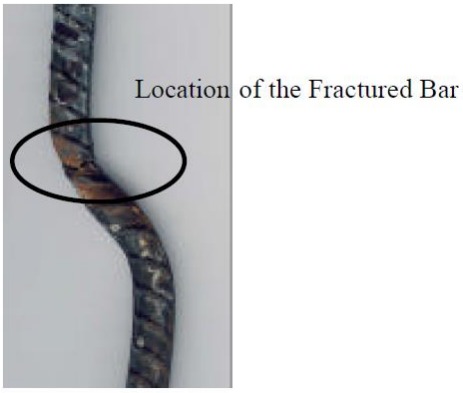

Figure 2.16 Dowel bar removed from shear key 5B (from Borzogzadeh et al., 2006)

Specimen 6 was tested by Bauer (2006). It consisted of two monolithic shear keys, 6A and 6B. The vertical dowel bars consisted of three rows of two U-shaped No. 3 bars, as shown in Figure 2.17. The horizontal shear reinforcement of the stem wall was significantly increased as compared to the previous shear keys. Shear key 6A had 4 No. 7 horizontal bars, while in shear key 6B four additional No. 7 bars were placed in a second row. The shrinkage and temperature reinforcement, consisting of No. 3 bars, stopped at the base of the shear key and did not continue into the stem wall.

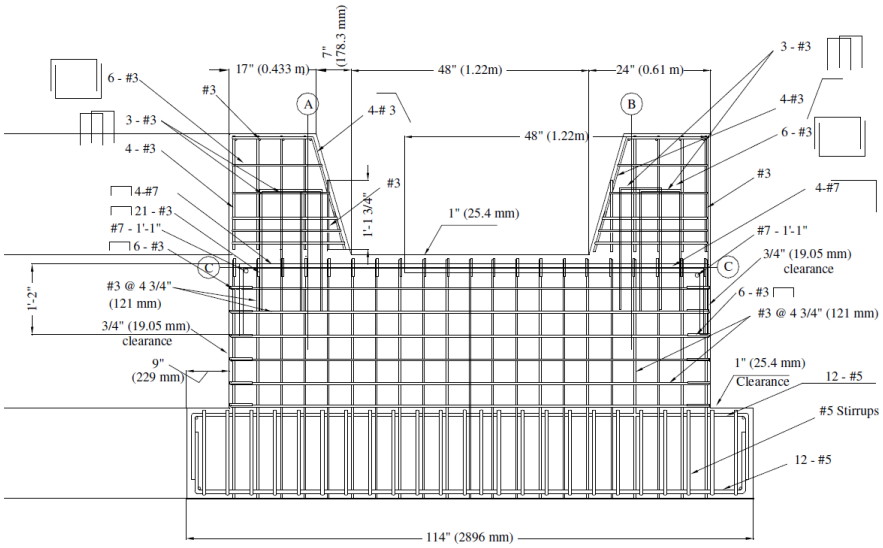

Figure 2.17 Elevation view of design details for Specimen 6 (from Bauer, 2006)

Shear key 6A failed with a diagonal crack forming in the stem wall, as shown in Figure 2.18. The maximum load resistance measured was 294 kips. Apart from the main diagonal crack, which started at the toe of the shear key and propagated to the toe of the stem wall, there were additional diagonal cracks which developed in the stem wall about 24 in. away from the shear key. This resulted in a premature bond-slip failure in the horizontal shear reinforcement when shear key 6B was tested, as the additional 4 No. 7 horizontal bars did not have sufficient development length. Shear key 6B reached a maximum resistance of about 209 kips. The conditions of the shear keys at the end of the tests are shown in Figure 2.18. A summary of all the aforementioned shear key tests and test observations is presented in Table 2.1.

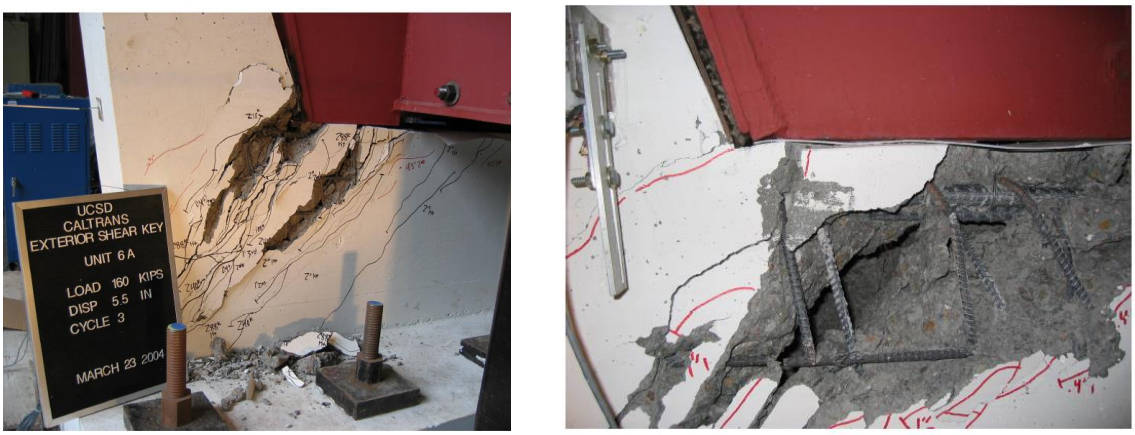

a) b)

Figure 2.18 Condition of shear keys at the end of the test: a) shear key 6A and; b) shear key 6B (from Bauer, 2006)

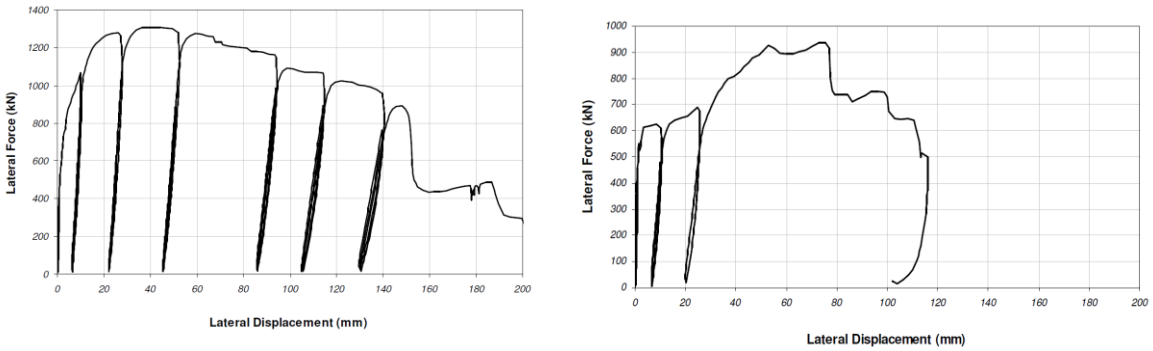

a) b)

Figure 2.19 Lateral force-vs.-lateral displacement curves for Specimen 6: a) shear key 6A; b) shear key 6B (from Bauer, 2006)

Table 2.1 Summary of past experimental test

Shear Key	Type of Shear Key	Construction joint preparation	Load capacity (kips)	Failure Mode
1A	Monolithic	-	222	Diagonal Shear
1B	Monolithic with back wall and wing wall	-	285	Diagonal Shear
2A	Isolated	Smooth with bond breaker	158	Diagonal Shear
2B	Monolithic (flexural-shear)	-	69	Flexural Shear
3A	Isolated	Smooth with bond breaker	267	Sliding Shear
3B	Isolated	Smooth with bond breaker	239	Sliding Shear
4A	Monolithic	-	329	Diagonal Shear
4B	Isolated	Rough	299	Diagonal Shear
5A	Partially Isolated	Smooth with foam**	165	Sliding Shear
5B	Isolated	Smooth with bond breaker	76	Sliding Shear
6A	Monolithic	-	294	Diagonal Shear
6B	Monolithic	-	209	Bond-Slip Failure

* The stem wall was post-tensioned horizontally to 320 kips
** An 8 x 8 in. rough construction between the shear key with the stem wall

2.3 Analytical Studies for Shear Key Resistance Calculation

Megally et al. (2002) have proposed an analytical method to calculate the diagonal shear strength of the stem wall. This method assumes that the total shear strength of the stem wall, V_n, consists of the resistance contributed by the concrete, V_c, and that by the steel, V_s:

$$V_n = V_c + V_s \tag{2.1}$$

To evaluate V_c, a formula similar to that provided in ACI 318-08 for the shear strength of concrete has been proposed:

$$V_c = 2.4 \cdot \sqrt{f_c'} \cdot b \cdot h \tag{2.2}$$

in which b is the width of the stem wall, h is the height of the stem wall, and f_c' is the compressive strength of the concrete. All units are in inches and kips. The steel resistance is calculated by considering the moment equilibrium of the shear key and the break-away portion of the stem wall about point *A* (see Figure 2.20):

$$V_s = \left[F_p \cdot h_p + T_1 \cdot h + T_2 \cdot d + n_h \cdot T_{1,h} \frac{h^2}{2 \cdot s} + n_v \cdot T_{i,v} \frac{d^2}{2 \cdot s} \right] \left(\frac{1}{h + a} \right) \tag{2.3}$$

In Eq. (2.3) T_1 is the total force at yielding developed by the horizontal reinforcement of the stem wall, T_2 is the yield force of the first row of steel bar crossing the shear key-stem wall interface, n_h and n_v are the numbers of layers of horizontal and vertical side reinforcement (equal to 2 for all the specimens presented in Section 2.2), which develop yield forces $T_{i,h}$ and $T_{i,v}$, respectively. Finally, $(h + a)$ is the moment arm of the horizontal load applied to the shear key and *s* is the center to center spacing of the vertical and horizontal side reinforcement. If the stem wall is prestressed, the prestressing force F_p should also be included in the equilibrium condition.

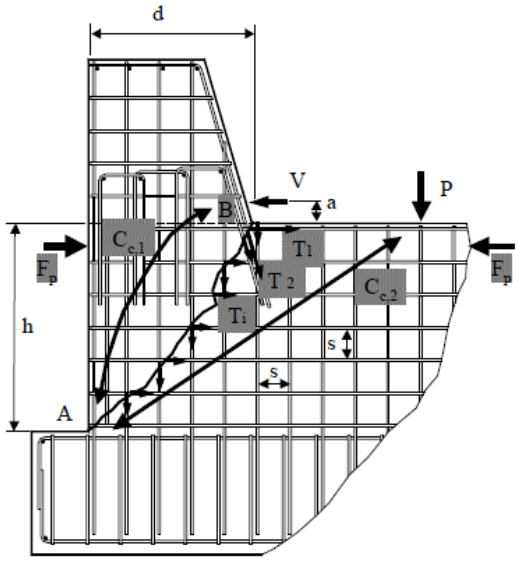

Figure 2.20 Strut-and-tie model to calculate diagonal shear strength of stem walls (from Megally et al., 2002)

A method to calculate the shear sliding resistance of isolated shear keys has been proposed by Borzogzadeh et al. (2006). In their study, it was observed that the vertical dowel bars developed significant tensile forces as the shear keys slid, bending the vertical bars, which finally assumed an inclined position before fracture. They observed that the bars developed an angle of kink of 37 degrees, as shown in Figure 2.16, before fracture. Based on this observation, they have suggested the following equation to calculate the shear resistance:

$$V_n = \frac{\mu_f \cdot \cos\alpha + \sin\alpha}{1 - \mu_f \cdot \tan\beta} \mathrm{A}_{vf} \cdot f_{su} \tag{2.4}$$

in which, μ_f is the friction coefficient of the joint surface, α is the angle of kink of the deformed vertical bars, which is taken to be equal to 37 degrees, β is the angle of the inclined face of the shear key with respect to a vertical plane, A_{vf} is the total area of the

vertical dowel bars crossing the joint and f_{su} the tensile strength. The above parameters are shown in Figure 2.21.

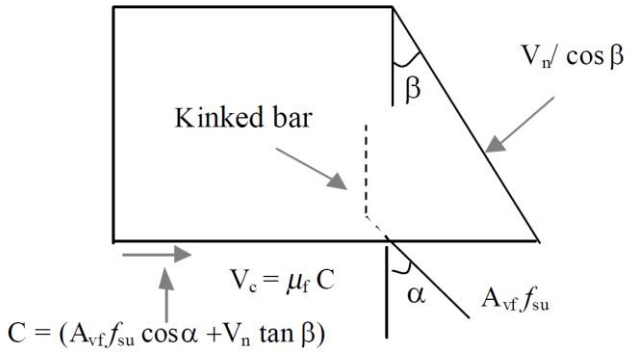

Figure 2.21 Shear sliding resistance mechanism in isolated shear keys proposed by Borzogzadeh et al. (2006)

2.4 Current Caltrans Design Approach

In the Caltrans Seismic Design Criteria, the following formula is provided to determine the target design capacity of shear keys in abutments on piles:

$$F_{sk} = a_{cl} \cdot \left(0.75 \cdot V_{piles} + V_{ww}\right) \tag{2.5}$$

in which V_{piles} is the lateral capacity of the abutment pile group, V_{ww} is the shear capacity of one wing wall, and a_{cl} is a parameter with a value between 0.5 and 1.0. The above equation is to have shear keys function as structure fuse and to protect the piles from damage in the event of a strong earthquake. For an abutment supported on a spread footing, the target capacity of a shear key is determined as follows:

$$F_{sk} = a_{cl} \cdot P_{dl} \tag{2.6}$$

in which P_{dl} is the superstructure dead load reaction at the abutment plus the weight of the abutment and its footing. Finally, in the case of abutments supported on a large number of piles, P_{dl} in Eq. (2.6) is replaced by P_{dl}^{sup}, which is only the superstructure dead load.

Two types of shear keys are considered in the specifications; isolated and non-isolated shear keys, as shown in Figure 2.22 and Figure 2.23, respectively. Isolated shear keys are required to have a smooth and unbonded construction joint with the back wall and the stem wall. The vertical reinforcement should be located at the center of the shear key, such that the concrete surrounding the bars is sufficiently confined. The cross-sectional area of the vertical reinforcement required for an isolated shear key is calculated with the following equation, which is based on the method proposed by Borzogzadeh et al. (2006), as discussed in the previous section.

$$A_{sk} = \frac{F_{sk}}{1.8 \cdot f_{ye}} \tag{2.7}$$

For the non-isolated shear keys, the following equation is suggested to calculate the amount of vertical reinforcement:

$$A_{sk} = \frac{1}{1.4 \cdot f_{ye}} \left(F_{sk} - 0.4 \cdot A_{cv} \right) \tag{2.8}$$

in which:

$$0.4 \cdot A_{cv} < F_{sk} \leq \min \begin{pmatrix} 0.25 \cdot f'_{ce} A_{cv} \\ 1.5 \cdot A_{cv} \end{pmatrix} \tag{2.9}$$

$$A_{sk} \geq \frac{0.05 \cdot A_{cv}}{f_{ye}} \tag{2.10}$$

In Eqs. (2.9) and (2.10), A_{cv} is the area of concrete engaged in interface shear transfer, f_{ye} is the expected yield strength of the steel and f'_{ce} is the confined compressive strength of the concrete. All units are in inches and kips.

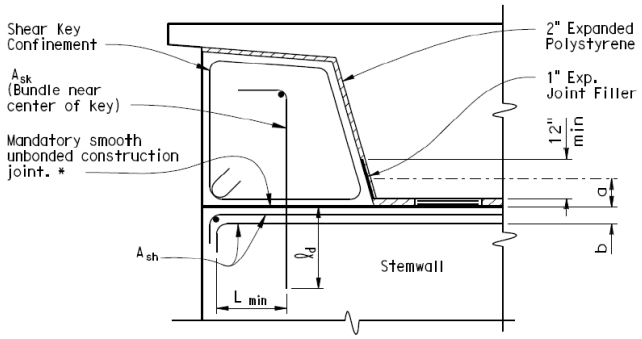

Figure 2.22 Isolated shear key design details (from Caltrans SDC, Version 1.7)

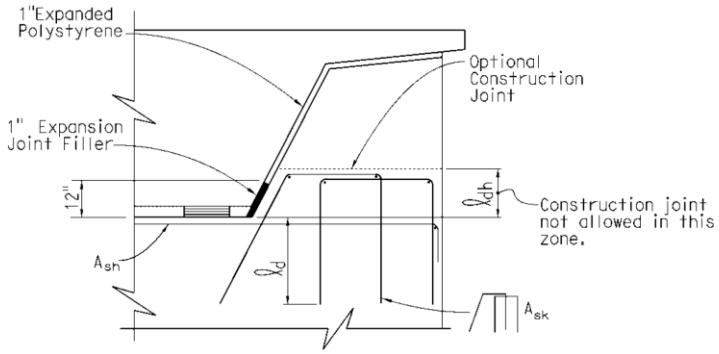

Figure 2.23 Non-isolated shear key design details (from Caltrans SDC, Version 1.7)

After determining the amount of vertical reinforcement, A_{sk}, the horizontal reinforcement area is calculated:

$$A_{sh} = 2.0 \cdot A_{sk}^{iso}$$
$$A_{sh} = \max\begin{cases} 2.0 \cdot A_{sk}^{Non-iso} \\ \dfrac{F_{sk}}{f_{ye}} \end{cases} \qquad (2.11)$$

In Eq. (2.11), A_{sk}^{iso} denotes the area of the vertical reinforcement in the isolated shear key, while $A_{sk}^{Non-iso}$ is that for the non-isolated shear key.

2.5 Summary of Past Studies

This chapter summarizes the tests of ten shear keys in past research studies. The results have shown that shear keys cast monolithic with the stem walls are prone to failing with a diagonal crack occurring in the stem wall. However, it has been shown that the diagonal shear failure of the stem wall can be avoided and failure can be governed by horizontal shear sliding of the shear key, by introducing a construction joint between the shear key and the stem wall and an appropriate amount of shear reinforcement in the stem wall. It is desired that the construction joint has a smooth surface and bond breaker applied to assure the sliding failure mode.

Analytical methods have been proposed to calculate the resistance of isolated and monolithic shear keys.

2.6 Acknowledgement of Publication

Part of this chapter is a reprint of the material that will appear in a technical report which will be submitted to the California Department of Transportation in 2016, Kottari, A., P. B. Shing, J. I. Restrepo, under the title "Design and Capacity Assessment of External Shear Keys in Bridge Abutments". The dissertation author will be the primary investigator and author of this report.

CHAPTER 3

SHEAR TRANSFER IN REINFORCED CONCRETE

3.1 Shear Transfer Mechanisms

The main mechanisms transferring shear across a crack in concrete are the dowel action of the reinforcing bars crossing the crack, the friction, the aggregate interlock mechanism, and the tangential component of the axial force developed by the reinforcing bars inclined with respect to the crack plane.

The frictional resistance across a crack depends on the normal compressive stress developed in the crack interface. The aggregate interlock mechanism is developed by the contact of the aggregates protruding from the opposite sides of a crack with each other. The tangential component of the axial force developed in the reinforcing bars inclined with respect to the crack plane may also contribute to the shear resistance across the crack, depending on the axial stress level and the inclination of the bar with respect to the crack plane.

In this section, we focus on the dowel action of steel reinforcing bars. The shear resistance provided by a bar as it reacts against the surrounding concrete is termed the dowel action. It involves the deformation of the bar in flexure and the compressive deformation of the surrounding concrete. Hence, shear resistance provided by the dowel

action depends on the compressive strength of the concrete surrounding the bar, and the shear and the flexural strengths of the bar.

When a bar is subjected to shear at the crack surface, there are three possible failure mechanisms. One is the shearing failure of the bar itself and the other two are governed by the behavior of the concrete. If the concrete cover is small, a splitting failure may occur in the concrete cover when the bar pushes against the exterior concrete. If sufficient concrete cover is provided to prevent splitting cracks, then the concrete in the vicinity of the bar will crush. Based on the observed behavior of shear keys in bridge abutments, as discussed in a later chapter, the failure mode governed by the crushing of concrete is of interest in this study.

3.2 Dowel Action in Shear Transfer

3.2.1 Past Experimental Studies

In this section, past experimental work conducted to investigate the dowel action of reinforcing bars is discussed. Three types of specimens were used in these studies: push-off specimens, cyclic push specimens, and block-type specimens. The configuration and loading conditions of the different specimens can be seen in Figure 3.1 through Figure 3.3.

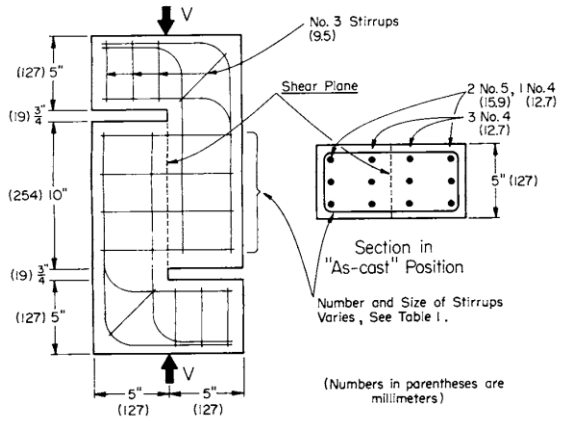

Figure 3.1 Typical push-off specimen (from Hofbeck et al., 1969)

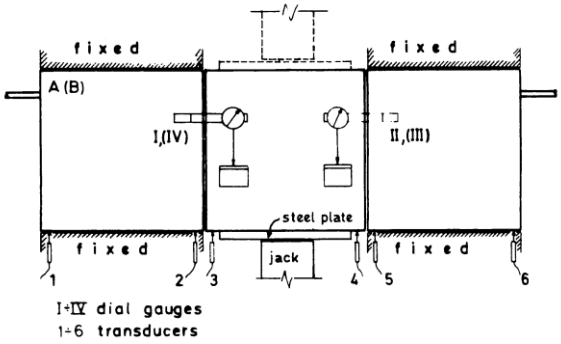

Figure 3.2 Cyclic push specimen (from Vintzeleou and Tassios, 1987)

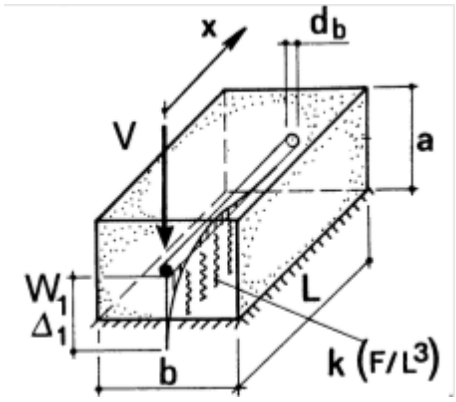

Figure 3.3 Block-type specimen (from Dei Poli et al., 1992)

Rasmussen (1963) was among the first to investigate the contribution of dowel resistance to the shear capacity of reinforced concrete members by experimental testing.

In his work, block-type specimens were used (Figure 3.3). For each specimen, reinforcing bars were embedded in a concrete block, perpendicularly protruding from the two sides. The bars were pushed on the protruding sides with the use of steel plates.

Hofbeck et al. (1969) conducted a number of tests to determine the contribution of the dowel action to the shear resistance of a rough joint after cracks had formed. The configuration for the push-off tests they conducted is shown in Figure 3.1. Slots were provided half-way through the concrete block section and close to the loaded ends to allow the development of a shear plane parallel to the loading direction. Each specimen was loaded from the two sides with a hydraulic jack in a test machine. In these tests, the specimens were first pushed to cause a shear crack. After the crack had formed, the specimens were loaded again to determine the shear resistance. With this procedure, the engendered shear plane was not smooth, and the shear strength measured also included the contribution of the aggregate interlock mechanism. By comparing the behavior of the monolithic specimens with the specimens in which a crack had been introduced, they concluded that the contribution of the dowel bars is relatively small as compared to the cohesive forces. However, the dowel resistance was not directly determined from their tests.

Dulacska (1972) conducted a number of tests to study the dowel action. The specimen configuration resembled that of the tests conducted by Hofbeck et al. and is depicted in Figure 3.4. Unlike Hofbeck et al., Dulacska divided the concrete block in two with a brass sheet between them to establish a smooth crack plane. Skewed and non-skewed stirrups connecting the two concrete blocks provided the dowel forces. Thus, the dowel resistance could be directly obtained from the measured test data. The embedded

bars were of different diameters and strengths and they were positioned in concrete with different angles. It was the first attempt made to relate the dowel strength to the inclination of bars with respect to the crack plane.

Mills (1975) also conducted three tests with bars inclined at 45 degrees to quantify the decrease in the dowel resistance induced by the skewed reinforcement.

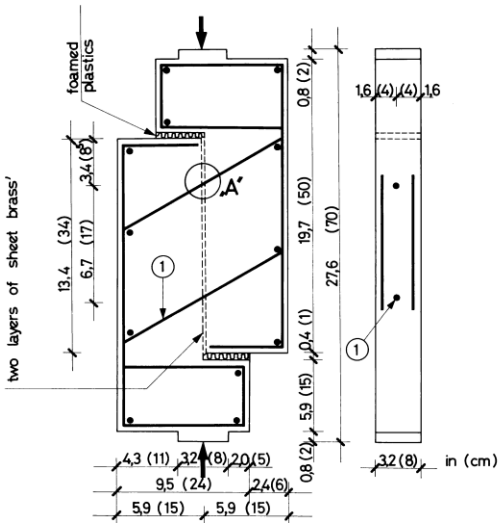

Figure 3.4 Test set-up with inclined dowel bars (from Dulacska, 1972)

Paulay et al. (1974) examined the influence of different construction joints on the shear strength. Their study included numerous types of joint construction. Surfaces were made smooth with a trowel, roughened by washing off the cement to expose the aggregate particles or by a chisel and a hammer, or were keyed. They applied melted wax to the joints to eliminate any bond between the concrete blocks so that the dowel strength of bars could be isolated.

Bennett and Banerjee (1976) examined the dowel resistance in an effort to determine the shear strength of beam-column joints. To achieve that, they used the same method as Dulacska, i.e., using brass sheets to isolate the dowel action. They also

examined the influence of transverse reinforcement and different types of interface conditions in the dowel resistance.

Millard and Johnson (1984) conducted a number of tests to examine the resistance provided by dowel bars and the aggregate interlock. A cyclic push test set-up was used. Each specimen was cast in two stages. The first half was cast against a flat plate, which was later removed. The exposed face of the specimen was covered with thin polythene sheeting. The second half of the specimen was then cast against this sheeting. Unlike what is shown in Figure 3.2, the specimen had one sliding interface.

In their tests, Vintzeleou and Tassios (1987) varied the thickness of the cover concrete in order to obtain the concrete splitting and the crushing failure modes induced by the dowel action. It was found that when the concrete cover was larger than six to eight times the bar diameter, the crushing failure mode governed the dowel behavior. In their study, the dowel bars were subjected to cyclic loading.

Dei Poli et al. (1992) carried out a series of tests with single dowel bars protruding from a block of concrete as shown in Figure 3.3. They examined the stiffness and the deterioration of concrete underneath the bar. The tests consisted of normal-strength as well as high-strength concrete.

Tanaka and Murakoshi (2011), using the same testing setup as Dei Poli et al. (1992), performed a series of 24 tests with concrete blocks containing dowel bars.

Results of the above experiments on dowel resistance are summarized in Table 3.1 and Table 3.2. It should be noted that the eccentricity of the applied shear (distance of the shear force from the crack/concrete surface) in these tests was insignificant and can be ignored.

Table 3.1 Summary of material properties, bar sizes and results for various tests

Study	d_b (in.)	f_c' (ksi)	f_y (ksi)	Inclination Angle (degrees)	Dowel Force, F (kips)
Paulay et al. (1974)	0.25	3.60	46.00	0	1.24
	0.375	3.60	46.00	0	2.50
	0.50	3.60	46.00	0	4.20
Dei Poli et al. (1992)	0.94	10.44	64.00	0	26.50
	0.71	10.44	64.00	0	16.90
	0.55	10.44	64.00	0	11.20
	0.94	4.68	64.00	0	17.98
	0.71	4.47	64.00	0	10.12
	0.55	4.80	64.00	0	6.07
	0.55	4.35	64.00	45	3.82
	0.71	4.35	64.00	45	7.00
	0.94	4.35	64.00	45	11.07
Benett and Banerjee (1976)	0.25	5.29	59.45	0	1.52
	0.625	5.29	59.45	0	8.80
	0.50	5.29	59.45	0	5.35
	0.75	5.29	59.45	0	12.10
Millard and Johnson (1984)	0.47	4.36	67.00	0	5.09
	0.47	4.47	67.00	0	4.62
	0.47	6.26	67.00	0	5.36
	0.63	3.20	67.00	0	7.28
	0.31	3.74	67.00	0	0.98
	0.47*	4.32	67.00	0	4.27
	0.47*	4.51	67.00	0	3.40

*The bars were subjected to axial tensile loads as well.

Table 3.2 Summary of material properties, bar sizes and results for various tests (continued from Table 3.1**)**

Study	d_b (in.)	f_c' (ksi)	f_y (ksi)	Inclination Angle (degrees)	Dowel Force, F (kips)
Dulacska (1972)	0.39	3.63	41.89	10	2.33
	0.24	3.41	35.07	20	0.92
	0.39	1.14	41.89	20	1.41
	0.39	3.63	41.89	20	2.33
	0.55	3.41	36.49	20	3.83
	0.39	2.73	41.89	30	1.71
	0.39	2.73	41.89	40	1.63
Mills (1975)	1.50	5.22	30.45	45	17.08
Vintzeleou and Tassios (1987)	0.31	3.55	60.90	0	4.74
	0.55	4.61	60.90	0	7.10
	0.55	6.24	60.90	0	3.82
	0.55	6.53	60.90	0	7.91
	0.55	6.86	60.90	0	7.94
	0.71	7.25	60.90	0	9.55
Tanaka and Murakoshi (2011)	0.75	3.55	49.59	0	7.42
	0.38	4.90	51.48	0	2.14
	0.50	4.52	49.01	0	3.62
	0.63	4.76	50.03	0	6.92
	0.75	4.83	49.59	0	9.17
	0.75	4.83	54.23	0	9.24
	0.75	4.83	64.53	0	9.71
	0.75	6.64	49.59	0	10.43
	0.38	8.58	51.48	0	2.81
	0.50	8.58	49.01	0	4.79
	0.63	8.58	50.03	0	7.64
	0.75	8.57	49.59	0	11.04

3.2.2 Existing Analytical Models for Dowel Resistance

Various analytical models have been presented in the literature to predict the dowel resistance. Paulay et al. (1974) have suggested that the dowel action depends on three mechanisms. The first is the bending of the bar with the formation of plastic hinges.

The second is the kinking of the bars: when a crack has a large relative tangential displacement, the bar crossing the crack is axially stretched and the tangential component of the axial force contributes to the shear resistance. The third mechanism is the shear strength of the bar.

However, it has been shown by Mills (1975) that the concrete between the bars can undergo severe deterioration. Thus, for the cases he examined, the shear capacity of the bars could not be fully developed and it was the bending of the bar that dominated the dowel action behavior.

Many formulations have been proposed for the calculation of the dowel strength due to bar bending and the compressive resistance of the surrounding concrete. Among the most common are the models of Rasmussen (1963), Dulacska (1972), Vintzeleou and Tassios (1987) and Pruijsser (1988), which are summarized below.

Rasmussen (1963), assuming that plastic hinges in the bar form at the same time as the concrete below the bar crushes, has suggested that:

$$\begin{aligned} F_d &= B \cdot d_b^2 \sqrt{f_c' \cdot f_y} \\ B &= C_r \cdot \left(\sqrt{1 + \left(\varepsilon \cdot C_r \right)^2} - \varepsilon \cdot C_r \right) \\ \varepsilon &= 3 \cdot \frac{e}{d_b} \cdot \sqrt{\frac{f_c'}{f_y}} \end{aligned} \tag{3.1}$$

in which F_d is the dowel strength (in N), f_c' is the concrete cylinder compressive strength (in MPa), f_y is the bar yield strength, C_r is a constant taken to be 1.30, e is the eccentricity of the dowel force (as shown in Figure 3.6) and d_b is the bar diameter.

Dulacska (1972) has proposed the following equation:

$$F_d = \rho \cdot d_b^2 \cdot \gamma \cdot f_y \cdot n \cdot \cos\varphi \left[\sqrt{1 + \frac{f_{ck}}{3 \cdot \rho \cdot \gamma^2 \cdot f_y \cdot n \cdot \cos^2 \varphi}} - 1 \right] \tag{3.2}$$

in which φ is the complementary angle of that between the bars and the crack plane, f_{ck} is the concrete cube compressive strength (in MPa), γ is a constant taken to be 0.05, n is a coefficient accounting for the local confinement on concrete in the vicinity of the bar and is taken to be 4.0, and $\rho = 1 - N^2 / N_y^2$, where N is the tension force in the bar and N_y is the tensile yield force of the bar. Dulacska did not consider the case of an eccentric load applied to a dowel bar.

Vintzeleou and Tassios (1987) have proposed a model similar to that of Rasmussen based on their experimental results. Assuming that the compressive bearing strength of concrete is 5 times the concrete cube strength because of the local confinement effect, they have proposed that:

$$F_d = 1.30 \cdot d_b^2 \cdot \sqrt{f_{ck} \cdot f_y \cdot \left(1 - \alpha_f{}^2\right)} \tag{3.3}$$

in which α_f is defined as $\alpha_f = \sigma_s / f_y \le 1.0$, where σ_s is the tensile stress in the bar.

For the case that the eccentricity, e, of the load is not zero, they have proposed the following equation to calculate the dowel strength:

$$F_d^2 + \left(10 \cdot f_{ck} \cdot d_b \cdot e\right) \cdot F_d - 1.7 \cdot d_b^4 \cdot f_{ck} \cdot f_y = 0 \tag{3.4}$$

Pruijsser (1988) have modified Rasmussen's model and proposed that:

$$\begin{aligned} F_d &= 1.35 \cdot d_b^2 \cdot \sqrt{f_y \cdot f_c'} \cdot \left[\sqrt{1 + 9 \cdot \varepsilon^2} - 3 \cdot \varepsilon \right] \\ \varepsilon &= \frac{e}{d_b} \cdot \sqrt{\frac{f_c'}{f_y}} \end{aligned} \tag{3.5}$$

It should be noted that the above models have different assumptions to determine the bearing strength of concrete. Dulacska (1972) and Vintzeleou and Tassios (1987) have assumed that the bearing strength of concrete is $4 f_c'$ (which is equivalent to 5 times the concrete cube strength as originally suggested by them); Rasmussen has assumed a bearing strength of $5.1 f_c'$; Pruijsser has assumed that it is $5.5 f_c'$ and Dei Poli et al. (1988) have assumed a value of $6.5 f_c'$.

Dei Poli et al. found that the plasticization of the bar starts at a distance d_b from the crack face and extends over a distance of $1.0 d_b$ to $2.0 d_b$. However, most models assume a concentrated plastic hinge. Rasmussen has reported that the value of the concentrated plastic hinge is located between $0.7 d_b$ and $1.5 d_b$, and Vintzeleou and Tassios have observed that it is between $0.6 d_b$ and $1.0 d_b$. If a dowel bar is modeled as a beam on elastic foundation (Fridberg 1938; Timoshenko 1956), as shown in Figure 3.5, Dei Poli et al. (1992) have found that the location of the section subjected to the maximum bending stresses is at $1.6 d_b$ to $1.7 d_b$ from the crack face.

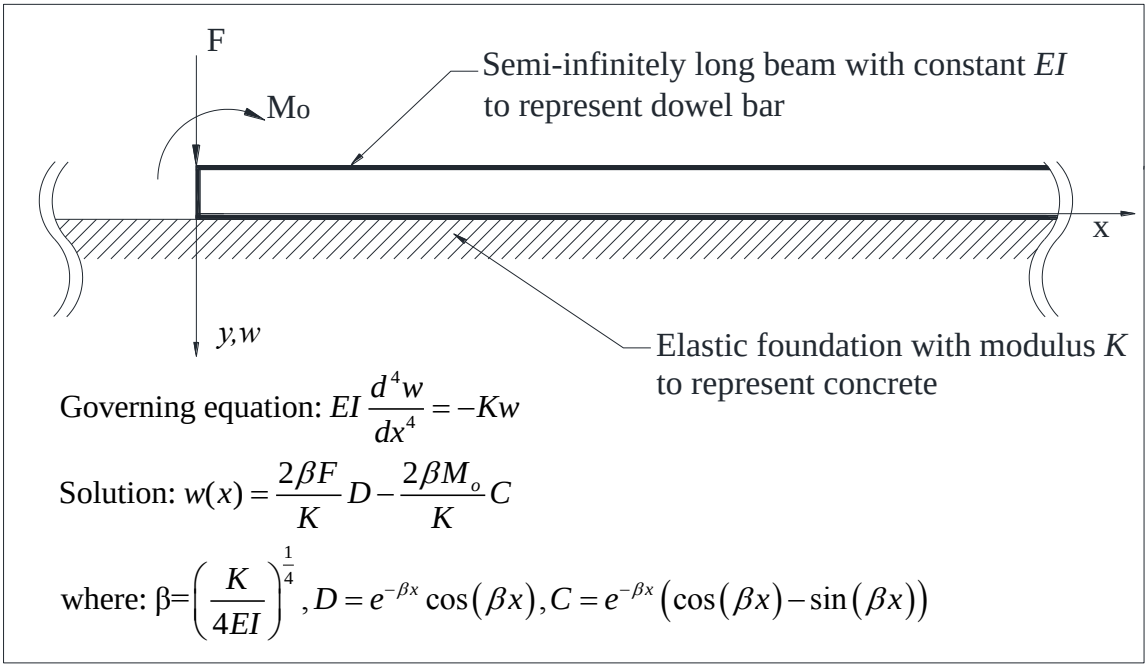

Figure 3.5 Beam on elastic foundation

The bearing stiffness of concrete has also been the focus of various researchers. Soroushian et al. (1987), based on curve fitting of their test data, have suggested that the bearing stiffness of concrete can be given as:

$$k_c = 127 \cdot c_1 \cdot \sqrt{f_c'} \cdot (1/d_b)^{\frac{2}{3}} \tag{3.6}$$

in which f_c' is the concrete compressive strength (in MPa), d_b is the bar diameter (in mm) and c_1 is a coefficient varying from 0.6 for a clear bar spacing of 1 in. to 1.0 for larger bar spacing. The bearing stiffness k_c is in MPa/mm.

Dei Poli et al. (1992) have suggested that the bearing stiffness is not constant for higher load levels, and have introduced a modification factor ω to Eq.(3.6):

$$k = \omega \cdot k_c \tag{3.7}$$

where

$$\omega = 2.12 \text{ for } F/F_d \le 0.4$$
$$\omega = \left(0.0544 + 0.026 \cdot \cosh\left(8 \cdot \left(F / F_d - 0.4\right)\right)\right)^{-4/3} \text{ for } F/F_d > 0.4$$

which gives the bearing stiffness as a function of the dowel force. Brenna et al. (1990) have proposed an alternative formulation for k :

$$k = \omega \cdot k_0 \tag{3.8}$$

in which

$$\begin{aligned} k_0 &= 600 \cdot f_c'^{0.7} / d_b \\ \omega &= \left[1.5 \cdot \left(\alpha + \sqrt{f^2 \cdot \left(40 \cdot \delta / d_b - b\right)^2 + c^2}\right)\right]^{-4/3} \\ \alpha &= 0.59 - 0.011 \cdot f_c' \\ b &= 0.0075 \cdot f_c' - 0.23 \\ c &= 0.0038 \cdot f_c' + 0.44 \\ f &= 0.0025 \cdot f_c' + 0.58 \end{aligned} \tag{3.9}$$

which gives the dowel stiffness as a function of the dowel displacement δ . The formula by Brenna et al. (1990) or that by Dei Poli et al. (1992) can be used to calculate the dowel force F as a function of the displacement δ by using the beam-on-elastic foundation model shown in Figure 3.5. With this model, it can be taken that $\delta = w(0)$. With the moment M_o equal to zero, we have:

$$\delta = w(0) = \frac{2 \cdot \beta \cdot F}{K} \tag{3.10}$$

which gives:

$$F = 2 \cdot \beta^3 \cdot E \cdot I \cdot \delta \tag{3.11}$$

in which $\beta = \sqrt[4]{K/\left(4 \cdot E \cdot I\right)}$, E is the Young's modulus of steel, and I is the moment of inertia of the bar. The stiffness of the foundation K is related to the bearing stiffness as

$K = kd_b$. By introducing the expression for *k* of Eq. (3.7) or Eq. (3.8) into Eq. (3.11), we obtain a nonlinear equation which can be solved to find F for a given δ.

3.3 Proposed Analytical Model for Dowel Resistance

3.3.1 Analytical Model Derivation

The models by Rasmussen, Vintzeleou and Tassios, and Pruijsser for the prediction of the dowel resistance of a bar due to bending have been derived in a similar manner, by assuming that the plastic hinge on the dowel bar is formed at the same time when the concrete underneath the bar has reached its peak strength. However, they do not consider the case of inclined reinforcement, i.e. reinforcement crossing the crack plane with an angle other than 90 degrees, with the exception of Dulacska's formulation.

Dulacska's model has been extensively used in different studies. It predicts well the resistance of dowels with different material properties. However, the physical basis of Eq. (3.2) is not explained in detail (Dulacska, 1972). The assumptions over which it is based are not presented. Hence, it is difficult to modify the formula to account for other factors, such as the eccentricity of the applied shear force.

As the bar is pushed against the concrete, the concrete deforms and eventually crushes. The bearing strength of the concrete adjacent to the bar is difficult to estimate because it is difficult to quantify the local confinement effect and there may be other factors affecting the bearing strength. The experimental study of Soroushian et al. (1987) has concluded that the bearing strength of the concrete is proportional to its uniaxial compressive strength and the confinement level, and is inversely proportional to the bar

diameter. However, the results they obtained are scattered as compared to those of other researchers. The reason is probably that the specimens considered in their experiments failed with splitting cracks and the necessary cover was not provided to allow for higher bearing stresses to develop.

A new analytical model is presented herein to address the above-mentioned shortcomings of Dulacska's model and to provide a comprehensive formulation to calculate dowel resistance accounting for the material properties, the angle of skew of the dowel bars, and the increased bearing strength of the surrounding concrete due to the confinement effect.

The new model is based on the same assumption as the models of Rasmussen, Vintzeleou and Tassios, and Pruijsser in that the formation of a plastic hinge in the dowel bar coincides with the crushing of the concrete adjacent to the dowel bar.

Let us first consider the case of a dowel bar perpendicular to the shear plane. A schematic illustration of the assumptions for the model is given in Figure 3.6. As shown, the dowel force is applied with an eccentricity *e* from the crack face. It is assumed that when the plastic hinge forms and the bar reaches the plastic moment capacity M_{pl}, the bearing stress in the concrete is uniform along the effective length l_y and reaches the bearing strength f_{cb}. It is also assumed that the plastic hinge is not able to develop any shear resistance. The equilibrium of the bar segment over the effective length l_y requires that:

$$M_{pl} = M_o + \frac{f_{cb} \cdot d_b \cdot l_y^2}{2}$$
$$F_d = f_{cb} \cdot d_b \cdot l_y \qquad (3.12)$$

in which $M_o = F_d \cdot e$ and $M_{pl} = \frac{f_y \cdot d_b^3}{6}$. From Eq. (3.12), F_d can be determined as:

$$F_d = \sqrt{2 \cdot f_{cb} \cdot d_b \cdot \left(M_{pl} - M_o\right)} \tag{3.13}$$

In the case of zero eccentricity, the dowel strength is $F_d = \sqrt{2 \cdot M_{pl} \cdot d_b \cdot f_{cb}}$.

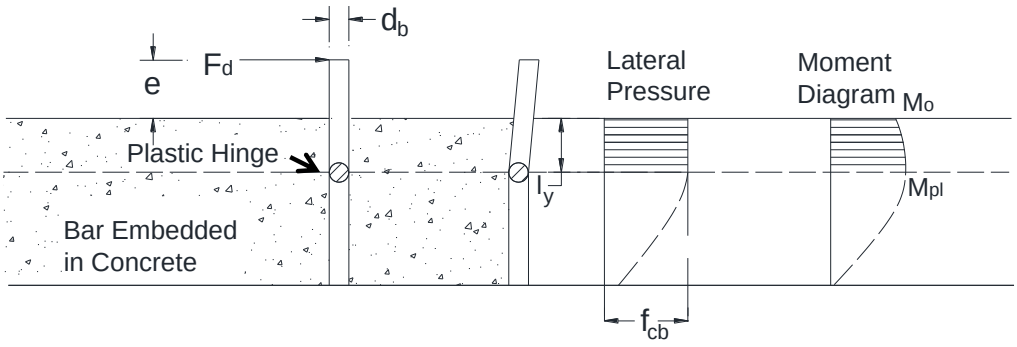

Figure 3.6 Schematic of proposed model

To calculate the dowel resistance, the value of the bearing strength, f_{cb}, is needed. Based on the test data summarized in Table 3.1 and Table 3.2, the following equation is proposed to estimate f_{cb}:

$$\begin{aligned} f_{cb} &= a \cdot f_c'^{1.2} \\ a &= 2.0 + \frac{0.5}{d_b} \end{aligned} \tag{3.14}$$

in which f_c' is in ksi and d_b in inches. This equation has been validated for commonly used bar sizes. Hence, it is recommended that $d_b \geq 0.375"$.

If the dowel bar is not perpendicular to the crack plane, there is a region in the vicinity of the bar close to the crack that is not well confined. The concrete in that region is not adequate to develop a high bearing stress, and may be damaged prematurely from the dowel action. The term “inactive zone” is used to describe this region of low

confinement, and “active zone” the region away from it that is well confined. The active and inactive zones are depicted in Figure 3.7, where the effective length l_y is exaggerated for illustration purposes. It is assumed that in the inactive zone, the concrete will not provide any resistance towards the dowel capacity. For the active zone, the bearing stresses are given by Eq. (3.14). The distance of the inactive zone is l_c, as shown in Figure 3.7, and can be calculated based on the angle of inclination of the bar with respect to the crack plane and the bar diameter as it will be explained below.

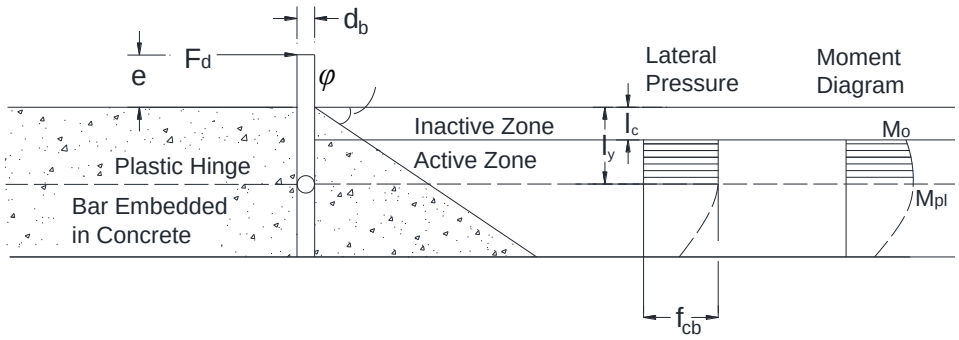

Figure 3.7 Schematic of dowel model with inclined steel bars

For this case, the equilibrium conditions for the bar segment are:

$$F_d = f_{cb} \cdot \left(l_y - l_c \right) \cdot d_b$$
$$M_{pl} = \frac{f_{cb} \cdot d_b \cdot \left({l_y}^2 - {l_c}^2 \right)}{2} + M_o \tag{3.15}$$

in which $M_o = F_d \cdot \left(e + l_c \right)$.

With the above equation and Eq. (3.14), the lengths of the inactive zones, l_c, for the tests of Dulacska (1972), Dei Poli et al. (1992), and Mills (1975) with inclined bars, as summarized in Table 3.1 and Table 3.2, have been estimated. Based on these data, the following empirical equation has been derived to estimate l_c:

$$l_c = 2.2 \cdot \sin^2 \varphi \cdot \sqrt{\left(\frac{2 \cdot M_{pl}}{f_{cb} \cdot d_b} \right)} \tag{3.16}$$

in which φ is the inclination angle and l_c is in inches. The above equation has been validated for inclination angles between 0^o and 45^o and for $d_b \geq 0.375"$.

3.3.2 Analytical Model Validation with Experimental Data

The correlation between the values of l_c obtained from the test data and those estimated with Eq. (3.16) is shown in Figure 3.8.

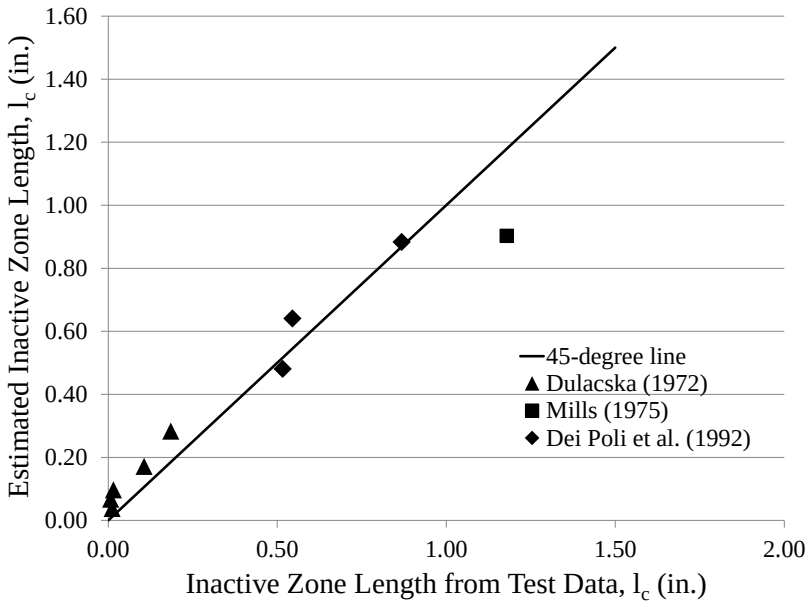

Figure 3.8 Comparison of inactive zone lengths from test data and from analytical prediction

When the dowel bars are subjected to tension, their moment capacity will be reduced. The interaction between the axial strength and the moment capacity of a bar should be accounted for in the calculation of the dowel resistance of a bar. For this

purpose, the formula proposed by Dulacska (1972) and Vintzeleou and Tassios (1987) has been adopted here:

$$\left(\frac{N}{N_y}\right)^2 + \left(\frac{F}{F_d}\right)^2 = 1.0 \tag{3.17}$$

in which N is the axial force carried by the dowel bar, N_y is the uniaxial tensile yield force of the bar, F is the dowel resistance, and F_d is the dowel strength in the absence of the axial force as predicted from Eq.(3.15). The available test data for bars subjected to shear and axial loading simultaneously are very limited, and the above approximation seems to yield satisfactory results for the limited data. In Figure 3.9, the curve given by Eq. (3.17) is plotted and compared with the data found in Millard and Johnson (1984) for a bar with $d_b = 0.47$ in. and $f_y = 67$ ksi .

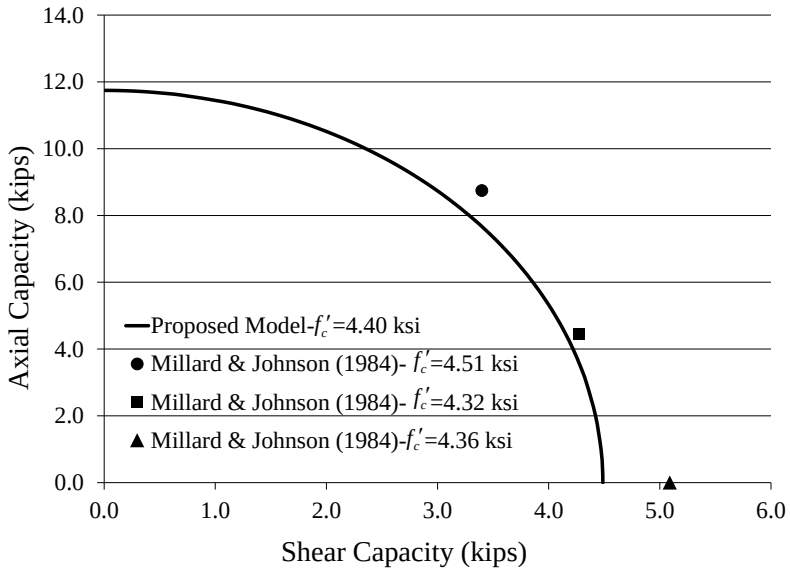

Figure 3.9 Interaction diagram for the axial force and dowel capacity of a bar

The dowel model proposed here is also validated with the test data summarized in Table 3.1 and Table 3.2. In this data set, the bar diameters vary from 0.24 in. to 1.50 in.,

the concrete strength is between 1.14 and 8.58 ksi, and the yield strength of the bars is between 30.45 and 67 ksi. The comparison of the analytical prediction with the experimental data is shown in Figure 3.10. An excellent correlation can be observed.

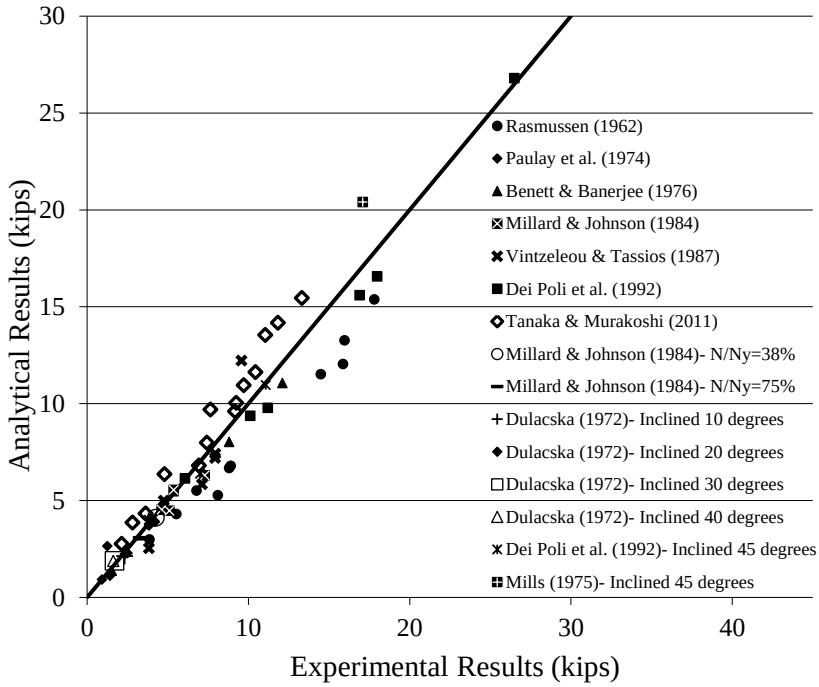

Figure 3.10 Comparison of experimental and analytical results for dowel strengths

3.4 Inclined Bar Tension due to Sliding

3.4.1 Past Experimental Observations

When sliding occurs across a shear plane, the bar crossing the plane perpendicularly will bend, as shown in Figure 3.11. When sliding is large, the bar will bend significantly and the horizontal component of the axial force developed by the bar may resist a significant shear force. The angle between the axis of the deformed and undeformed bar is defined as the angle of kink as shown in Figure 3.11, and the

magnitude of the horizontal component of the bar force can be determined from this angle and the tensile strength of the bar. An important question is, however, what this angle will be when the bar fractures.

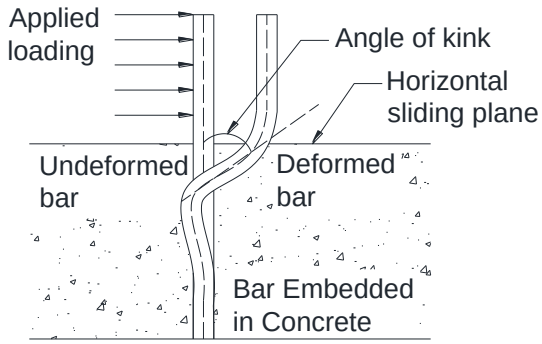

Figure 3.11 Deformed configuration of a bar due to sliding

Borzogzadeh et al. (2006) performed tests on external shear keys in bridge abutments and measured the angle of kink in one of the dowel bars removed from a test specimen after the bar had fractured. The specimen was built at 2/5-scale of a prototype bridge. The vertical reinforcement crossing the shear plane consisted of 4 No. 4 bars. In that specimen, the shear key was constructed as follows. The stem wall concrete was poured first and allowed to harden. The top face of the stem wall was smooth. On the surface that would be in contact with the shear key, several layers of bond breaker were applied to eliminate bonding with the shear key. The shear key was poured afterwards. The shear key was tested by applying a horizontal load on its inclined inner surface when the compressive strength of the concrete reached 4.45 ksi. The shear key slid and the vertical bars crossing the shear plane fractured when the sliding of the shear key was between 1.5 and 2.0 inches. After the test, one of the bars was removed from the

specimen and the angle of kink was measured to be 37^{o}. Figure 3.12 shows the bar extracted from the specimen.

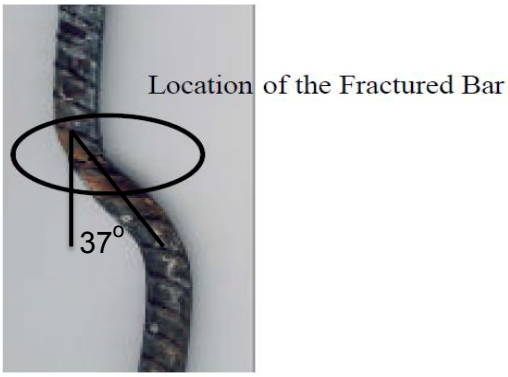

Figure 3.12 Angle of kink of a fractured bar (from Borzogzadeh et al., 2006)

From this experimental observation, they proposed an analytical model to calculate the shear resistance of an isolated shear key, assuming that the angle of kink of the dowel bar is always 37^{o}. The model has shown good correlation with experimental results obtained from other similar specimens that had different amounts of dowel bars. However, no data is available to confirm that the angle of kink is independent of the concrete properties and the bar size.

3.4.2 Description of Model to Study Large Deformation of Dowel Bars

To understand the behavior of dowel bars crossing shear planes subjected to severe sliding and examine the sensitivity of the angle of kink reached by the bar before rupture to the material properties and bar size, a numerical model is developed using the software OpenSees (McKenna et al., 2000). A 2-D model is used to represent the dowel behavior. The model consists of displacement-based, fiber-section beam elements to

simulate the linear and nonlinear behavior of a dowel bar and spring elements to represent the resistance developed by the concrete surrounding the bar. The spring elements are placed on both sides of the beam elements. A schematic of the model is presented in Figure 3.13. A crack plane divides the assembly into two parts. The nodes of the spring elements away from the bar in the lower half of the assembly are uniformly displaced to simulate the loading condition of a dowel test like that shown in Figure 3.1, while those in the upper half of the assembly are fixed.

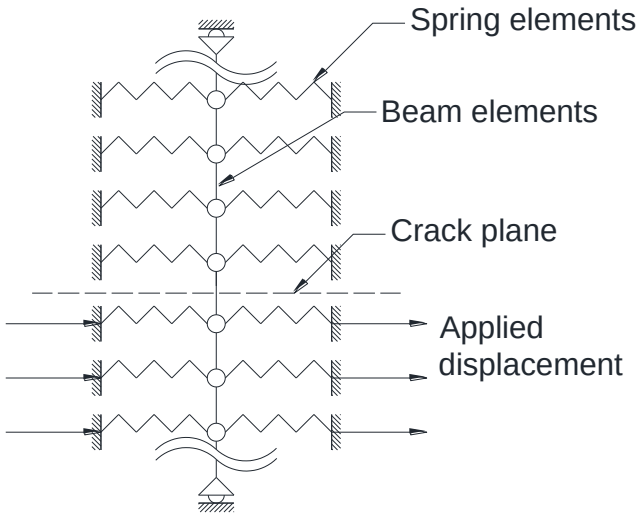

Figure 3.13 Schematic representation of OpenSees model

Steel is modeled with an elastic-perfectly plastic material law. Geometric nonlinearity is considered for the beam elements by using the co-rotational formulation. For the spring elements representing concrete, the nonlinear compressive stress-displacement law proposed by Brenna et al. (1990) for dowel action, as described in Eq. (3.8), is used, and the tensile resistance is assumed to be zero. The stress obtained from Eq. (3.8) is assumed to act on a rectangular area, which represents the projection of the contact surface between the bar and the concrete, defined by the bar diameter and the

length of contact of the bar. For each spring element, the force at each displacement increment is obtained by multiplying the stress by the tributary area of each spring. A schematic representation of the material law is shown in Figure 3.14.

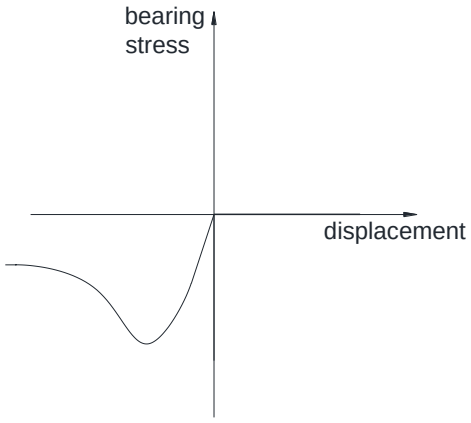

Figure 3.14 Concrete behavior considered in the analysis

The model proposed here is first validated with experimental results from Paulay et al. (1974) and Dei Poli et al. (1992), and a parametric study is subsequently performed to investigate the influence of the material parameters and bar size on the angle of kink.

3.4.3 Validation of Model with Experimental Data

The ability of the model to predict the dowel force associated with the bending deformation of a bar at different deformation levels is evaluated by the test data of Paulay et al. (1974) and Dei Poli et al. (1992). The comparison of the analytical and experimental force-vs.-displacement curves in small displacements is shown in Figure 3.15 and Figure 3.16. Figure 3.17 shows a further validation of the ability of the model to predict dowel resistance using the test data summarized in Table 3.1 and Table 3.2. The

tests were performed with small dowel deformations, for which the geometric nonlinearity is not significant.

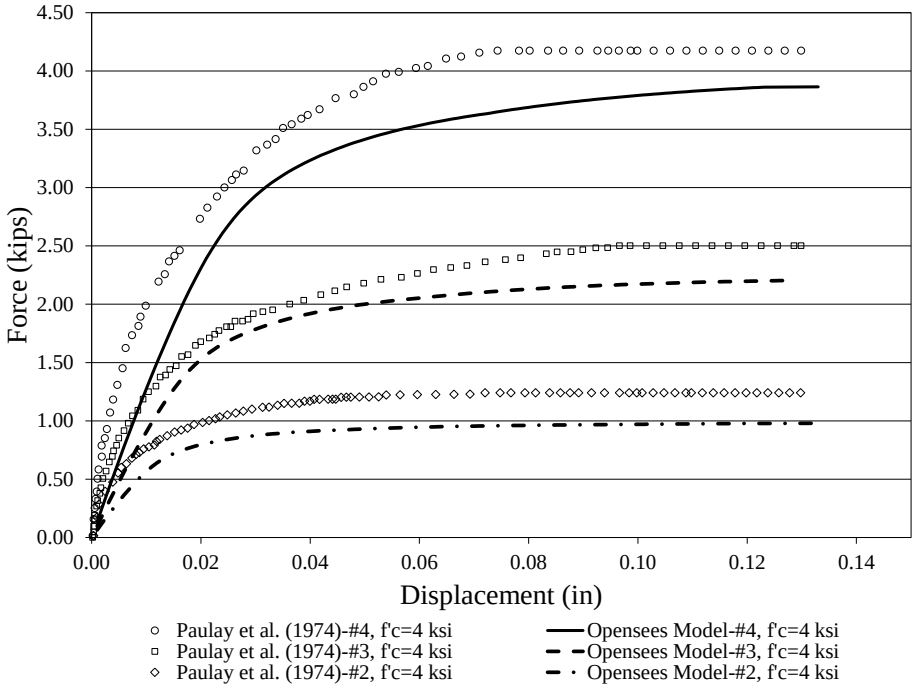

Figure 3.15 Comparison of analytical results with test data of Paulay et al. (1974)

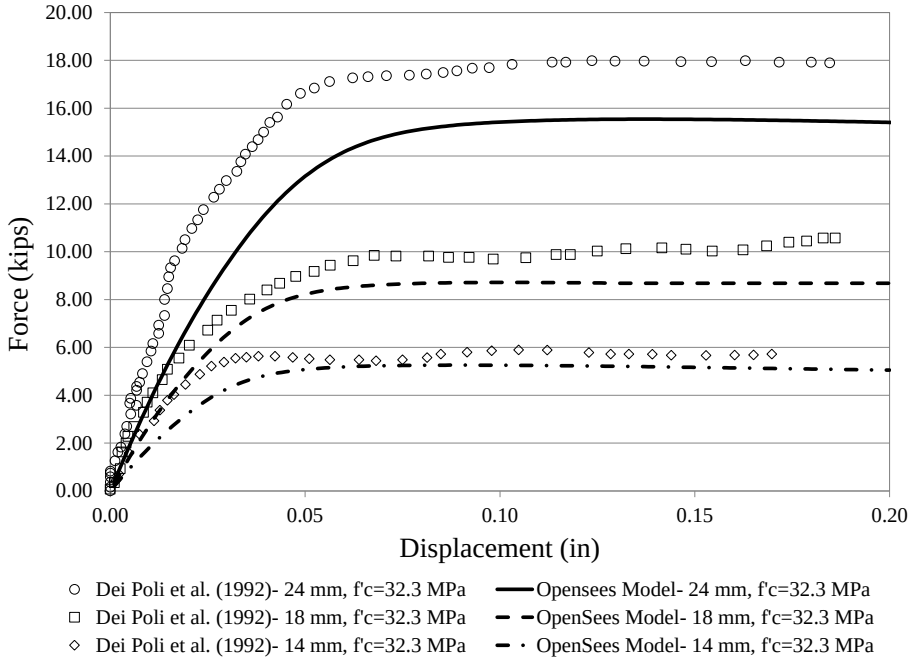

Figure 3.16 Comparison of analytical results with test data of Dei Poli et al. (1992)

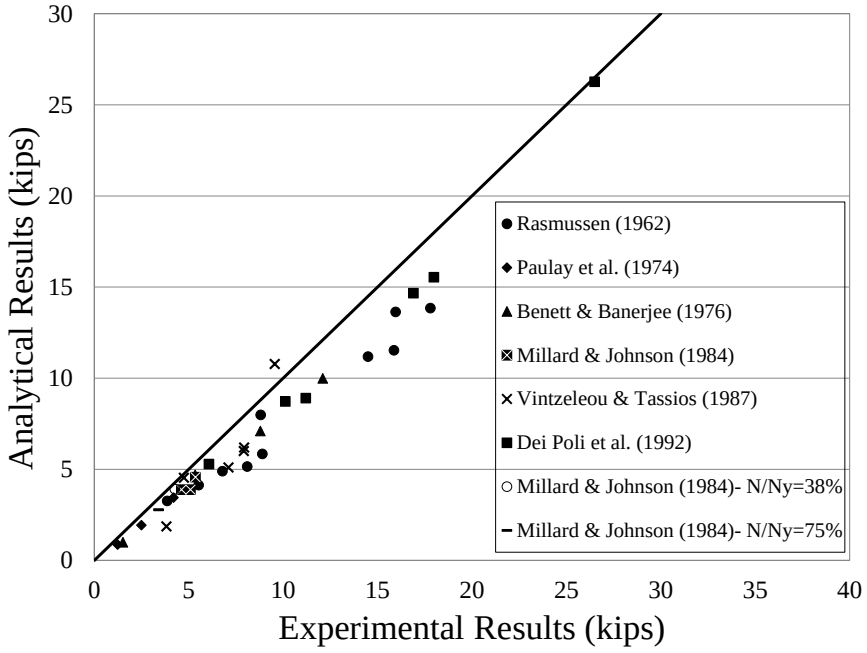

Figure 3.17 Validation of analytical model for dowel resistance

As shown in Figure 3.15 and Figure 3.16, the model in OpenSees captures the behavior of the dowel action well. It successfully predicts the stiffness of the dowels but tends to underestimate the dowel force. However, the error in the strength prediction is within 15% of the test results. It can also be observed that the accuracy is slightly lower for larger-diameter bars. Figure 3.17 shows a similar trend in strength prediction by the OpenSees model for a large set of test data. However, for this data set, the maximum difference between the analytical and experimental results is 35%.

3.4.4 Plastic-Hinge Locations in Dowel Bars

The locations of the plastic hinges developed in the bar have an important influence on the dowel resistance, as implied in the analytical model for the dowel mechanism presented in Section 3.3. In this section, the distances of the plastic hinges from the crack interface predicted by the OpenSees model are compared to the values extracted from the test data shown in Table 3.1 and Table 3.2 by means of the analytical model presented in Section 3.3. In the analytical model, this distance is defined as the effective length l_y, as shown in Figure 3.6.

First, Eq. (3.13), which is based on the idealized model shown in Figure 3.6, is used to compute the uniform bearing stress f_{cb} developed by the concrete for each test, using the dowel resistance F_d, the bar diameter d_b given in Table 3.1 and Table 3.2, and the plastic moment capacity computed with the formula $M_{pl} = f_y \cdot d_b^3 / 6$. After the bearing strength has been calculated, the effective length l_y is then determined with Eq.

(3.12). The experimental results extracted by the model are compared to those given by OpenSees in Figure 3.18. It can be seen that the correlation between the two sets of values is good. However, the OpenSees model tends to give a higher value.

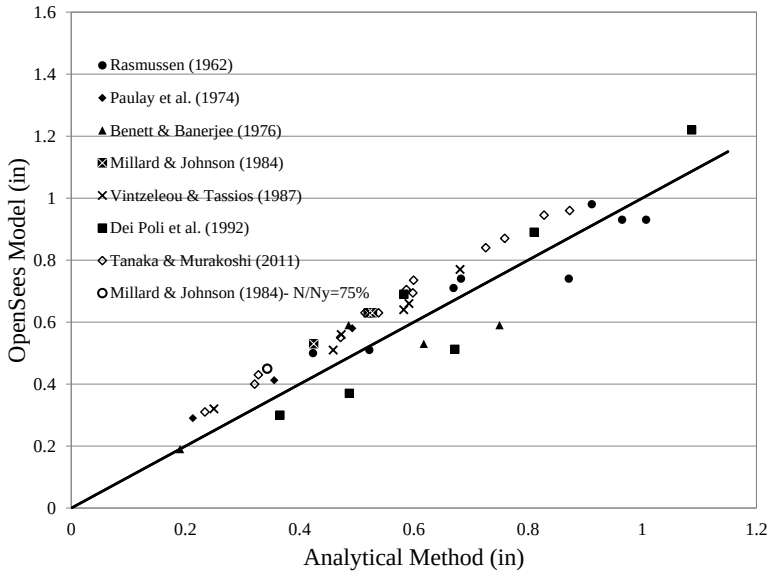

Figure 3.18 Comparison of effective lengths from OpenSees model to values extracted from test data

3.4.5 Parametric Study on the Angle of Kink

The OpenSees model is used in this section to predict the behavior of dowels subjected to large deformations and to determine the influence of the material properties and bar sizes on the angle of kink of the dowel bar at the ultimate resistance.

The model has the same configuration as that shown in Figure 3.13 and is subjected to a displacement level of 3 to 5 times the bar diameter, which corresponds to the displacement level observed in the shear key tests of Borzogzadeh et al. (2006) when the ultimate shear resistance was reached. The hardening behavior of steel may influence

the plastic-hinge location in the bar and the angle of kink. Thus, a material law that better simulates the hardening behavior of steel is used. This steel material law has a trilinear curve, in which the elastic branch with a yield strength f_y is followed by a hardening branch till the stress reaches the ultimate strength, f_{su}, after which the stress remains constant. The ultimate strength of the steel is first reached at 6% strain. Results of the large deformation analysis are compared to the test data of Borzogzadeh et al. (2006). Hence, the yield strength of the bar is set equal to $f_y = 68$ ksi and the ultimate strength is $f_{su} = 105$ ksi, which are the steel properties reported in Borzogzadeh et al. (2006). The steel model is compared to the test data for a bar having the same yield strength but a lower ultimate strength in Figure 3.19 because Borzogzadeh et al. did not provide such a curve for the bars used in their tests.

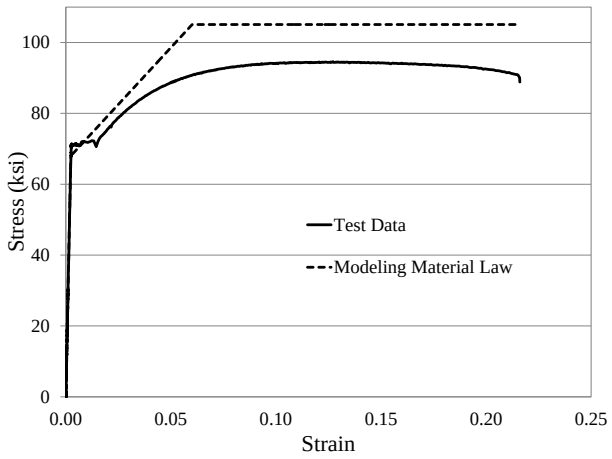

Figure 3.19 Trilinear steel material model

A parametric study has been conducted with this model. First, the influence of the concrete strength is examined. A No. 3 bar is considered. The deflected shape of the bar embedded in a concrete block with a compressive strength of 4.0 ksi is shown in Figure

3.20. In Figure 3.20, the elevation of the bar has been normalized by the length of the bar considered in the OpenSees model, which is 16 in. The deflected shape is similar to what was observed in the test, as shown in Figure 3.12.

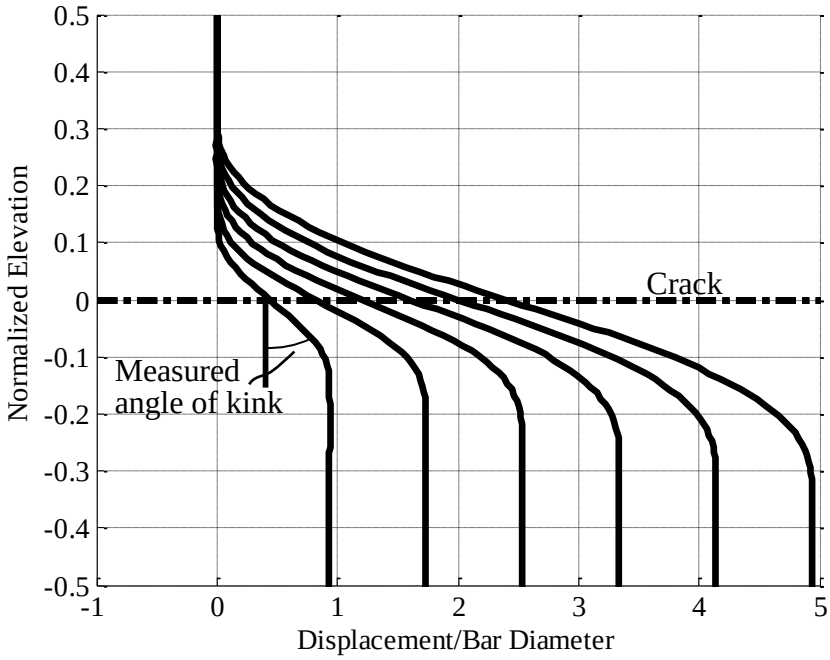

Figure 3.20 Progression of deformation of a bar

As the bottom part is displaced with respect to the top, the bar bends, forming plastic hinges. The location of the plastic hinges changes as the imposed displacement increases. To show the change in the distance between the plastic hinges, the curvature profiles for the bar at horizontal displacements of $d_b/6$, d_b and $2\,d_b$ are shown in Figure 3.21. The curvature is normalized by the maximum curvature observed for the respective displacement level and it is plotted against the elevation of the bar, which is normalized by the bar diameter. The curvature is shown for the region that spans 6 times the bar diameter, $3d_b$ from both sides of the crack plane.

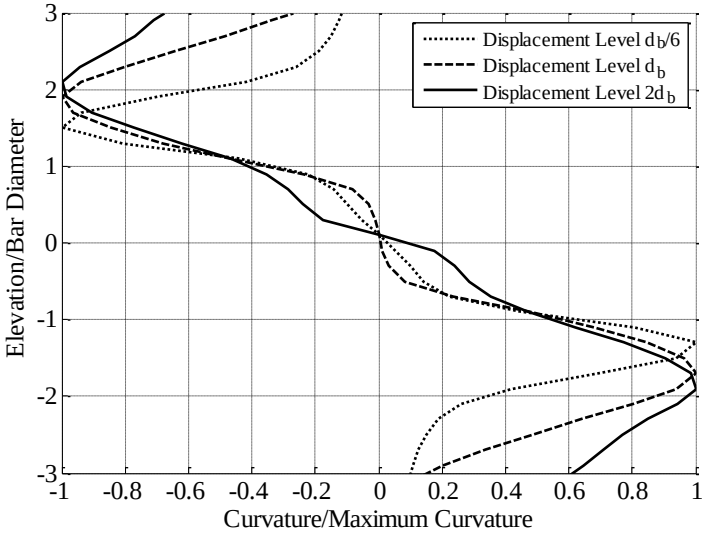

Figure 3.21 Bar Curvature

The distance between the plastic hinges changes from $2.8\,d_b$ at a displacement level of $d_b/6$ to $3.6\,d_b$ when the bar experiences a displacement of d_b, which is a 29% increase. At a displacement level of $2\,d_b$ the distance between the plastic hinges was measured to be $4.0\,d_b$. As shown in the figure, the curvature changes rapidly within a small length of the bar. This indicates that a sufficiently fine element discretization should be used.

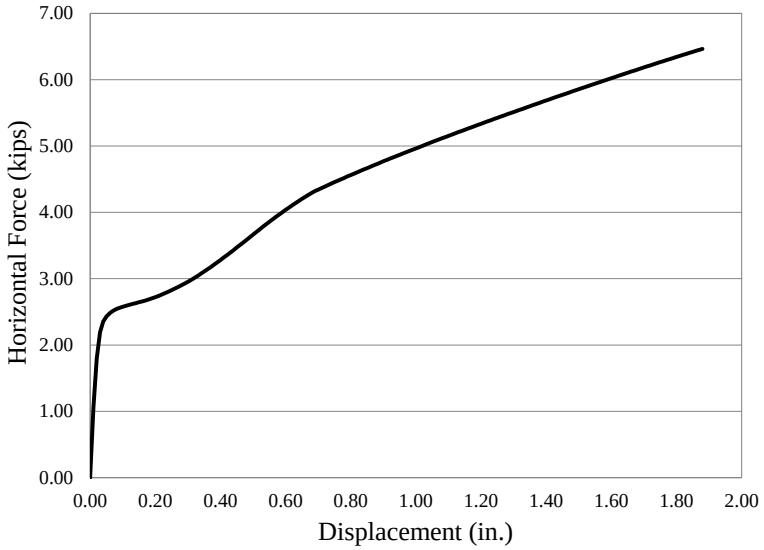

Figure 3.22 Horizontal force-vs.-displacement curve for the bar under large deformation

The force-displacement curve for the dowel bar is shown in Figure 3.22. It can be observed that the first major change of the slope of the curve occurs at about 2.5 kips as a result of plastic hinging in the bar. In fact, from the analytical formula in Eq. (3.12), the dowel force is estimated to be 2.79 kips. The influence of the horizontal component of the bar is more pronounced after 0.20 in. of displacement in that a stiffer behavior is observed.

In the parametric study that follows, the dowel action is simulated for concrete with compressive strengths varying from 4.0 ksi to 9.0 ksi. For each concrete strength, the angle of kink is calculated based on the rotation of the bar element at the crack elevation. The results are plotted in Figure 3.23 against the displacement of the bottom half normalized by the bar diameter. In this investigation, the bar is considered fractured when the strain in the element close to the crack location has reached a value of 12%. Thus, the curves in Figure 3.23 terminate at the point when this value is reached in the analysis and the angle of kink observed is termed ultimate angle of kink.

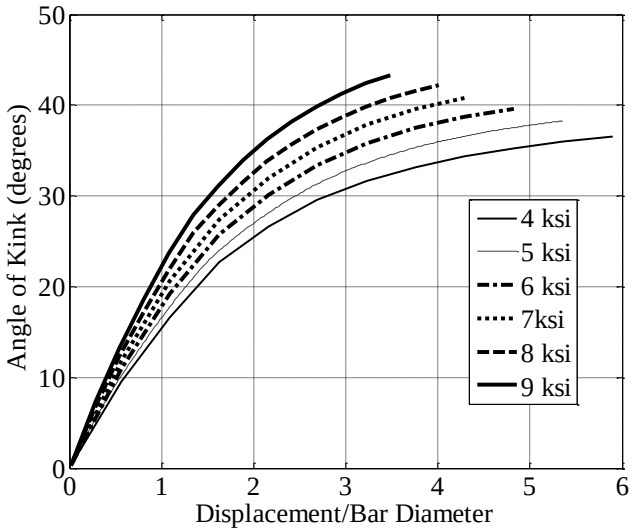

Figure 3.23 Angle of kink for a No. 3 bar with different concrete strengths

Figure 3.23 shows that the ultimate angle of kink (at the termination point of each curve) is proportional to the compressive strength of the concrete. However, for the range of the concrete strengths shown in the figure, which is normally encountered in RC structures, the variation of the angle is not very significant. It can also be observed that the displacement level at which bar fracture occurs decreases with increasing concrete strength and it is between 3.5 and 6.0 times the bar diameter. Since the ultimate angle of kink increases with the concrete strength, the decrease of the displacement implies that the plastic hinges in the dowel bar will be closer to each other (i.e., the effective length l_y will be shorter). This is consistent with the analytical dowel model presented in Section 3.3. The ultimate angles of kink determined in the parametric study are summarized in Table 3.3. A variation of less than 7 degrees is observed for the different analyses.

Table 3.3 Ultimate angles of kink for a No. 3 bar embedded in concrete of different strengths

Concrete Strength (ksi)	4.00	5.00	6.00	7.00	8.00	9.00
Ultimate angle of kink (degrees)	36.6	38.8	39.7	40.9	42.1	43.3

In addition, a parametric study is carried out to study the sensitivity of the ultimate angle of kink to the bar size. In this study, the compressive strength of the concrete is 5 ksi. The angle of kink is plotted against the normalized displacement up to the bar fracture point in Figure 3.24. Again, it can be observed that the change of the ultimate angle of kink is relatively small, and the angle is inversely proportional to the bar size. The results for the ultimate angle of kink are summarized in Table 3.4. Bar fracture occurs between 3.50 to 5.50 times the bar diameter.

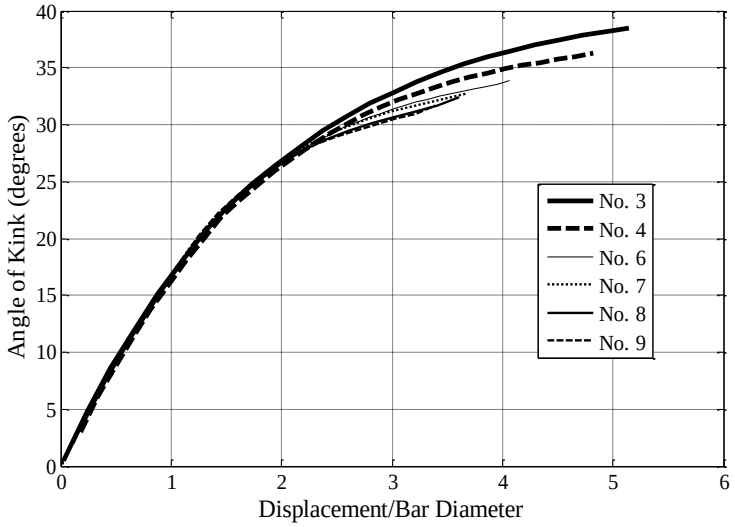

Figure 3.24 Angle of kink for different bar sizes with 5-ksi concrete

Table 3.4 Ultimate angles of kink for different bar sizes

Bar size	No. 3	No. 4	No. 6	No. 7	No. 8	No. 9
Ultimate angle of kink (degrees)	38.8	36.6	33.9	33.3	32.4	31.8

For the case of the No. 4 bar with 5-ksi concrete, the angle predicted (36.6 degrees) is very close to the value measured in the test of Borzogzadeh et al. (37 degrees), which had the same bar size. However, the displacement level at which bar fracture occurs differs from what was observed in the test by approximately 20-25%.

For different bar sizes and concrete strengths considered here, the range of variation of the angle of kink is 7 degrees.

3.5 Acknowledgement of Publication

Part of this chapter is a reprint of the material that will appear in a technical report which will be submitted to the California Department of Transportation in 2016, Kottari, A., P. B. Shing, J. I. Restrepo, under the title "Design and Capacity Assessment of External Shear Keys in Bridge Abutments". The dissertation author will be the primary investigator and author of this report.

CHAPTER 4

PHENOMENOLOGICAL DOWEL ACTION MODEL FOR FINITE ELEMENT ANALYSIS

4.1 Introduction

Dowel action is one of the shear resisting mechanisms across a cracked sliding surface in reinforced concrete (RC) and reinforced masonry (RM) structures. When the sliding surface is smooth and has little cohesive force, sliding shear resistance is mainly provided by the dowel action of the bars crossing the crack. The modeling of dowel action in a precise manner, in finite element analysis, presents a major challenge. It requires a 3-D constitutive model for concrete that can accurately account for the increased compressive resistance of confined concrete as it interacts with the dowel bar. This confinement effect is localized in the vicinity of the bar and is introduced by the surrounding concrete. The experimental data presented in Chapter 3 have indicated that this increase in strength can be significant and cannot be ignored. The finite element model also requires a sufficiently refined mesh to capture the variation of the dowel force along the bar in an accurate manner. Such models are often impractical for the analysis of RC and RM structures, which may have dowel action developed in a number of reinforcing bars.

To circumvent the aforementioned issues, an efficient modeling approach to represent the dowel behavior in finite element analysis has been developed in this study. In this approach, the compressive behavior of the concrete that interacts with the dowel bar is modeled in a zero-thickness interface element that connects a concrete element to a bar element, so that the very localized confinement effect does not have to be represented in the concrete element. As it will be discussed in the following paragraph, this approach has an added advantage that the size of the concrete elements does not have to be as small as that of the bar elements to accurately model the dowel behavior. It is similar to the way the bond-slip behavior of a reinforcing bar is normally modeled. To model the dowel behavior in an interface element, the formulation proposed by Brenna et al. (1990), as presented in Chapter 3, has been adopted and extended to account for the dowel behavior under cyclic loading. This model has been implemented in an interface element together with the bond-slip law proposed by Murcia-Delso and Shing (2015). However, for simplicity, it is assumed that the dowel behavior is not affected by bond slip, and vice versa. This model can be used for both 2-D and 3-D finite element analysis.

It has been shown in Chapter 3 with beam and spring elements that the change of curvature of a dowel bar can be rapid within a small distance from the crack face. Hence, the size of the steel elements needs to be sufficiently small to accurately capture this behavior and the dowel resistance. For finite element analysis, this would require a mesh that is much more refined than what would normally be required when the dowel action is ignored. To overcome this problem, and improve the computational efficiency, the proposed dowel model has been implemented in a special interface element, proposed by

Mavros (2015), which allows the reinforcing bars and concrete to be represented by different mesh refinements.

The proposed model has been validated with experimental data from monotonic and cyclic load tests of dowel bars conducted by Paulay et al. (1974) and Vintzeleou and Tassios (1987) with relatively small displacement levels. Furthermore, the model has been validated with experimental data of reinforced masonry shear walls, whose behavior was dominated by base sliding. In the following sections, the formulation of the interface element and the bond-slip constitutive law developed in the other studies are concisely summarized, and the dowel action constitutive law extended for cyclic loading is described in detail. Finally, the validation analyses are presented.

4.2 Description of the Interface Element

A zero thickness interface model is used to connect the steel to the concrete elements. This interface model is proposed by Mavros (2015) and can connect steel and concrete elements with different sizes. An example of a beam element connected to a larger concrete element is shown in Figure 4.1.

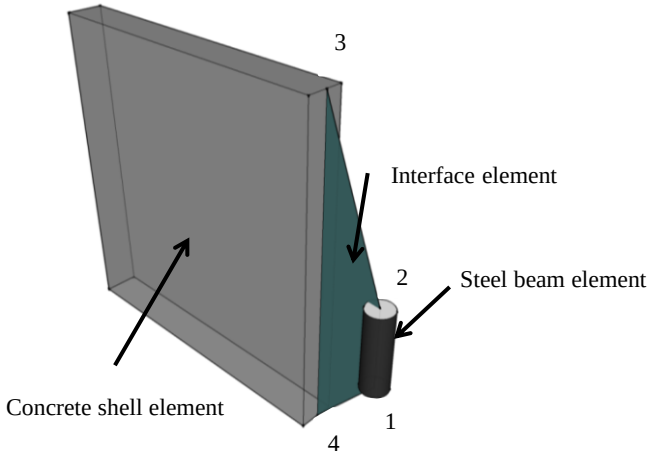

Figure 4.1 Steel-to-concrete connectivity with interface element (from Mavros, 2015)

The shear stress τ and the normal stress σ in the interface depend on the relative displacements $\tilde{u}$ and $\tilde{v}$, in the tangential and normal directions, respectively. The relative displacements are defined as the difference of the displacements of the steel element and the concrete element as follows:

$$\begin{Bmatrix} \tilde{u} \\ \tilde{v} \end{Bmatrix} = \begin{Bmatrix} u_s(x) - u_c(x) \\ v_s(x) - v_c(x) \end{Bmatrix} \tag{4.1}$$

in which the subscript s denotes the displacements on the steel side of the interface and the subscript c denotes the displacements on the concrete side. The displacements on each side of the interface are determined by linear shape functions and the nodal displacements. The interface element is shown in Figure 4.2. The steel side and the concrete side, i.e., side 1-2 and side 3-4, as shown in Figure 4.2, have different natural coordinates, η_s and η_c, respectively, which satisfy the following relation:

$$\eta_c = \alpha + \beta \cdot \eta_s \tag{4.2}$$

in which

$$\alpha = \frac{L_{14} - L_{23}}{L_{34}} \tag{4.3}$$

$$\beta = \frac{L_{12}}{L_{34}} \tag{4.4}$$

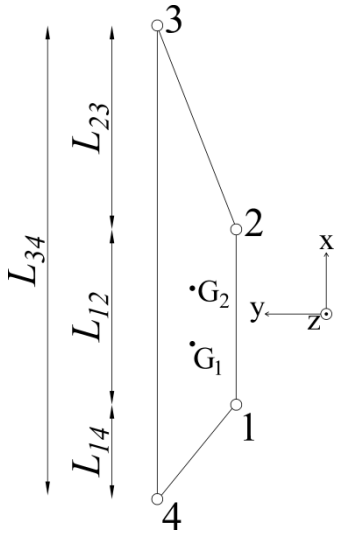

Figure 4.2 Single interface element (from Mavros, 2015)

The relative displacements can then be calculated in terms of η_s as:

$$\begin{Bmatrix} \tilde{u} \\ \tilde{v} \end{Bmatrix} = \begin{Bmatrix} u_s(\eta_s) - u_c \cdot (\alpha + \beta \cdot \eta_s) \\ v_s(\eta_s) - v_c \cdot (\alpha + \beta \cdot \eta_s) \end{Bmatrix} = \begin{bmatrix} \boldsymbol{b}(\eta_s) & \mathbf{0} \\ \mathbf{0} & \boldsymbol{b}(\eta_s) \end{bmatrix} \cdot \begin{Bmatrix} \boldsymbol{u} \\ \boldsymbol{v} \end{Bmatrix} \tag{4.5}$$

in which $\boldsymbol{b}$ is defined as:

$$\boldsymbol{b}(\eta_s) = \begin{bmatrix} N_1(\eta_s) & N_2(\eta_s) & -N_2 \cdot (\alpha + \beta \cdot \eta_s) & -N_1 \cdot (\alpha + \beta \cdot \eta_s) \end{bmatrix} \tag{4.6}$$

Finally, the forces in *x* and *y* directions are calculated as:

$$\begin{aligned} \boldsymbol{f}_x &= \pi d_b \int_{-1}^{1} \boldsymbol{b}^T(\eta_s) \cdot \tau(\eta_s) \cdot J d\eta_s \\ \boldsymbol{f}_y &= d_b \int_{-1}^{1} \boldsymbol{b}^T(\eta_s) \cdot \sigma(\eta_s) \cdot J d\eta_s \end{aligned} \tag{4.7}$$

In Eq. (4.7), J is the Jacobian given by:

$$J = \frac{dx}{d\eta_s} = \frac{L_{12}}{2} \tag{4.8}$$

For the relative displacement in the *x* direction, the bond-slip material law of Murcia-Delso and Shing (2015) is implemented, whereas in the *y* direction an appropriate law for the bearing strength of concrete is proposed.

4.3 Bond-Slip Constitutive Law

The bond-slip constitutive law proposed by Murcia-Delso and Shing (2015) accounts for the bond-strength degradation due to bar slip, cyclic slip reversals, and the tensile yielding of a bar. The bearing forces on the bar ribs and the frictional forces between the concrete and steel surfaces contribute to the bond resistance. The two mechanisms are shown in Figure 4.3a for the monotonic shear stress-vs.-slip relation. The bond-slip law is given by Eqs. (4.9), (4.10) and (4.11).

$$\tau = \rho_{b,y} \cdot \rho_{b,c} \cdot \tau_b + \rho_{f,y} \cdot \rho_{f,c} \cdot \tau_f \tag{4.9}$$

where

$$\tau_b(\tilde{u}) = \begin{cases} 3.0 \cdot \dfrac{\tau_{\max}}{s_{peak}} \cdot \tilde{u} & for \;\; 0 \le \tilde{u} < 0.1 \cdot s_{peak} \\ sign(\tilde{u}) \cdot \tau_{\max} \cdot \left[0.75 - 0.45 \cdot \left(\dfrac{|\tilde{u}| - s_{peak}}{0.9 \cdot s_{peak}} \right)^4 \right] & for \;\; 0.1 \cdot s_{peak} \le |\tilde{u}| < s_{peak} \\ sign(\tilde{u}) \cdot 0.75 \cdot \tau_{\max} & for \;\; s_{peak} \le |\tilde{u}| < 1.1 \cdot s_{peak} \\ sign(\tilde{u}) \cdot 0.75 \cdot \tau_{\max} \cdot \left[1 - \dfrac{|\tilde{u}| - 1.1 \cdot s_{peak}}{s_R - 1.1 \cdot s_{peak}} \right] & for \;\; 1.1 \cdot s_{peak} \le |\tilde{u}| < s_R \\ 0 & for \;\; |\tilde{u}| \ge s_R \end{cases} \tag{4.10}$$

and

$$\tau_f(\tilde{u}) = \begin{cases} \dfrac{\tau_{\max}}{s_{peak}} \cdot \tilde{u} & \text{for } 0 \le |\tilde{u}| < 0.1 \cdot s_{peak} \\ sign(\tilde{u})\,\tau_{\max}\left[0.25 - 0.15 \cdot \left(\dfrac{\tilde{u} - s_{peak}}{0.9 \cdot s_{peak}}\right)^4\right] & \text{for } 0.1 \cdot s_{peak} \le |\tilde{u}| < s_{peak} \\ sign(\tilde{u}) \cdot 0.25 \cdot \tau_{\max} & \text{for } |\tilde{u}| \ge s_{peak} \end{cases} \quad (4.11)$$

in which $\tilde{u}$ is the slip displacement, $\tau_{\max}$ and τ_{res} are the maximum and residual bond strengths for monotonic loading, $\rho_{b,s}$ and $\rho_{f,s}$ control the reduction of the bearing and frictional resistances due to the tensile yielding of the bar, and $\rho_{b,c}$ and $\rho_{f,c}$ account for the strength degradation due to cyclic slip reversals, as shown in Figure 4.3b.

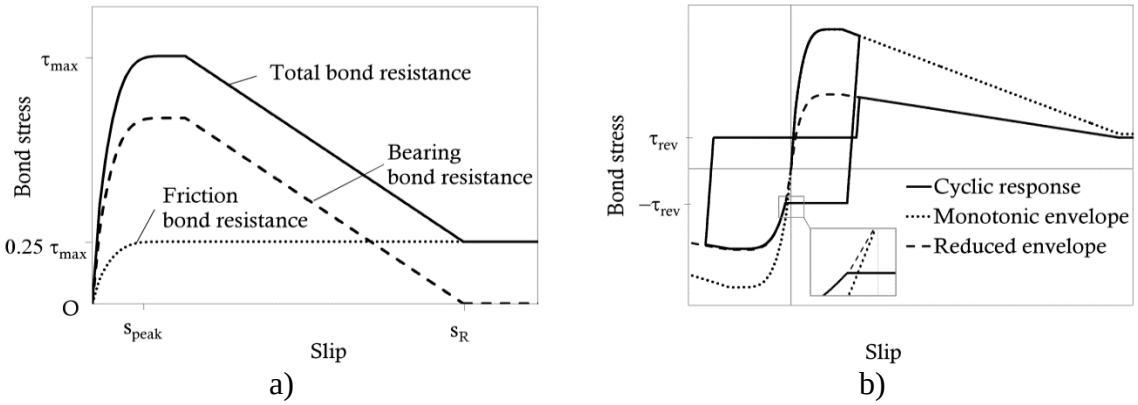

Figure 4.3 Bond-slip model: a) monotonic response; b) cyclic response (from Murcia-Delso and Shing, 2015)

The model is calibrated with the following empirical relations:

$$\tau_{\max} = 2.4 \cdot \left(f_c'/5.0\right)^{0.75} \quad (4.12)$$

$$s_{peak} = 0.07 \cdot d_b \quad (4.13)$$

$$s_R = 0.5 \cdot d_b \quad (4.14)$$

in which d_b is the bar diameter and f_c' is the concrete compressive strength, with all units in inches and kips. Details of the model can be found in Murcia-Delso and Shing (2015).

4.4 Proposed Constitutive Law for Dowel Action

The empirical formulation proposed by Brenna et al. (1990) to model the dowel action of a reinforcing bar under monotonic loading has been adopted to establish the normal stress-compressive displacement ($\sigma - \tilde{v}$) relation for the interface. The model is based on the test data of Soroushian et al. (1987) and is formulated as follows:

$$\sigma(\tilde{v}) = \omega(\tilde{v}) \cdot k_0 \cdot \tilde{v} \tag{4.15}$$

in which

$$\begin{aligned} k_0 &= 600 \cdot f_c'^{0.7} / d_b \\ \omega(\tilde{v}) &= \left[1.5 \cdot \left(a + \sqrt{d^2 \cdot \left(40 \cdot \tilde{v} / d_b - b \right)^2 + c^2} \right) \right]^{-4/3} \\ a &= 0.59 - 0.011 \cdot f_c' \\ b &= 0.0075 \cdot f_c' - 0.23 \\ c &= 0.0038 \cdot f_c' + 0.44 \\ d &= 0.0025 \cdot f_c' + 0.58 \end{aligned} \tag{4.16}$$

In Eq. (4.16) f_c' is the concrete compressive strength in MPa, d_b is the bar diameter in mm and $\tilde{v}$ is the imposed displacement in mm. Notice that the model parameters depend solely on the concrete strength and the bar diameter.

To account for cyclic loadings, an appropriate law is proposed in this study. Consider that the reinforcing bar is embedded in a concrete block, as shown in Figure 4.4a. First, consider that the reinforcing bar deforms in flexure towards Side 1, as shown in Figure 4.4b. The concrete in the vicinity of the bar on Side 1 experiences compression

and can be severely damaged. However, due to the confinement provided by the surrounding concrete, the compressive strength of the concrete in contact with the bar is significantly higher than that under uniaxial compression, and the increased compressive resistance is calculated with Eqs. (4.15) and (4.16).

Once the imposed displacement is reversed, the bar loses contact with concrete on Side 1 and the compressive stress on the bar diminishes. The decrease in stress is calculated as elastic unloading:

$$\begin{aligned} \dot{\sigma}(\tilde{v}) &= K_{un} \cdot \dot{\tilde{v}} \\ K_{un} &= \gamma \cdot K_{in} \end{aligned} \tag{4.17}$$

in which the superposed dot represents the rate of change, γ is a multiplication factor greater than 1.0 and K_{in} is given by:

$$\begin{aligned} K_{in} &= \omega_{in} \cdot k_0 \\ \omega_{in} &= \omega(\tilde{v} = 0) = \left[1.5 \cdot \left(a + \sqrt{d^2 \cdot b^2 + c^2} \right) \right]^{-4/3} \end{aligned} \tag{4.18}$$

Once the stress reaches zero, a gap δ_g is created as shown in Figure 4.4c, and the stress will remain zero until the concrete on Side 2 assumes contact with the bar or the bar resumes contact with the concrete on Side 1 upon reloading. For the reloading towards Side 1, the increase in stress is given by the following equation:

$$\sigma(\tilde{v}) = \omega(\tilde{v} - \delta_r) \cdot k_0 \cdot \langle \tilde{v} - \delta_r \rangle \tag{4.19}$$

In Eq. (4.19), $\langle \bullet \rangle$ are the Macaulay brackets, the expressions for $\omega(\cdot)$ and k_0 are given in Eq. (4.16), and δ_r is the displacement at which reloading starts. If complete unloading occurs, δ_r is equal to δ_g, and the compressive stress will remain zero until the

displacement $\tilde{v}$ reaches δ_g, as shown in Figure 4.5, at which the gap closes and the reinforcing bar resumes contact with the undamaged concrete. The displacement δ_r is calculated as follows:

$$\delta_r = \begin{cases} \delta_g = \delta_u - \dfrac{\sigma_u}{K_{un}} & \text{complete unload} \\ \delta_{cur} & \text{partial unload} \end{cases} \tag{4.20}$$

in which σ_u and δ_u are the stress and the normal displacement at which the unloading starts and δ_{cur} is the displacement at reloading. The parameters defining the behavior of dowel are shown in Figure 4.5. For the analyses that follow, the multiplication factor γ is taken to be 4.0, which provides a sufficiently stiff unloading slope. Equation (4.19) remains valid until the stress reaches the monotonic envelope as shown in Figure 4.5. After that point, the stress is given by Eq. (4.15) and (4.16).

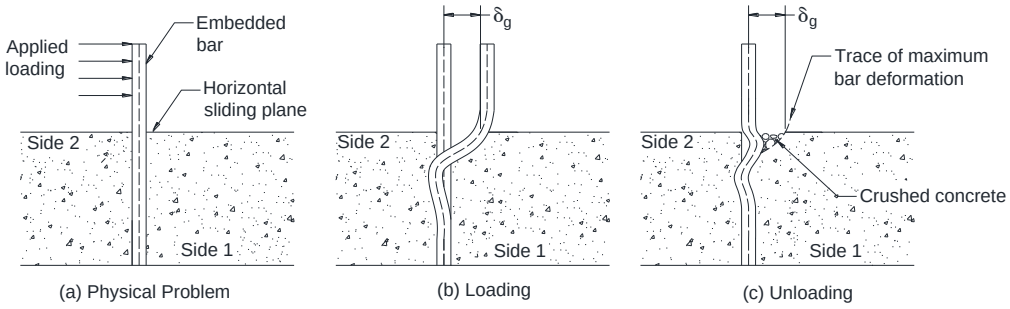

Figure 4.4 The damage of concrete during dowel action

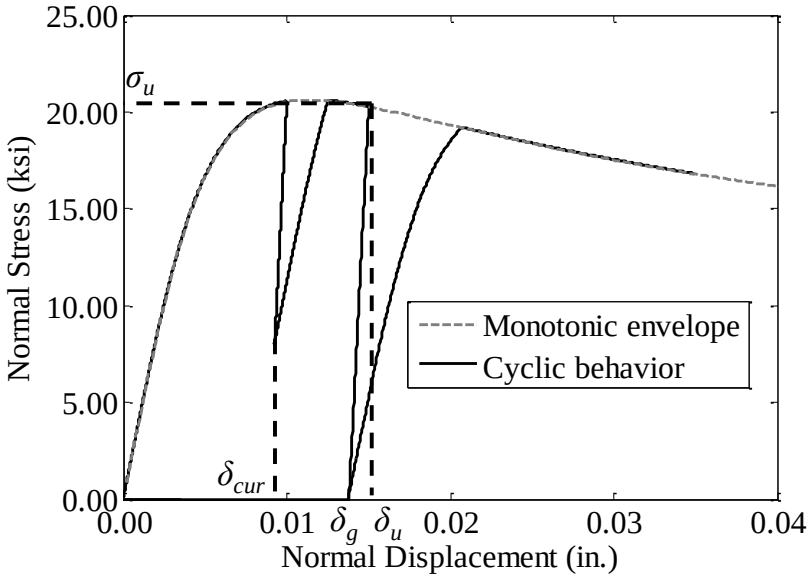

Figure 4.5 Normal stress-vs.-normal displacement curve for the dowel action model

The interface element and the constitutive laws for dowel action and bond slip have been implemented in the finite element program FEAP (Taylor, 2014). The following sections show the validation of the dowel law with experimental results for both monotonic and cyclic loadings. The results are for bars with sufficient concrete cover so that splitting failure of concrete did not occur.

4.5 Calibration and Validation Analyses

4.5.1 Dowel Tests of Single Bars in RC Blocks

The ability and efficiency of the constitutive law proposed here to simulate the dowel action of reinforcing bars has been evaluated with the experimental data of Paulay et al. (1974), who conducted dowel tests on No. 2, No. 3, and No. 4 bars, each embedded in two concrete blocks separated by a joint, and the data from the cyclic loading tests of

Vintzeleou and Tassios (1987). Paulay et al. applied melted wax to the joint between the blocks to eliminate any cohesive resistance so that the dowel resistance of the bar can be directly measured. Vintzeleou and Tassios separated the concrete blocks with 0.16-in. thick metal sheets, which were later removed and the gap was filled with paraffin to create a sliding plane.

The concrete blocks used by Paulay et al. had an average compressive strength of 3.58 ksi, and the steel bars had yield strengths between 42.7 and 50 ksi. For the tests of Vintzeleou and Tassios, the actual strengths of the materials have not been reported. The concrete had a nominal compressive strength of 6.525 ksi and the steel bars had a nominal yield strength of 61 ksi (Vintzeleou 1984). The testing apparatus they used are shown in Figure 4.6.

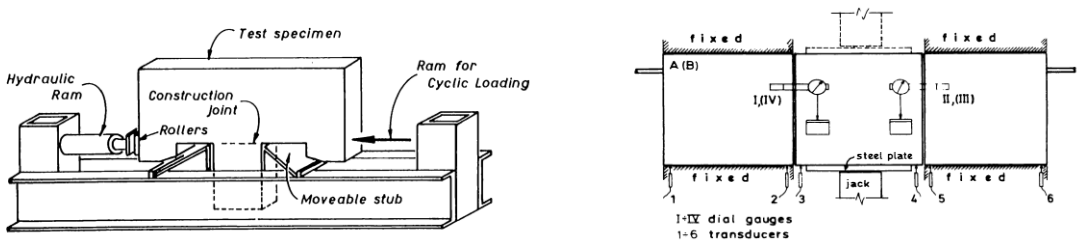

a) b)

Figure 4.6 Testing apparatus: a) Paulay et al. (1974); b) Vintzeleou and Tassios (1987)

In the finite element analyses presented here, beam elements are used for the reinforcing steel. The configuration of the test specimens and the finite element model are schematically shown in Figure 4.7, in which the interface elements modeling the dowel action are represented by the shaded and unshaded trapezoidal areas for illustration purposes. Since the resistance developed by the concrete that interacts with the dowel bar

is represented by the interface elements, the concrete blocks need not be explicitly modeled.

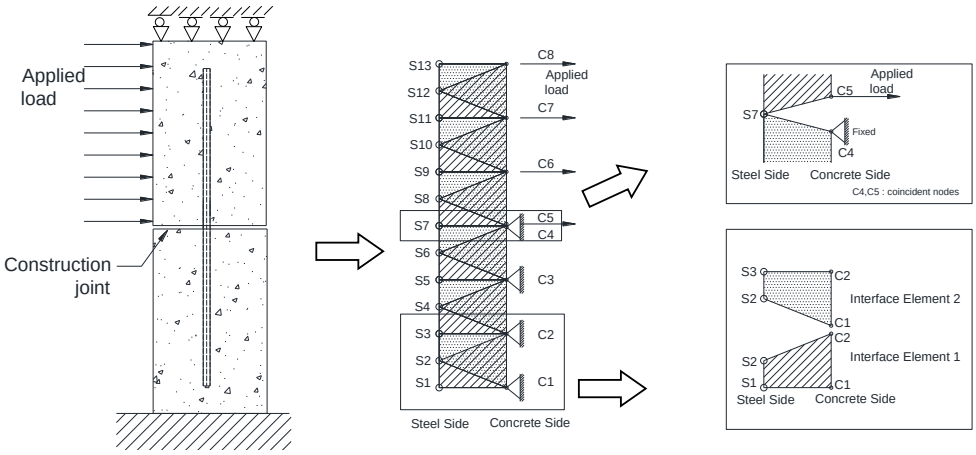

a) b) c)

Figure 4.7 Model used in finite element analysis: a) physical model; b) FE model; c) connectivity details

Past experimental studies, such as Dei Poli et al. (1988), Vintzeleou and Tassios (1987), Rasmussen (1963), have shown that the curvature of a bar developing dowel action can change rapidly within a small distance between $0.6d_b$ and $3.0d_b$ from the crack face. Thus, it is important that the size of the steel elements be sufficiently small to capture this behavior. To determine this size, a sensitivity study has been conducted for a No. 4 bar, and the results are shown in Figure 4.8.

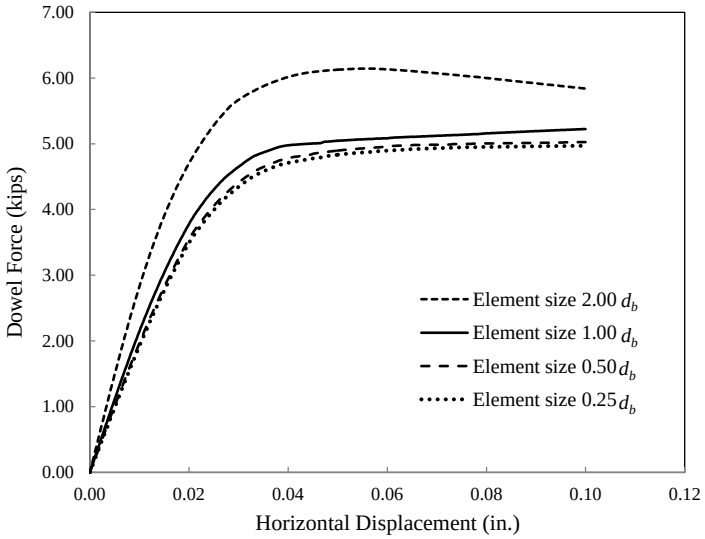

Figure 4.8 Sensitivity of dowel behavior to beam element size for a No. 4 bar

It can be observed that the solution converges when the element size is between $0.25d_b$ and $0.50d_b$. An element size of $0.25d_b$ has been chosen for the analyses presented in this section. Numerical results are compared to the experimental results of Paulay et al. (1974) in Figure 4.9, which shows that the proposed model is able to capture the dowel behavior well.

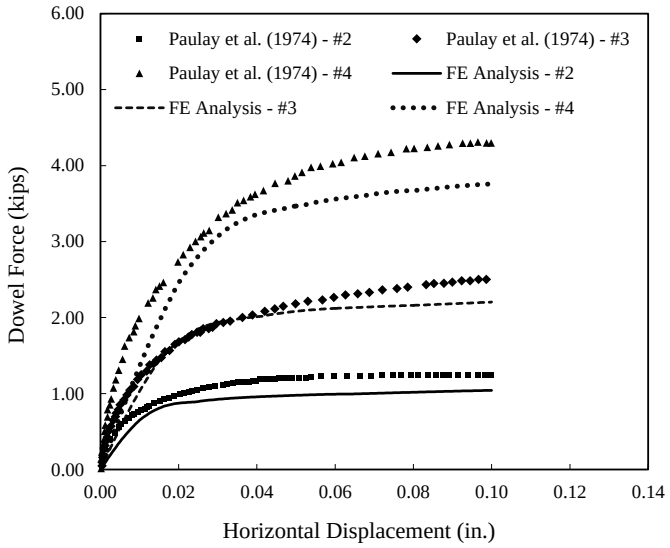

Figure 4.9 Comparison of experimental and numerical results for monotonic dowel action $\left(f_c' = 3.58 \text{ ksi} \right)$

In Figure 4.10, the result of an FE analysis is compared to the experimental data of Vintzeleou and Tassios (1987) on a cyclic dowel test. The numerical result is in good agreement with the experimental data in terms of the stiffness and force capacity. In the second loading cycle, the stiffness reduction at reloading is due to the damage of the concrete at the interface and the resulting gap. The stiffness increases as the gap is being closed until further damage has been inflicted.

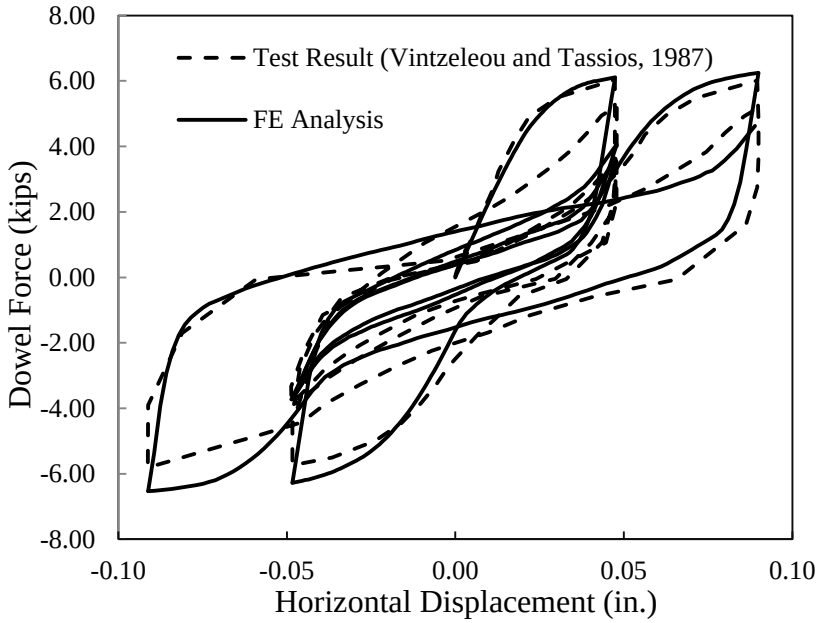

Figure 4.10 Experimental and numerical results for cyclic dowel action

4.5.2 Cyclic Load Tests of Reinforced Masonry Walls

4.5.2.1 Description of Test Specimens

The dowel action model has been used to analyze the behavior of two reinforced masonry walls subjected to cyclic in-plane loads. One wall was tested at the University of Auckland (Voon, 2007) and its behavior was dominated by diagonal shear cracks. The other wall was tested at University of Texas at Austin (Ahmadi, 2012), and its behavior was dominated by sliding shear near the base. For both cases, dowel action plays an important role.

The wall tested by Voon (2007) had fully grouted concrete masonry blocks. It had a very low amount of shear reinforcement and no axial load applied. The vertical reinforcement consisted of 5Ø20 (0.79-in. diameter) reinforcing bars distributed evenly

every at 400 mm (15.75 in.) on center. One horizontal bar of 6-mm (0.24-in.) diameter was placed in the top masonry course.

The concrete masonry units used were 140 mm (5.51 in.) wide. The height of the wall was 1800 mm (70.9 in.) with an aspect ratio of 1.0. The load was applied at the top of the masonry wall with an actuator attached to a steel loading beam. The reinforcing details of the specimen are shown in Figure 4.11. The reinforcing bars used had a nominal yield strength of 300 MPa (43.5 ksi). The average measured yield strength of the bars was 318 MPa (46.1 ksi). The masonry had a measured compressive strength, f'_m, of 17.6 MPa (2.552 ksi) based on prism tests.

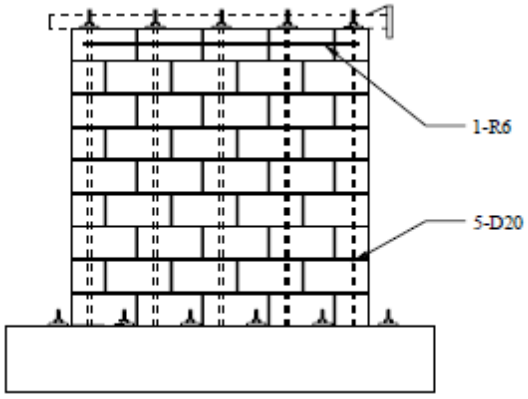

Figure 4.11 Reinforcing details of the wall tested by Voon (2007)

The second wall considered in this study, was tested by Ahmadi (2012). The wall was constructed of concrete masonry blocks and was fully grouted. It was 96 in. long and 96 in. tall. No axial load was applied in the test. The reinforcement consisted of No. 4 bars distributed uniformly at 8 in. on center in the horizontal and vertical directions. The design details are shown in Figure 4.12. The average measured yield strength of the vertical and horizontal reinforcement 61.4 ksi and the tensile strength was 98.7 ksi. The

specimens were constructed of 8 x 8 x 16 in. concrete masonry units. The average compressive strength of the masonry measured from prism tests was 4.45 ksi.

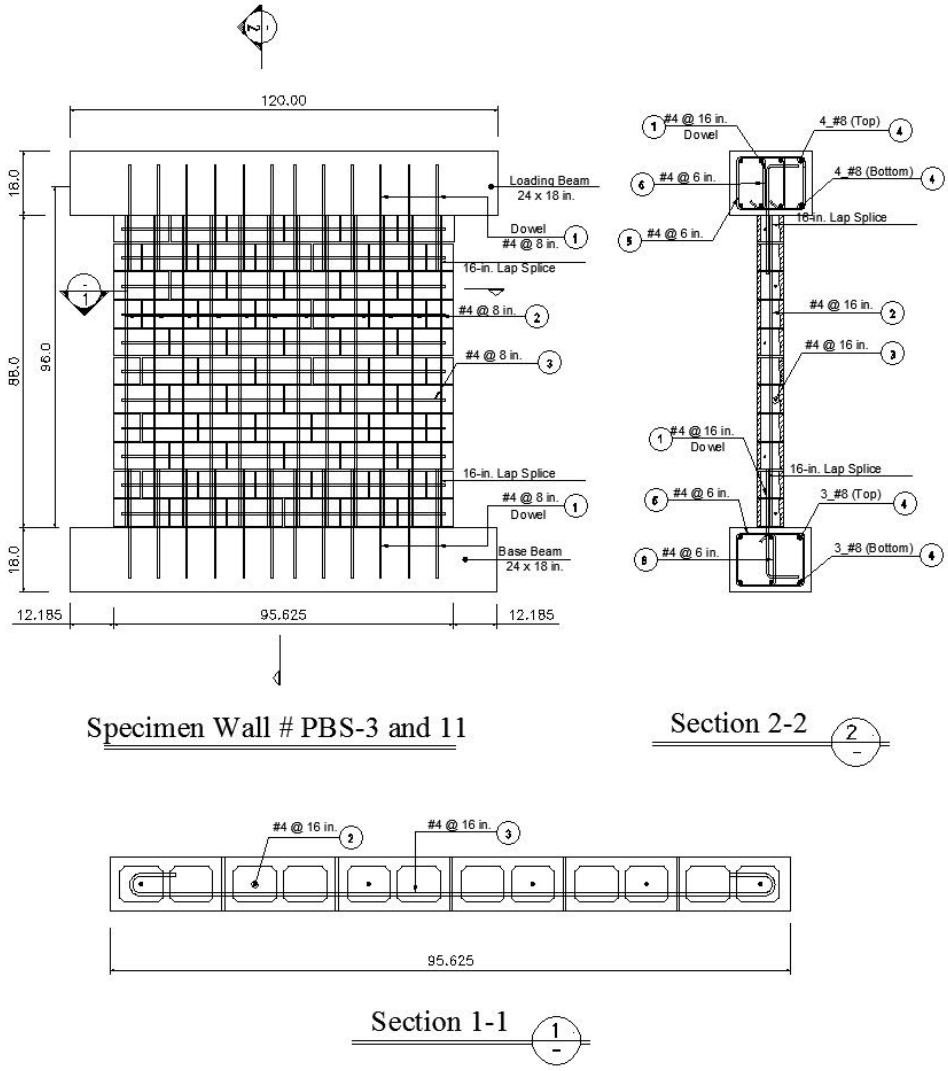

Figure 4.12 Reinforcing details of the wall tested by Ahmadi (2012)

4.5.2.2 Finite Element Analyses

In the following analyses, masonry is modeled with shell elements, whose formulation is described in Burchnall (2014). Each element consists of five membrane

layers across the thickness, and each layer has the plane-stress condition. The element uses a smeared-crack approach to simulate the behavior of masonry and concrete. The constitutive law adopted for masonry and concrete was developed by Lotfi and Shing (1991) and later improved by Koutromanos and Shing (2011). For the modeling purpose, the material has two states. One is the uncracked state and the other is the cracked state. In the uncracked state, the model adopts the J_2-plasticity formulation, with the yield and failure surfaces governed by the von Mises criterion and the tension cutoff condition. The material can have isotropic strain hardening and softening in compression before tensile cracking. When the maximum principal stress reaches the tensile strength, the material is considered cracked and its behavior in directions normal and parallel to the crack is governed by an orthotropic stress-strain law. The model can have a second crack in the direction perpendicular to the first. However, the directions of the cracks remain fixed. The orthotropic stress-strain law for a cracked material is shown in Figure 4.13.

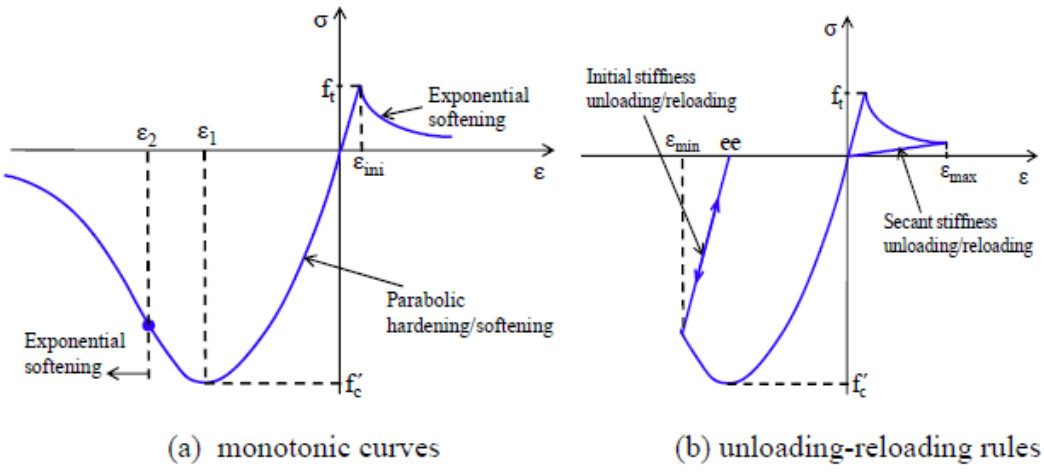

Figure 4.13 Stress-strain relation for a cracked material
(from Koutromanos and Shing, 2011)

In addition to the smeared-crack shell elements, zero-thickness interface elements with a cohesive crack constitutive law are also used to model dominant cracks in the masonry wall in a discrete fashion. The constitutive law for the interface elements was developed by Koutromanos and Shing (2011), and it can effectively simulate the crack opening and closing in addition to the reversible shear dilatation and irreversible joint compaction. It has a failure surface providing a mixed mode, Mode-I and Mode-II, fracture condition, and a set of softening laws governing the gradual degradation of the tensile strength, frictional resistance, and cohesion. In Figure 4.14, the uniaxial behavior of the model in tension and compression is presented. The parameters d_{n1} and d_{n2} govern crack closing and re-opening, and are functions of the normal plastic displacement and the geometric dilatation.

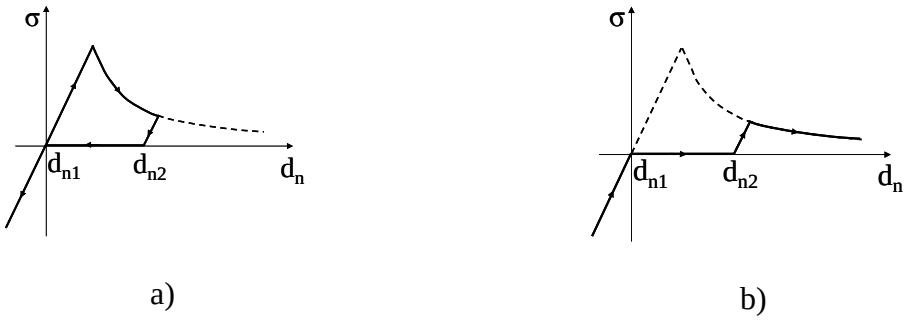

a) b)

Figure 4.14 Uniaxial behavior of cohesive crack interface: (a) normal loading and unloading; (b) reloading in tension (from Koutromanos and Shing, 2011)

The reinforcement is modeled with inelastic beam elements, including the geometric nonlinearity. The material law used for the steel reinforcement was proposed by Dodd and Restrepo-Posada (1995). The model can simulate the Bauschinger effect, reduced elastic modulus, isotropic and kinematic strain hardening. The beam elements are connected to the shell elements through the interface elements presented in Sections

4.2 through 4.5, which account for the bond-slip behavior as well as the dowel mechanism of the reinforcing bars.

To analyze the wall tested by Voon (2007), the horizontal load is applied at the second row of nodes from the top, while the bottom nodes of the model are fixed. The final finite element model is shown Figure 4.15, in which the element size shown is shrunk for clarity. In the same figure, the connectivity between a reinforcing bars and the surrounding masonry unit is also shown.

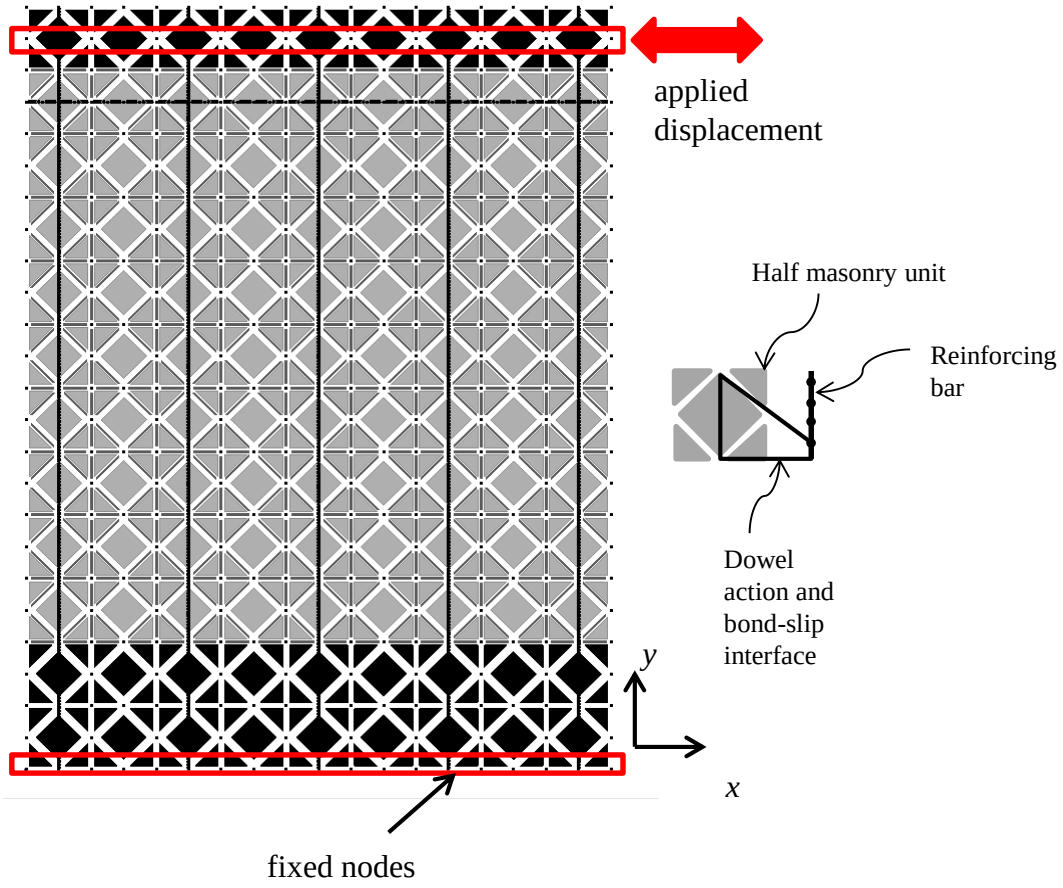

Figure 4.15 Finite element model of the wall tested by Voon (2007)

The compressive strength from the prism test is used to calibrate the smeared-crack elements and determine the tensile strength for both the smeared and the cohesive

crack interface elements. The tensile strength is set to be 10% of the compressive strength, which is 2.55 ksi. The Mode-I fracture energy for the interface elements is specified to be 0.0004 kips/in., based on the recommendation of Koutromanos and Shing (2011). The value of Mode-II fracture energy is assumed to be 10 times the value of Mode-I fracture energy. The yield and tensile strengths of the vertical reinforcing bars are 46 and 68 ksi, respectively, based on the data of Voon (2007). The initial friction coefficient assumed is 1.40, which is suggested by ACI 318-08 for concrete placed monolithically, and the residual friction coefficient is assumed to be 1.0, reflecting a smoothened surface condition. The length of each beam element is chosen to be $0.50\,d_b$ to accurately predict the dowel force as discussed in Section 4.5.1. Figure 4.16 compares the lateral load-vs.-lateral displacement curves from the analysis and the test. The stiffness and the strength degradations are well captured by the model.

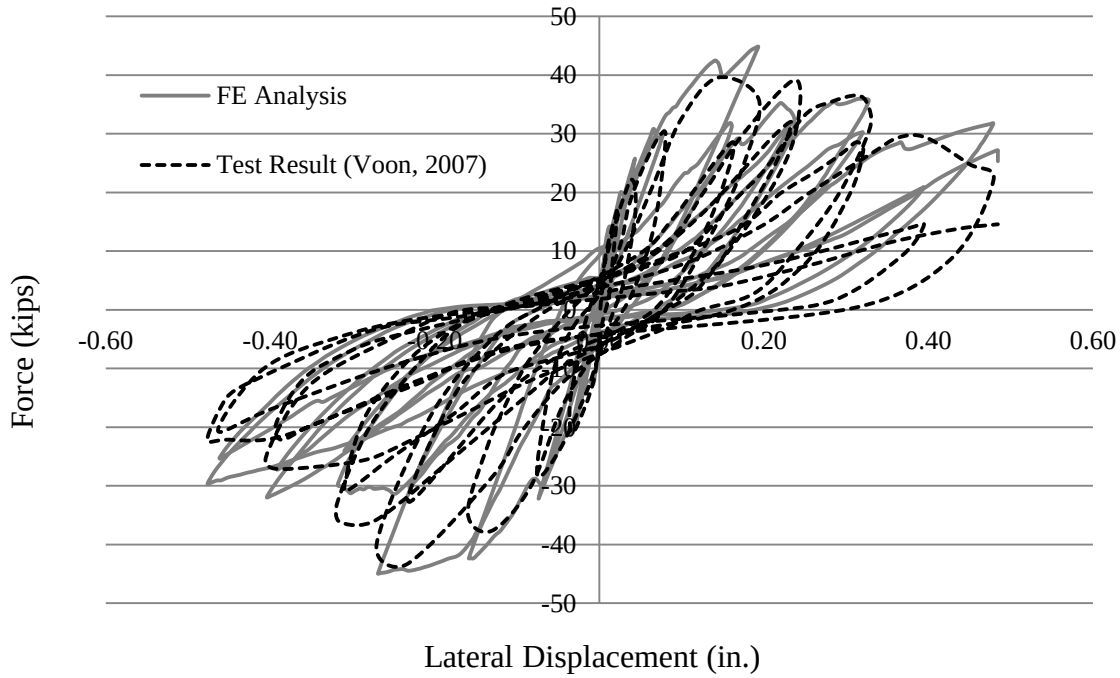

Figure 4.16 Lateral force-vs.-lateral displacement curves for the wall tested by Voon (2007)

In the analysis, the wall shows a behavior similar to that in the test. Horizontal flexural cracks develop initially, which are then superseded by wide diagonal cracks. The flexural cracks can be seen in Figure 4.17. Further widening of these cracks and the crushing of masonry at the toe of the wall led to a significant stiffness degradation. The deformed mesh for the wall in the last cycle of the analysis is shown in Figure 4.18. Diagonal cracks form in both directions and additional vertical cracks are observed. The damage pattern obtained by the analysis compares favorably to the experimental observations as shown in Figure 4.19.

To identify the influence of the dowel action of the vertical bars in this analysis, the numerical results are further examined. When the wall forms a horizontal crack at the base, base sliding is prevented by a combination of the dowel forces and the frictional resistance. The wall exhibits a rocking movement. When the maximum resistance is

reached in the positive direction, the dowel forces contribute 15 kips and frictional resistance contributes 29 kips to the total resistance. However, in the next cycle, when the displacement has reached 0.22 in. and the diagonal cracks have widened, the contribution of the frictional resistance drops to 13 kips, while the dowel forces increase to 22 kips.

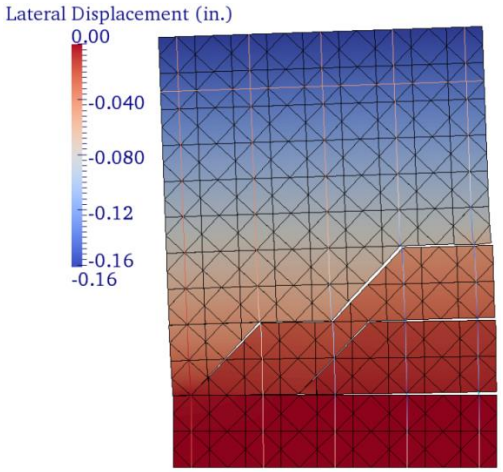

Figure 4.17 Flexural cracks in initial steps of analysis of the wall tested by Voon (2007)

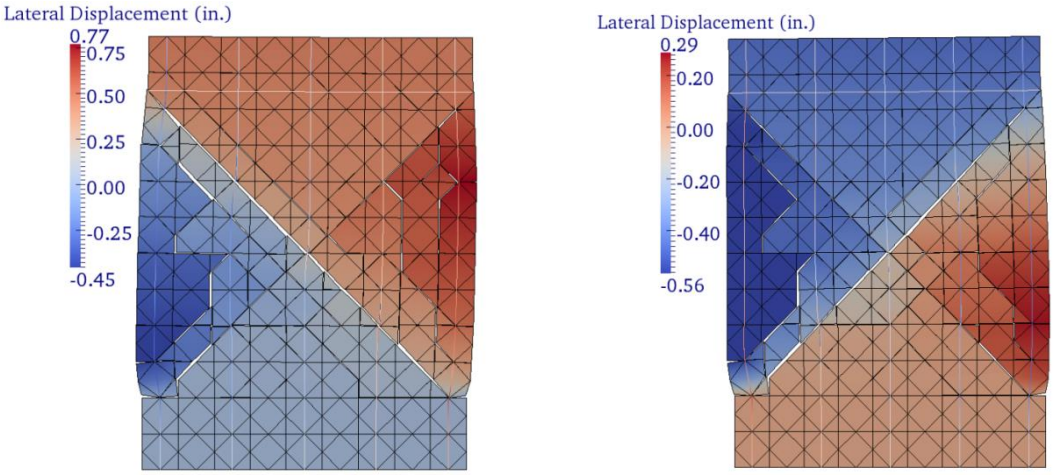

a) b)

Figure 4.18 Deformed mesh at horizontal displacements of: a) 0.47 in.; b) -0.46 in. for the wall tested by Voon (2007)

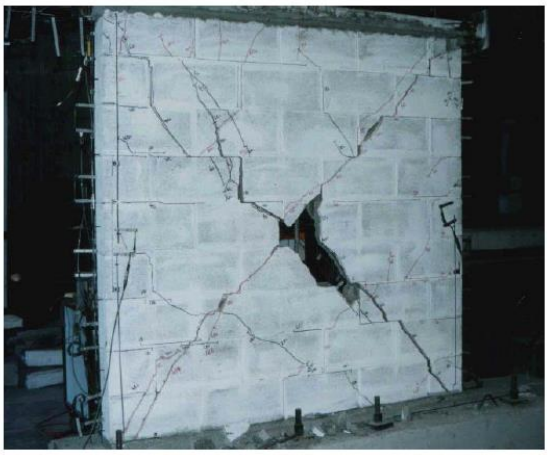

Figure 4.19 Damage at the end of the test of Voon (2007)

The finite element model used to simulate the wall tested by Ahmadi (2012) is shown in Figure 4.20, in which the element size shown is shrunk for clarity. The horizontal load is applied at the third row of nodes from the top, while the bottom nodes of the model are fixed.

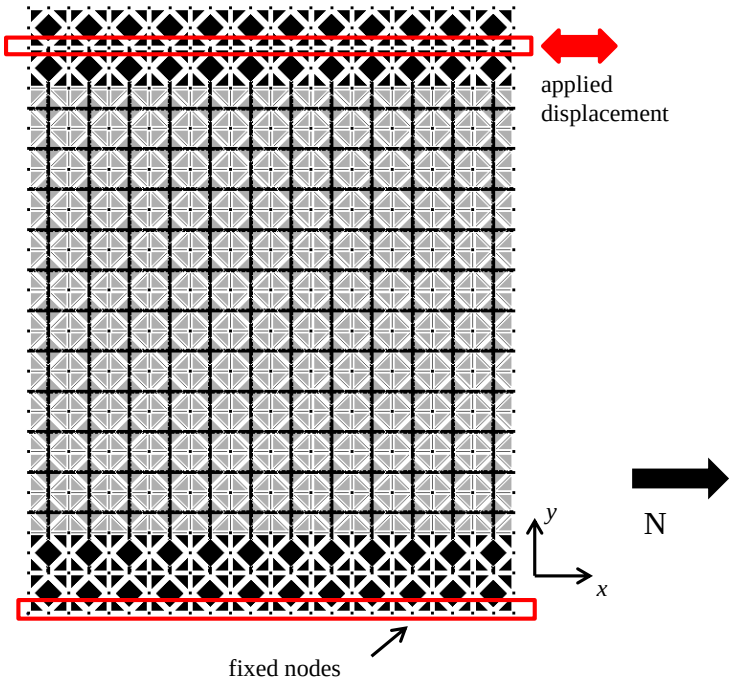

Figure 4.20 Finite element model of the wall tested by Ahmadi (2012)

The yield and tensile steel strengths of the vertical and horizontal reinforcing bars are 61 ksi and 99 ksi, respectively, as reported by Ahmadi (2012). The length of each beam element is chosen to be $0.50\,d_b$, to accurately predict the dowel force, as discussed in Section 4.5.1. The tensile strength of the masonry is set to be 10% of the compressive strength, which is 4.45 ksi. The Mode-I fracture energy used is 0.0004 kips/in., as in the previous simulation, and the value of the Mode-II fracture energy is assumed to be 10 times the value of the Mode-I fracture energy. The assumed initial friction coefficient of the masonry is 1.40, which is suggested by ACI 318-08 for concrete in monolithic construction, and the residual friction coefficient used is 1.0, reflecting the smoothened surface. Finally, the interfaces connecting the foundation of the specimen to the first course of masonry units have a constant and lower friction coefficient than the interfaces in the rest of the wall. This is because right after casting the foundation, the surface was smoothened with the use of a trowel. The value of the friction coefficient assumed is 0.60, which is suggested by ACI 318-08 for concrete placed against concrete surface which has not been intentionally roughened.

It has been reported by Ahmadi (2012) that flexural cracks were observed in the wall before the displacement of 0.1 in. was reached, while the first shear cracks appeared at a displacement of 0.2 in. The horizontal reinforcement in the fifth masonry course from the base of the wall developed the yield strength at a displacement of 0.6 in. Toe crushing was observed at 1.4 in. displacement on the south end of the wall, and at 1.6 in. on the north end. Four bars fractured on the north side of the wall.

In the analysis, a horizontal crack starts to form at the base of the wall in the first loading step. The activation of the dowel and frictional resistance initially prevents the

sliding of the wall, which is observed in later loading cycles due to the damage of the masonry grout by the dowel action. Another horizontal crack appears between the second and third course of masonry units from the base at a displacement of 0.24 in., while a larger diagonal shear crack starts right above the seventh course and propagates diagonally to the third course of masonry units from the north to the south at a displacement of about 0.49 in. This crack is shown in Figure 4.21. The load-vs.-displacement curves from the analysis and the test are plotted in Figure 4.22. When the maximum resistance is reached at a displacement of 0.6 in., the force provided by the dowel bars is 47 kips and the rest is contributed by the frictional resistance developed in the interfaces at the toes of the wall. The analysis stopped due to numerical instability when fracture occurred in the extreme bars of the north and of the south side. The final deformed configuration of the wall is shown in Figure 4.23 and can be compared to the test observations shown in Figure 4.24**.** It can be seen that the two main horizontal cracks near the base of the wall and above the second row of masonry units have been captured in the analysis. However, fewer shear cracks developed in the middle of the wall, as compared to the test.

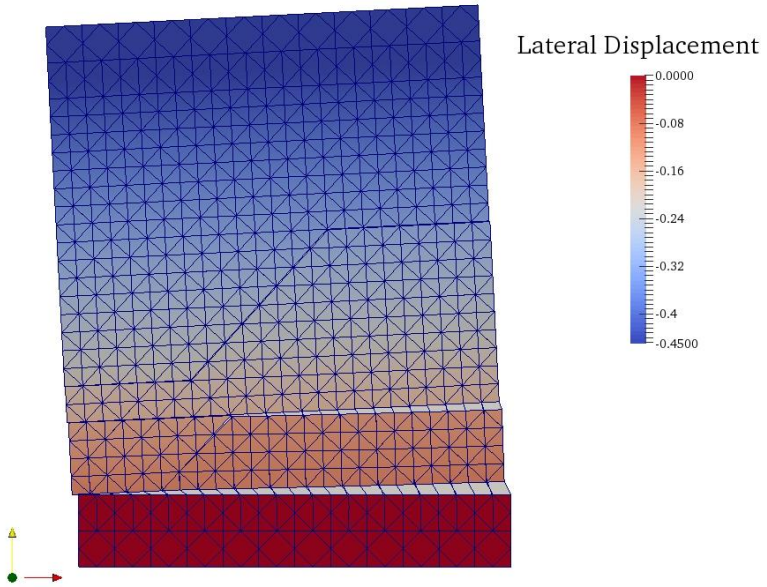

Figure 4.21 Shear crack starting above the seventh masonry course from the base of the wall (displacement amplified 15 times)

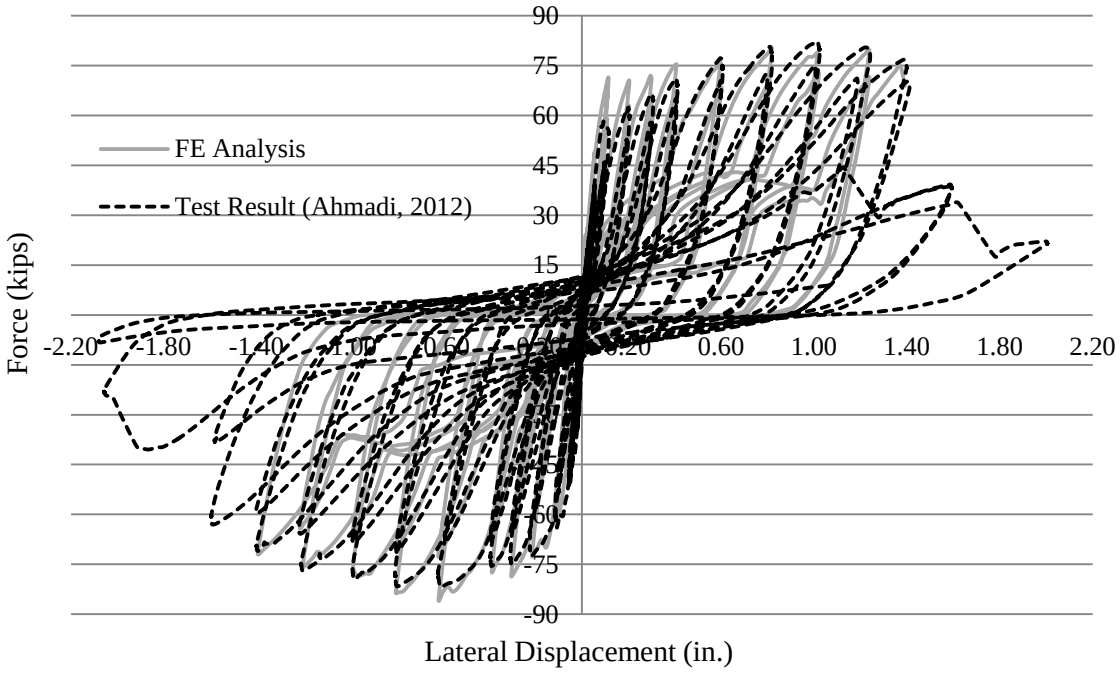

Figure 4.22 Force-vs.-horizontal displacement curves for the wall tested by Ahmadi (2012)

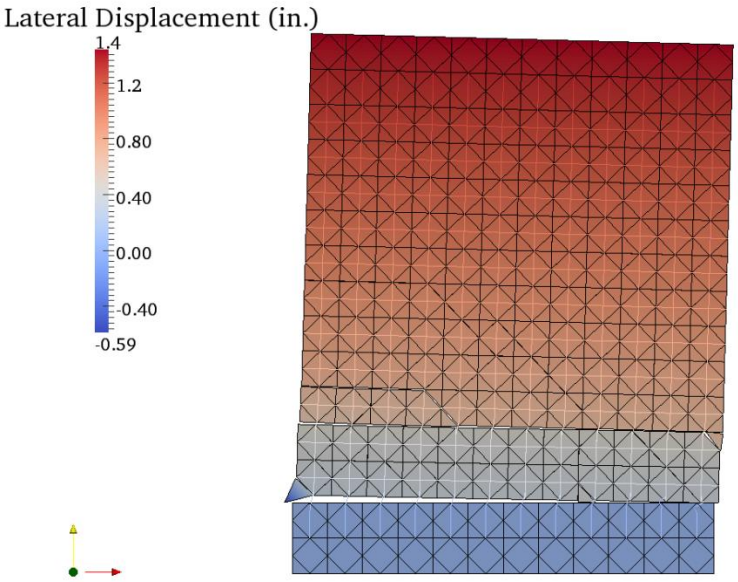

Figure 4.23 Deformed mesh at the end of the analysis (displacement amplified 3 times)

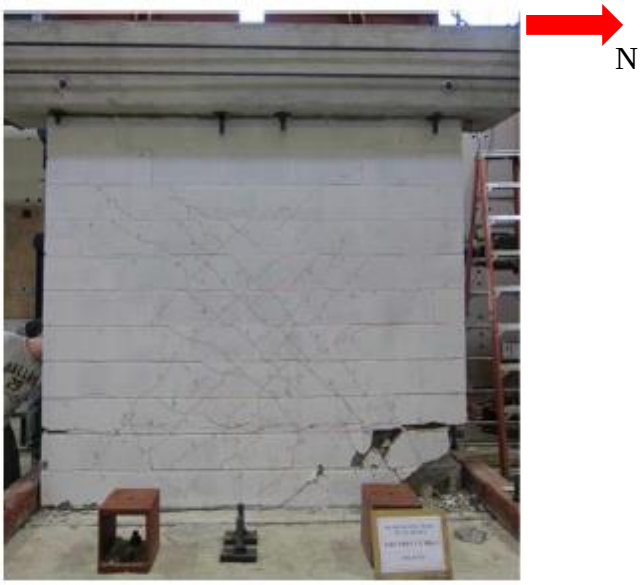

Figure 4.24 Damage at the end of the test of Ahmadi (2012)

4.6 Summary and Conclusions

In this chapter, a model developed to simulate the dowel action of a reinforcing bar crossing a crack is presented. The model is based on the formulation of Brenna et al.

(1990), which has been extended to account for the dowel behavior under cyclic loading. The proposed model is implemented in an interface model, which connects steel elements to concrete elements and allows the reinforcing bars and concrete to be represented by different mesh refinements. This special interface element allows a coarser mesh for concrete, and a fine mesh for the reinforcing bars to capture the curvature of a bar near a crack face in an accurate manner. The interface also models the bond-slip behavior of a bar. However, the bond slip and the dowel action are assumed to be independent.

Validation analyses have been conducted with dowel bars embedded in concrete blocks under monotonic and cyclic loading. The results are compared to experimental data and a good agreement has been observed. Finally, the model has been successfully used to analyze two fully grouted reinforced masonry shear walls. One was dominated by sliding shear failure at the wall base, while the other had a diagonal shear failure. The model is able to capture the failure mechanisms and predict their load capacity and stiffness degradation with good accuracy.

4.7 Acknowledgement of Publication

Part of this chapter is a reprint of the material that will appear in a technical report which will be submitted to the California Department of Transportation in 2016, Kottari, A., P. B. Shing, J. I. Restrepo, under the title "Design and Capacity Assessment of External Shear Keys in Bridge Abutments". The dissertation author will be the primary investigator and author of this report.

CHAPTER 5

EXPERIMENTAL STUDY OF ISOLATED EXTERNAL SHEAR KEYS IN BRIDGE ABUTMENTS

5.1 Description of Test Specimen

This chapter presents the experimental study conducted at UC San Diego to examine the behavior of isolated shear keys in bridge abutments. As discussed in previous chapters, a shear key should be so designed that its failure as a structural fuse should not incur significant repair costs. One way to achieve this goal is to introduce a construction joint between the shear key and the stem wall of the abutment so that the shear key is permitted to slide along the construction joint without causing damage in the stem wall when significant seismic forces occur. This method was first introduced in Caltrans Seismic Design Criteria (SDC) in 2010 and is referred to as isolated shear key method.

Several isolated shear key designs were evaluated with physical tests at UC San Diego (Megally et al. 2002, Borzogzadeh et al. 2006). The variables considered in these studies include the amount and arrangement of dowel bars crossing the construction joints from the stem walls to the shear keys, the amount of horizontal shear reinforcing steel in the stem walls and the construction joint preparation. A specimen with horizontally prestressed stem wall and isolated shear keys was also tested. While most of

the shear keys developed sliding failure, two tests had diagonal shear failure occurring in the stem wall (Megally et al. 2002, Borzogzadeh et al. 2006). One of the two had a smooth construction joint in which hydraulic oil was applied as a bond breaker, while the other had a rough joint. In both cases, the amount of horizontal reinforcement provided in the stem wall was not sufficient to prohibit diagonal shear failure.

To validate the analytical methods proposed in this study for calculating the diagonal shear strength of stem walls and the sliding resistance of isolated shear keys, and to further verify the formula proposed by Borzogzadeh et al. (2006) for calculating the ultimate shear resistance of isolated shear keys, an additional specimen consisting of one stem wall and two isolated shear keys was tested. This specimen had different amounts of dowel bars connecting the shear keys to the stem wall than those studied before. One shear key had a smooth construction joint, while the other had a rough joint. This specimen is the 7^{th} in the series tested at UC San Diego, considering all the previous specimens tested by Megally et al., Bauer, and Borzogzadeh et al., and it is thus identified as Specimen 7.

5.2 Design of Test Specimen

Specimen 7 consisted of a stem wall and two shear keys, termed 7A and 7B. The shear keys were completely isolated from the stem wall with a bond breaker, except for the vertical reinforcement crossing the construction joint. They had the same geometry and dimensions as the specimens tested in the past at UC San Diego. The specimen represented a 40%-scale model of the original prototype bridge, which is the South Ave

OC (Caltrans Br #39-0146). However, the length of the stem wall was much shorter than that required according to the scaling, but sufficient to develop the horizontal bars in the stem wall. Hence, the shorter length would not affect the performance of the shear keys.

In shear key 7A, 4 No. 5, Grade 60, vertical bars with a total cross-sectional area of 1.23 in^2, were used as dowels crossing the construction joint. Shear key 7A had a smooth construction joint, while 7B had a rough joint with the aggregate exposed to an amplitude of 3/16 in. The number of dowel bars and bar size for shear key 7A were selected such that it would extend the existing database to validate the analytical formulas proposed in this and prior studies for calculating the resistance of shear keys and stem walls (see Chapter 2 and Section 5.3), and to confirm whether the past experimental observation on the angle of kink (see Chapter 2) of the vertical dowel bars at the point of rupture is applicable to bars of a different size. The vertical dowel bars for shear key 7B consisted of 4 No. 4, Grade 60 bars. In both shear keys, the vertical dowel bars were anchored in the footing of the stem wall, and in the shear keys with 90 degree hooks satisfying the detailing requirements of the AASHTO LRFD Bridge Design Specifications (2010). All the vertical bars were placed in a single row, as shown in Figure 5.1 and Figure 5.2.

Side reinforcement consisting of No. 3 bars was placed near both faces of the stem wall and shear keys, according to the AASHTO LRFD Specifications, for temperature and shrinkage. The reinforcement was placed horizontally and vertically at 4.0 in. and 4.5 in. center-to-center spacing, respectively. The vertical side reinforcement did not cross the construction joints of the shear keys. Two No. 3 bars were placed near and parallel to the inclined face of each of the shear keys.

Shear keys 7A and 7B were designed to ensure that they would exhibit a sliding shear failure at the construction joints, instead of a diagonal shear failure in the stem wall. To prohibit diagonal shear failure, which was observed in past studies (Megally et al. 2002, Borzogzadeh et al. 2006), 6 No. 5, Grade 60, headed bars were placed at the top of the stem wall in two rows, as shown in Figure 5.1. Their quantity was determined with the strength prediction formulas proposed in this study (see Section 5.3). The reinforcement layout is shown in Figure 5.1 through Figure 5.4.

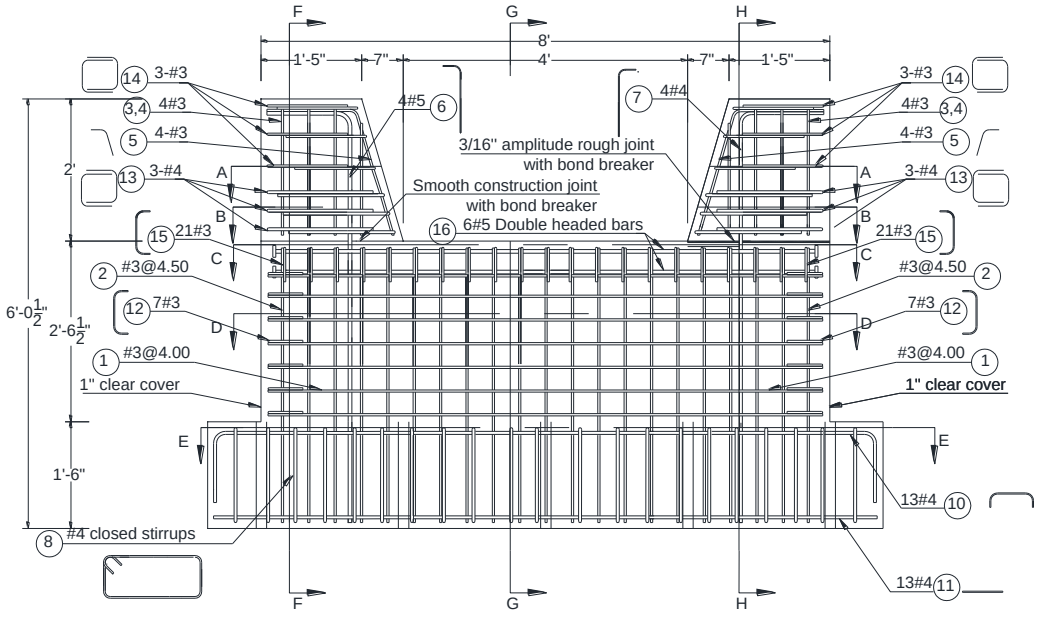

Figure 5.1 Elevation view of design details for Specimen 7

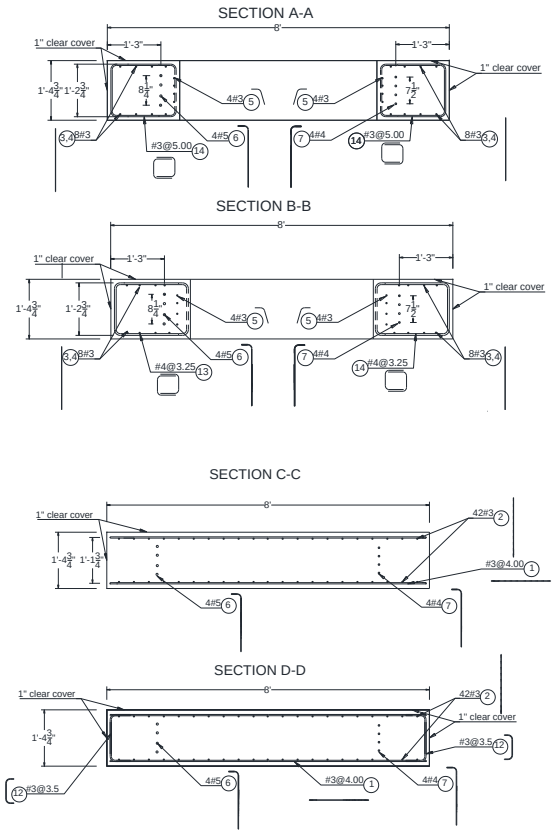

Figure 5.2 Sections A-A, B-B, C-C and D-D in design drawing for Specimen 7
(see Figure 5.1 for the location of the sections)

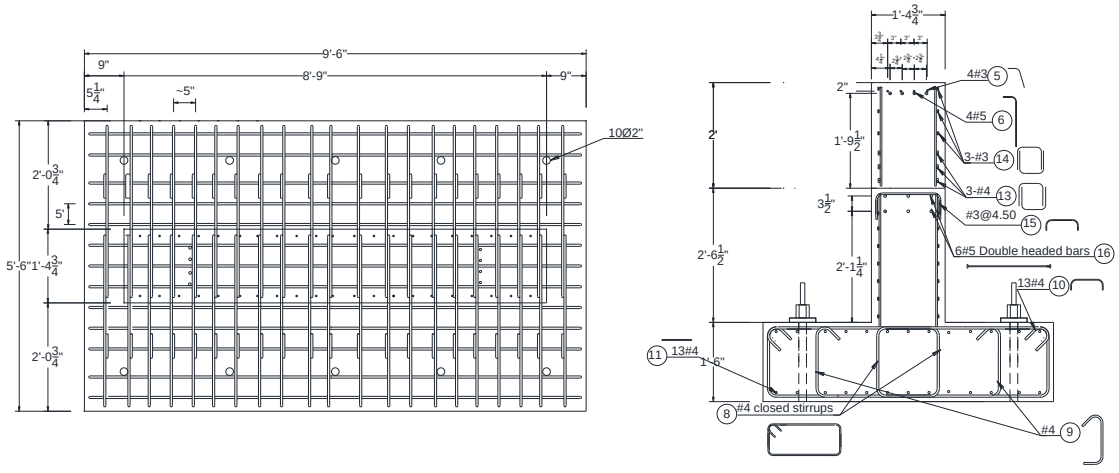

Figure 5.3 Sections E-E (left) and F-F (right) in design drawing for Specimen 7
(see Figure 5.1 for the location of the sections)

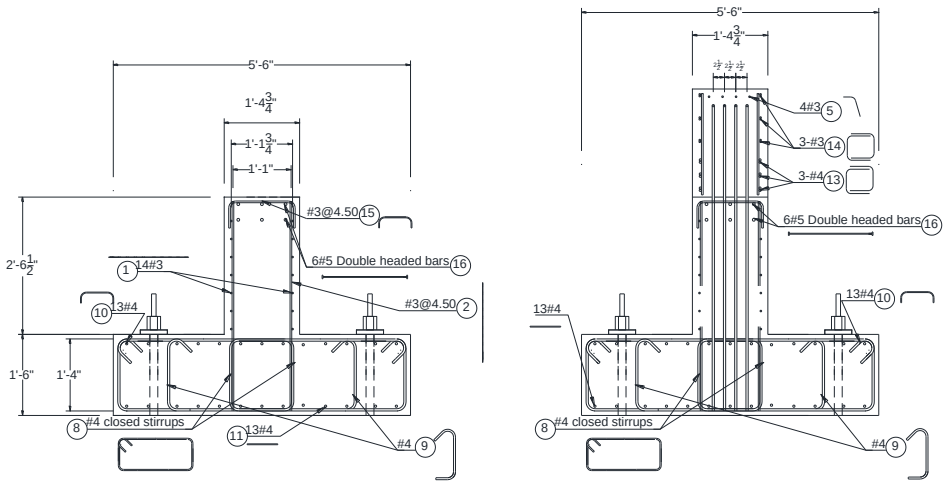

Figure 5.4 Sections G-G (left) and H-H (right) in design drawing for Specimen 7 (see Figure 5.1 for the location of the sections)

The concrete compressive strength on the day of the test was 4.54 ksi for the stem wall and 4.4 ksi for the shear keys. The compressive strengths were obtained from the tests of concrete cylinders, which were cast and kept in plastic molds till the day of testing. The slump of the concrete mix for the shear keys was measured to be 3.0 in. The reinforcement properties are summarized in Table 5.1.

Table 5.1 Measured strengths of reinforcing bars in Specimen 7

Reinforcement Description	Bar Size	f_y (ksi)	f_{su} (ksi)
Vertical and horizontal side reinforcement of the stem wall	No. 3	79.30	102.60
Horizontal shear reinforcement of the stem wall	No. 5	67.20	94.92
Vertical reinforcement of shear key 7A	No. 5	70.00	93.60
Vertical reinforcement of shear key 7B	No. 4	70.00	94.50

Specimen 7A had a smooth and flat construction joint. After casting the abutment stem wall, the surface was finished with a steel trowel, and three layers of water-based

bond breaker were applied. Each layer of bond breaker was applied two hours after the previous. The surface with applied bond breaker is shown in Figure 5.5.

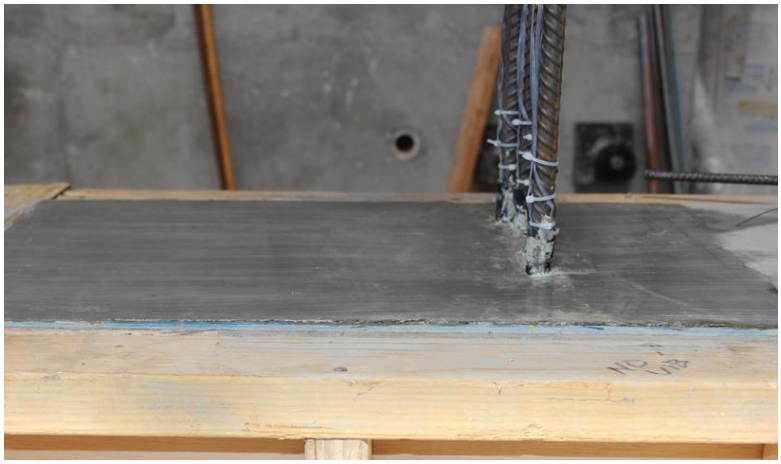

Figure 5.5 Smooth construction joint with bond breaker for shear key 7A

The surface of the construction joint for shear key 7B was intentionally roughened. The shear key was expected to ride over the protruding aggregate when sliding occurred. This would quickly engage the clamping force of the vertical dowel bars and increase the effective coefficient of friction for the surface.

The surface of shear key 7B was finished with a trowel and left to dry for one and one-half hour. Then, a thin cement layer in the surface was removed by applying pressured water and also with the aid of a brush to expose the aggregate to an amplitude of 3/16 in. No retarder was used in this procedure. The roughness of the surface was measured with a dial caliper at five locations across the surface. Three coats of water-based bond breaker were applied. The surface condition and the measurement of roughness are shown in Figure 5.6.

a) b)

Figure 5.6 Construction joint of shear key 7B: a) roughened surface; b) roughness measurement

5.3 Prediction of Load Resistance of Isolated Shear Keys

5.3.1 Diagonal Shear Strength of Stem Wall

Megally et al. (2002) have proposed an analytical method to calculate the diagonal shear strength of the stem wall. This method, presented in detail in Chapter 2, assumes that the total shear strength of the stem wall consists of the resistances contributed by the concrete and by the steel. For the former, a formula similar to that provided in ACI 318-08 for the shear strength of concrete was proposed. The shear resistance provided by the steel is calculated by considering the moment equilibrium of the forces developed by the vertical and horizontal reinforcement in the stem wall. While this method predicted well the shear resistance of the stem walls tested in the past, it ignores the influence of the vertical component of the force applied to the shear key and the equilibrium of forces in the horizontal and vertical directions.

To overcome the aforementioned deficiencies, a new analytical method is proposed in this study. This method is derived as follows by considering the equilibrium of the free body shown in Figure 5.7, which consists of a shear key and a portion of the stem wall that has been isolated from the rest of the wall by a diagonal crack. It is assumed that the horizontal shear reinforcement of the stem wall has reached the ultimate tensile strength, f_{su}, while the remaining reinforcement has reached the yield strength, f_y. Thus, the forces developed by the steel are calculated as follows:

$$\begin{aligned} F_{t,s} &= A_{t,s} \cdot f_{su} \\ F_{i,h} &= A_{i,h} \cdot f_y \\ F_{j,v} &= A_{j,v} \cdot f_y \end{aligned} \tag{5.1}$$

in which $F_{t,s}$ is the force developed by the horizontal shear reinforcing bar *t* in the stem wall, with area $A_{t,s}$, and $F_{i,h}$ and $F_{j,v}$ are the forces of the horizontal reinforcing bar *i* and vertical reinforcing bar *j*, respectively, with the respective areas $A_{i,h}$ and $A_{j,v}$.

The external load applied to the shear key has a horizontal component, V_w, and a vertical component P_w. If the friction on the inclined face of the shear key is assumed to be zero, the external load has to be perpendicular to the surface, and thus V_w and P_w are related by the following geometric relation:

$$P_w = V_w \cdot \tan\beta \tag{5.2}$$

The length of the region in compression at the toe of the stem wall is denoted by α_c. It is assumed that the compressive stress in this region is uniform and equal to $0.85 f_c'$, similar to a concrete section in bending. The forces developed in the compression

region are V_c and C_c, which act in the horizontal and vertical direction, respectively. The vertical force is thus calculated as:

$$C_c = 0.85 \cdot f_c' \cdot d \cdot \alpha_c \tag{5.3}$$

in which d is the width of the shear key. Vertical bars located in the compression zone are assumed to have reached their yield strength in compression.

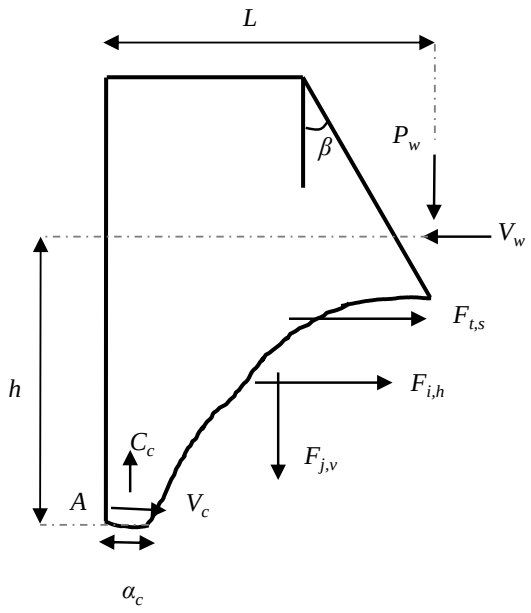

Figure 5.7 Free-body diagram for diagonal shear resistance calculation

The procedure for calculating the diagonal shear resistance of the stem wall, V_w, is as follows:

1. Assume a compression zone length α_c .

2. Based on the moment equilibrium of the free body about the toe of the stem wall (point *A* in Figure 5.7) and Equation (5.2), calculate V_w:

$$V_w = \frac{\sum_{i=1}^{\#hor.\ bars} F_{i,h} \cdot l_{i,h} + \sum_{j=1}^{\#vert.\ bars} F_{j,v} \cdot l_{j,v} - C_c \cdot \alpha_c \cdot 0.5 + \sum_{t=1}^{\#hor.\ shear\ bars} F_{t,s} \cdot l_{t,s}}{h - L \cdot \tan\beta} \tag{5.4}$$

in which $l_{i,h}$ is the vertical distance of horizontal bar *i* from point *A*, $l_{j,v}$ is the horizontal distance of vertical bar *j* from point *A*, and $l_{t,s}$ is the vertical distance of horizontal shear reinforcing bar *t* in the stem wall from point *A*.

3. Calculate the vertical force P_w:

$$P_w = V_w \cdot \tan\beta$$

4. Check if equilibrium in the vertical direction is satisfied.

5. If equilibrium in the vertical direction is not satisfied, a new compression zone length α_c is selected and steps (2-4) are repeated. If the equilibrium is satisfied, then the procedure can stop and the value of V_w calculated is the final value. It should be noted that in this method, the value of V_c need not be calculated.

5.3.2 Sliding Shear Strength of Shear Key

Sliding shear failure has been observed in specimens with isolated shear keys tested in the past, as summarized in Chapter 2. Based on past experimental observations, the sliding shear resistance of an isolated shear key can be associated with two states. One is the shear resistance at first sliding and the second is the ultimate sliding shear resistance right before the rupture of the dowel bars. They are denoted by V_{slid} and V_u, respectively. Right after V_u has been reached, the vertical dowel bars rupture and the load resistance drops significantly. The peak sliding shear resistance depends on the preparation of the construction joint, and can be either V_u or V_{slid}. If a significant cohesive force develops in the sliding surface, which was the case for shear key 5A as

presented in Chapter 2, it is more likely that V_{slid} is larger than V_u. If bond breaker is applied on the construction joint, as for shear key 5B discussed in Chapter 2, the peak resistance will most likely be the ultimate shear sliding resistance, V_u. The resistances associated with the two states for shear keys 5A and 5B are shown in Figure 5.8 and Figure 5.9.

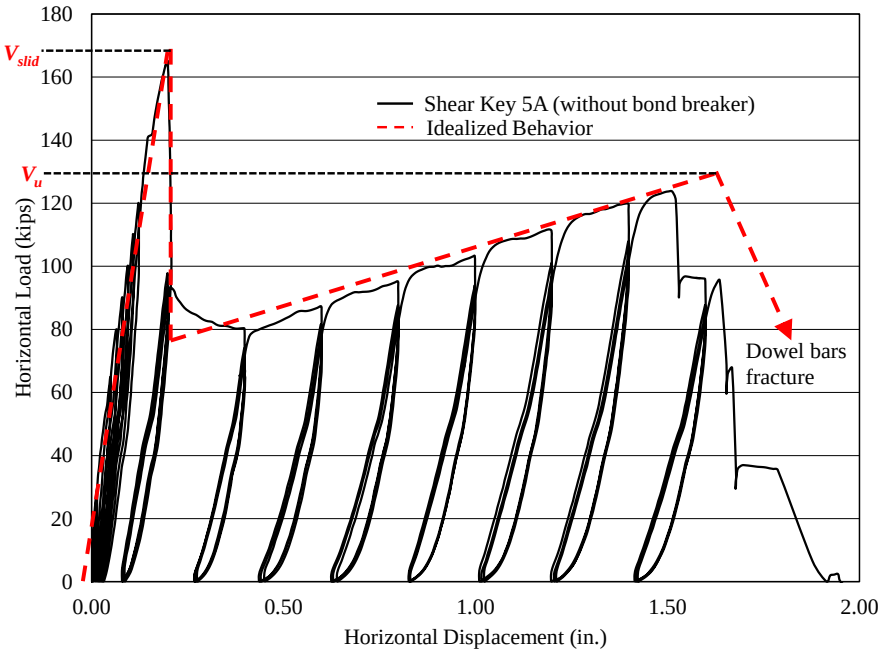

Figure 5.8 Idealized and experimental behavior of isolated shear keys without bond breaker

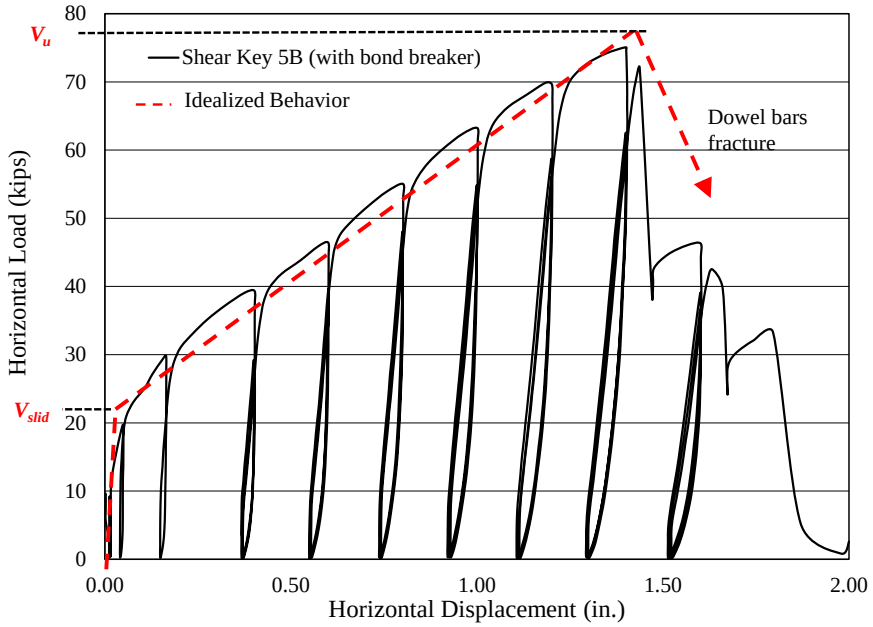

Figure 5.9 Idealized and experimental behavior of isolated shear keys with bond breaker

The roughness of the construction joint also influences the behavior of the shear key. For a smooth construction joint, the sliding resistance of the shear key is mainly provided by the dowel action. The shear resistance, F_d, due to the dowel action of a bar can be calculated with the following equation proposed in Chapter 3:

$$F_d = \sqrt{2 \cdot M_{pl} \cdot f_{cb} \cdot d_b}$$
$$M_{pl} = \frac{f_y \cdot d_b^3}{6} \tag{5.5}$$

in which M_{pl} is the plastic moment capacity of the bar, and the strength of concrete, f_{cb}, can be calculated as follows:

$$f_{cb} = a \cdot f_c'^{1.2}$$
$$a = 2.0 + \frac{0.5}{d_b} \tag{5.6}$$

in which f_c' is the uniaxial concrete compressive strength in ksi, d_b is the bar diameter in in and f_{cb} is in ksi/in.

The free-body diagram of a shear key, isolated from the stem wall, is shown in Figure 5.10. It is assumed that the friction coefficient is zero on the inclined face of the shear key. Thus, the external load applied to the shear key has to be perpendicular to its inclined face and can be resolved into a horizontal component, denoted by V_{slid}, and a vertical component, denoted by P_{slid}, which are geometrically related as follows:

$$P_{slid} = V_{slid} \cdot \tan\beta \tag{5.7}$$

in which β is the angle of the inclined face of the shear key with respect to a vertical plane, as shown in Figure 5.10. The friction coefficient of the horizontal sliding surface of the shear key is denoted by μ_f, and the cohesive force is denoted by *T*.

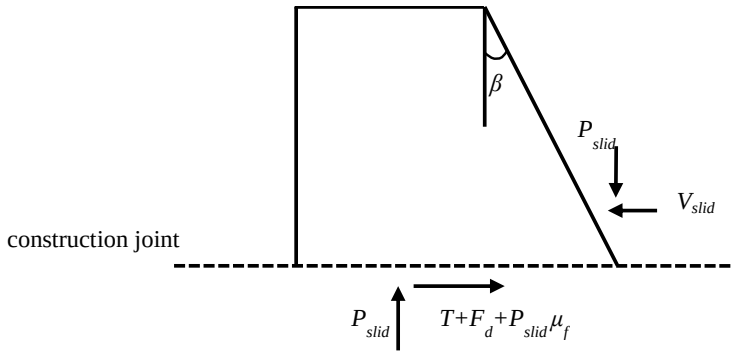

Figure 5.10 Free-body diagram of shear key with smooth construction joint for the calculation of shear resistance at first sliding

Based on the equilibrium of horizontal and vertical forces in the free-body diagram shown in Figure 5.10 and Eq. (5.7), the shear resistance at first sliding, V_{slid}, can be calculated as follows:

$$V_{slid} = \frac{T + F_d}{(1 - \mu_f \cdot \tan\beta)} \tag{5.8}$$

If the construction joint surface is rough, the shear key will experience a significant vertical uplift when it starts to slide. Thus, the vertical dowel bars will elongate and reach the yield strength, f_y.The axial forces developed by the vertical dowel bars introduce additional clamping forces to the construction joint. To calculate the sliding shear resistance, V_{slid} , the horizontal and vertical equilibrium of the forces in the free-body diagram of the shear key, shown in Figure 5.11, are considered. This results in:

$$V_{slid} = \frac{T + \mu_f \cdot F_s}{\left(1 - \mu_f \cdot \tan\beta\right)} \tag{5.9}$$

in which β is the angle of the inclined face of the shear key with respect to a vertical plane, *T* is the cohesive force, F_s is the yield force of the vertical dowel bars, and μ_f is the coefficient of friction of the rough construction joint. It is assumed that the friction coefficient for the inclined face of the shear key is zero. Hence, Eq. (5.7) applies here as well. In Eqs. (5.8) and (5.9), if bond breaker is applied on the construction joint, then *T* can be taken to be zero.

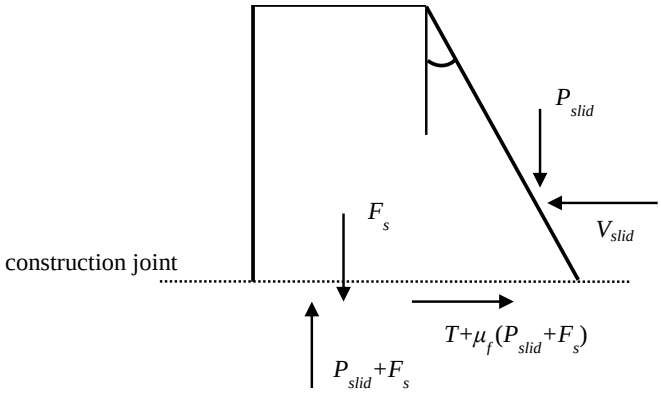

Figure 5.11 Free-body diagram of shear key with a rough joint for the calculation of shear resistance at first sliding

When the shear key has slid significantly on the stem wall, the behavior of shear keys with smooth and rough joints will be governed by the same resisting mechanisms. The ultimate shear resistance can be calculated by the method proposed by Borzogzadeh et al. (2006), as presented in Chapter 2. This method has been adopted by the Caltrans Seismic Design Criteria. It assumes that the vertical dowel bars has reached their ultimate tensile strength, f_{su}, and the dowel bars has been bent with an angle of inclination of 37 degrees with respect to a vertical plane when the ultimate shear resistance of the shear key, V_u, has been reached. It has been shown in Chapter 3 that the angle of kink is practically independent of the bar size and the concrete strength. Thus, the angle of kink is assumed to be 37 degrees in this study, as measured by Borzogzadeh et al. (2006). Based on the equilibrium of the horizontal and vertical forces, shown in Figure 5.12, the following equation can be obtained:

$$V_u = \frac{\mu_f \cdot \cos a_k + \sin a_k}{1 - \mu_f \cdot \tan \beta} A_{vs} \cdot f_{su} \tag{5.10}$$

in which a_k is the angle of kink of the vertical dowel bar with respect to the vertical axis, μ_f is the coefficient of friction of the construction joint, f_{su} is the ultimate tensile strength of the vertical dowel bars with a total area of A_{vs}.

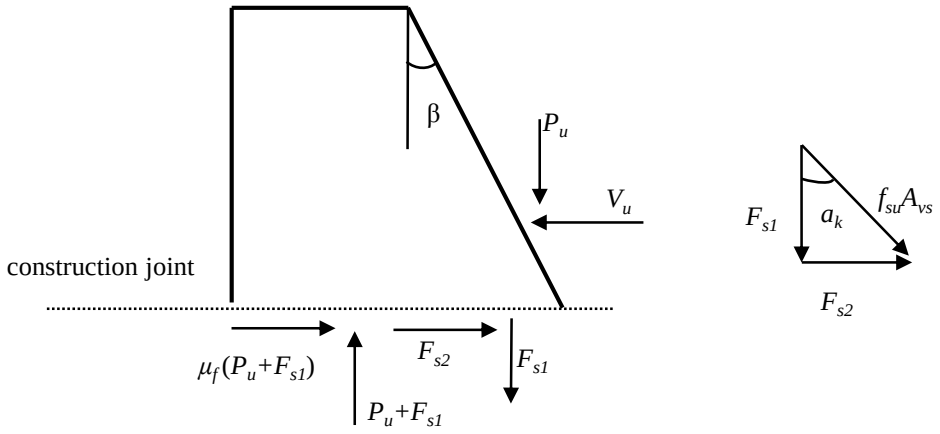

Figure 5.12 Free-body diagram of shear key for the calculation of ultimate shear resistance

5.3.3 Calculation of Load Resistance of Shear Keys 7A and 7B

The calculations for the expected sliding shear resistances of shear keys 7A and 7B are presented in this section. The expected material strengths assumed are:

- Yield strength of vertical dowel bars and side reinforcement f_y = 68 ksi
- Ultimate tensile strength of horizontal shear reinforcement f_{su} = 105 ksi
- Coefficient of friction μ_f is taken to be 0.36 for shear key 7A (smooth joint) and 1.00 for shear key 7B (rough joint)
- Concrete strength f_c' = 5.0 ksi

The friction coefficient for smooth joints with bond breaker was estimated from the test data of Borzogzadeh et al. (2006). For rough joints, the coefficient of friction was assumed to be 1.0, based on the recommendations in ACI 318-08 and the AASHTO LRFD Bridge Design Specifications for concrete placed against concrete with intentionally roughened surface. The yield strength of the steel was based on the expected properties for Grade 60 bars suggested in the Caltrans Seismic Design Criteria (SDC, Version 1.6, Section 3.2.3), while the ultimate tensile strength of the steel was based on that measured by Borzogzadeh et al. (2006), which is higher than that suggested in the SDC. The expected concrete compressive strength was taken to be equal to 5.0 ksi.

The shear resistance at first sliding, V_{slid}, was calculated with Eqs. (5.8) and (5.9) for shear keys 7A and 7B, respectively, and the ultimate sliding shear resistance, V_u, was calculated with Eq. (5.10). The results are presented in Table 5.2. Since bond breaker was to be applied in the construction joints of the two shear keys, the cohesive force in Eqs. (5.8) and (5.9) was assumed to be zero. From these calculations, the peak shear resistance of each shear key was identified as the larger of the two.

To avoid diagonal shear failure in the stem wall, the stem wall was sufficiently reinforced so that the peak shear resistance of shear keys 7A and 7B would be lower than the diagonal shear resistance of the stem walls. The diagonal shear resistance of the stem wall was calculated with the procedure described in Section 5.3.1, and the values of the parameters used and the calculated strengths are summarized in Table 5.3 and Table 5.4. The strengths of the stem wall are compared to the peak strengths of the shear keys in Table 5.5. It can be seen that the stem wall was capacity protected with a good margin. It

should be noted that the strength of the stem wall is affected by the amount of the vertical reinforcement, based on the model presented in Section 5.3.1. For this reason, the strengths of the stem wall are different for the two ends, even though the specimen had the same horizontal reinforcement along the entire wall.

Table 5.2 Calculated sliding shear resistances of shear keys in Specimen 7

Shear Key	Shear Resistance at First Sliding (kips)	Ultimate Sliding Shear Resistance (kips)
7A	34	128
7B	75	163

Table 5.3 Diagonal shear resistance of stem wall in shear key 7A

Shear Key	Bars	Number of bars crossing diagonal crack	Total bar area (in^2)	Distance of bars, $l_{i,h}$, $l_{j,v}$, or $l_{t,s}$ (in.)	Stress in bars (ksi)	α_c (in.)	Diagonal Shear Resistance (kips)
7A	Vertical side bars	2	0.22	3.5	68	3.10	286
	Vertical side bars	2	0.22	8.0			
	Vertical side bars	2	0.22	12.5			
	Vertical side bars	2	0.22	17.0			
	Vertical dowel bars	4	1.23	15.0			
	Horizontal shear reinforcement	3	0.92	29.0	105		
	Horizontal shear reinforcement	3	0.92	25.5			
	Horizontal side bars	2	0.22	25.5	68		
	Horizontal side bars	2	0.22	21.5			
	Horizontal side bars	2	0.22	17.5			
	Horizontal side bars	2	0.22	13.5			
	Horizontal side bars	2	0.22	9.5			
	Horizontal side bars	2	0.22	5.5			
	Horizontal side bars	2	0.22	1.5			

Table 5.4 Diagonal shear resistance of stem wall in shear key 7B

Shear Key	Bars	Number of bars crossing diagonal crack	Total bar area (in^2)	Distance of bars, $l_{i,h}$, $l_{j,v}$, or $l_{i,s}$ (in.)	Stress in bars (ksi)	α_c (in.)	Diagonal Shear Resistance (kips)
7B	Vertical side bars	2	0.22	3.5	68	2.65	278
	Vertical side bars	2	0.22	8.0			
	Vertical side bars	2	0.22	12.5			
	Vertical side bars	2	0.22	17.0			
	Vertical dowel bars	4	0.785	15.0			
	Horizontal shear reinforcement	3	0.92	29.0	105		
	Horizontal shear reinforcement	3	0.92	25.5			
	Horizontal side bars	2	0.22	25.5	68		
	Horizontal side bars	2	0.22	21.5			
	Horizontal side bars	2	0.22	17.5			
	Horizontal side bars	2	0.22	13.5			
	Horizontal side bars	2	0.22	9.5			
	Horizontal side bars	2	0.22	5.5			
	Horizontal side bars	2	0.22	1.5			

Table 5.5 Comparison of horizontal load resistance of stem wall and peak horizontal resistance of shear keys in Specimen 7

Shear Key	Diagonal Shear Resistance of Stem Wall (kips)	Peak Sliding Shear Resistance of Shear Key (kips)
7A	286	128
7B	278	163

5.4 Test Setup

The test setup consisted of the test specimen, a steel loading beam and two hold-down frames, placed on the two sides of the specimen parallel to the stem wall. The specimen was secured to the lab floor with post-tensioned rods. A total of ten rods were

used, with each post-tensioned to 150 kips. This force was sufficient to avoid sliding along the lab floor and to prevent uplift of the specimen during the test.

The load was applied to the shear keys with a steel loading beam, as shown in Figure 5.13, which was connected to two 220-kip load capacity, 48-inch stroke actuators. The beam was prevented from moving upward by two hold-down frames, assembled with hollow steel sections. The frames were post-tensioned with 4 rods (2 rods for each) to the lab floor. The rods were hand-tightened and the initial strain was negligible. Figure 5.14 shows a hold-down frame, the vertical rods, and the steel loading beam in their final position. The friction between the loading beam and the frames was minimized with the use of PTFE (Polytetrafluorethylene-Teflon) bearings and grease.

Figure 5.13 Steel beam

a)

b)

Figure 5.14 Test setup: a) north view; b) south view

5.5 Instrumentation of Test Specimen

The specimen was instrumented to monitor the strains in the reinforcing bar and the deformation of the specimen. Electrical resistance strain gages were attached to the longitudinal and transverse reinforcing bars. A total of 92 strain gages were installed. The locations and numbering of the strain gages are shown in Figure 5.15 through Figure 5.20. The strain gage numbers are preceded by an S.

The positions of the strain gages were selected to measure strains in the bars at the potential locations of main cracks in the stem wall. Those cracks included the horizontal construction joints between the shear keys and the stem wall as well as possible diagonal cracks developing in the stem wall. The latter was however unlikely to be significant based on the design calculations. Since the vertical dowel bars could bend as sliding increased, strain gages were placed on the two opposite sides of the bars. All the vertical dowel bars had 4 strain gages each; 2 strain gages were 1.0 in. above the construction joint and 2 gages 1.0 in. below the joint.

In addition, linear potentiometers were installed external to the specimen to measure the horizontal displacements along the height of each shear key, as well as the expected uplift of the shear key with respect to the stem wall. Two string potentiometers were used to measure the horizontal displacement of the loading beam, and a tilt meter was attached to each of the shear keys to measure in-plane rotation. The strain in each of the vertical post-tensioned bars for the hold-down steel frames was monitored with a strain gage. These strain readings were used to calculate the vertical reaction force exerted on the shear key through the loading beam. The positions and numbering of the external transducers are shown in Figure 5.21 through Figure 5.23. In these figures, the

linear potentiometer numbers are preceded by an L, while those of the string potentiometers and tilt meters are preceded by SP and TM, respectively.

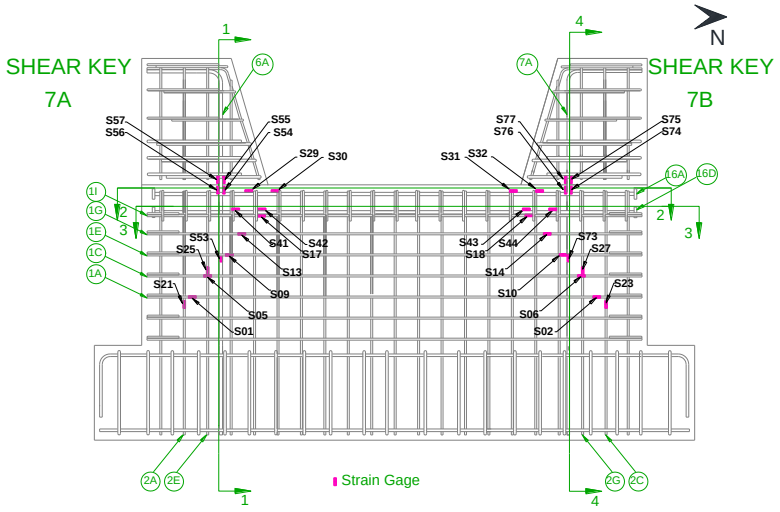

Figure 5.15 Strain gages located on the east side of Specimen 7

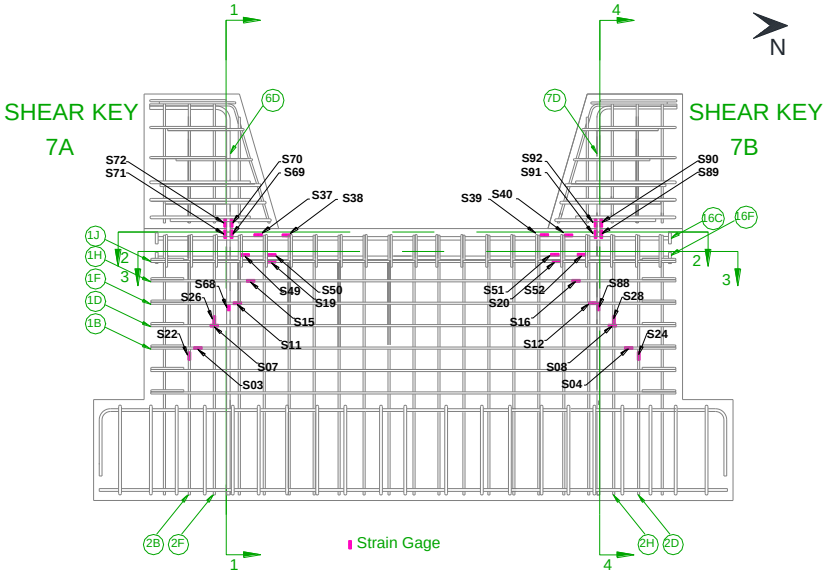

Figure 5.16 Strain gages located on the west side of Specimen 7

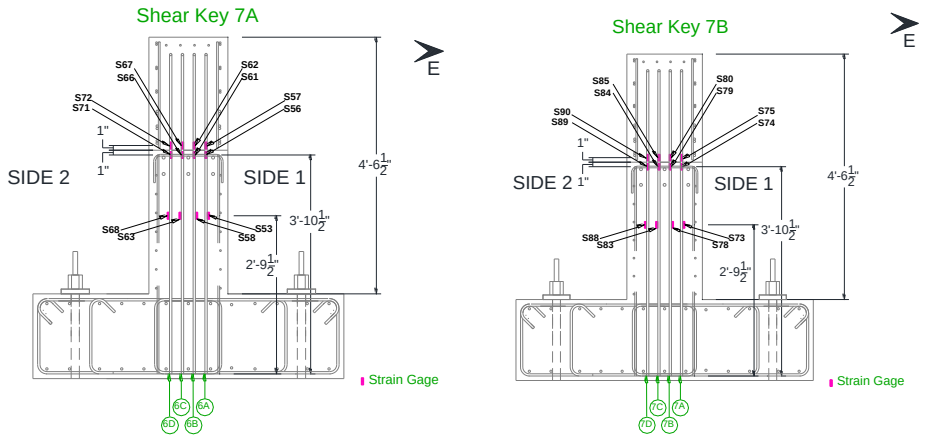

Figure 5.17 Sections 1-1 (left) and 4-4 (right) for Specimen 7
(see Figure 5.16 for the location of the sections)

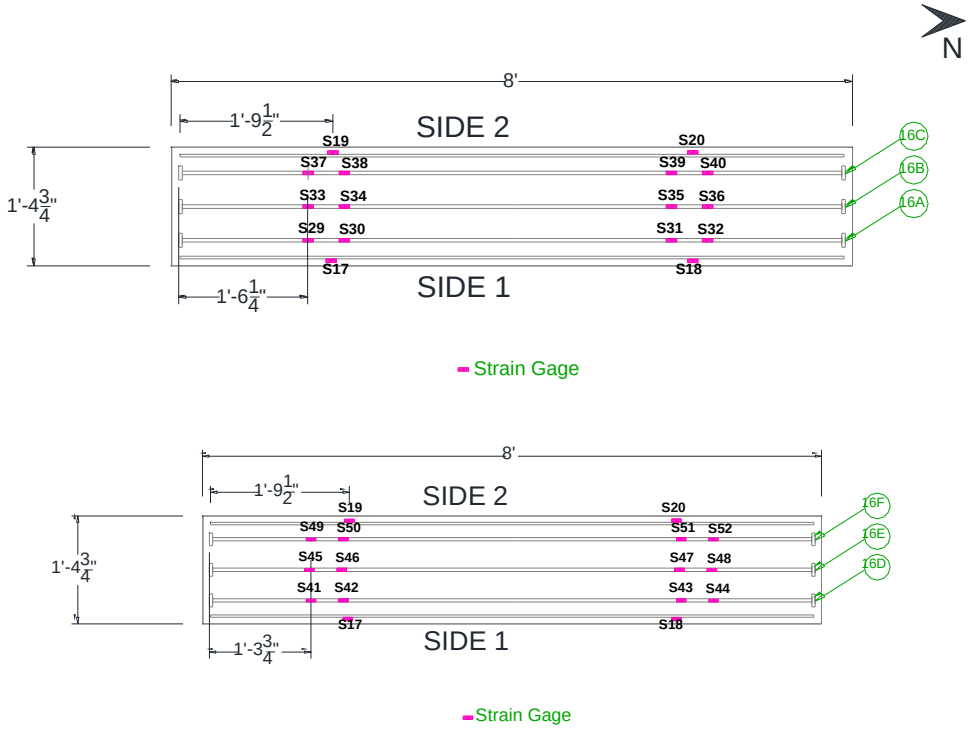

Figure 5.18 Sections 2-2 (top) and 3-3 (bottom) for Specimen 7
(see Figure 5.16 for the location of the sections)

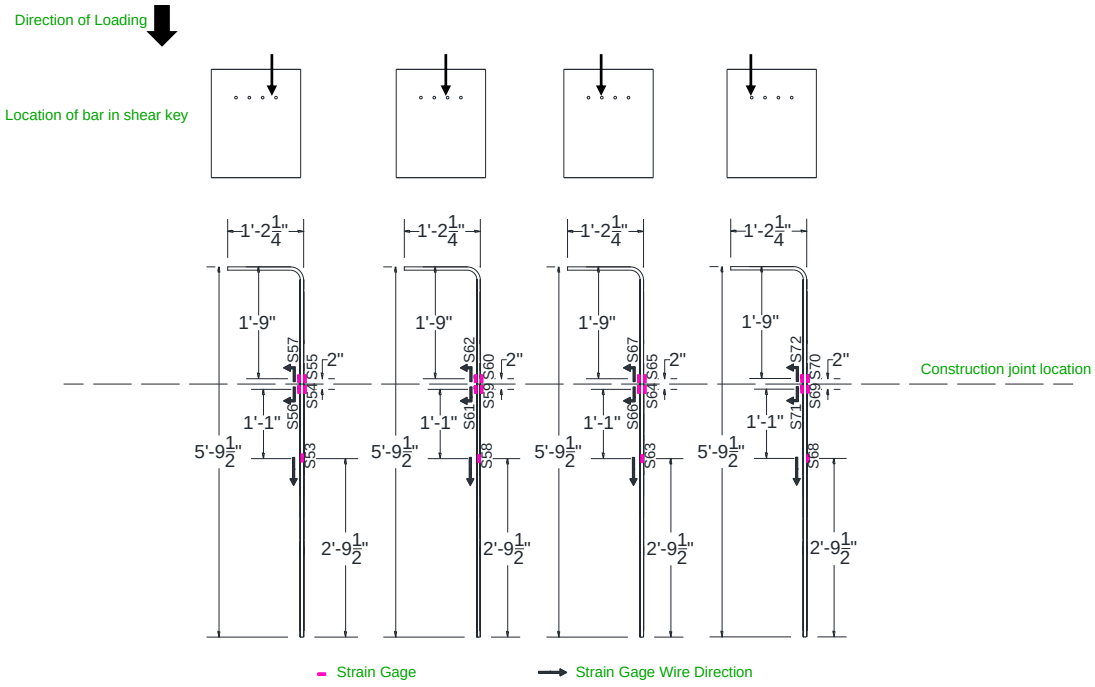

Figure 5.19 Strain gages on the vertical dowel bars of shear key 7A

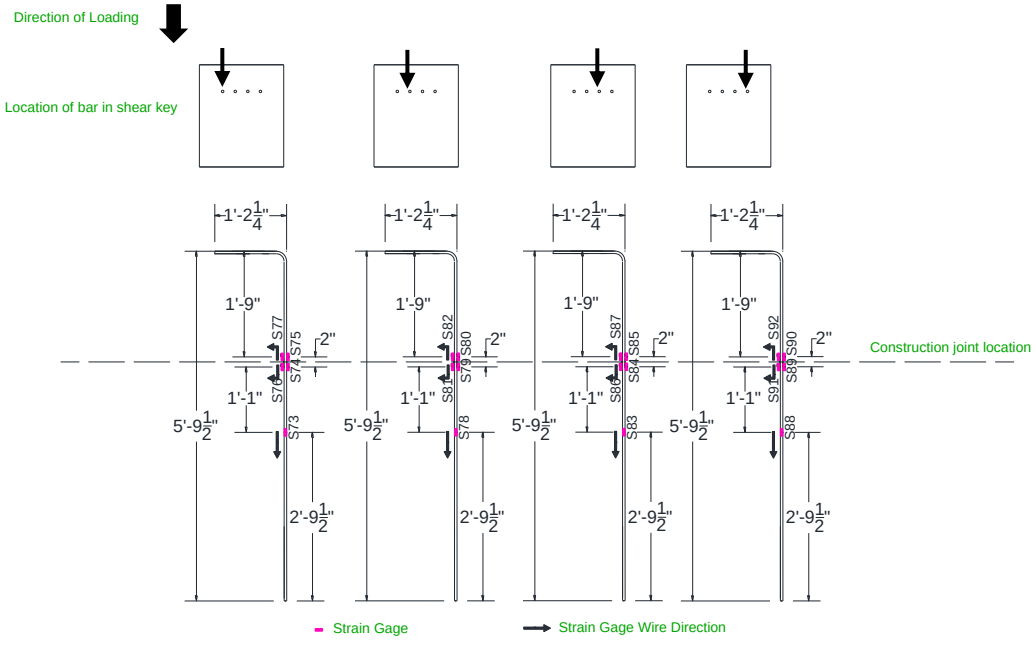

Figure 5.20 Strain gages on the vertical dowel bars of shear key 7B

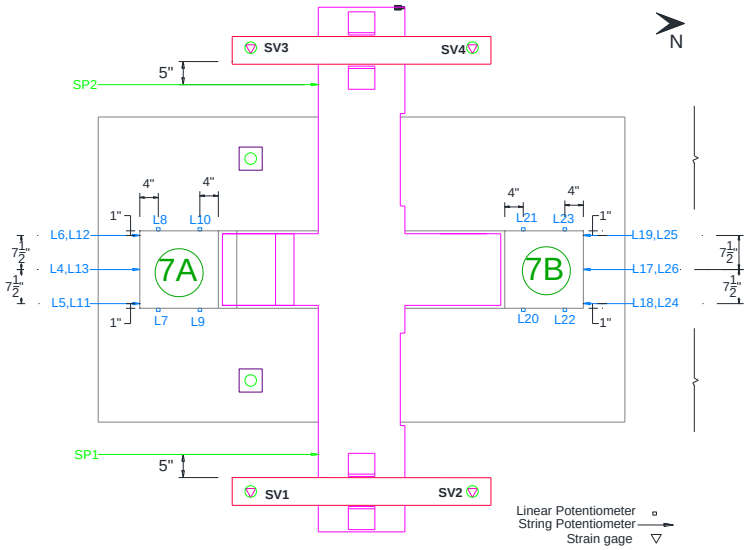

Figure 5.21 Plan view of external instrumentation for Specimen 7

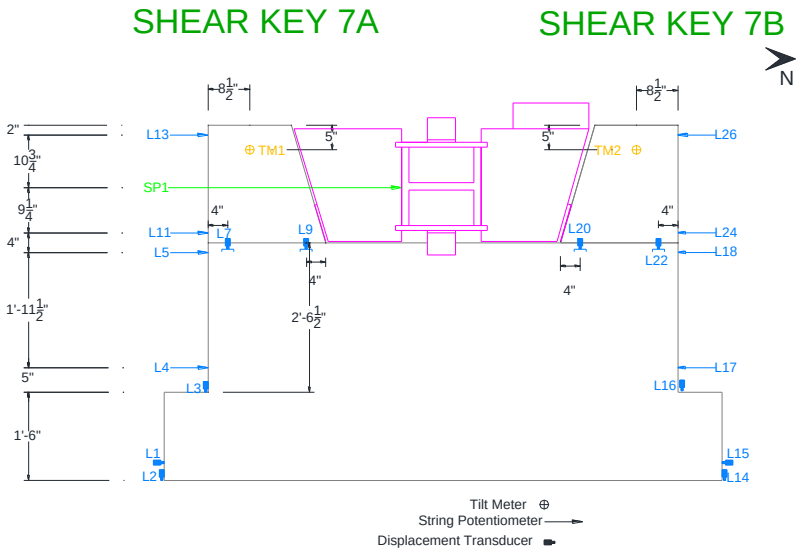

Figure 5.22 External instrumentation located on the east side of Specimen 7

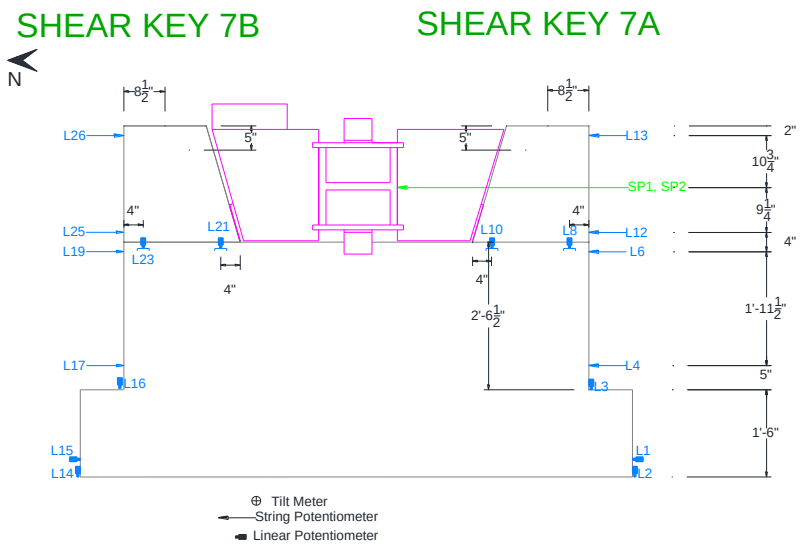

Figure 5.23 External instrumentation located on the west side of Specimen 7

5.6 Loading Protocols and Test Results

5.6.1 Shear Key 7A

Shear key 7A was on the south side of the stem wall. The loading protocol for the shear key consisted of incremental loading, unloading, and reloading, with the target loads and displacements shown in Table 5.6. The shear key was initially loaded in force control to 30 kips in increments of 10 kips. Then, it was loaded in displacement control up to failure, which occurred at 2.0 in. displacement. The displacement was based on the average of the readings from displacement transducers L11 and L12, located on the south side of the shear key, as shown in Figure 5.21 through Figure 5.23. The specimen was unloaded 5 times at 20 kips load, and at displacements of 0.50 in., 1.00 in., 1.50 in. and 1.80 in., respectively, to obtain the unloading stiffness.

Table 5.6 Loading protocol for shear key 7A

Step	Control	Target Load/Displacement
1-3	Load	30 kips with 10 kip increments
4-23	Displacement	2.00 in. with 0.10 in. increments

The shear key slid on the horizontal construction joint. The first crack in the stem wall was observed on the east face of the wall at a horizontal load of 70 kips. It was located near one of the vertical dowel bars and propagated with a small inclination towards the base of the wall. A similar crack was observed on the west face at a horizontal load of 107 kips. At that load, minor spalling of concrete was observed on the south side of the shear key at the elevation of the construction joint. At a horizontal load of 137 kips, a diagonal crack initiated from the top of the stem wall. The crack initiation point was 12 in. away from the toe of the shear key. The width of all diagonal cracks remained small throughout the test. The cracks on the east face are shown in Figure 5.24 and those on the west face are shown in Figure 5.25.

Figure 5.24 First two cracks observed on the east face of shear key 7A

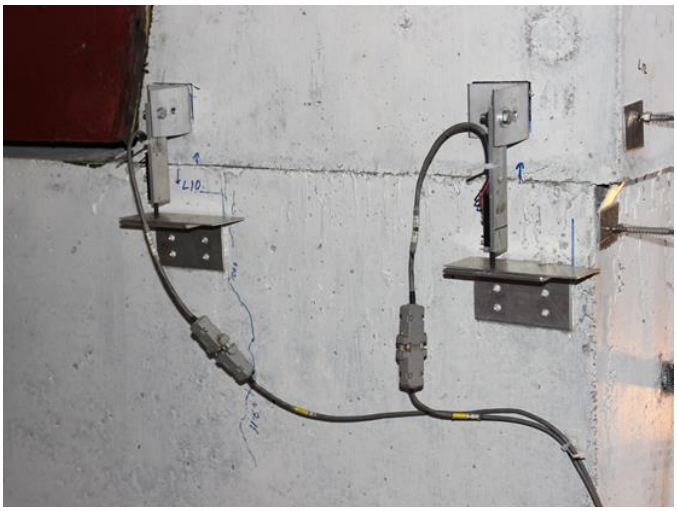

Figure 5.25 First crack on the west face of shear key 7A

The horizontal load resistance of the shear key is plotted against its horizontal displacement in Figure 5.26. The horizontal displacement plotted is the averaged readings of linear potentiometers L11 and L12, whose locations are shown in Figure 5.21 and Figure 5.22. The maximum load resistance of 145 kips was reached at a displacement of 1.60 in., as shown in the figure. Right after the maximum load resistance was reached, the vertical dowel bars started to fracture leading to a sudden substantial decrease of the load resistance of the shear key. At the end of the test, the shear key had experienced an uplift of about 0.08-0.10 in. with respect to the stem wall. This was measured by a crack gage, as shown in Figure 5.27.

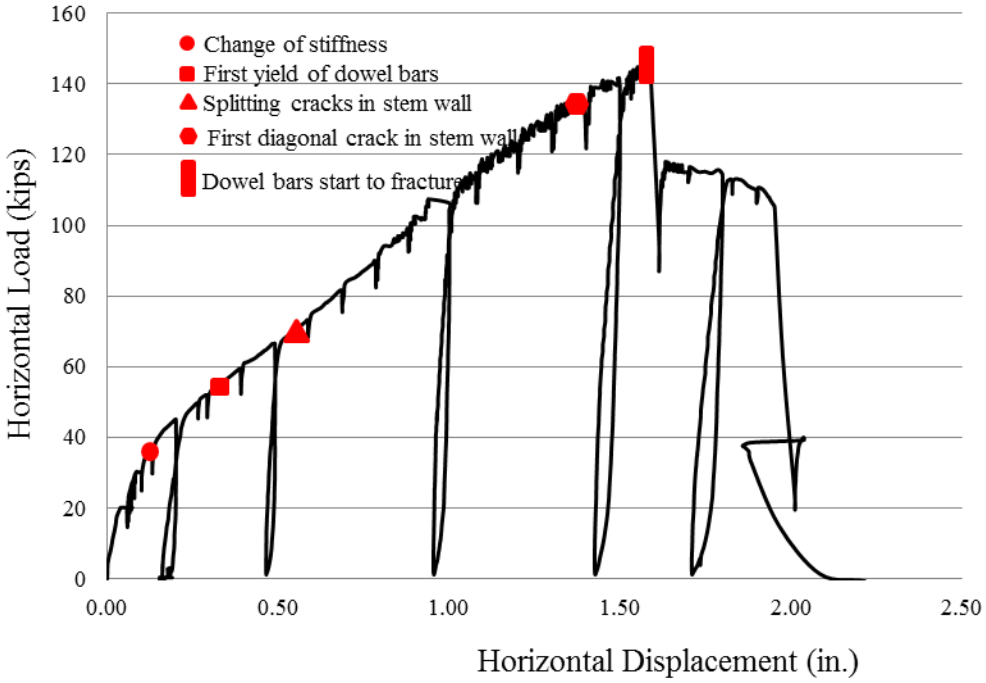

Figure 5.26 Horizontal load-vs.-horizontal displacement for shear key 7A

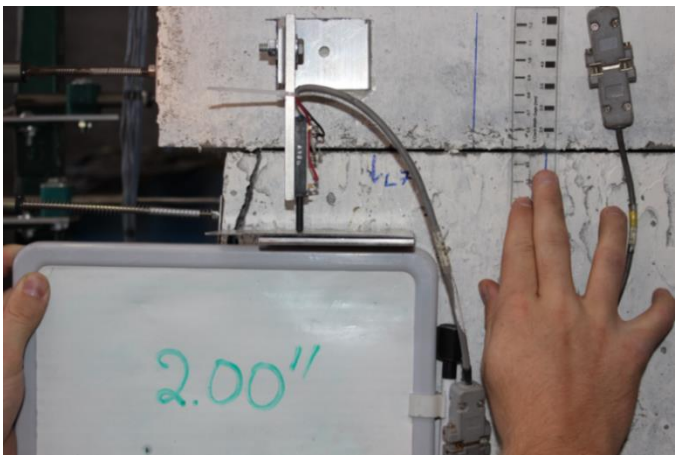

Figure 5.27 Measuring uplift at the end of the test of shear key 7A

After the end of the test, the vertical No. 5 dowel bars were removed from the specimen. The average angle of kink measured was found to be 42 degrees. Two of the bars extracted from the specimen are shown in Figure 5.28. The bottom face of the shear key is shown in Figure 5.29. The sliding plane was smooth. No damage was detected.

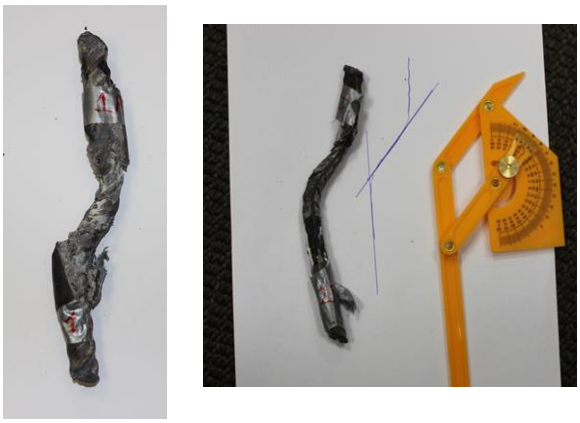

Figure 5.28 Extracted dowel bars from shear key 7A showing the angle of kink

Figure 5.29 Sliding plane condition for shear key 7A after the completion of the test

Vertical Load on Shear Key

The measurements from the strain gages on the bars in the hold-down frames indicate that at the peak horizontal load, a 30-kip vertical force was applied to the shear key. In Figure 5.30, the measured and the theoretical vertical forces are plotted against the measured horizontal load. The theoretical vertical force is calculated from the measured horizontal load and the angle of the inclined face of the shear key, which is assumed to have zero friction. However, based on the least-squares fit of the measured

vertical force plotted in Figure 5.30, the friction coefficient between the shear key and the loading beam is estimated to be 0.125.

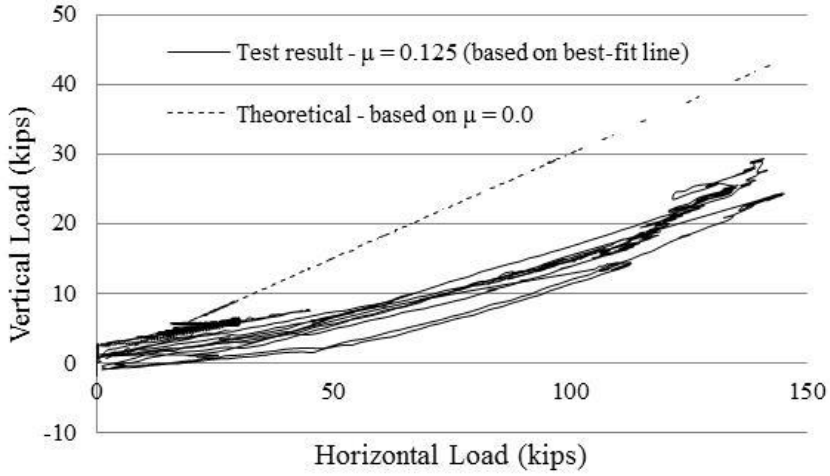

Figure 5.30 Measured and theoretical vertical forces on shear key 7A

Strains in Horizontal Shear Reinforcement of Stem Wall

Strains in the horizontal shear reinforcement in the stem wall near the shear key were measured. Readings from strain gages registering the largest strains are plotted against the horizontal load in Figure 5.31 and Figure 5.32. The locations of these gages are shown in Figure 5.18. The stain-gage readings (S33 and S49) show that only two of the horizontal bars reached the yield strain, whereas all other strain-gage readings show that the strains were within the elastic regime. The change in the slope of the curves indicates that a diagonal crack probably initiated in the stem wall at about 40 kips load. However, this was not visible during the test.

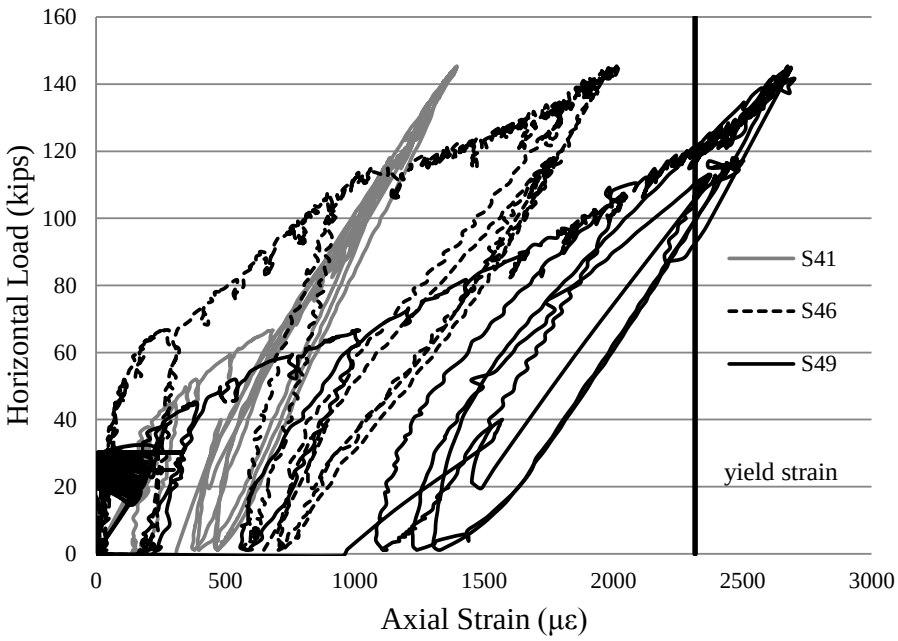

Figure 5.31 Horizontal load-vs.-axial strain in the horizontal shear reinforcement in the bottom row in the stem wall (near shear key 7A)

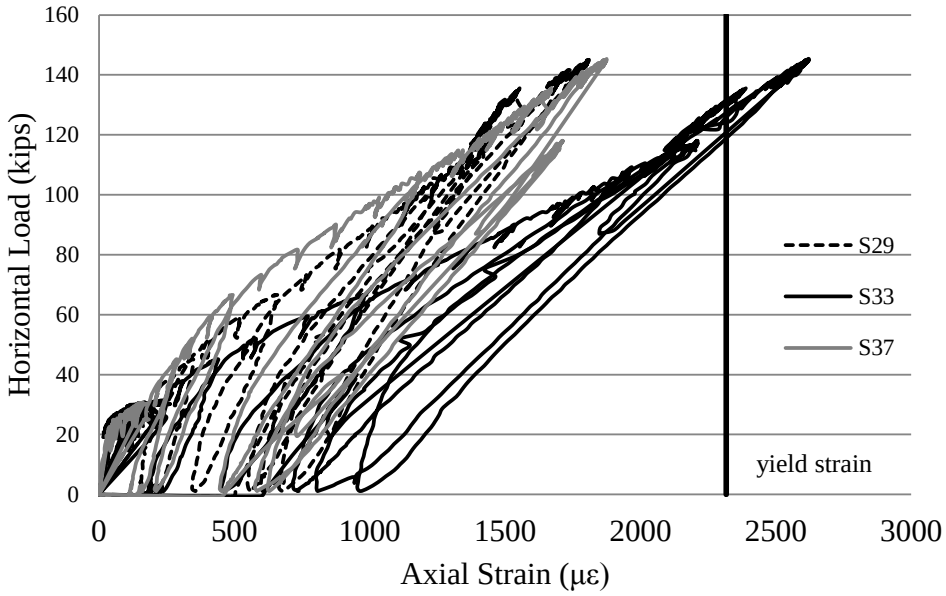

Figure 5.32 Horizontal load-vs.-axial strain in the horizontal shear reinforcement in the top row in the stem wall (near shear key 7A)

Strains in Vertical Dowel Bars

The averaged readings from the pair of strain gages on the opposite sides of each vertical dowel bar are plotted against the horizontal displacement in Figure 5.33. The locations of these gages are shown in Figure 5.19. Strain gages S56 and S69 were damaged early in the test and are not plotted. It can be observed that the tensile strains in the bars exceeded the yield strain soon after the horizontal displacement of the shear key had reached 0.2 in. For one bar, compressive strains were registered. This was probably due to the out-of-plane tilting of the shear key. Soon after 0.2 in., there is a change in the slope of the curves with the strains increasing at a higher rate.

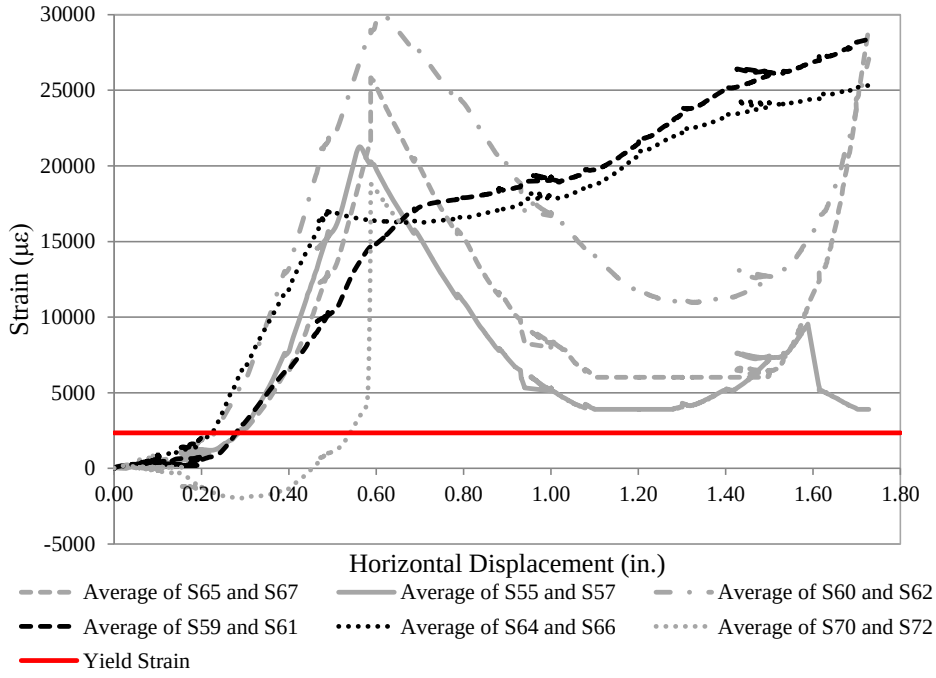

Figure 5.33 Average of strain-gage readings from vertical dowel bars in shear key 7A

Opening of Construction Joint

The opening of the construction joint between the shear key and the stem wall during the test was monitored by displacement transducers L7 through L10, whose positions are shown in Figure 5.21 and Figure 5.22. Transducers L7 and L8 were close to the south end of the shear key, while L9 and L10 were close to the north end. Readings from these transducers are plotted against the horizontal displacement of the shear key in Figure 5.34 and Figure 5.35 and show limited joint opening during shear key sliding. This can be attributed to the smooth surface of the joint.

Figure 5.34 and Figure 5.35 show that the shear key rotated in the plane of loading with more joint opening at the loaded side. Readings from L7 and L8, which were positioned on the east and west face of the stem wall, suggest that there was a small out-of-plane rotation of the shear key. This rotation should have negligible effect on the performance of the shear key.

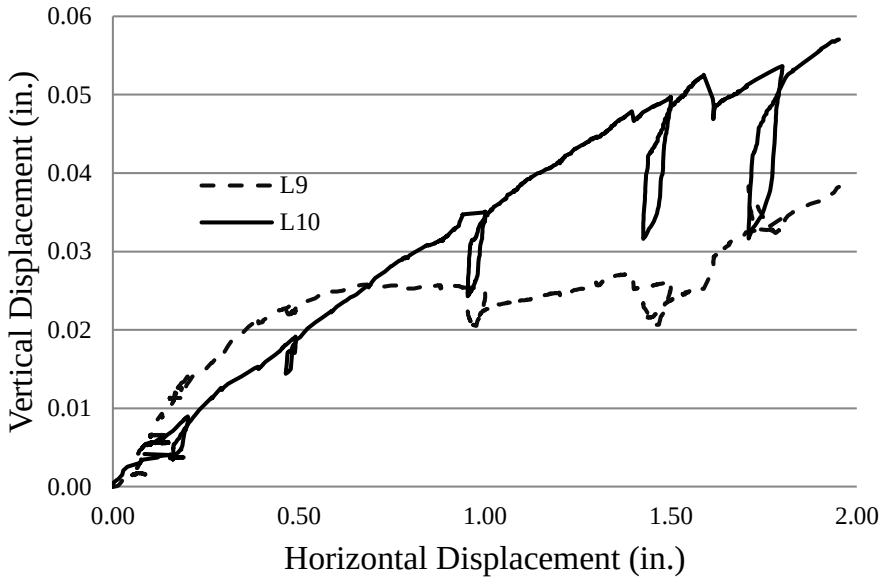

Figure 5.34 Vertical construction joint opening near the loaded end of shear key 7A

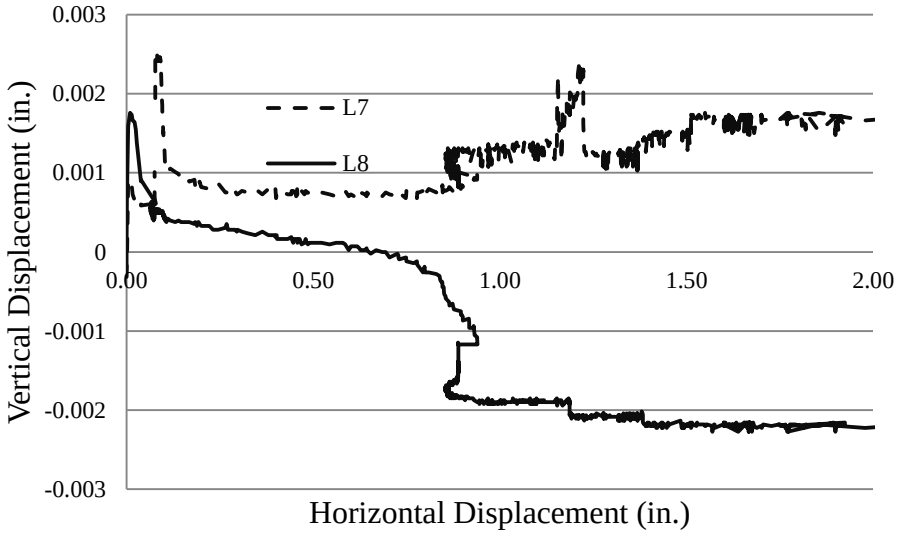

Figure 5.35 Vertical construction joint opening near the free end of shear key 7A

Concluding Remarks

Based on the above observations, one can conclude that the frictional resistance developed in the construction joint at the initial loading stage was small. This is because of the smooth contact surfaces, which also resulted in small clamping forces developed by the vertical dowel bars. The resistance was mainly provided by the dowel action of the vertical bars. As the horizontal sliding increased, the dowel bars were bent and stretched, developing more tensile forces. The shear resistance was provided by the horizontal component of the axial tensile forces developed in the dowel bars as well as the frictional resistance induced by the clamping forces exerted by the dowel bars.

5.6.2 Shear Key 7B

Shear key 7B was on the north side of the stem wall. The loading protocol for the shear key consisted of incremental loading, unloading, and reloading, with the target loads and displacements shown in Table 5.7. The shear key was initially loaded in force control to 56 kips in increments of 18.50 kips. Then, it was loaded in displacement control up to failure, which occurred at 2.0 in. displacement. The specimen was unloaded five times, when the load reached 38 kips, and when the displacement reached 0.50 in., 1.00 in., 1.20 in. and 1.50 in., respectively. The horizontal displacements of the shear key were monitored with linear potentiometers L24, L25, and L26, located on the north side of the shear key, as shown in Figure 5.21 through Figure 5.23. Potentiometers L24 and L25 were located near the base of the shear key, while L26 was at the top.

Table 5.7 Loading protocol for shear key 7B

Step	Control	Target Load/Displacement
1-3	Load	56 kips with ~18.50 kip increments
4-23	Displacement	2.00 in. with 0.10 in. increments

Early in the test, the shear key started to rotate about its toe at the free end. The shear key separated from the stem wall at the loaded end, while the construction joint remained closed at the free end. However, no horizontal sliding of the shear key was observed. At a horizontal load of 56 kips, the construction joint had an opening of 0.016 in. (0.4 mm) on the loaded side. The condition of the shear key at this load level is shown in Figure 5.36. The opening kept increasing as the horizontal load increased.

Figure 5.36 Construction joint condition at 56 kips for shear key 7B

As the load increased, the shear key continued to rotate about its free end, and diagonal cracks started to develop in the stem wall underneath the shear key at about 60 kip load. At 115 kip load, additional diagonal cracks formed in the stem wall, away from the shear key, as shown in Figure 5.37. The width of the diagonal cracks remained small throughout the test.

Figure 5.37 Diagonal cracks on the east side at 115 kips load in shear key 7B

When the horizontal load reached 132 kips, a diagonal crack occurred at the free end of the stem wall breaking away an approximately 4 in. x 8 in. triangular-shaped concrete piece, as shown in Figure 5.38. At that point, the load dropped significantly and the shear key started to slide. At the load of 108 kips (~1.60 in. displacement), the vertical dowel bars started to fracture, leading to a decreasing resistance. The test stopped at 2.00 in. displacement. The load-vs.-displacement curve is shown in Figure 5.39.

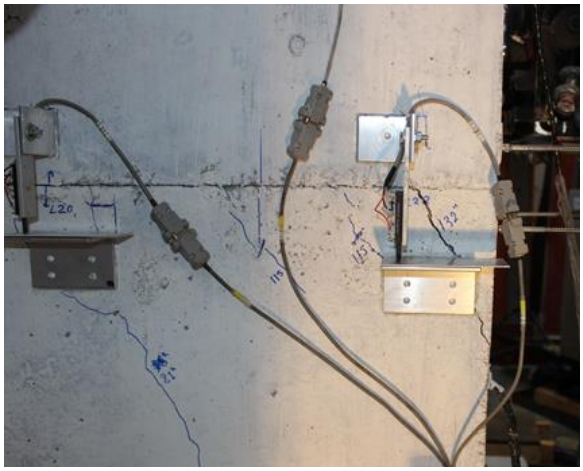

Figure 5.38 Triangular-shaped concrete piece broke off from stem wall

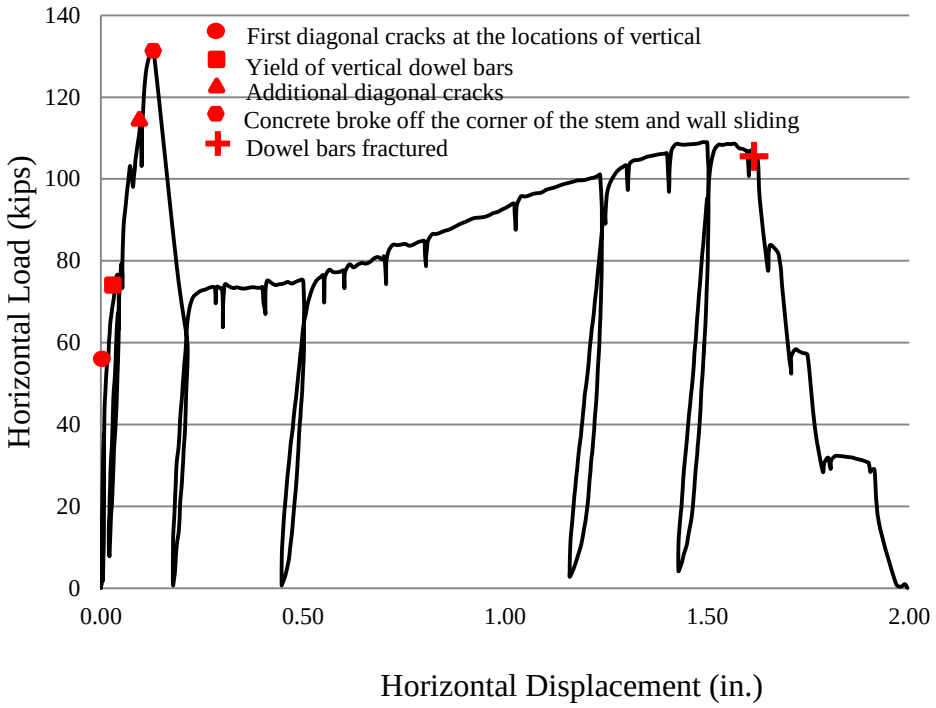

Figure 5.39 Horizontal load-vs.-horizontal displacement for shear key 7B

After the end of the test, parts of the vertical dowel bars were extracted from the shear key. These parts were located close to the construction joint and provided information on the angle of kink of the bars when fracture occurred. The average angle of kink was measured to be 42 degrees. One bar sample is shown in Figure 5.40.

Figure 5.40 Angle of kink observed in vertical reinforcement of shear key 7B

The shear key was removed from the stem wall and the condition of its bottom face was inspected. The roughness of the sliding plane is shown in Figure 5.41. Splitting cracks were observed at the locations of the vertical dowel bars. Away from the locations of the vertical bars and towards the free end of the shear key, the sliding plane had a smoother surface, seen in brighter color in Figure 5.44. This was probably due to the grinding action introduced by sliding. The smoothened area had probably provided most of the aggregate interlock action, while the area near the free end was not effective because of the concrete break-off failure at the corner of the stem wall as shown in Figure 5.38.

Figure 5.41 Sliding plane condition for shear key 7B after the completion of the test

Vertical Load on Shear Key

Based on the strain-gage readings from the four vertical bars in the steel restraining frame (SV1-SV4 shown in Figure 5.21), the vertical load exerted on the shear key is calculated. It is found that when the maximum horizontal load of 132 kips was reached, the shear key was subjected to a vertical force of 17 kips. The measured and the theoretical vertical forces are plotted in Figure 5.42 against the measured horizontal load. The theoretical vertical force is calculated from the measured horizontal load and the angle of the inclined face of the shear key, which is assumed to have zero friction. Based on the least-squares approximation of the measured vertical force, the friction coefficient between the shear key and the loading beam is estimated to be 0.19.

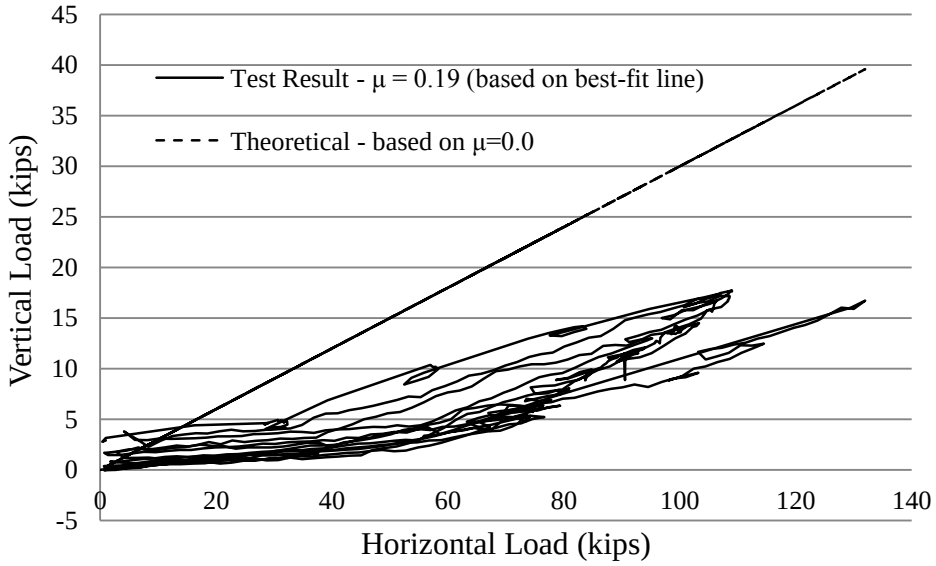

Figure 5.42 Measured and theoretical vertical forces on shear key 7B

Strains in Horizontal Shear Reinforcement of the Stem Wall

The strains in the horizontal shear reinforcement of the stem wall near the shear key are presented in Figure 5.43. Readings of the strain gages showing the largest strains

are plotted against the measured horizontal load. The locations of these strain gages are shown in Figure 5.18. The strain-gage readings show that only one of the horizontal bars (gage S40) exceeded the yield strain, while the rest remained in the elastic regime. The change of the slope of the curves indicates that diagonal cracking in the stem wall probably occurred between 50 and 60 kips. This cracking was not visible during the test.

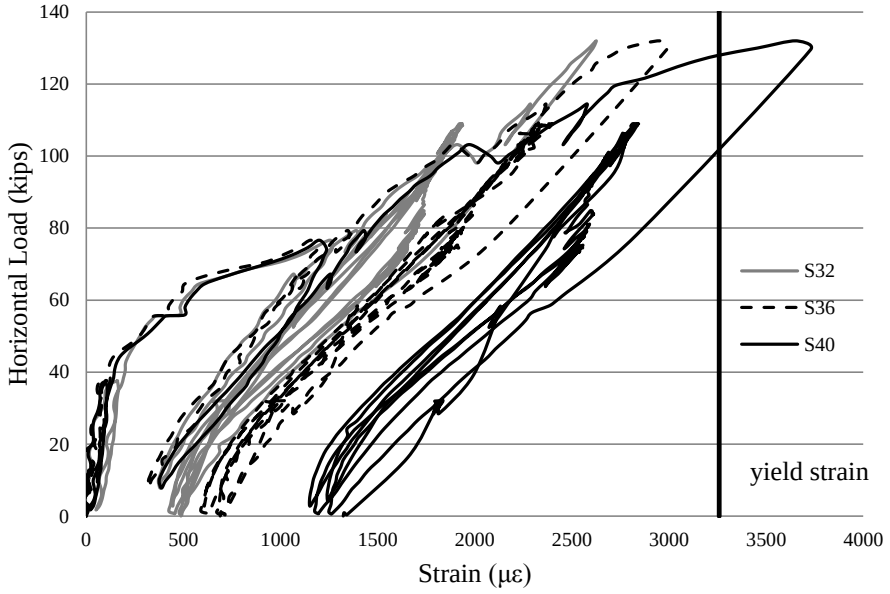

Figure 5.43 Horizontal load-vs.-strain in the horizontal shear reinforcement in the top row in the stem wall (near shear key 7B)

Strains in Vertical Dowel Bars

The averaged readings of the strain gages located on the opposite sides of each vertical dowel bar are plotted in Figure 5.44. The locations of the strain gages are presented in Figure 5.20. It is shown that most bars reached the yield strain before 0.12 in. of displacement, which is when the peak force was observed, as shown in Figure 5.39. The average strains registered by the strain gages located above the construction joint are

plotted with darker-color lines. Even though many of the strain gages were damaged early in the test, it can be seen that significant tensile strains were developed in the vertical bars.

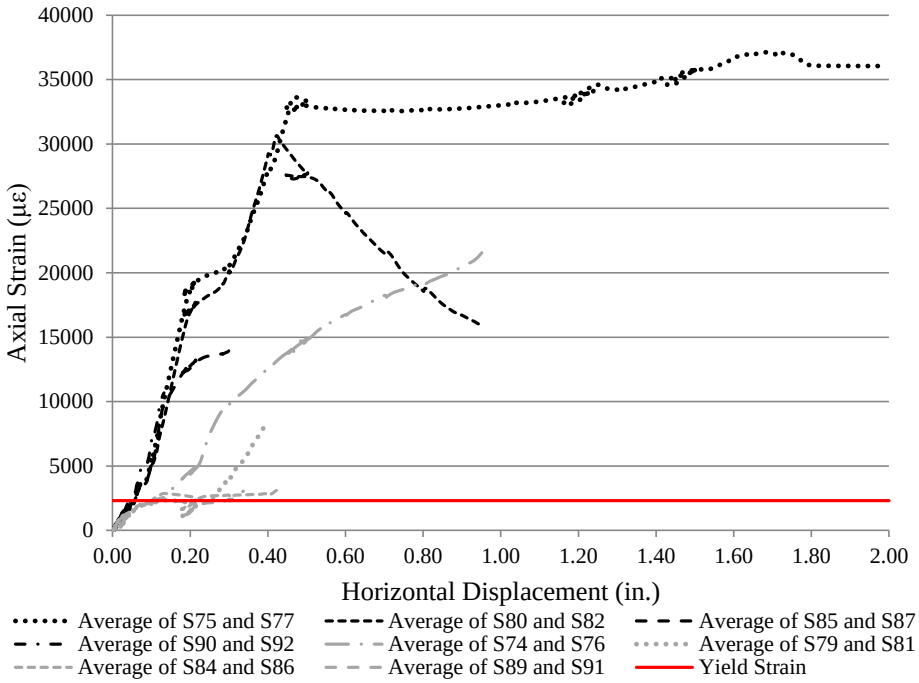

Figure 5.44 Average of strain-gage readings from vertical dowel bars in shear key 7B

Opening of Construction Joint

Displacement transducers L20 through L23, whose positions are shown in Figure 5.21 and Figure 5.22, measured the opening of the construction joint. Transducers L20 and L21 were close to the south end of the shear key, while L22 and L23 were close to the north end. Readings from these transducers are plotted against the horizontal displacement in Figure 5.45 and Figure 5.46. The readings of L20 and L21 are significantly larger than L22 and L23, showing that the shear key rotated in the plane of loading with more joint opening at the loaded side. Readings from L22 and L23, which

were positioned on the east and west faces of the stem wall, respectively, suggest that there was an out-of-plane rotation of the shear key. This rotation should have negligible effect on the performance of the shear key.

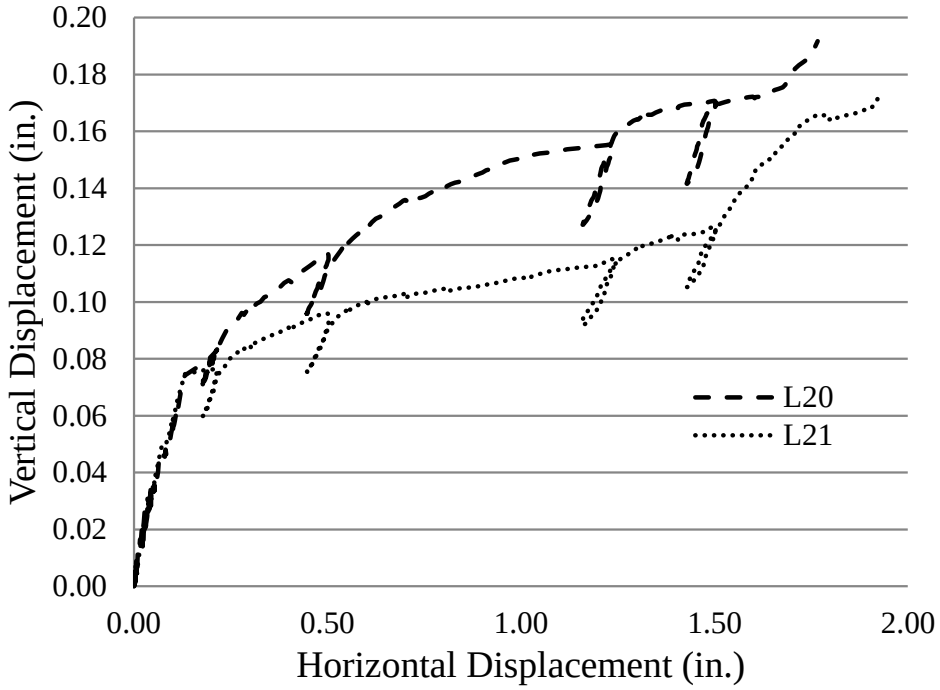

Figure 5.45 Vertical construction joint opening near the loaded end of shear key 7B

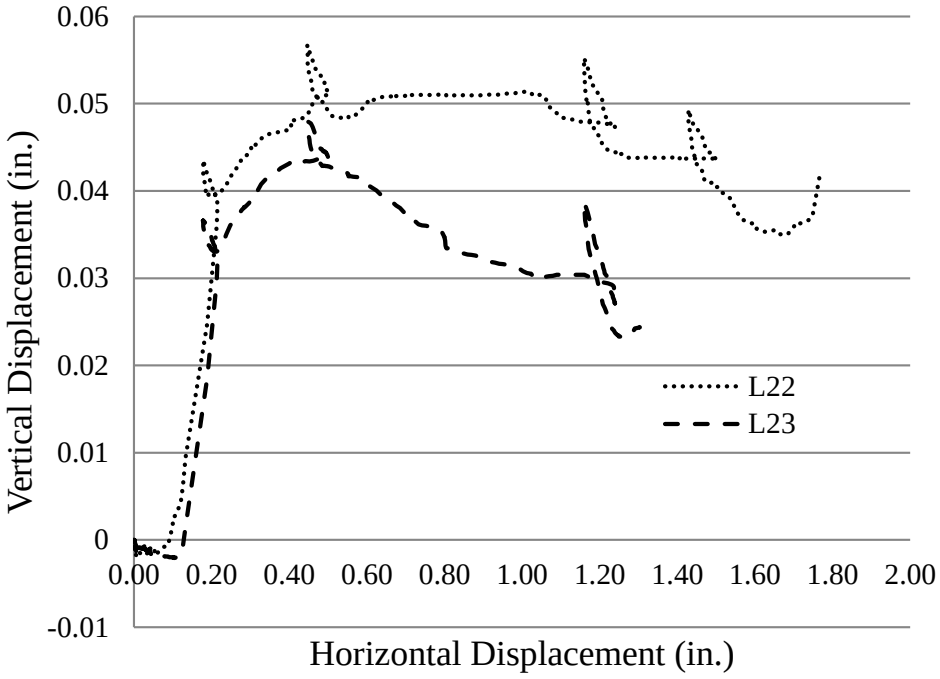

Figure 5.46 Vertical construction joint opening near the free end of shear key 7B

Concluding Remarks

Initially, the shear key experienced in-plane rotation without sliding. This led to the development of significant tensile forces in the vertical dowel bars. No sliding was observed in the shear key until the peak load was reached. The peak resistance of the shear key was provided in part by the aggregate-interlock mechanism and in part by the cohesive force in the construction joint. In spite of the application of the bond breaker, it was likely that the cohesive force was not completely eliminated from the construction joint. This could be due to the fact that the water-based bond break tended to run off from the surface of the protruded aggregate, making it less effective. After passing the peak resistance, when the shear key started to slide, the horizontal resistance was provided by the combined action of the horizontal component of the tensile forces in the bent dowel

bars and the friction introduced by the clamping force exerted by the vertical component of the bar forces. The vertical bars continued to tilt with increasing sliding until fracture occurred.

5.7 Summary and Conclusions

Specimen 7 had two isolated shear keys. Shear key 7A had a smooth construction joint with the stem wall, while 7B had a rough construction joint. The two shear keys had the same number but different sizes of vertical dowel bars. Shear key 7A had four No. 5 bars, while 7B had four No. 4 bars.

The results of the tests showed that the shear keys were designed properly to achieve a sliding governed mechanism. The diagonal cracks observed in the stem wall were minor. However, for shear key 7B, which had a rough joint, the peak resistance was reached at a displacement much smaller than that for 7A. This was the result of the aggregate-interlock mechanism as well as the cohesive force present in the sliding plane. The bond breaker could effectively eliminate the cohesive force when it was applied on a flat smooth surface. However, on the rough surface, the water-based bond breaker ran off the exposed aggregate making it less effective. After shear key 7B started to slide, its load resistance dropped due to the loss of the cohesive force and its behavior became similar to that of 7A. As sliding progressed in both shear keys, the horizontal load resistances increased due to the tensile forces developed in the vertical dowel bars, and the tilting of these bars. At the final stage, the resistances of the shear keys dropped rapidly due to bar fracture.

The calculated horizontal load resistances of the shear keys based on the expected material properties are compared to the measured horizontal resistances in Table 5.8. Based on the values in Table 5.8, it can be seen that the peak resistance of shear key 7A is under-predicted while that of shear key 7B is over-predicted.

For shear key 7A, this can be attributed to the nature of the construction joint. The construction joint surface was prepared with a water-based bond breaker and could have a larger friction coefficient than what was assumed in the design calculation, which was based on the value suggested by Borzogzadeh et al. (2006), who used an oil-based bond breaker. However, it should be noted that the friction on the inclined face of the shear key would decrease the sliding shear resistance of the shear key, off-setting the increase introduced by the increased friction in the construction joint.

For shear key 7B, the calculated peak resistance was the ultimate shear resistance V_u developed at the point right before the fracture of the vertical dowel bars. However, this was not the case in the test probably due to the unanticipated large cohesive force in the construction joint, which increased V_{slid}. In addition, the presence of friction on the inclined face of the shear key, which was ignored in the design calculations, is expected to decrease the V_u.

The calculated horizontal load resistances at first sliding based on the expected material properties are also compared to the measured horizontal resistances in Table 5.8. It can be seen that for shear key 7A the calculated resistance is very close to the measured resistance, while for 7B this is not the case. This can be attributed to the cohesive force

that existed right before the shear key started to slide but not considered in the calculation as discussed above.

Table 5.8 Calculated and measured sliding shear resistances for Specimen 7

Tested Shear Key	Calculated Shear Resistance at First Sliding (kips)	Calculated Ultimate Sliding Shear Resistance (kips)	Measured Resistance at First Sliding (kips)	Measured Ultimate Shear Sliding Resistance (kips)
7A	34	128	37	142
7B	75	163	132	109

5.8 Acknowledgement of Publication

Part of this chapter is a reprint of the material that will appear in a technical report which will be submitted to the California Department of Transportation in 2016, Kottari, A., P. B. Shing, J. I. Restrepo, under the title "Design and Capacity Assessment of External Shear Keys in Bridge Abutments". The dissertation author will be the primary investigator and author of this report.

CHAPTER 6

EXPERIMENTAL STUDY OF MONOLITHIC EXTERNAL SHEAR KEYS IN BRIDGE ABUTMENTS

6.1 Description of Test Specimens

Most of the external shear keys in bridge abutments are monolithic with the stem walls without construction joints. They require less construction effort and are therefore more economical and faster to construct as compared to isolated shear keys. However, past experimental studies by Megally et al. (2002), Borzogzadeh et al. (2006), and Bauer (2006), as discussed in Chapter 2, have shown that the failure of these shear keys under horizontal loading was often caused by the development and opening of diagonal shear cracks in the stem walls. This can result in costly repairs in the event of a major earthquake.

This chapter presents a further experimental study conducted at UC San Diego to examine the behavior of monolithic shear keys in bridge abutments. The main objective of this study was to investigate if the stem wall and shear key could be appropriately reinforced such that diagonal shear failure could be prevented in the stem wall and the shear key could develop a horizontal failure plane like an isolated shear key when subjected to strong earthquake loads. For this purpose, three specimens were tested, each with a stem wall and two shear keys. The main difference of this study in comparison to

the aforementioned past studies is that all the specimens considered here had a higher amount of horizontal shear reinforcement in the stem wall and a lower amount of dowel bars connecting the shear keys to the stem walls.

The specimens considered are identified as Specimens 8, 9 and 10. Each specimen consisted of two shear keys. One had an inclined face and the other had a vertical face. Specimens 8 and 10 had the same amount of reinforcement and reinforcing details but different concrete strengths, while Specimen 9 had the same amount of horizontal shear reinforcement in the stem wall and concrete strength as Specimen 8 but an increased amount of vertical dowel bars.

6.2 Design of Specimens

6.2.1 Specimens 8 and 10

Specimens 8 and 10 consisted of a stem wall and two shear keys each. The shear keys are identified as 8A and 8B, and 10A and 10B, respectively. The shear keys were cast together with the stem wall. The specimen represented a 40%-scale model of the original prototype bridge, which is the South Ave OC (Caltrans Br #39-0146). The stem wall length was 10 ft., as opposed to 8 ft. used in the previous specimens. This length increase was to provide a longer embedment length for the horizontal shear reinforcement in the stem wall, which had bar sizes larger than those used in the previous specimens. However, the length of the stem wall was still much shorter than that required according to the scaling, but sufficient to develop the horizontal bars in the stem wall. Hence, the shorter length would not affect the performance of the shear keys. Shear keys 8A and

10A had an inclined shear key face and, shear keys 8B and 10B had a vertical face, as shown in Figure 6.1. Specimens 8 and 10 had the same amount of reinforcement and reinforcing details, but Specimen 10 had a higher concrete strength. The specimens were designed with the strength prediction formulas developed in this study, as will be discussed in Section 6.3.

Specimens 8 and 10 were designed to have the shear keys fail in sliding shear like an isolated shear key. To prohibit the diagonal shear failure in the stem wall, 8 No. 8, Grade 60, headed bars were placed at the top of the stem wall in two rows with 5.0 in. center-to-center spacing in the vertical direction, as shown in Figure 6.1. Their quantity was determined with the strength prediction formulas proposed in this study (see Section 6.3).

Side reinforcement, consisting of No. 3 bars, was placed near both faces of the stem wall and shear keys, according to the AASHTO LRFD Specifications, for temperature and shrinkage. The reinforcement was placed horizontally and vertically at 4.0 in. and 4.5 in. center-to-center spacing, respectively. In shear keys 8B and 10B, six out of the ten vertical No. 3 bars for the side reinforcement of the shear keys were used as dowels and continued from the shear key into the stem wall, whereas the rest stopped at the base of the shear key and did not continue into the stem wall. In shear keys 8A and 10A, which had an inclined face on the loading side, four out of eight vertical No. 3 bars for the side reinforcement of the shear keys were used as dowels and continued from the shear key into the stem wall. Two additional No. 3 dowel bars were placed near and parallel to the inclined face of these shear keys. The reinforcement layout is shown in Figure 6.1 through Figure 6.5.

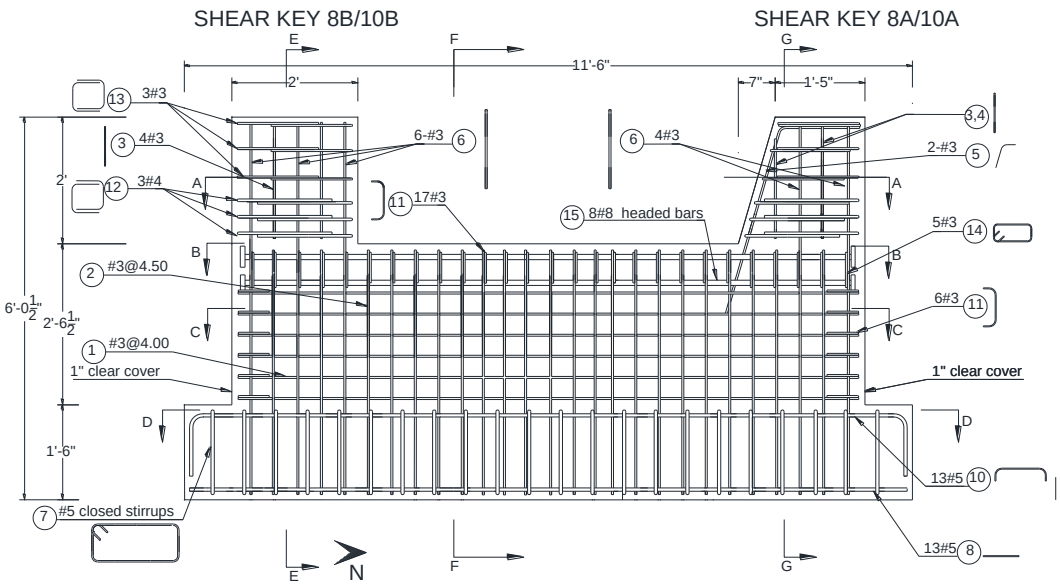

Figure 6.1 Elevation view of design details for Specimens 8 and 10

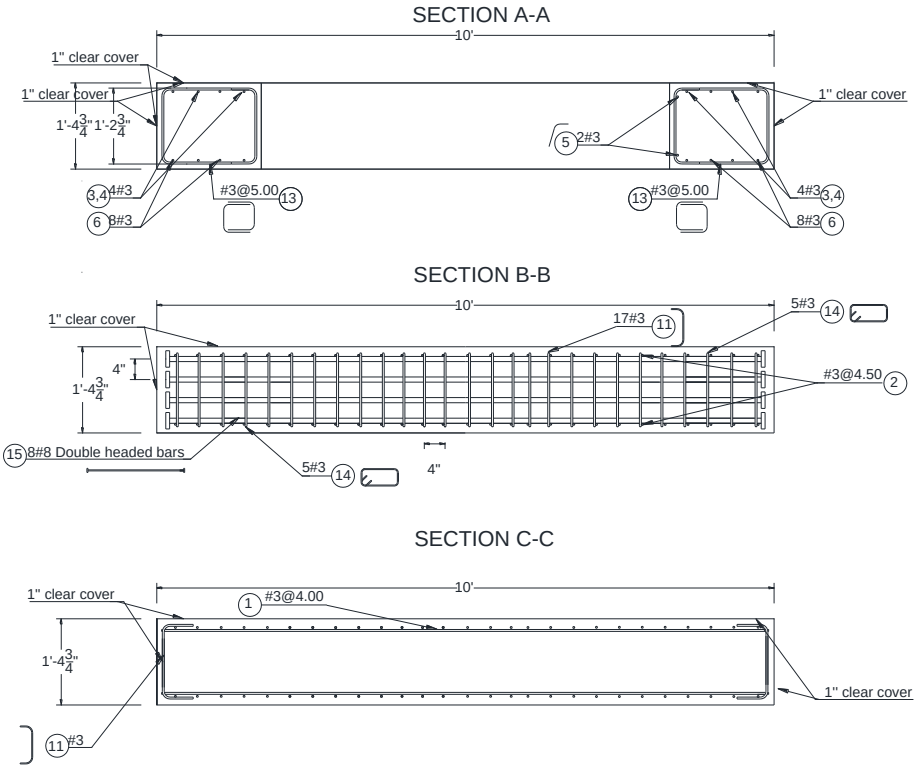

Figure 6.2 Section A-A, B-B and C-C in design drawings for Specimens 8 and 10 (see Figure 6.1 for the location of the sections)

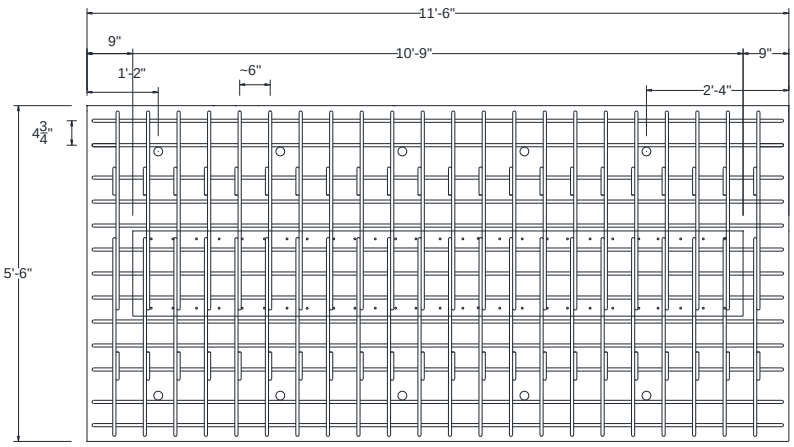

Figure 6.3 Section D-D in design drawings for Specimens 8 and 10
(see Figure 6.1 for the location of the sections)

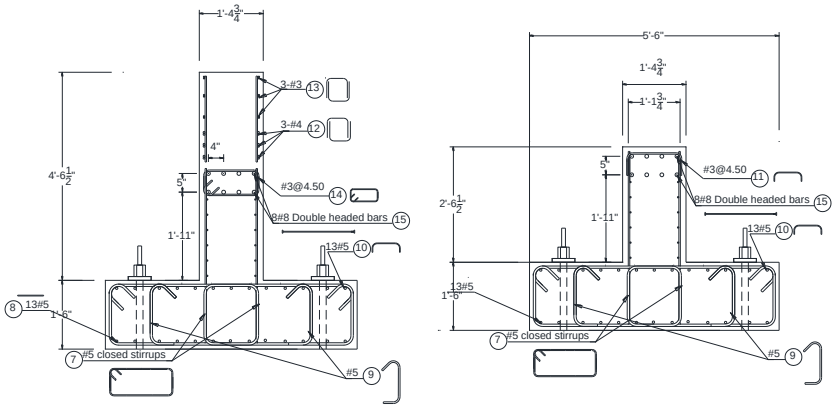

Figure 6.4 Section E-E (left) and F-F (right) in design drawings for Specimens 8 and 10
(see Figure 6.1 for the location of the sections)

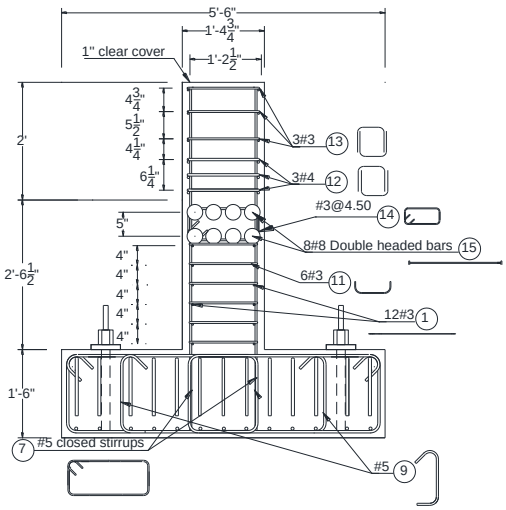

Figure 6.5 Side view in design drawings for Specimens 8 and 10
(see Figure 6.1 for the location of the sections)

The specified concrete compressive strength for Specimen 8 was 4.0 ksi. On the day of the test the concrete strength reached 4.71 ksi. The specified compressive strength for the concrete mix ordered for Specimen 10 was 6.0 ksi, and the actual strength on the day of the test was 6.74 ksi. The compressive strengths of the specimens were obtained from the tests of concrete cylinders, which were cast and kept in plastic molds till the day of testing. The slump of the concrete mix was 3.50 in. and 3.75 in. for Specimens 8 and 10, respectively. The reinforcement properties for Specimen 8 are summarized in Table 6.1 and those for Specimen 10 are shown in Table 6.2.

Table 6.1 Measured strengths of reinforcing bars in Specimen 8

Reinforcement Description	Bar Size	f_y (ksi)	f_{su} (ksi)
Vertical and horizontal side reinforcement of the stem wall	No. 3	67.00	104.00
Horizontal shear reinforcement of the stem wall	No. 8	70.00	93.60

Table 6.2 Measured strengths of reinforcing bars in Specimen 10

Reinforcement Description	Bar Size	f_y (ksi)	f_{su} (ksi)
Vertical and horizontal side reinforcement of the stem wall	No. 3	67.20	104.00
Horizontal shear reinforcement of the stem wall	No. 8	67.50	89.10

6.2.2 Specimen 9

Specimen 9 had the same design as Specimens 8 and 10, except that all the vertical side reinforcement in the shear keys continued into the stem wall. This resulted in a higher shear key load capacity. However, the shear keys were still expected to fail by horizontal sliding over the stem wall according to the strength prediction formulas presented in Section 6.3. The design details for Specimen 9 are shown in Figure 6.6 through Figure 6.10. The main purpose of this test was to provide an additional variable to verify the strength prediction formulas.

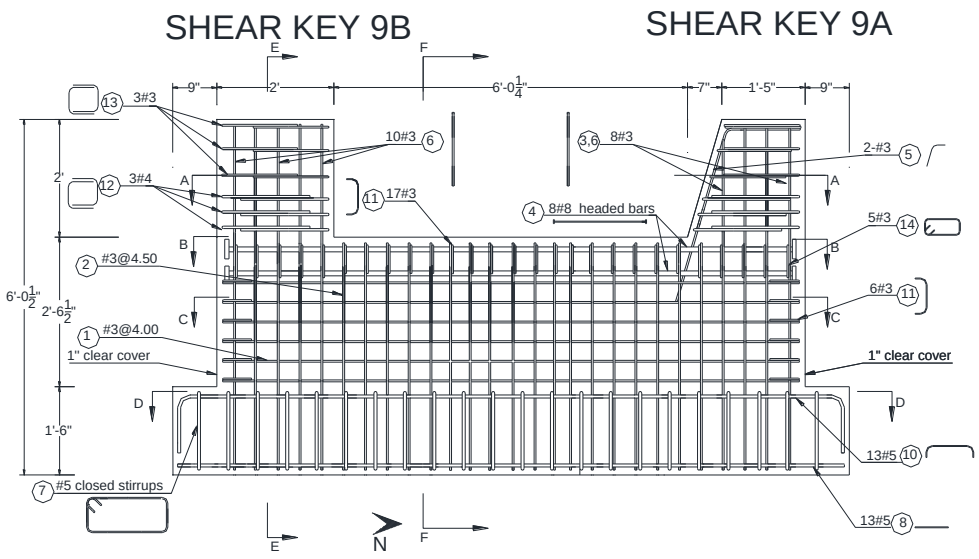

Figure 6.6 Elevation view of design details for Specimen 9

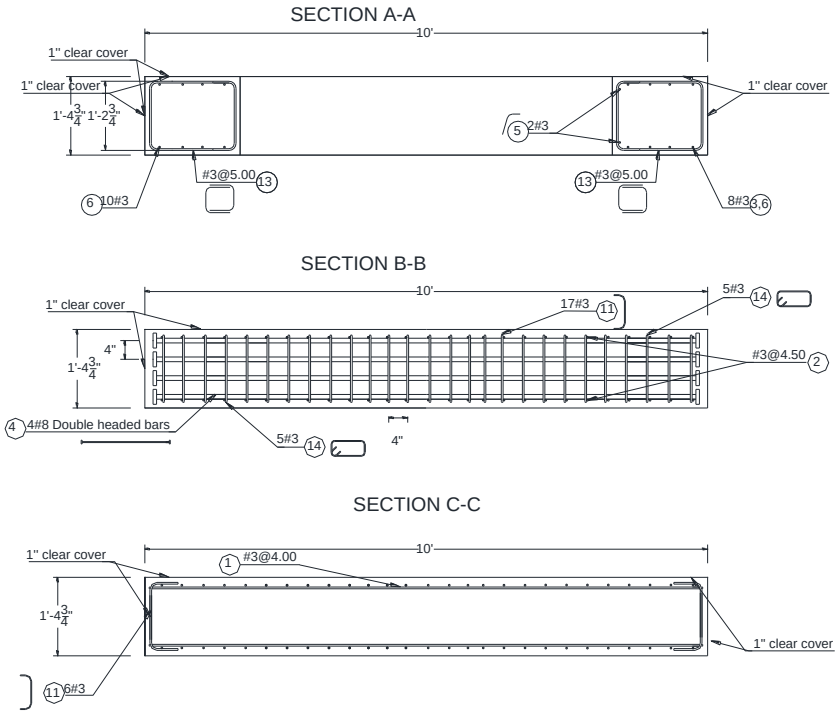

Figure 6.7 Sections A-A, B-B and C-C in design drawings for Specimen 9
(see Figure 6.6 for the location of the sections)

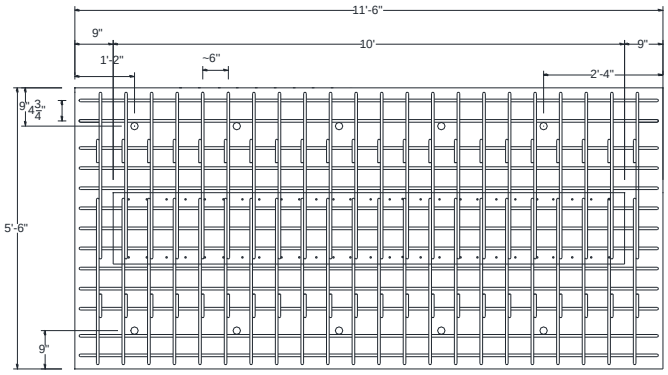

Figure 6.8 Section D-D in design drawings for Specimen 9
(see Figure 6.6 for the location of the section)

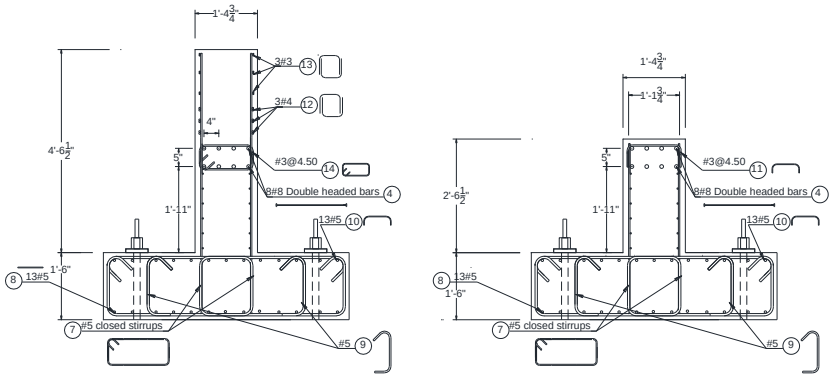

Figure 6.9 Sections E-E (left) and F-F (right) in design drawings for Specimen 9 (see Figure 6.6 for the location of the sections)

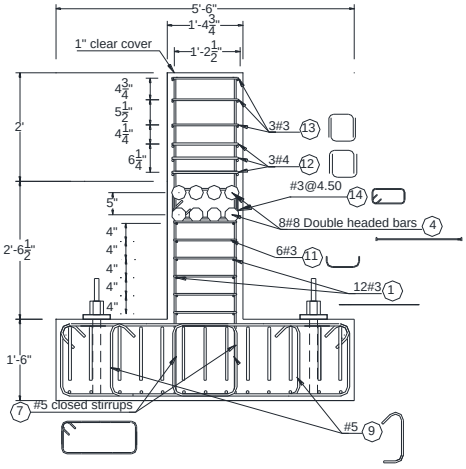

Figure 6.10 Side view in design drawings for Specimen 9

The specified concrete compressive strength was 4.0, which on the day of the test reached 5.1 ksi. The slump of the concrete mix was measured to be around 3.75 in. The reinforcement properties are summarized in Table 6.3.

Table 6.3 Measured strengths of reinforcing bars in Specimen 9

Reinforcement Description	Bar Size	f_y (ksi)	f_{su} (ksi)
Vertical and horizontal side reinforcement of the stem wall	No. 3	67.20	104.00
Horizontal shear reinforcement of the stem wall	No. 8	67.50	89.10

6.3 Prediction of Sliding Shear Resistance of Monolithic Shear Keys

To calculate the shear resistance of a monolithic shear key failing in a horizontal sliding mode, the following failure process is assumed. Initially, a diagonal shear crack forms at the toe of the shear key on the loading side. The diagonal shear crack then propagates downward until it reaches the top horizontal shear reinforcement in the stem wall. The horizontal shear reinforcement prohibits the opening and propagation of the diagonal crack, which then turns direction to propagate as a horizontal crack due to the overturning moment induced by the applied load, creating a sliding plane as shown in Figure 6.11.

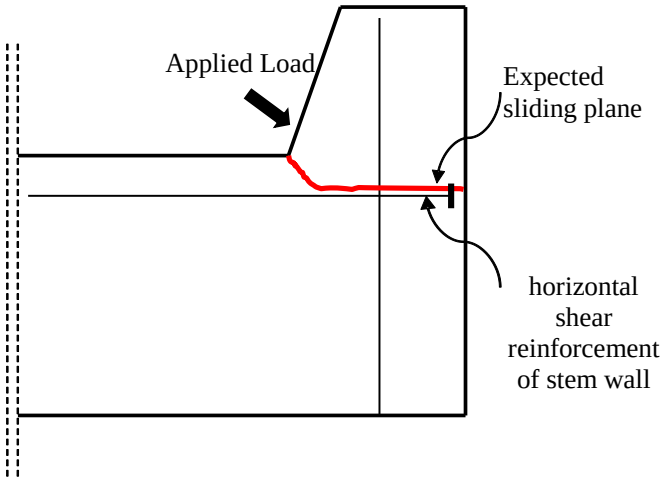

Figure 6.11 Assumed crack pattern in a monolithic shear key at failure

It is assumed that the shear resistance is partially provided by the cohesive force in the sliding plane. The shear key will also experience a significant rotation with the opening of the horizontal crack, causing the vertical dowel bars to yield in tension. The axial forces developed by the vertical dowel bars introduce additional clamping forces to the sliding plane. These forces are shown in the free-body diagram in Figure 6.12, in

which the shear key and part of the stem wall are isolated from the remaining part of the stem wall by the crack shown in Figure 6.11.

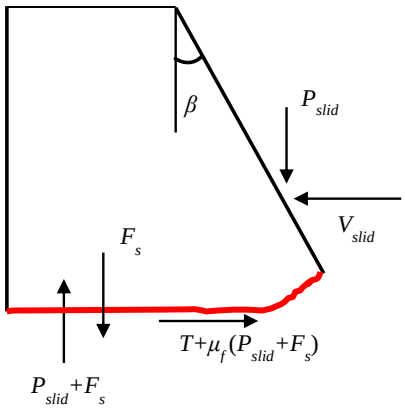

Figure 6.12 Free-body diagram of monolithic shear keys for the calculation of sliding shear resistance

It is assumed that the friction coefficient is zero on the inclined face of the shear key. Thus, the external load applied to the shear key has to be perpendicular to its inclined face and can be resolved into a horizontal component, denoted by V_{slid}, and a vertical component, denoted by P_{slid}, which are geometrically related as follows:

$$P_{slid} = V_{slid} \cdot \tan\beta \tag{6.1}$$

in which β is the angle of the inclined face of the shear key with respect to a vertical plane, as shown in Figure 6.12. The friction coefficient of the horizontal sliding surface of the shear key is denoted by μ_f, and the cohesive force is denoted by *T*. It should be noted that if the external force is applied to shear keys with a vertical face, the vertical component, P_{slid}, is zero.

To calculate the sliding shear resistance, V_{slid}, the equilibrium of forces in the horizontal and vertical directions in the free-body diagram shown in Figure 6.12 are considered. This results in:

$$V_{slid} = \frac{T + \mu_f \cdot F_s}{\left(1 - \mu_f \cdot \tan\beta\right)} \tag{6.2}$$

in which β is the angle of the inclined face of the shear key with respect to a vertical plane, T is the cohesive force, F_s is the yield force of the vertical dowel bars, and μ_f is the coefficient of friction assumed for the sliding plane. This equation is similar to Eq. (5.9) presented in Chapter 5 for isolated shear keys with rough construction joints.

For the diagonal shear strength of the stem wall, the method presented in Section 5.3.1 in Chapter 5 can be used.

6.3.1 Load Resistance Calculations for Test Specimens

The calculations for the expected sliding shear resistances of Specimens 8, 9 and 10 are presented in this section. The expected material strengths assumed are:

- Yield strength of side reinforcement f_y = 68 ksi
- Ultimate tensile strength of horizontal shear reinforcement f_{su} = 105 ksi
- Concrete strength f_c' = 5.00 ksi for Specimens 8 and 9, and f_c' = 6.50 ksi for Specimen 10
- Coefficient of friction μ_f = 1.40

The friction coefficient was based on the recommendations in ACI 318-08 and the AASHTO LRFD Bridge Design Specifications for concrete in monolithic construction. The yield strength of the steel was based on the expected properties for Grade 60 bars suggested in the Caltrans Seismic Design Criteria (SDC, Version 1.6, Section 3.2.3), while the ultimate tensile strength of the steel was based on that measured by Borzogzadeh et al. (2006), which is higher than that suggested in the SDC. The cohesive force, *T*, for concrete was calculated by the formula proposed by Bazant and Pfeiffer (1986) as follows:

$$T = c \cdot d \cdot l$$
$$c = \frac{0.15 \cdot f_c'}{\sqrt{0.0099 \cdot X + 0.3659}} \tag{6.3}$$

in which *c* is the cohesive strength of concrete in ksi, and *d* and *l* are the dimensions of the contact surface in inches, with the latter being in the direction of loading. Finally, parameter *X* can be calculated as:

$$X = \frac{1.50 \cdot l}{d_a} \tag{6.4}$$

in which d_a is the maximum aggregate size in inches. Equation (6.3) was developed by Bazant and Pfeiffer (1986) by the curve-fitting of data from a large number of Mode-II fracture tests. For the test specimens, *d* = 16.75 in., *l* = 24 in., and the maximum aggregate size used was ⅜ in. Based on these values and the expected concrete compressive strengths, the cohesive strength for the concrete in Specimens 8 and 9 was calculated to be 0.68 ksi, and that in Specimen 10 was 0.85 ksi.

To avoid diagonal shear failure in the stem walls, the stem walls were sufficiently reinforced so that the peak shear resistance of shear keys would be lower than the

diagonal shear resistance of the stem walls. The diagonal shear resistance of the stem wall was calculated with the procedure described in Section 5.3.1, and the values of the parameters used and the calculated strengths are presented in Table 6.4 and Table 6.5. The strengths of the stem walls are compared to the strengths of the shear keys in Table 6.6. It can be seen that the stem walls were capacity protected with a good margin for all the cases, except for shear key 10A, which had the calculated sliding shear resistance higher than the diagonal shear strength of the stem wall.

It should be noted that the strength of the stem wall is affected by the load applied to the shear key, based on the model presented in Section 5.3.1. For this reason, the strengths of the stem wall in each specimen are different for the two ends, even though they had the same reinforcement along the entire wall. Specimens 8 and 9 had the same reinforcement in the stem wall, the same geometry of the shear keys and the same expected material properties. For this reason, the strengths of the two stem walls were expected to be the same, as shown in Table 6.4 and Table 6.5. For Specimen 10, the expected material properties are different from those for Specimens 8 and 9, even though the reinforcement in the stem wall was the same.

Table 6.4 Diagonal shear resistance of stem walls in Specimens 8 and 9

Shear Key	Bars	Number of bars crossing diagonal crack	Total bar area (in^2)	Distance of bars, $l_{i,h}$, $l_{j,v}$ or $l_{t,s}$ (in.)	Stress in bars (ksi)	α_c (in.)	Diagonal Shear Resistance (kips)
8A/9A	Vertical side bars	2	0.22	3.5	68	3.50	689
	Vertical side bars	2	0.22	8.0			
	Vertical side bars	2	0.22	12.5			
	Vertical side bars	2	0.22	17.0			
	Horizontal shear reinforcement	4	3.14	29.0	105		
	Horizontal shear reinforcement	4	3.14	24.0			
	Horizontal side bars	2	0.22	21.5	68		
	Horizontal side bars	2	0.22	17.5			
	Horizontal side bars	2	0.22	13.5			
	Horizontal side bars	2	0.22	9.5			
	Horizontal side bars	2	0.22	5.5			
	Horizontal side bars	2	0.22	1.5			
	Inclined side bars	2	0.22	37.80			
8B/9B	Vertical side bars	2	0.22	3.5	68	1.00	563
	Vertical side bars	2	0.22	8.0			
	Vertical side bars	2	0.22	12.5			
	Vertical side bars	2	0.22	17.0			
	Vertical side bars	2	0.22	21.5			
	Horizontal shear reinforcement	4	3.14	29.0	105		
	Horizontal shear reinforcement	4	3.14	24.0			
	Horizontal side bars	2	0.22	21.5	68		
	Horizontal side bars	2	0.22	17.5			
	Horizontal side bars	2	0.22	13.5			
	Horizontal side bars	2	0.22	9.5			
	Horizontal side bars	2	0.22	5.5			
	Horizontal side bars	2	0.22	1.5			

Table 6.5 Diagonal shear resistance of stem wall in Specimen 10

Shear Key	Bars	Number of bars crossing diagonal crack	Total bar area (in^2)	Distance of bars, $l_{i,h}$, $l_{j,v}$ or $l_{t,s}$ (in.)	Stress in bars (ksi)	α_c (in.)	Diagonal Shear Resistance (kips)
10A	Vertical side bars	2	0.22	3.5	68	2.80	682
	Vertical side bars	2	0.22	8.0			
	Vertical side bars	2	0.22	12.5			
	Vertical side bars	2	0.22	17.0			
	Horizontal shear reinforcement	4	3.14	29.0	105		
	Horizontal shear reinforcement	4	3.14	24.0			
	Horizontal side bars	2	0.22	21.5	68		
	Horizontal side bars	2	0.22	17.5			
	Horizontal side bars	2	0.22	13.5			
	Horizontal side bars	2	0.22	9.5			
	Horizontal side bars	2	0.22	5.5			
	Horizontal side bars	2	0.22	1.5			
	Inclined side bars	2	0.22	37.80			
10B	Vertical side bars	2	0.22	3.5	68	0.80	563
	Vertical side bars	2	0.22	8.0			
	Vertical side bars	2	0.22	12.5			
	Vertical side bars	2	0.22	17.0			
	Vertical side bars	2	0.22	21.5			
	Horizontal shear reinforcement	4	3.14	29.0	105		
	Horizontal shear reinforcement	4	3.14	24.0			
	Horizontal side bars	2	0.22	21.5			
	Horizontal side bars	2	0.22	17.5			
	Horizontal side bars	2	0.22	13.5			
	Horizontal side bars	2	0.22	9.5			
	Horizontal side bars	2	0.22	5.5			
	Horizontal side bars	2	0.22	1.5			

Table 6.6 Calculated horizontal load resistances of stem walls and shear keys in Specimens 8, 9 and 10

Shear key	Diagonal Resistance (kips)	Sliding Shear Resistance (kips)
8A	689	576
8B	563	326
9A	689	629
9B	563	368
10A	682	691
10B	563	405

6.4 Test Setup

The test setup consisted of the test specimen, a steel loading beam and two hold-down frames, placed on the two sides of the specimen parallel to the stem wall, as for Specimen 7, which was presented in Chapter 5. The specimen was secured to the lab floor with post-tensioned rods. A total of ten rods were used, with each post-tensioned to 150 kips. This force was sufficient to avoid sliding along the lab floor and to prevent uplift of the specimen during the test.

The load was applied to the shear keys with the steel loading beam presented in Chapter 5. However, in each of these specimens, one of the shear keys had a vertical face on the loading side and the other had an inclined face. Thus, the loading beam was modified to accommodate the vertical face. To this end, a concrete block was added to one end of the loading beam. This block was made of high-strength concrete, and was connected to the loading beam with the steel plates, as shown in Figure 6.13. Six days after casting it, the compressive strength of the concrete block reached 6.1 ksi.

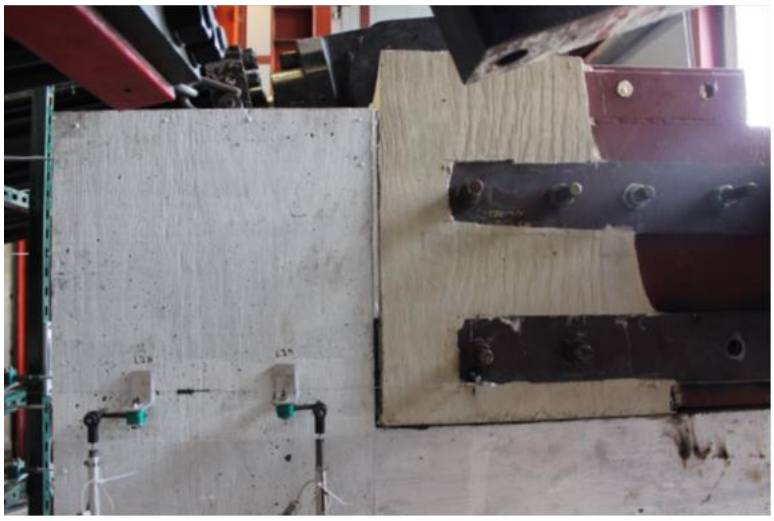

Figure 6.13 Concrete block attached to loading beam

The loading beam was prevented from moving upward by two hold-down frames, assembled with hollow steel sections. The frames were post-tensioned with 4 rods (2 rods for each) to the lab floor. The rods were hand-tightened and the initial strain in the rods was negligible. Figure 6.14 shows a hold-down frame, the vertical rods, and the steel loading beam in their final positions.

Figure 6.14 East view of test setup

To reduce the friction between the loading beam and the shear key observed in Specimen 7, a piece of 8 in. x 16.75 in. x 0.5 in. joint filler satisfying ASTM 1751 was placed against the loaded face of the shear key. This type of joint filler contains strips of fibers saturated with asphalt and is commonly used to fill gaps in bridge abutments. The friction between the loading beam and the restraining frames was minimized with the use of PTFE (Polytetrafluorethylene-Teflon) bearings and grease.

6.5 Instrumentation of Specimens

6.5.1 Specimens 8 and 10

The specimens were instrumented to monitor the strains in the reinforcing bars as well as the deformation of the specimens. The instrumentation schemes for Specimens 8 and 10 were the same. Electrical resistance strain gages were attached to the longitudinal and transverse reinforcing bars. A total of 100 strain gages were installed. The location and numbering of the strain gages, preceded by an S, are shown in Figure 6.15 through Figure 6.18.

The positions of the strain gages were selected to measure strains in the bars at the potential locations of main cracks in the stem wall. Those cracks included the major diagonal crack that could occur in the stem wall, and the horizontal crack below a shear key. For this purpose, strain gages were attached to the side reinforcement and horizontal shear reinforcement in multiple locations.

In addition, linear potentiometers were installed external to the specimens to measure the horizontal displacements along its height, as well as the expected vertical

uplift of the shear key with respect to the stem wall. A tilt meter was attached to each of the shear keys to measure the in-plane rotation. Two string pots were used to measure the horizontal displacement of the loading beam. The strain in each of the vertical post-tensioning bars for the hold-down frames was monitored with a strain gage. These strain readings were used to calculate the vertical reaction force exerted on the shear key through the loading beam. The positions and numbering of the external transducers are shown in Figure 6.19 through Figure 6.21. In these figures, the linear potentiometer numbers are preceded by an L, while those of the string potentiometers and tilt meters are preceded by SP and TM, respectively.

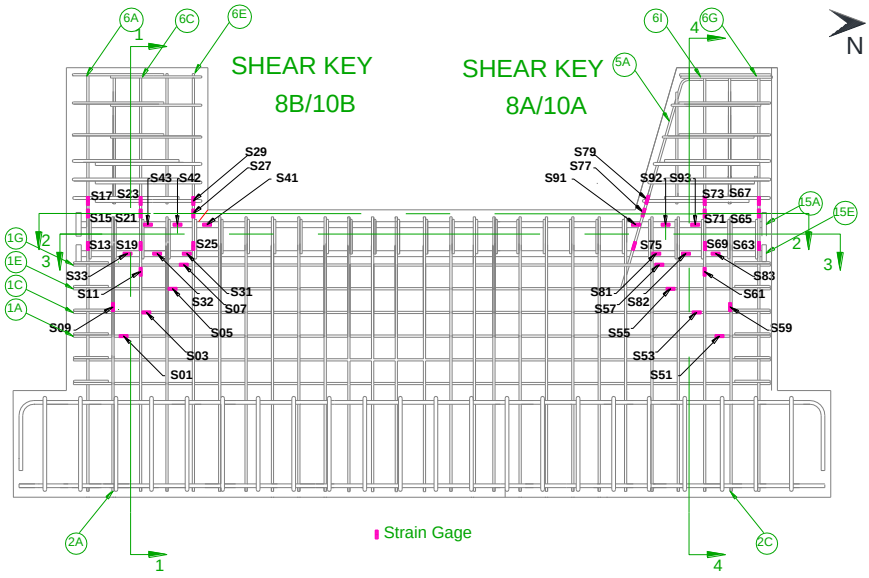

Figure 6.15 Strain gages located on the east side of Specimens 8 and 10

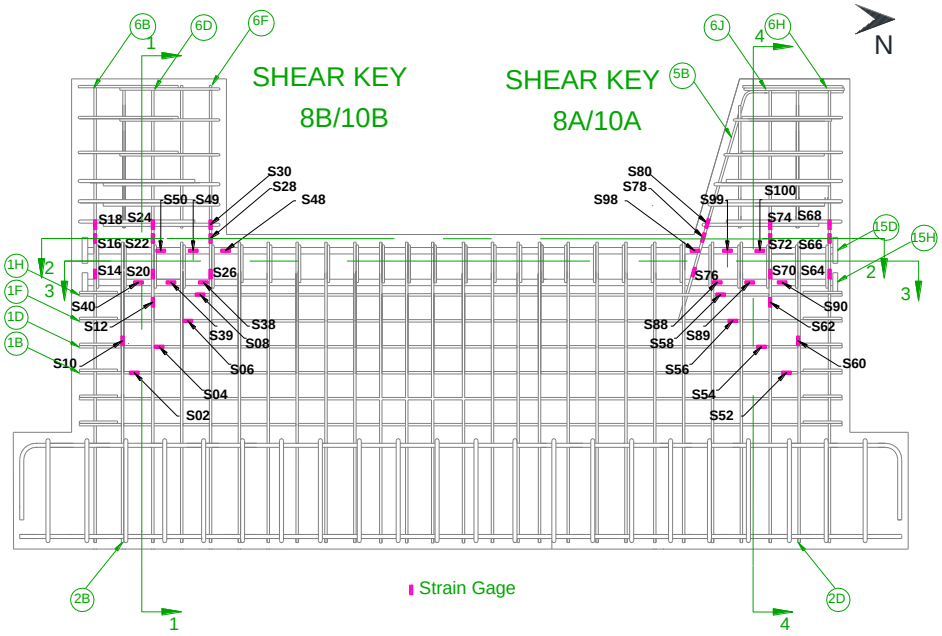

Figure 6.16 Strain gages located on the west side of Specimens 8 and 10

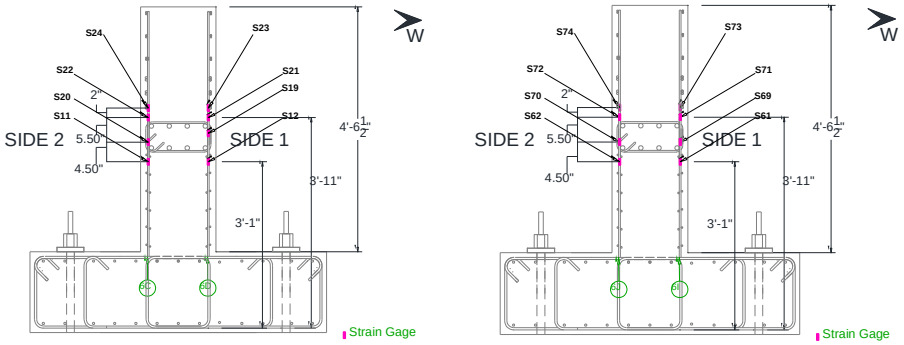

Figure 6.17 Sections 1-1 (left) and 4-4 (right) for Specimens 8 and 10
(see Figure 6.16 for the location of the sections)

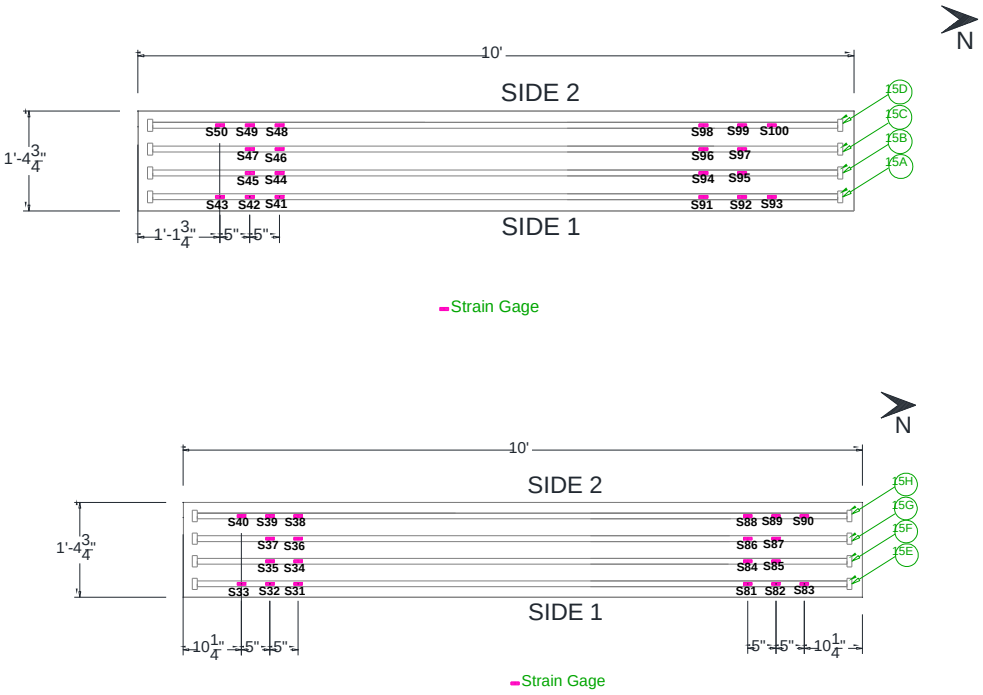

Figure 6.18 Sections 2-2 (top) and 3-3 (bottom) for Specimens 8 and 10 (see Figure 6.16 for the location of the sections)

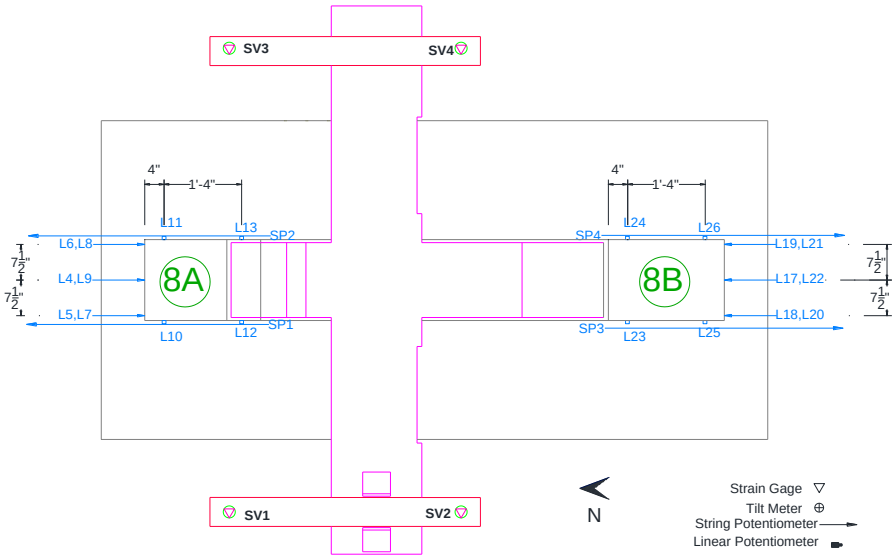

Figure 6.19 Plan view of external instrumentation for Specimens 8 and 10

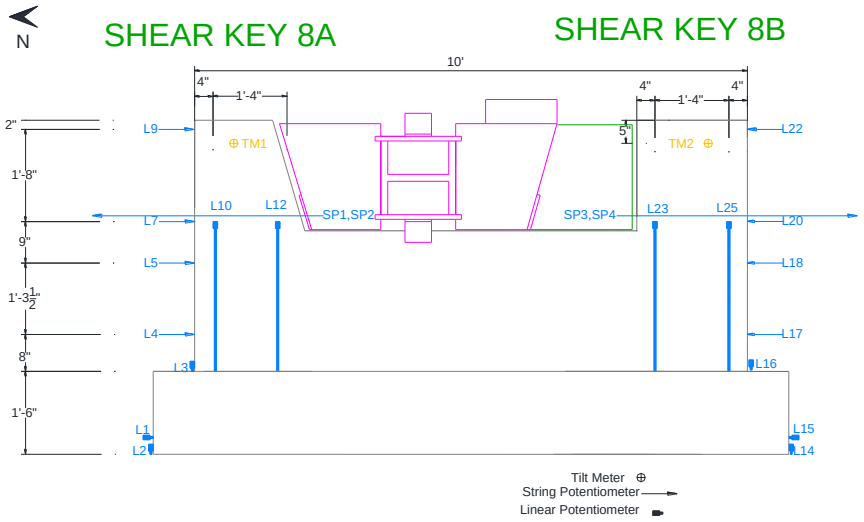

Figure 6.20 External instrumentation located on the west side of Specimens 8 and 10

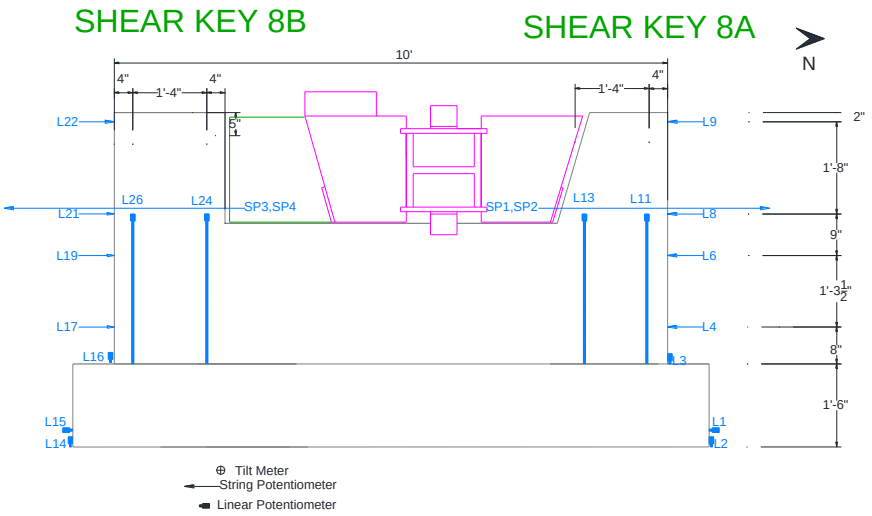

Figure 6.21 External instrumentation located on the east side of Specimens 8 and 10

6.5.2 Specimen 9

To monitor the strains in Specimen 9, a total of 116 electrical resistance strain gages were installed in the longitudinal and transverse reinforcement. The locations of the strain gages were selected to measure strains in the bars at the potential locations of main cracks in the stem wall. These locations included the diagonal cracks in the stem wall and horizontal cracks in the region below the shear key. The location and numbering of these strain gages, preceded by S, is shown in Figure 6.22 through Figure 6.25.

To monitor the deformation of the shear keys, linear potentiometers, string potentiometers and tilt meters were installed external to the specimen, as shown in Figure 6.26 through Figure 6.28. The external instrumentation of the specimen is the same as in Specimens 8 and 10.

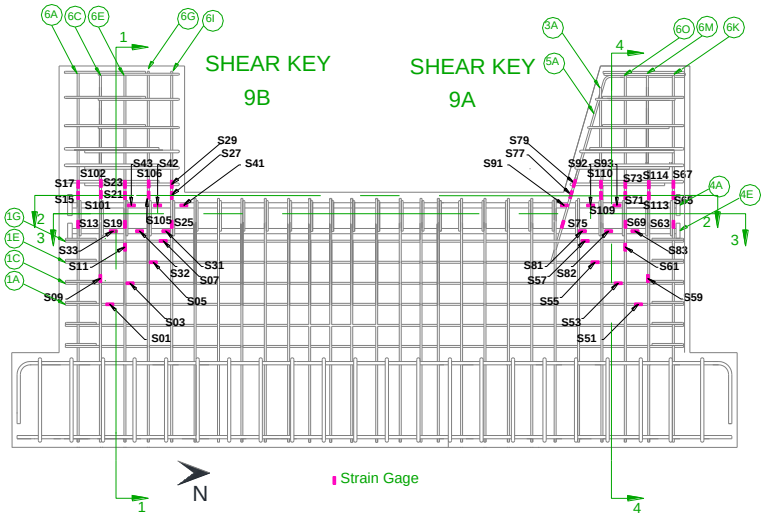

Figure 6.22 Strain gages located on the east side of Specimen 9

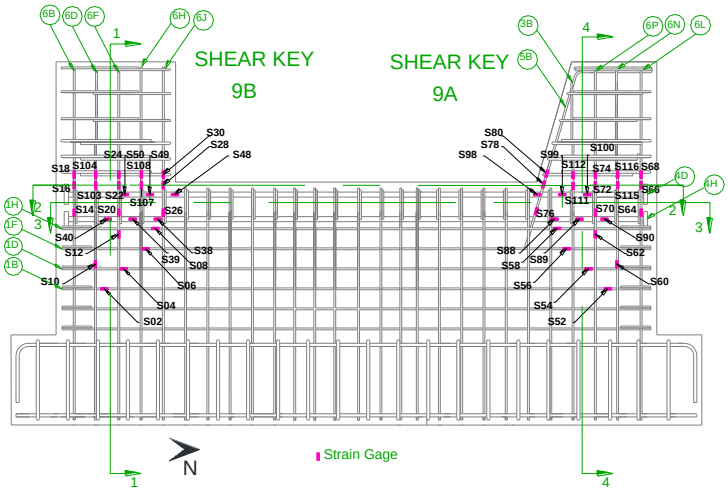

Figure 6.23 Strain gages located on the west side of Specimen 9

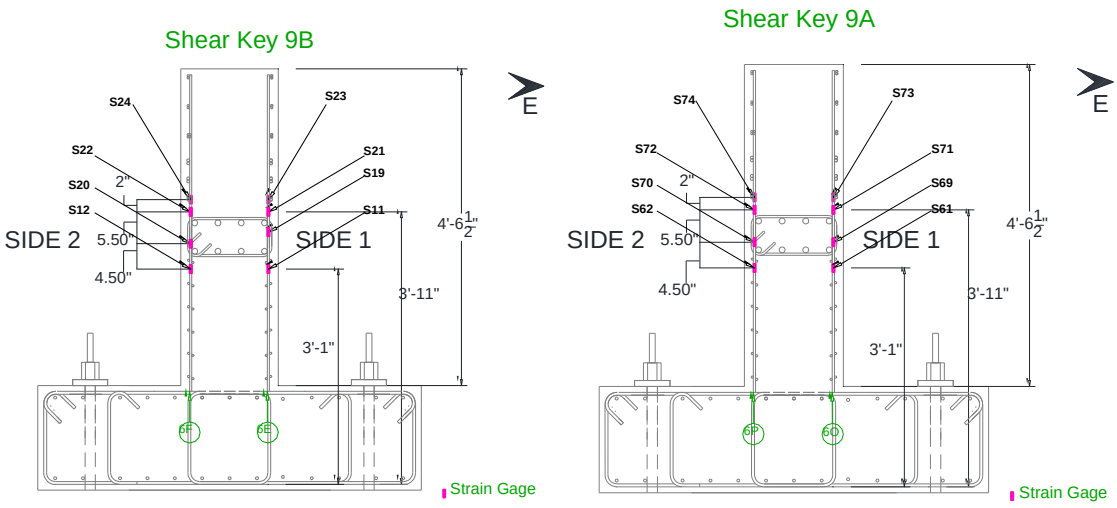

Figure 6.24 Sections 1-1 (left) and 4-4 (right) for Specimen 9
(see Figure 6.22 for the location of the sections)

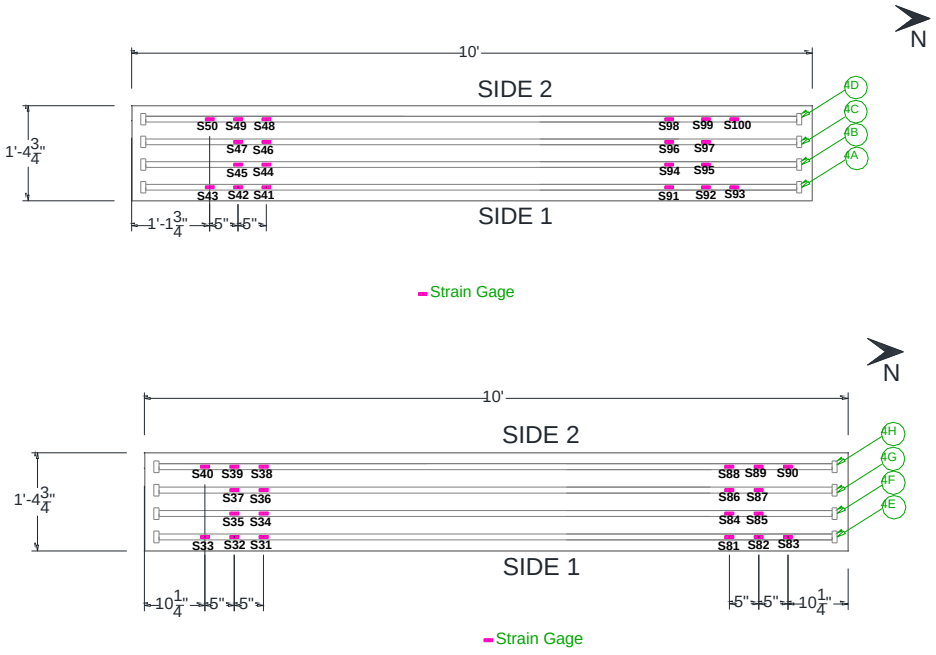

Figure 6.25 Sections 2-2 (top) and 3-3 (bottom) for Specimen 9
(see Figure 6.22 for the location of the sections)

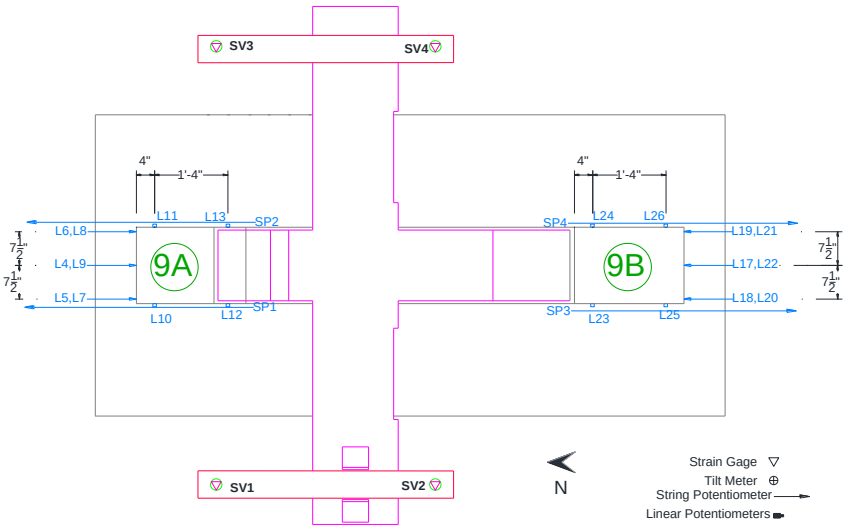

Figure 6.26 Plan view of external instrumentation for Specimen 9

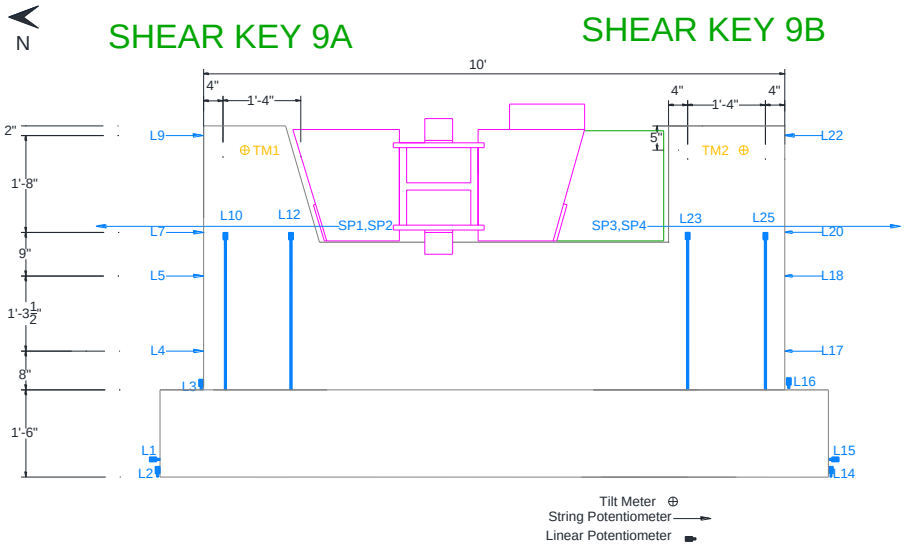

Figure 6.27 External instrumentation located on the west side of Specimen 9

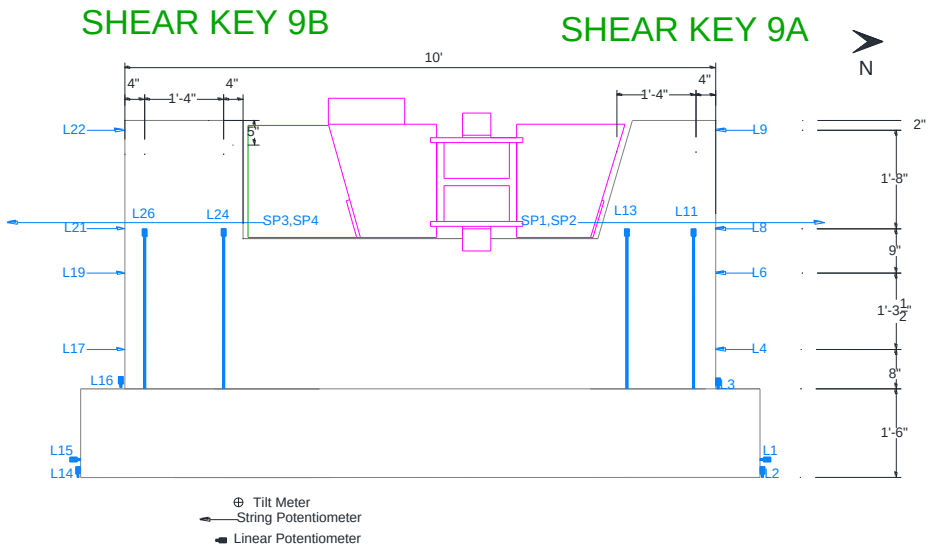

Figure 6.28 External instrumentation located on the east side of Specimen 9

6.6 Loading Protocols and Test Results

6.6.1 Shear Key 8A

Shear key 8A was on the north side of the stem wall. It had an inclined face on the loading side. The loading protocol for the shear key consisted of incremental loading, unloading and reloading with the target loads and displacements shown in Table 6.7. The shear key was initially loaded in force control to 30 kips and then to 150 kips in increments of 20 kips. Then, it was loaded in displacement control up to failure, which occurred at 4.20 in. displacement. The displacement was based on the average of the readings of the displacement transducers L7 and L8, located on the north side of the shear key, as shown in Figure 6.19 through Figure 6.21. The specimen was unloaded 6 times at

90 kips and 130 kips load, and at displacements of 0.10 in, 0.60 in., 1.20 in. and 2.60 in., respectively, to obtain the unloading stiffness.

Table 6.7 Loading protocol for shear key 8A

Step	Control	Target Load/Displacement
1-7	Load	150 kips with 20-kip increments (first step to 30 kips)
8-28	Displacement	4.20 in. with 0.20 in. increments

The first crack on the stem wall was observed on the east face of the specimen, at a horizontal load of 50 kips. It initiated at the toe of the shear key and propagated diagonally, as shown in Figure 6.29. A similar crack was observed on the west face of the shear key at a horizontal load of 70 kips, as shown in Figure 6.30. The load increased, and these diagonal cracks propagated downwards, until a load of 90 kips was reached. At that load, an additional diagonal crack parallel to the first formed on the west face of the stem wall below the shear key, as shown in Figure 6.30.

Figure 6.29 First diagonal crack observed on the east face of shear key 8A

Figure 6.30 Propagation of diagonal crack and formation of additional diagonal crack on the west face of shear key 8A

At a horizontal load of 110 kips, some of the existing diagonal shear cracks started to propagate horizontally. The change in the direction of the crack propagation is shown in Figure 6.31.

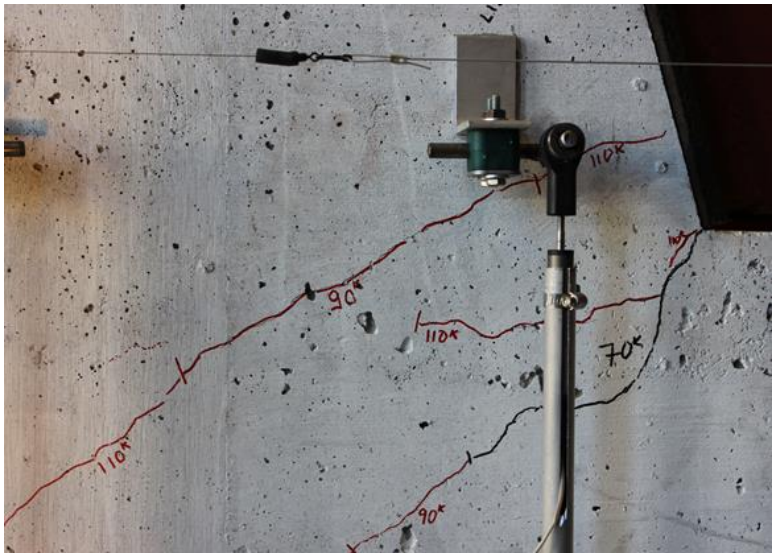

Figure 6.31 Change in the direction of crack propagation on the west face of shear key 8A

At a horizontal load of 130 kips, a diagonal crack initiated from the top of the stem wall. The crack initiation point was 14 in. away from the toe of the shear key. The width of this crack remained small throughout the test. At this load level, additional short diagonal cracks formed on the stem wall, below the shear key. The maximum crack width measured was 0.08 in. The cracks on the east face are shown in Figure 6.32.

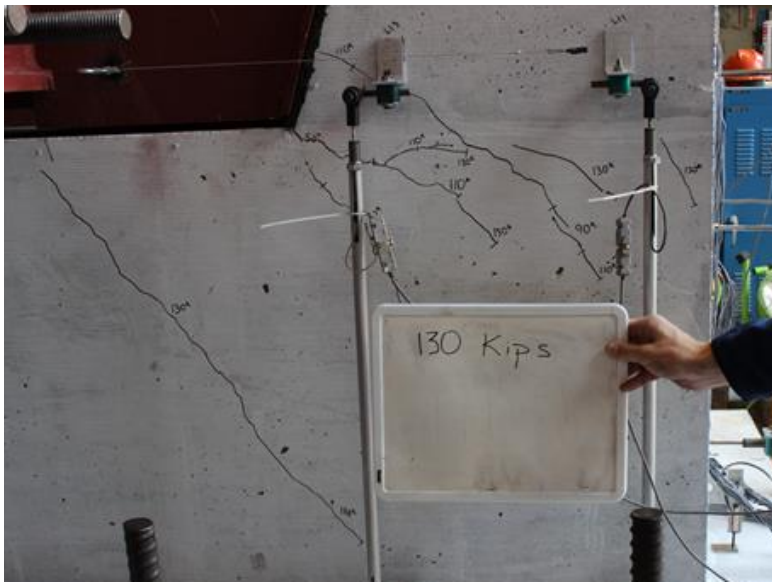

Figure 6.32 Cracks on the east face of shear key 8A at 130 kips load

As the load increased to 230 kips, additional diagonal cracks appeared on the stem wall closer to shear key 8B. These cracks remained small throughout the test. The existing cracks below the shear key increased in size. A diagonal crack appeared behind the heads of the horizontal shear reinforcement in the stem wall.

Figure 6.33 Cracks on the east face of shear key 8A at 230 kips load

Right after the maximum resistance of 286 kips was reached, a decrease of the horizontal load resistance of the shear key was observed. At that load, the cracks below the shear key joined together and formed a horizontal sliding shear plane, as shown in Figure 6.34. The sliding shear plane was located right above the top horizontal shear reinforcement in the stem wall. The sliding shear plane continued with an increased slope towards the free end of shear key. It was then joined with the diagonal crack, which opened exposing the heads of the horizontal shear reinforcement in the stem wall, as shown in Figure 6.34.

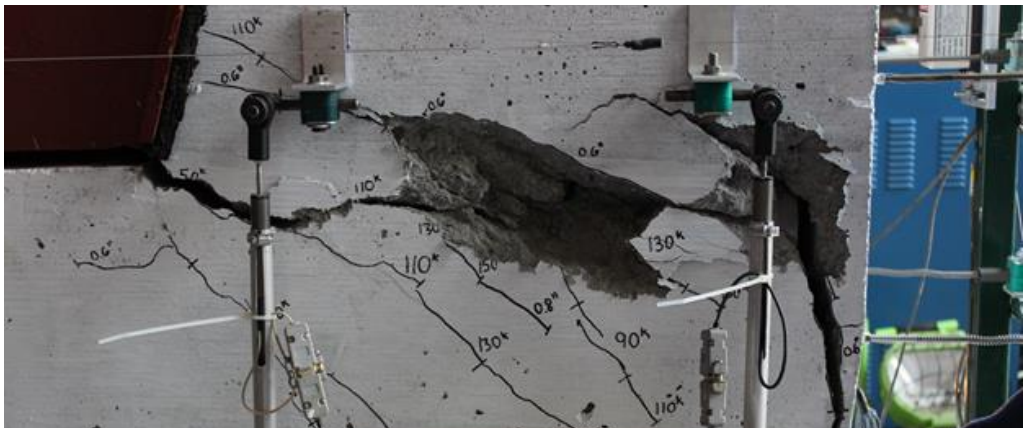

Figure 6.34 Sliding shear plane from the east face of shear key 8A

Additional drops of the horizontal load were observed at displacements of 1.20 in., 2.70 in. and 3.60 in. due to the fracture of the vertical dowel bars. The horizontal load resistance is plotted against the horizontal displacement in Figure 6.35. The horizontal displacement is the averaged reading of the linear potentiometers L7 and L8, whose locations are shown in Figure 6.19 through Figure 6.21.

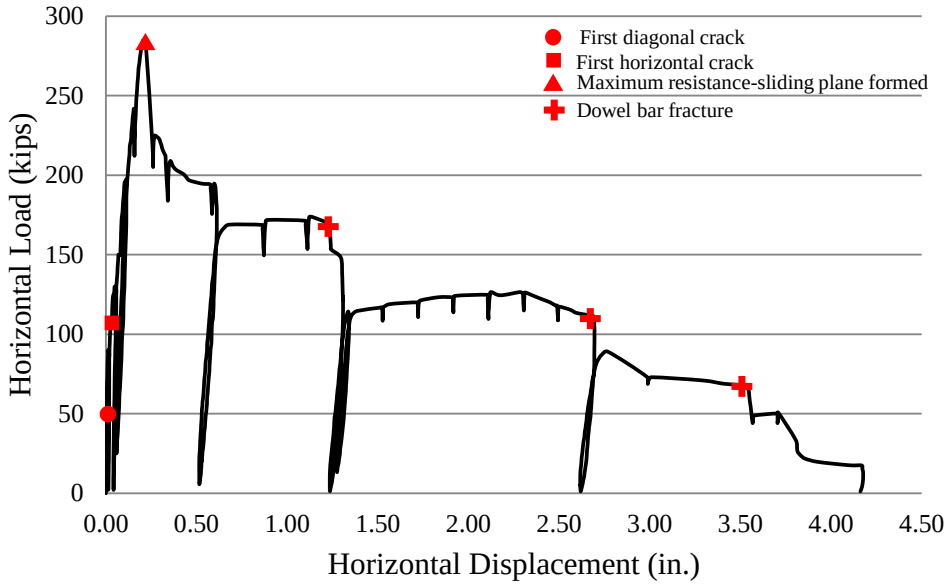

Figure 6.35 Horizontal load-vs.-horizontal displacement for shear key 8A

After the test, the shear key was removed from the stem wall and the sliding surface was inspected, and shown in Figure 6.36.

Figure 6.36 Sliding surface on stem wall after removing shear key 8A

Vertical load on Shear Key

The measurements from the strain gages on the bars in the hold-down frames indicate that at the peak horizontal load, a 90-kip vertical force was applied to the shear key. In Figure 6.37, the measured and the theoretical vertical forces are plotted against the measured horizontal load. The theoretical vertical force is calculated from the measured horizontal load and the angle of the inclined face of the shear key, which is assumed to have zero friction. A good correlation between the theoretical and the measured values of the vertical force is observed. The use of the expansion joint filler reduced the friction along the inclined surface of the shear key, as compared to Specimen 7.

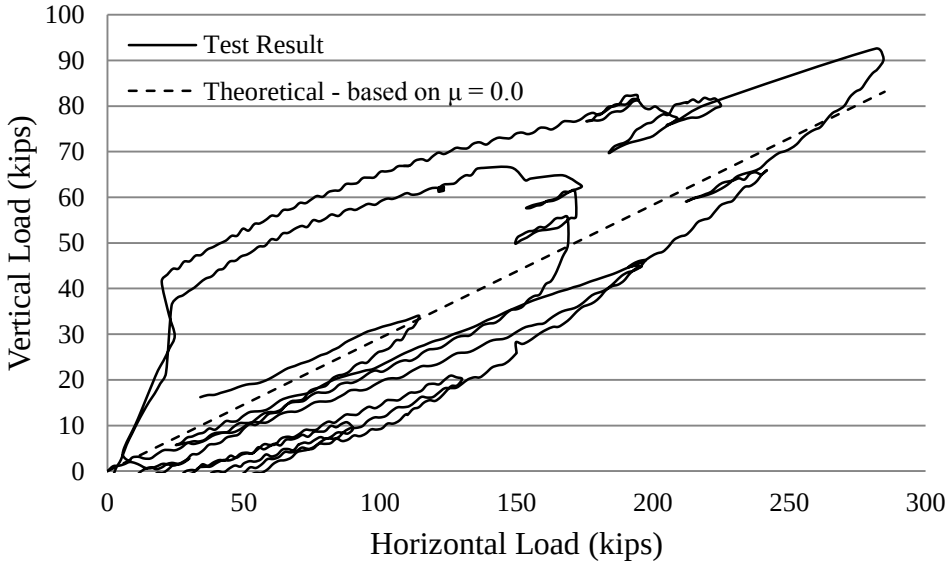

Figure 6.37 Measured and theoretical vertical forces on shear key 8A

Strains in Horizontal Shear Reinforcement of Stem Wall

Strains in the horizontal shear reinforcement of the stem wall were measured. Readings from strain gages registering the largest strains in each bar are plotted against the horizontal load in Figure 6.38 and Figure 6.39. The locations of these gages are shown in Figure 6.18. All the stain-gage readings were within the elastic regime. The change in the slope of the curves coincides with the formation of the first horizontal crack below the shear key, as shown in Figure 6.31.

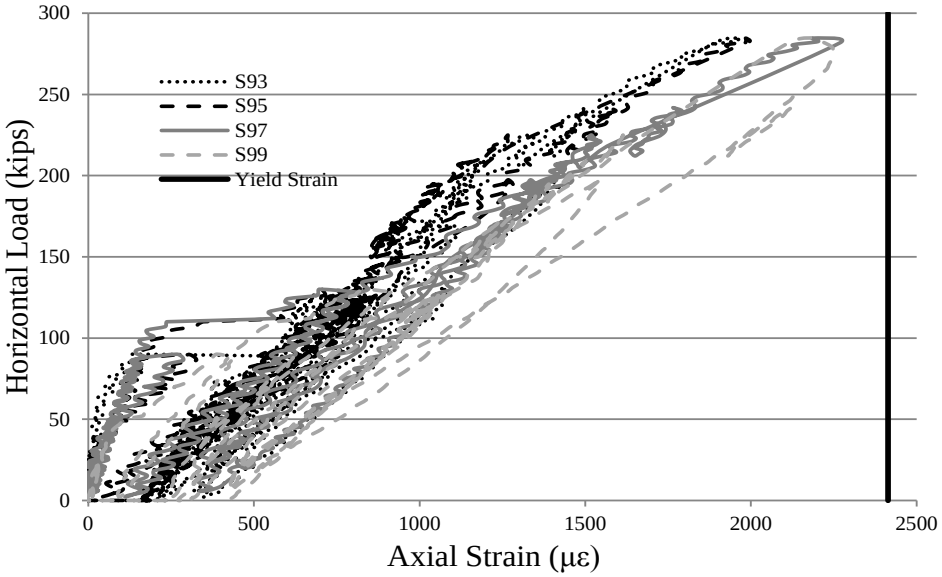

Figure 6.38 Horizontal load-vs.-axial strain in the horizontal shear reinforcement in the top row in the stem wall (near shear key 8A)

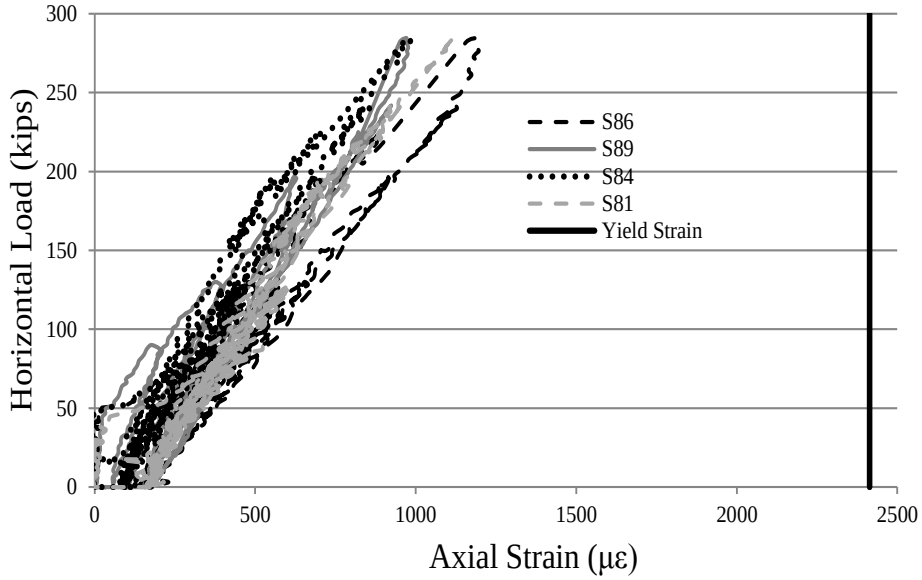

Figure 6.39 Horizontal load-vs.-axial strain in the horizontal shear reinforcement in the bottom row in the stem wall (near shear key 8A)

Strains in Vertical Dowel Bars

The averaged strain readings of the strain gages in the vertical dowel bars are plotted in Figure 6.40 against the horizontal displacement. The locations of the strain

gages are shown in Figure 6.15 and Figure 6.16. Only the strain gages that were close to the sliding plane are plotted.

Based on Figure 6.40, it can be observed that S77 and S78 reached the yield strain very early in the test, followed by S71 and S72 and lastly by S65 and S66. This can be attributed to the in-plane rotation of the shear key, as discussed in the next section. The readings show that appreciable tensile forces developed by the vertical dowel bars from the beginning of the test.

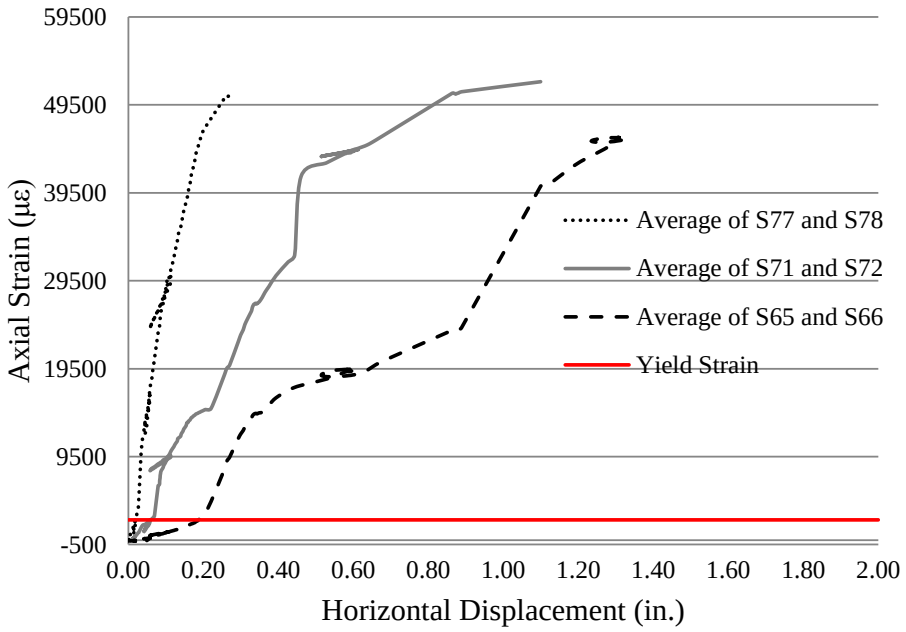

Figure 6.40 Average of strain-gage readings from dowel bars in shear key 8A

In-Plane Rotation of Shear Key

The in-plane rotation of the shear key was monitored with the tilt meter TM1, whose location is shown in Figure 6.20. The readings of the tilt meter are plotted in Figure 6.41 against the horizontal displacement. Most of the rotation of the shear key occurred before the maximum horizontal resistance was reached. After this point, the

displacement of the shear key was dominated by sliding. A small drop is observed right after the maximum resistance was reached and additional rotations can be observed after the vertical dowel bar fractured at 1.20 and 2.70 in.

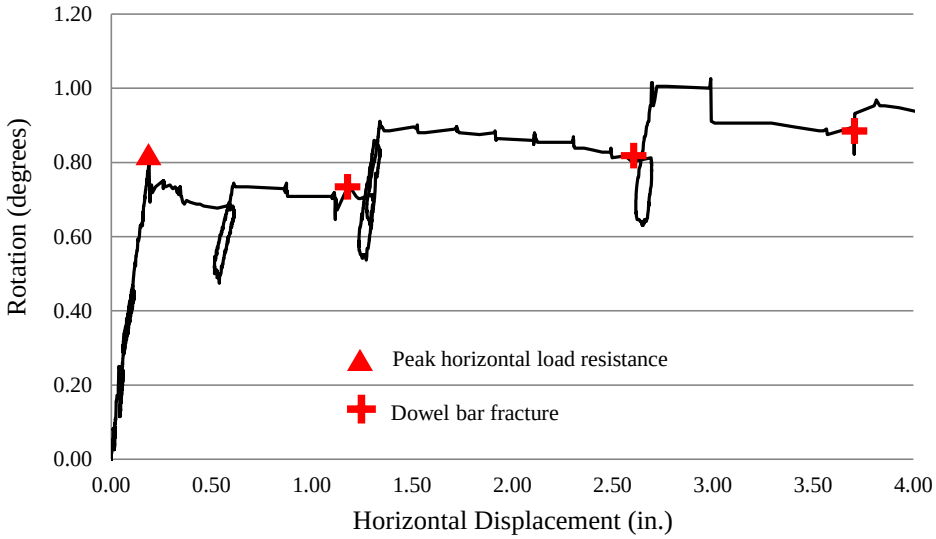

Figure 6.41 In-plane rotation of shear key 8A

Vertical Uplift of Shear Key

The vertical uplift of the shear key was monitored in four locations with the displacement transducers L10-L13, whose locations are shown in Figure 6.19 through Figure 6.21. The readings of L11 and L13, which were located on the east face of the shear key, suggest that the shear key experienced a significant vertical uplift and that the uplift was larger at the loaded end of the shear key. Readings from these transducers are plotted against the horizontal displacement of the shear key in Figure 6.42.

Figure 6.43 shows the readings of the displacement transducers L10 and L11, which were positioned on the free end of the shear key at the east and west faces, respectively, plotted against the horizontal displacement of the shear key. The

comparison of the two linear potentiometers shows that there was a negligible out-of-plane rotation of the shear key. The linear potentiometer L12 was damaged early in the test and is not considered in the following plots.

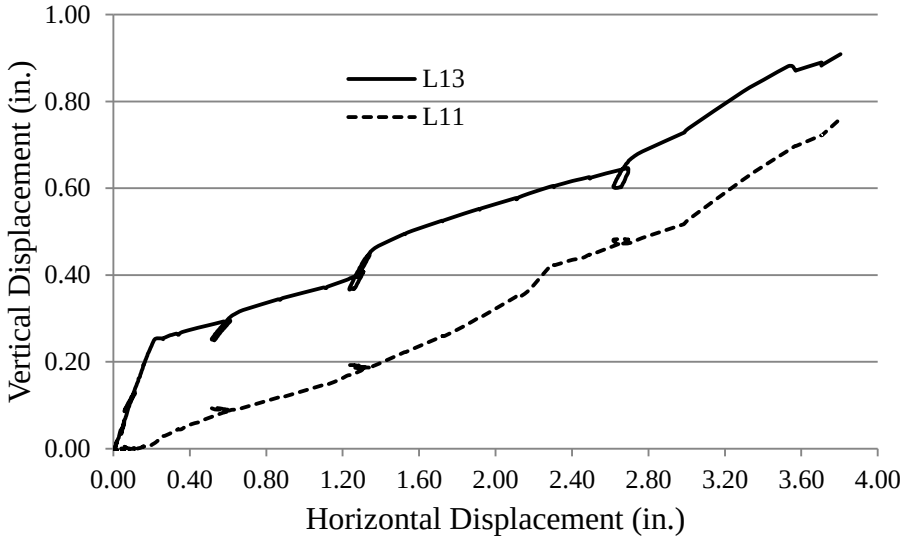

Figure 6.42 Vertical uplift of the east face of shear key 8A

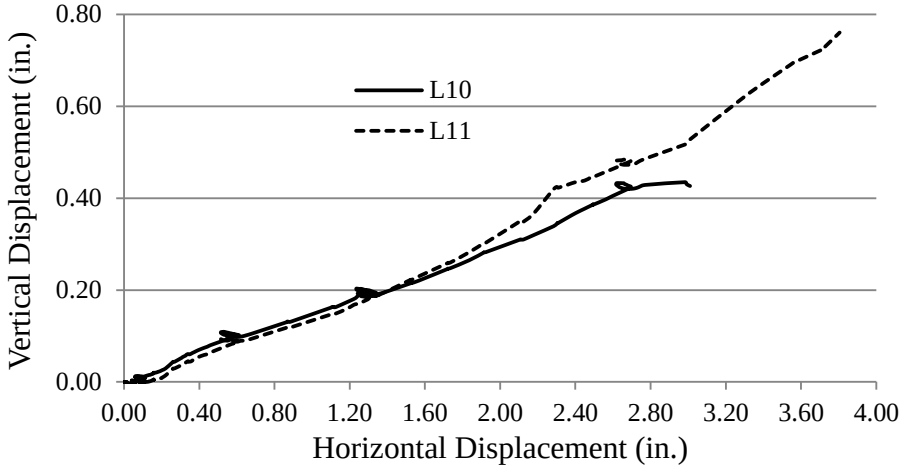

Figure 6.43 Vertical uplift near the free end of shear key 8A

6.6.2 Shear Key 8B

Shear key 8B was on the south side of the stem wall and had a vertical face on the loading side. The loading protocol for the shear key consisted of incremental loading, unloading, and reloading, with the target loads and displacements shown in Table 6.8. The shear key was initially loaded in force control to 20 kips, then to 40 kips and then to 80 kips in increments of 10 kips. Then, it was loaded in displacement control up to failure, which occurred at 3.20 in. displacement. The displacement was based on the average of the readings from displacement transducers L20 and L21, located on the south side of the shear key, as shown in Figure 6.19 through Figure 6.21. The specimen was unloaded 6 times at 60 kips and 80 kips load, and at displacements of 0.10 in., 0.40 in., 1.00 in., 1.60 in., respectively, to obtain the unloading stiffness.

Table 6.8 Loading protocol for shear key 8B

Step	Control	Target Load/Displacement
1	Load	20 kips
2	Load	40 kips
3-6	Load	80 kips with 10-kip increments
7-10	Displacement	0.40 in. with 0.10 in. increments
11-24	Displacement	3.20 in. with 0.20 in. increments

The first cracks in the stem wall were observed on the east and west faces of the shear key at a horizontal load of 50 kips. They initiated at the toe of the shear key and propagated diagonally, as shown in Figure 6.44. As the load increased to 80 kips, the diagonal cracks propagated downwards, as shown in Figure 6.45.

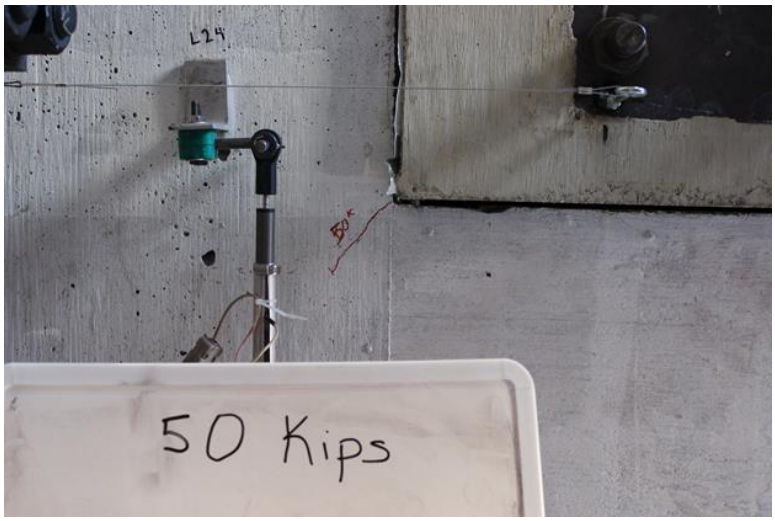

Figure 6.44 First crack on the east face of shear key 8B

Figure 6.45 Propagation of first diagonal crack on the east face of shear key 8B

At a load of 93 kips, an almost horizontal crack formed in the stem wall below the shear key. In Figure 6.46, this crack was marked with “0.02 in”.

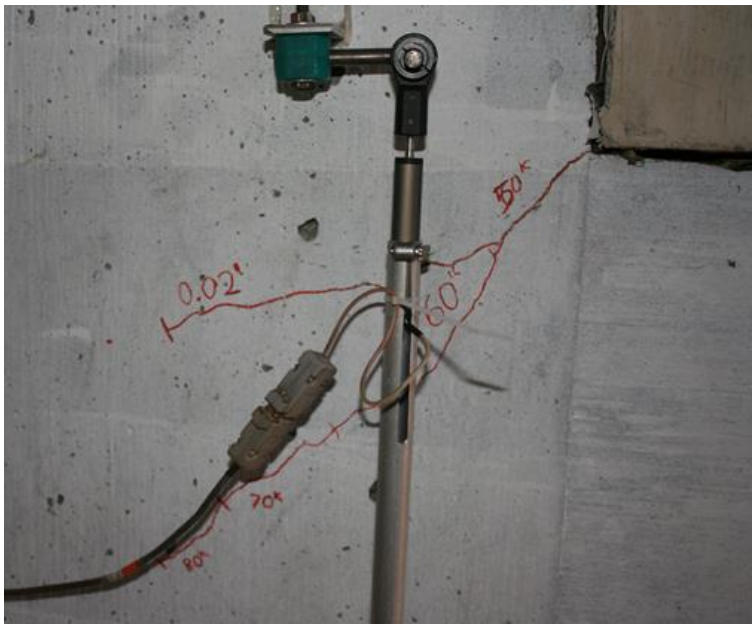

Figure 6.46 First horizontal crack on the east face of shear key 8B

As the load increased, additional diagonal cracks formed on the stem wall below the shear key. The angle of these diagonal cracks with respect to a horizontal plane was smaller than that of the initial diagonal crack. At a horizontal load of 132 kips, an additional diagonal crack initiated from the top of the stem wall. This crack was located 14 in. away from the toe of the shear key. The width of this crack remained small throughout the test.

The specimen reached a maximum horizontal resistance of 198 kips. At that load, a steep diagonal crack formed at the free end of the shear key behind the heads of the horizontal shear reinforcement of the stem wall. Soon after the maximum resistance was reached, the diagonal cracks under the shear key joined to form a sliding shear plane and a decrease of the horizontal load resistance was observed. The sliding plane and cracks on the west face of the shear key are shown in Figure 6.47.

Figure 6.47 Sliding plane from the west face of shear key 8B

As the test progressed, additional drops in the horizontal load resistance were observed due to the fracture of the vertical dowel bars. These drops occurred at 0.56 in., 1.80 in., 2.25 in. and 2.90 in. At the end of the test, only the two vertical dowel bars located at the free end of the shear key had not fractured. The horizontal load resistance of the specimen is plotted against the horizontal displacement in Figure 6.48. The horizontal displacement plotted is the averaged readings of the linear potentiometers L20 and L21, whose locations are shown in Figure 6.20 and Figure 6.21. The condition of the stem wall after the shear key was removed is shown in Figure 6.49.

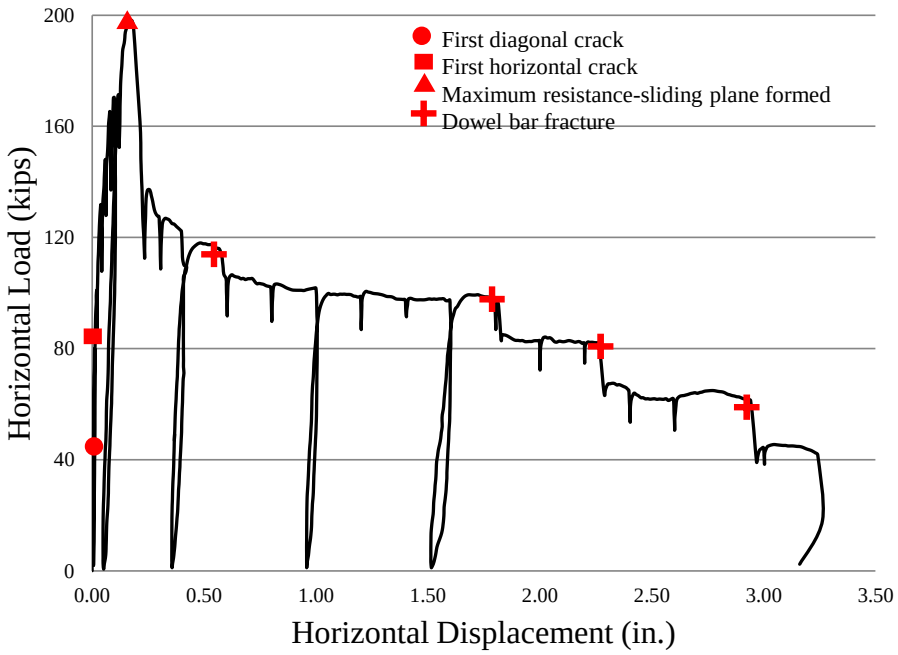

Figure 6.48 Horizontal load-vs.-horizontal displacement for shear key 8B

Figure 6.49 Sliding plane of shear key 8B

Vertical Load on Shear Key

The measurements from the strain gages on the post-tensioning bars in the hold-down frames indicate that a 27-kip vertical force was applied to the shear key at the

maximum horizontal load. In Figure 6.50, the measured vertical forces are plotted against the measured horizontal load. It can be observed that at the first loading steps there is a sudden increase of the vertical load to 8 kips. After that, the vertical load increases almost linearly to 27 kips.

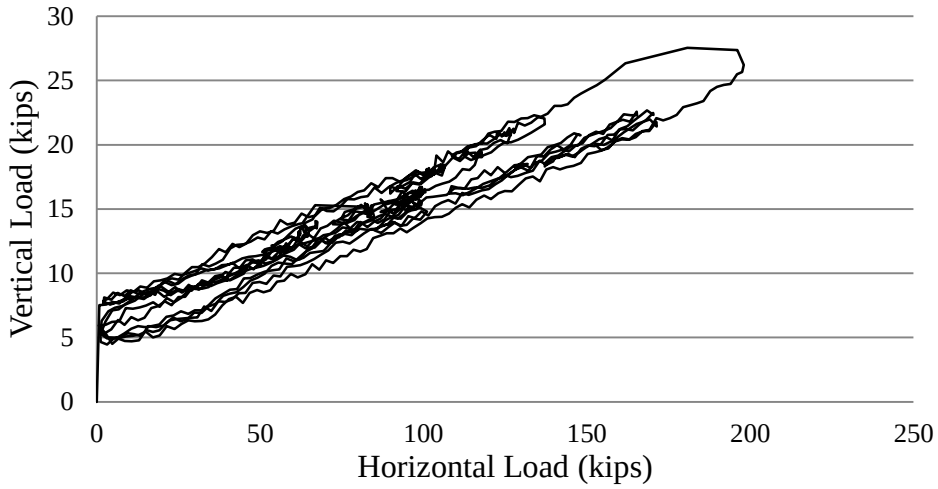

Figure 6.50 Measured vertical force on shear key 8B

Strains in Horizontal Shear Reinforcement of Stem Wall

Strains in the horizontal shear reinforcement of the stem wall were measured. Readings from strain gages registering the largest strains in each bar are plotted against the horizontal load in Figure 6.51 and Figure 6.52. The locations of these gages are shown in Figure 6.18. The stain-gage readings show that all the strains were within the elastic the elastic regime.

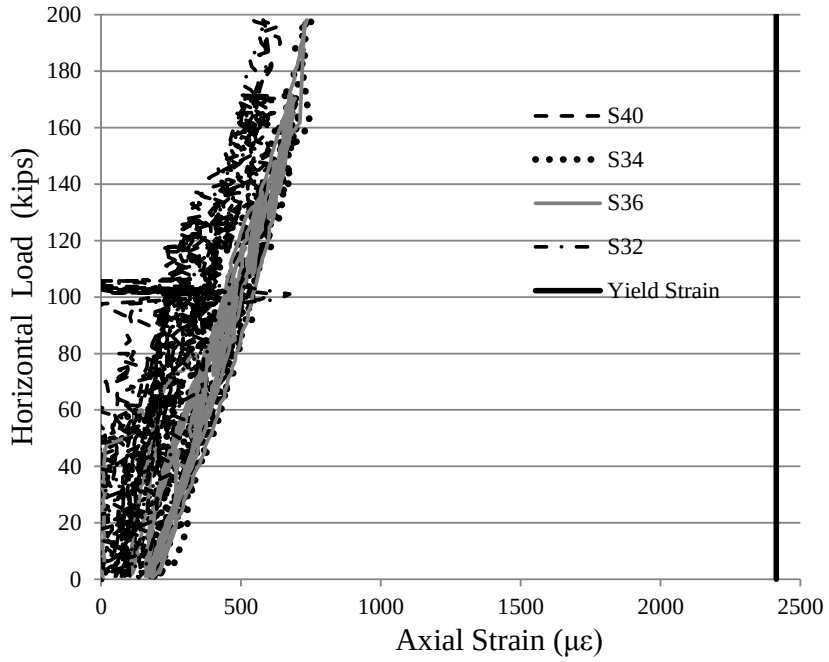

Figure 6.51 Horizontal load-vs.-axial strain in the horizontal shear reinforcement in the bottom row in the stem wall (near shear key 8B)

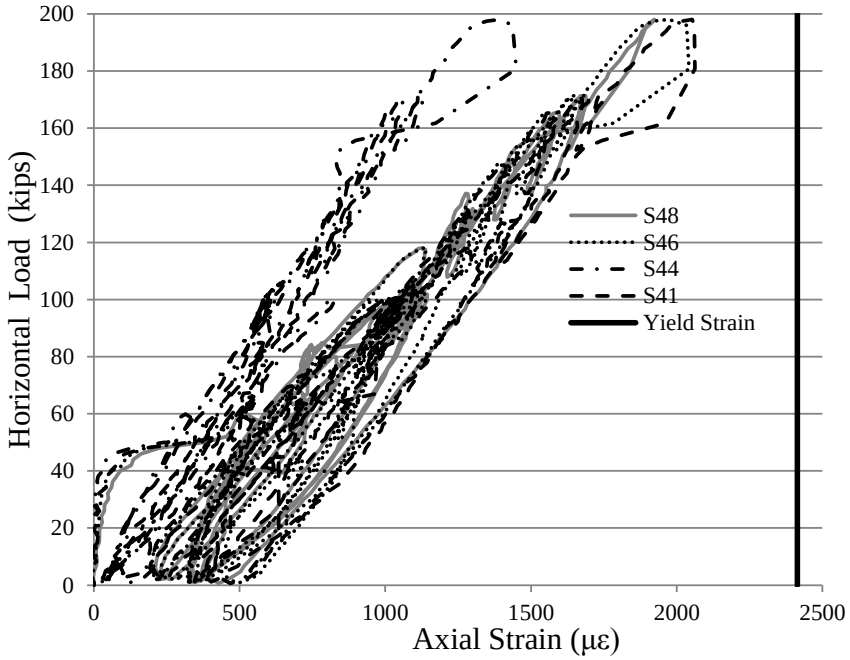

Figure 6.52 Horizontal load-vs.-axial strain in the horizontal shear reinforcement in the top row in the stem wall (near shear key 8B)

Strains in Vertical Dowel Bars

The averaged strain readings of the strain gages in the vertical dowel bars are plotted in Figure 5.33 against the horizontal displacement. The locations of the strain gages are shown in Figure 6.15 and Figure 6.16. Only the strain gages that were closer to the sliding plane are considered.

Based on Figure 5.33, it can be observed that S27 and S28 reached the yield strain very early in the test, followed by S21 and S22 and lastly by S15 and S16. This can be attributed to the in-plane rotation of the shear key, as discussed in the following section. The readings also show that appreciable tensile forces developed by the vertical dowel bars from the beginning of the test.

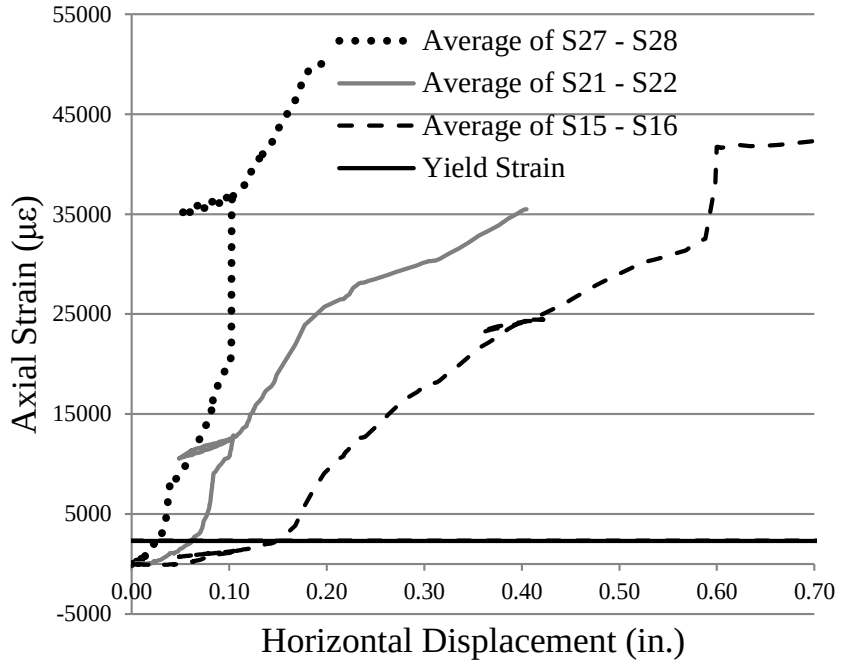

Figure 6.53 Average of strain-gage readings from vertical dowel bars in shear key 8B

In-Plane Rotation of Shear Key

The in-plane rotation of the shear key was monitored with the tilt meter TM2, whose location is shown in Figure 6.20. The readings of the tilt meter are plotted in Figure 6.54 against the horizontal displacement. Almost half of the total rotation of the shear key occurred before the maximum horizontal resistance was reached. The rotation continues to increase until the first bar fractured and then it started to decrease. At a displacement of 2.25 in., the rotation increased again. At the end of the test, the shear key had rotated 2.1 degrees.

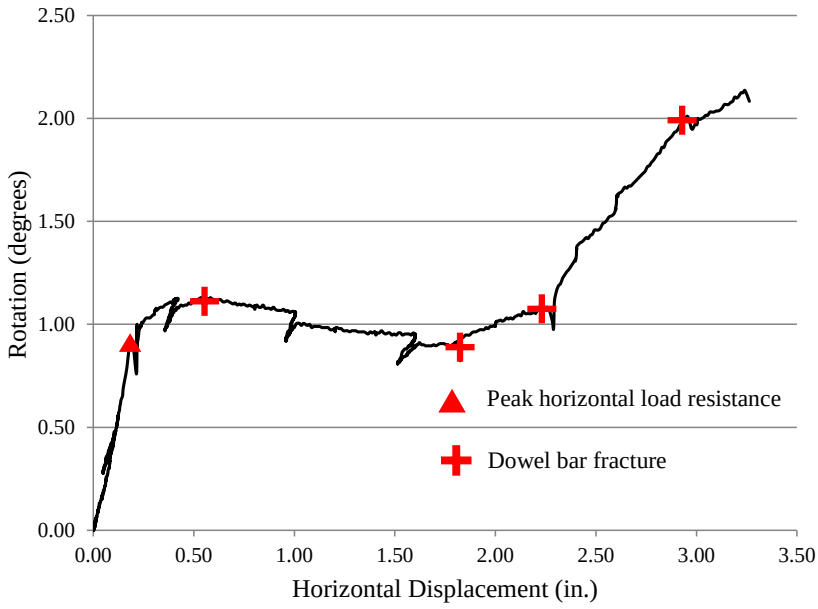

Figure 6.54 In-plane rotation for shear key 8B

Vertical Uplift of Shear Key

The vertical uplift of the shear key was monitored in four locations with the linear potentiometers L23-L26, whose locations are shown in Figure 6.20 and Figure 6.21. Transducers L23 and L24 were located at the north (loaded) end of the shear key, while

L25 and L26 were located at the south end. The averaged readings of L23 and L24, and L25 and L26 suggest that the shear key experienced a significant uplift and that the vertical uplift was larger at the loaded end of the shear key. Readings from these transducers are plotted against the horizontal displacement of the shear key in Figure 6.55.

Figure 6.56 shows the averaged readings of linear potentiometers L23 and L25, and L24 and L26, which were positioned on the west and east faces of the stem wall, respectively, plotted against the horizontal displacement of the shear key. The comparison of the two curves shows that there was practically no out-of-plane rotation.

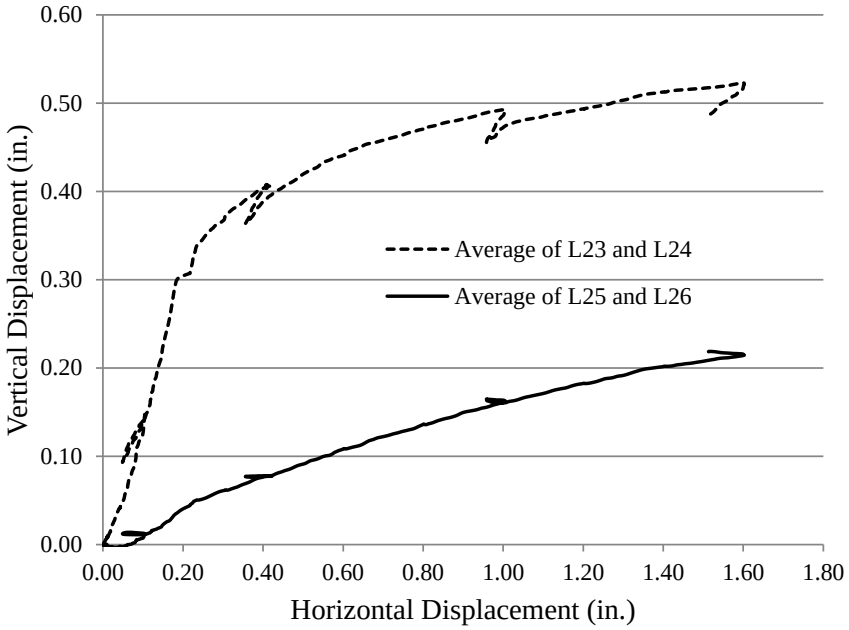

Figure 6.55 Vertical uplift of the north and south ends of shear key 8B

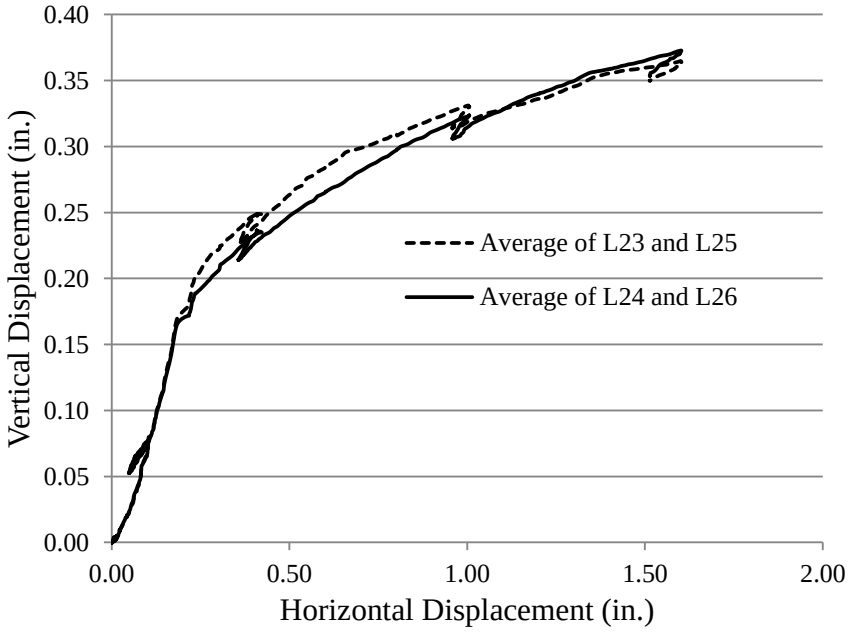

Figure 6.56 Vertical uplift of the east and west faces of shear key 8B

6.6.3 Shear Key 9A

Shear key 9A was on the north side of the stem wall of Specimen 9 and had an inclined face on the loading side. It had more vertical dowel bars connecting the shear key to the stem wall as compared to shear key 8A. The loading protocol for the shear key consisted of incremental loading, unloading, and reloading, with the target loads and displacements shown in Table 6.9. The shear key was initially loaded in force control to 30 kips, then to 150 kips in increments of 20 kips and then to 180 kips and 210 kips. Finally, it was loaded in displacement control up to failure, which occurred at 5.50 in. displacement. The displacement was based on the averaged readings of the displacement transducers L7 and L8, located on the north side of the shear key, as shown in Figure 6.26 through Figure 6.28. The specimen was unloaded 7 times at 90 kips, 130 kips and 180

kips load, and at displacements of 0.60 in., 1.00 in., 1.60 in., 2.20 in., respectively, to obtain the unloading stiffness.

Table 6.9 Loading protocol for shear key 9A

Step	Control	Target Load/Displacement
1	Load	30 kips
2-7	Load	150 kips with 20-kip increments
8-9	Load	150-210 with 30-kip increments
10-20	Displacement	2.60 in. with 0.20 in. increments
21	Displacement	3.00 in.
22-26	Displacement	5.50 in with 0.50 in. increments

The first cracks on the stem wall were observed on the east and west face of the specimen at a horizontal load of 30 kips. They initiated at the toe of the shear key and propagated diagonally, as shown in Figure 6.57. As the load increased to 110 kips, the diagonal cracks propagated downwards. At that load, additional diagonal cracks formed on the stem wall below the shear key, which had smaller inclination than the initial diagonal crack. A diagonal crack initiated from the top of the stem wall 12 in. away from the toe of the shear key. The width of this crack remained small throughout the test. The cracks on the east face of the specimen are shown in Figure 6.58.

Figure 6.57 First crack on the east face of shear key 9A

Figure 6.58 Propagation of first diagonal crack and additional cracks on the east face of shear key 9A

The cracks of the stem wall at 210 kips are shown in Figure 6.59. Several diagonal cracks formed in the region below the shear key and a crack was observed in the area behind the heads of the horizontal shear reinforcement of the stem wall at 180 kips, also shown in the same figure.

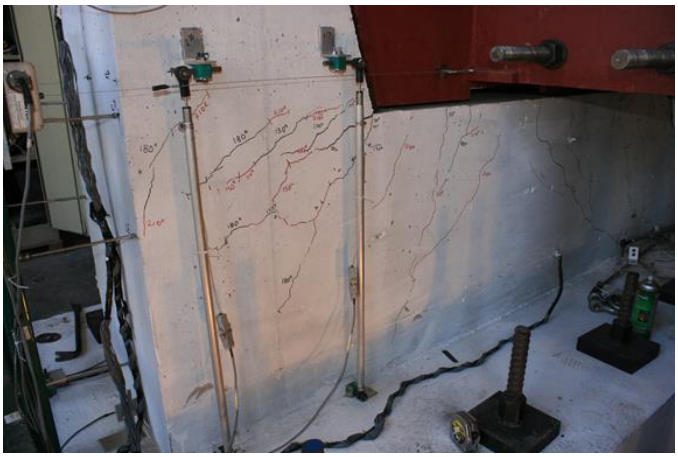

Figure 6.59 Cracks on the west face of shear key 9A at 210 kips

The specimen reached a maximum horizontal resistance of 336 kips. At that load, the diagonal cracks under the shear key joined to form a sliding shear plane and a drop in the horizontal load resistance was observed. The sliding plane and cracks of the east face of the shear key are shown in Figure 6.60. As the test progressed, additional drops in the horizontal load resistance were observed due to the fracture of the vertical dowel bars. These drops occurred at 1.00 in., 1.10 in., 1.70 in., 3.70 in., 4.00 in. and 5.00 in. The horizontal load resistance of the specimen is plotted against the horizontal displacement in Figure 6.61. The horizontal displacement plotted is the averaged readings of the linear potentiometers L7 and L8, whose locations are shown in Figure 6.26 through Figure 6.28.

Figure 6.60 Sliding plane on the east face of shear key 9A

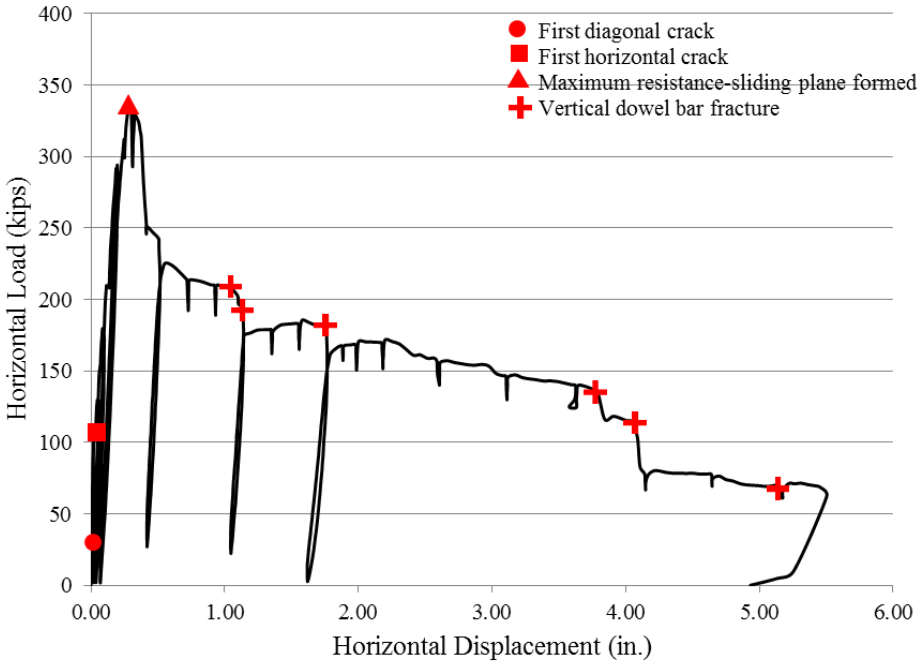

Figure 6.61 Horizontal load-vs.-horizontal displacement for shear key 9A

The condition of the specimen at the end of the test is shown in Figure 6.62 and the horizontal shear sliding plane is shown in Figure 6.63.

Figure 6.62 Deformed configuration of shear key 9A at the end of the test

Figure 6.63 Sliding plane condition after shear key 9A was removed

Vertical load on Shear Key

The measurements from the strain gages on the post-tensioning bars in the hold-down frames indicate that a 127-kip vertical force was applied to the shear key at the maximum horizontal load. In Figure 6.64, the measured and the theoretical vertical forces are plotted against the measured horizontal load. The theoretical vertical force is calculated from the measured horizontal load and the angle of the inclined face of the

shear key, which is assumed to have zero friction. It can be observed that the vertical forces applied on the shear key are close to the theoretical prediction.

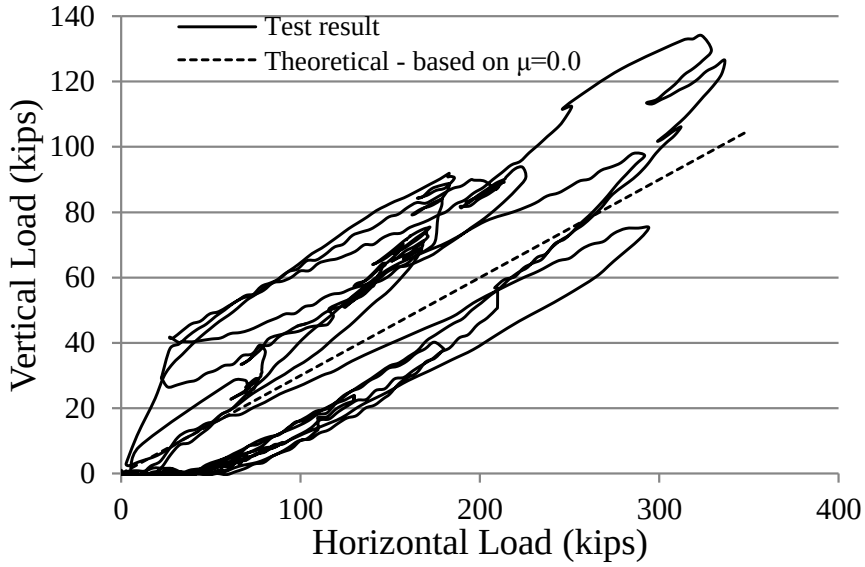

Figure 6.64 Measured and theoretical vertical forces on shear key 9A

Strains in Horizontal Shear Reinforcement of Stem Wall

Strains in the horizontal shear reinforcement of the stem wall were measured. Readings from strain gages registering the largest strains are plotted against the horizontal load in Figure 6.65 and Figure 6.66. The locations of these gages are shown in Figure 6.25. The stain-gage readings show that one of the horizontal bars in the bottom row reached the yield strain, whereas all the horizontal bars in the top row reached their yield strength.

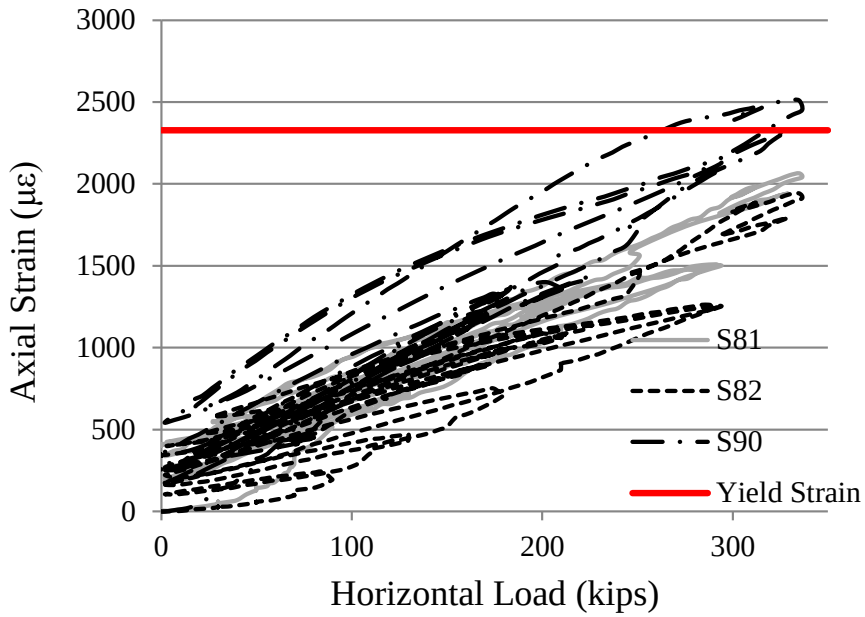

Figure 6.65 Horizontal load-vs.-axial strain in the horizontal shear reinforcement in the bottom row in the stem wall (near shear key 9A)

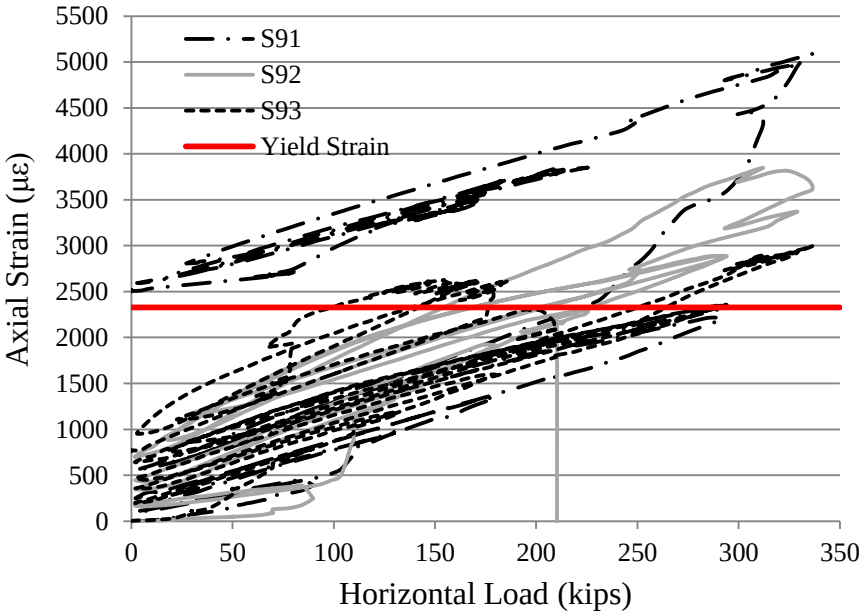

Figure 6.66 Horizontal load-vs.-axial strain in the horizontal shear reinforcement in the top row in the stem wall (near shear key 9A)

Strains in Vertical Dowel Bars

The averaged strain readings of the strain gages in the vertical dowel bars are plotted in Figure 6.67 against the horizontal displacement. The locations of the strain gages are shown in Figure 6.22 and Figure 6.23. Only the strain gages that were close to the sliding plane are considered. Strain gage S78 was damaged early in the test and is not plotted.

Based on Figure 6.67, it can be observed that the strain gages that were closer to the loaded end of the shear key reached the yield strength earlier in the test, while the strain gages at the free end of the shear key reached the yield strain last. This is the result of the in-plane rotation of the shear key, as discussed in the next section. The readings also show that appreciable tensile forces developed by the vertical dowel bars from the beginning of the test.

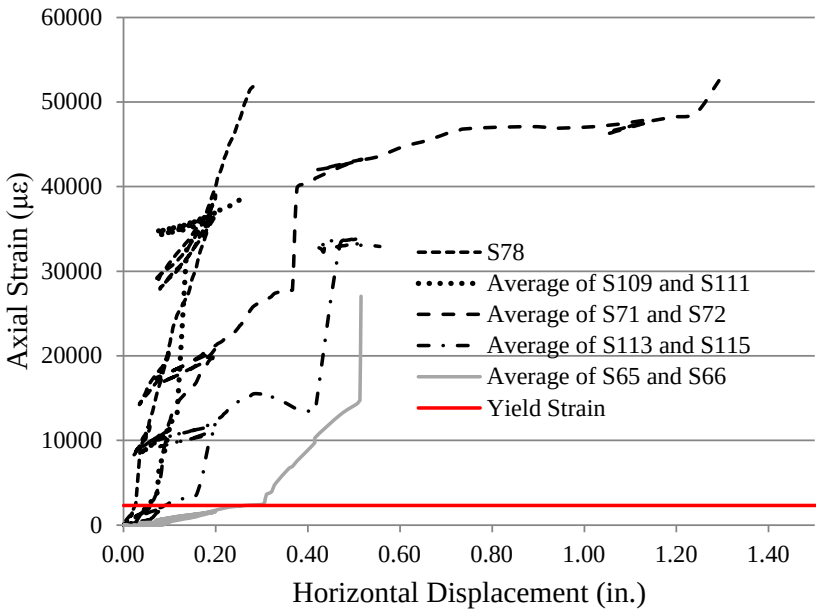

Figure 6.67 Average of strain-gage readings from dowel bars in shear key 9A

In-Plane Rotation of Shear Key

The in-plane rotation of the shear key was monitored with the tilt meter TM1, whose location is shown in Figure 6.27. The readings of the tilt meter are plotted in Figure 6.68 against the horizontal displacement. Almost half of the total rotation of the shear key occurred before the maximum horizontal resistance was reached. At that load level, the rotation dropped and started to increase again at 1.70 in. displacement, after the fracture of some of the vertical dowel bars. An additional increase is shown at 4.00 in. displacement when another vertical dowel bar fractured.

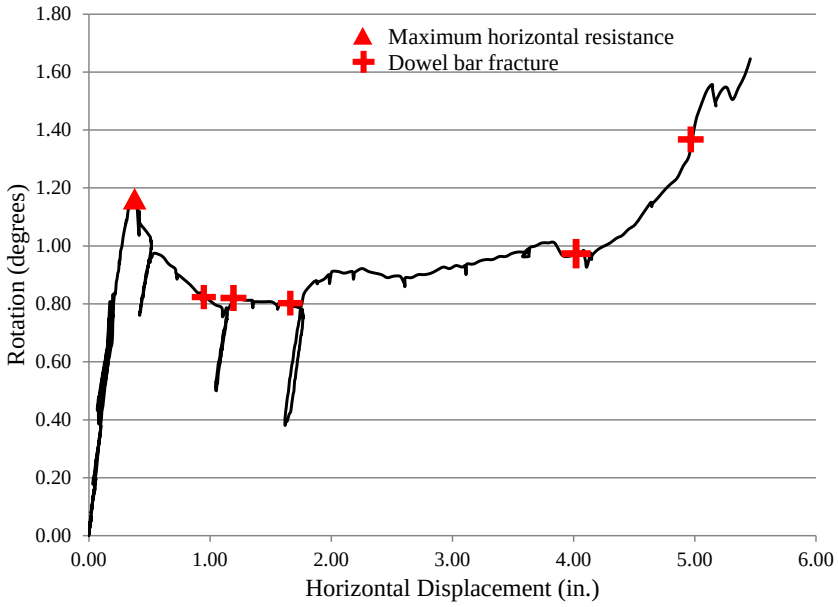

Figure 6.68 In-plane rotation of shear key 9A

Vertical Uplift of Shear Key

The vertical uplift of the shear key was monitored in four locations with the linear potentiometers L10-L13, whose locations are shown in Figure 6.26 through Figure 6.28. Transducers L10 and L11 were close to the free end of the shear key, while L12 and L13

were close to the loaded end. The readings of L10 and L13, suggest that the shear key experienced a significant uplift as the test progressed and that the vertical uplift was higher at the loaded end of the shear key. Readings from these transducers are plotted against the horizontal displacement of the shear key in Figure 6.69.

Figure 6.70 shows the readings of linear potentiometers L13 and L12, which were positioned in the west and east face of the stem wall, respectively, plotted against the horizontal displacement of the shear key. The comparison of the two linear potentiometers shows that there was almost zero out-of-plane rotation up to 3.0 in. horizontal displacement. After 3.0 in., the readings of the L12 are anomalous and are not presented.

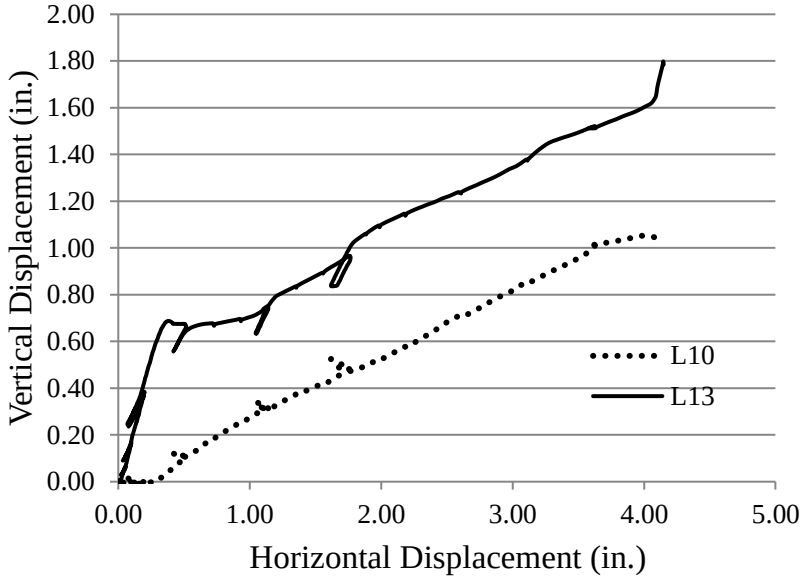

Figure 6.69 Vertical uplift of the free and loaded sides of shear key 9A

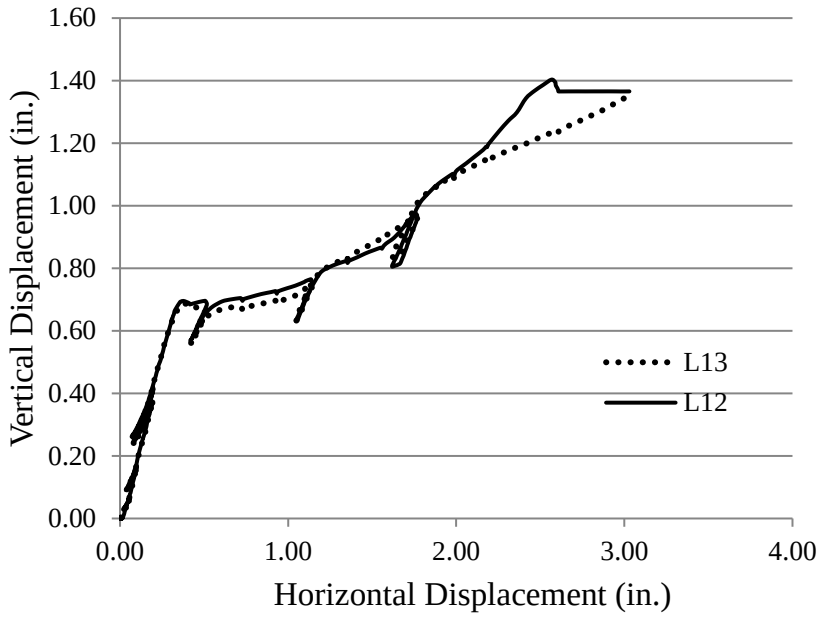

Figure 6.70 Vertical uplift of the east and west faces of shear key 9A

6.6.4 Shear Key 9B

Shear key 9B was on the south side of the stem wall of Specimen 9 and had a vertical face on the loaded side. The loading protocol for the shear key consisted of incremental loading, unloading, and reloading, with the target loads and displacements shown in Table 6.10. The shear key was initially loaded in force control to 150 kips in increments of 20 kips and then to 175. Then, it was loaded in displacement control up to failure, which occurred at 3.20 in. displacement. The displacement was based on the average of the readings from displacement transducers L20 and L21, located on the south side of the shear key, as shown in Figure 6.26 through Figure 6.28. The specimen was unloaded 8 times at 90 kips, 130 kips and 180 kips load, and at displacements of 0.30 in., 0.80 in., 1.20 in., 1.80 in. and 2.40 in., respectively, to obtain the unloading stiffness.

Table 6.10 Loading protocol for shear key 9B

Step	Control	Target Load/Displacement
1-7	Load	150 kips with 20-kip increments
8	Load	175 kips
9-22	Displacement	3.20 in. with 0.20 in. increments

The first cracks on the stem wall were observed on the east and west faces of the specimen at a horizontal load of 50 kips. They initiated at the toe of the shear key and propagated diagonally, as shown in Figure 6.71. At a horizontal load of 110 kips, the diagonal cracks propagated further down and additional diagonal cracks formed on the stem wall below the shear key. These diagonal cracks had smaller inclination with respect to a horizontal plane than the first diagonal crack. At that load, additional diagonal cracks initiated from the top of the stem wall. The width of these cracks remained small throughout the test. The cracks on the east face of the specimen are shown in Figure 6.72.

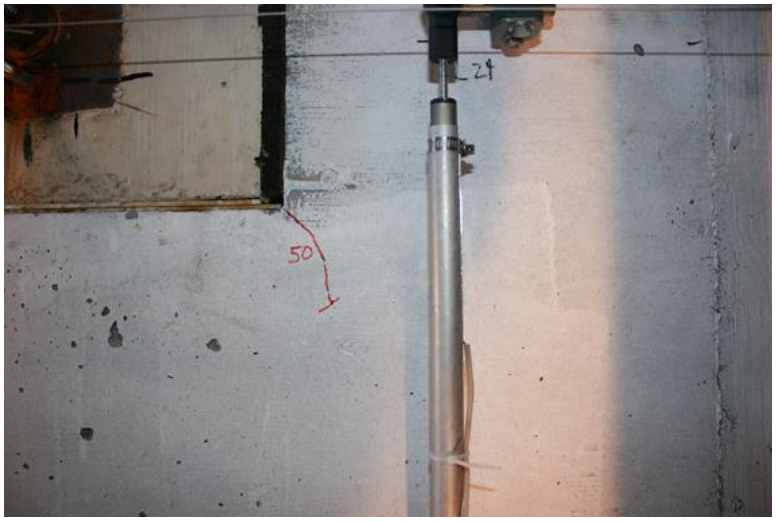

Figure 6.71 First crack on the west face of shear key 9B

Figure 6.72 Propagation of first diagonal crack and additional cracks on the east face of shear key 9B

The cracks of the stem wall at a horizontal displacement of 0.20 in. are shown in Figure 6.73. Several diagonal cracks formed in the region below the shear key and a crack was observed in the area behind the heads of the horizontal shear reinforcement of the stem wall, also shown in the same figure.

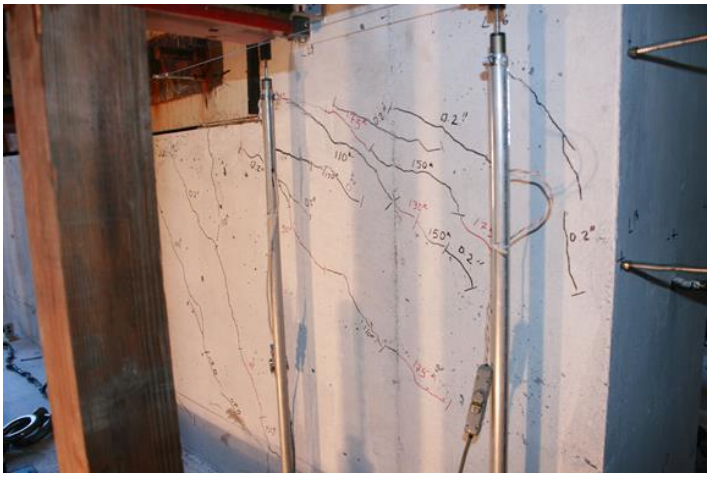

Figure 6.73 Cracks on the west face of shear key 9B at a displacement of 0.20 in.

The specimen reached a maximum horizontal resistance of 316 kips at a displacement of 0.40 in. At that load, the diagonal cracks under the shear key joined and formed a sliding shear plane, and a drop in the horizontal load resistance was observed.

The sliding plane and cracks on the east face of the shear key are shown in Figure 6.74. As the test progressed, additional drops in the horizontal load resistance were observed due to the fracture of the vertical dowel bars. These drops occurred at 1.25 in., 1.45 in., 1.65 in., 1.85 in. and 2.45 in. The fractured bars were visible after the spalling of the concrete occurred, as shown in Figure 6.75. The horizontal load resistance of the specimen is plotted against the horizontal displacement in Figure 6.76. The horizontal displacement plotted is the averaged readings of the linear potentiometers L21 and L22, whose locations are shown in Figure 6.26 through Figure 6.28. After the end of the test, the shear key was removed from the specimen and the surface of the sliding plane was inspected, as shown in Figure 6.77.

Figure 6.74 Sliding plane from the east face of shear key 9B

Figure 6.75 Fractured bars near the east face of shear key 9B

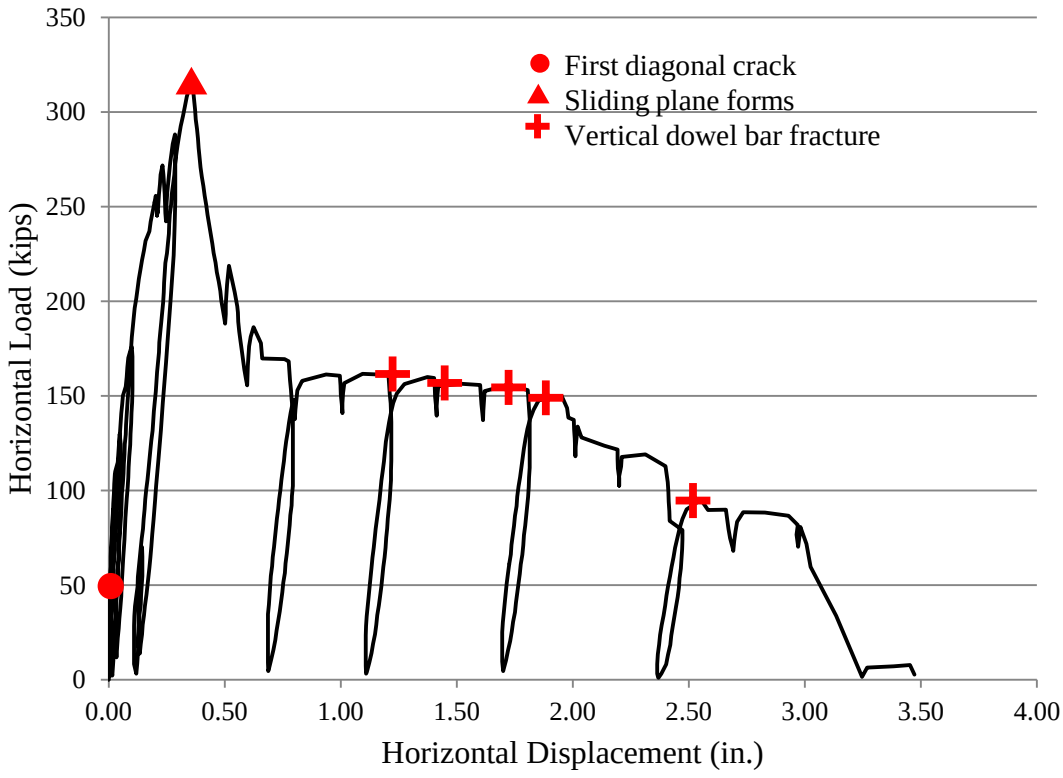

Figure 6.76 Horizontal load-vs.-horizontal displacement for shear key 9B

Figure 6.77 Sliding plane surface after shear key 9B was removed

Vertical load on Shear Key

The measurements from the strain gages on the post-tensioning bars in the hold-down frames indicate that at the maximum horizontal load, a 47-kip vertical force was applied to the shear key. In Figure 6.78, the measured vertical force is plotted against the measured horizontal load.

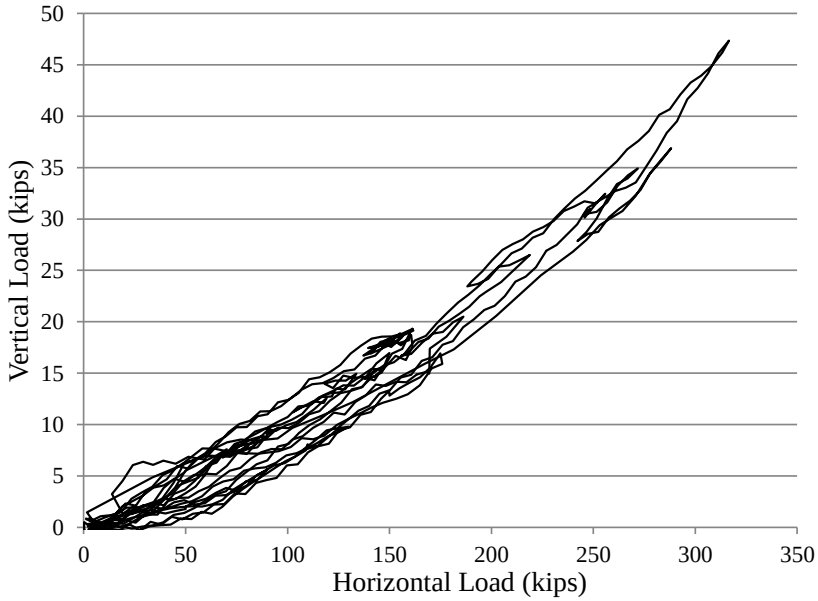

Figure 6.78 Measured vertical force on shear key 9B

Strains in Horizontal Shear Reinforcement of Stem Wall

Strains in the horizontal shear reinforcement of the stem wall were measured. Readings from strain gages registering the largest strains are plotted against the horizontal load in Figure 6.79 and Figure 6.80. The locations of these gages are shown in Figure 6.25. The stain-gage readings show that one of the horizontal bars in the bottom row (S34) reached the yield strain. In the top row, three bars slightly exceeded the yield strain (S49, S45 and S41) and one of the bars developed higher tensile strain (S46). The strain gage recording this strain was located close to the loaded side of the shear key, as shown in Figure 6.25.

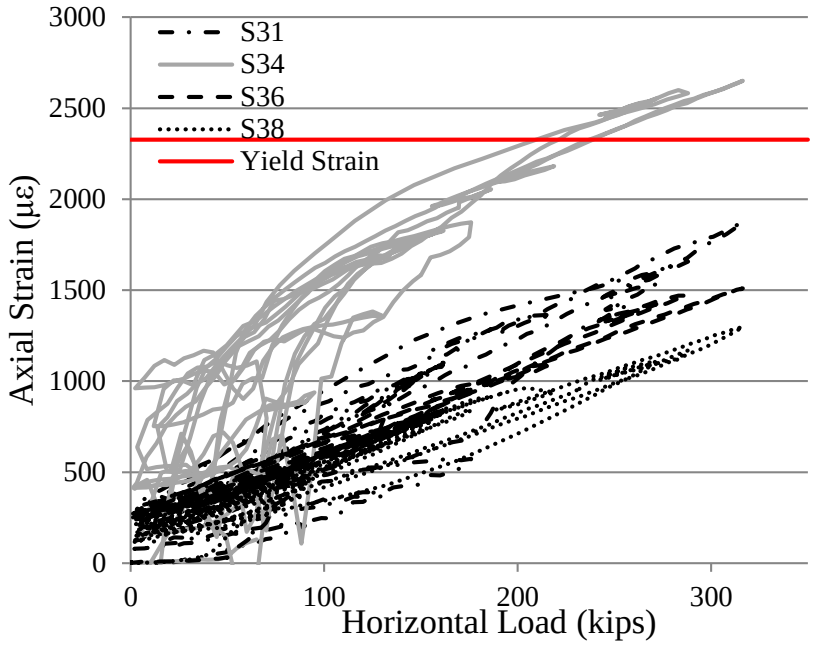

Figure 6.79 Horizontal load-vs.-axial strain in the horizontal shear reinforcement in the bottom row in the stem wall (near shear key 9B)

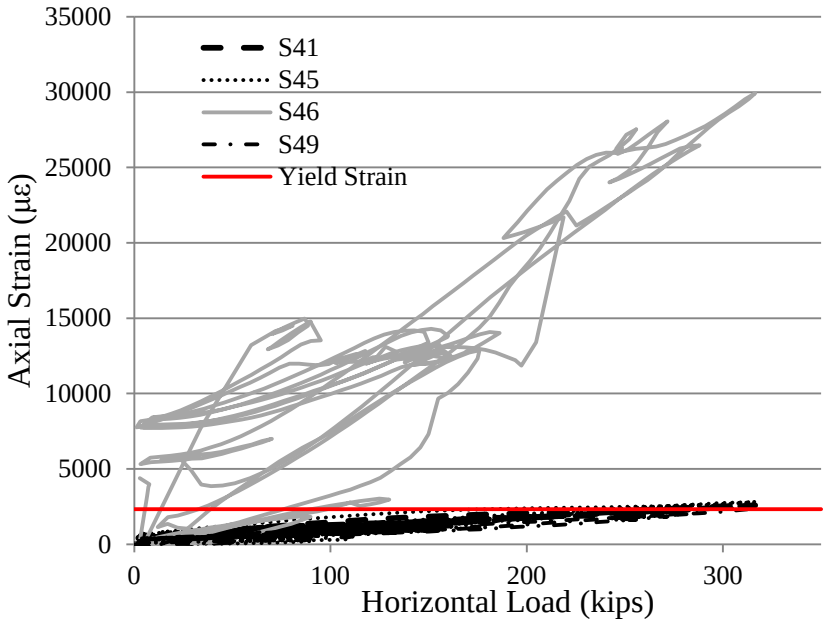

Figure 6.80 Horizontal load-vs.-axial strain in the horizontal shear reinforcement in the top row in the stem wall (near shear key 9B)

Strains in Vertical Dowel Bars

The averaged strain readings of the strain gages in the vertical dowel bars are plotted in Figure 6.81 against the horizontal displacement. The locations of the strain gages are shown in Figure 6.22 and Figure 6.23. Only the strain gages that were close to the sliding plane are considered.

Based on Figure 6.81, it can be observed that the strain gages that were closer to the loaded end of the shear key reached the yield strength earlier in the test, while the strain gages at the free end of the shear key reached the yield strain last. This is the result of the in-plane rotation of the shear key, as discussed in the next section. The readings also show that appreciable tensile forces developed in the vertical dowel bars from the beginning of the test.

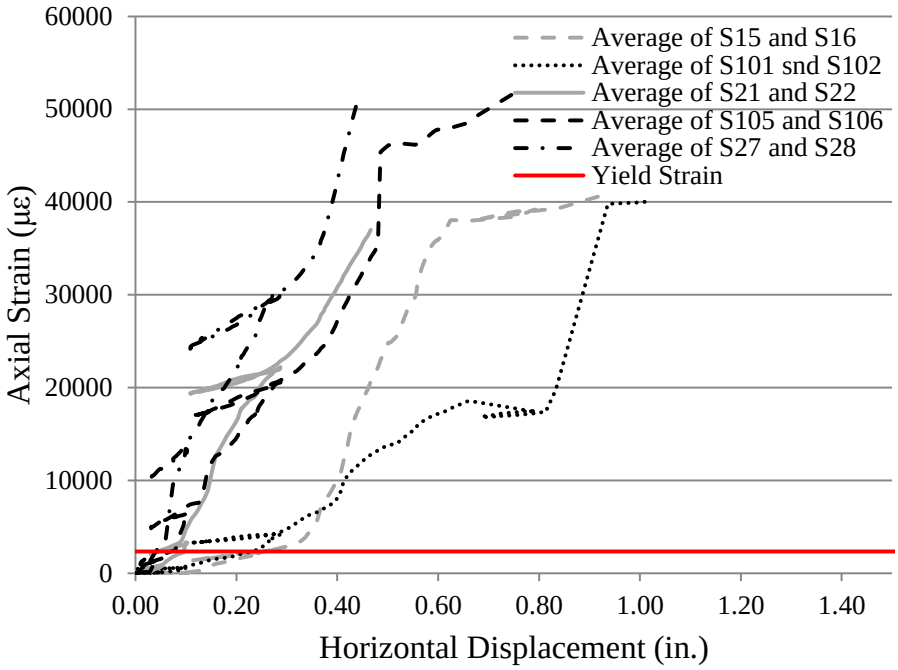

Figure 6.81 Average of strain-gage readings from vertical dowel bars in shear key 9B

In-Plane Rotation of Shear Key

The in-plane rotation of the shear key was monitored with the tilt meter TM2, whose location is shown in Figure 6.27. The readings of the tilt meter are plotted in Figure 6.82 against the horizontal displacement. Almost half of the total rotation of the shear key occurred before a horizontal displacement of 0.50 in. was reached. After that displacement level, the rotation remained at 1.50 degree until the last fracture of the vertical dowel bars occurred. At that point, the rotation increased again and reached 3.25 degrees at the end of the test.

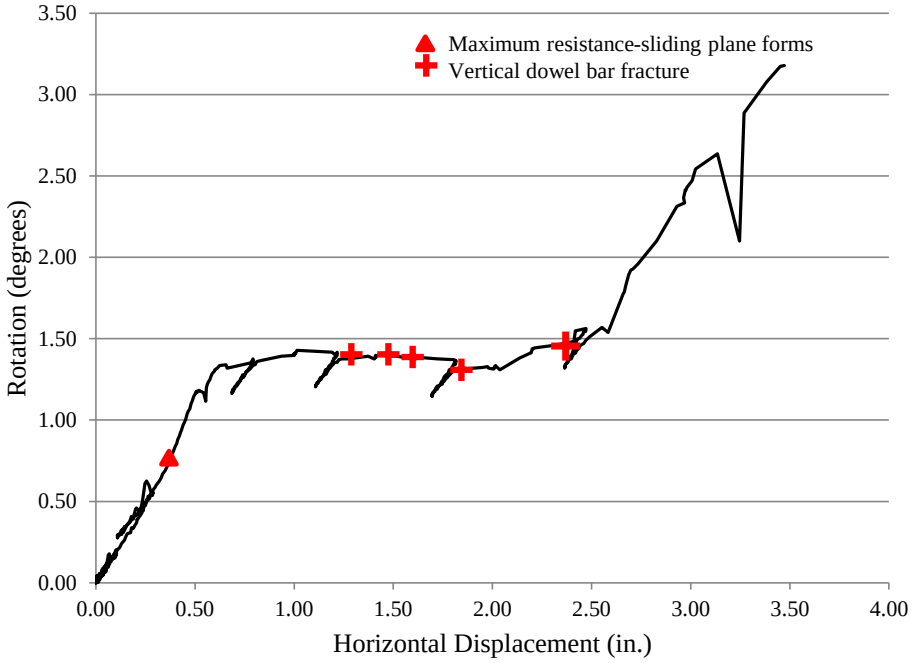

Figure 6.82 In-plane rotation of shear key 9B

Vertical Uplift of Shear Key

The vertical uplift of the shear key was monitored in four locations with the linear potentiometers L23-L26, whose locations are shown in Figure 6.26 through Figure 6.28.

Transducers L23 and L24 were close to the free end of the shear key, while L25 and L26 were close to the loaded end. The transducers L23 and L25, located on the west side of the shear key, were removed from the specimen after a displacement of 2.00 and 2.20 in. was reached.

The readings suggest that the shear key experienced a significant uplift as the test progressed and that the vertical uplift was higher at the loaded end of the shear key, as shown in Figure 6.83. In Figure 6.84, the averaged readings of the displacement transducers L23 and L25, located on the east side of the shear key, and L24 and L26, located on the west side of the shear key, are plotted against the horizontal displacement of the shear key. It can be seen that no out-of-plane rotation occurred.

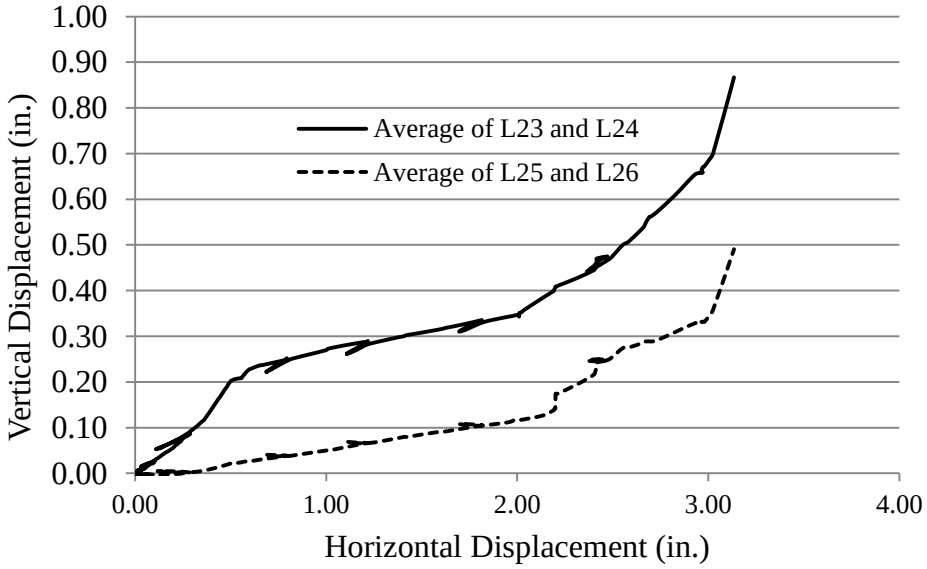

Figure 6.83 Vertical uplift of the free and loaded side of shear key 9B

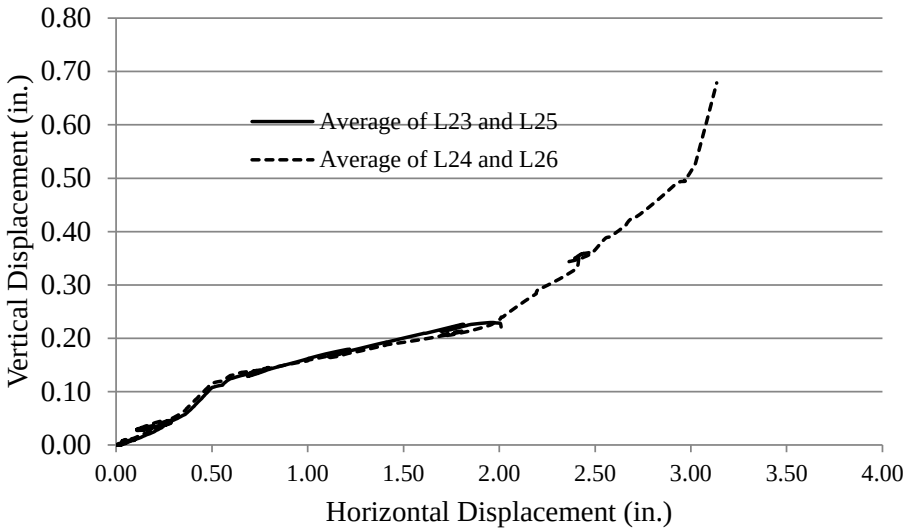

Figure 6.84 Vertical uplift of the east and west faces of shear key 9B

6.6.5 Shear Key 10A

Shear key 10A was on the north side of the stem wall and had an inclined face on the loading side. Specimen 10 had the same amount of reinforcement and reinforcing details as Specimen 8 but a higher concrete strength. The loading protocol for the shear key consisted of incremental loading, unloading and reloading with the target loads and displacements shown in Table 6.11. The shear key was initially loaded in force control and then in displacement control up to failure, which occurred at 3.50 in. displacement. The displacement was based on the averaged readings of the displacement transducers L7 and L8, located on the north side of the shear key, as shown in Figure 6.19 through Figure 6.21. The specimen was unloaded 7 times at 108 kips, 180 kips and 234 kips load, and at displacements of 0.30 in, 0.70 in., 1.30 in. and 2.10 in., respectively, to obtain the unloading stiffness.

Table 6.11 Loading protocol for shear key 10A

Step	Control	Target Load/Displacement
1	Load	36 kips
2	Load	52 kips
3	Load	90 kips
4	Load	108 kips
5	Load	144 kips
6	Load	180 kips
7	Load	216 kips
8	Load	234 kips
9-21	Displacement	to 3.50 in. with 0.20 in. increments

The first crack on the stem wall was observed on the east face of the specimen, at a horizontal load of 36 kips. It initiated at the toe of the shear key and propagated diagonally, as shown in Figure 6.85. A similar crack was observed on the west face of the shear key at a horizontal load of 52 kips. At a load of 108 kips, a diagonal crack parallel to the first crack was observed in the east face of the stem wall below the shear key, as shown in Figure 6.86. As the load increased to 144 kips, many almost parallel diagonal cracks developed in the stem wall below the shear key. Additional diagonal cracks initiated from the top of the stem wall away from the shear key. The width of these diagonal cracks remained small throughout the test. The cracks on the east face of the shear key are shown in Figure 6.87. At a load of 180 kips, a longer, almost vertical, crack formed behind the heads of the horizontal shear reinforcement of the stem wall on the west and east faces of the shear key. This crack on the west face of the shear key is shown in Figure 6.88. Right after the maximum resistance of 340 kips was reached, a substantial decrease of the load resistance of the specimen was observed. At that load, the diagonal cracks below the shear key started to join and form a horizontal siding plane.

The shear key at 0.30 in. displacement is shown in Figure 6.89. As the load increased, the horizontal sliding plane became visible due to the excessive spalling of concrete in the stem wall area above the horizontal shear reinforcement and below the shear key, as shown in Figure 6.90.

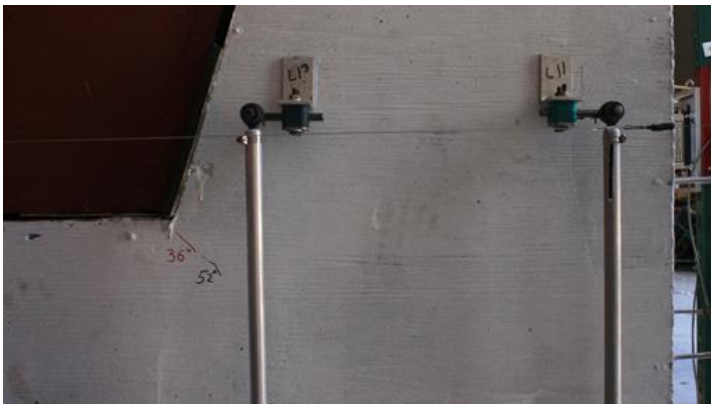

Figure 6.85 First diagonal crack observed on the east face of shear key 10A

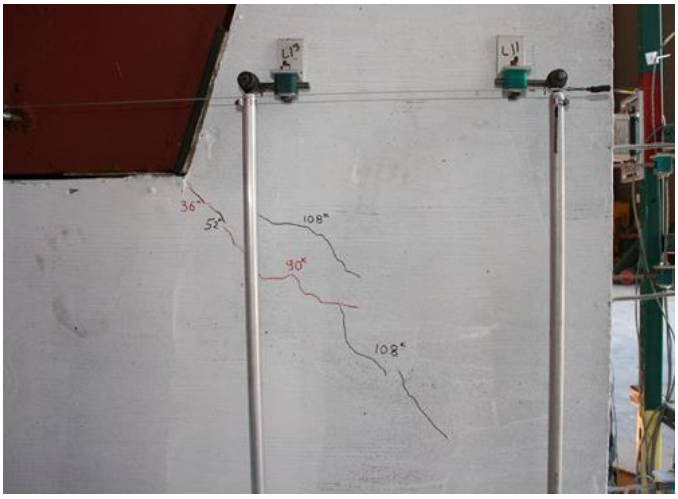

Figure 6.86 Propagation of diagonal cracks and formation of additional diagonal cracks on the east face of shear key 10A

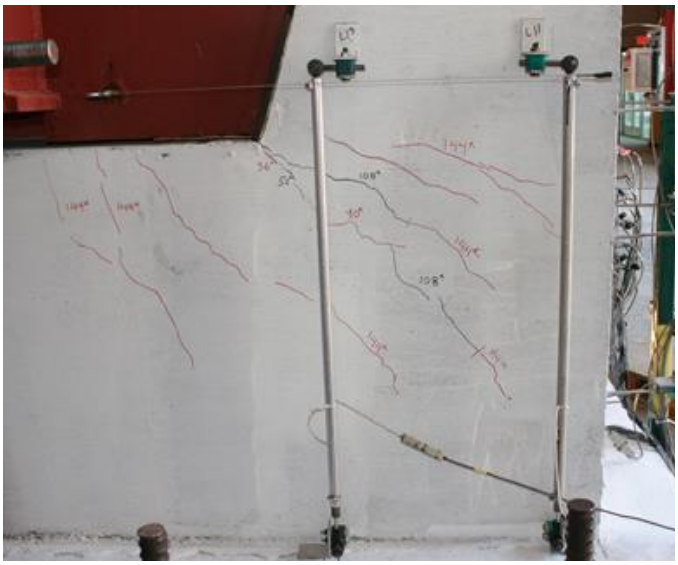

Figure 6.87 Cracks on the east face of shear key 10A at 144 kips

Figure 6.88 Crack behind the horizontal shear reinforcement of the stem wall on the west face of shear key 10A

Figure 6.89 Diagonal cracks join to form a sliding plane on the west face of shear key 10A

Figure 6.90 Sliding shear plane from the east face of shear key 10A

Additional horizontal load drops were observed at displacements of 0.70 in., 1.30 in., 1.60 in., 1.70 in., 2.0 in. and 3.25 in. due to the fracture of the vertical dowel bars. The horizontal load resistance is plotted against the horizontal displacement in Figure

6.91. The horizontal displacement is the averaged reading of the linear potentiometers L7 and L8, whose locations are shown in Figure 6.19 through Figure 6.21.

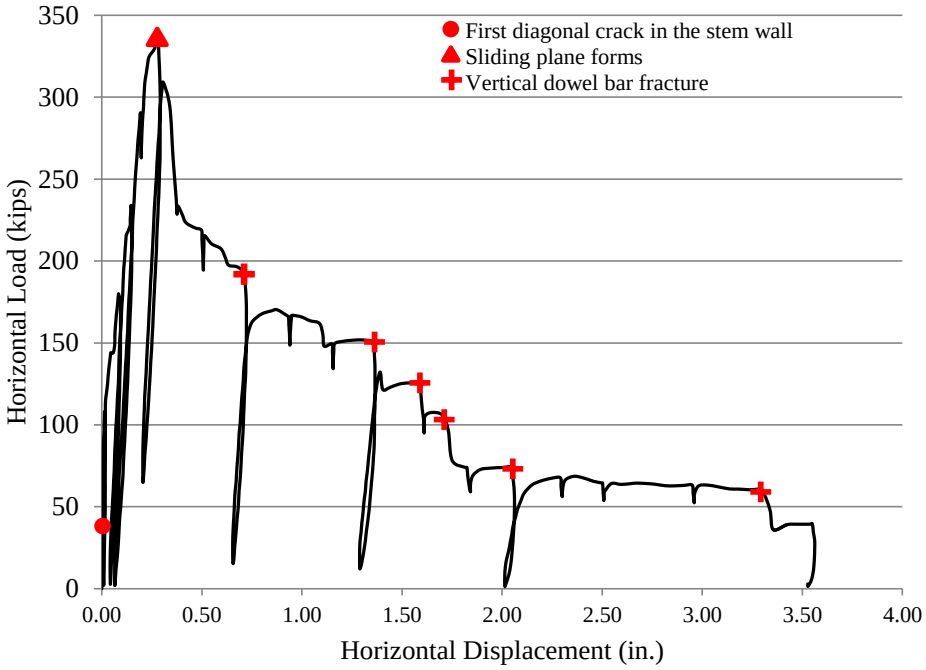

Figure 6.91 Horizontal load-vs.-horizontal displacement for shear key 10A

After the end of the test, the shear key with part of the stem wall was removed from the specimen and the sliding surface was inspected, as shown in Figure 6.92.

Figure 6.92 Sliding surface after removing shear key 10A

Vertical Load on Shear Key

The measurements from the strain gages on the bars in the hold-down frames indicate that a 120-kip vertical force was applied to the shear key at the peak horizontal load. In Figure 6.93, the measured and the theoretical vertical forces are plotted against the measured horizontal load. The theoretical vertical force is calculated from the measured horizontal load and the angle of the inclined face of the shear key, which is assumed to have zero friction. A good correlation between the theoretical and the measured values of the vertical force is observed.

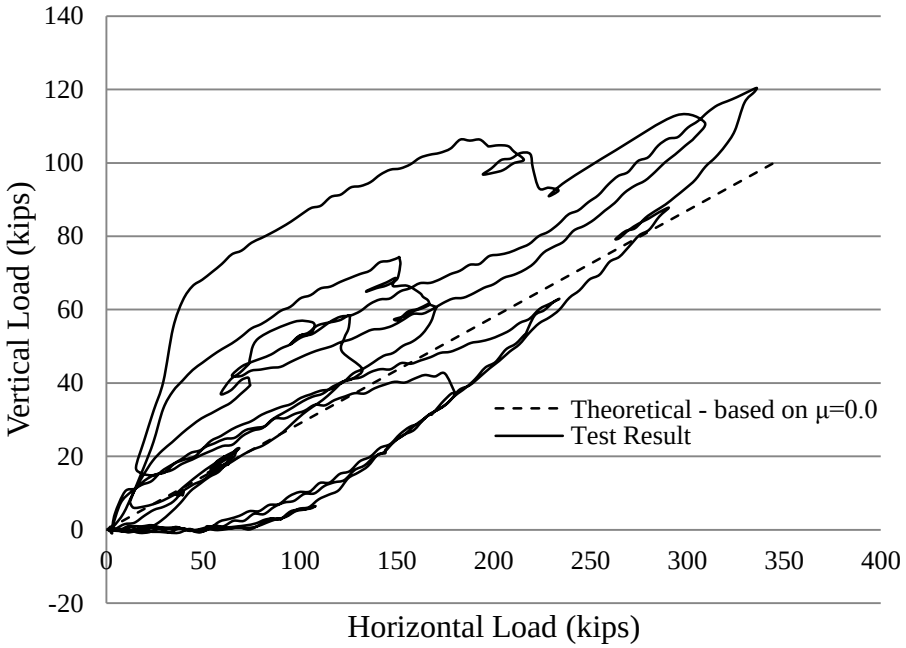

Figure 6.93 Measured and theoretical vertical forces on shear key 10A

Strains in Horizontal Shear Reinforcement of Stem Wall

Strains in the horizontal shear reinforcement of the stem wall were measured. Readings from strain gages registering the largest strains are plotted against the

horizontal load in Figure 6.94 and Figure 6.95. The locations of these gages are shown in Figure 6.18. Strain gages S94, S95, S96 and S100 were damaged early in the test and their readings are not considered. The strain-gage readings show that only one of the horizontal bars (gage S90) exceeded the yield strain, while the rest remained in the elastic regime.

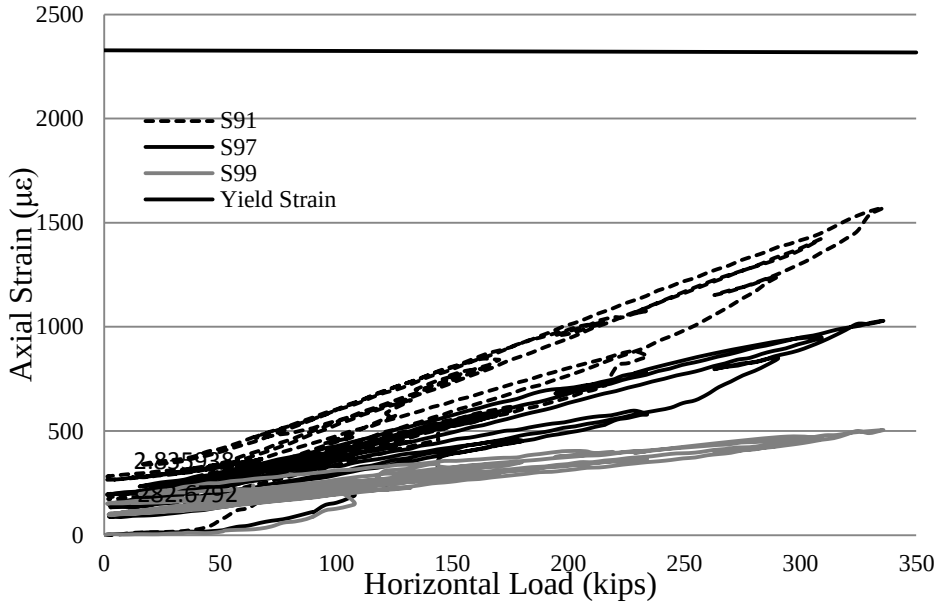

Figure 6.94 Horizontal load-vs.-axial strain in the horizontal shear reinforcement in the top row in the stem wall (near shear key 10A)

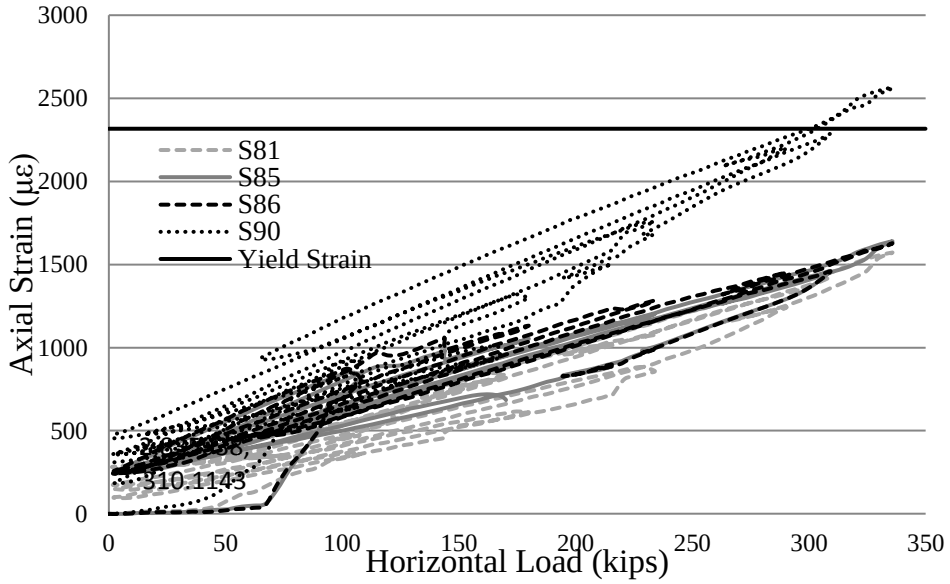

Figure 6.95 Horizontal load-vs.-axial strain in the horizontal shear reinforcement in the bottom row in the stem wall (near shear key 10A)

Strains in Vertical Dowel Bars

The averaged strain readings of the strain gages in the vertical dowel bars are plotted in Figure 6.96 against the horizontal displacement. The locations of the strain gages are shown in Figure 6.15 and Figure 6.16. Only the strain gages that were close to the sliding plane are considered.

Strain gages S77 and S78 were located on the inclined dowel bars close to the inclined face of the shear key, S71 and S72 were on the vertical dowel bars between the loaded and the free ends of the shear key, and S65 and S66 were close to the free end of the shear key. Based on Figure 6.96, it can be observed that S77 and S78 reached the yield strain very early in the test, followed by S71 and S72 and lastly by S65 and S66. This can be attributed to the in-plane rotation of the shear key, presented in the next

section. The readings also show that appreciable tensile forces developed by the dowel bars from the beginning of the test.

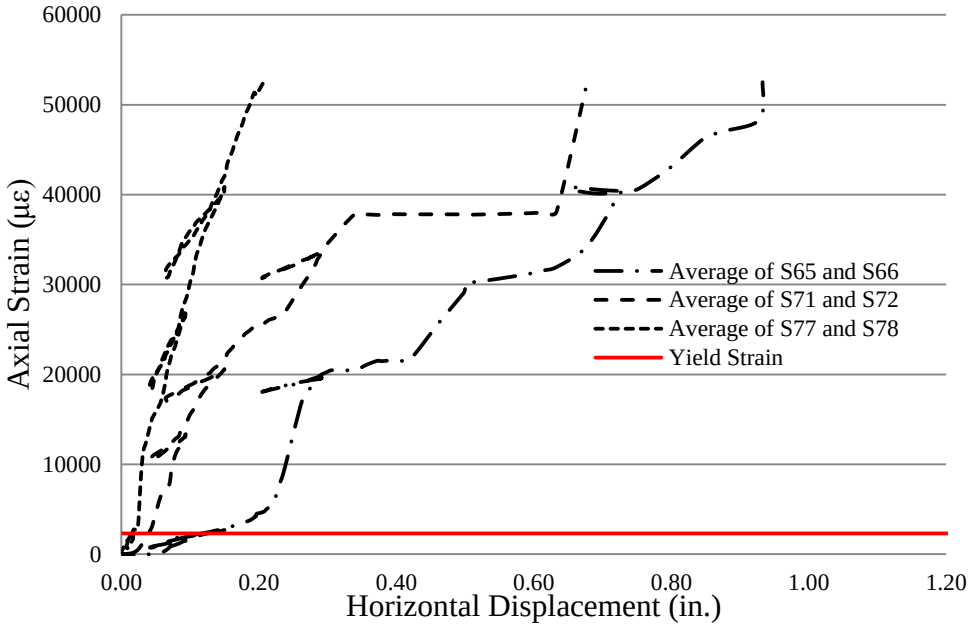

Figure 6.96 Average of strain-gage readings from dowel bars in shear key 10A

In-Plane Rotation of Shear Key

The in-plane rotation of the shear key was monitored with the tilt meter TM1, whose location is shown in Figure 6.20. The readings of the tilt meter are plotted in Figure 6.41 against the horizontal displacement. Most of the rotation of the shear key occurred before the maximum horizontal resistance was reached. A small decrease is observed right after the maximum resistance and additional increases of the rotation are observed after the vertical dowel bar fractured at a displacement of 2.00 in.

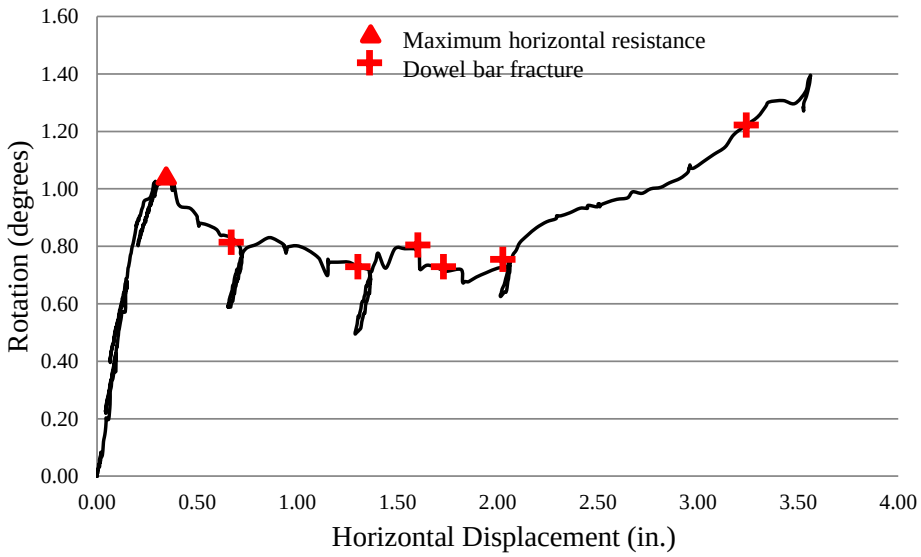

Figure 6.97 In-plane rotation of shear key 10A

Vertical Uplift of Shear Key

The vertical uplift of the shear key was monitored in four locations with the linear potentiometers L10-L13, whose locations are shown in Figure 6.20 and Figure 6.21. The readings suggest that the shear key experienced a significant uplift as the test progressed and that the vertical uplift was higher at the loaded end of the shear key. The averaged readings from the transducers L10 and L11, located on the free end of the shear key, and transducers L12 and L13, located on the loaded end of the shear key, are plotted against the horizontal displacement of the shear key in Figure 6.42.

Figure 6.43 shows the averaged readings of linear potentiometers L10 and L12, and L11 and L13, which were positioned in the west and east faces of the stem wall respectively, plotted against the horizontal displacement of the shear key. The comparison of the two curves shows that there was no out-of-plane rotation until a

displacement of 1.70 in. was reached. After that, significant out-of-plane rotation can be observed.

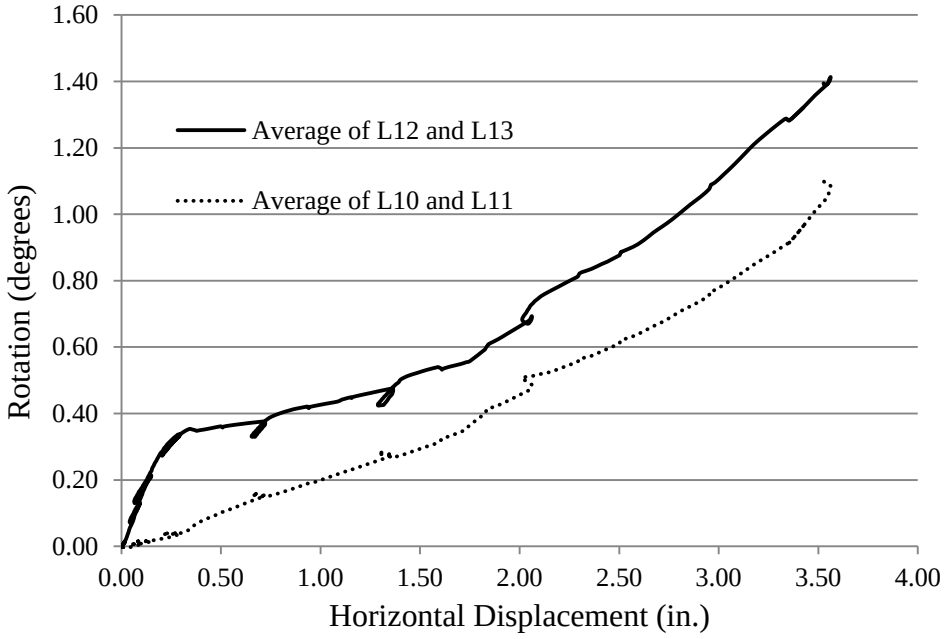

Figure 6.98 Vertical uplift of the east face of shear key 10A

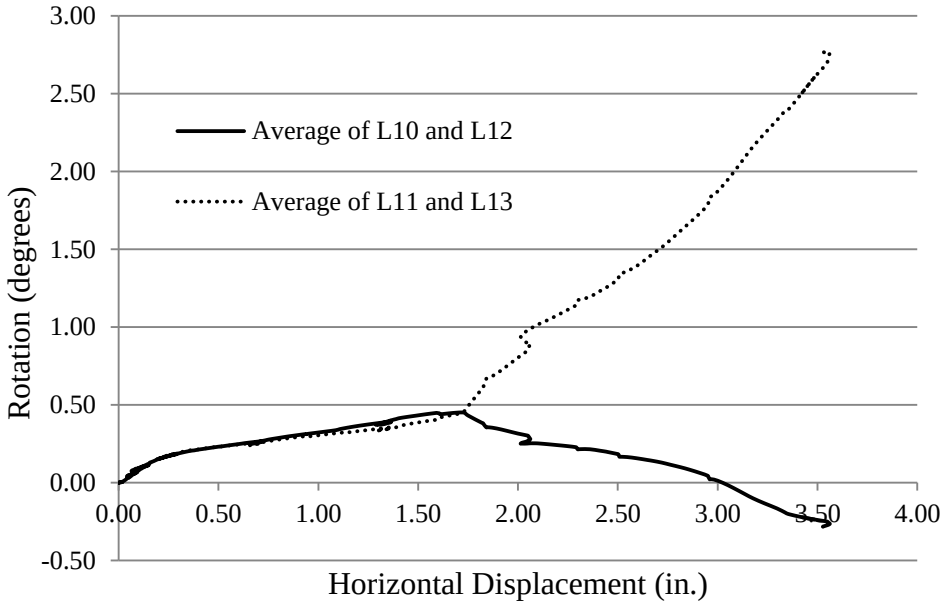

Figure 6.99 Vertical uplift near the free end of shear key 10A

6.6.6 Shear Key 10B

Shear key 10B was on the south side of the stem wall and had a vertical face on the loading side. The loading protocol for the shear key consisted of incremental loading, unloading, and reloading, with the target loads and displacements shown in Table 6.12. The shear key was initially loaded in force control to 140 kips in increments of 20 kips. Then, it was loaded in displacement control up to failure, which occurred at 1.60 in. displacement. The specimen was unloaded five times, when the load reached 60 kips, 100 kips and 140 kips and when the displacement reached 0.20 in., 0.60 in. and 1.00 in. The displacement was based on the average of the readings from displacement transducers L20 and L21, located on the south side of the shear key, as shown in Figure 6.19 through Figure 6.21.

Table 6.12 Loading protocol for shear key 10B

Step	Control	Target Load/Displacement
1-7	Load	50 kips
2	Load	60 kips
3-8	Load	140 kips with 20-kip increments
9-16	Displacement	1.60 in. with 0.20 in. increments

The first cracks in the stem wall were observed on the east and west faces of the wall at a horizontal load of 50 kips. They initiated from the toe of the shear key and propagated diagonally downwards. This crack is shown in Figure 6.100 at a horizontal load of 80 kips.

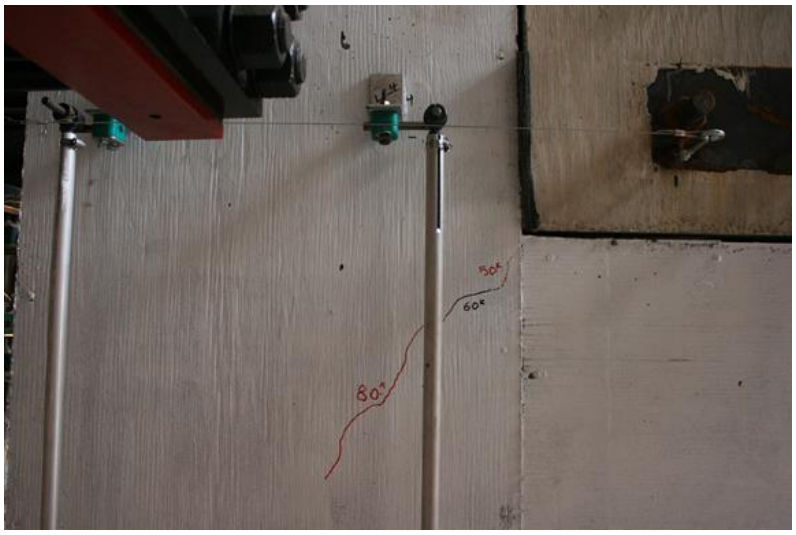

Figure 6.100 First crack observed on the east face of shear key 10B

When the horizontal load reached 120 kips, this crack stopped propagating. An additional crack, parallel to the first, formed on the stem wall, below the shear key, at a horizontal load of 140 kips. Several diagonal cracks initiated from the top of the stem wall, away from the toe of the shear key, which remained small throughout the test. These cracks are shown in Figure 6.101 and Figure 6.103.

Figure 6.101 Cracks on the east face of shear key 10B at 190 kips

When the maximum horizontal resistance of 250 kips was reached, several cracks appeared on the stem wall in the region below the shear key. These cracks propagated with smaller inclination, with respect to a horizontal plane, than the initial cracks. A crack also developed behind the heads of the horizontal shear reinforcement of the stem wall. After that point, a significant drop in the horizontal load resistance was observed. These cracks are shown in Figure 6.102. As the load increased, one of the cracks extended through the entire shear key and formed a well-defined sliding plane, as shown in Figure 6.103.

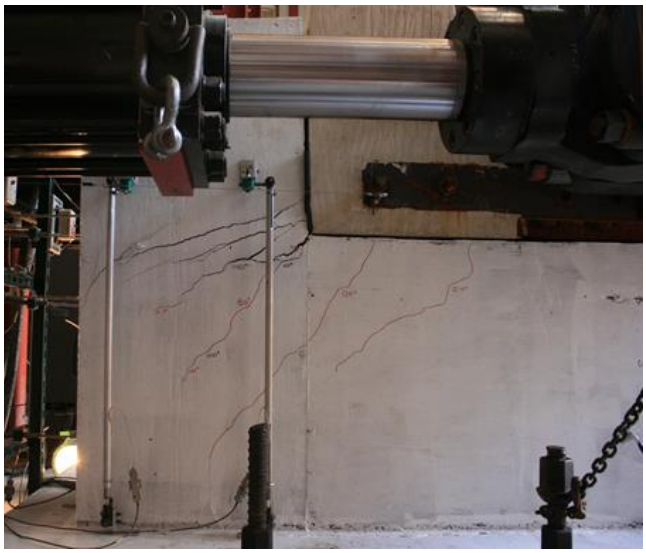

Figure 6.102 Cracks on the east face of shear key 10B at 250 kips

Figure 6.103 Sliding plane from the east face of shear key 10B

After the maximum resistance was reached, the shear key started to slide. The vertical dowel bars fractured progressively, leading to small sudden drops of the horizontal load. At the end of the test, all the bars located on the east side of the wall had fractured. The surface of the sliding plane after removing the shear key is shown in Figure 6.104. The horizontal load resistance of the shear key is plotted against its horizontal displacement in Figure 6.105.

Figure 6.104 Sliding plane surface after removing shear key 10B

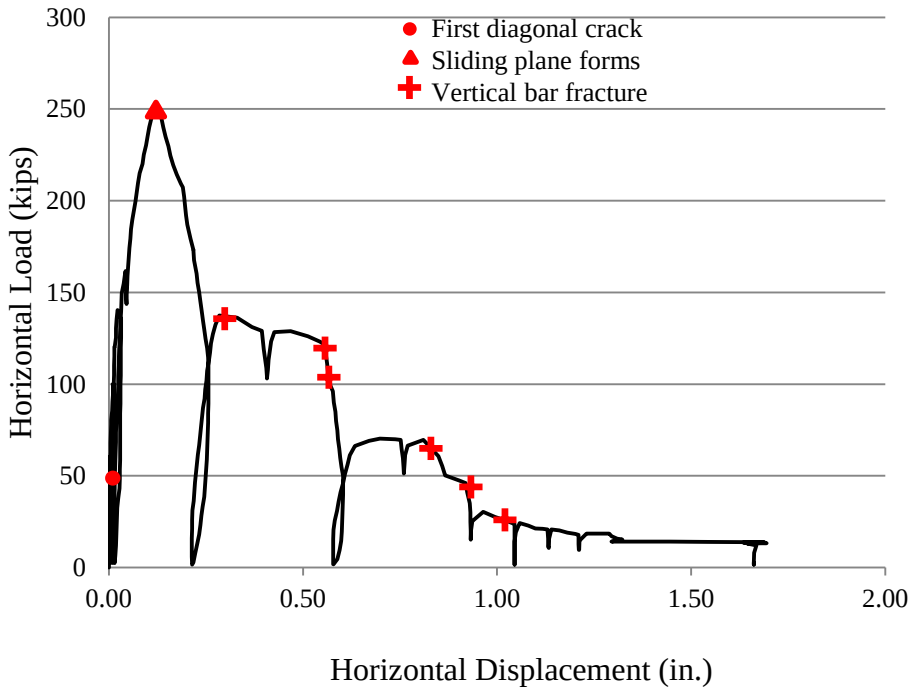

Figure 6.105 Horizontal load-vs.-horizontal displacement for shear key 10B

Vertical Load on Shear Key

The measurements from the strain gages on the bars in the hold-down frames indicate that a 45-kip vertical force was applied to the shear key at the peak horizontal load. In Figure 6.106, the measured vertical force is plotted against the measured horizontal load.

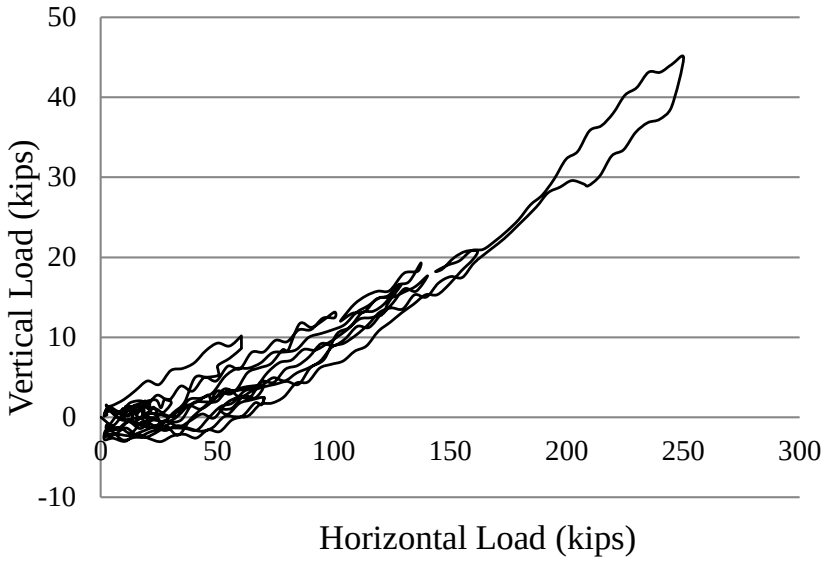

Figure 6.106 Measured vertical force on shear key 10B

Strains in Horizontal Shear Reinforcement of Stem Wall

Strains in the horizontal shear reinforcement in the stem wall near the shear key were measured. Readings from strain gages registering the largest strains in each bar are plotted against the horizontal load in Figure 6.107 and Figure 6.108. The locations of these gages are shown in Figure 6.18. The stain-gage readings show that the strains were the elastic regime.

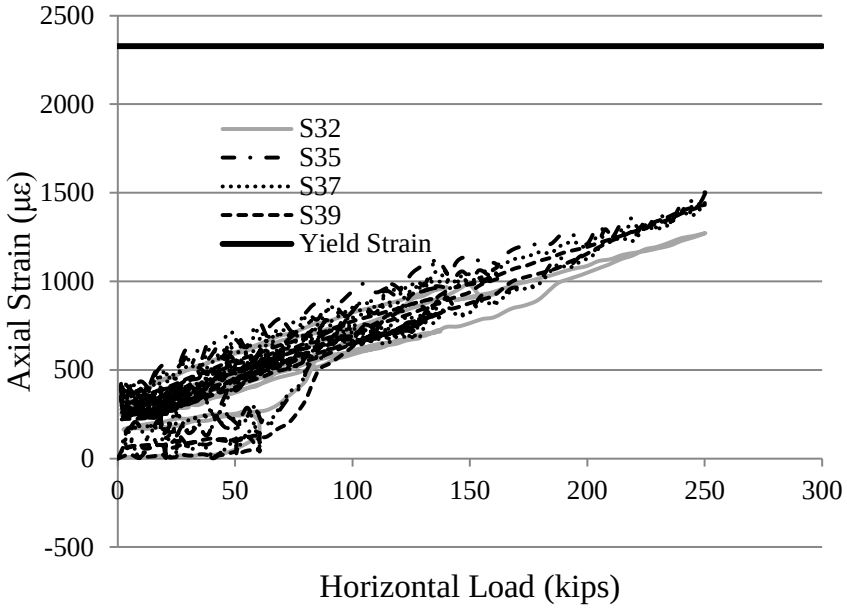

Figure 6.107 Horizontal load-vs.-axial strain in the horizontal shear reinforcement in the bottom row in the stem wall (near shear key 10B)

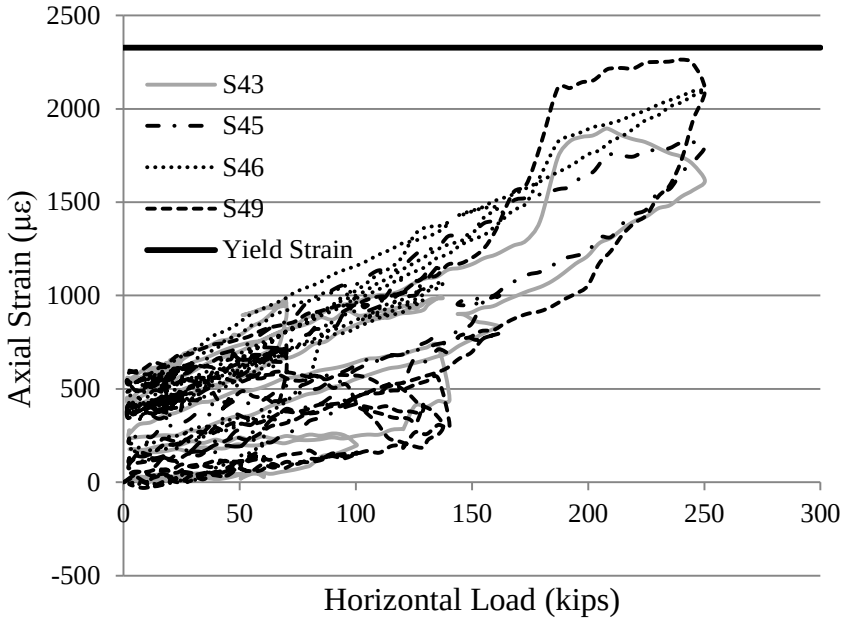

Figure 6.108 Horizontal load-vs.-axial strain in the horizontal shear reinforcement in the top row in the stem wall (near shear key 10B)

Strains in Vertical Dowel Bars

The averaged readings of the strain gages in the vertical dowel bars are plotted against the horizontal displacement in Figure 6.109. The locations of the strain gages are shown in Figure 6.15 and Figure 6.16. Only the strain gages that were close to the sliding plane are considered.

From Figure 6.109, it can be observed that S27 and S28 registered the yield strain very early in the test, followed by S21 and S22 and lastly by S15 and S16. This can be attributed to the in-plane rotation of the shear key, as discussed in the following section. The readings also show that appreciable tensile forces are developed in the vertical dowel bars from the beginning of the test.

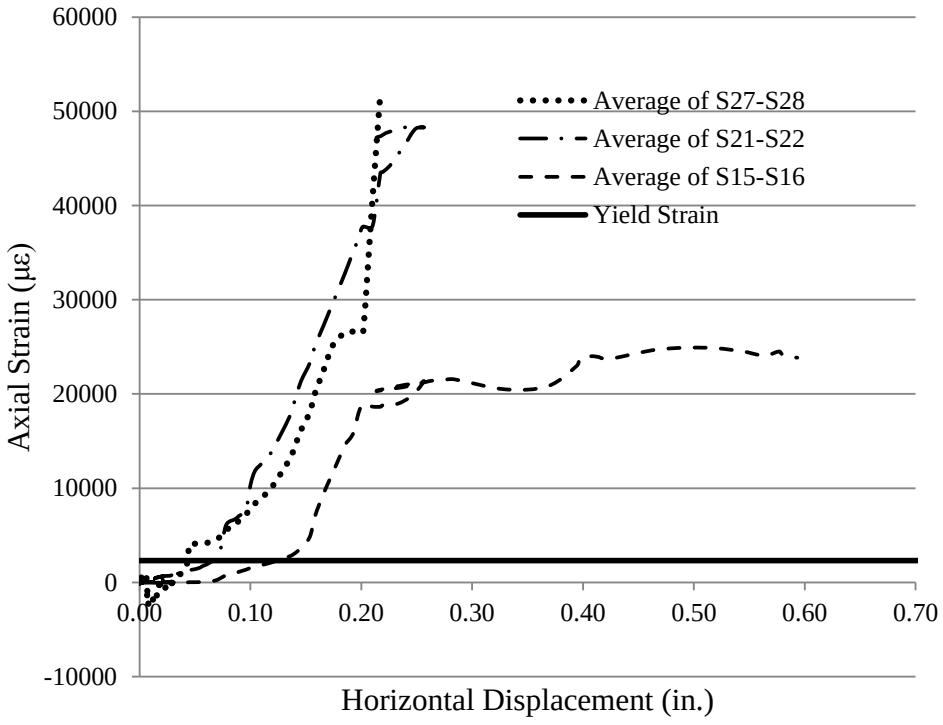

Figure 6.109 Average of strain-gage readings from vertical dowel bars in shear key 10B

In-Plane Rotation of Shear Key

The in-plane rotation of the shear key was monitored with the tilt meter TM2, whose location is shown in Figure 6.20. The readings of the tilt meter are plotted in Figure 6.110 against the horizontal displacement. It can be noticed that the in-plane rotation continuously increased and reached 14 degrees at the end of the test.

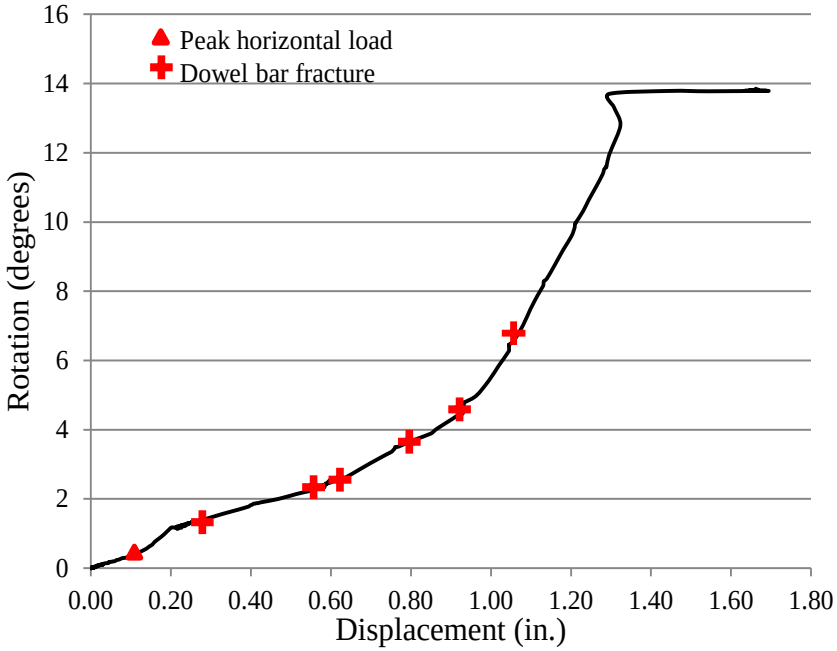

Figure 6.110 In-plane rotation of shear key 10B

Vertical Uplift of Shear Key

The vertical uplift of the shear key was monitored in four locations with the linear potentiometers L23-L26, whose locations are shown in Figure 6.20 and Figure 6.21. Transducers L23 and L24 were located at the north (loaded) end of the shear key, while L25 and L26 were located at the south end. The averaged readings of L23 and L24, and L25 and L26, suggest that the shear key experienced a significant uplift and that the

vertical uplift was larger at the loaded end of the shear key. Readings from these transducers are plotted against the horizontal displacement of the shear key in Figure 6.111.

Figure 6.112 shows the averaged readings of linear potentiometers L23 and L25, and L24 and L26, which were positioned on the west and east faces of the stem wall, respectively, plotted against the horizontal displacement of the shear key. The comparison of the two curves shows that there was practically no out-of-plane rotation.

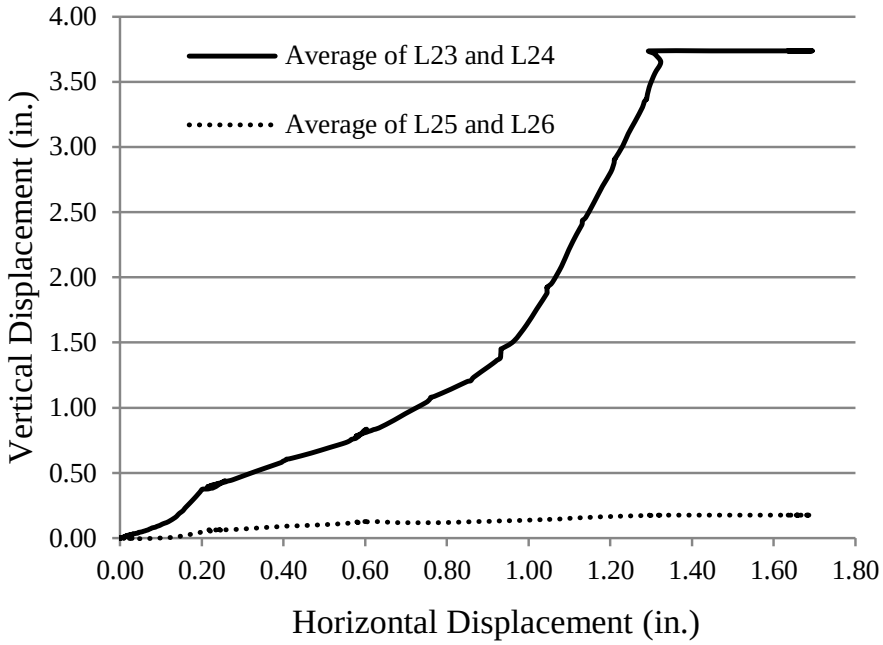

Figure 6.111 Vertical uplift of the north and south ends of shear key 10B

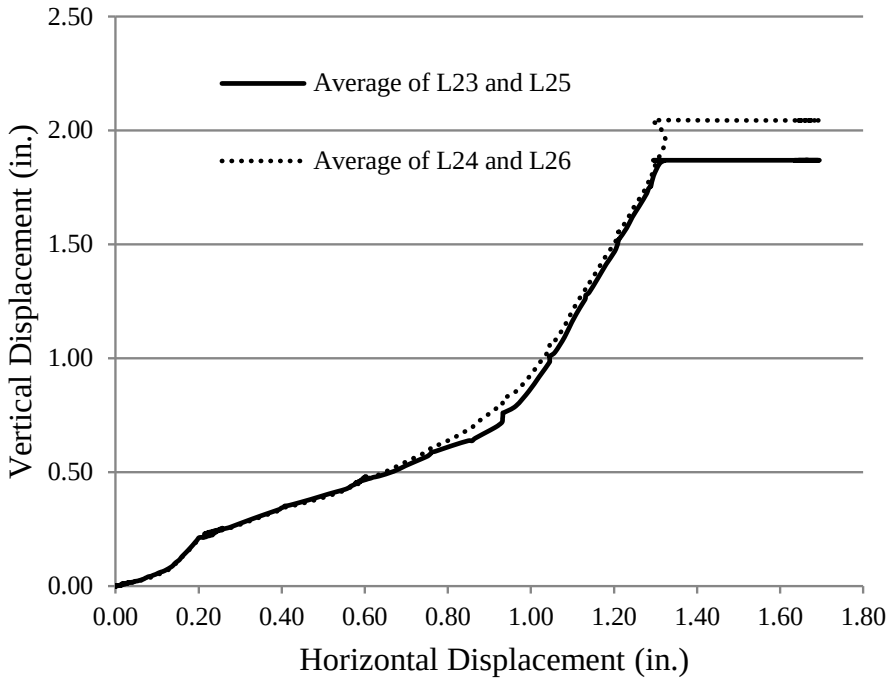

Figure 6.112 Vertical uplift of the east and west faces of shear key 10B

6.7 Summary and Conclusions

The experimental results on three abutment wall specimens with monolithic shear keys are presented in this chapter. The specimens had different amounts of dowel bars, connecting the shear keys to the stem walls and concrete strengths, but the same amount of horizontal shear reinforcement in the stem walls. Diagonal shear failure of the stem walls was not observed in these tests. Diagonal shear cracks formed on the stem walls, but remained small throughout the tests.

The failure mechanisms of the shear keys were similar and were governed by shear sliding. Initially, the shear keys experienced in-plane rotation without sliding. This led to the development of significant tensile forces in the dowel bars. A number of almost parallel diagonal cracks formed on the stem walls, in the regions below the shear keys. In

every shear key test, some of the diagonal cracks eventually propagated horizontally forming a sliding plane. When the maximum horizontal load was reached, the shear key started to slide. At that point, the in-plane rotation of the shear key leveled off between 0.80 and 1.50 degrees, except for shear key 10B, which experienced very large in-plane rotation. The shear key continued to slide and the dowel bars fractured sequentially starting at the loaded end leading to sudden drops of the horizontal load.

The calculated horizontal load resistances of the shear keys based on the expected material properties are compared to the measured horizontal resistances in Table 6.13. Based on the values in Table 6.13, it can be seen that the peak resistance was over-predicted for all of the shear keys. This can be attributed to the resisting mechanism that developed in the tests, which was different from what was assumed in the design calculations.

The rotation of the shear keys in the tests suggests that the shear key resistance was governed by the tensile forces of the dowel bars. As a shear key rotated about the free end of the stem wall, this region experienced large shear and compressive forces. This led to the development of a steep diagonal crack in the stem wall behind the heads of the horizontal shear reinforcement. When the sliding plane formed and the corner of the stem wall at the free end of the shear keys broke off, the shear keys stopped to rotate and started to slide on that plane. The corner diagonal crack limited the horizontal load resistance of the shear key.

Table 6.13 Calculated and measured sliding shear resistances for Specimens 8, 9 and 10

Tested Shear Key	Calculated Shear Resistance (kips)	Measured Peak Resistance (kips)
8A	576	286
8B	326	198
9A	629	334
9B	368	313
10A	682	334
10B	405	250

6.8 Acknowledgement of Publication

Part of this chapter is a reprint of the material that will appear in a technical report which will be submitted to the California Department of Transportation in 2016, Kottari, A., P. B. Shing, J. I. Restrepo, under the title "Design and Capacity Assessment of External Shear Keys in Bridge Abutments". The dissertation author will be the primary investigator and author of this report.

CHAPTER 7

EXPERIMENTAL STUDY OF PRE-STRESSED EXTERNAL SHEAR KEYS IN BRIDGE ABUTMENTS

7.1 Description of Test Specimen

This chapter presents an experimental study conducted on Specimen 11, which had two external shear keys that were connected to the stem wall with horizontal, unbonded, post-tensioned bars, as shown in Figure 7.1. The stem wall and the shear keys were cast separately. The post-tensioned bars were anchored on the exterior side of the shear keys with a hinge mechanism to avoid the bending of the bars. This system allowed the shear keys to move and rotate when subjected to a horizontal load.

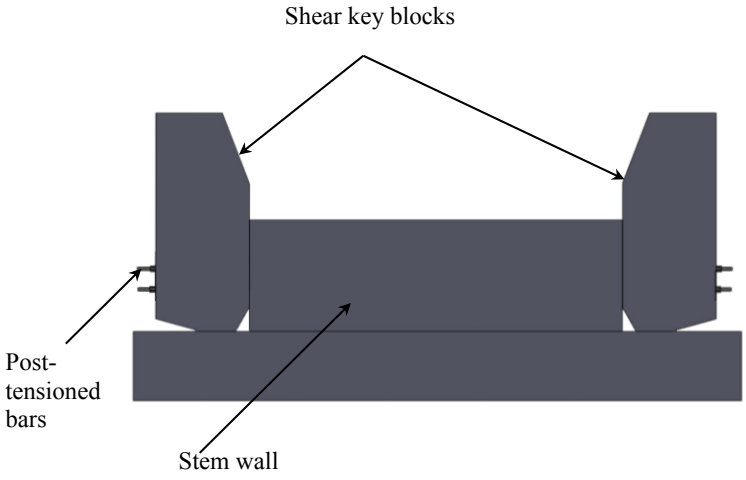

Figure 7.1 Main parts of Specimen 11 with pre-stressed shear keys

This shear key design has a number of beneficial features as compared to isolated and monolithic shear keys. First, the on-site construction effort can be reduced since the shear keys can be precast and then transferred to the construction site. Second, the unbonded, post-tensioned, bars allow the shear keys to displace and rotate without damage to the shear keys and the stem wall, and the bars if not yielded can restore the shear keys to their original positions. Hence, such shear keys can reduce repair costs in the event of a major earthquake. Third, the shear keys can be designed in such a way that they provide strength and deformation capabilities compatible to the bridge columns. Hence, they can remain functional in a major seismic event.

Specimen 11 consisted of two shear keys blocks with inclined loading faces. The shear key blocks had the same reinforcement details. On one side of the specimen, neoprene pads were attached to the stem wall and the footing to distribute the contact forces between the wall and the shear key blocks more evenly, while the other side had concrete-to-concrete contacts. Five tests were conducted with the pre-stressed shear key blocks. However, the first three (Test 1 through Test 3) stopped early due to the unexpected behavior of either the neoprene pads or the hinge mechanism for the bar anchor. After the neoprene pads had been replaced and the hinge mechanism had been modified, the tests were repeated. Only the revised hinge design and the results of Test 4 and Test 5 are presented in this chapter.

7.2 Design of Specimen 11

Specimen 11 consisted of a stem wall and two shear key blocks. The specimen represented a 40%-scale model of the prototype bridge, which is the Lenwood Overhead (Caltrans Br. #54-1112). The length of the specimen was 12 ft. and was much shorter than that required according to the scaling. The shear key width was 12 in. Two 5 ½ in. x 1 ½ in. steel ducts were placed in parallel inside the stem wall, and two 7 ⅝ in. x 1 ½ in. steel ducts were placed inside the shear key blocks, as shown in Figure 7.2. Two 2-in.-thick, 90-durometer neoprene pads satisfying ASTM D4014 were placed on one side of the stem wall, as shown in Figure 7.2, to spread the contact force more evenly. Four ⅝-in. diameter, Grade 150, DYWIDAG bars were used to pre-stress the shear key blocks and the stem wall. The base corner of the shear key blocks was shaped to avoid a sharp 90-degree angle.

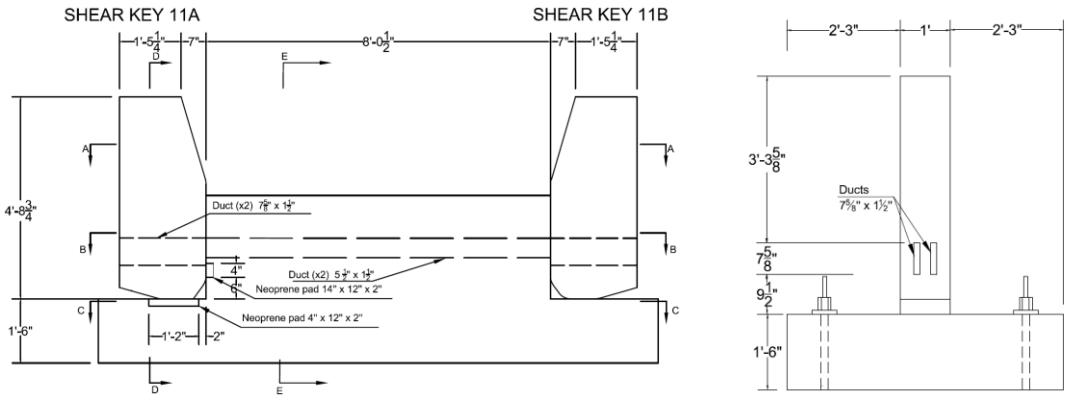

a) b)

Figure 7.2 Neoprene pads and steel ducts in Specimen 11: a) elevation view; b) side view

The vertical reinforcement of the shear key block consisted of 6 No. 4, Grade 60, bars placed near the loaded face of the shear key block. Their quantity was determined

with a strut-and-tie model as will be explained in the next section. For temperature and shrinkage crack control, No. 3, Grade 60, bars were placed near each face of the shear keys. Horizontal stirrups consisting of No. 3 bars were placed along the height of the shear key block at a center-to-center spacing of 3 ⅝-in. To prevent splitting cracks, 5 No. 3 vertical stirrups were placed around the ducts to confine the concrete in the bar anchorage region, as shown in Figure 7.3.

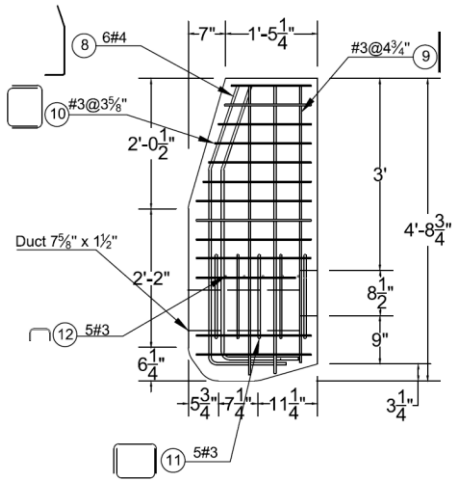

Figure 7.3 Reinforcement details for shear key blocks

Since the stem wall did not have to resist the shear forces transmitted from the shear keys, the amount of horizontal shear reinforcement was significantly reduced as compared to the previous specimens. The side reinforcement was the same as that in the previous specimens. The reinforcement of the footing and the stem wall is shown in Figure 7.4. Additional detailed drawings are shown in Figure 7.5 through Figure 7.8.

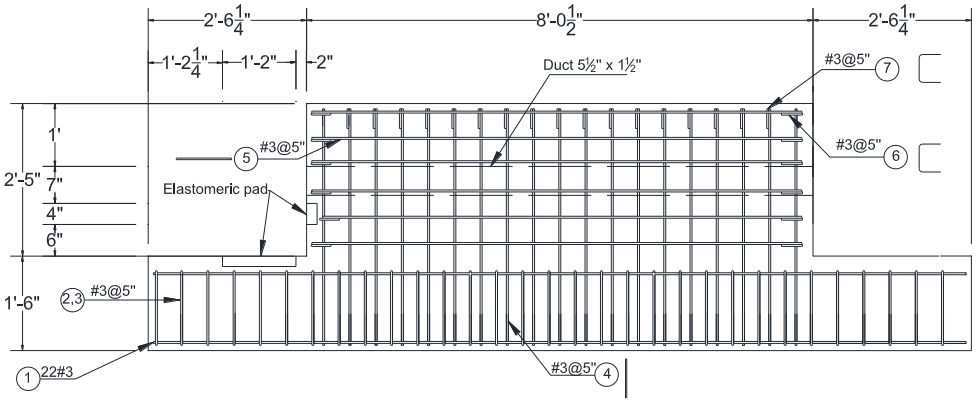

Figure 7.4 Reinforcement details for stem wall and footing

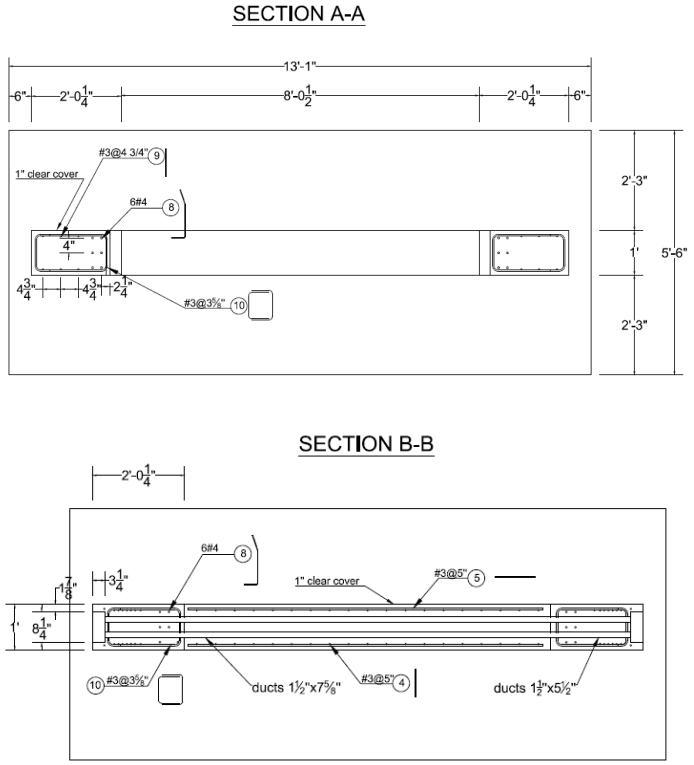

Figure 7.5 Sections A-A and B-B in design drawings in Figure 7.2

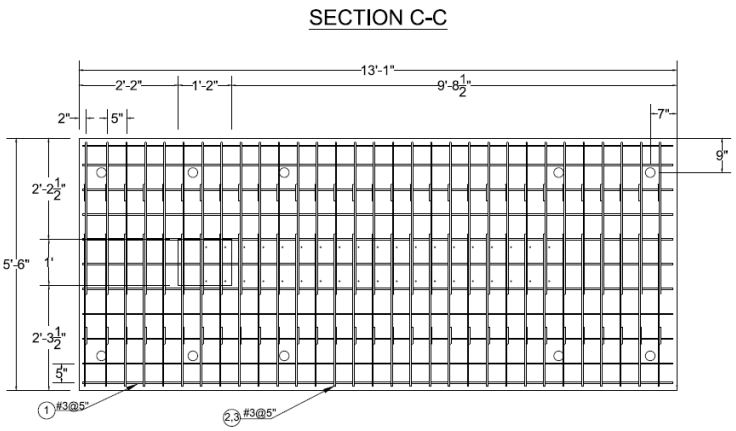

Figure 7.6 Section C-C in design drawings in Figure 7.2

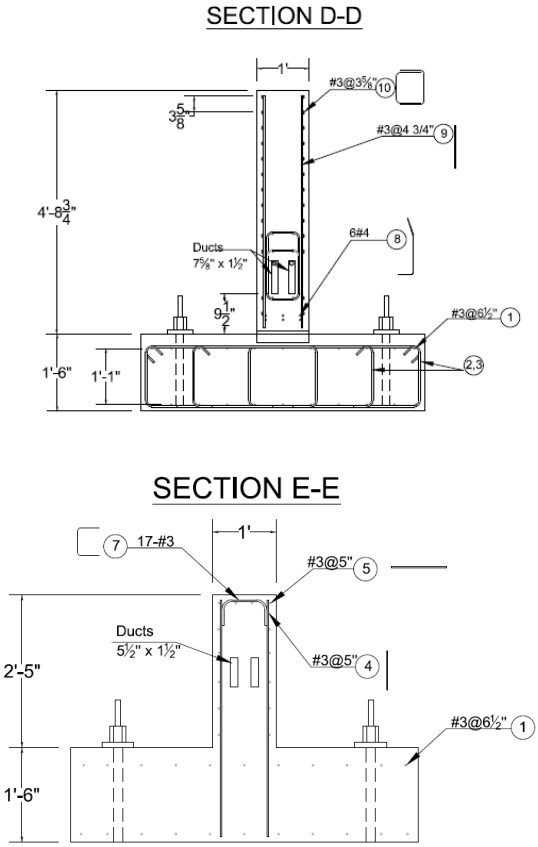

Figure 7.7 Sections D-D (top) and E-E (bottom) in design drawings in Figure 7.2

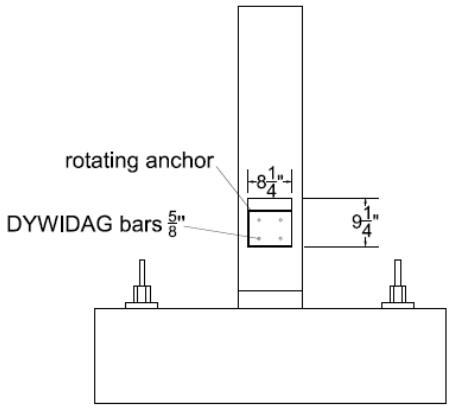

Figure 7.8 Side view in design drawings for Specimen 11 (Figure 7.2)

Hinge Mechanism for Bar Anchor

Four post-tensioned bars were used to secure the shear keys to the stem wall. A custom-made hinge system was used to allow the rotation of the bar anchors with respect to the shear key block and thus to avoid the bending of the post-tensioned bars as the shear key block rotated. The hinge system consisted of two plates. One was in contact with the shear key block and would rotate with it, and the other was in direct contact the bar anchors and was to remain vertical as the shear key rotated. The two plates were able to rotate with respect to each other through a hinge mechanism. The first plate is referred to as the bearing plate as it exerted a bearing force on the shear key. The drawings of the plates are shown in Figure 7.9 and the system with the prestressing bars is shown in Figure 7.10. Appropriate slots were provided in the bearing plate to avoid touching the bars as the shear key rotated, as shown in the picture in Figure 7.10b. The vertical distance of the two rows of prestressing bars was selected to be the maximum permissible for the given shear key dimensions. When a shear key block rotated, the top post-

tensioned bars would experience a larger tension than the bottom bars. As a result, the outer plate would rotate with respect to the bearing plate to balance the forces in the two rows of bars, thus avoiding the bending of the bars. The larger the vertical spacing of the bars is, the higher will be the restoring moment to overcome the friction in the system.

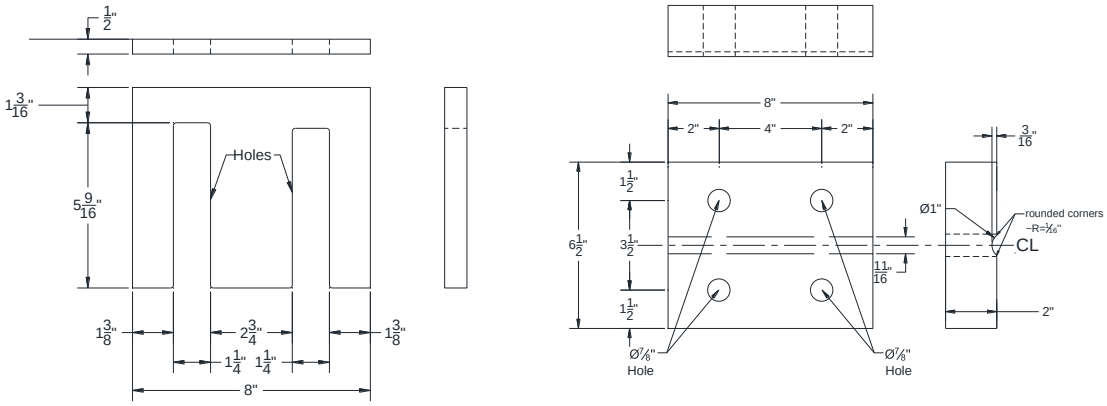

a) b)

Figure 7.9 Design details of the hinge mechanism for bar anchorage

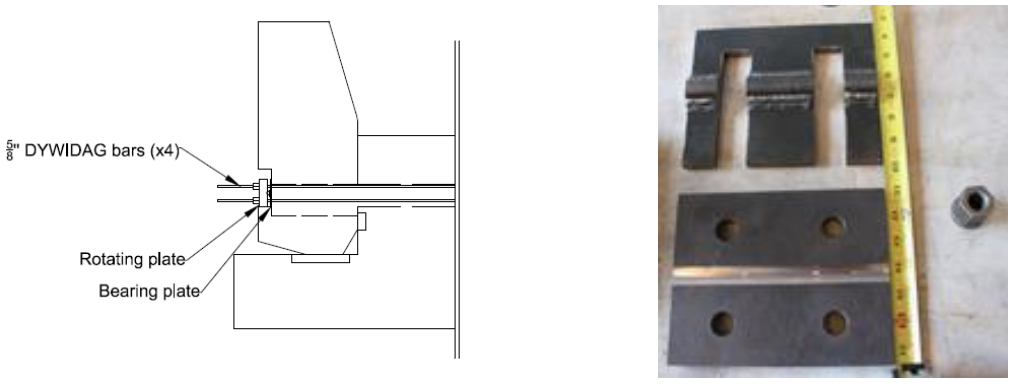

a) b)

Figure 7.10 Hinge mechanism for bar anchorage: a) design drawing; b) bearing plate (top) and outer plate (bottom)

Material Properties

The compressive strength of the concrete for the shear key blocks and the stem wall was specified to be 7.0 ksi. The actual 28-day compressive strength of the shear key

concrete was 6.7 ksi, while that for the stem wall was 6.6 ksi. The compressive strengths were obtained from the tests of concrete cylinders, which were cast and kept in plastic molds till the day of testing. The strengths of the reinforcing bars are summarized in Table 7.1 and Table 7.2.

Table 7.1 Measured strengths of reinforcing bars in Specimen 11

Reinforcement Description	Bar Size	f_y (ksi)	f_{su} (ksi)
Vertical and horizontal side reinforcement of the stem wall and shear key blocks	No. 3	63.00	101.00
Vertical reinforcement of the shear key blocks	No. 4	62.00	92.60

Table 7.2 Measured strengths of prestressing bars in Specimen 11

Reinforcement Description	Bar Diameter (in.)	Bar Area (in^2)	f_{pu} (ksi)
Prestressing bars	0.625	0.31	`169.00

7.3 Calculation of Load Resistance of Shear Keys

Specimen 11 was designed such that the prestressing bars would not exceed 70% of their ultimate strength, f_{pu}. The shear key blocks are assumed to behave as rigid bodies. As the shear key rotates, it is expected to slide and resume contact with the stem wall. The free-body diagram of a shear key block is shown in Figure 7.11. It is assumed that the friction coefficient on the inclined face of the shear key block is zero. Thus, the external load applied to the shear key has to be perpendicular to the inclined face. This load can be resolved into a horizontal component, F_h, and a vertical component, F_v, which are geometrically related as follows:

$$F_h = \frac{F_v}{\tan\beta} \tag{7.1}$$

in which β is the angle between the inclined face of the shear key block and a vertical plane. In Figure 7.11, point *O* is the point about which the shear key rotates and the distances shown are as follows:

- h_p = 13.75 in. is the vertical distance of the resultant force F_p of the prestressing bars from point *O*
- l_h = 13 in. and l_v = 33.5 in.; they are the distances of F_v and F_h from point *O*
- l_{cv} = 8 in.; it is the distance of contact force F_{ch} between the shear key and the stem wall from point *O*

In addition, T_{cv} and T_{ch} are the frictional forces due to the contact forces F_{cv} and F_{ch}, respectively. The friction coefficient μ for the concrete-to-concrete contact is assumed to be 0.4.

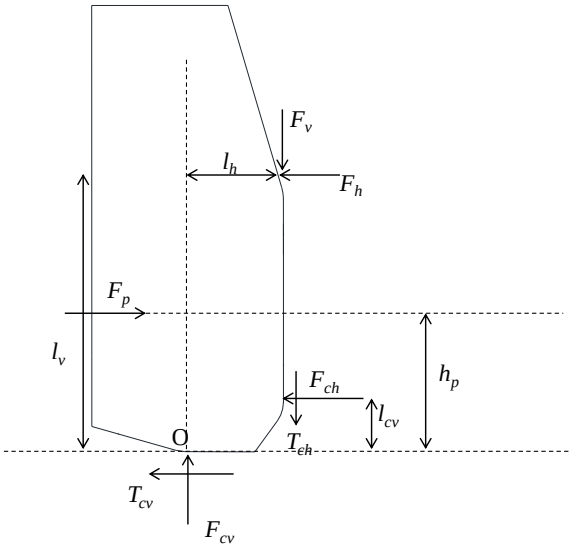

Figure 7.11 Free-body diagram of shear key block for the calculation of horizontal resisting force

Based on the force and moment equilibrium conditions for the free-body diagram shown in Figure 7.11, the horizontal resisting force, F_h, can be calculated as follows:

$$\begin{aligned}
&\Sigma F_h = 0 \Rightarrow\ F_{ch} = -F_h + F_p - T_{cv} \\
&\Sigma F_v = 0 \Rightarrow\ F_{cv} = F_v + T_{ch} \\
&\Sigma \mathrm{M}_o = 0\ \Rightarrow \\
&h_p \cdot F_p - F_h \cdot l_v + F_v \cdot l_h - F_{ch} \cdot l_{cv} + T_{ch} \cdot l_h = 0 \\
&F_h = \frac{F_p\left(h_p \cdot \left(1+\mu^2\right) + \mu \cdot l_h - l_{cv}\right)}{\left(\left(1+\mu^2\right) \cdot l_v - l_{cv} + \mu \cdot l_h\right) - \left(\tan\beta\right) \cdot \left(\left(1+2 \cdot \mu^2\right) \cdot l_h - \mu \cdot l_{cv}\right)}
\end{aligned} \tag{7.2}$$

For a maximum bar stress of 70% of the expected f_{pu} = 180 ksi, F_p = 156 kips. This results in a maximum horizontal resisting force F_h of 64 kips based on Eq. (7.2).

For the maximum horizontal resistance of 64 kips, a strut-and-tie model, as shown in Figure 7.12, is used to determine the amount of reinforcement provided in the shear key block. Along the vertical tie, the force is F_t = 55 kips, as shown in Figure 7.12. Assuming that the expected yield strength of the reinforcing bars is f_y = 68 ksi, the necessary reinforcement should be:

$$A_b = \frac{F_t}{f_y} = \frac{55}{68} = 0.81\ in^2 \tag{7.3}$$

The vertical reinforcement used in this area is 6 No. 4 bars with a total area of A_b = 1.20 in^2, which satisfies this requirement. Also, to provide sufficient resistance for the struts, and given that the width of the shear key block which was 12 in., the concrete compressive strength was specified to be 7.0 ksi, which is higher than the concrete strength used in most tests.

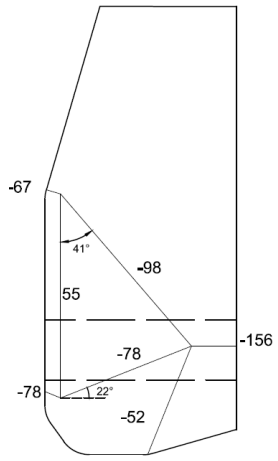

Figure 7.12 Strut-and-tie model for determining the reinforcing bars in the shear keys

For the calculation of the displacement of the shear key block, it is assumed that the shear key block rotates α degrees about point *O*, as shown in Figure 7.13. Based on this figure, the elongation of the prestressing bars is:

$$\Delta l_p = \left(h_p - l_{cv}\right) \cdot \sin\alpha \tag{7.4}$$

The horizontal displacement at the point of load application is:

$$\delta = \left(l_v - l_{cv}\right) \cdot \sin\alpha \tag{7.5}$$

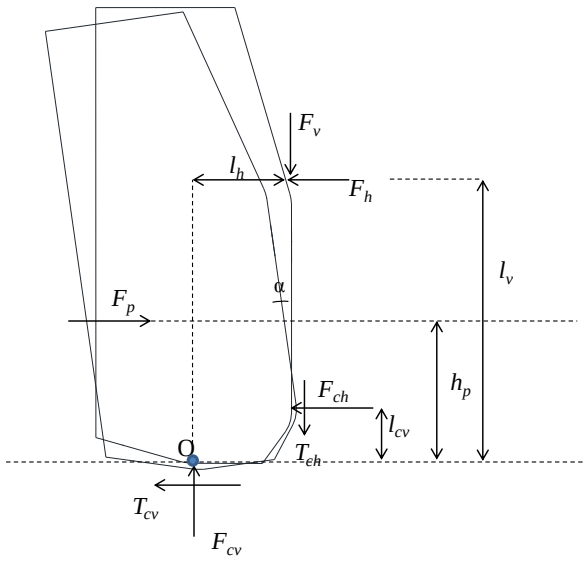

Figure 7.13 Displaced configuration of shear key block for determining the horizontal displacement

As mentioned before, the shear keys were designed to reach 70% of the expected ultimate strength f_{pu}. Assuming the modulus of elasticity to be 29,700 ksi (based on the DYWIDAG manual), and from the length of the prestressing bars, l =138.50 in., the expected elongation of these bars is:

$$\Delta l_p = \frac{0.7 \cdot f_{pu}}{E} \cdot l = 0.59 \; in. \tag{7.6}$$

From Eq. (7.4) and from the elongation of the prestressing bars, the rotation of the shear key blocks can be calculated to be α = 5.9 degrees. Using Eq. (7.5), the displacement at the point of load application is calculated to be δ = 2.60 in. However, when the neoprene pads are used, the horizontal displacement is expected to be larger than the aforementioned value.

7.4 Test Setup

The test setup was the same as that for Specimen 7, as described in Chapter 5. The specimen was secured to the lab strong floor with post-tensioned rods. A total of eight rods were used, with each post-tensioned to 150 kips. This force was sufficient to avoid sliding along the lab floor and to prevent the uplift of the specimen during the test. The load was applied to the shear keys with the steel loading beam presented in Chapter 6. The steel loading beam was prevented from moving upward by the two hold-down frames. The test assembly with the specimen, the hold-down frames and the actuators in their final positions is shown in Figure 7.14.

Figure 7.14 Test setup for Specimen 11

To reduce the friction between the shear key block and the loading beam, a piece of 8 in. x 12 in. x 0.5 in. joint filler satisfying ASTM 1751 was placed against the loaded face of the shear key, which was also used in Specimens 7 through 10. The friction between the loading beam and the frames was minimized with the use of PTFE (Polytetrafluorethylene-Teflon) bearings and grease.

7.5 Instrumentation of Specimen 11

The specimens were instrumented to monitor the strains in the reinforcing and prestressing bars, as well as the deformation of the specimen. Electrical resistance strain gages were attached to the prestressing bars and the vertical reinforcing bars of the shear keys. Test 4 was conducted on shear key block 11B (with neoprene pads between the shear key and stem wall and the footing) and Test 5 was conducted on shear key block 11A. Six strain gages were installed in each shear key block at the locations and with the numbering, preceded by an S, shown in Figure 7.15 and Figure 7.16. The positions of the strain gages were selected to measure strains in the reinforcing bars at potential crack locations, in the vicinity of the contact region of the shear key block with the stem wall. The strain gages used to monitor strains in each prestressing bar are shown in Figure 7.17. At each location, two strain gages were installed on opposite sides of the bar to monitor the axial as well as the bending deformation. The numbering and position of each prestressing bar are shown in Figure 7.18. Finally, the positions of the strain gages along the length of the specimen are shown in Figure 7.19. The side of the specimen with the neoprene pads (shear key 11B) was tested first. Then the prestressing bars were replaced and the side without the neoprene pads (shear key 11A) was tested. However, the numbering of the strain gages in the prestressing bars remained the same in the two tests.

In addition, linear potentiometers were installed external to the specimen to measure the horizontal displacements along its height. A tilt meter was attached to each shear key block to measure the in-plane rotation. Two string potentiometers were used for each test to measure the horizontal displacement of the loading beam. The strain in each

of the vertical post-tensioning bars for the hold-down frames was monitored with a strain gage. These strain readings were used to calculate the vertical reaction force exerted on the shear key through the loading beam. The positions and numbering of the external transducers are shown in Figure 7.20 and Figure 7.21. In these figures, the linear potentiometer numbers are preceded by an L, while those of the string potentiometers and tilt meters are preceded by SP and TM, respectively. To test the side of the specimen without the neoprene pads (shear key 11A), the specimen was rotated 180 degrees, so the numbering and positioning of the external instrumentation are the same as those shown in Figure 7.20 and Figure 7.21.

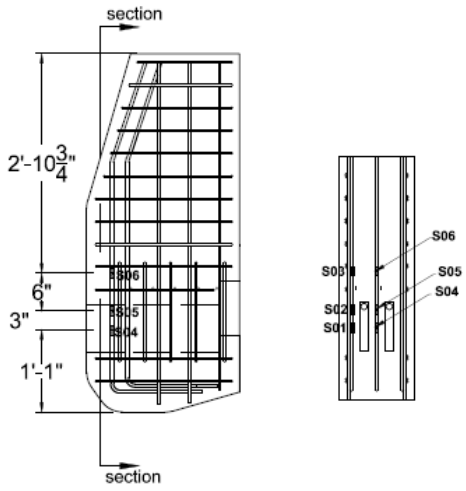

Figure 7.15 Strain gages installed in shear key block 11A

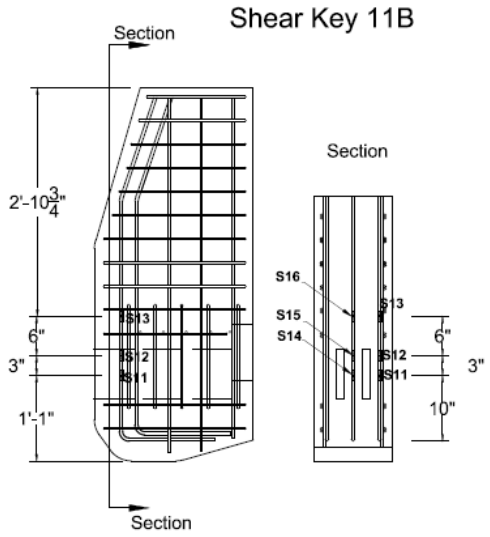

Figure 7.16 Strain gages installed in shear key block 11B

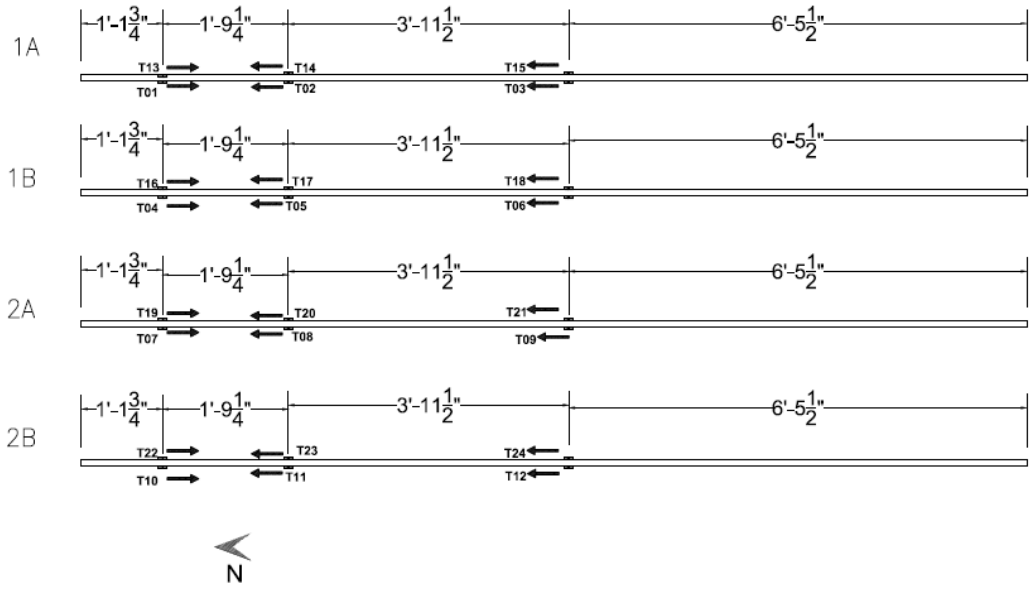

Figure 7.17 Strain gages installed in individual prestressing bars in Specimen 11

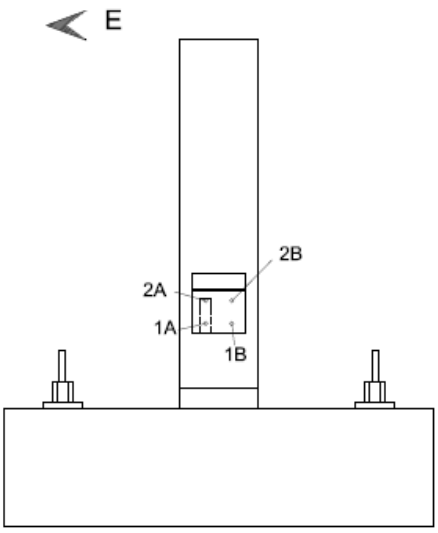

Figure 7.18 Position of each prestressing bar in Specimen 11

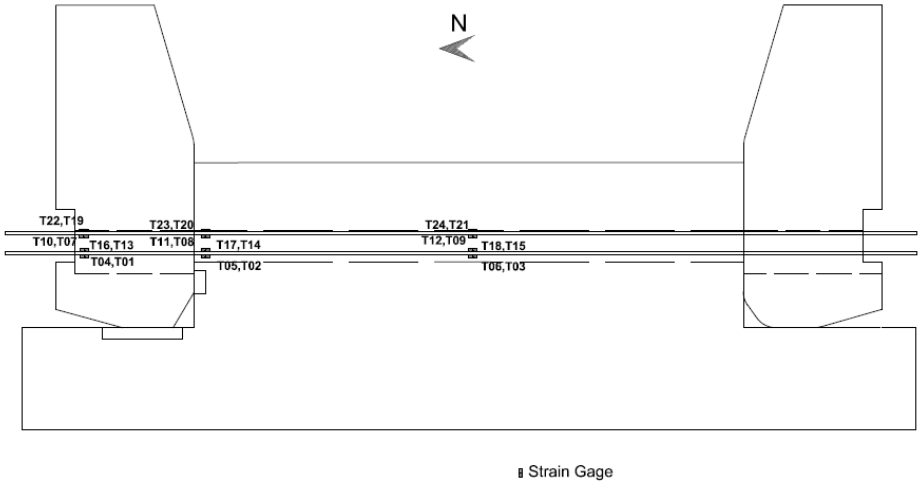

Figure 7.19 Positions of strain gages along the length of Specimen 11

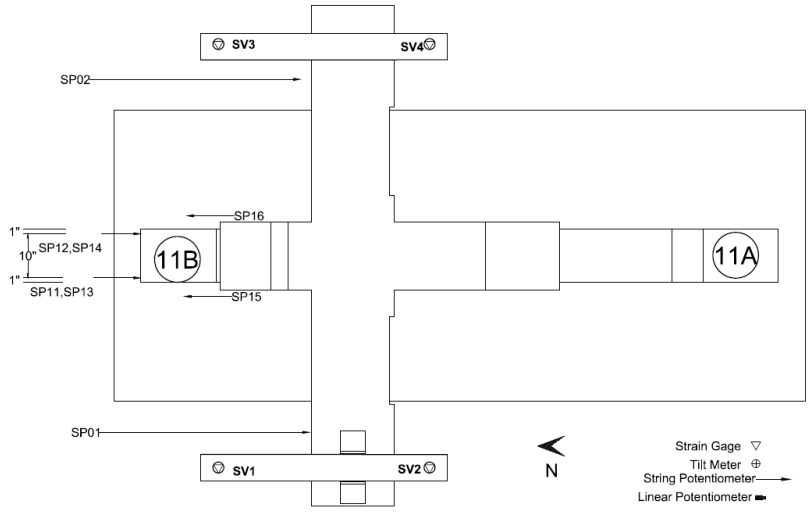

Figure 7.20 Plan view of external instrumentation for Specimen 11

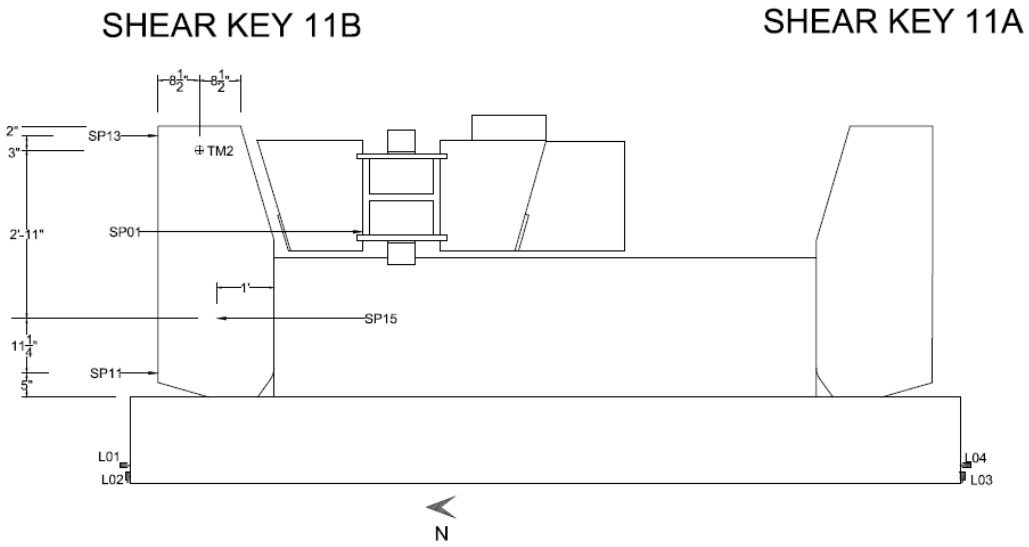

Figure 7.21 External instrumentation located on the west side of Specimen 11

7.6 Loading Protocols and Test Results

7.6.1 Test 4

Test 4 was conducted on shear key 11B, which was on the side that had neoprene pads. The prestressing bars were post-tensioned to a strain of 244 microstrain. The total prestressing force exerted to the shear key blocks was 9 kips. The loading protocol for this test consisted of incremental loading, unloading and reloading with the target loads and displacements shown in Table 7.3. The shear key was loaded in displacement control to 50 kips in increments of 5 kips. The test stopped when the stress in one of the bars reached 70% of the ultimate strength, f_{pu}. The stress was calculated from the strain-gage readings. The specimen was unloaded 6 times at 5 kips, 10 kips, 15 kips, 20 kips, 25 kips and 35 kips load, respectively, to obtain the unloading stiffness.

Table 7.3 Loading protocol for Test 4

Step	Control	Target Load/Displacement
1-10	Displacement	50 kips with 5-kip increments

The shear key block rotated about its toe on the neoprene pad. A small horizontal crack appeared in the shear key block at a horizontal load of 15 kips. The crack was close to the stem wall, as shown in Figure 7.22. In this figure, a larger crack is shown at 15 kips load. This crack occurred in one of the previous tests, which did not provide satisfactory performance of the shear key.

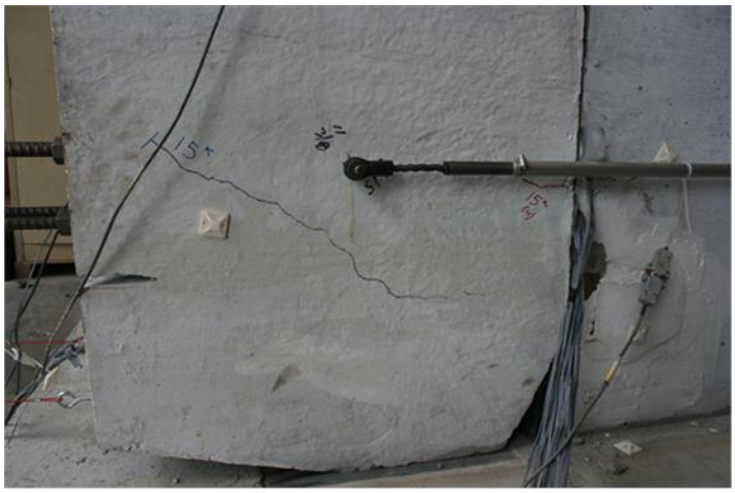

Figure 7.22 First crack (marked in red) observed on the west face of the shear key block in Test 4

The rotation of the outer plate was monitored manually with a level, as shown in Figure 7.23. It was observed that the outer plate remained vertical until a horizontal load of 30 kips was reached. After that load, the plate started to rotate together with the shear key block. This can be attributed to the fact that the axial force developed in the bottom row of prestressing bars was approaching that of the top row and the resultant moment was not sufficient to counteract the bending moments of the prestressing bars. Hence, the hinge mechanism did not perform exactly as expected.

Figure 7.23 Monitoring the rotation of the outer plate in Test 4

The test stopped at a horizontal load of 50 kips when 70% of the ultimate strength was reached in one of the prestressing bars. The displacement of the shear key block is shown in Figure 7.24. At that load, the average horizontal displacement registered by the string potentiometers SP1 and SP2, whose locations are shown in Figure 7.20 and Figure 7.21, was 3.60 in. The load-vs.-displacement curve for Test 4 is shown in Figure 7.25.

Figure 7.24 Displacement of shear key block at a horizontal load of 50 kips in Test 4

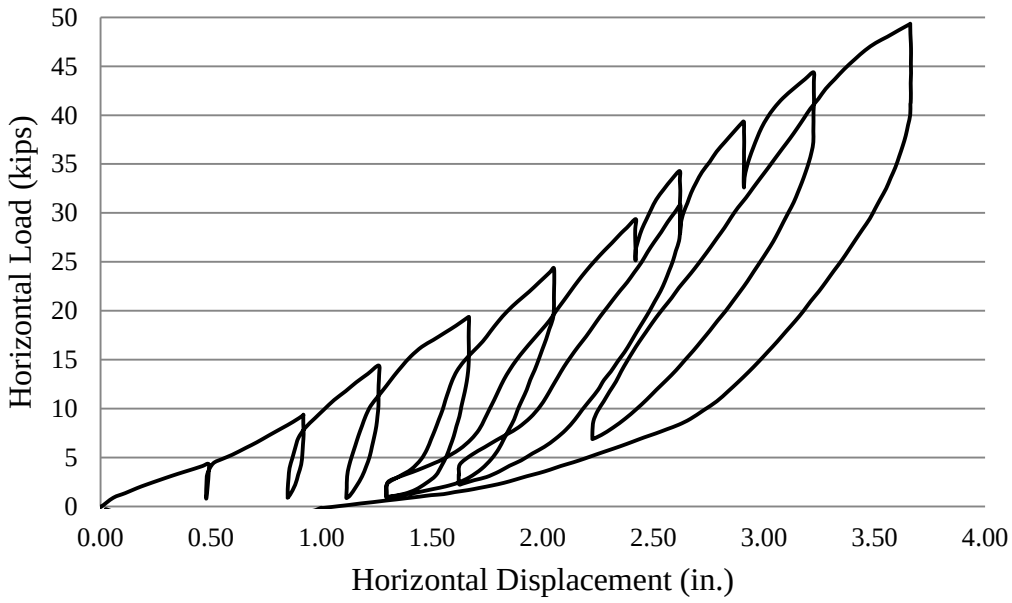

Figure 7.25 Horizontal load-vs.-horizontal displacement for Test 4

After the end of the test, the shear key block was removed from the specimen and the stem wall and neoprene pads were inspected, as shown in Figure 7.26. It should be mentioned that this side of the specimen had been first tested with a softer pad prior to Test 4, causing some damage in the stem wall. In Test 4, minor concrete spalling was observed.

Figure 7.26 Stem wall and neoprene pads after shear key block was removed in Test 4

Vertical load on Shear Key Block

The measurements from the strain gages on the bars in the hold-down frames indicated that at the peak horizontal load, a 10-kip vertical force was applied to the shear key. In Figure 7.27, the measured and the theoretical vertical forces are plotted against the measured horizontal load. The theoretical vertical force is calculated from the measured horizontal load and the angle of the inclined face of the shear key, which is assumed to have zero friction.

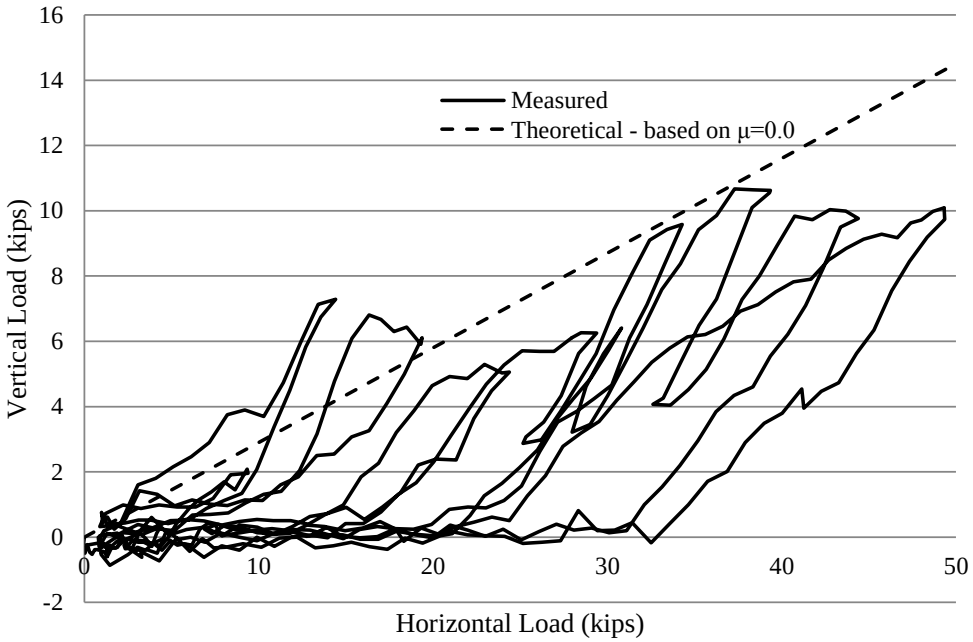

Figure 7.27 Measured and theoretical vertical forces in Test 4

Strains in Vertical Reinforcing Bars of Shear Key Block

Strains in the vertical reinforcing bars of the shear key block were measured. Readings from the strain gages in each bar are plotted against the horizontal load in Figure 7.28. The locations of these gages are shown in Figure 7.16. All the stain-gage readings were within the elastic regime.

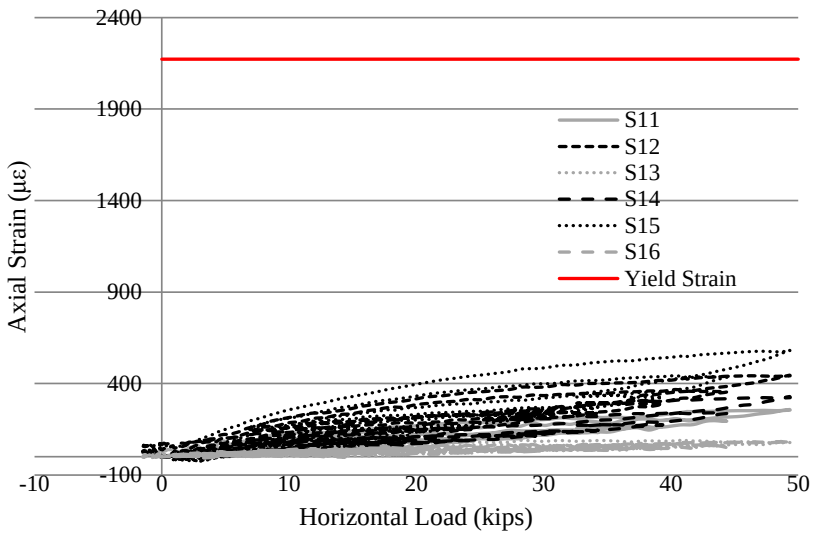

Figure 7.28 Axial strain-vs.-horizontal load in the vertical reinforcing bars of shear key block 11B in Test 4

Strains in Prestressing Bars

The strain readings from the strain gages in the prestressing bars are plotted against the horizontal displacement in Figure 7.28 through Figure 7.32 for each prestressing bar. The locations of the strain gages are shown in Figure 7.17 and Figure 7.19, and the numbering of the prestressing bars is shown in Figure 7.18.

Based on the figures, it can be observed that the top row of prestressing bars registered larger strains. For the bottom bars, bars 1A and 1B, the maximum strain was observed at the strain gage located in the middle of the prestressing bar, away from the tested shear key block. For the top bars, bars 2A and 2B, the strains measured were at the same levels. Readings from the bars suggest that the bars experienced limited bending towards the end of the test.

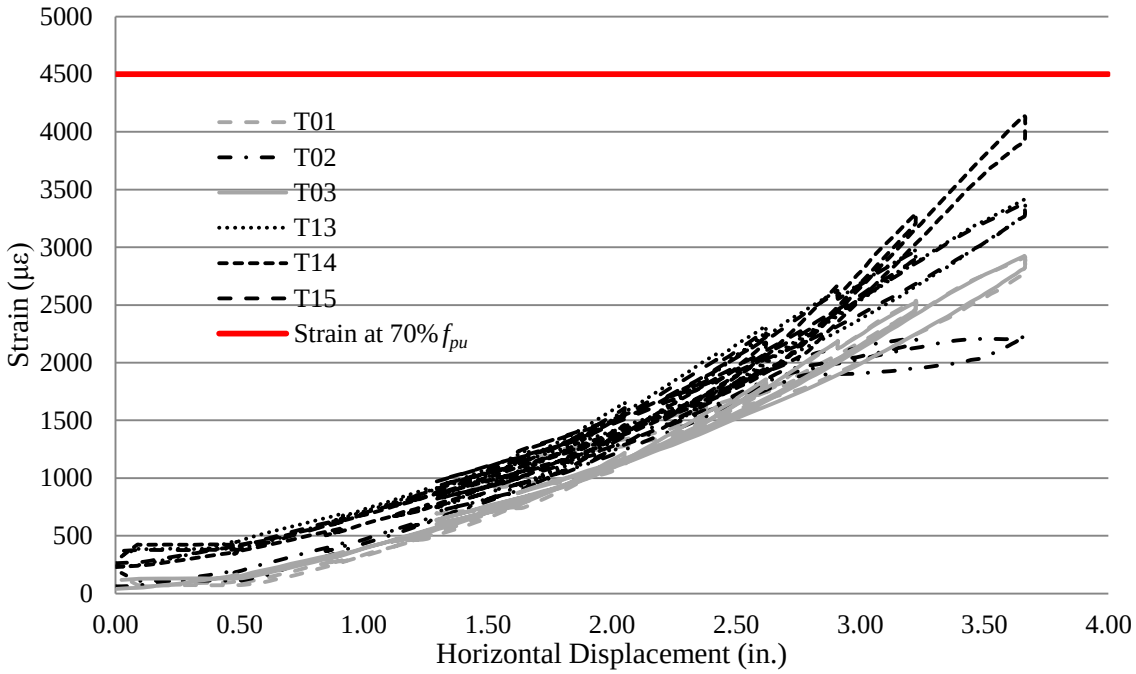

Figure 7.29 Axial strain-vs.-horizontal displacement for prestressing bar 1A in Test 4

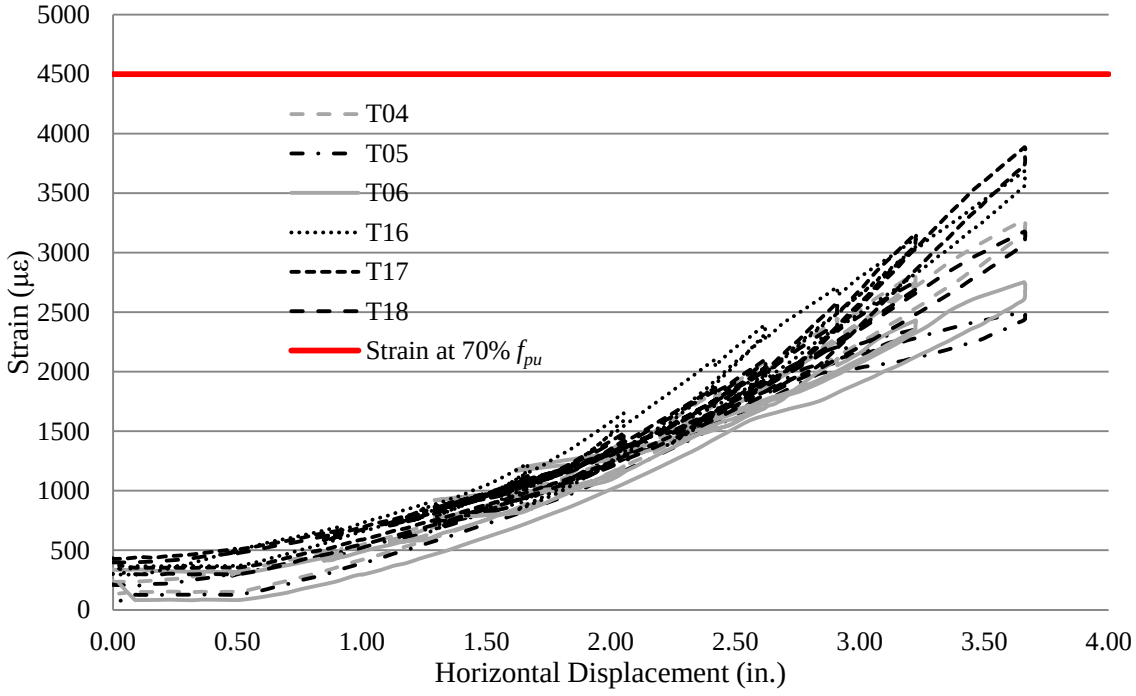

Figure 7.30 Axial strain-vs.-horizontal displacement for prestressing bar 1B in Test 4

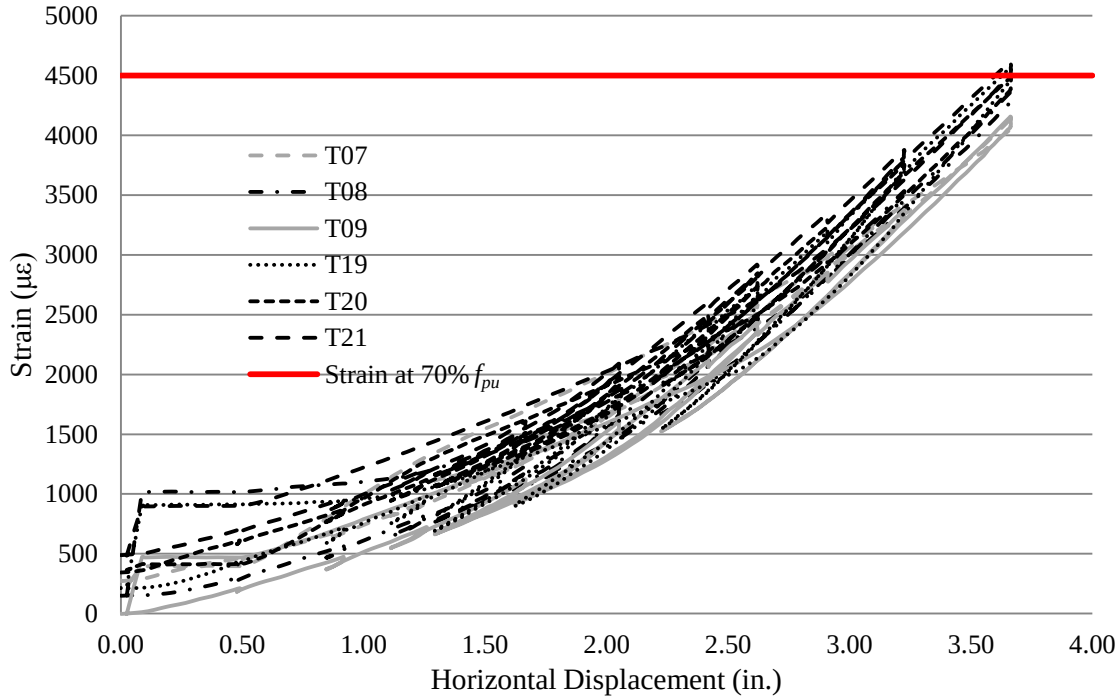

Figure 7.31 Axial strain-vs.-horizontal displacement for prestressing bar 2A in Test 4

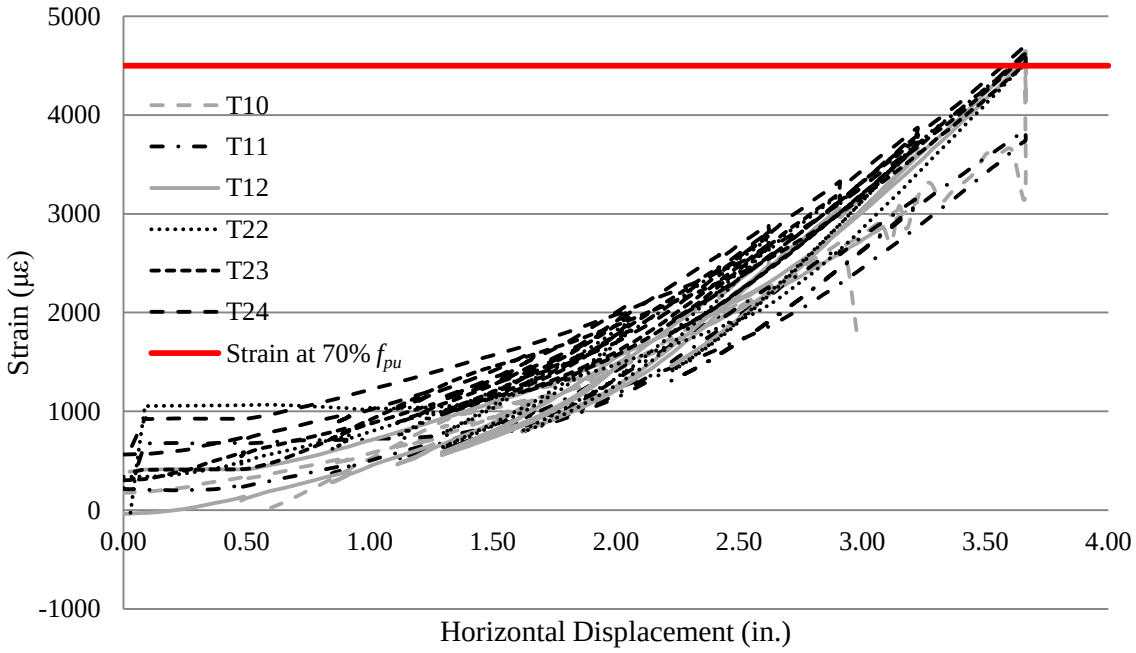

Figure 7.32 Axial strain-vs.-horizontal displacement for prestressing bar 2B in Test 4

In-Plane Rotation of Shear Key Block

The in-plane rotation of the shear key block was monitored with the tilt meter TM2, whose location is shown in Figure 7.21. The readings of the tilt meter are plotted against the horizontal displacement in Figure 7.33. The rotation is directly proportional to the horizontal displacement. At the end of the test, the tilt-meter shows that the residual rotation was one degree.

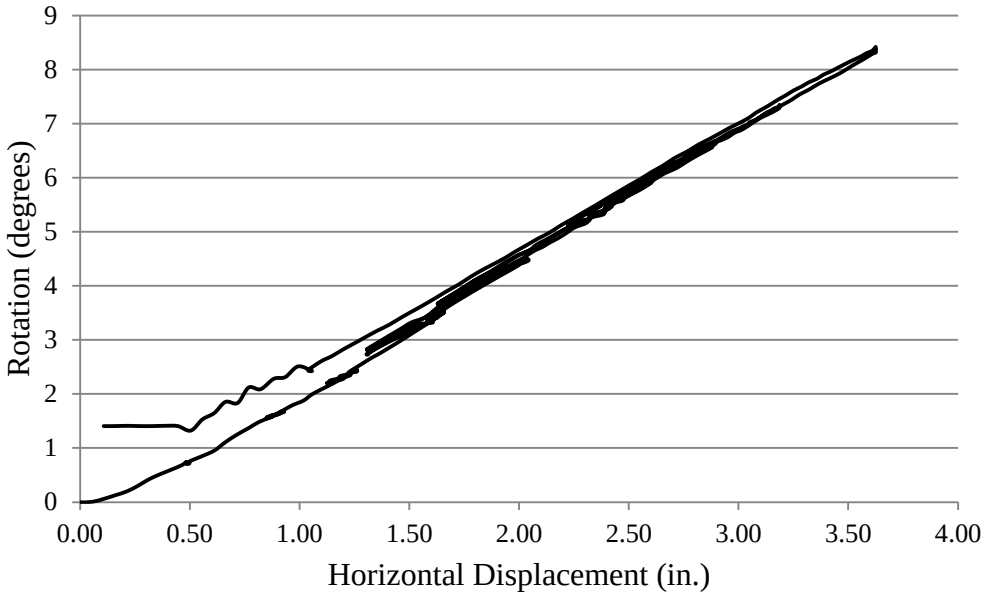

Figure 7.33 In-plane rotation of shear key block 11B in Test 4

7.6.2 Test 5

Test 5 was conducted on shear key 11A, which was on the side with no neoprene pads between the shear key and the stem wall or the footing. The prestressing bars were loaded to a strain of 241 microstrain. The total prestressing force exerted to the shear key blocks was measured to be 9 kips. The loading protocol for this test consisted of incremental loading, unloading and reloading with the target loads shown in Table 7.4.

The shear key was loaded in displacement control to 55 kips in increments of 5 kips. As in Test 4, the test was stopped when the stress in one of the post-tensioned bars reached 70% of the ultimate strength. The specimen was unloaded 7 times at 5 kips, 10 kips, 15 kips, 20 kips, 25 kips and 35 kips, and 45 kips, respectively, to obtain the unloading stiffness.

Table 7.4 Loading protocol for Test 5

Step	Control	Target Load/Displacement
1-11	Displacement	55 kips with 5-kip increments

The shear key block rotated about its toe. At a horizontal load of 15 kips, a horizontal crack developed in the shear key block and propagated towards the middle of the block. The crack is shown in Figure 7.34. The width of the crack remained very small throughout the test.

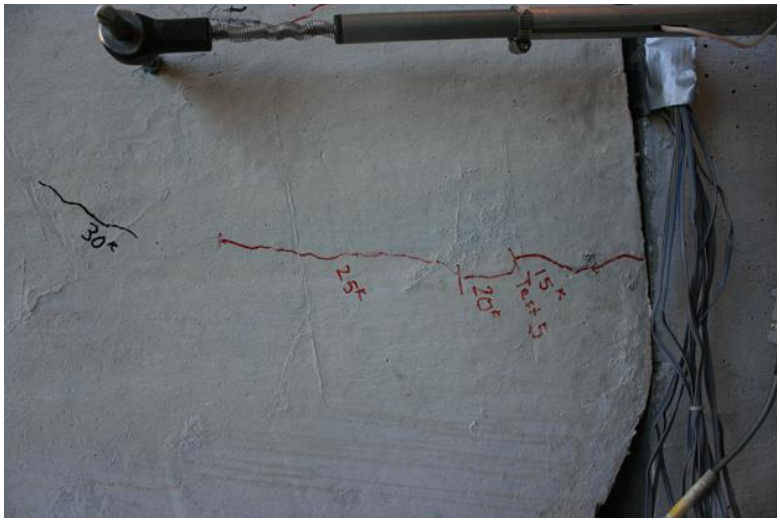

Figure 7.34 Crack observed on the west face of the shear key block in Test 5

The rotation of the outer plate was monitored continuously with a level attached to the plate, as shown in Figure 7.35. It was observed that the rotating plate remained vertical until the end of the test.

Figure 7.35 Monitoring the rotating plate in Test 5

The test was stopped at a horizontal load of 55 kips, when 70% of the ultimate tensile strength was reached in one of the prestressing bars. The displacement of the shear key block is shown in Figure 7.36. At that load, the average horizontal displacement registered by the string potentiometers SP1 and SP2, whose locations are shown in Figure 7.20 and Figure 7.21, was 2.60 in. The load-vs.-displacement curve for Test 5 is shown in Figure 7.37.

Figure 7.36 Displacement of shear key block at a horizontal load of 55 kips in Test 5

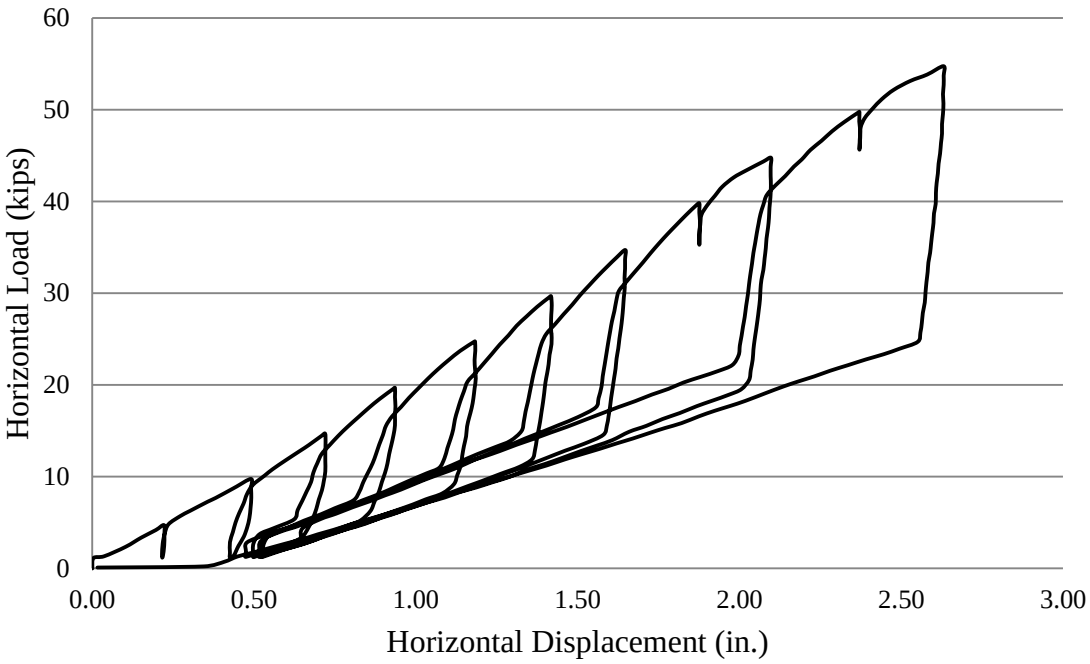

Figure 7.37 Horizontal load-vs.-horizontal displacement for Test 5

After the end of the test, the shear key block was removed from the specimen, and the stem wall and footing condition is shown in Figure 7.38. It can be noticed that no damage occurred in the footing and the stem wall.

Figure 7.38 Stem wall and footing after shear key block was removed in Test 5

Vertical load on Shear Key Block

The measurements from the strain gages on the bars in the hold-down frames indicated that at the peak horizontal load, a 24-kip vertical force was applied to the shear key. In Figure 7.39, the measured and the theoretical vertical forces are plotted against the measured horizontal load. The theoretical vertical force is calculated from the measured horizontal load and the angle of the inclined face of the shear key, which is assumed to have zero friction. The vertical load was about 44% of the horizontal load and is significantly higher than what has been measured in the previous tests.

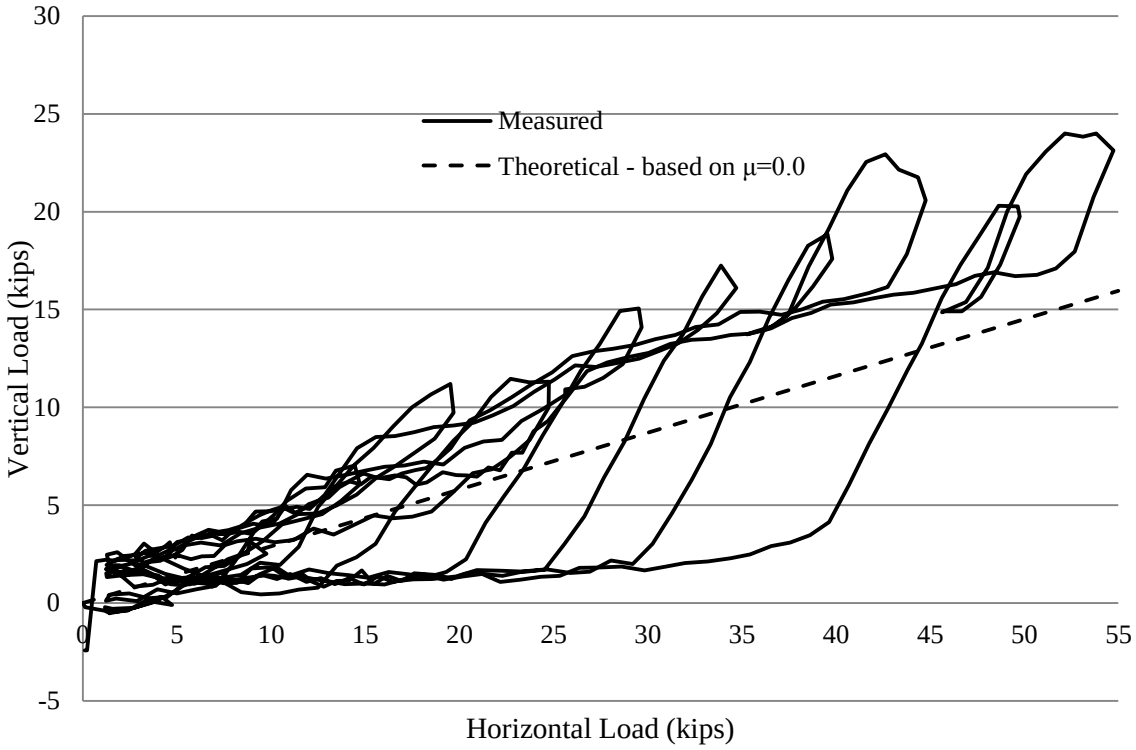

Figure 7.39 Measured and theoretical vertical forces in Test 5

Strains in Vertical Reinforcing Bars of Shear Key Block

Strains in the vertical reinforcing bars of the shear key block were measured. Readings from the strain gages in each bar are plotted against the horizontal load in Figure 7.40. The locations of these gages are shown in Figure 7.15. All the stain-gage readings were within the elastic regime.

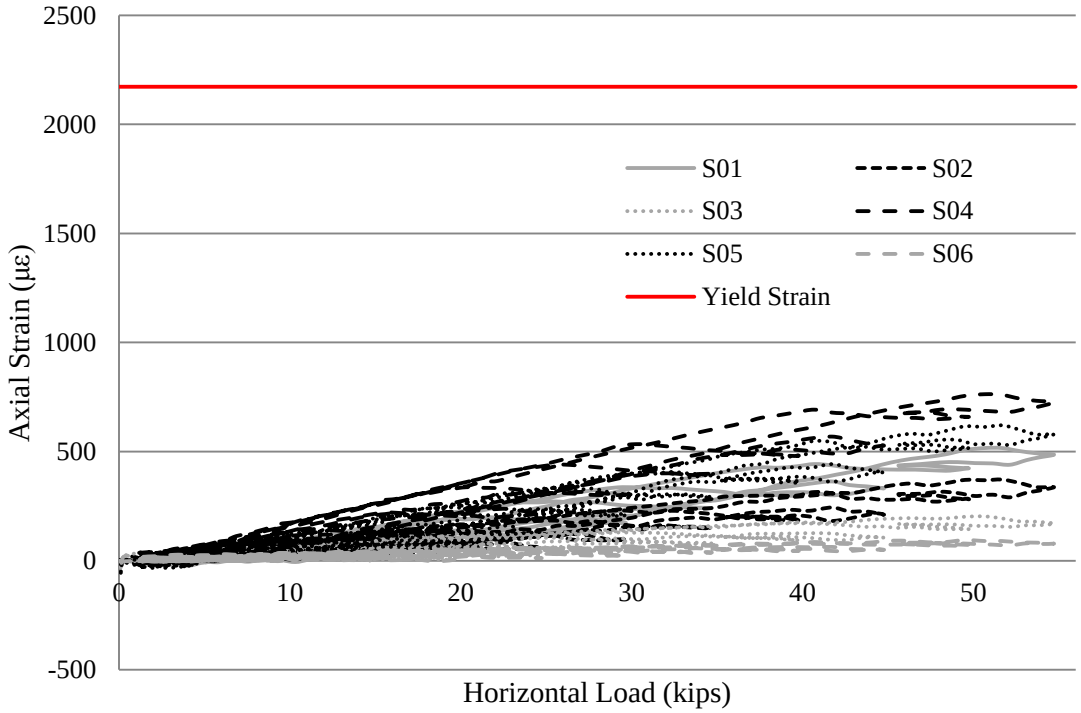

Figure 7.40 Axial Strain-vs.-horizontal load in the vertical reinforcing bars of shear key block 11A in Test 5

Strains in Prestressing Bars

Readings from the strain gages in the prestressing bars are plotted against the horizontal displacement in Figure 7.41 through Figure 7.44. The locations of the strain gages are shown in Figure 7.17 and Figure 7.19, and the numbering of the prestressing bars in Figure 7.18.

From the figures, it can be observed that the top prestressing bars registered larger strains. The highest strain was measured in the middle of bar 2B (gage T24). For the bottom bars, the highest strain was measured in bar 1B at a location (gage T16) close to the bar anchor. Finally, the readings from bar 1B suggest that the bar experienced limited bending towards the end of the test.

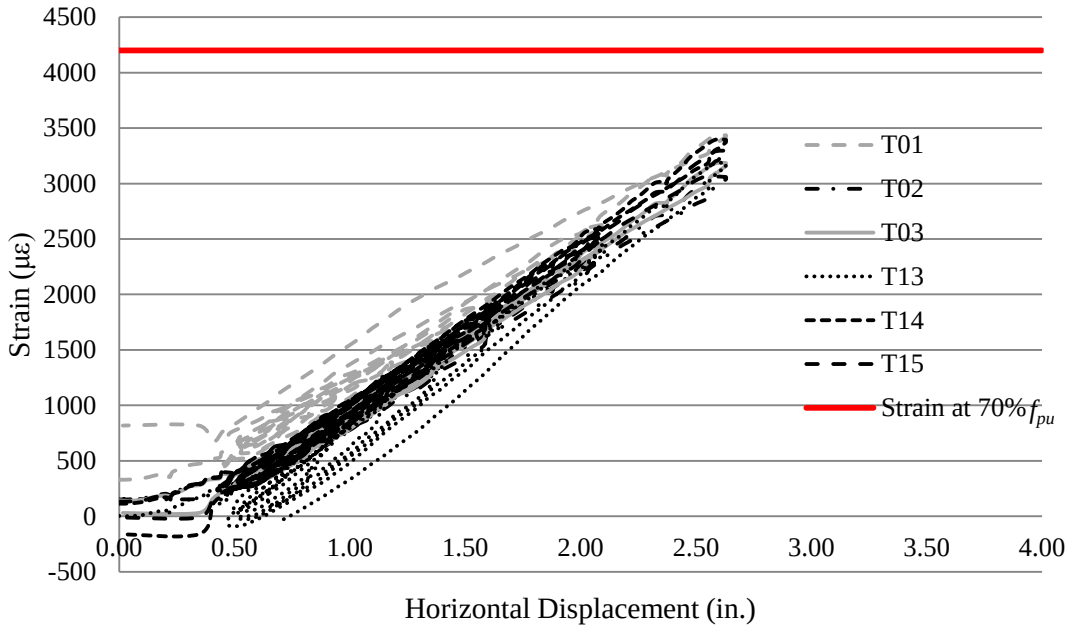

Figure 7.41 Axial strain-vs.-horizontal displacement in the prestressing bar 1A in Test 5

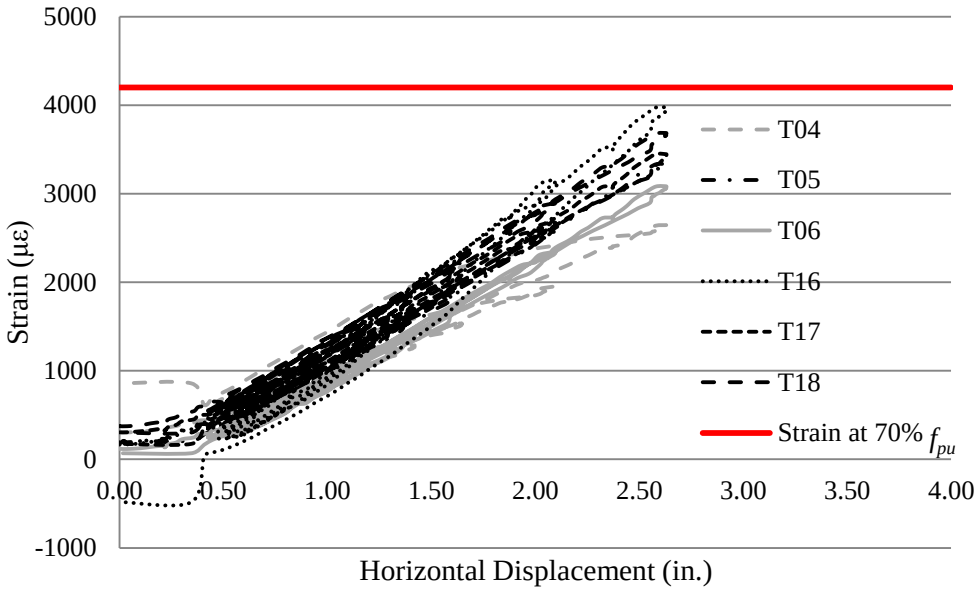

Figure 7.42 Axial strain-vs.-horizontal displacement in prestressing bar 1B in Test 5

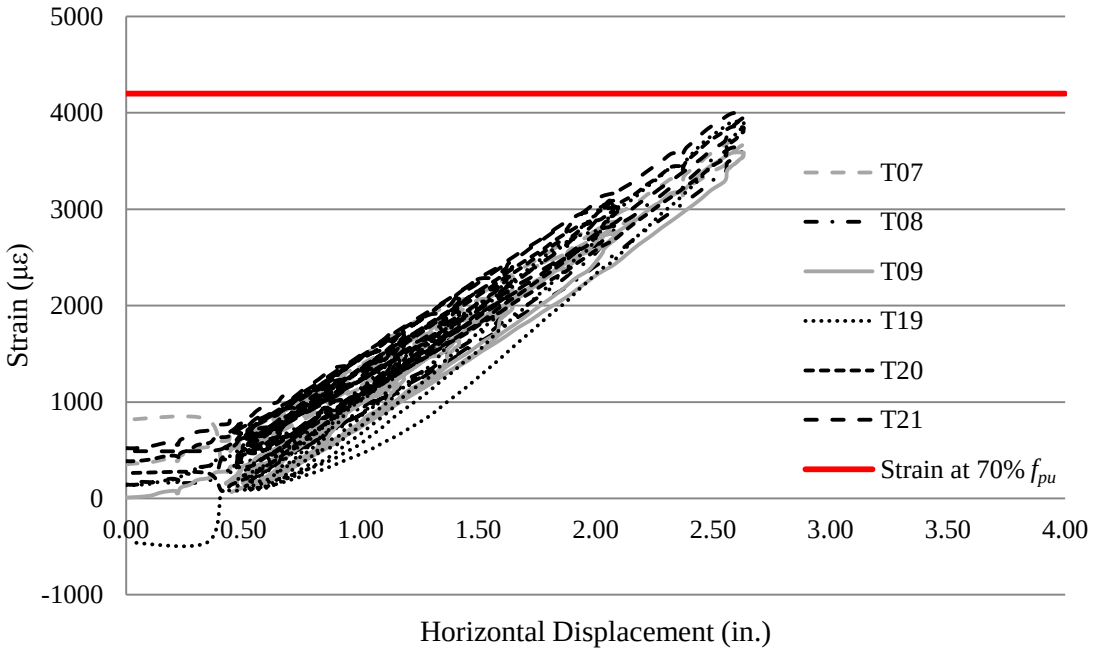

Figure 7.43 Axial strain-vs.-horizontal displacement in prestressing bar 2A in Test 5

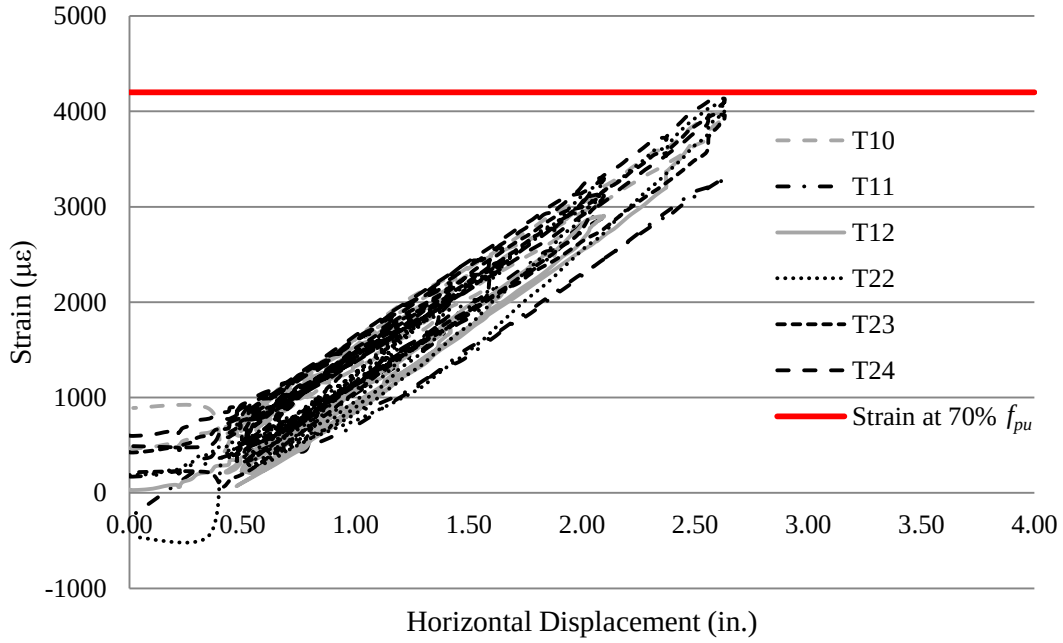

Figure 7.44 Axial strain-vs.-horizontal displacement in prestressing bar 2B in Test 5

In-Plane Rotation of Shear Key Block

The in-plane rotation of the shear key block was monitored with the tilt meter TM1, whose location is shown in Figure 7.21. The readings of the tilt meter are plotted in Figure 7.45 against the horizontal displacement. The rotation is directly proportional to the horizontal displacement.

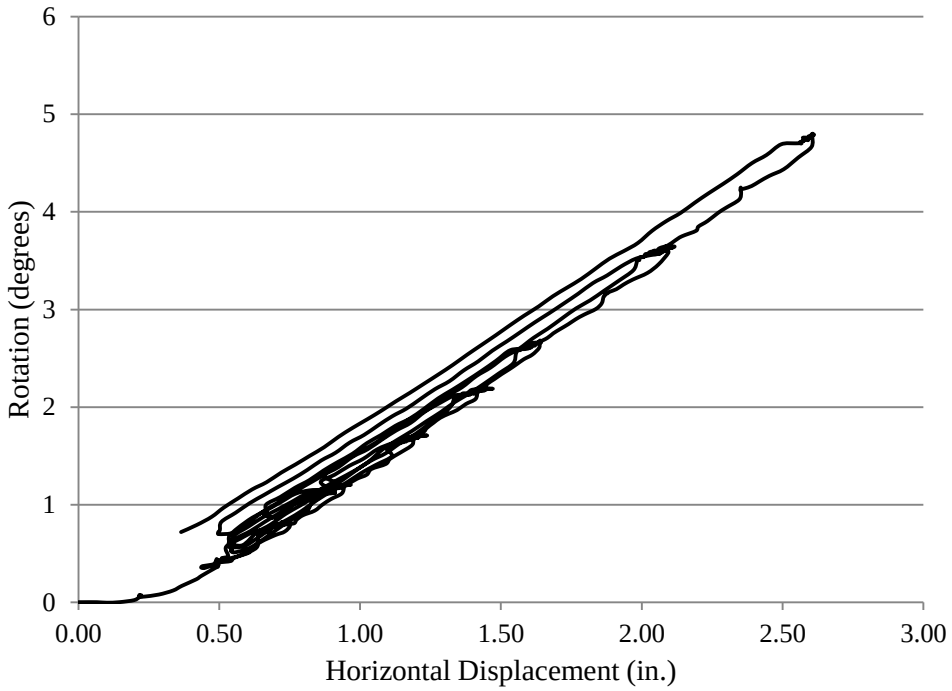

Figure 7.45 In-plane rotation of shear key block in Test 5

7.7 Summary and Conclusions

Experimental results on two prestressed shear keys were presented in this chapter. Both had the same reinforcement details. For the first shear key (11B), neoprene pads were inserted between the shear key block and the footing and the stem wall, while the contacts were concrete-to-concrete for the second shear key.

The shear key blocks displaced by rocking on the footing surface. Limited cracking appeared in the lower part of the shear keys. However, the widths of these cracks remained very small throughout the tests. The hinge system developed in this study for anchoring the prestressing bars mitigated the bending of the bars as the shear keys rocked. The test results have shown that the neoprene pads between the shear key and the stem wall and the footing provided no advantage. The concrete-to-concrete contact for shear key 11A did not cause noticeable damage on the contact surfaces. However, the presence of neoprene pads in shear key 11B resulted in a softer response.

Based on the tests results, one can conclude that the shear keys performed as they were designed for. However, the maximum horizontal resistances developed by shear keys 11B and 11A when the prestressing bars reached 70% of their ultimate tensile force were 50 kips and 55 kips, respectively, which are a bit lower than the 64 kips prior to the tests (as presented in Section 7.3). This can be attributed to the frictional forces between the shear key blocks and the stem wall and the footing higher than what was assumed in the calculation. In Table 7.5, the displacements at which the two tests were stopped are compared to the displacements at failure for the two isolated shear keys (7A and 7B) presented in Chapter 5. The displacements shown in Table 7.5 are measured by displacement transducers mounted at the elevation of the applied horizontal load. It can be seen that the prestressed shear keys reached much higher displacements with only minor damage.

Table 7.5 Comparison of displacement capacities for isolated and prestressed shear keys

Shear key 7A	Shear key 7B	Shear key 11B	Shear key 11A
1.60 in.	1.60 in.	3.60 in.	2.60 in.

7.8 Acknowledgement of Publication

Part of this chapter is a reprint of the material that will appear in a technical report which will be submitted to the California Department of Transportation in 2016, Kottari, A., P. B. Shing, J. I. Restrepo, under the title "Design and Capacity Assessment of External Shear Keys in Bridge Abutments". The dissertation author will be the primary investigator and author of this report.

CHAPTER 8

EXPERIMENTAL STUDY OF SKEWED MONOLITHIC EXTERNAL SHEAR KEYS IN BRIDGE ABUTMENTS

8.1 Description of Test Specimen

Very often, a bridge superstructure is not perpendicularly aligned with the abutments and piers, as illustrated in Figure 8.1. The angle of skew as defined in the figure is normally between 0 and 60 degrees. The strength and behavior of the exterior shear keys in a bridge abutment under horizontal loading are expected to depend significantly on the angle of skew. However, the influence of the angle of skew has not been studied before.

This chapter presents the experimental study conducted on an abutment stem wall with two monolithic shear keys for a bridge deck which has an angle of skew of 60 degrees. This specimen is identified as Specimen 12 with shear keys 12A and 12B. The specimen had the same amount of horizontal shear reinforcement in the stem wall as Specimens 8 and 9, which had zero-degree skew, as presented in Chapter 7. The amounts of vertical dowel bars connecting shear keys 12A and 12B to the stem wall were the same as those in shear keys 8B and 9B, respectively, so that the influence of the angle of skew can be identified from the test results. All the shear keys had a vertical face on the loading side.

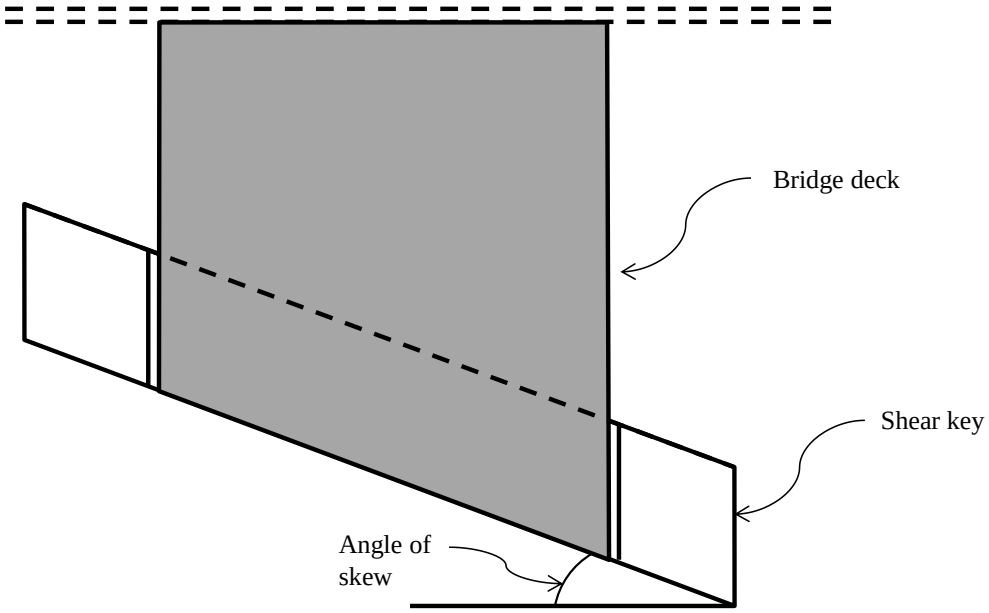

Figure 8.1 Angle of skew of a bridge abutment

8.2 Design of Specimen 12

The reinforcing details of Specimen 12 are shown in Figure 8.2 through Figure 8.6. To arrange the vertical dowel bars properly, the length of the shear keys was increased to 28 in., as compared to 24 in. used in the other specimens presented in Chapter 6. To have the same contact area between a shear key and the stem wall as that in the other specimens, the width of the shear keys was decreased from 16.75 in. to 15 in. Shear keys 12A and 12B had a vertical face on the loading side, as shown in Figure 8.2. The reinforcement of the stem wall was the same as that in Specimens 8 and 9. Shear key 12A had 6 No. 3 vertical dowel bars, which was the same as that for shear key 8B, whereas 12B had 10 No. 3 vertical dowel bars, which was the same as that for shear key 9B.

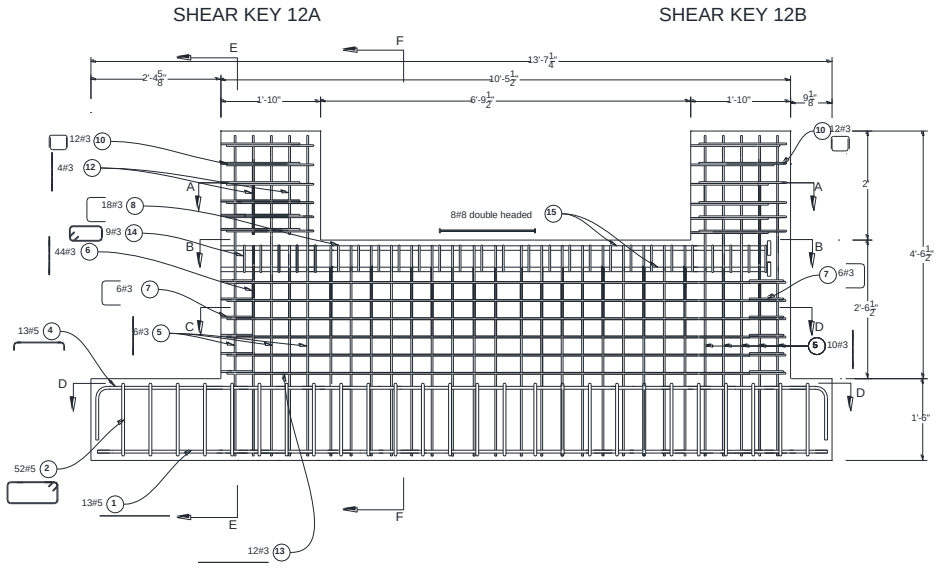

Figure 8.2 Elevation view of design details for Specimen 12

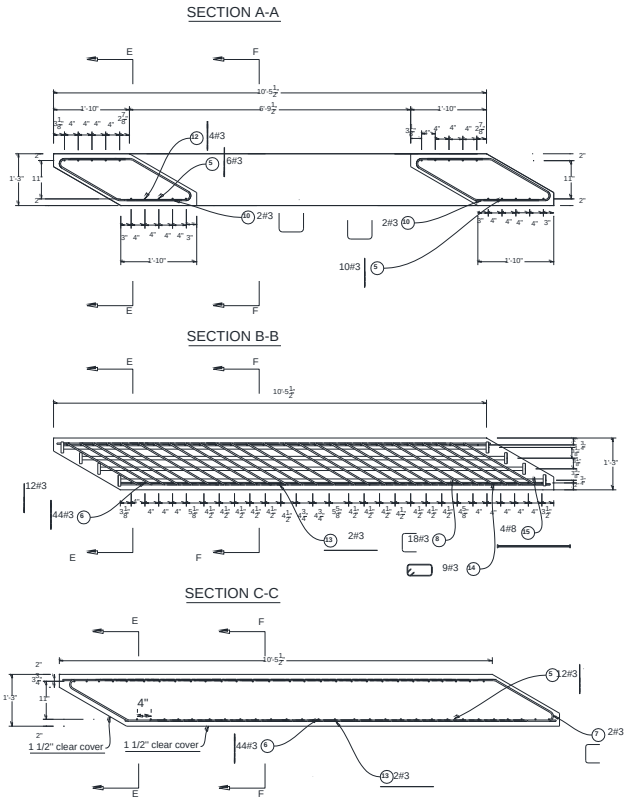

Figure 8.3 Section A-A, B-B and C-C in design drawings for Specimen 12 (see Figure 8.2 for the location of the sections)

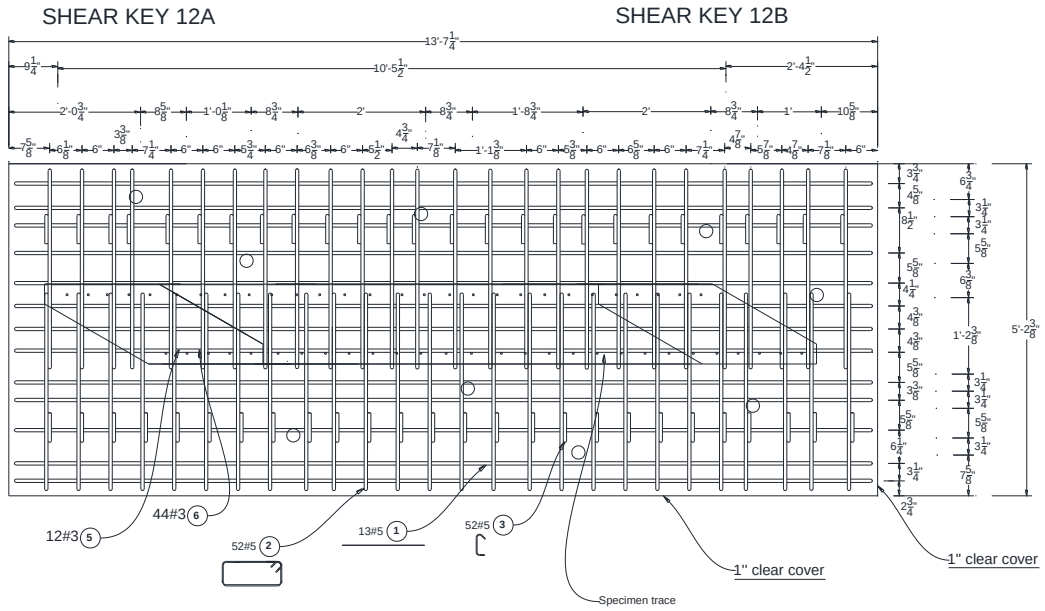

Figure 8.4 Section D-D in design drawings for Specimen 12
(see Figure 8.2 the location of the section)

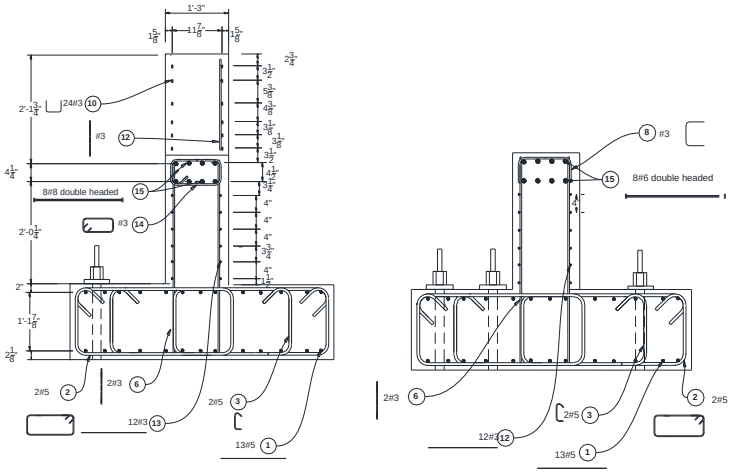

Figure 8.5 Section E-E (left) and F-F (right) in design drawings for Specimen 12
(see Figure 8.2 for the location of the sections)

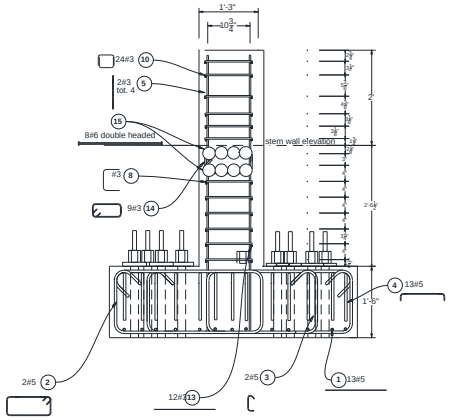

Figure 8.6 Side view in design drawings for Specimen 12

The concrete compressive strength specified for Specimen 12 was 4.0 ksi. On the day of the first shear key test, the strength reached 6.0 ksi. The compressive strength was obtained from the tests of concrete cylinders, which were cast and kept in plastic molds till the day of testing. The slump of the concrete mix was 4.50 in. The reinforcement properties are summarized in Table 8.1.

Table 8.1 Measured strengths of reinforcing bars in Specimen 12

Reinforcement Description	Bar Size	f_y (ksi)	f_{su} (ksi)
Vertical and horizontal side reinforcement of the stem wall	No. 3	65.75	93.00
Horizontal shear reinforcement of the stem wall	No. 8	67.20	96.20

8.3 Test Setup

The setup for testing shear key 12A is shown in Figure 8.7. The specimen was rotated 180 degrees for testing shear key 12B so that loading direction remained the same. The load was applied to the shear keys with the steel loading beam presented in Chapter 6. The loading beam was supported on concrete blocks in three locations, as

shown in Figure 8.7. The loading beam was prevented from moving upward by two hollow steel section beams and two hold-down frames, assembled with 5 x 5 x ½ in. steel angle sections. The two hold-down frames, shown in Figure 8.8, also prevented the out-of-plane movement of the steel loading beam. The specimen was secured to the lab floor with 1 ⅜ in. post-tensioned rods. A total of seven rods were used, with each post-tensioned to 150 kips. This force was sufficient to avoid sliding along the lab floor and to prevent uplift of the specimen during the test. The rods were hand-tightened and the initial strain in the rods was negligible. Figure 8.8 shows the hold-down frames and beams, the vertical rods, the steel loading beam and the actuators in their final positions. A piece of 8 in. x 15 in. x 0.5 in. joint filler satisfying ASTM 1751 was placed between the loading beam and the vertical face of the shear key to minimize the friction of the loading surface, as for Specimens 8 through 10. In addition, the friction between the loading beam and the concrete supports, the steel frames and the steel beams was minimized with the use of PTFE (Polytetrafluorethylene-Teflon) bearings and grease.

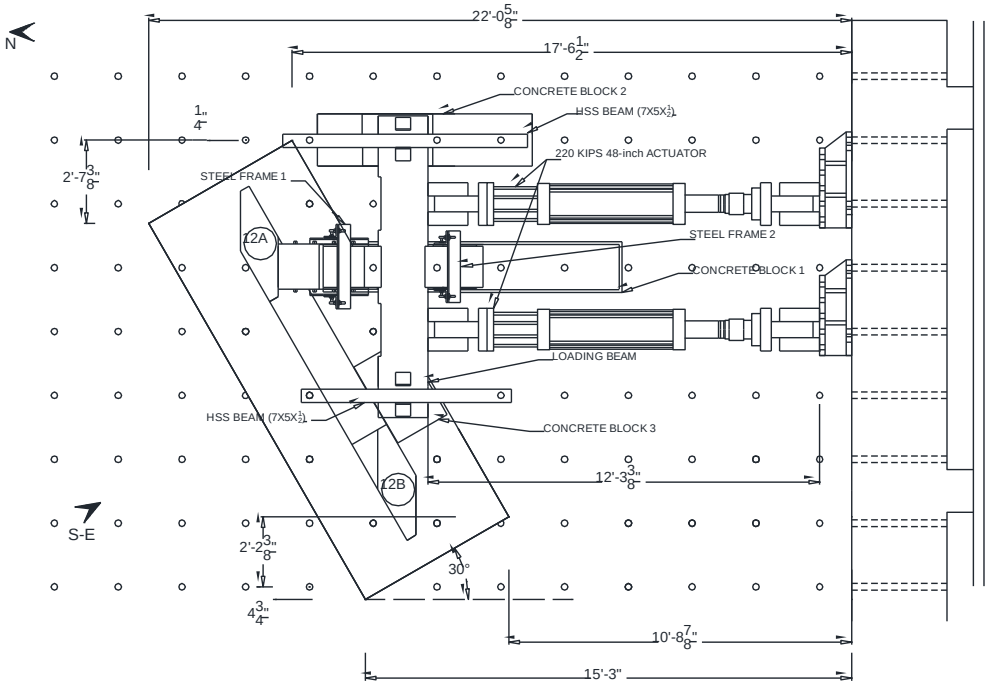

Figure 8.7 Plan view of test setup for shear key 12A (the specimen was rotated 180 degrees for the test of shear key 12B)

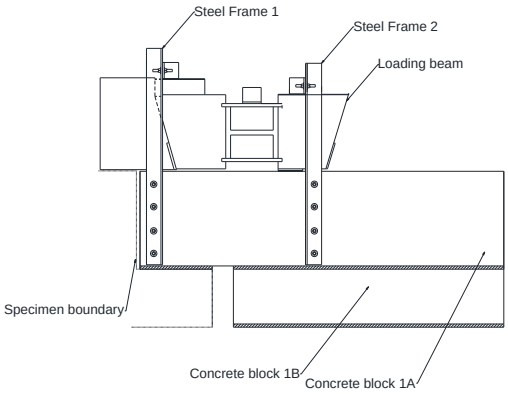

Figure 8.8 Side view of hold-down frames in test setup for Specimen 12

Figure 8.9 Picture of test setup for Specimen 12

8.4 Instrumentation of Specimen 12

The specimens were instrumented to monitor the strains in the reinforcing bars as well as the deformation of the specimen. Electrical resistance strain gages were attached to the longitudinal and transverse reinforcing bars. A total of 96 strain gages were installed. The location and numbering of the strain gages, preceded by an S, are shown in Figure 8.10 through Figure 8.12.

The positions of the strain gages were selected to measure strains in the bars at the potential locations of main cracks in the stem wall. Those cracks included the diagonal cracks in the stem wall underneath and away from the shear key. For this reason, strain gages were attached to the side reinforcement and horizontal shear reinforcement in multiple locations.

In addition, linear potentiometers were installed external to the specimen to measure the horizontal displacements along its height in the north and east side of the

shear key, as well as the expected vertical uplift of the shear key with respect to the stem wall. The directions are identified in Figure 8.7. A tilt meter was attached to each of the shear keys to measure the in-plane rotation. Two string pots were used to measure the horizontal displacement of the loading beam. The strain in each of the vertical post-tensioning bars of the steel beams and those in the vertical steel angles of the hold-down frames, shown in Figure 8.8, were monitored with strain gages. These strain readings were used to calculate the vertical reaction force exerted on the shear key through the loading beam. The positions and numbering of the external transducers are shown in Figure 8.13 through Figure 8.15. In these figures, the linear potentiometer numbers are preceded by an L, while those of the string potentiometers and tilt meters are preceded by SP and TM, respectively. It should be noted that to test shear key 12B, the specimen was rotated 180 degrees with respect to the position shown in Figure 8.7. The numbering and positioning of the external instrumentation were the same for the two shear keys.

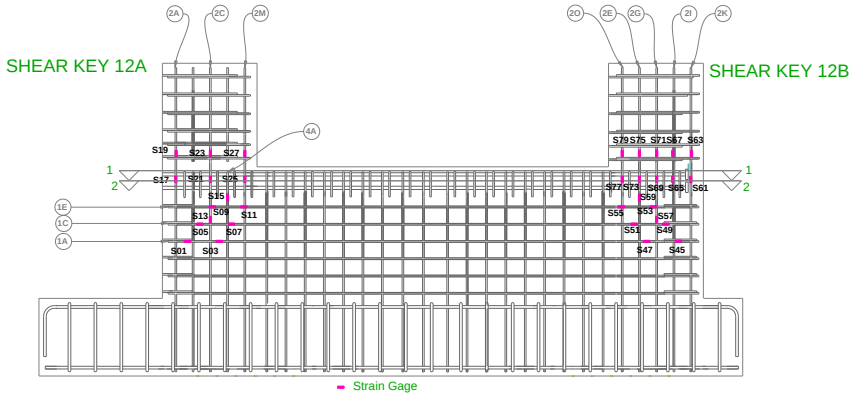

Figure 8.10 Strain gages located on the northwest side of Specimen 12

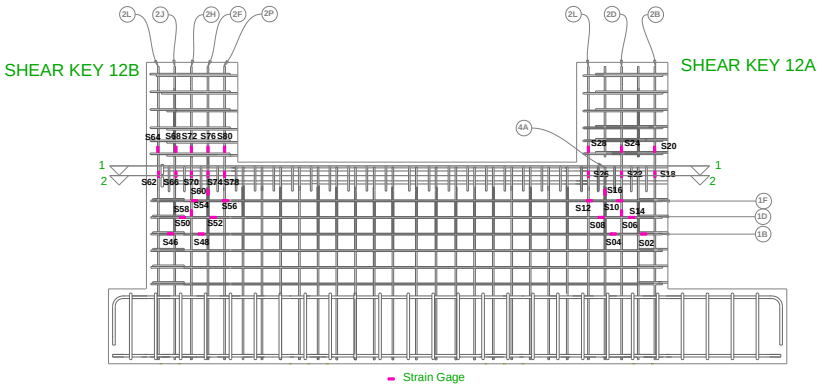

Figure 8.11 Strain gages located on the southeast side of Specimen 12

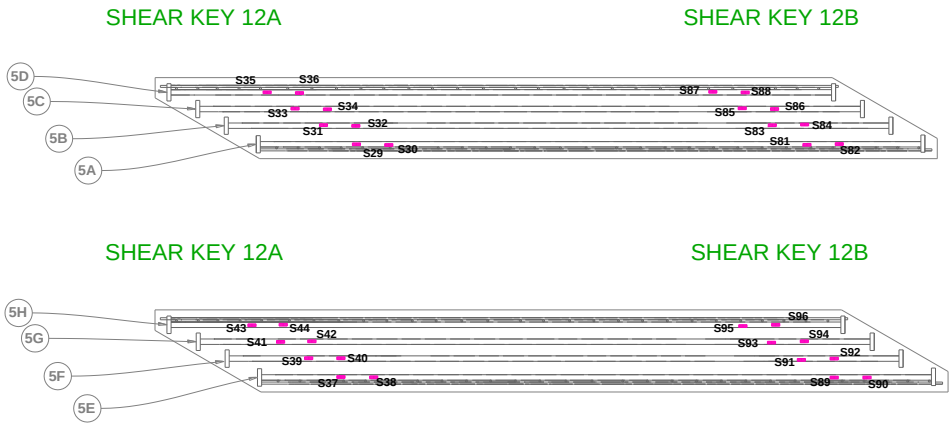

Figure 8.12 Sections 1-1 (top) and 2-2 (bottom) for Specimen 12
(see Figure 8.11 for the location of the sections)

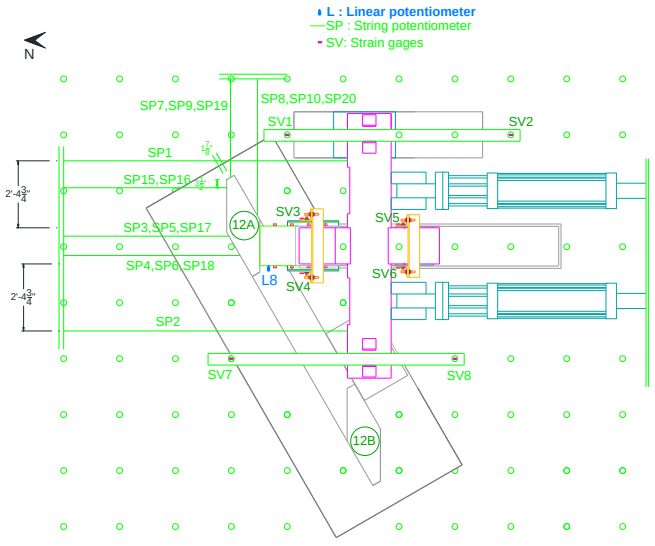

Figure 8.13 Plan view of external instrumentation for Specimen 12

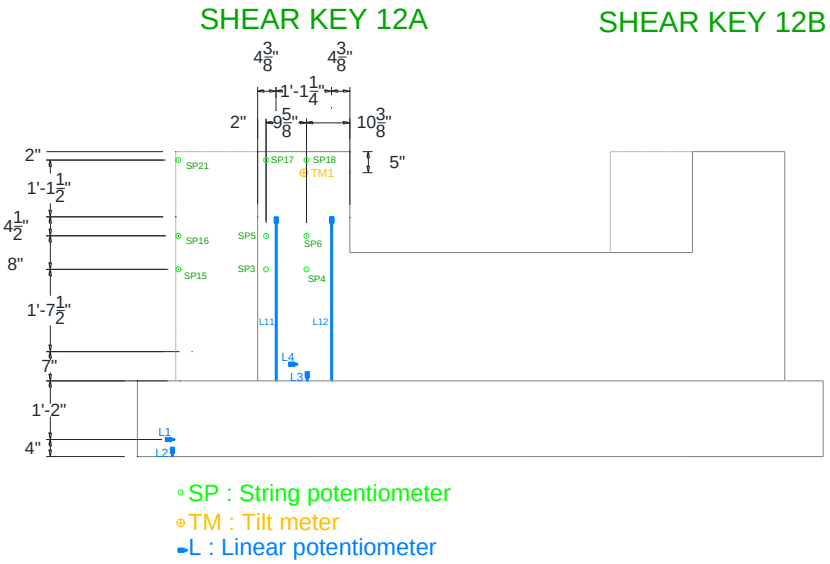

Figure 8.14 External instrumentation located on the northwest side of Specimen 12

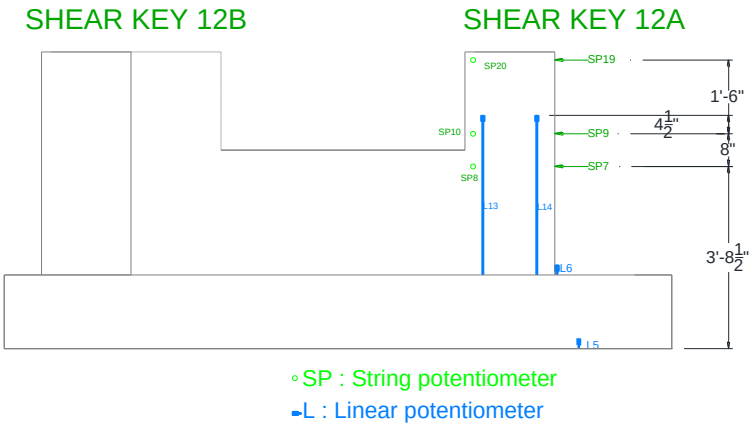

Figure 8.15 External instrumentation located on the southeast side of Specimen 12

8.5 Loading Protocols and Test Results

8.5.1 Shear Key 12A

The loading protocol for the shear key consisted of incremental loading, unloading and reloading with the target loads and displacements shown in Table 8.2. The

shear key was initially loaded in force control to 20 kips in increments of 5 kips and then in displacement control to 70 kips in increments of 10 kips. Then, it was loaded in displacement control up to failure, which occurred at 2.40 in. displacement. The displacement was based on the average of the readings of the displacement transducers SP5 and SP6, located on the northwest side of the shear key, as shown in Figure 8.13 and Figure 8.14. The specimen was unloaded 5 times at 20 kips and 50 kips load, and at displacements of 0.80 in, 1.40 in., and 2.00 in., respectively, to obtain the unloading stiffness.

Table 8.2 Loading protocol for shear key 12A

Step	Control	Target Load/Displacement
1-4	Load	20 kips with 5-kip increments
5-8	Displacement	70 kips with 10-kip increments
9-19	Displacement	2.40 in. with 0.20-in. increments

The first cracks were observed at a horizontal load of 50 kips. On the southeast side of the shear key, a crack initiated at the toe of the shear key and propagated horizontally across the interface between the shear key and the stem wall. Another horizontal crack formed 10 in. lower than the first, as shown in Figure 8.16. The maximum crack width was measured to be 1.3-1.4 mm in the region closest to the location of load application. On the northwest side of the shear key, three diagonal cracks formed. One was in the stem wall and the other two started from the shear key and continued into the stem wall. One of the cracks was connected to the top horizontal crack on the southeast side of the shear key. Due to the presence of the loading beam, visibility was limited in that region. The cracks had almost the same inclination and propagated

towards the toe of the stem wall. These cracks are shown in Figure 8.17. At a horizontal load of 70 kips, the existing horizontal cracks on the southeast side had propagated towards the northwest side and the top crack was inclined towards the toe of the stem wall on the northwest side. On the northwest side, an additional diagonal crack formed on the stem wall 11 in. away from the shear key and the existing cracks continued to propagate with their original inclination, as shown in Figure 8.18.

The shear key reached a maximum horizontal force of 72 kips at a displacement of 0.46 in. This load was maintained until a horizontal displacement of about 1.20 in. was reached. At this displacement, the shear plane was well defined by the top horizontal crack on the southeast side that propagated diagonally to the northwest side, which is shown in Figure 8.16. The cracks defining the shear plane on the two sides of the shear key are shown in Figure 8.19. The shear key rotated about the toe of the stem wall on the northwest side. After a displacement of 1.20 in. was reached, the resistance started to drop gradually to 36 kips. At that load, a vertical dowel bar fractured. The bar was located on the southeast side and was close to the location of the load application. The bars of the south east side were in tension, as the shear key rotated about the toe of the northwest side of the shear key. At 2.40 in. displacement, the test was stopped. Towards the end of the test and when concrete spalling had occurred, bar buckling was also observed on the northwest side of the shear key. At the end of the test, the shear key was removed and the shear plane surface is shown in Figure 8.20.

Figure 8.16 First cracks observed on the southeast side of shear key 12A

Figure 8.17 First cracks observed on the northwest side of shear key 12A

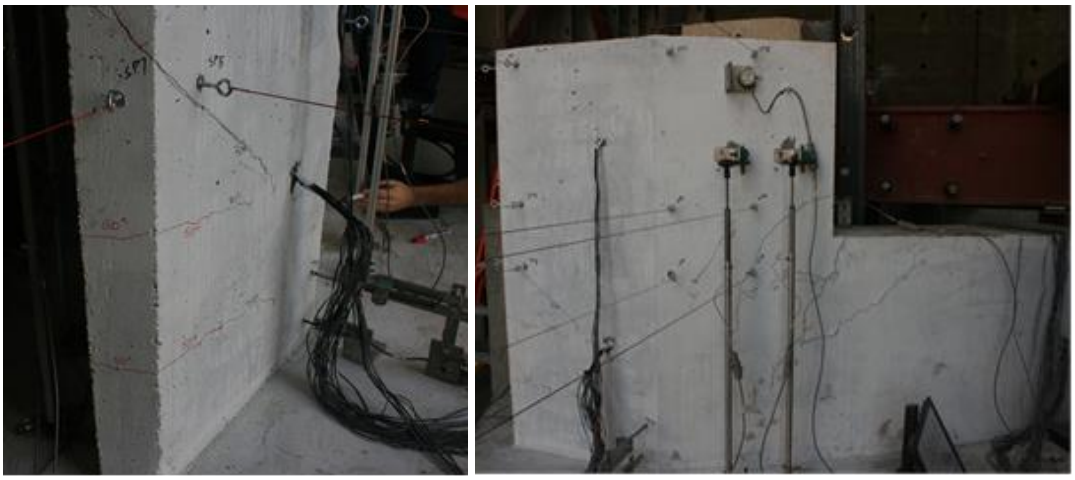

Figure 8.18 Cracks on the southeast side propagating to the northwest side (left) and cracks on the northwest side (right) of shear key 12A at a horizontal load of 70 kips

Figure 8.19 Cracks defining the shear plane on the southeast side (left) and northwest side (right) of shear key 12A

Figure 8.20 Shear plane from the northwest side (left) and from the southeast side (right) after removing shear key 12A

The horizontal load resistance is plotted against the horizontal displacement in Figure 8.21. The horizontal displacement is the averaged reading of the string potentiometers SP5 and SP6, whose locations are shown in Figure 8.13 and Figure 8.14.

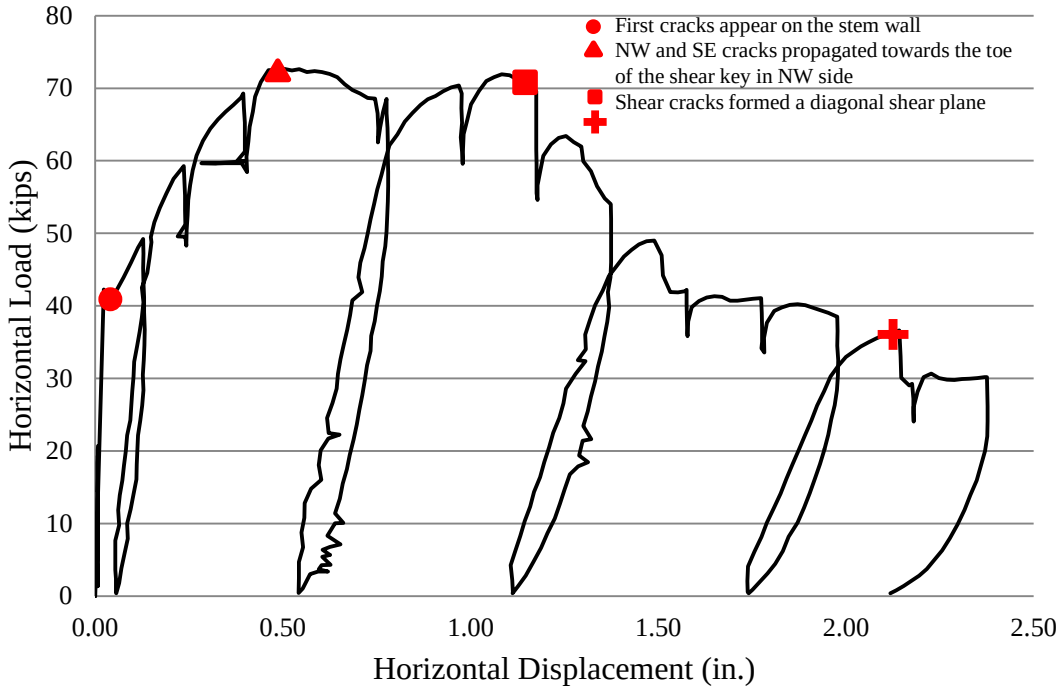

Figure 8.21 Horizontal load-vs.-horizontal displacement for shear key 12A

Vertical Load on Shear Key

The measurements from the strain gages of the bars in the hold-down beams and the steel angles indicate that the vertical force that was applied to the shear key at the peak horizontal load was negligible. The measured vertical load is plotted against the horizontal load in Figure 8.22. It can be seen that the vertical load increased early in the test and then decreased. Bending of the bars and steel angles of the hold-down frames observed in the test could have influenced the strain gage readings.

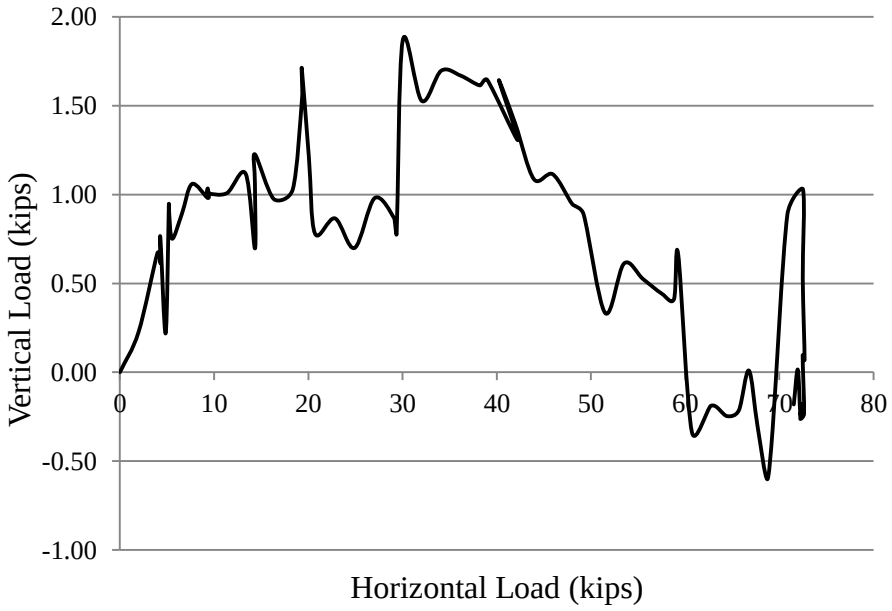

Figure 8.22 Measured vertical force on shear key 12A

Strains in Horizontal Shear Reinforcement of Stem Wall

Strains in the horizontal shear reinforcement of the stem wall were measured. Readings from strain gages registering the largest strains in each bar are plotted against the horizontal load in Figure 8.23 and Figure 8.24. The locations of these gages are

shown in Figure 8.12. All the stain-gage readings were within the elastic regime, apart from one bar (S38) which exceeded the yield strain.

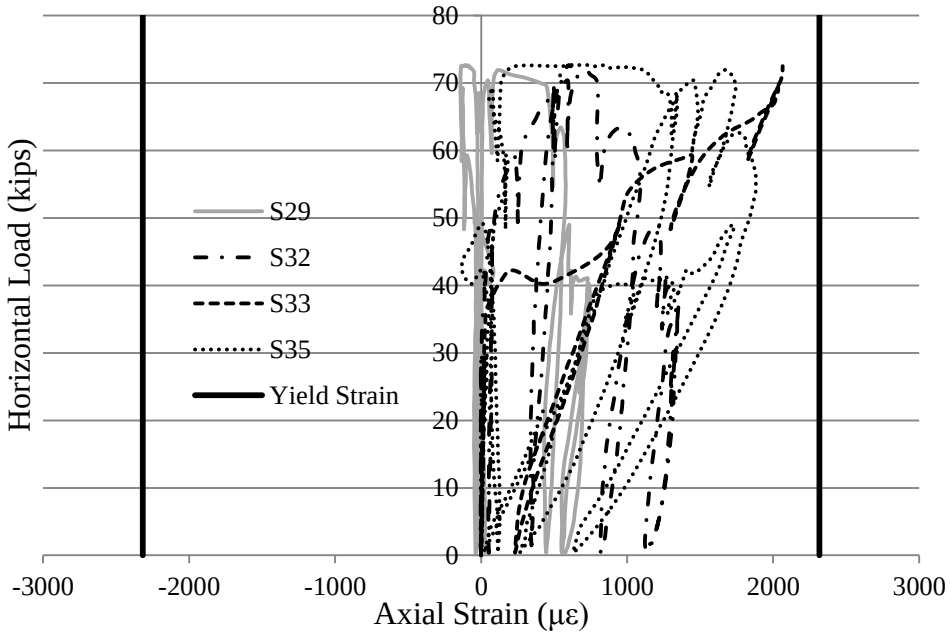

Figure 8.23 Horizontal load-vs.-axial strain in the horizontal shear reinforcement in the top row in the stem wall (near shear key 12A)

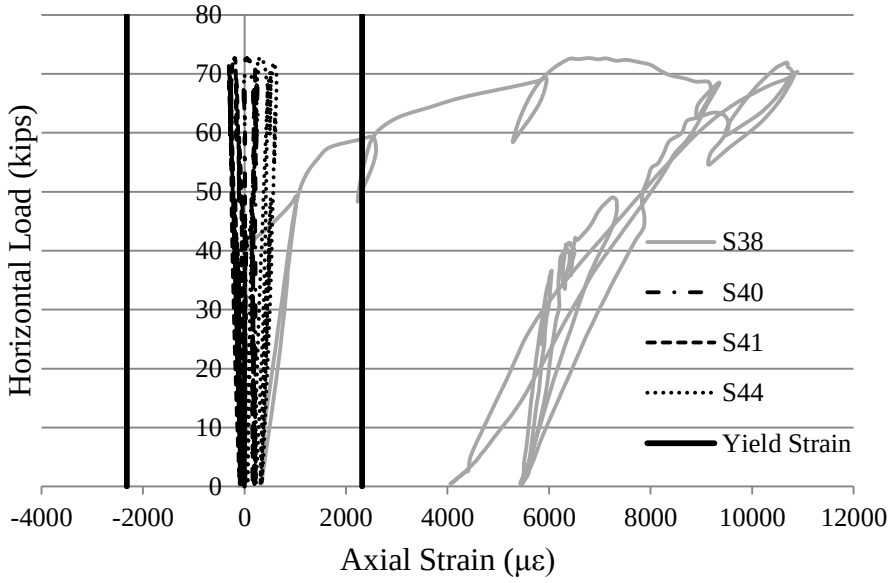

Figure 8.24 Horizontal load-vs.-axial strain in the horizontal shear reinforcement in the bottom row in the stem wall (near shear key 12A)

Strains in Vertical Dowel Bars

The strain readings of the strain gages in the vertical dowel bars are plotted in Figure 8.25 against the horizontal displacement. The locations of the strain gages are shown in Figure 8.10 and Figure 8.11. Only the strain gages that were close to the shear plane are plotted.

Based on Figure 8.25, it can be observed that most bars reached the yield strain very early in the test. Only strain gage S17 registered the yield strain at a displacement of about 1 in., after the peak load had been reached. This strain gage was located close to the toe of the north west side of the shear key, about which the shear key rotated. When the strain gages stopped recording, the bars had developed significant tensile forces.

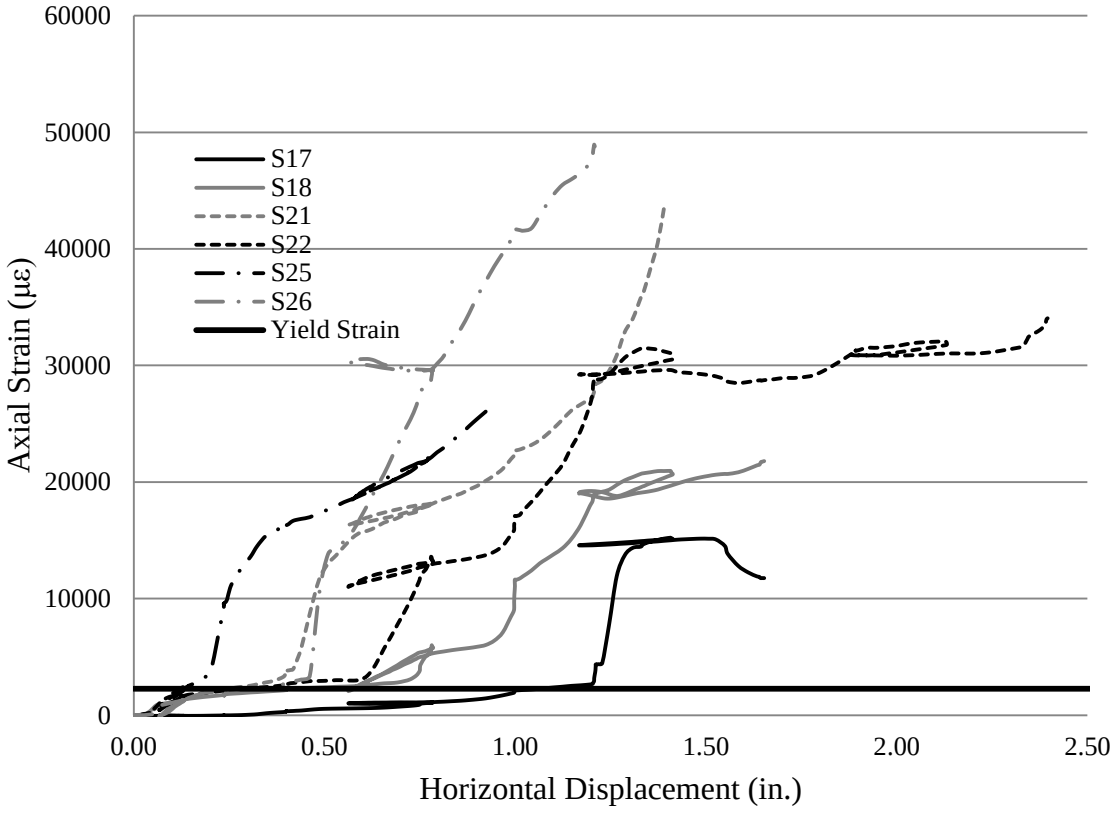

Figure 8.25 Strain-gage readings from vertical dowel bars in shear key 12A

Strains in Horizontal Side Bars

The strain readings of the strain gages in the horizontal side bars are plotted in Figure 8.26 against the horizontal displacement. The locations of the strain gages are shown in Figure 8.10 and Figure 8.11. It can be observed that strain-gage readings of S09, S05 and S12 have exceeded the yield strain in tension. S01 shows that the bar has yielded in compression, while the remaining readings are in the elastic regime.

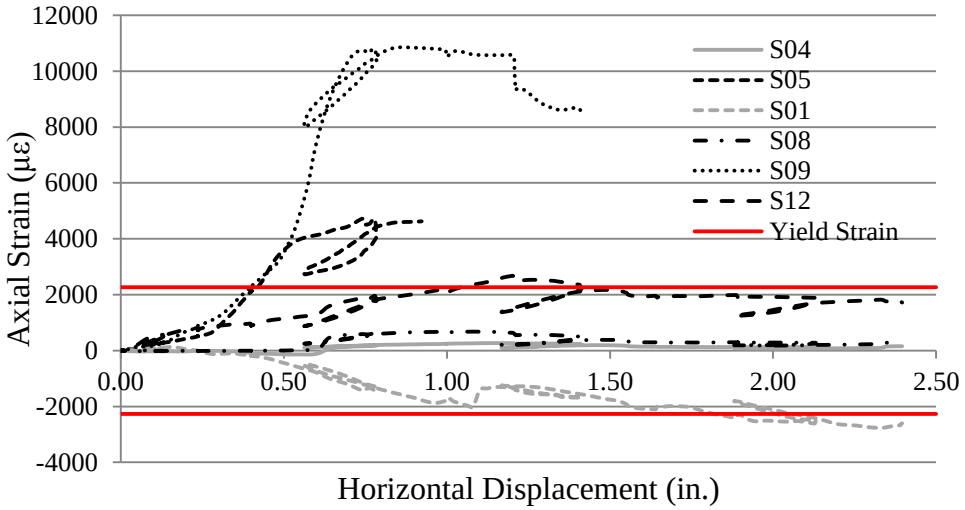

Figure 8.26 Strain-gage readings from horizontal side bars in shear key 12A

In-Plane Rotation of Shear Key

The in-plane rotation of the shear key was monitored with the tilt meter TM1, whose location is shown in Figure 8.14. The readings of the tilt meter are plotted in Figure 8.27 against the horizontal displacement. The rotation increased to 0.75 degree when the shear key reached a displacement of 1.50 in., and then it increased at a higher rate. At the end of the test, the shear key had rotated 2.50 degrees.

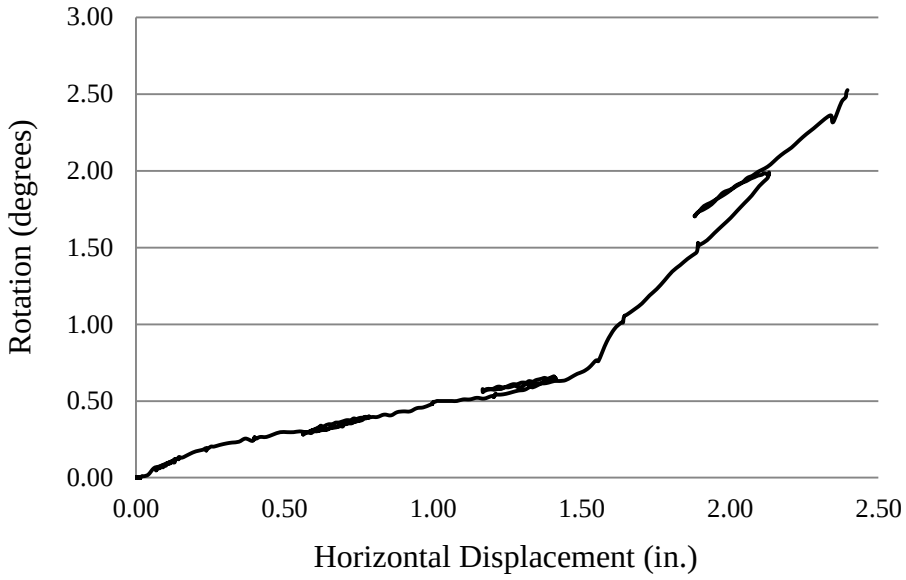

Figure 8.27 In-plane rotation of shear key 12A

Out-of-Plane Rotation of Shear Key

The vertical displacements of the northwest and southeast sides of the shear key were monitored by the displacement transducers L11 through L14, whose locations are shown in Figure 8.10 and Figure 8.11. Transducers L11 and L12 were on the northwest side of the shear key, while L12 and L13 were on the southeast side. Readings from these transducers show a significant out-of-plane rotation of the shear key, which is also observed in Figure 8.19. This is of course expected for shear keys in a skewed bridge. The averaged readings of L11 and L12, and of L13 and L14 are plotted against the horizontal displacement of the shear key in Figure 8.28.

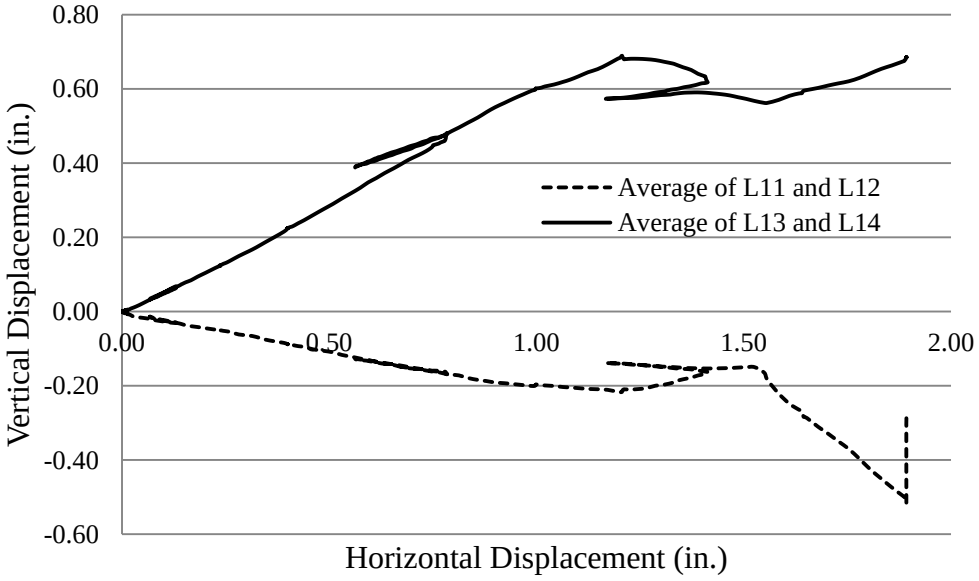

Figure 8.28 Out-of-plane rotation of shear key 12A

Displacement of the Shear Key in the East-West Direction

The horizontal displacement in the east-west direction was monitored with the displacement transducers SP7 through SP10, whose locations are shown in Figure 8.13 and Figure 8.15. The readings of these transducers are plotted in Figure 8.29 against the horizontal displacement of the shear key in the north-south direction, obtained from the averaged readings of the displacement transducers SP5 and SP6. The readings show that SP9 and SP10 recorded significant displacement in the east-west direction, while SP7 and SP8 did not. This is attributed to the fact that SP7 and SP8 were located in the part of the stem wall located below the shear plane, which did not experience significant deformations.

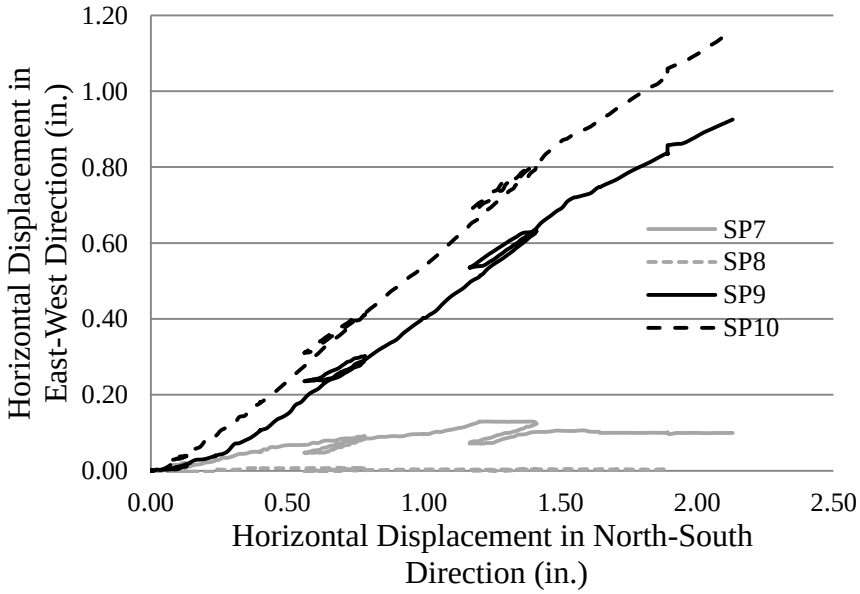

Figure 8.29 Displacement in the east-west direction of shear key 12A

8.5.2 Shear Key 12B

After testing shear key 12A, the specimen was rotated 180 degrees with respect to the stem wall axis so that shear key 12B was tested in the same orientation and position as shear key 12A. The loading protocol for the shear key consisted of incremental loading, unloading and reloading with the target loads and displacements shown in Table 8.3. The shear key was initially loaded in force control to 40 kips in increments of 5 kips and then in displacement control to 55 kips in increments of 5 kips. Then, it was loaded in displacement control up to failure, which occurred at 3.20 in. displacement. The displacement was based on the average of the readings of the displacement transducers SP5 and SP6, located on the northwest side of the shear key, as shown in Figure 8.13 and Figure 8.14. The specimen was unloaded 6 times at 20 kips, 30 kips, 40 kips and 50 kips

load, and at displacements of 0.60 in and 1.40 in., respectively, to obtain the unloading stiffness.

Table 8.3 Loading protocol for shear key 12B

Step	Control	Target Load/Displacement
1-8	Load	40 kips with 5-kip increments
9-11	Displacement	55 kips with 5-kip increments
12-26	Displacement	3.20 in. with 0.20 in. increments

The first cracks were observed at a horizontal load of 35 kips. On the southeast side of the shear key, a horizontal crack initiated at the toe of the shear key and propagated upwards to the lower part of the shear key. Another almost horizontal crack formed below the first, as shown in Figure 8.30. On the northwest side, two diagonal cracks started to form from the shear key toe and propagated diagonally into the stem wall. One of the cracks was connected to the top horizontal crack on the southeast side. Due to the presence of the loading beam, visibility was limited in that region. The cracks had almost the same inclination and propagated towards the toe of the stem wall. These cracks are shown in Figure 8.31. At a horizontal load of about 88 kips, the existing cracks of the southeast side had propagated towards the northwest side and they were inclined towards the toe of the stem wall on the northwest side, as shown in Figure 8.32.

The shear key reached a maximum horizontal load of 88 kips at 0.6 in. displacement. At that load, the shear plane was well defined by the top horizontal crack on the southeast side that propagated diagonally to the northwest side, as shown in Figure 8.30. The cracks defining the shear plane on the two sides of the shear key are shown in Figure 8.33. The shear key rotated about the toe of the stem wall on the northwest side. After the maximum horizontal load was reached, the resistance started to drop gradually

to 40 kips. At 3.20 in. displacement, the test was stopped. Towards the end of the test and when concrete spalling had occurred, bar buckling was also observed on the northwest side of the shear key. At the end of the test, the shear key was removed and the shear plane surface is shown in Figure 8.34.

Figure 8.30 First cracks observed on the southeast side of shear key 12B

Figure 8.31 First cracks observed on the northwest side of shear key 12B

Figure 8.32 Cracks on the southeast side propagating to the northwest side (left) and cracks on the northwest side of shear key 12B at a horizontal load of 88 kips

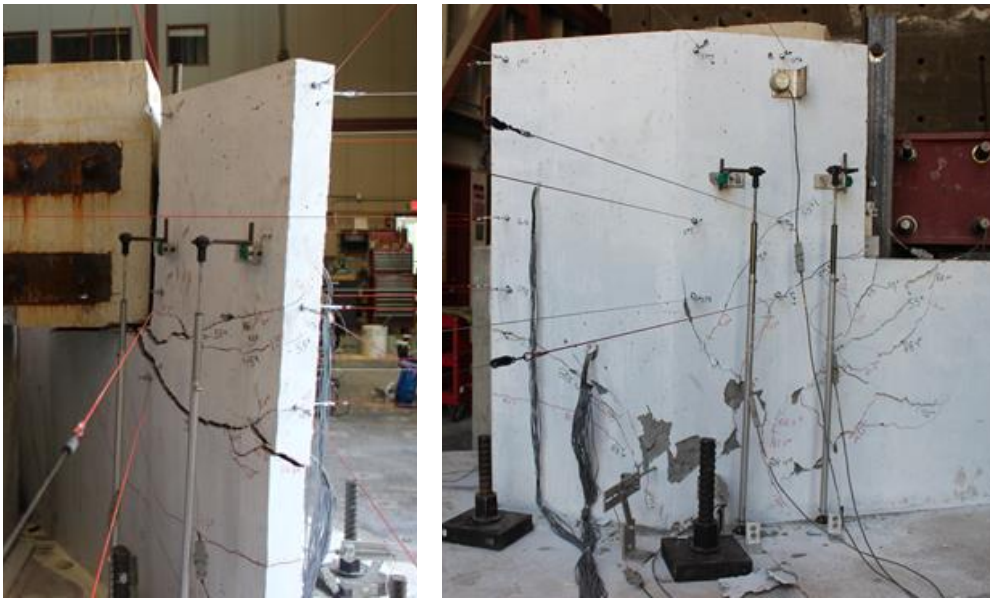

a) b)

Figure 8.33 Cracks defining the shear plane of shear key 12B: a) on the southeast side; b) on the northwest side

Figure 8.34 Shear plane from the southeast side (left) and from the northwest side (right) after removing shear key 12B

The horizontal load resistance is plotted against the horizontal displacement in Figure 8.35. The horizontal displacement is the averaged reading of the string potentiometers SP5 and SP6, whose locations are shown in Figure 8.13 and Figure 8.14.

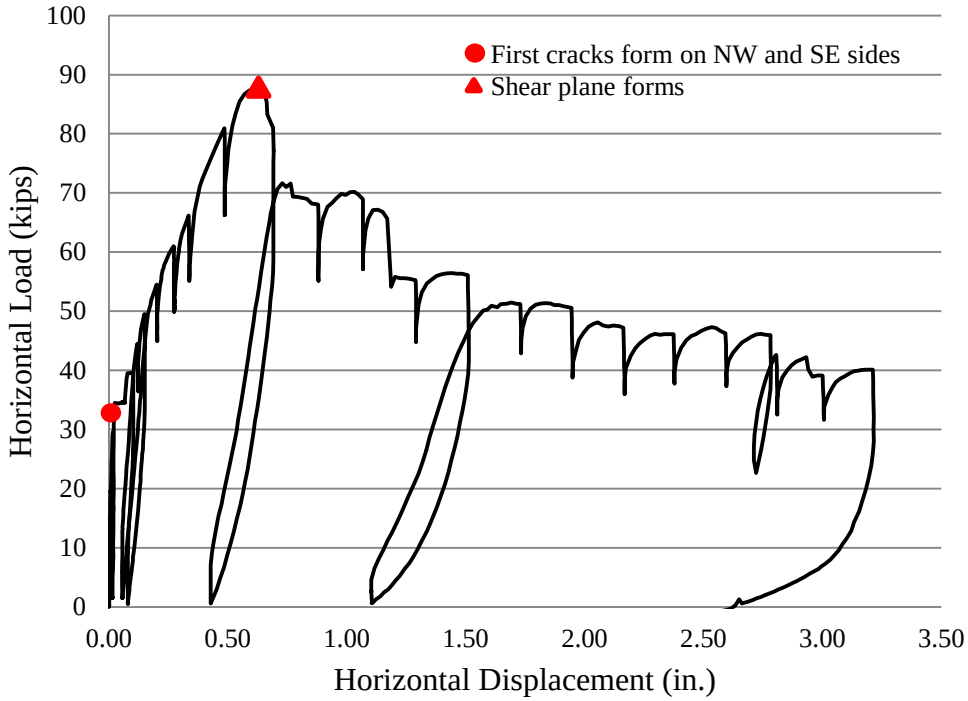

Figure 8.35 Horizontal load-vs.-horizontal displacement for shear key 12B

Vertical Load on Shear Key

The measurements from the strain gages on the bars in the hold-down beams and the steel angles indicated that the vertical force that was applied to the shear key at the peak horizontal load was negligible.

Strains in Horizontal Shear Reinforcement of Stem Wall

Readings from strain gages in the horizontal shear reinforcement of the stem wall registering the largest strains in each bar are plotted against the horizontal load in Figure 8.36 and Figure 8.37. The locations of these gages are shown in Figure 8.12. For the top row of bars, two of the strain gages (S84 and S87) registered strains higher than the yield strength, while the rest were in the elastic regime. The strain-gage readings from the bottom row of bars show that one bar developed a high tensile force (reading S91) and another bar (reading S93) reached the yield strength. Two of the bars, one in the top and one in the bottom row, registered compressive strains.

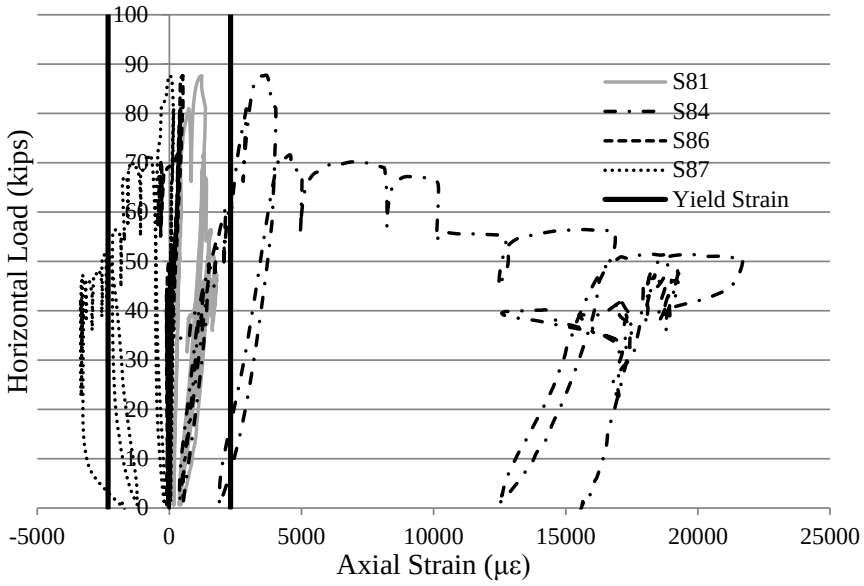

Figure 8.36 Horizontal load-vs.-axial strain in the horizontal shear reinforcement in the top row in the stem wall (near shear key 12B)

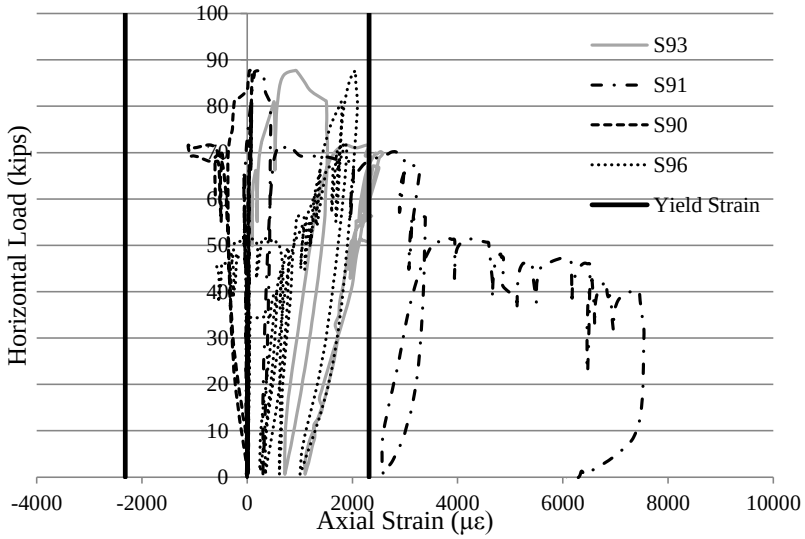

Figure 8.37 Horizontal load-vs.-axial strain in the horizontal shear reinforcement in the bottom row in the stem wall (near shear key 12B)

Strains in Vertical Dowel Bars

The strain readings of the strain gages in the vertical dowel bars are plotted in Figure 8.38 against the horizontal displacement. The locations of the strain gages are

shown in Figure 8.10 and Figure 8.11. Only the strain gages that were close to the sliding plane are plotted. However, the lower strain gages in the vertical dowel bars were still a lot higher than the crack on the south east side of the specimen as shown in Figure 8.33. The readings show that only two bars developed high tensile strains (S77 and S78), at location close to the main diagonal crack of the stem wall on the northwest side of the shear key.

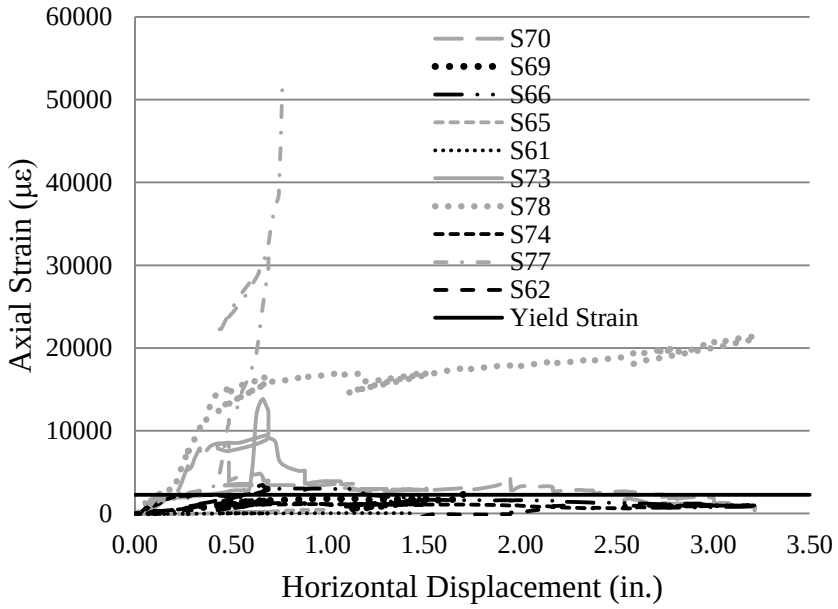

Figure 8.38 Strain-gage readings from dowel bars in shear key 12B

Strains in Horizontal Side Bars

The readings of the strain gages in the horizontal side bars are plotted in Figure 8.40 against the horizontal displacement. The locations of the strain gages are shown in Figure 8.10 and Figure 8.11. It can be observed that strain-gage readings of S52 and S54, located at the second and first horizontal side bars measured from the top, exceeded the

yield strain in tension. Strain gage S48 shows that the bar yielded in compression, while readings from the remaining gages are in the elastic regime.

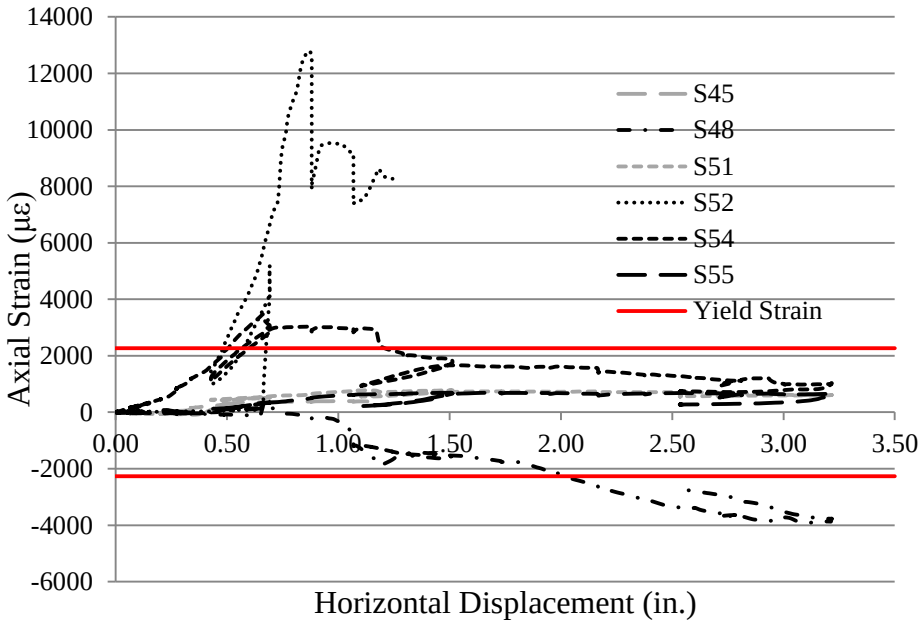

Figure 8.39 Strain-gage readings from horizontal side bars in shear key 12B

In-Plane Rotation of Shear Key

The in-plane rotation of the shear key was monitored with the tilt meter TM1, whose location is shown in Figure 8.14. The readings of the tilt meter are plotted in Figure 8.40 against the horizontal displacement. The rotation increased to 0.20 degrees when the displacement reached 0.60 in. After that point, the shear key stopped to rotate up to the end of the test.

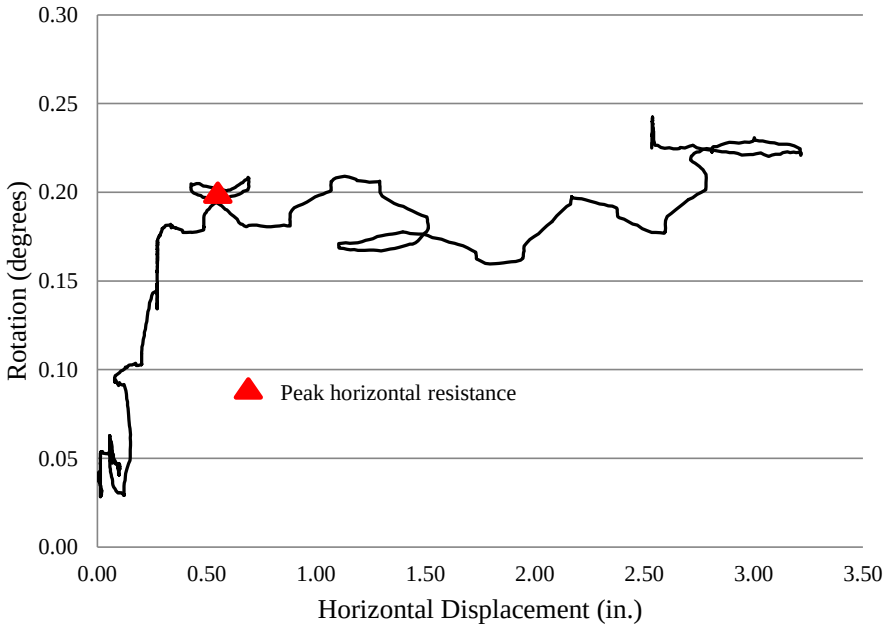

Figure 8.40 In-plane rotation of shear key 12B

Out-of-Plane Rotation of Shear Key

The vertical displacements of the northwest and southeast sides of the shear key were monitored by the displacement transducers L11 through L14, whose locations are shown in Figure 8.10 and Figure 8.11. Transducers L11 and L12 were on the northwest side of the shear key, while L12 and l13 were on the southeast side. Readings from these transducers show a significant out-of-plane rotation of the shear key, which is also observed in Figure 8.33. The averaged readings of L11 and L12, and of L13 and L14 are plotted against the horizontal displacement of the shear key in Figure 8.41.

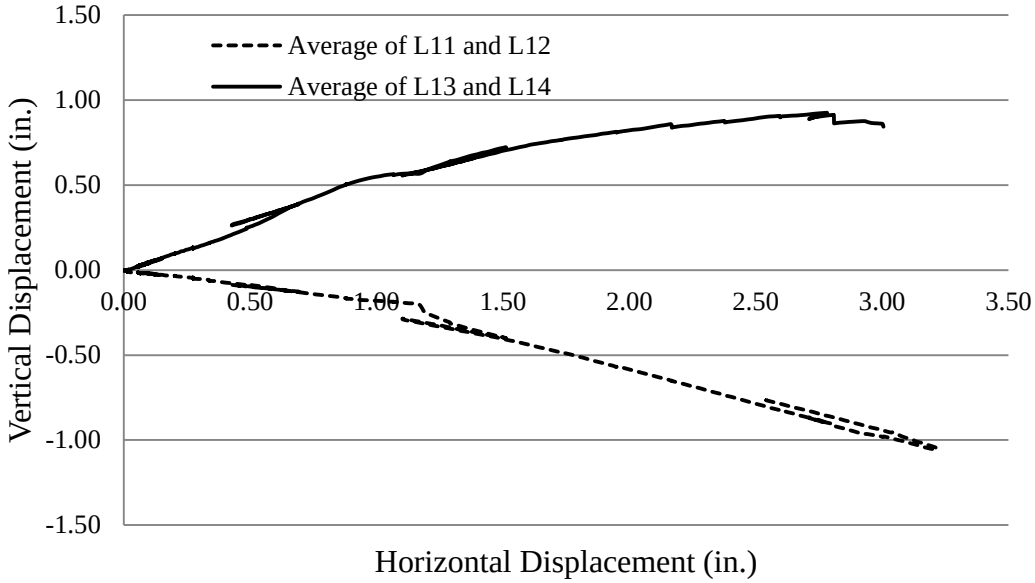

Figure 8.41 Out-of-plane rotation of shear key 12B

Displacement of the Shear Key in the East-West Direction

The horizontal displacement in the east-west direction was monitored with the displacement transducers SP7 through SP10, whose locations are shown in Figure 8.13. The readings of these transducers are plotted in Figure 8.42 against the horizontal displacement of the shear key in the north-south direction, obtained from the averaged readings of the displacement transducers SP5 and SP6. The readings show that a significant displacement occurred in the east-west direction. Displacement transducer SP8 did not provide reliable readings and is not considered in Figure 8.42.

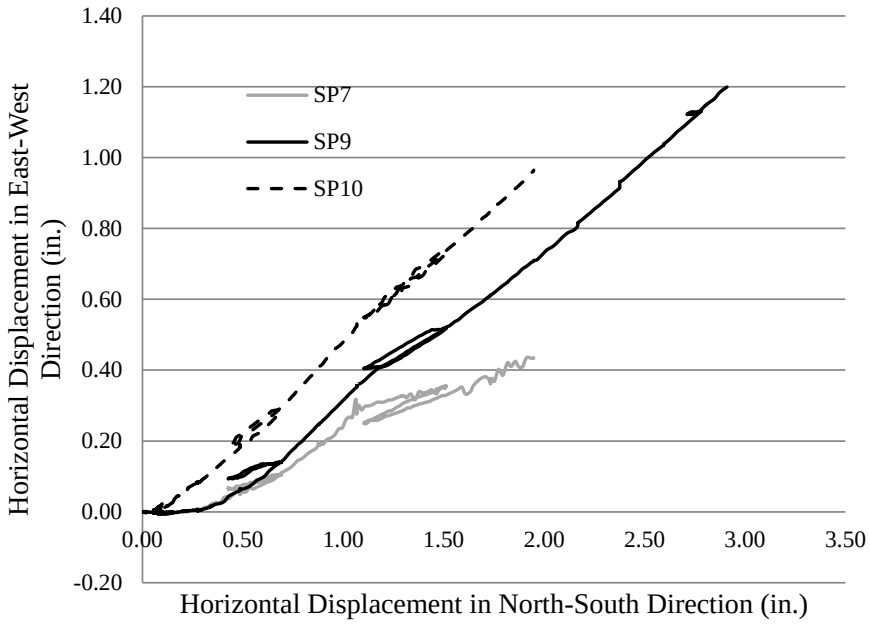

Figure 8.42 Displacement in the east-west direction of shear key 12B

8.6 Summary and Conclusions

The experimental results from a skewed abutment wall specimen with monolithic shear keys are presented in this chapter. The shear keys had the same amount of vertical dowel bars connecting the shear keys to the stem wall and the same amount of horizontal shear reinforcement in the stem wall as the non-skewed shear keys 8B and 9B, discussed in Chapter 7.

Initially, multiple horizontal flexural cracks formed on one side of the stem wall. The cracks continued to propagate diagonally to the other side of the shear keys towards the toe of the stem wall. Thus, the shear keys experienced combined in- and out-of-plane rotations. Some vertical dowel bars developed high tensile strains, and one of the bars fractured in each shear key. Due to the diagonal cracking and the in-plane rotation, some

of the horizontal side reinforcing bars stretched and reached the yield strength. The shear keys continued to rotate about the toe of the stem wall, which experienced compressive forces. When the concrete of the toe of the stem wall was damaged, the load resistance started to drop.

In Table 8.4, the load resistances from the non-skewed and the skewed shear keys are compared. It can be seen that the skewed shear keys had considerably lower load capacities. In addition, the damage observed in the skewed shear keys is more severe, as compared to non-skewed shear keys. This can be attributed to the different load resistance and failure mechanisms.

Table 8.4 Comparison of the measured shear resistances of non-skewed and skewed shear keys

Shear Key	Amount of Vertical Dowel Bars (in^2)	Angle of skew (degrees)	Measured Peak Resistance (kips)
8B	0.66	0	286
12A	0.66	60	72
9B	1.10	0	313
12B	1.10	60	87

8.7 Acknowledgement of Publication

Part of this chapter is a reprint of the material that will appear in a technical report which will be submitted to the California Department of Transportation in 2016, Kottari, A., P. B. Shing, J. I. Restrepo, under the title "Design and Capacity Assessment of External Shear Keys in Bridge Abutments". The dissertation author will be the primary investigator and author of this report.

CHAPTER 9

INTERFACE MODELS FOR THREE-DIMENSIONAL ANALYSIS OF RC STRUCTURES

9.1 Introduction

This chapter presents two interface models developed in this study for the analysis of three-dimensional concrete structures. One is a cohesive crack model that has been implemented in a planar interface element. The second is an interface model for simulating the dowel action and bond-slip behavior in three-dimensional reinforced concrete (RC) structures. It is an extension of the model presented in Chapter 4 developed for two-dimensional problems. These models have been implemented in the finite element program FEAP (Taylor, 2014).

9.2 Proposed Cohesive Crack Model for Three-Dimensional Analysis

Finite element models based on the smeared-crack continuum concept can account for the effect of cracking, while maintaining the continuity of the displacement field. While the smeared-crack approach is computationally efficient and suitable for capturing the effect of diffuse cracks (Bazant and Oh, 1983) in concrete, it has several issues, such as the spurious mesh-size sensitivity of numerical results for softening materials (Bazant, 1976), and stress locking (Rots and Blaauwendraad, 1989).

To avoid inaccuracies associated with stress locking, discrete cohesive crack interface elements can be used. Carol et al. (1997) have proposed a cohesive crack line interface model using a hyperbolic failure surface to capture mixed-mode fracture. The failure criterion involves three parameters, namely, the tensile strength, the cohesive shear strength and the frictional coefficient of the material. Lotfi and Shing (1994) have proposed a model based on the same failure criterion but with different softening laws. The mixed-mode fracture energy release law adopted in their model is based on the work of Stankowski et al. (1993). They have proposed additional softening laws that govern the shape of the failure surface as functions of frictional work. Mehrabi and Shing (1997) have improved the model of Lotfi and Shing (1994) to account for the reversible shear dilatation associated with joint roughness. Koutromanos and Shing (2011) have further refined this model to simulate the reversible shear dilatation and crack closing and reopening in a more realistic manner. All these models are formulated for two-dimensional problems.

In this section, a cohesive crack model that has been developed and implemented in a planar interface element for analyzing the fracture behavior of three-dimensional concrete structures is presented. The model is based on the formulation of Koutromanos and Shing (2011), which has been developed for two-dimensional analysis.

9.2.1 Element Formulation

The model is implemented in a zero-thickness planar interface element. Figure 9.1 shows the global and local coordinate systems, (x,y,z) and (t, s, n), for the element

together with the top and bottom surfaces of the interface. For the convenience of presentation, the two coordinate systems are shown to coincide with one another, which is normally not the case. Nodes 1 - 4 define the bottom surface of the interface, while nodes 5 - 8 define the top surface. Figure 9.2 shows the Gauss integration points in the element and the natural coordinates (η, ξ) .

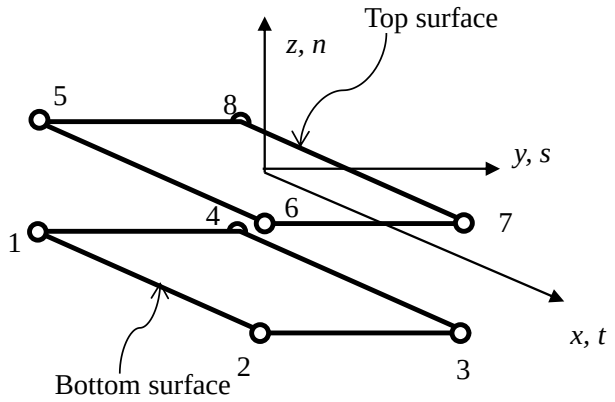

Figure 9.1 Global coordinate system for the 8-node zero-thickness interface element

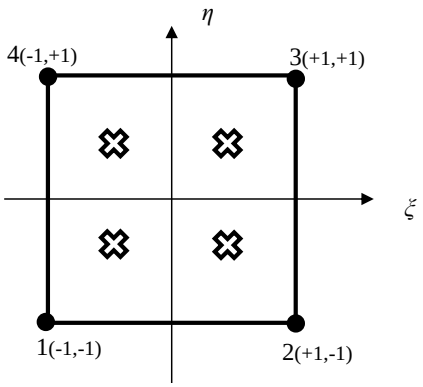

Figure 9.2 Gauss integration points in the natural coordinate space

Same shape functions are used to describe the spatial coordinates and displacement fields of the element. Thus, the global spatial coordinates of the element, $\boldsymbol{x} = \{x \quad y \quad z\}^T$, are related to its natural coordinates (η, ξ) as follows:

$$\boldsymbol{x} = \boldsymbol{N}\boldsymbol{x}_l \tag{9.1}$$

in which $\boldsymbol{x}_l$ is a vector containing the global coordinates of the nodes of one surface of the interface, i.e.,

$$\boldsymbol{x_l} = \left\{ x_{1/5} \quad x_{2/6} \quad x_{3/7} \quad x_{4/8} \quad y_{1/5} \quad . \quad . \quad z_{4/8} \right\}^T \tag{9.2}$$

and matrix $\boldsymbol{N}(\xi,\eta)$ is defined as:

$$\boldsymbol{N}(\xi,\eta) = \begin{bmatrix} \left[\boldsymbol{N_s}(\xi,\eta)\right] & & \\ & \left[\boldsymbol{N_s}(\xi,\eta)\right] & \\ & & \left[\boldsymbol{N_s}(\xi,\eta)\right] \end{bmatrix} \tag{9.3}$$

with $\boldsymbol{N_s}(\xi,\eta) = \left[N_1(\xi,\eta) \quad N_2(\xi,\eta) \quad N_3(\xi,\eta) \quad N_4(\xi,\eta) \right]$ containing the linear shape functions defined in the natural coordinates ξ and η as follows:

$$\begin{aligned} N_1(\xi,\eta) &= \frac{1}{4}\cdot(1-\xi)\cdot(1-\eta) \\ N_2(\xi,\eta) &= \frac{1}{4}\cdot(1+\xi)\cdot(1-\eta) \\ N_3(\xi,\eta) &= \frac{1}{4}\cdot(1+\xi)\cdot(1+\eta) \\ N_4(\xi,\eta) &= \frac{1}{4}\cdot(1-\xi)\cdot(1+\eta) \end{aligned} \tag{9.4}$$

Each node *i* has three degrees of freedom, i.e., displacements in the *t, s* and *n* directions, denoted by u_i, v_i and w_i, respectively. The nodal displacements can be collected in the vector ***u***:

$$\boldsymbol{u} = \left[u_1 \quad v_1 \quad w_1 \quad u_2 \quad . \quad . \quad w_8 \right]^T \tag{9.5}$$

The displacement field of the top surface is represented by u_t, v_t, and w_t, while that of the bottom surface by u_b, v_b, and w_b. These displacement fields are expressed in terms of the nodal displacements by interpolation as follows:

$$
\begin{aligned}
u_b &= N_1(\xi,\eta)\cdot u_1 + N_2(\xi,\eta)\cdot u_2 + N_3(\xi,\eta)\cdot u_3 + N_4(\xi,\eta)\cdot u_4 \\
u_t &= N_1(\xi,\eta)\cdot u_5 + N_2(\xi,\eta)\cdot u_6 + N_3(\xi,\eta)\cdot u_7 + N_4(\xi,\eta)\cdot u_8 \\
v_b &= N_1(\xi,\eta)\cdot v_1 + N_2(\xi,\eta)\cdot v_2 + N_3(\xi,\eta)\cdot v_3 + N_4(\xi,\eta)\cdot v_4 \\
v_t &= N_1(\xi,\eta)\cdot v_5 + N_2(\xi,\eta)\cdot v_6 + N_3(\xi,\eta)\cdot v_7 + N_4(\xi,\eta)\cdot v_8 \\
w_b &= N_1(\xi,\eta)\cdot w_1 + N_2(\xi,\eta)\cdot w_2 + N_3(\xi,\eta)\cdot w_3 + N_4(\xi,\eta)\cdot w_4 \\
w_t &= N_1(\xi,\eta)\cdot w_5 + N_2(\xi,\eta)\cdot w_6 + N_3(\xi,\eta)\cdot w_7 + N_4(\xi,\eta)\cdot w_8
\end{aligned}
\tag{9.6}
$$

Equation (9.6) can be written as:

$$\bar{\boldsymbol{u}} = \boldsymbol{M}\boldsymbol{u} \tag{9.7}$$

where

$$\bar{\boldsymbol{u}} = \begin{Bmatrix} u_b & u_t & v_b & v_t & w_b & w_t \end{Bmatrix}^T \tag{9.8}$$

and $\boldsymbol{M}$ is a 6 x 24 matrix containing the shape functions.

The shear stresses and the normal stress in the interface are calculated based on the relative shear displacements, d_t and d_s, and the relative normal displacement, d_n, which are defined as:

$$\boldsymbol{d} = \boldsymbol{L}\bar{\boldsymbol{u}} \tag{9.9}$$

in which

$$\boldsymbol{d} = \begin{bmatrix} d_t & d_s & d_n \end{bmatrix}^T \tag{9.10}$$

and

$$\boldsymbol{L} = \begin{bmatrix} -1 & 1 & 0 & 0 & 0 & 0 \\ 0 & 0 & -1 & 1 & 0 & 0 \\ 0 & 0 & 0 & 0 & -1 & 1 \end{bmatrix} \tag{9.11}$$

By combining Eqs. (9.7) and (9.9), the relative displacements can be expressed in terms of the nodal displacements as:

$$\boldsymbol{d} = \boldsymbol{L}\boldsymbol{M}\boldsymbol{u} = \boldsymbol{B}\boldsymbol{u} \tag{9.12}$$

in which $\boldsymbol{B} = \boldsymbol{LM}$. The relative displacements are used to calculate the normal and shear stresses shown in Figure 9.3. The normal stress is denoted by σ and the shear stresses by τ_s and τ_t. They are collected in the stress vector $\boldsymbol{\sigma} = \{\sigma \quad \tau_t \quad \tau_s\}^T$.

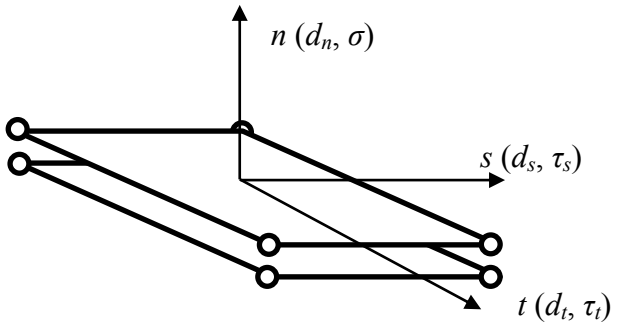

Figure 9.3 Relative displacement and stress in each direction

9.2.2 Constitutive Model

The proposed constitutive model is able to simulate mixed-mode fracture, including crack opening, shear sliding, irreversible normal joint compaction due to damage, and reversible joint dilatation due to joint roughness. To capture the aforementioned mechanisms, the relative displacements in the interface are decomposed into three parts, as proposed by Mehrabi and Shing (1997):

$$\boldsymbol{d} = \{d_n \quad d_t \quad d_s\}^T = \boldsymbol{d}^e + \boldsymbol{d}^p + \boldsymbol{d}^g \tag{9.13}$$

in which $\boldsymbol{d}^e = \{d_n^e \quad d_t^e \quad d_s^e\}^T$ is the elastic part, $\boldsymbol{d}^p = \{d_n^p \quad d_t^p \quad d_s^p\}^T$ is the plastic part, and $\boldsymbol{d}^g = \{d_n^g \quad 0 \quad 0\}^T$ is the geometric part, which consists of only a normal component to account for the reversible dilatation associated with surface roughness.

The normal and shear stresses are calculated from the interface relative displacements using the following constitutive relations proposed by Koutromanos and Shing (2011):

$$\sigma = -D_{nn} \cdot \langle d_{n1} - d_n \rangle + D_{nn} \cdot \langle d_n - d_{n2} \rangle \tag{9.14}$$

$$\tau_t = D_{tt} \cdot \left(d_t - d_t^p \right) \tag{9.15}$$

$$\tau_s = D_{ss} \cdot \left(d_s - d_s^p \right) \tag{9.16}$$

Parameters D_{nn}, D_{tt} and D_{ss} in Eqs. (9.14) through (9.16) are the elastic stiffness constants for the normal and shear displacements. It can be assumed that the stiffness constants D_{ss} and D_{tt}, corresponding to shear in directions *s* and *t*, have the same values. Equations (9.15) and (9.16) represent shear sliding with elastoplastic stress-displacement laws, while Eq. (9.14) describes cyclic crack opening and closing behavior as illustrated in Figure 9.4. The evolution of parameters d_{n1} and d_{n2} in Equation (9.14) is governed by the following expressions with the superposed dot representing the rate of change with respect to time. The value of parameter d_{n2} cannot smaller than d_{n1}.

$$\dot{d}_{n1} = -\langle -\dot{d}_n^p \rangle + \dot{d}_n^g \tag{9.17}$$

$$\dot{d}_{n2} = \dot{d}_n^p \tag{9.18}$$

a) b)

Figure 9.4 Cyclic crack opening-closing behavior of interface element in the normal direction: (a) loading and unloading; (b) reloading (from Koutromanos and Shing, 2011)

Plastic displacements occur when the stress state reaches a yield surface denoted by *F=0*. The yield surface adopted here is generated by the revolution of the hyperbolic yield function suggested by Lotfi and Shing (1994) about the σ axis to describe Mode-I and -II fractures:

$$F = \tau_s^2 + \tau_t^2 - \mu^2 \cdot (\sigma - s)^2 - 2 \cdot r \cdot (\sigma - s) = 0 \tag{9.18}$$

in which *s* is the tensile strength of the interface, *r* is the radius of curvature at the apex of the yield surface, and μ is the slope of the asymptotes of the hyperboloid, which is illustrated in Figure 9.5. The subscript *o* shown in the figure represents the initial values of the variables. These three variables are collected in the internal variable vector $\boldsymbol{q} = \{s \quad r \quad \mu\}^T$. For given values of *s* and μ, *r* can be used to specify cohesion, *c*, with the following equation:

$$c = \sqrt{\mu^2 \cdot s^2 + 2 \cdot r \cdot s} \tag{9.19}$$

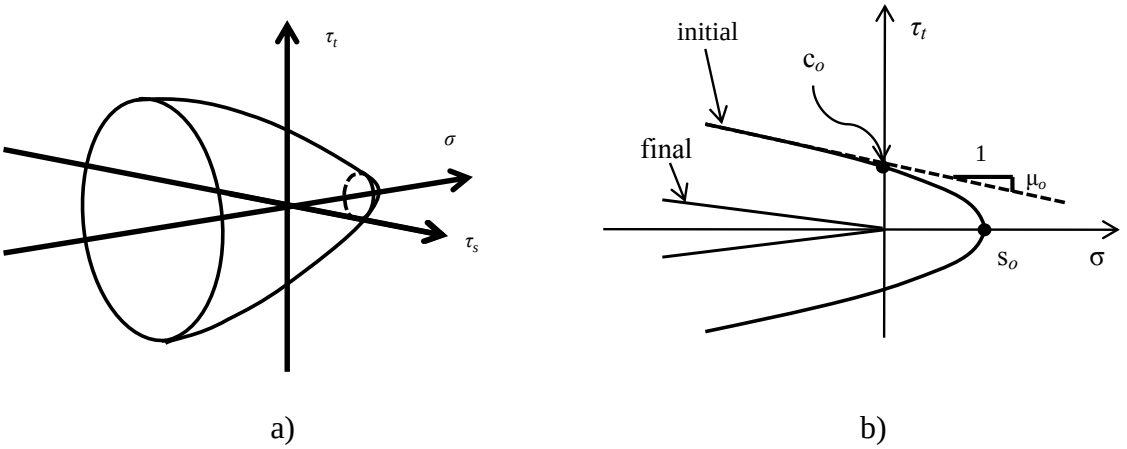

a) b)

Figure 9.5 Yield Surface: a) 3-D representation; b) initial and final yield surfaces projected on the σ-τ_t plane

Once the stress state reaches the yield surface, the rate of the plastic relative displacements is given by a flow rule as follows:

$$\dot{\boldsymbol{d}}^{\boldsymbol{p}} = \dot{\lambda}\boldsymbol{m} \tag{9.20}$$

in which $\dot{\lambda}$ is the plastic multiplier and vector $\boldsymbol{m}$ defines the direction of the plastic flow. The vector $\boldsymbol{m} = \{m_1 \quad m_2 \quad m_3\}^T$ is given by a plastic potential, Q, as follows:

$$\boldsymbol{m} = \frac{\partial Q}{\partial \boldsymbol{\sigma}} \tag{9.21}$$

or

$$m_1 = \frac{\partial Q}{\partial \sigma} = \sigma,\ m_2 = \frac{\partial Q}{\partial \tau_t} = \eta \cdot \tau_t,\ m_3 = \frac{\partial Q}{\partial \tau_s} = \eta \cdot \tau_s \tag{9.22}$$

Similar to the 2-D model of Koutromanos and Shing (2011), the following plastic potential is adopted when the elastic predictor stresses are in the compression regime.

$$Q = \frac{1}{2} \cdot \eta \cdot \tau_s^2 + \frac{1}{2} \cdot \eta \cdot \tau_t^2 + \sigma^2 \tag{9.23}$$

in which η is a parameter controlling plastic compaction due to damage. This is an extension of the plastic potential originally proposed by Mehrabi and Shing (1997) for a 2-D model.

When the elastic predictor stresses are in the tension regime, the vector ***m*** is calculated with the following equations, which are an extension of the expressions proposed by Koutromanos and Shing (2011):

$$m_1 = \frac{\sigma^{el} / D_{nn}}{\sqrt{\left(\frac{\sigma^{el}}{D_{nn}}\right)^2 + \left(\frac{\tau_t^{el}}{D_{tt}}\right)^2 + \left(\frac{\tau_s^{el}}{D_{ss}}\right)^2}}$$

$$m_2 = \frac{\tau_t^{el} / D_{tt}}{\sqrt{\left(\frac{\sigma^{el}}{D_{nn}}\right)^2 + \left(\frac{\tau_t^{el}}{D_{tt}}\right)^2 + \left(\frac{\tau_s^{el}}{D_{ss}}\right)^2}} \tag{9.24}$$

$$m_3 = \frac{\tau_s^{el} / D_{ss}}{\sqrt{\left(\frac{\sigma^{el}}{D_{nn}}\right)^2 + \left(\frac{\tau_t^{el}}{D_{tt}}\right)^2 + \left(\frac{\tau_s^{el}}{D_{ss}}\right)^2}}$$

in which σ^{el}, τ_t^{el} and τ_s^{el} are the elastic predictor stresses calculated in the stress update process. This flow rule provides a robust solution algorithm and is similar to that proposed by Cervenka (1994) and Puntel et al. (2006).

To describe the degradation of the cohesive resistance during inelastic displacements, the following softening law, proposed by Stankowski et al. (1993), has been adopted:

$$s = s_o \left(1 - \frac{\kappa_1}{G_f^I} - \frac{\kappa_2}{G_f^{II}}\right) \tag{9.25}$$

Parameter s_o in Eq. (9.25) is the tensile strength of the undamaged material, while κ_1 and κ_2 represent the plastic work associated with Mode-I and Mode-II fracture, respectively. Parameters G_f^I and G_f^{II} represent the total fracture energy release for the respective fracture modes. The plastic work κ_1 is calculated with the following rate equation:

$$\dot{\kappa}_1 = \langle \sigma \rangle \cdot \dot{d}_n^p \tag{9.26}$$

in which $\dot{d}_n^p$ is the rate of change of the plastic normal displacement, and $\langle \bullet \rangle$ are the Macaulay brackets. By extending the expression proposed by Lotfi and Shing (1994), the rate of the plastic work $\dot{\kappa}_2$ is defined as follows:

$$\dot{\kappa}_2 = \left(\tau_s - \tau_{r1} \cdot \text{sign}\left(\tau_s\right) \cdot \cos\gamma\right) \cdot \dot{d}_s^p + \left(\tau_t - \tau_{r1} \cdot \text{sign}\left(\tau_t\right) \cdot \sin\gamma\right) \cdot \dot{d}_t^p \tag{9.27}$$

in which τ_{r1} is the shear strength under a normal stress σ when the tensile strength has diminished to zero, i.e.,

$$\tau_{r1} = \sqrt{\mu^2 \cdot \sigma^2 + 2 \cdot r \cdot \sigma} \tag{9.28}$$

Parameter τ_{r1} is shown in Figure 9.6. The angle γ in Eq. (9.27) is used to calculate the projection of τ_{r1} on the τ_s and τ_t axes, and is determined by the following expression:

$$\gamma = \tan^{-1}\left(\tau_t^{el} / \tau_s^{el}\right) \tag{9.29}$$

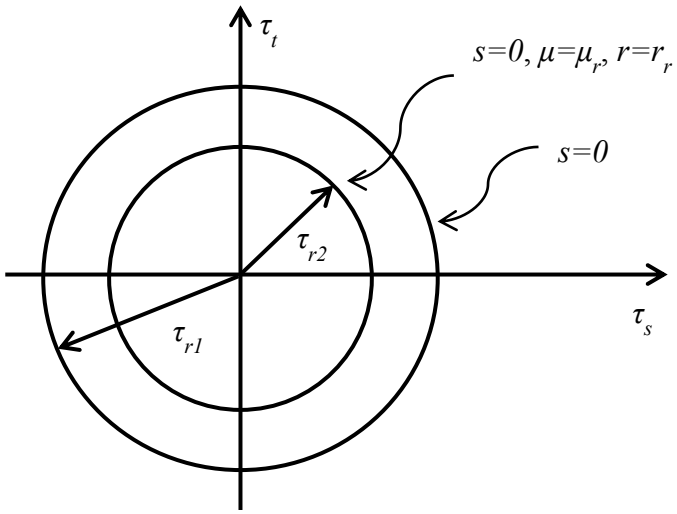

Figure 9.6 Shear strengths τ_{r1} and τ_{r2} for a given normal stress σ

The reduction in the roughness of the surface during the sliding process results in the gradual degradation of the frictional resistance. To capture this degradation, the following laws proposed by Lotfi and Shing (1994) have been adopted:

$$r = \left(r_o - r_r\right) \cdot e^{-\beta \cdot \kappa_3} + r_r \quad \text{and} \quad \mu = \left(\mu_o - \mu_r\right) \cdot e^{-\alpha \cdot \kappa_3} + \mu_r \tag{9.30}$$

in which κ_3 is the plastic work associated with the smoothening of the sliding surface, α and β govern the rate of change of μ and r with respect to the plastic work, and r_o, μ_o, r_r, and μ_r represent the initial and residual values of the respective parameters. As damage progresses, the yield surface changes from the initial shape to the final shape, as shown in Figure 9.5(b). The rate of the plastic work $\dot{\kappa}_3$ is defined as:

$$\dot{\kappa}_3 = (\tau_{r1} - \tau_{r2}) \cdot \left[\text{sign}\left(\tau_s\right) \cdot \cos\gamma \cdot \dot{d}_s^p + \text{sign}\left(\tau_t\right) \cdot \sin\gamma \cdot \dot{d}_t^p \right] \tag{9.31}$$

in which τ_{r2} is the shear strength under a normal stress σ when the tensile strength s has diminished to zero and the material parameters have reached their residual values as illustrated in Figure 9.6. It can be calculated as follows:

$$\tau_{r2} = \sqrt{\mu_r{}^2 \cdot \sigma^2 + 2 \cdot r_r \cdot \sigma} \tag{9.32}$$

Equations (9.26), (9.27) and (9.31) can be written in a matrix form as follows:

$$\dot{\boldsymbol{\kappa}} = \boldsymbol{\Lambda}(\boldsymbol{\sigma})\dot{\boldsymbol{d}}^{\boldsymbol{p}} \tag{9.33}$$

in which $\dot{\boldsymbol{\kappa}} = \{\dot{\kappa}_1 \quad \dot{\kappa}_2 \quad \dot{\kappa}_3\}^T$ and $\Lambda(\boldsymbol{\sigma})$ is:

$$\boldsymbol{\Lambda}(\boldsymbol{\sigma}) = \begin{bmatrix} 0 & 0 & \langle\sigma\rangle \\ \tau_t - \tau_{r1} \cdot \text{sign}(\tau_t) \cdot \sin\gamma & \tau_s - \tau_{r1} \cdot \text{sign} \cdot (\tau_s) \cdot \cos\gamma & 0 \\ (\tau_{r1} - \tau_{r2}) \cdot \text{sign}(\tau_t) \cdot \sin\gamma & (\tau_{r1} - \tau_{r2})\text{sign}(\tau_s) \cdot \cos\gamma & 0 \end{bmatrix} \tag{9.34}$$

The geometric dilatation component of the relative displacement vector is calculated with the following expression:

$$\dot{d}_n^g = \zeta_{dil} \cdot \dot{d}_{res}^p \tag{9.35}$$

in which the dilatation coefficient, ζ_{dil}, accounts for the wedging action of the interface asperities and is a measure of the surface roughness, and d_{res}^p is the resultant plastic shear displacement defined as:

$$d_{res}^p = \sqrt{\left(d_s^p\right)^2 + \left(d_t^p\right)^2} \tag{9.36}$$

When shear deformation occurs, the sliding surface can be smoothened. To account for this, the following softening rule, proposed by Koutromanos and Shing (2011), has been adopted:

$$\zeta_{dil} = \left(\zeta_{dil,o} - \zeta_{dil,r}\right) \cdot \exp\left(-\frac{d_{res}^p}{d_o}\right) + \zeta_{dil,r} \tag{9.37}$$

in which the subscripts *o* and *r* represent the initial and residual values of ζ_{dil}, which along with d_o are material parameters.

9.2.3 Numerical Implementation – Stress Update Algorithm

To calculate the stress update with the constitutive relations presented in the previous section, a numerical solution scheme has been implemented. For this purpose, the stress-displacement relations are written in a discrete incremental form. In each computation step *m*, the state of a joint is represented by the stress vector $\boldsymbol{\sigma}_m = \{\sigma_m \quad \tau_{t,m} \quad \tau_{s,m}\}^T$ and the internal variable vector $\boldsymbol{q}_m = \{s_m \quad r_m \quad \mu_m\}^T$. Knowing the values of the stresses, internal variables, and displacement increments $\Delta d_n = d_{n,m+1} - d_{n,m}$ at *m*, the stress vector $\boldsymbol{\sigma}_{m+1}$ and the internal variable vector $\boldsymbol{q}_{m+1}$ for the next step are to be calculated so that they satisfy $F(\boldsymbol{\sigma}_{m+1}, \boldsymbol{q}_{m+1}) = 0$.

Equations (9.14) - (9.16) can be rewritten in a discrete incremental form as follows:

$$\begin{aligned}
&\sigma_{m+1} = \sigma_m + D_{nn} \cdot (\Delta d_n - \Delta d_{n1}) = \sigma^{el}_{m+1} - D_{nn} \cdot (\Delta d_n^p + \Delta d_n^g) \ \text{(in compression)} \\
&\sigma_{m+1} = D_{nn} \cdot \langle d_{n,m+1} - d_{n2,m} - \Delta d_n^p \rangle - D_{nn} \cdot \langle d_{n1,m} + \Delta d_n^g - d_{n,m+1} \rangle \ \text{(in tension)} \\
&\tau_{t,m+1} = \tau_{t,m} + D_{tt} \cdot (\Delta d_t - \Delta d_t^p) = \tau^{el}_{t,m+1} - D_{tt} \cdot \Delta d_t^p \\
&\tau_{s,m+1} = \tau_{s,m} + D_{ss} \cdot (\Delta d_s - \Delta d_s^p) = \tau^{el}_{s,m+1} - D_{ss} \cdot \Delta d_s^p
\end{aligned} \tag{9.38}$$

in which the elastic predictor stresses are given by the following set of equations:

$$\begin{aligned}
\sigma^{el}_{m+1} &= D_{nn} \cdot \langle d_{n,m+1} - d_{n2,m} \rangle - D_{nn} \cdot \langle d_{n1,m} - d_{n,m+1} \rangle \\
\tau^{el}_{t,m+1} &= \tau_{t,m} + D_{tt} \cdot \Delta d_t \\
\tau^{el}_{s,m+1} &= \tau_{s,m} + D_{ss} \cdot \Delta d_s
\end{aligned} \tag{9.39}$$

The incremental plastic displacements are to be calculated with Eq. (9.20). With the backward Euler rule, Eqs. (9.38), (9.39), (9.35), and (9.20) result in:

$$\begin{aligned}
&\sigma_{m+1} = \sigma_{m+1}^{el} - \Delta\lambda \cdot D_{nn} \cdot \left[m_{1,m+1} + \zeta_{dil} \cdot \sqrt{\left(m_{2,m+1}^2 + m_{3,m+1}^3 \right)} \right] \text{ (in compression)} \\
&\sigma_{m+1} = D_{nn} \cdot \left\langle d_{n,m+1} - d_{n2,m} - \Delta\lambda \cdot m_{1,m+1} \right\rangle \text{ (in tension)} \\
&\tau_{t,m+1} = \tau_{t,m+1}^{el} - \Delta\lambda \cdot D_{tt} \cdot m_{2,m+1} \\
&\tau_{s,m+1} = \tau_{s,m+1}^{el} - \Delta\lambda \cdot D_{ss} \cdot m_{3,m+1}
\end{aligned} \tag{9.40}$$

When the elastic predictor normal stress is compressive, the components of the direction vector $\boldsymbol{m}$ are as follows:

$$m_{1,m+1} = \sigma_{m+1} \text{ , } m_{2,m+1} = \eta \cdot \tau_{t,m+1} \text{ , } m_{3,m+1} = \eta \cdot \tau_{s,m+1} \tag{9.41}$$

When the elastic predictor normal stress is tensile or zero, the direction vector components are calculated as:

$$\begin{aligned}
m_{1,m+1} &= \frac{\sigma_{m+1}^{el} / D_{nn}}{\sqrt{\left(\frac{\sigma_{m+1}^{el}}{D_{nn}} \right)^2 + \left(\frac{\tau_{t,m+1}^{el}}{D_{tt}} \right)^2 + \left(\frac{\tau_{s,m+1}^{el}}{D_{ss}} \right)^2}} \\
m_{2,m+1} &= \frac{\tau_{t,m+1}^{(el)} / D_{tt}}{\sqrt{\left(\frac{\sigma_{m+1}^{el}}{D_{nn}} \right)^2 + \left(\frac{\tau_{t,m+1}^{el}}{D_{tt}} \right)^2 + \left(\frac{\tau_{s,m+1}^{el}}{D_{ss}} \right)^2}} \\
m_{3,m+1} &= \frac{\tau_{s,m+1}^{el} / D_{ss}}{\sqrt{\left(\frac{\sigma_{m+1}^{el}}{D_{nn}} \right)^2 + \left(\frac{\tau_{t,m+1}^{el}}{D_{tt}} \right)^2 + \left(\frac{\tau_{s,m+1}^{el}}{D_{ss}} \right)^2}}
\end{aligned} \tag{9.42}$$

Hence, when the predictor normal stress is compressive, Eqs. (9.40) and (9.41) lead to:

$$\begin{aligned}
\sigma_{m+1} &= \frac{\sigma_{m+1}^{\text{el}} - \Delta\lambda \cdot D_{nn} \cdot \left[\sigma_m + \zeta_{dil} \cdot \eta \sqrt{\tau_{t,m+1}^2 + \tau_{s,m+1}^2} \right]}{\left(1 + \Delta\lambda \cdot D_{nn} \right)} \\
\tau_{t,m+1} &= \frac{\tau_{t,m+1}^{el}}{\left(1 + \Delta\lambda \cdot D_{tt} \cdot \eta \right)} \\
\tau_{s,m+1} &= \frac{\tau_{s,m+1}^{el}}{\left(1 + \Delta\lambda \cdot D_{ss} \cdot \eta \right)}
\end{aligned} \tag{9.43}$$

When the predictor normal stress is tensile, the components of the direction vector in Eq. (9.42) can be directly calculated from the elastic predictor stresses and substituted in Eq. (9.40) to obtain the stresses in step *m+1*.

The internal variables are updated with the softening laws using the updated stresses as follows:

$$s_{m+1} = s_m - \Delta\lambda \cdot s_o \cdot \left[\begin{array}{l} \dfrac{\langle \sigma_{m+1} \rangle}{G_f^I} \cdot m_{1,m+1} + \dfrac{\left(\tau_{t,m+1} - \tau_{r1,m+1} \cdot \text{sign}\left(\tau_{t,m+1} \right) \cdot \cos\gamma \right)}{G_f^{II}} \cdot m_{2,m+1} \\ + \dfrac{\left(\tau_{s,m+1} - \tau_{r1,m+1} \cdot \text{sign}\left(\tau_{s,m+1} \right) \cdot \cos\gamma \right)}{G_f^{II}} \cdot m_{3,m+1} \end{array} \right] \tag{9.44}$$

To provide a robust and efficient numerical solution procedure, the friction coefficient, μ, and the radius of curvature, r, are calculated with the approximation suggested by Koutromanos and Shing (2011) as follows:

$$\begin{array}{l} \mu_{m+1} \approx \mu_m - \Delta\lambda \cdot \alpha \cdot \left(\mu_m - \mu_r \right) \cdot (\tau_{r1,m} - \tau_{r2,m}) \cdot \\ \left[\text{sign}(\tau_{t,m+1}) \cdot m_{2,m+1} \cdot \sin\gamma + \text{sign}(\tau_{s,m+1}) \cdot m_{3,m+1} \cdot \cos\gamma \right] \\ \\ r_{m+1} \approx r_m - \Delta\lambda \cdot \beta \left(r_m - r_r \right) \left(\tau_{r1,m} - \tau_{r2,m} \right) \cdot \\ \left[\text{sign}(\tau_{t,m+1}) \cdot m_{2,m+1} \cdot \sin\gamma + \text{sign}(\tau_{s,m+1}) \cdot m_{3,m+1} \cdot \cos\gamma \right] \end{array} \tag{9.45}$$

The computation procedure is as follows. The yield function is first evaluated using the elastic predictor stresses calculated in step *m+1*, with Eq. (9.39), and the internal variables of the previous step *m*. If the value calculated lies in the elastic region, i.e., if $F\left(\boldsymbol{\sigma}_{m+1}^{el}, \boldsymbol{q}_m \right) < 0$, the elastic predictor stresses are taken as the updated stresses for step *m+1*. This procedure is repeated until the elastic predictor stresses result in $F\left(\boldsymbol{\sigma}_{m+1}^{el}, \boldsymbol{q}_m \right) > 0$. When this happens, the value of $\Delta\lambda$ is calculated iteratively until the stresses and the internal variables given by Eqs. (9.40) - (9.45) satisfy that the condition

that $F\left(\boldsymbol{\sigma}_{m+1}, \boldsymbol{q}_{m+1}\right) = 0$ with a set tolerance. The numerical solution procedure to calculate the plastic multiplier $\Delta\lambda$ when $F\left(\boldsymbol{\sigma}^{el}_{m+1}, \boldsymbol{q}_{m}\right) > 0$ can be summarized as follows:

1. Select a trial value for the plastic multiplier, $\Delta\lambda$.
2. Calculate the elastic predictor stresses with Eq. (9.39).
3. If the elastic predictor normal stress is negative, then:
  a. Calculate $\tau_{t,m+1}$ and $\tau_{s,m+1}$ with Eq. (9.43).
  b. Calculate the normal stress σ_{m+1} with Eq. (9.43).
  c. Calculate $m_{1,m+1}$, $m_{2,m+1}$ and $m_{3,m+1}$ with Eq. (9.41).
  else
  a. Calculate $m_{1,m+1}$, $m_{2,m+1}$ and $m_{3,m+1}$ with Eq. (9.42).
  b. Calculate $\tau_{t,m+1}$ and $\tau_{s,m+1}$ and the normal stress σ_{m+1} with the second equation in Eq. (9.40).
4. Calculate the angle γ with Eq. (9.29).
5. Calculate s_{m+1}, r_{m+1}, and μ_{m+1} with Eqs. (9.44) and (9.45).
6. Calculate the value of $F\left(\boldsymbol{\sigma}_{m+1}, \boldsymbol{q}_{m+1}\right)$.
7. If $F\left(\boldsymbol{\sigma}_{m+1}, \boldsymbol{q}_{m+1}\right) > 0$, select a larger value for $\Delta\lambda$ and go to Step 3.
Otherwise, the solution has been bracketed and an iterative procedure based on the bisection method can be used to find the value of $\Delta\lambda$ that yields $F\left(\boldsymbol{\sigma}_{m+1}, \boldsymbol{q}_{m+1}\right) = 0$ 7.

Figure 9.7 Stress Update Algorithm for the calculation of $\Delta\lambda$

9.2.4 Behavior of the Cohesive Crack Interface Model

To demonstrate the behavior of the proposed cohesive crack model, examples are considered with a single interface element of unit length for each side, as shown in Figure 9.8. The element is subjected to a uniform compressive stress of 100 psi (P = 0.025 kips). The bottom nodes are fixed and a uniform shear displacement is applied to the top four nodes. Two loading scenarios are investigated, as shown in Figure 9.9. First, the top

nodes are displaced in the *t* and *s* directions simultaneously by the same amount until a total resultant displacement δ is reached, as shown in Figure 9.9a, and then the displacement in the *s* direction is returned to zero. In the second scenario, the interface is displaced in the *s* direction first and then in the *t* direction, as shown in Figure 9.9b, and finally, its displacement in the *s* direction is returned to zero.

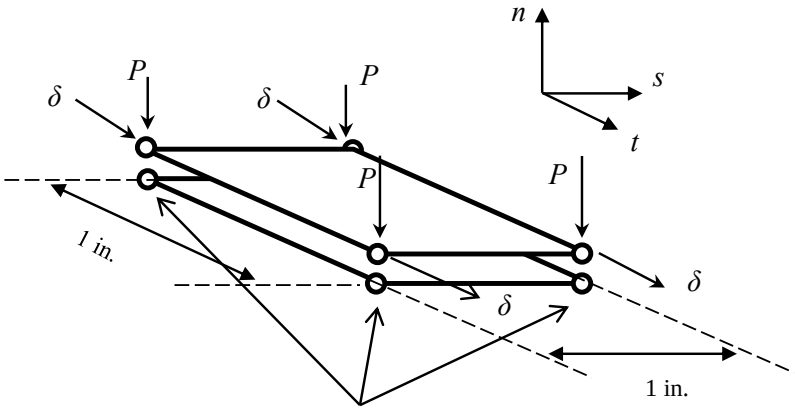

Figure 9.8 Interface element considered in examples

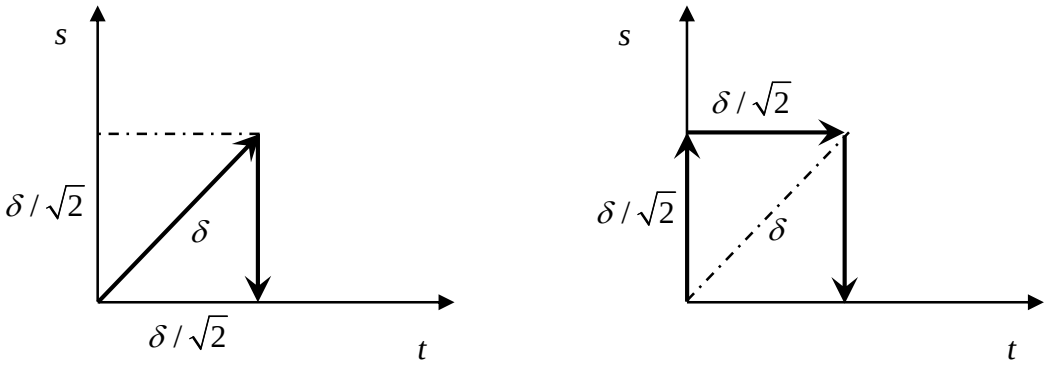

a) b)

Figure 9.9 Loading scenarios: a) scenario 1; b) scenario 2

The values of the model parameters used in the analysis are shown in Table 9.1. The Mode-II fracture energy is assumed to be 10 times that of Mode-I.

Table 9.1 Interface model parameters considered in the examples

D_{nn} (ksi/in.)	300	$\zeta_{dil,o}$	0.15
$D_{tt} = D_{ss}$ (ksi/in.)	125	$\zeta_{dil,r}$	0.001
s_o (ksi)	0.03	d_o (in.)	0.40
r_o (ksi)	0.01	α (in./kip)	2000
r_r (ksi)	0.005	β (in./kip)	2000
μ_o	0.95	G_f^I (kips/in.)	0.0001
μ_r	0.9	η	30

In the first loading scenario, cohesive and frictional forces develop simultaneously in the *t* and *s* directions. As the displacement progresses, the cohesive force decreases and the resistance levels off to the frictional force, as shown in Figure 9.10. The total frictional resistance is divided equally in the *s* and *t* directions. It can be observed that when displacement reversal occurs in the *s* direction, the force in the *t* direction drops to zero while the frictional resistance in the *s* direction is reversed. Thus, the total frictional force is developed only in the *s* direction. The dilation of the interface is plotted in Figure 9.11. As the displacement increases, the normal displacement increases due to the dilatation effect. When the displacement returns to zero in the *s* direction, displacement in the normal direction is negative, indicating joint compaction.

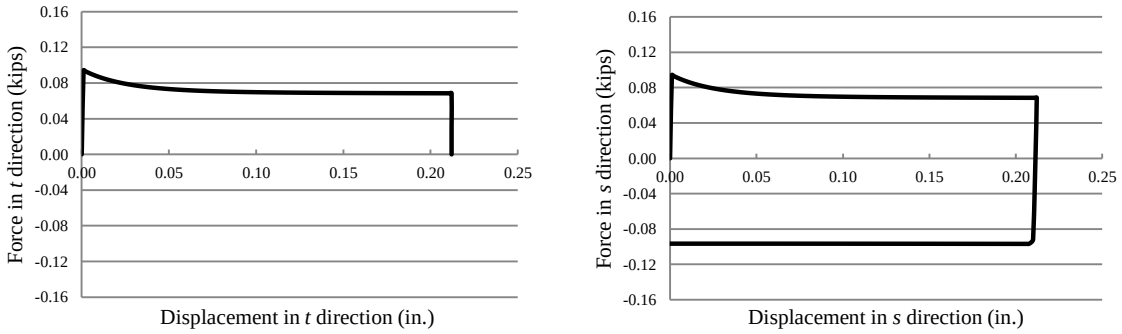

a) *t*-direction b) *s*-direction

Figure 9.10 Load-vs.-displacement curve for loading scenario 1

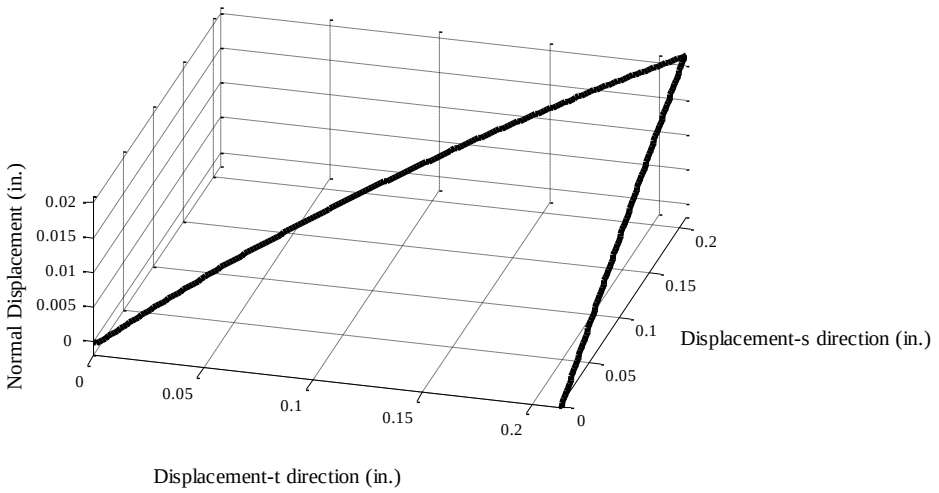

Figure 9.11 Normal displacement-vs-sliding displacement plot for loading scenario 1

For loading scenario 2, the load-vs.-displacement curve is shown in Figure 9.12. Initially, cohesive force is developed in the *s* direction. The cohesive force gradually disappears and the residual strength is provided by the friction. When the displacement shifts from the *s* direction to the *t* direction, a resisting force develops in the *t* direction, while that in the *s* direction drops to zero. Since the cohesive resistance of the interface has already diminished to zero in the first loading phase, the resisting force in the *t* direction is entirely due to friction.

In Figure 9.13, the normal displacement due to the dilatation effect is plotted against the sliding displacements. A comparison of Figure 9.11 and Figure 9.13 shows that the two scenarios result in slightly different maximum and residual normal displacements. Loading scenario 2 results in a higher joint dilatation. This can be attributed to the fact loading scenario 2 results in a higher net plastic shear displacements and thereby more joint dilatation according to Eq. (9.35). However, this is partially offset by the more severe plastic joint compaction in loading scenario 2.

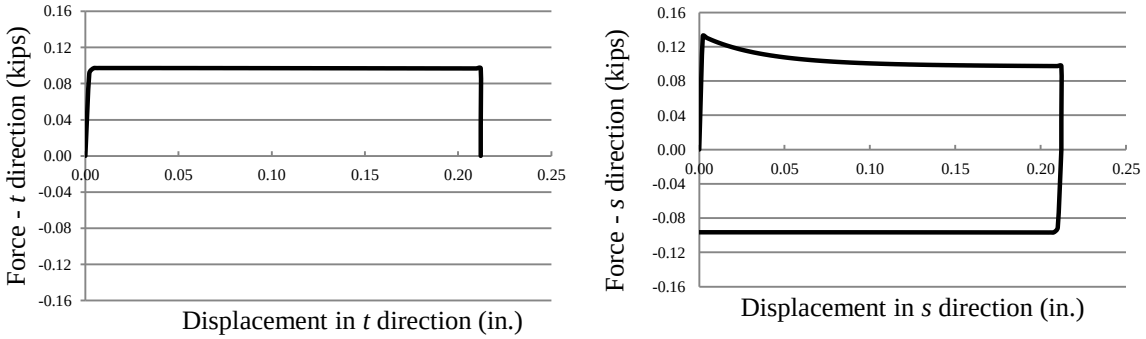

Figure 9.12 Load-vs.-displacement curve for loading scenario 2

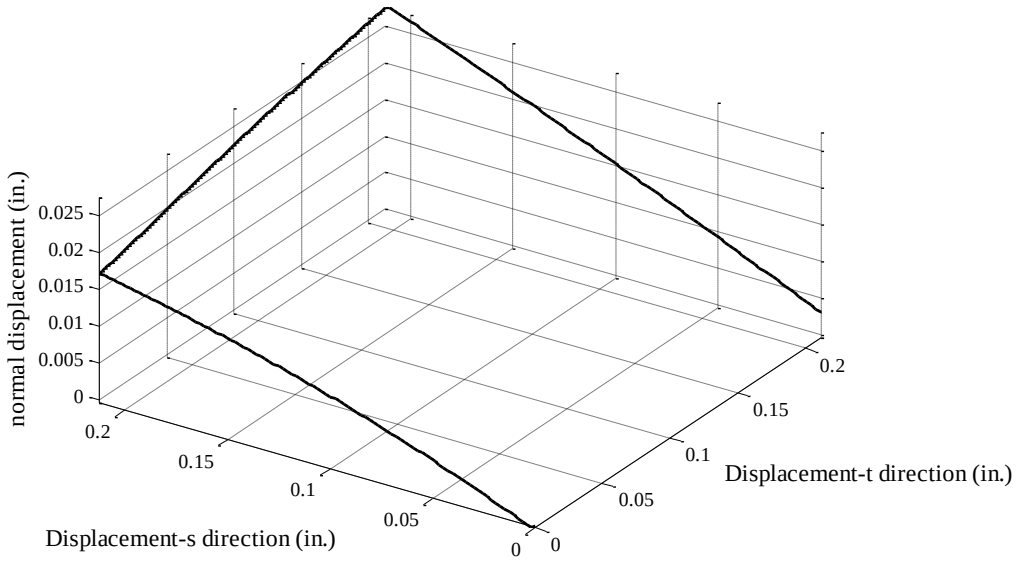

Figure 9.13 Normal displacement-vs.-sliding displacement plot for loading scenario 2

9.3 Proposed Three-Dimensional Model for Dowel Action and Bond-Slip

In this section, the formulation of the three-dimensional model for the dowel action behavior is described. This model is an extension of the two-dimensional model presented in Chapter 4.

9.3.1 Element Formulation

The zero thickness interface element presented in Chapter 4 has been extended for three-dimensional analysis. Like the element in Chapter 4, it is based on the formulation proposed by Mavros (2015), which can connect steel elements to more coarsely discretized concrete elements. An example of a block of concrete elements connected to a steel element is shown in Figure 9.14a. In this figure, the steel element is in the middle of the four concrete elements and can be seen in the plan view shown in Figure 9.14b. The concrete side and the steel side are shown in the close-up view in Figure 9.14c. The proposed interface element connects the concrete to the steel and is formulated in terms of the x coordinate and the radial coordinate r, as shown in Figure 9.14c.

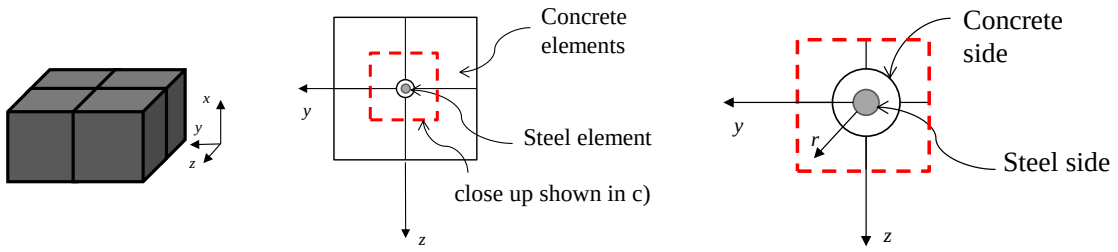

a) b) c)

Figure 9.14 Connectivity of interface element: a) element assembly; b) plan view showing concrete and steel elements; c) close-up view of concrete side and steel side of the interface

The interface element with the Gauss points G_1 and G_2 is shown in Figure 9.15. Nodes 3 and 4 are connected to the concrete elements, while nodes 1 and 2 are connected to the steel element. As discussed in Chapter 4, the model is so formulated that it allows the use of different element sizes for steel and concrete. Thus, the length of the steel element, denoted by L_{12}, can be equal to or shorter than that of the concrete element, denoted by L_{34}. The steel element also has to be located between nodes 3 and 4 at its undeformed state.

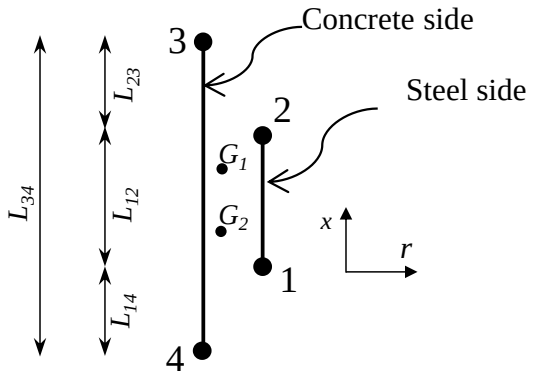

Figure 9.15 Interface element: Gauss points and geometric quantities (based on Mavros, 2015)

Following the work of Mavros (2015), the steel side (1-2) and the concrete side (3-4) have individual natural coordinate systems η and η_c, respectively, which are mapped by the following linear relation:

$$\eta_c = \alpha_f + \beta_f \cdot \eta \tag{9.46}$$

where

$$\alpha_f = \frac{L_{14} - L_{23}}{L_{34}} \tag{9.47}$$

$$\beta_f = \frac{L_{12}}{L_{34}} \tag{9.48}$$

The displacements in *x*, *y*, and *z* directions are denoted by *u*, *v* and *w*. The displacements of any point along the steel side, denoted by subscript *s*, are given by:

$$u_s(\eta) = N_1(\eta) \cdot u_1 + N_2(\eta) \cdot u_2 \tag{9.49}$$

$$v_s(\eta) = N_1(\eta) \cdot v_1 + N_2(\eta) \cdot v_2 \tag{9.50}$$

$$w_s(\eta) = N_1(\eta) \cdot w_1 + N_2(\eta) \cdot w_2 \tag{9.51}$$

in which u_i, v_i, and w_i are the nodal displacements and N_i are shape functions defined in the natural coordinate η as:

$$N_1(\eta) = \frac{1-\eta}{2},\ N_1(\eta) = \frac{1+\eta}{2} \tag{9.52}$$

The displacements along the concrete side, denoted by subscript *c*, are defined in the same way as follows:

$$u_c(\eta) = N_1(\eta) \cdot u_4 + N_2(\eta) \cdot u_3 \tag{9.53}$$

$$v_c(\eta) = N_1(\eta) \cdot v_4 + N_2(\eta) \cdot v_3 \tag{9.54}$$

$$w_c(\eta) = N_1(\eta) \cdot w_4 + N_2(\eta) \cdot w_3 \tag{9.55}$$

The stresses in the interface are calculated from the relative displacements between the concrete side and the steel side, denoted by $\tilde{u}$, $\tilde{v}$ and $\tilde{w}$. The relative displacements can be expressed as functions of η as follows:

$$\begin{Bmatrix} \tilde{u} \\ \tilde{v} \\ \tilde{w} \end{Bmatrix} = \begin{Bmatrix} u_s(\eta) - u_c(\alpha_f + \beta_f \cdot \eta) \\ v_s(\eta) - v_c(\alpha_f + \beta_f \cdot \eta) \\ w_s(\eta) - w_c(\alpha_f + \beta_f \cdot \eta) \end{Bmatrix} = \begin{bmatrix} \boldsymbol{b}(\eta) & 0 & 0 \\ 0 & \boldsymbol{b}(\eta) & 0 \\ 0 & 0 & \boldsymbol{b}(\eta) \end{bmatrix} \cdot \begin{Bmatrix} \boldsymbol{u} \\ \boldsymbol{v} \\ \boldsymbol{w} \end{Bmatrix} \tag{9.56}$$

where

$$\boldsymbol{b}(\eta) = \begin{bmatrix} N_1(\eta) & N_2(\eta) & -N_2(\alpha_f + \beta_f \cdot \eta) & -N_1(\alpha_f + \beta_f \cdot \eta) \end{bmatrix} \tag{9.57}$$

and

$$\begin{Bmatrix} \boldsymbol{u} \\ \boldsymbol{v} \\ \boldsymbol{w} \end{Bmatrix} = \begin{Bmatrix} u_1 & u_2 & u_3 & u_4 & v_1 & v_2 & v_3 & v_4 & w_1 & w_2 & w_3 & w_4 \end{Bmatrix}^T \tag{9.58}$$

9.3.2 Constitutive Model

The constitutive relation between the normal stress and the normal relative displacement of the interface element is formulated in terms of the resultant normal displacement, $\tilde{s}$, along the radial direction *r* as shown in Figure 9.16. Given $\tilde{v}$ and $\tilde{w}$ from Eq. (9.56), the resultant normal displacement can be calculated as:

$$\tilde{s} = \sqrt{\tilde{v}^2 + \tilde{w}^2} \tag{9.59}$$

In addition, the angle at which the resultant normal displacement occurs, also shown in Figure 9.16, is calculated as:

$$\gamma_d = \tan^{-1}\left(\tilde{w} / \tilde{v}\right) \tag{9.60}$$

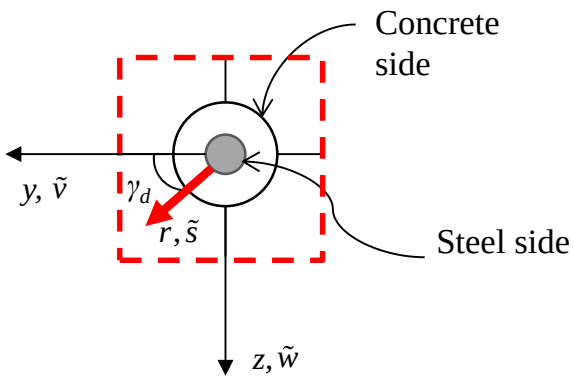

Figure 9.16 Resultant normal displacement and angle of displacement of interface model

From the resultant normal displacement, $\tilde{s}$, and the relative tangential displacement, $\tilde{u}$, along the x direction, the normal stress σ and the tangential stress τ can be computed. For the tangential stress τ, the constitutive model of Murcia-Delso and Shing (2015) for the bond-slip behavior presented in Section 4.3 is used. For the calculation of the normal stress σ, the dowel action law presented in Chapter 4 has been adopted. The normal stress-normal displacement backbone curve is based on the law proposed by Brenna et al. (1990):

$$\sigma(\tilde{s}) = \omega(\tilde{s}) \cdot k_0 \cdot \tilde{s} \tag{9.61}$$

in which

$$\begin{aligned}
k_0 &= 600 \cdot f_c'^{0.7} / d_b \\
\omega(\tilde{s}) &= \left[1.5 \cdot \left(a + \sqrt{d^2 \cdot \left(40 \cdot \tilde{s} / d_b - b \right)^2 + c^2} \right) \right]^{-4/3} \\
a &= 0.59 - 0.011 \cdot f_c' \\
b &= 0.0075 \cdot f_c' - 0.23 \\
c &= 0.0038 \cdot f_c' + 0.44 \\
d &= 0.0025 \cdot f_c' + 0.58
\end{aligned} \tag{9.62}$$

In Eq. (9.62), f_c' is the concrete compressive strength in MPa, d_b is the bar diameter in mm and $\tilde{s}$ is the imposed displacement in mm.

As soon as the normal compressive displacement is reversed, the bar loses contact with concrete and the compressive stress on the bar diminishes. The decrease in the contact stress is calculated as elastic unloading:

$$\begin{aligned} \dot{\sigma}(\tilde{s}) &= K_{un} \cdot \dot{\tilde{s}} \\ K_{un} &= \gamma \cdot K_{in} \end{aligned} \tag{9.63}$$

in which the superposed dot represent the rate of change, γ is a multiplication factor greater than 1.0 and K_{in} is given by:

$$\begin{aligned} K_{in} &= \omega_{in} \cdot k_0 \\ \omega_{in} &= \omega(\tilde{s}=0) = \left[1.5 \cdot \left(a + \sqrt{d^2 \cdot b^2 + c^2}\right)\right]^{-4/3} \end{aligned} \tag{9.64}$$

As discussed in Chapter 4, it is assumed that the concrete in the vicinity of the bar experiencing compression can be severely damaged. During unloading, when the stress reaches zero, a gap δ_g is created and the stress will remain zero until the bar resumes contact upon reloading. The increase in stress is then given by the following equation:

$$\sigma(\tilde{s}) = \omega(\tilde{s} - \delta_r) \cdot k_0 \cdot \langle \tilde{s} - \delta_r \rangle \tag{9.65}$$

in whcih $\langle \bullet \rangle$ are the Macaulay brackets, the expressions for $\omega(\cdot)$ and k_0 are given in Eq. (9.62), and δ_r is the displacement at which reloading starts. If complete unloading occurs, δ_r is equal to δ_g, and the compressive stress will remain zero until the resultant normal displacement $\tilde{s}$ reaches again δ_g, at which the gap closes and the reinforcing bar

resumes contact with the undamaged concrete. The displacement δ_r is calculated as follows:

$$\delta_r = \begin{cases} \delta_g = \delta_u - \dfrac{\sigma_u}{K_{un}} & \text{complete unload} \\ \delta_{cur} & \text{partial unload} \end{cases} \tag{9.66}$$

in which σ_u and δ_u are the stress and the normal displacement at which the unloading starts δ_{cur} and is the displacement at reloading.

The resultant normal displacement, as illustrated in Figure 9.17, can occur in any direction in the *y*-*z* plane. However, for simplicity, damage in concrete is assumed to be isotropic, and consequently, δ_g is independent of the loading direction. Based on this assumption, damaged region in cross section is circular of radius δ_g about the initial position of the reinforcing bar, as shown in Figure 9.17. This circular region expands when δ_g increases in any direction. It goes without saying that this simplifying assumption does not exactly correspond to the actual spread of concrete damage induced by dowel action. However, it is adequate for the analyses considered in this study.

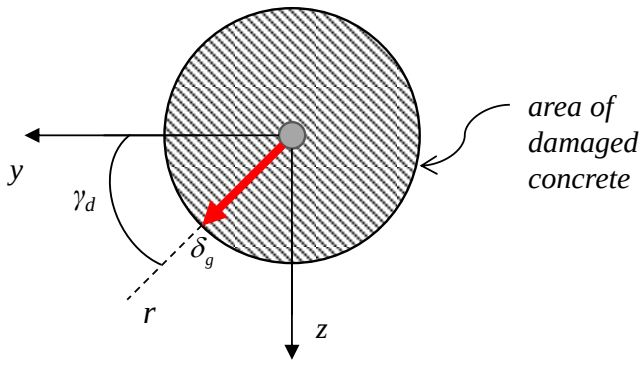

Figure 9.17 Assumed damaged region around a steel bar

After calculating the normal stress σ in the radial direction, it is resolved into components σ_y and σ_z in the *y* and *z* directions as follows:

$$\begin{aligned} \sigma_y &= \sigma \cdot \cos\gamma_d \\ \sigma_z &= \sigma \cdot \sin\gamma_d \end{aligned} \tag{9.67}$$

To calculate the element nodal forces, the following assumptions are made. The bond stress due to bar slip acts around the circumference of the bar, and the two components of the normal stress due to dowel action act on a rectangular area of width equal to the bar diameter d_b, as shown in Figure 9.18a and Figure 9.18b, respectively.

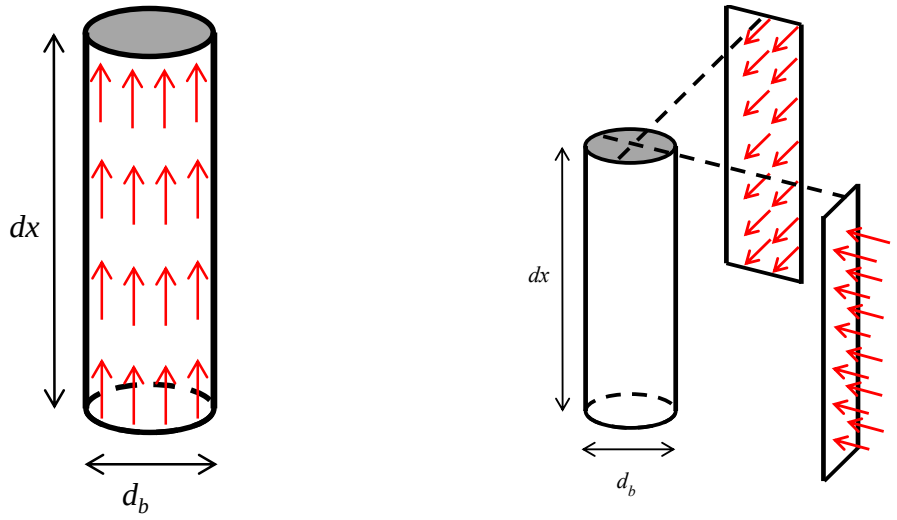

a) b)

Figure 9.18 Distribution of stresses for the calculation of element nodal forces: a) bond-slip stress; b) dowel action stress

The element nodal forces can be formulated using the principle of virtual displacements, with the internal virtual work given by:

$$\delta W_I = -\pi d_b \int_0^{L_{12}} \delta\tilde{u} \cdot \tau dx - d_b \int_0^{L_{12}} \delta\tilde{v} \cdot \sigma_y dx - d_b \int_0^{L_{12}} \delta\tilde{w} \cdot \sigma_z dx \tag{9.68}$$

and the external virtual work by:

$$\delta W_E = \delta \boldsymbol{u}^T \boldsymbol{f}_x + \delta \boldsymbol{v}^T \boldsymbol{f}_y + \delta \boldsymbol{w}^T \boldsymbol{f}_z \tag{9.69}$$

in which $\delta\tilde{u}$, $\delta\tilde{v}$ and $\delta\tilde{w}$ are the virtual relative displacements along the element, $\delta\boldsymbol{u}$, $\delta\boldsymbol{v}$ and $\delta\boldsymbol{w}$ are the vectors of virtual nodal displacements, and $\boldsymbol{f}_x$, $\boldsymbol{f}_y$ and $\boldsymbol{f}_z$ are vectors of element nodal forces in the *x*, *y* and *z* directions. From Eqs. (9.56), (9.68) and (9.69), and the condition that $\delta W_I + \delta W_E = 0$, we have:

$$\begin{aligned} \mathbf{F}_x &= \pi d_b \int_{-1}^{1} \boldsymbol{b}^T(\eta)\tau(\eta) J d\eta \\ \mathbf{F}_y &= d_b \int_{-1}^{1} \boldsymbol{b}^T(\eta)\sigma_y(\eta) J d\eta \\ \mathbf{F}_z &= d_b \int_{-1}^{1} \boldsymbol{b}^T(\eta)\sigma_z(\eta) J d\eta \end{aligned} \tag{9.70}$$

where

$$J = \frac{dx}{d\eta} = \frac{L_{12}}{2} \tag{9.71}$$

9.3.3 Behavior of the Dowel Action Interface Model

To demonstrate the behavior of the proposed dowel action model, simple examples using a single unit length interface element are considered. In these examples, nodes 4 and 3 (representing the concrete side) are fixed and displacement is applied to nodes 1 and 2. The model is shown in Figure 9.19.

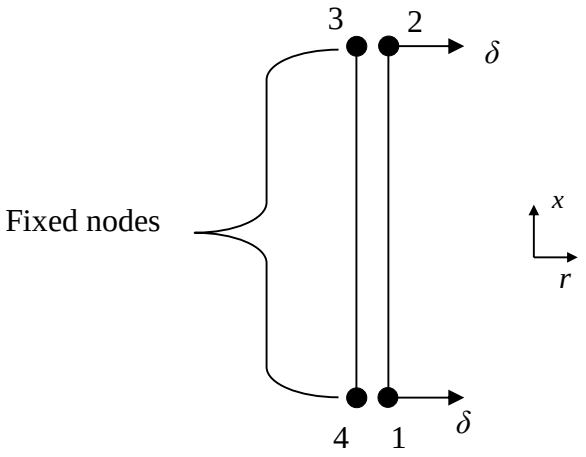

Figure 9.19 Model considered in examples

The four loading scenarios in the normal direction as shown in Figure 9.20 are considered. In all cases, the maximum resultant normal displacement δ is equal to 0.04 in. In the first scenario, the displacement δ is applied in the z direction only, while in scenarios 2 and 3 the displacement is applied at 45 and 20 degrees with respect to the y axis. In scenario 4, the displacement is first applied in the z direction and then in the y direction. After loading, the interface is unloaded to zero displacement in all cases. The compressive strength of concrete is assumed to be 5.0 ksi and the reinforcing bar has a diameter of 0.5 in. The load-vs.-displacement curves are shown in Figure 9.21 and Figure 9.22.

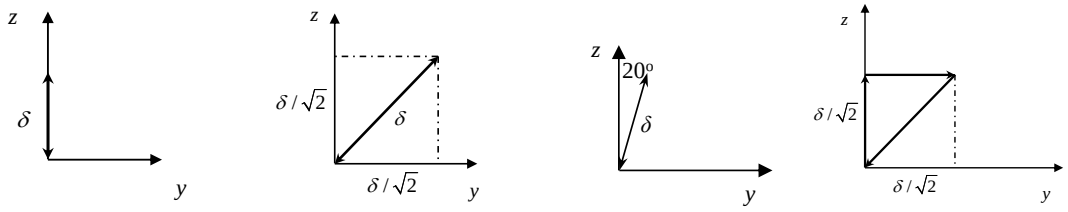

a) Loading Scenario 1 b) Loading Scenario 2 c) Loading Scenario 3 d) Loading Scenario 4

Figure 9.20 Loading scenarios applied in examples

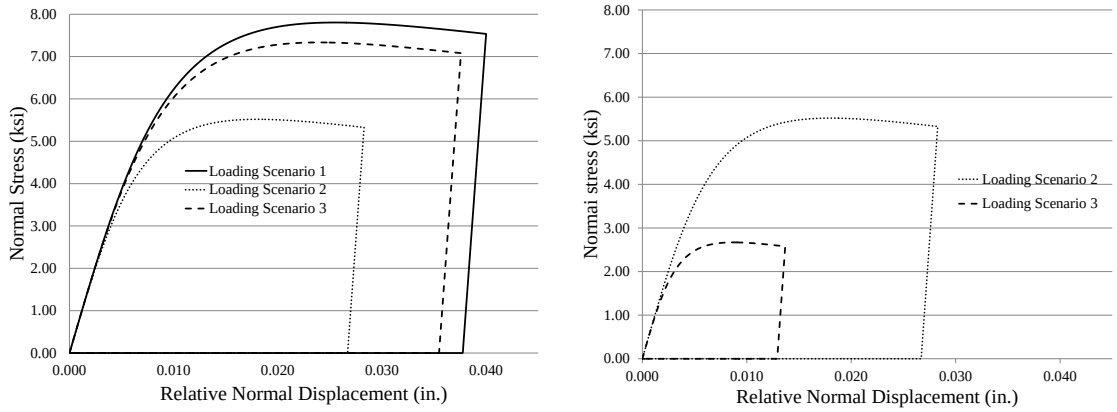

a) *z*-direction b) *y*-direction

Figure 9.21 Load-vs.-displacement curves for loading scenarios 1, 2 and 3

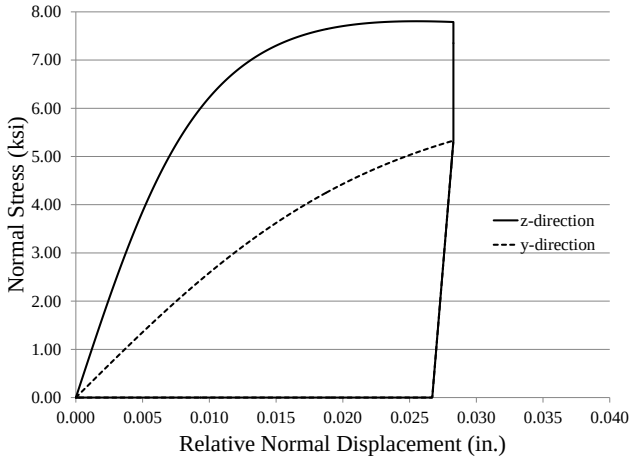

Figure 9.22 Load-vs.-displacement curves for loading scenario 4

The resultant normal stresses developed when the resultant displacements reach 0.04 in. are the same for all four cases as expected. For the non-proportional loading shown in Figure 9.22, the normal stress in the *z* direction initially increases as the displacement in that direction increases. When the displacement in the *y* direction occurs, the normal stress in the *y* direction increases and that in the *z* direction decreases until the stresses and displacemens in both directions reach the same values.

9.4 Acknowledgement of Publication

Part of this chapter is a reprint of the material that will appear in a technical report which will be submitted to the California Department of Transportation in 2016, Kottari, A., P. B. Shing, J. I. Restrepo, under the title "Design and Capacity Assessment of External Shear Keys in Bridge Abutments". The dissertation author will be the primary investigator and author of this report.

CHAPTER 10

FINITE ELEMENT ANALYSIS OF EXTERNAL SHEAR KEYS IN BRIDGE ABUTMENT

10.1 Introduction

Three-dimensional finite element models are needed to capture the failure behavior of skewed abutment shear keys. This chapter presents the analysis of shear keys in bridge abutments with three-dimensional finite element models. The modeling scheme is first validated for non-skewed shear keys and then applied to a skewed shear key. The numerical results are compared to experimental data from isolated and monolithic shear keys presented in Chapters 2, 5 and 6. For the skewed shear key, the numerical results are compared to the experimental observations presented in Chapter 8. For these analyses, the cohesive crack interface model and the interface model developed for the simulation of the bond-slip behavior and dowel action of reinforcing bars, as presented in Chapter 9, are used. To model the nonlinear behavior of concrete with 3-D solid elements, the smeared-crack constitutive model of Moharrami and Koutromanos (2016) is used and for the behavior of steel the model of Dodd and Restrepo-Posada (1995). The modeling schemes and the calibration of the material models are explained in this chapter.

10.2 Finite Element Analysis of Non-Skewed Shear Keys

10.2.1 Horizontal Shear Failure of Isolated Shear Keys

Shear keys 5A and 5B, tested by Borzogzadeh et al. (2006) as presented in Chapter 2, and shear keys 7A and 7B, tested in this study as described in Chapter 5, have been analyzed with three-dimensional finite element models. The specimen had four vertical dowel bars placed along the width of the shear key in a single row. Due to the symmetry of the specimen geometry, reinforcement layout, and loading conditions about the center plane of the stem wall, it can be assumed that all the dowel bars will contribute equally to the shear key resistance. Hence, only one-fourth of the width of the specimen (4.2 in.) is modeled with one layer of elements, as shown in Figure 10.1. The model has fixed boundary conditions in its base and is also prevented from moving in the horizontal direction at the end of the stem wall, away from the shear key. Quadrilateral solid elements are used to represent concrete. The elements have a size of 4 in. along the *x* and *z* directions. Their size is selected to allow the appropriate positioning of the vertical and horizontal reinforcing bars. The solid elements are separated by cohesive crack interface elements to allow the simulation of horizontal cracks and diagonal cracks, assumed to be at 45 degrees, in an accurate way. Horizontal displacement is applied to a block of elastic solid elements, as shown in Figure 10.1, which simulates the steel loading beam used in the test, as discussed in Chapter 5. Between the inclined face of the shear key and the loading block, zero-thickness, cohesive crack interface elements are placed to provide the contact condition. These interfaces have zero tensile strength and zero friction

coefficient. The loading block is prevented from moving in the vertical direction to simulate the restraint imposed by the hold-down frames in the test.

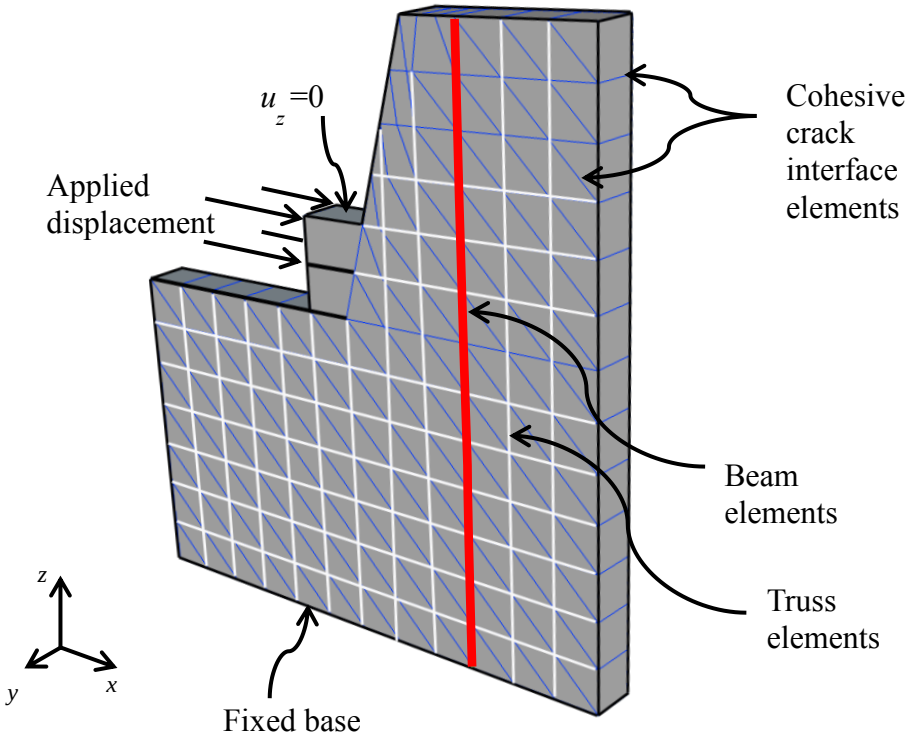

Figure 10.1 Finite element model for isolated shear keys

The three-dimensional concrete model developed by Moharrami and Koutromanos (2016) is used for the solid elements. This model can simulate the compressive crushing, and strength and stiffness degradation due to cracking, and the effect of confinement on the compressive behavior. The behavior of the model in compression is governed by an elastoplastic formulation with the yield surface shown in Figure 10.2 and a non-associative flow rule. After the tensile strength s_0 has been reached, the behavior in tension is governed by a rotating smeared-crack law. Moharrami and Koutromanos (2016) have suggested that the tensile fracture (Mode-I) energy be multiplied by 100 to obtain the compressive fracture energy. The behavior in

compression is governed by the normalized fracture energy g_c (compressive fracture energy divided by the characteristic element length), the dilatancy parameter α_p, factor d, which controls the effect of the hydrostatic pressure on the hardening behavior of the material, and parameter α_c, which is a material constant. The values of these three parameters used in all the analyses presented in this chapter are shown in Table 10.1. The modulus of elasticity of concrete used in all the analyses is calculated with the formula $E_c = 57,000\sqrt{f'_c}$, as suggested in ACI 318-08, and the parameter λ_t controlling the tensile softening behavior of the cracked material is set equal to 500. All the parameters are explained in the paper by Moharrami and Koutromanos (2016).

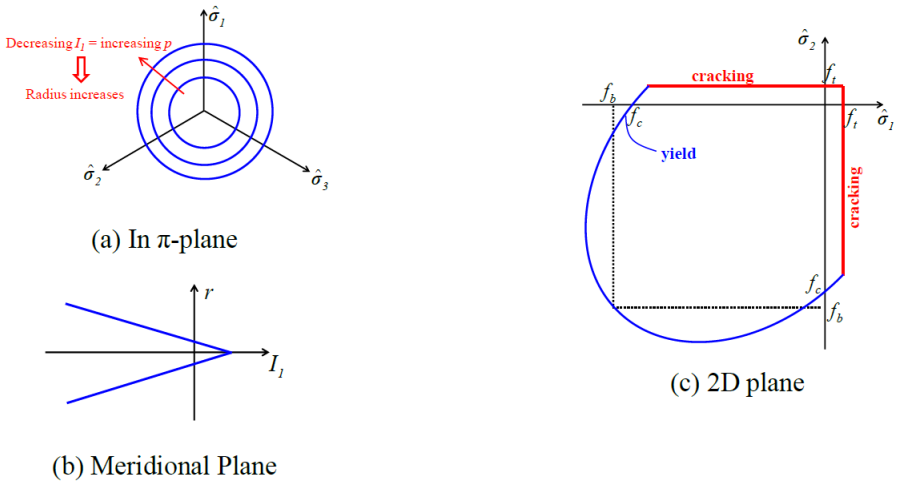

Figure 10.2 Yield surface for elastoplastic material model for concrete (from Moharrami and Koutromanos, 2016)

Table 10.1 Material properties for concrete model used in all the analyses

α_p	α_c	d
0.15	0.35	3.7

The vertical and horizontal side reinforcing bars of the stem wall are modeled with elastoplastic truss elements, which have a 2% strain hardening slope. Since one-fourth of the specimen is modeled, the area of each truss element is equal to one-fourth of the total area of the steel reinforcing bars of the two sides. To simulate the dowel action, the vertical reinforcing bars crossing the construction joint of a shear key are modeled with fiber-section beam elements, which are connected to the solid elements through the interface elements that simulate the bond-slip and dowel action behavior. The length of the beam elements is chosen to be $0.5d_b$, as recommended in Chapter 4. The beam elements have both geometric and material nonlinearities. The constitutive model for steel developed by Dodd and Restrepo-Posada (1995) is used to describe the material nonlinearity of the beams. This model has been modified to be able to capture the fracture of the dowels. After the strain, ε_f, at which fracture is expected to occur is reached, the stress starts to decrease, following a linearly decaying law in which the slope is 0.2% of the elastic stiffness.

Shear Keys 5A and 5B

Shear key 5A was isolated from the stem wall, but it had an 8 in. x 8 in. rough construction joint at the center. In the construction joint, bond breaker was not applied. In the area around the rough construction joint, foam was applied prior to casting the shear key to eliminate the bond between the shear key and stem wall surface. More information regarding the construction joint preparation can be found in Borzogzadeh et al. (2006). To simulate the rough construction joint, the corresponding interface elements connecting the shear key to the stem wall are calibrated accordingly. The remaining interface

elements representing the unbonded part of the construction joint have zero tensile strength and a coefficient of friction of 0.01. This small coefficient of friction is needed to avoid numerical problems in the analysis. It should be noted that the yield surface for the interface model is so calibrated that the parameter μ represents the coefficient of friction.

Shear key 5B was completely isolated from the stem wall. Thus, all the interface elements representing the construction joint have zero tensile strength, and a constant coefficient of friction of 0.36, as identified by Borzogzadeh et al. (2006).

For the interface elements outside the construction joints used to model the behavior of the stem wall and the shear keys, the tensile strength is assumed to be 0.5 ksi, which is about 10% of the 28-day compressive strength of the concrete, and the cohesive shear strength is assumed to be 2 times the tensile strength.

The values of the material parameters selected for the interface elements modeling the behavior of the construction joints, the stem walls, and the shear keys are shown in Table 10.2 and Table 10.3 and the parameters for the concrete model are shown in Table 10.4. It should be noted that for all the cases, the Mode-II fracture energy is taken to be 10 times that of Mode-I.

Table 10.2 Cohesive crack model parameters for shear keys 5A and 5B, part I

Type of Interface	D_{nn} (ksi/in.)	D_{tt} (ksi/in.)	s_o (ksi)	r_o (ksi)	r_r (ksi)	μ_o	μ_r
Construction Joint 5A (rough part)	5000	10000	0.5	0.5	0.01	1.0	0.7
Construction Joint 5A (unbonded part)	5000	10000	0.0	0.0	0.00	0.01	0.01
Construction Joint 5B	5000	10000	0.0	0.0	0.0	0.36	0.36
Stem Wall and Shear Key	5000	10000	0.5	0.5	0.01	1.4	1.0

Table 10.3 Cohesive crack model parameters for shear keys 5A and 5B, part II

Type of Interface	$\zeta_{dil,o}$	$\zeta_{dil,r}$	d_o	α (in./kip)	β (in./kip)	G_f^I (kip / in.)	η
Construction Joint 5A (rough part)	0.7	0.1	0.25	100	100	0.0006	300
Construction Joint 5A (unbonded part)	0.01	0.01	0.05	100	100	0.0	300
Construction Joint 5B	0.01	0.01	0.25	100	100	0.0	300
Stem Wall and Shear Key	0.7	0.1	0.25	100	100	0.0006	300

Table 10.4 Material properties for concrete model used for shear keys 5A and 5B

f_c' (ksi)	s_0 (ksi)	g_c (ksi)
5.0	0.5	0.015

The tensile strength of the vertical dowel bars is based on the values reported by Borzogzadeh et al. (2006). For the vertical dowel bars (No. 4 bars), the yield strength was 63 ksi and the ultimate strength was 104 ksi. The modulus of elasticity is equal to 29,000 ksi. It is assumed that the bars will fracture at a tensile strain of 20%.

The side reinforcement (No. 3 bars) and horizontal shear reinforcement of the stem wall are modeled with elastoplastic truss elements. The yield strength used is 68 ksi and the modulus of elasticity is 29,000 ksi. The strain hardening slope considered is 2%.

The finite element models are able to reproduce the behavior observed in the tests with good accuracy. The failure mode is horizontal shear sliding along the construction joints for both shear keys, as shown in Figure 10.3 and Figure 10.4. The cohesive shear force developed in shear key 5A resulted in a high peak horizontal resistance as shown in the horizontal load-vs.-horizontal displacement curve in Figure 10.5.

This figure and Figure 10.6, show that the finite element analyses are able to reproduce the stiffness and the strengths of both shear keys very accurately. In addition,

for both cases, the fracture of the vertical dowel bars occurs at displacement levels similar to that observed in the tests. For shear key 5A, the fracture of all the vertical dowel bars occurs at a displacement of 1.86 in., while it started at 1.50 in. with the last bar fractured at 1.75 in. in the test. For shear key 5B, bar fracture of all the vertical dowel bars occurs at 1.70 in. This is close to the displacement of 1.75 in. at which the last bar fracture occurred in the test. It should be noted that fracture is considered to occur in the analysis when all the fibers in the beam element section reach a tensile strain of 20%.

The angle of kink is calculated for the dowel bar crossing the construction joint based on the deformation of the beam elements. For shear key 5A, this angle is found to be 34 degrees and for shear key 5B, it is 35 degrees. These values are in good agreement with the 37 degrees observed in the experiment by Borzogzadeh et al. (2006).

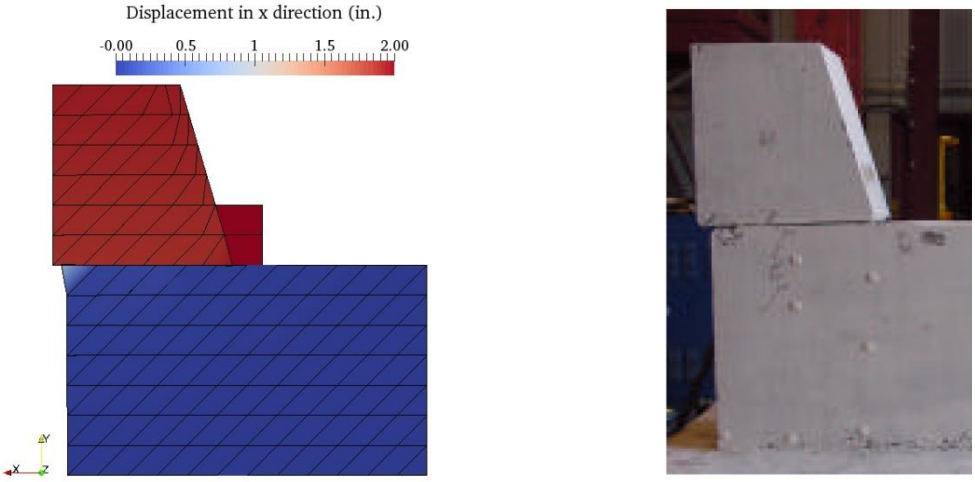

a) b)

Figure 10.3 Sliding of shear key 5A at the end of loading: a) FE analysis; b) test (from Borzogzadeh et al., 2006)

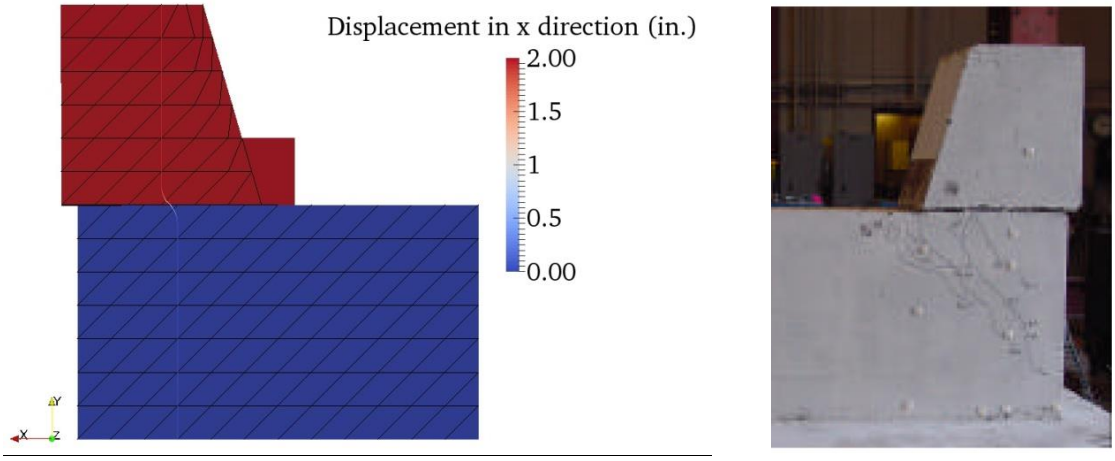

a) b)

Figure 10.4 Sliding of shear key 5B: a) at the end of the FE analysis; b) at the end of the test (from Borzogzadeh et al., 2006)

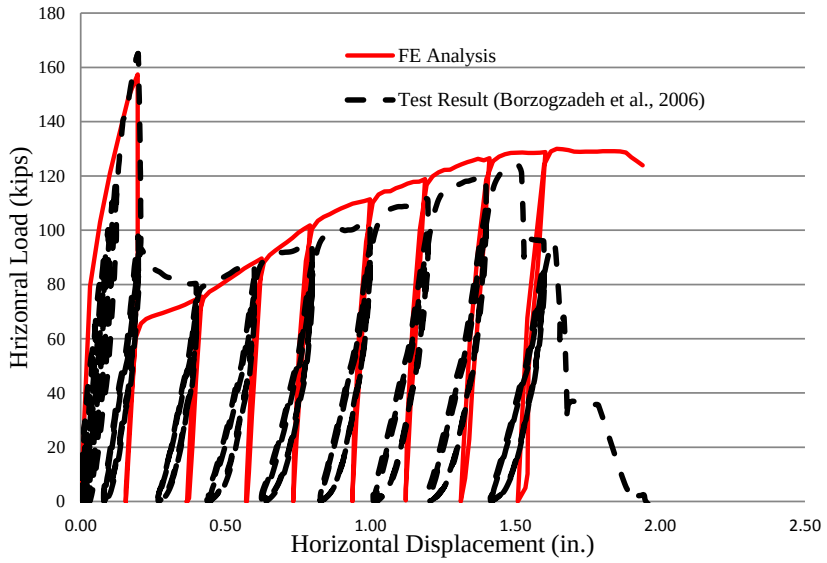

Figure 10.5 Numerical and experimental horizontal load-vs.-horizontal displacement curves for shear key 5A

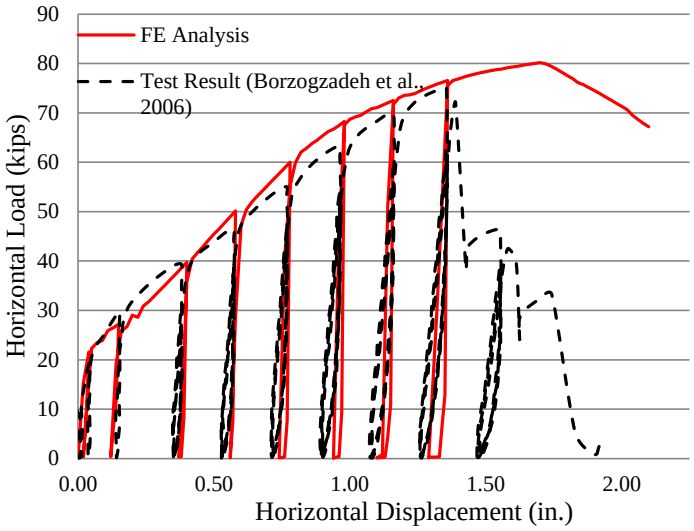

Figure 10.6 Numerical and experimental horizontal load-vs.-horizontal displacement curves for shear key 5B

Shear Keys 7A and 7B

Shear key 7A had a smooth construction joint, in which several layers of water-based bond breaker were applied. Thus, in the analysis, the interface elements of the construction joint are modeled with zero cohesive strength, and a friction coefficient of 0.36, as in shear key 5B. It should be mentioned that the yield surface of the interface elements are calibrated such that μ represents the coefficient of friction.

Shear key 7B was constructed with a rough joint, and bond breaker was applied to the joint surface to eliminate the cohesive force. However, this was not entirely effective, and limited cohesive force was developed, as indicated by the experimental results presented in Chapter 5. The influence of the bond breaker is difficult to determine from the test data. Thus, two analyses have been performed, one without cohesive force and the other with cohesive force in the construction joint. These analyses will be referred to as "analysis with bond breaker" and "analysis without bond breaker", respectively. For

the analysis in which the cohesive force is considered, the cohesive strength is set equal to 2 times the tensile strength. The tensile strength is about 10% of the 28-day compressive strength of concrete.

For the interfaces used to simulate the behavior of concrete in the stem wall and the shear keys, the tensile strength is assumed to be 0.5 ksi, which is close to 10% of the concrete compressive strength and their cohesive strength is 2 times the tensile strength. The Mode-I fracture energy for all the interfaces with cohesive strength is 0.006 kips/in. The Mode-II fracture energy is set equal to 10 times that of Mode-I. The values of all the parameters used in the interfaces are summarized in Table 10.5 and Table 10.6.

As in Specimen 5, the side reinforcement (No. 3 bars) and the horizontal shear reinforcement of the stem wall are modeled with elastoplastic truss elements and the vertical dowel bars with beam elements. The properties of the beam and truss elements are based on the tensile tests of the reinforcing bars, summarized in Chapter 5 and presented in Table 10.7. The modulus of elasticity of the steel is 29,000 ksi. The tensile strain at which fracture occurs in the beam elements is assumed to be 20% and the truss elements have a strain hardening slope of 2% of the initial modulus of elasticity. Finally, the parameters used for the concrete model are shown in Table 10.8.

Table 10.5 Cohesive crack model parameters for shear keys 7A and 7B, part I

Type of Interface	D_{nn} (ksi/in.)	D_{tt} (ksi/in.)	s_o (ksi)	r_o (ksi)	r_r (ksi)	μ_o	μ_r
Construction Joint 7A	5000	10000	0.0	0.0	0.0	0.36	0.36
Construction Joint 7B (without bond breaker)	5000	10000	0.5	0.5	0.01	1.0	0.7
Construction Joint 7B (with bond breaker)	5000	10000	0.0	0.0	0.0	1.0	0.7
Stem Walls and Shear Keys	5000	10000	0.5	0.5	0.01	1.5	1.0

Table 10.6 Cohesive crack model parameters for shear keys 7A and 7B, part II

Type of Interface	$\zeta_{dil,o}$	$\zeta_{dil,r}$	d_o	α (in./kip)	β (in./kip)	G_f^I (kip/in.)	η
Construction Joint 7A	0.01	0.01	0.05	100	100	0.0	300
Construction Joint 7B (without bond breaker)	0.3	0.1	0.05	100	100	0.0006	300
Construction Joint 7B (with bond breaker)	0.3	0.1	0.05	100	100	0.0	300
Stem Wall and Shear Keys	0.7	0.1	0.05	100	100	0.0006	300

Table 10.7 Measured strengths of reinforcing bars in Specimen 7

Reinforcement Description	Bar Size	f_y (ksi)	f_{su} (ksi)
Vertical and horizontal side reinforcement of the stem wall	No. 3	79.30	102.60*
Horizontal shear reinforcement of the stem wall	No. 5	67.20	94.92*
Vertical dowel bars of shear key 7A	No. 5	70.00	93.60
Vertical dowel bars of shear key 7B	No. 4	70.00	94.50

* they are not reached in the analysis

Table 10.8 Material properties for concrete model used for shear keys 7A and 7B

f_c' (ksi)	s_0 (ksi)	g_c (ksi)
5.0	0.5	0.015

The numerical and experimental load-vs.-displacement curves for shear key 7A are shown in Figure 10.7. It can be observed that the model overestimates the initial stiffness before sliding occurs. However, as the horizontal displacement increases, it accurately predicts the stiffness and the load resistance. All the dowel bars fracture at a horizontal displacement of 1.70 in. This is in good agreement with the test observation, in which the dowel bars started to fracture at 1.60 in.

The failure mode is horizontal shear sliding, as shown in Figure 10.8. The angle of kink of the dowel bars at fracture is 32 degrees. The angle measured in the test was 42 degrees.

Figure 10.9 presents the load-vs.-displacement curves obtained for shear key 7B from the analysis and the test. In the analysis without bond breaker, the peak load occurs when the shear key starts to slide at about 0.16 in. displacement, due to the cohesive and frictional forces developing in the construction joint. At this same displacement, the analysis with bond breaker predicts a much lower resistance, which is provided by the friction and the dowel force. As shown in Figure 10.9, the peak load resistance observed in the test is close to the average of the values obtained at the same displacement in the two analyses. After the cohesive strength has diminished, a load drop is observed in the analysis without bond breaker. At the point of bar fracture, the two analyses predict almost the same load resistance, which is also in agreement with the test result. The first bar fracture observed in the test occurred at a displacement of 1.56 in., while in the analyses all the bars fracture at displacements between 1.70 and 1.80 in. Finally, the damage of the concrete at the free end of the specimen is also reproduced in the analysis without bond breaker, and can be seen in Figure 10.10a. Figure 10.10b shows the deformed mesh at the end of the analysis with bond breaker. Figure 10.10c shows the sliding of the shear key and damage in the stem wall at the end of the test. The angle of kink of the dowel bars right before fracture is 32 degrees for both analyses, while in the test it was measured to be 42 degrees.

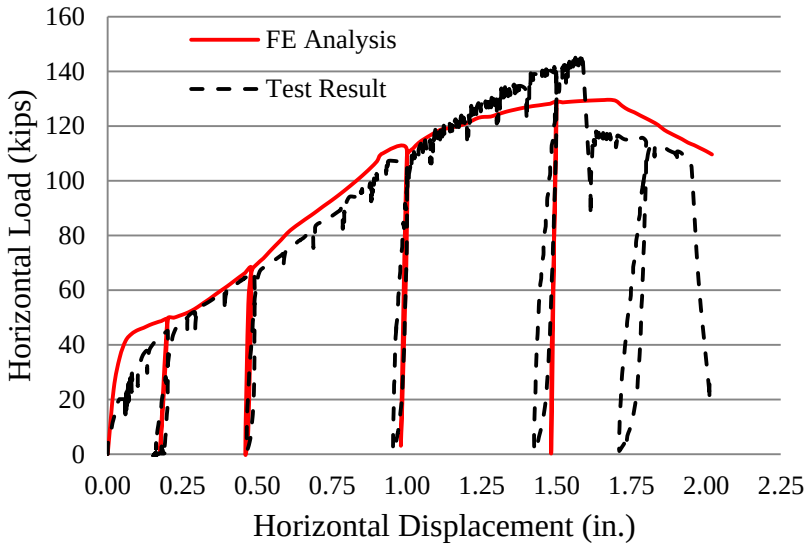

Figure 10.7 Numerical and experimental horizontal load-vs.-horizontal displacement curves for shear key 7A

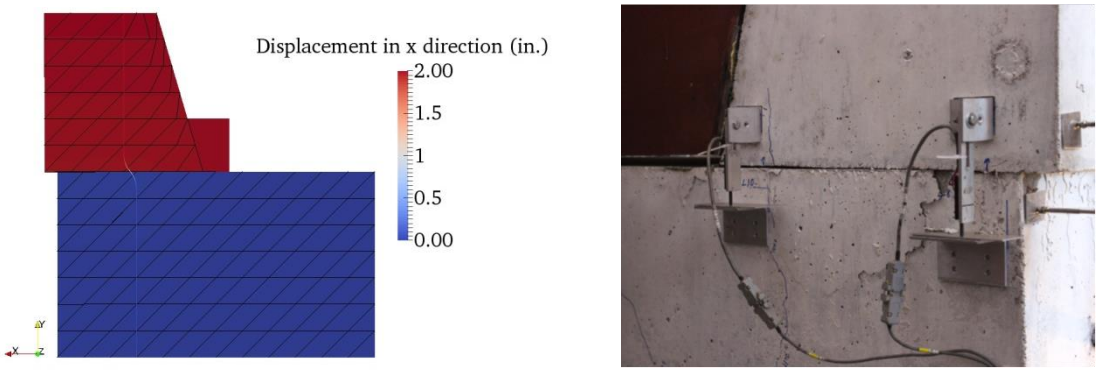

a) b)

Figure 10.8 Sliding of shear key 7A at the end of: a) the FE analysis; b) the test

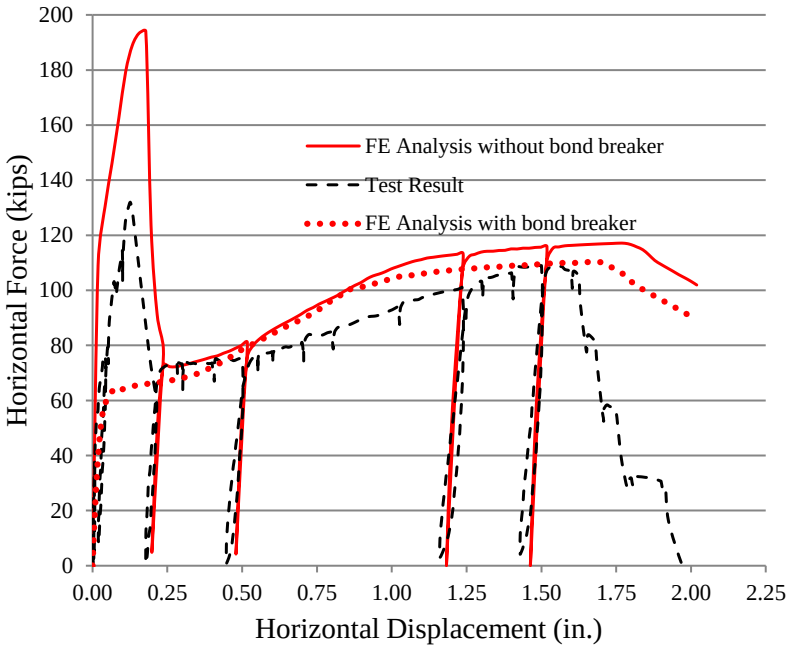

Figure 10.9 Numerical and experimental horizontal load-vs.-horizontal displacement curves for shear key 7B

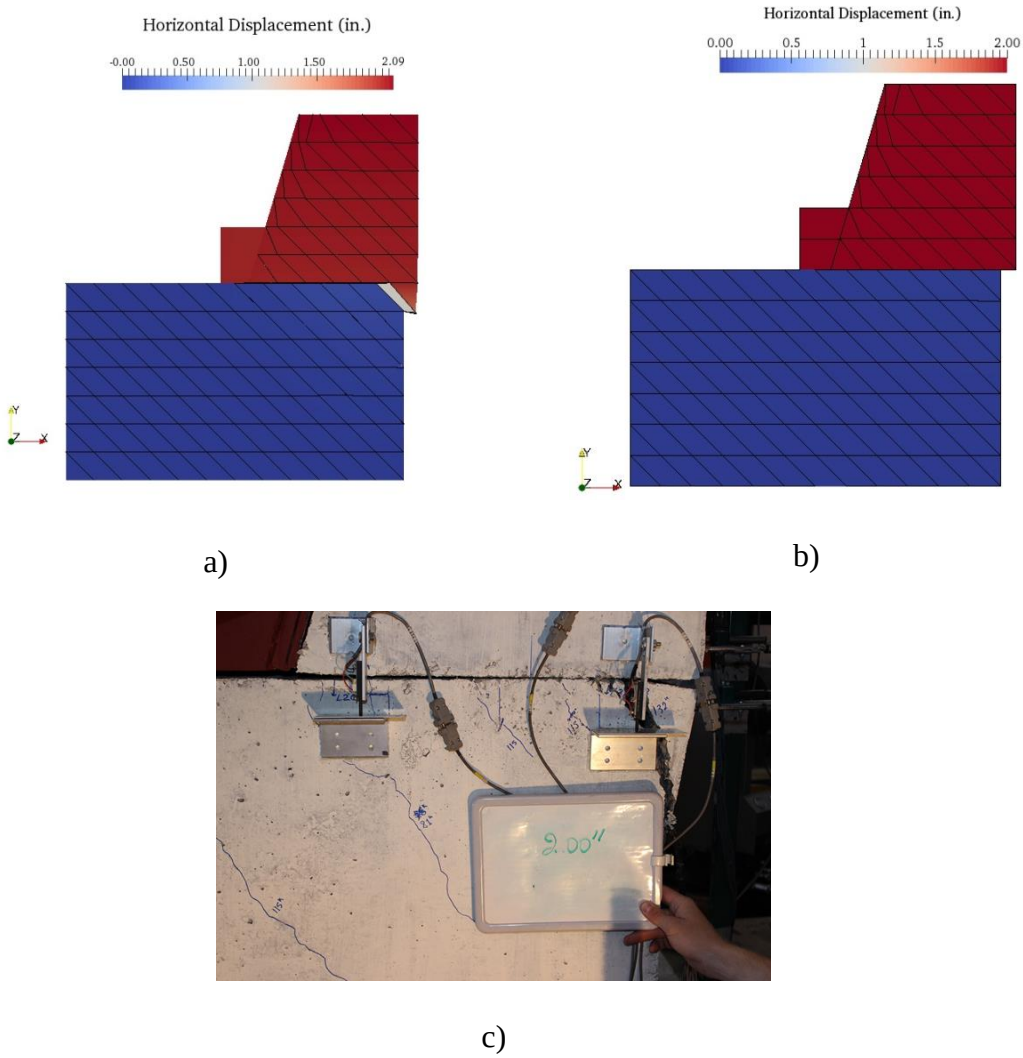

a) b)

c)

Figure 10.10 Sliding of shear key 7B: a) at the end of the FE analysis without bond breaker; b) at the end of the FE analysis with bond breaker; c) at the end of the test

10.2.2 Modeling of Diagonal Shear Failure of Stem Wall

In this section, Specimen 4 tested by Borzogzadeh et al. (2006) is considered. As shown in Chapter 2, shear key 4A was monolithically connected to the stem wall and failed with a diagonal shear crack developed in the stem wall. Shear key 4B was isolated from the stem wall with a rough construction joint. In spite of the construction joint, the

failure mechanism was the same as that for shear key 4A. The two specimens had the same amount and arrangement of horizontal and vertical reinforcement. Thus, almost identical behavior was observed for the two tests.

Since shear keys 4A and 4B had almost identical behavior, only shear key 4B is analyzed here. The shear key was reinforced with 4 rows of vertical dowel bars along its width. Each row consisted of 3 No. 3 U-shaped reinforcing bars, as shown in Figure 10.11. In shear key 4B, the vertical side reinforcement of the stem wall did not continue into the shear key. The mesh used for this shear key is shown in Figure 10.12.

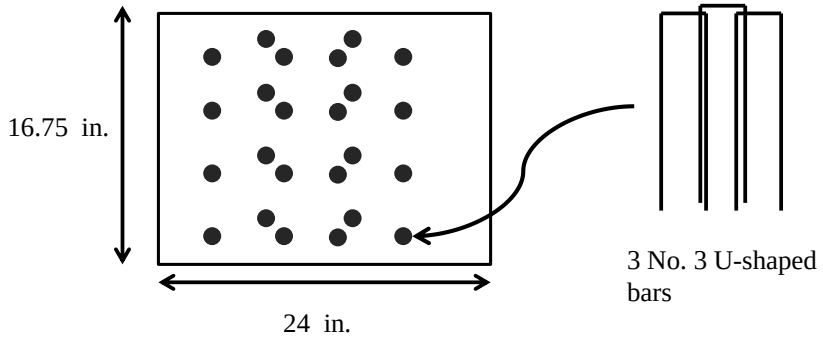

Figure 10.11 Plan view of the construction joint of shear key 4B

Only one-fourth of the width of the specimen (4.2 in.) is modeled with one layer of elements in the *z* direction, as shown in Figure 10.12. The model has fixed boundary conditions at its base and is also prevented from moving in the horizontal direction at the end of the stem wall away from the shear key. The elements have a size of 4.0 in. along the *x* and *y* directions. Their size allows the appropriate positioning of the vertical and horizontal reinforcing bars. A block of elastic solid elements is modeled to simulate the loading beam used in the tests to apply the displacement. Between the inclined face of the shear key and the loading block, zero-thickness, cohesive crack interface elements with

zero tensile strength and zero friction are placed, to provide the contact condition. As in the isolated shear keys analyses, the loading block is prevented from moving in the vertical direction.

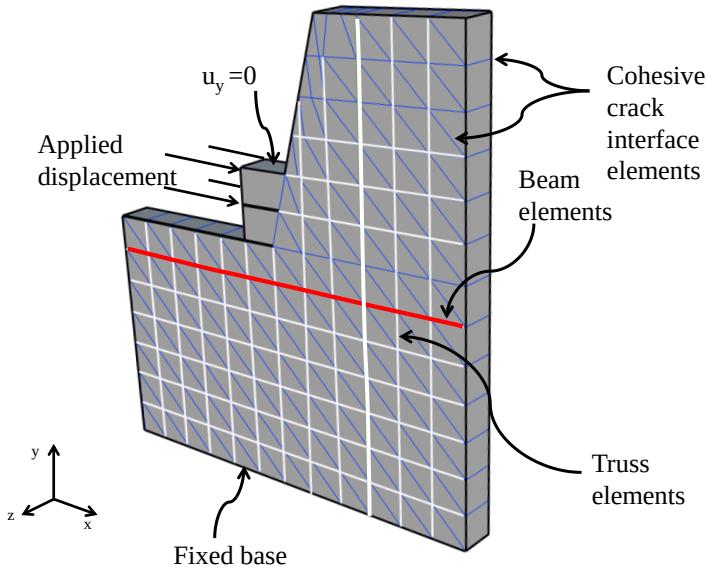

Figure 10.12 Finite element model for shear key 4B

Quadrilateral solid elements are used to represent concrete, which are separated by cohesive crack interface elements to allow the simulation of horizontal cracks and diagonal cracks at 45 degrees. The material parameters used for the cohesive interface elements are shown in Table 10.9 and Table 10.10. The concrete model of Moharrami and Koutromanos (2016) is used to simulate the behavior of solid elements. The values of parameters used for the concrete model, as defined in Moharrami and Koutromanos (2016), are shown in Table 10.1 and Table 10.11.

Table 10.9 Cohesive crack model parameters for shear key 4B, part I

Type of Interface	D_{nn} (ksi/in.)	D_{tt} (ksi/in.)	s_o (ksi)	r_o (ksi)	r_r (ksi)	μ_o	μ_r
Construction Joint 4B	5000	10000	0.5	0.5	0.01	1.0	0.7
Shear Key and Stem Wall	5000	10000	0.5	0.5	0.01	1.4	1.0

Table 10.10 Cohesive crack model parameters for shear key 4B, part II

Type of Interface	$\zeta_{dil,o}$	$\zeta_{dil,r}$	d_o	α (in./kip)	β (in./kip)	G_f^I (kip/in.)	η
Construction Joint 4B	0.3	0.01	0.05	100	100	0.0006	300
Shear Key and Stem Wall	0.7	0.1	0.05	100	100	0.0006	300

Table 10.11 Material properties for concrete model used for shear key 4B

f_c' (ksi)	s_0 (ksi)	g_c (ksi)
5.0	0.5	0.015

The horizontal shear reinforcement of the stem wall is modeled with beam elements, which are connected to the solid elements through the dowel action/bond-slip interface elements presented in Chapter 9. The beam element size used is $0.50d_{b.}$ Finally, the side reinforcement and the vertical dowel bars are modeled with truss elements. The Dodd and Restrepo-Posada (1995) model is used to describe the behavior of the truss and beams elements. For the beam elements, geometric nonlinearity is included. The steel model was modified as follows to account for the fracture of the dowel bars. When the strain at which fracture is considered to occur, ε_f , is reached, the tensile stress drops to a residual value which is set equal to 10% of the tensile strength. The values of the material parameters for steel are shown in Table 10.12.

Table 10.12 Parameters of steel model for shear key 4B

E (ksi)	f_y (ksi)	f_{su} (ksi)	ε_f
29,000	68.0	105.0	0.20

The deformed mesh at the end of the analysis is shown in Figure 10.13a, and it compares well with the specimen damage and deformation observed in the test, as shown in Figure 10.13b. It can be observed that both in the analysis and the test, a diagonal crack formed at the toe of the shear key and propagated diagonally towards the toe of the stem wall. The load-vs.-displacement curve obtained in the analysis also matches the test result well, as shown in Figure 10.14, except that it shows a more drastic load drop at a displacement of 2.15 in. This is caused by the fracture of the horizontal shear reinforcement of the stem wall. This also occurred in the test.

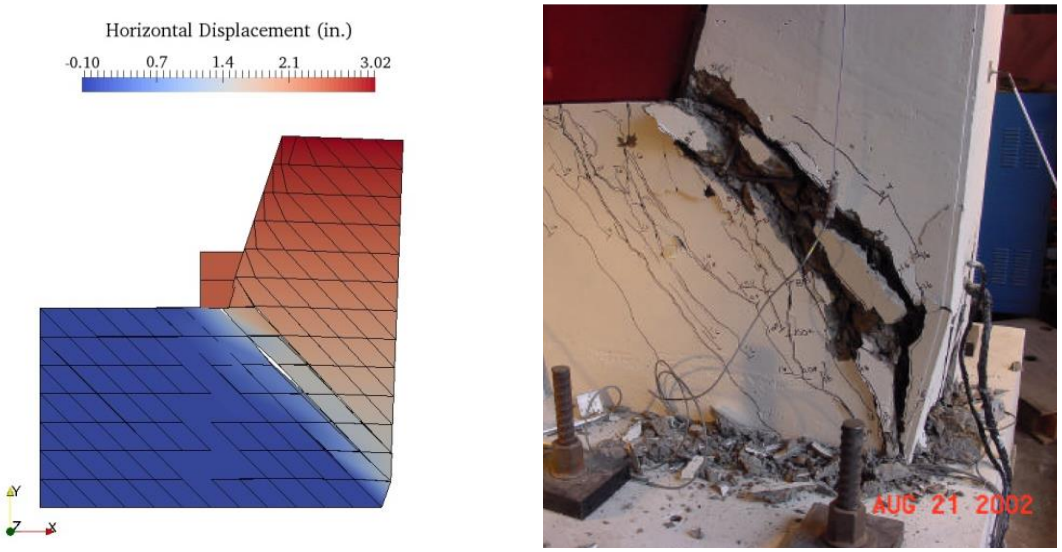

a) b)

Figure 10.13 Deformation of shear key 4B: a) at the end of the FE analysis; b) at the end of the test (from Borzogzadeh et al., 2006)

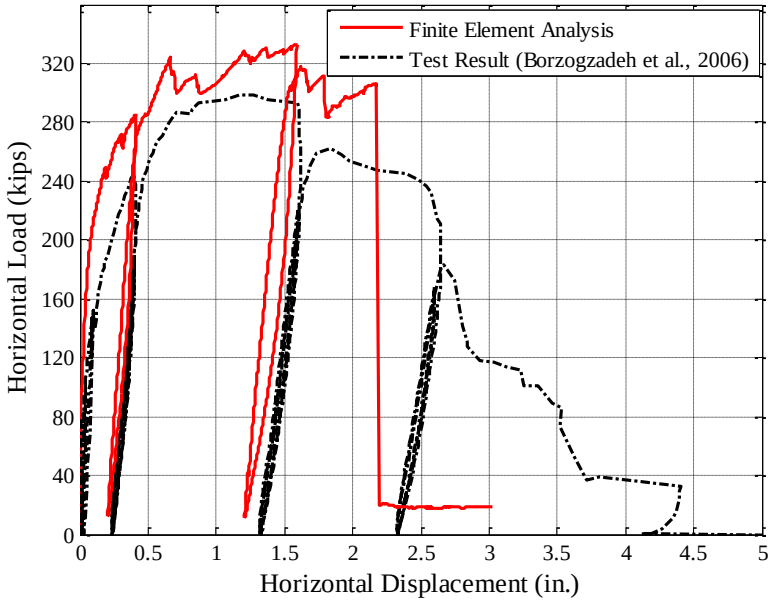

Figure 10.14 Numerical and experimental horizontal load-vs.-horizontal displacement curves for shear key 4B

10.2.3 Horizontal Shear Failure of Monolithic Shear Keys

The analysis of Specimens 8 and 10, whose tests are described in Chapter 6, are presented in this section. Each of the specimens had two shear keys. One shear key had an inclined face and in the other had a vertical on the loading side. The symmetry of the specimen geometry, reinforcement layout, and loading conditions allows the modeling of only one half of the width of the specimen (8.4 in.), as shown in Figure 10.15. The model has fixed boundary conditions in its base and is prevented from moving in the horizontal direction at the end of the stem wall away from the shear key. Quadrilateral solid elements are used to represent concrete. To better capture the multiple cracks observed in the tests of the shear keys, the mesh is refined as compared to the previous analyses. Thus, the element size in the *x* direction is reduced to 2 in., while in the *y* direction it

remains at 2 in. Two layers of elements of 4.2 in. length are used in the *z* direction. The solid elements are separated by cohesive crack interface elements to allow the simulation of horizontal cracks and diagonal cracks, assumed to be at 45 degrees. The horizontal displacement is applied to a block of elastic solid elements, which is prevented from moving in the vertical direction. For the shear keys with an inclined face, the interface between the loading block and the shear key has zero cohesive strength and zero friction coefficient, and for the shear keys with a vertical surface, the interface is assumed to have a friction coefficient of 0.15. This is in agreement with the experimental observations obtained in Chapter 6.

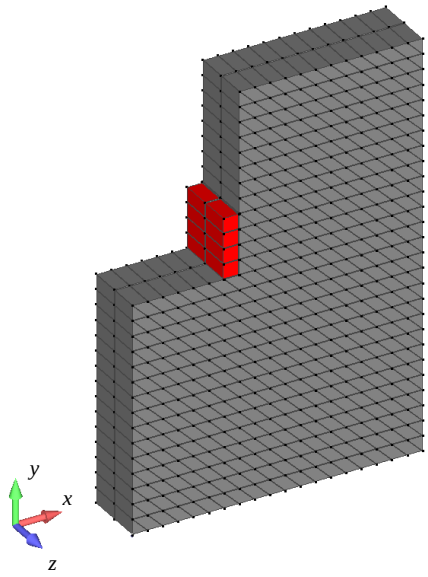

Figure 10.15 Finite element model for a monolithic shear key

To simulate the dowel action, the vertical dowel bars are modeled with beam elements and they are connected to the concrete solid elements with dowel action/bond-slip interface elements. The modified Dodd and Retrepo-Posada (1995) model is used to model the steel. The length of the steel elements is $0.5d_b$. The reinforcing bars that did

not cross the construction joint are not expected to contribute to the horizontal shear resistance of the shear keys, and they are modeled with elastoplastic truss elements, with a 2% strain hardening slope.

Shear Keys 8A and 8B

In this section, the model shown in Figure 10.15 is used for the analysis of shear keys 8A and 8B. Both shear keys were cast together with the stem wall. One shear key had a vertical face on the loading side, while the other had an inclined face. Six No. 3 vertical side reinforcement bars continued from the shear keys into the stem wall. The horizontal shear reinforcement of the stem wall consisted of 8 No. 8 bars placed in two rows. A detailed description of the specimen can be found in Chapter 6.

The values of the material parameters used for the solid elements, cohesive crack interface elements, and beam elements are summarized in Table 10.13 through Table 10.15. The truss elements used have a modulus of elasticity of 29,000 ksi, the yield strength is equal to 68 ksi, and have a strain hardening slope of 2% of initial modulus of elasticity. For all the analyses, the energy for Mode-II fracture is taken to be 10 times that of Mode-I.

Table 10.13 Cohesive crack model parameters for shear keys 8A and 8B

D_{nn} (ksi/in.)	5000	$\zeta_{dil,o}$	0.70
$D_{tt,}=D_{ss}$(ksi/in.)	10000	$\zeta_{dil,r}$	0.001
s_o (ksi)	0.47	d_o (in.)	0.25
r_o (ksi)	0.5	α (in./kip)	100
r_r (ksi)	0.01	β (in./kip)	100
μ_o	1.5	G_f^I (kip / in.)	0.0007
μ_r	1.0	η	300

Table 10.14 Concrete model parameters for shear keys 8A and 8B

f_c' (ksi)	s_0 (ksi)	g_c (ksi)
4.7	0.47	0.035

Table 10.15 Beam model parameters for shear keys 8A and 8B

E (ksi)	f_y (ksi)	f_{su} (ksi)	ε_f
29,000	67.0	104.0	0.20

In the test, shear keys 8A and 8B initially rotated about the free end of the specimen. Small cracks initiated below the shear keys and propagated diagonally. However, when loading continued, horizontal cracks developed right above the shear reinforcement of the stem wall. After severe horizontal cracks developed, the shear keys started to slide. This behavior is captured in the analyses. Figure 10.16 shows the deformed meshes for the shear keys at the peak load, and Figure 10.17 shows the deformed meshes at the end of the analyses.

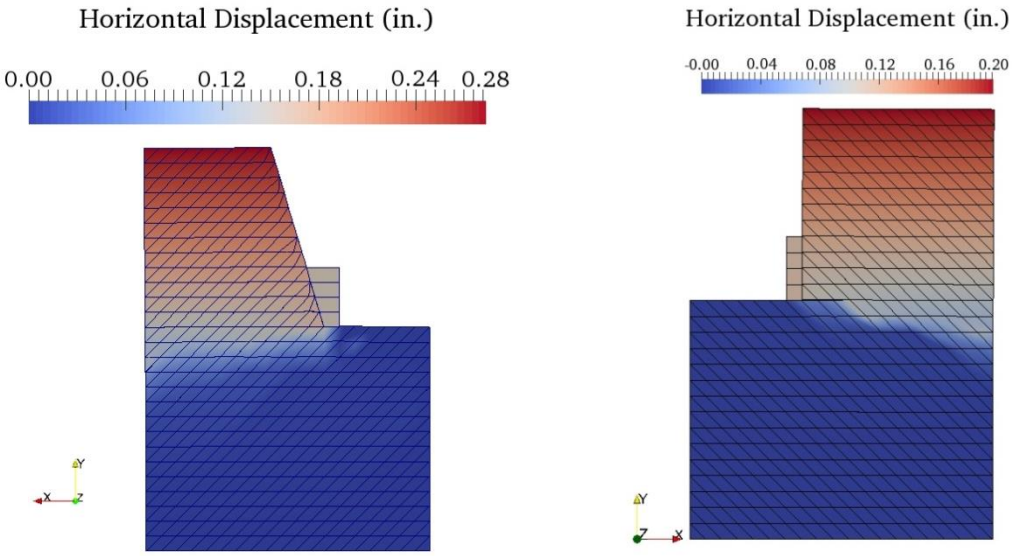

a) b)

Figure 10.16 Deformed mesh at peak load resistance: a) shear key 8A; b) shear key 8B

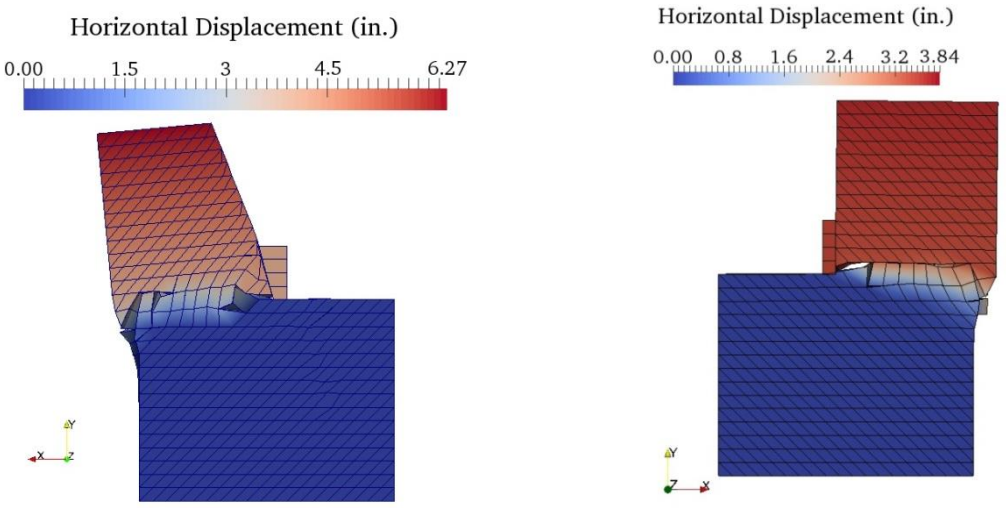

a) b)

Figure 10.17 Deformed mesh at the end of the analysis: a) shear key 8A; b) shear key 8B

The numerical load-vs.-displacement curves from the analyses are compared to the experimental results in Figure 10.18 and Figure 10.19. It can be observed that for both shear keys, the peak load obtained in the analysis is within 10% of the measured. However, for shear key 8A, the initial stiffness is overestimated.

Since only half of the width of the specimen is modeled, due to the symmetry of the specimen, vertical bar fracture occurs two at a time in the analysis. In the case of shear key 8A, vertical dowel bars fractured at 0.65 in. displacement and at 2.20 in. displacement. In the analysis of shear key 8B, fracture of vertical bars is observed at displacements of 0.40 in., 0.80 in. and 1.0 in. In the test of shear key 8A, fracture of vertical dowel bars was observed at displacements of 1.20 in., 2.70 in. and 3.60 in. and in the test of shear key 8B, it was observed at displacements of 0.56 in., 1.80 in., 2.25 in. and 2.90 in., one bar at a time. In the analysis, fracture of the vertical bars is considered

to occur when all the fibers in a section of the beam element have reached the fracture strain, ε_f. In the vertical bars that have not fractured, most of the fibers have reached ε_f.

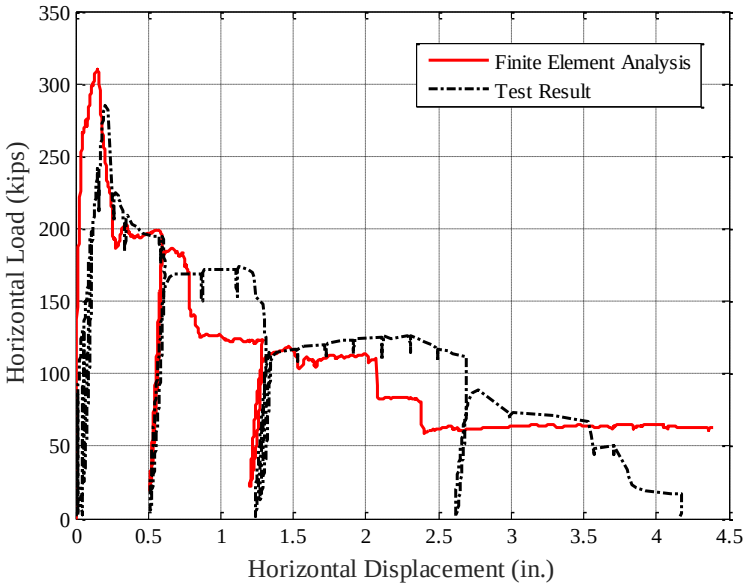

Figure 10.18 Comparison of experimental and numerical load-vs.-displacement curves for shear key 8A

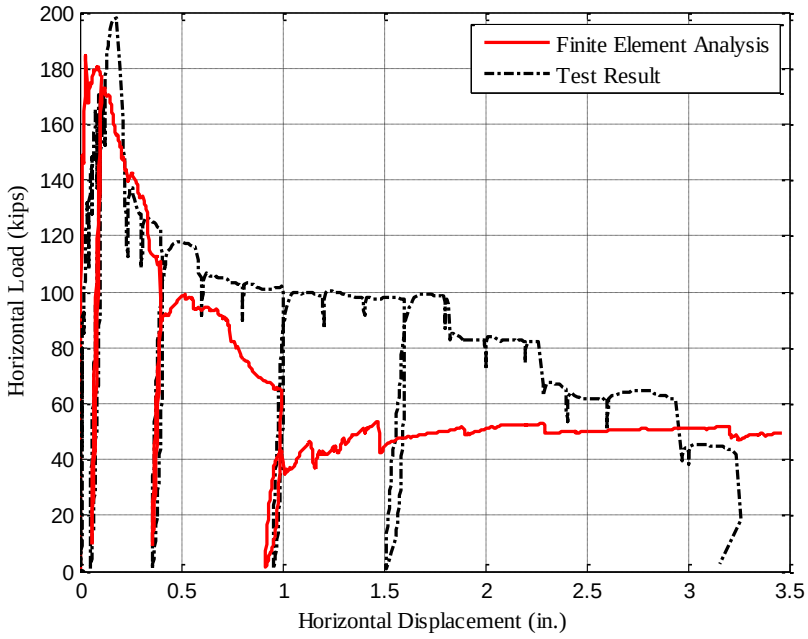

Figure 10.19 Comparison of experimental and numerical load-vs.-displacement curves for shear key 8B

Shear Keys 10A and 10B

In this section, the analysis of Specimen 10, consisting of shear keys 10A and 10B, is presented. Shear key 10A had an inclined face and shear key 10B had a vertical one. The shear keys were cast together with the stem wall and had the same amounts of vertical and horizontal reinforcing bars as shear keys 8A and 8B. The only difference was that the shear keys in Specimen 10 had a higher concrete strength.

The values of the material parameters for the cohesive crack interfaces, the beam elements, and the solid elements are presented in Table 10.16 through Table 10.18. For the truss elements, the yield strength assumed is 68 ksi and the modulus of elasticity is 29,000 ksi with a 2% strain hardening slope.

Table 10.16 Cohesive crack model parameters for shear keys 10A and 10B

D_{nn} (ksi/in.)	5000	$\zeta_{dil,o}$	0.70
D_{tt} =D_{ss} (ksi/in.)	10000	$\zeta_{dil,r}$	0.001
s_o (ksi)	0.67	d_o (in.)	0.25
r_o (ksi)	0.5	α (in./kip)	100
r_r (ksi)	0.01	β (in./kip)	100
μ_o	1.5	G_f^I (kip / in.)	0.0007
μ_r	1.0	η	300

Table 10.17 Concrete model parameters for shear keys 10A and 10B

f_c' (ksi)	s_0 (ksi)	g_c (ksi)
6.74	0.67	0.035

Table 10.18 Beam model parameters for shear keys 10A and 10B

E (ksi)	f_y (ksi)	f_{su} (ksi)	ε_f
29,000	67.0	104.0	0.20

In an early stage during the tests of shear keys 10A and 10B, the shear keys rotated about their toes at the free end of the specimen. Many diagonal cracks formed below the shear keys. After the maximum load was reached, a horizontal sliding plane formed above the horizontal shear reinforcement of the stem wall, and the shear keys started to slide. This behavior is well captured by the numerical analysis. The deformed meshes of the shear keys at the peak load are shown in Figure 10.20 and at the end of the analyses in Figure 10.21.

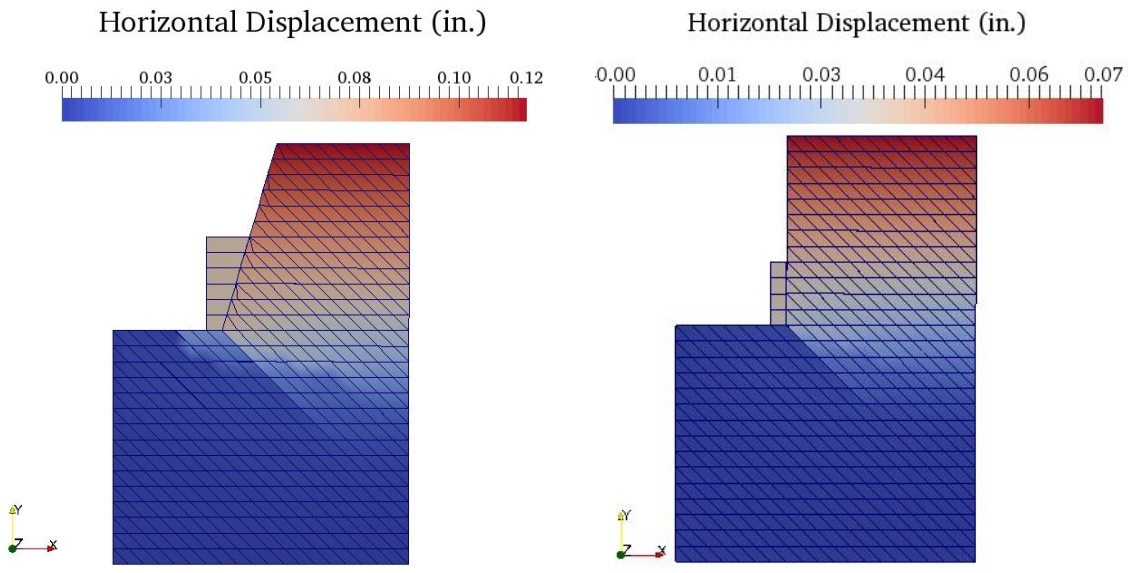

a) b)

Figure 10.20 Deformed mesh at peak load resistance: a) shear key 10A; b) shear key 10B

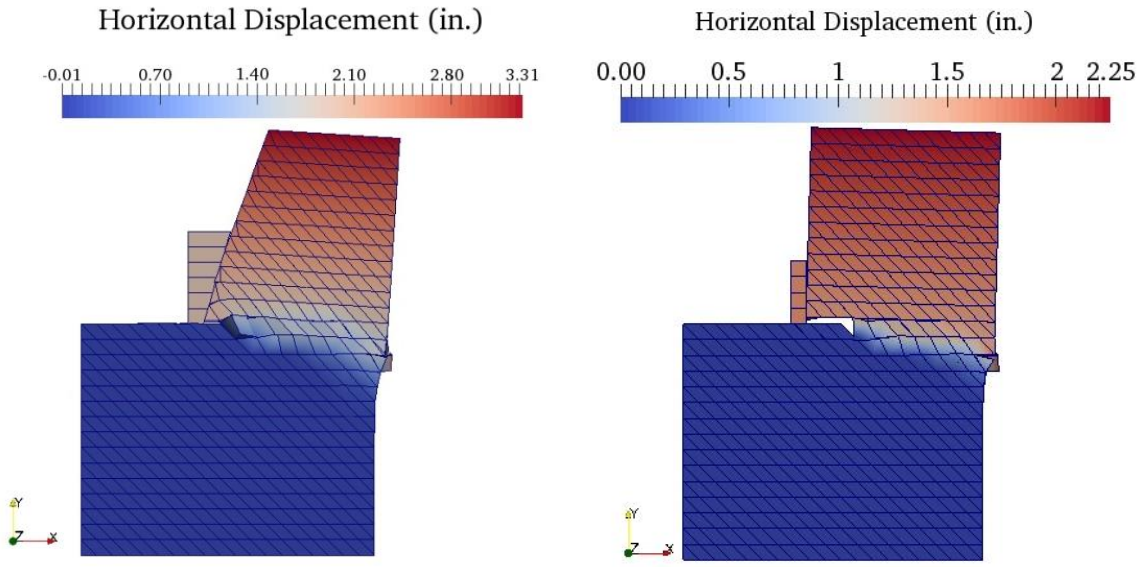

a) b)

Figure 10.21 Deformed mesh at the end of the analysis: a) shear key 10A; b) shear key 10B

The numerical and experimental load-vs.-displacement curves are shown in Figure 10.22 and Figure 10.23. The load capacity of shear key 10A is accurately

predicted, while that of shear key 10B is underestimated in the FE analysis by about 15%. Since only one half of the specimen is modeled, due to the symmetry of the specimen about the middle plane, vertical bar fracture occurs two at a time. In the analysis of shear key 10A, vertical dowel bars located close to the loaded end of the shear key fracture at a displacement of 0.70 in. and at 1.70 in. In the analysis of shear key 10B, the vertical dowel bars fracture at displacements of 0.20 in., 0.70 in. and 1.30 in. In the test of shear key 10A, all the vertical dowel bars fractured at displacements of 0.70 in., 1.30 in., 1.60 in., 1.70 in., 2.0 in. and 3.25 in. In the test of shear key 10B, all the bars fractured, occurring at displacements of 0.30 in., 0.50 in. (two bars), 0.8 in., 0.9 in., and 1.0 in.

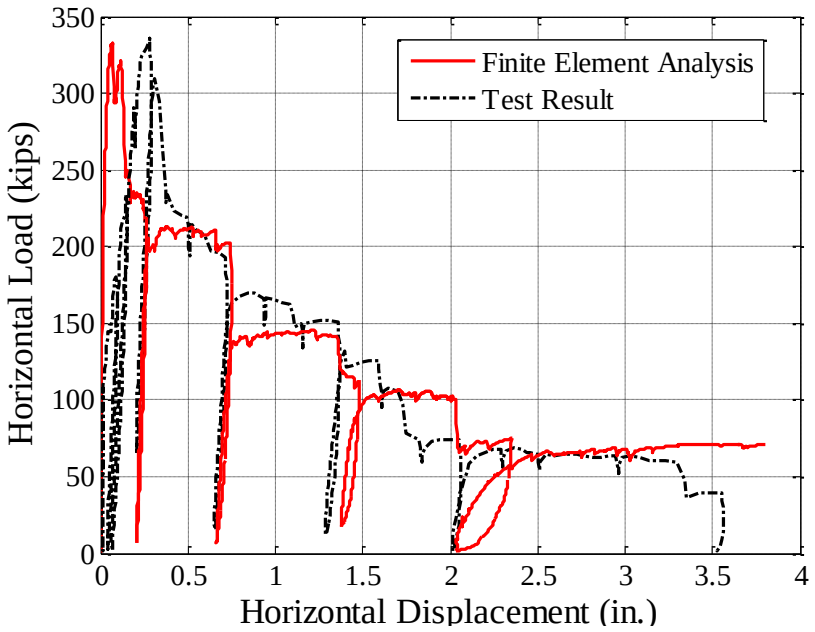

Figure 10.22 Comparison of experimental and numerical load-vs.-displacement curves for shear key 10A

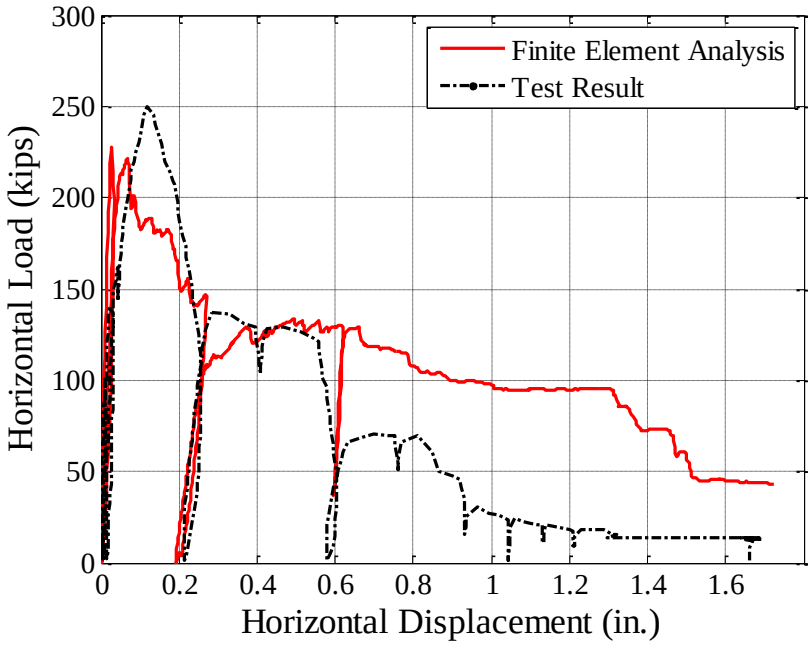

Figure 10.23 Comparison of experimental and numerical load-vs.-displacement curves for shear key 10B

10.3 Finite Element Analysis of Skewed Shear Keys

To simulate the behavior of the skewed shear key 12A, whose test results are presented in Chapter 8, the three-dimensional model shown in Figure 10.24 is used. The meshing scheme used is different than that for the shear keys described in Section 10.2, due to the more complex geometry and loading conditions.

As shown in Figure 10.24a, the longitudinal axis of the stem wall is oriented in the *x*-*z* plane. The nodes at the bottom of the stem wall are fixed from translations and rotations. The nodes of the stem wall away from the shear key are prevented from moving in the *x* and *z* directions. The displacement is applied in the *x* direction and the loading block is prevented from moving in the *y* and *z* directions. As in the previous

simulations, cohesive crack interface elements are placed between the vertical face of the shear key and the block of elastic solid elements to simulate the contact conditions. The interfaces have zero cohesive strength and the friction coefficient used is 0.15.

Concrete is modeled with quadrilateral solid elements. The element size along the direction of the stem wall is 2.4 in., in the *z* direction it is 3.75 in., and in the *y* direction it is 2 in. The dimensions of the concrete elements are selected to allow the proper positioning of the vertical and horizontal reinforcing bars, while their shape is to facilitate the connection of concrete and steel with the dowel action and bond-slip interface element presented in Chapter 9. Between the solid elements, cohesive crack interface elements are used to simulate cracks in the horizontal and vertical directions. It should be noted that one cohesive crack interface element is placed every two solid elements, in each direction.

The material model used for the 6 No. 3 vertical dowel bars is the modified Dodd and Restrepo-Posada (1995) which accounts for the bar fracture when the tensile strain reaches the value ε_f, as discussed in the previous section. The vertical dowel bars are modeled with beam elements, whose length is $0.5d_b$. The bars that do not cross the construction joint are not expected to contribute to the resistance of the shear key. They are modeled with elastoplastic truss elements with a 2% strain hardening slope. The yield strength of the truss elements is 68 ksi and the modulus of elasticity is 29,000 ksi.

To facilitate the presentation and comparison of this shear key with the test results presented in Chapter 8, the two sides of the shear key will be referred to as the “northwest side” and the “southeast side”, as shown in Figure 10.24a.

The values of the material parameters used for the beam elements, the solid concrete elements, and the cohesive crack interface model are presented in Table 10.19 through Table 10.21, and are based on the measured properties presented in Chapter 8.

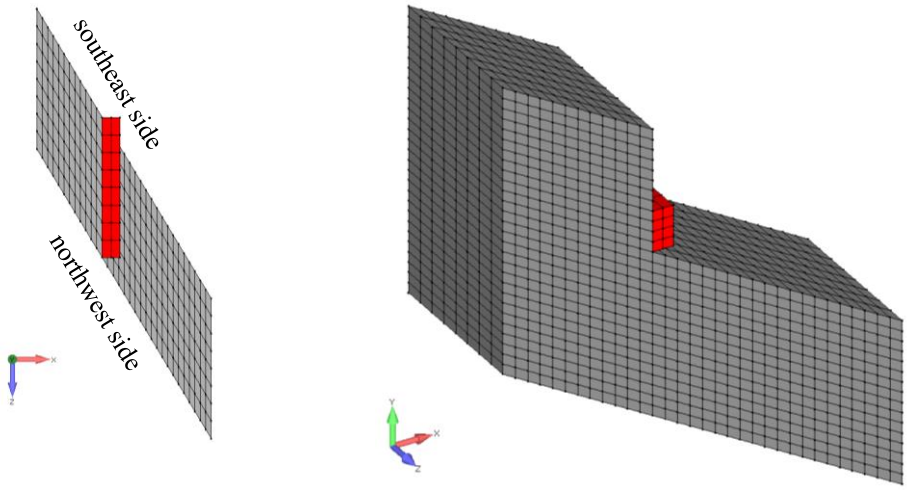

a) b)

Figure 10.24 Finite element mesh for a skewed monolithic shear key: a) plan view; b) northwest side view

Table 10.19 Cohesive crack model parameters for shear key 12A

D_{nn} (ksi/in.)	5000	$\zeta_{dil,o}$	0.70
D_{tt} =D_{ss} (ksi/in.)	10000	$\zeta_{dil,r}$	0.001
s_o (ksi)	0.6	d_o (in.)	0.25
r_o (ksi)	0.5	α (in./kip)	100
r_r (ksi)	0.01	β (in./kip)	100
μ_o	1.5	G_f^I (kip / in.)	0.0007
μ_r	1.0	η	300

Table 10.20 Concrete model parameters for shear key 12A

f_c' (ksi)	s_0 (ksi)	g_c (ksi)
6.00	0.6	0.035

Table 10.21 Beam model parameters for shear key 12A

E (ksi)	f_y (ksi)	f_{su} (ksi)	ε_f
29,000	66.0	93.0	0.20

The numerical results obtained closely match the experimental results presented in Chapter 8. The shear key deformation observed at the end of the analysis is shown in Figure 10.25 and Figure 10.26, respectively. Figure 10.25 shows the displacement in the *x* direction for the two sides of the shear key, while Figure 10.26 shows the displacement in the *z* direction. Initially, the shear key rotated about an axis perpendicular to *x*-*z* plane similar to what was observed in the test. As the analysis progressed, the damage of the specimen concentrated in the region above the horizontal shear reinforcement of the stem wall.

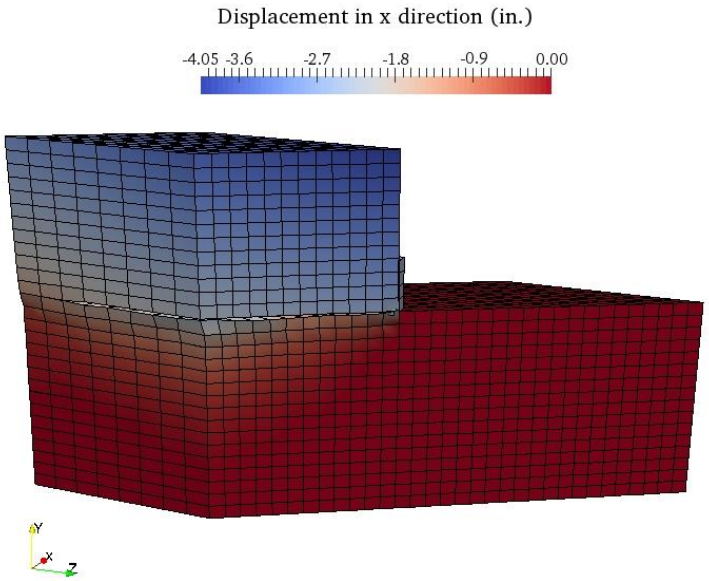

a)

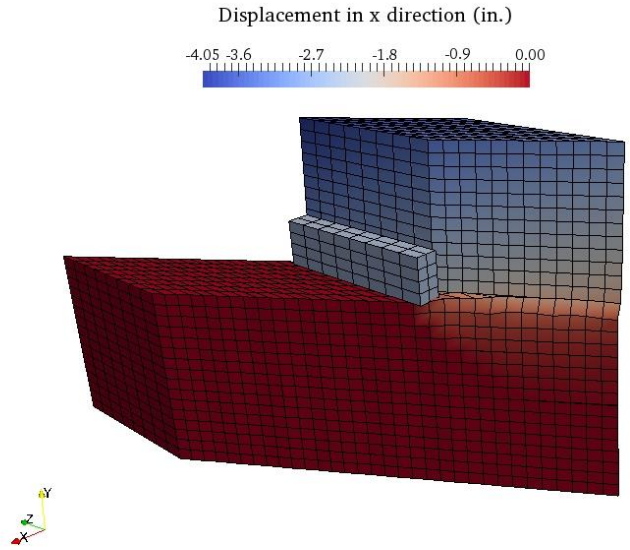

b)

Figure 10.25 Displacement in *x* direction at the end of the analysis of shear key 12A: a) northwest side; b) southeast side;

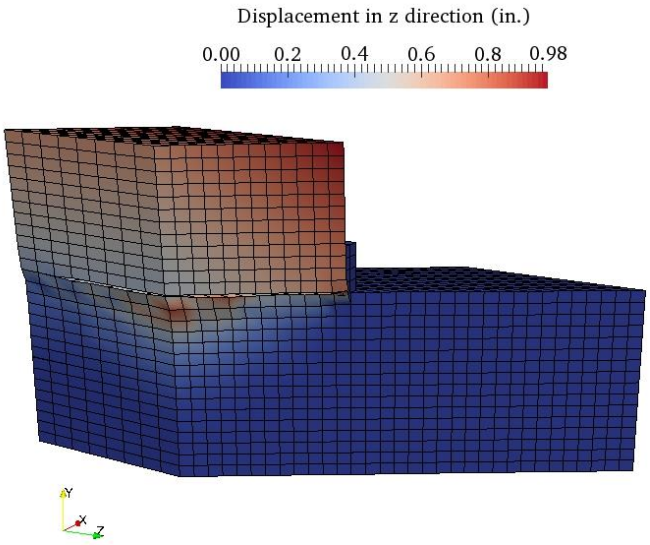

a)

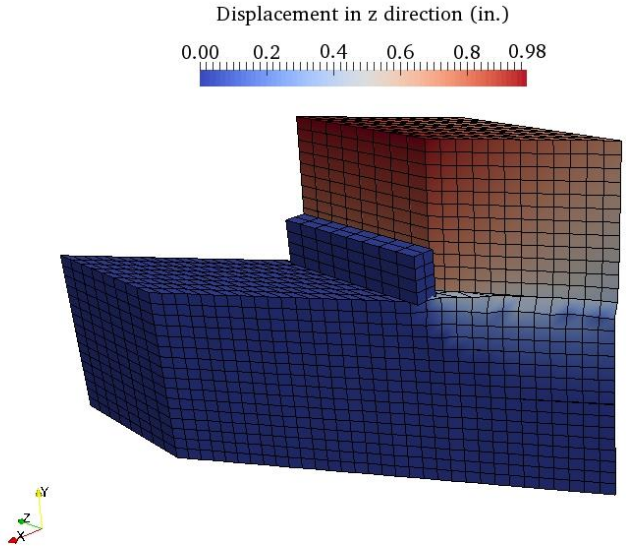

b)

Figure 10.26 Displacement in *z* direction at the end of the analysis of shear key 12A: a) northwest side; b) southeast side

The horizontal load-vs.-horizontal displacement curve in the *x* direction obtained form the analysis is compared to that from the test in Figure 10.27. The displacement plotted is the average of the numerical values registered at the same locations as the string potentiometers SP5 and SP6 shown in Chapter 8. At the end of the analysis, four of the bars located on the southeast side and close to the loaded end of the shear key fractured. The fracture of the bars occurred between 1.70 and 1.75 in. In the test one dowel bar fractured at a displacement of 2.0 in. The bar was located on the southeast side and was close to the location of the load application.

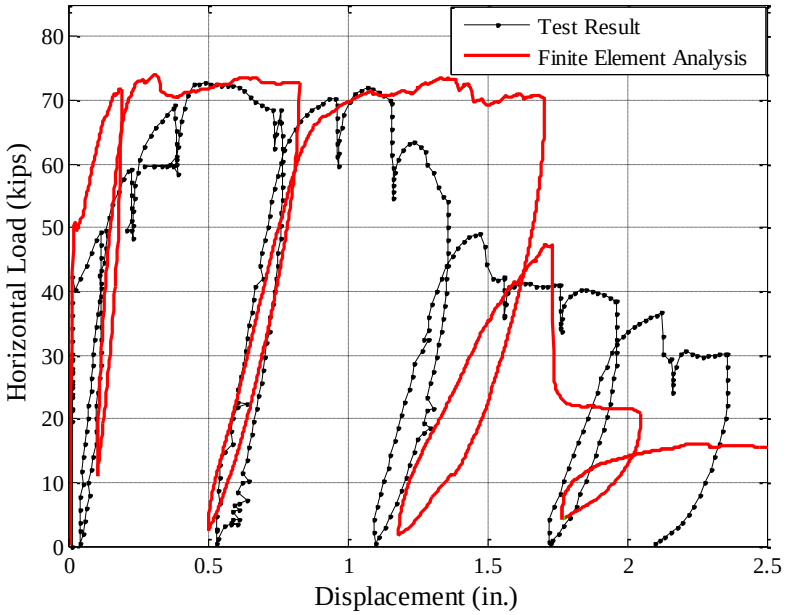

Figure 10.27 Comparison of experimental and numerical load-vs.-displacement curves for shear key 12A

10.4 Acknowledgement of Publication

Part of this chapter is a reprint of the material that will appear in a technical report which will be submitted to the California Department of Transportation in 2016, Kottari,

A., P. B. Shing, J. I. Restrepo, under the title "Design and Capacity Assessment of External Shear Keys in Bridge Abutments". The dissertation author will be the primary investigator and author of this report.

CHAPTER 11

CALCULATION OF LOAD CAPACITY OF SHEAR KEYS IN BRIDGE ABUTMENTS

11.1 Introduction

It has been shown in this and prior studies that the failure mechanisms of shear keys in bridge abutments can vary significantly depending on the reinforcement and construction details, as well as the angle of shew of the abutment. As shown in Chapter 5, isolated shear keys can fail by horizontal shear sliding along the construction joint when the stem wall is adequately reinforced to resist the shear force transmitted by the shear keys. The tests reported in Chapter 6 have shown that a monolithic shear key can fail with the formation of a horizontal crack in the stem wall right above the horizontal shear reinforcement, when the amount of the vertical bars connecting the shear key to the stem wall is sufficiently small. Nevertheless, as shown in past experimental studies, diagonal shear failure could occur in the stem wall if the wall does not have a sufficient amount of horizontal shear reinforcement.

To have shear keys effectively function as structural fuse and develop the desired failure mechanism that will minimize the repair cost in the event of a major earthquake, it is important to have reliable analytical methods to calculate the resistance of shear keys associated with any of the aforementioned failure mechanisms. This chapter presents

these analytical methods and their validation with test data. Some of the methods have been presented in the previous chapters for the pre-test analyses, and some have been developed based the new experimental data acquired in this study.

11.2 Shear Keys in Non-Skewed Abutment Walls

11.2.1 Shear Resistance of Stem Wall

The diagonal shear strength of a stem wall can be calculated from the analytical method presented in Section 5.3.1. This method is based on the equilibrium of the forces in the free-body diagram shown in Figure 11.1, and has been validated with the experimental results from shear keys 1A and 2A, tested by Megally et al. (2002), and shear keys 4A and 4B, tested by Borzogzadeh et al. (2006). These tests are summarized in Chapter 2.

When the shear capacity of the stem wall has been reached, it is assumed that the horizontal shear reinforcement in the wall has reached the ultimate tensile strength, f_{su}, while the rest of the reinforcement in the wall has reached the yield strength, f_y. It should be noted that the horizontal shear reinforcement referred to here is the reinforcement placed near the top of the stem wall to provide the necessary shear strength in addition to the normal side reinforcement in the wall. These bars can be distributed across the wall width in two or more layers. Thus, the axial forces in the reinforcing bars are as follows:

$$\begin{aligned} F_{t,s} &= A_{t,s} \cdot f_{su} \\ F_{i,h} &= A_{i,h} \cdot f_y \\ F_{j,v} &= A_{j,v} \cdot f_y \end{aligned} \tag{11.1}$$

in which $F_{t,s}$ is the tensile force developed by the horizontal shear reinforcing bar *t* in the stem wall, $A_{t,s}$ is the cross-sectional area of bar *t*, and $F_{i,h}$ and $F_{j,v}$ are the tensile forces in the horizontal reinforcing bar *i* and vertical reinforcing bar *j*, respectively, whose cross-sectional areas are $A_{i,h}$ and $A_{j,v}$.

The external load applied to the shear key has a horizontal component V_w and a vertical component P_w. If the friction on the inclined face of the shear key is assumed to be zero, the external load has to be perpendicular to the surface, and thus V_w and P_w are related by the following geometric relation:

$$P_w = V_w \cdot \tan\beta \tag{11.2}$$

in which β is the angle of the loaded face of the shear key with respect to a vertical plane. For the tests conducted on shear keys with $\beta = 0$, as reported in Chapter 6, a vertical force that was about 15% of the horizontal force was measured. This was probably caused by the interaction of the lower corner of the shear key with the loading beam as the shear key rotated. Hence, one should assume that the value of $\tan\beta$ be no less than 0.15 as the limiting condition to represent this vertical force.

Normally, the diagonal crack propagating from the toe of the shear key towards the toe of the stem wall is not straight, as shown in Figure 11.1. Observations from the shear key-and-abutment stem wall specimens considered here show that the angle of this diagonal crack is around than 38 degrees with respect to a vertical plane. In Figure 11.1, the part of the shear key and stem wall separated from the rest of the stem wall by a diagonal crack is shown. The crack propagates from the toe of the shear key to point *A*, in

which a region of length α_c is assumed to be in compression. It is assumed that the compressive stress in this region is uniform and reaches the maximum value of 0.85 f_c', similar to a concrete section in bending. The forces developed in the compression region are V_c and C_c, which act in the horizontal and vertical directions, respectively. The vertical force is thus calculated as:

$$C_c = 0.85 \cdot f_c' \cdot d \cdot \alpha_c \tag{11.3}$$

in which *d* is the width of the shear key. Vertical bars located in the compression zone are assumed to have reached their yield strength in compression. These forces are shown in Figure 11.1. The distances *h* and *L* are measured from the point of load application to point *A* in the vertical and horizontal direction, respectively.

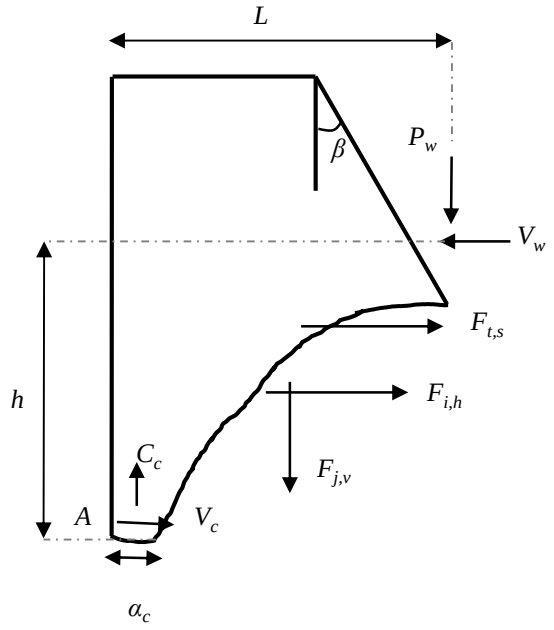

Figure 11.1 Free-body diagram for the calculation for diagonal shear resistance calculation

Based on the free-body diagram in Figure 11.1, the calculation of the diagonal shear resistance of the stem wall, V_w, can be carried out as follows:

1. Determine the elevation of point *A*. It can be assumed to be at the base of the stem wall. If the line from the toe of the shear key to *A* has an angle less than 45 degrees with respect to a vertical plane, assume that the angle of the diagonal crack is 45 degrees and point *A* will be at the intersection of the crack line and the edge of the wall.
2. Assume a compression zone length α_c.
3. Based on the moment equilibrium of the free body about point *A* in Figure 11.1 and Equation (11.2), calculate V_w:

$$V_w = \frac{\sum_{i=1}^{\#hor.\ bars} F_{i,h} \cdot l_{i,h} + \sum_{j=1}^{\#vert.\ bars} F_{j,v} \cdot l_{j,v} - C_c \cdot \alpha_c \cdot 0.5 + \sum_{t=1}^{\#hor.\ shear\ bars} F_{t,s} \cdot l_{t,s}}{h - L \cdot \tan\beta} \qquad (11.4)$$

in which $l_{i,h}$ is the vertical distance of horizontal bar *i* from point *A*, $l_{j,v}$ is the horizontal distance of vertical bar *j* from point *A*, and $l_{t,s}$ is the vertical distance of horizontal shear reinforcing bar *t* in the stem wall from point *A*.

4. Calculate the vertical force P_w:

$$P_w = V_w \cdot \tan\beta$$

5. Check if equilibrium in the vertical direction is satisfied.
6. If equilibrium in the vertical direction is not satisfied, a new compression zone length α_c is selected and steps (2-5) are repeated. If the equilibrium is satisfied, then the procedure can stop and the value of V_w calculated is the final value.

It should be noted that in this method, the value of V_c need not be calculated. For simplicity, the term for C_c in Eq. (11.4) can be ignored and it can be assume that $\alpha_c = 0$. This will avoid iteration in the calculation. As shown in the following examples, this simplification will not affect the results significantly.

Validation with Test Data

To validate this analytical method, shear keys 1A and 2A, tested by Megally et al. (2002), and shear keys 4A and 4B, tested by Borzogzadeh et al. (2006), are considered. The material properties used are based on the measured values reported by Megally et al. (2002) and Borzogzadeh et al. (2006) and are summarized in Table 11.1 and Table 11.2. It should be noted that in shear keys 1A and 2A, No. 3 bars were used for reinforcing the specimen, while for shear keys 4A and 4B, the horizontal shear reinforcement of the stem wall consisted of No. 4 bars, for which the measured material properties were not reported. For these bars, a tensile strength of 105 ksi is assumed for the calculation of the diagonal shear resistance.

The measured and calculated load resistance values are shown in Table 11.3. Two values are reported for the calculated diagonal shear resistance of the stem walls. One is calculated with the aforementioned iterative scheme and the other is calculated without iteration by ignoring the term for C_c in Eq. (11.4) and assuming $\alpha_c = 0$. It can be seen that the method (with or without iterations) is able to predict the diagonal shear resistance of the stem walls well and the influence of the term for C_c is very small. The difference in

percentage between the measured and calculated strengths as shown in the table is calculated with respect to the measured strength and is below 10% for all the cases.

Table 11.1 Measured concrete strengths in ksi for shear keys 1A, 2A, 4A and 4B (from Megally et al. and Borzogzadeh et al.)

Shear Key 1A	Shear Key 2A	Shear Key 4A	Shear Key 4B
4.96	3.11	5.78	5.78

Table 11.2 Measured steel strengths for No. 3 bars in shear keys 1A, 2A, 4A and 4B (from Megally et al. and Borzogzadeh et al.)

	Shear Key 1A	Shear Key 2A	Shear Key 4A	Shear Key 4B
Yield strength (ksi)	65	84	61	61
Tensile strength (ksi)	98	124	not reported	not reported

Table 11.3 Tested and calculated diagonal shear resistances for shear keys 1A, 2A, 4A and 4B

Shear Key	Measured Resistance (kips)	Calculated Resistance (kips)	Difference
1A	222	205/207*	-8% / -7%*
2A	158	151/160*	-4% / +1%*
4A	329	324/333*	-2% /+1%*
4B	299	289/297*	-3% / -0.5%*

*Calculated without iteration

11.2.2 Sliding Shear Resistance of Isolated Shear Keys

For the design of isolated shear keys, two shear resistance values are important to consider. One is the ultimate shear resistance, which can be calculated with the method proposed by Borzogzadeh et al. (2006), as presented in Chapter 2, and the other is the shear resistance at first sliding, which can be calculated with the method proposed in this study, as presented in Section 5.3.2. These methods are summarized below. It is very likely that an isolated shear key will have to be repaired or replaced once sliding has occurred. For this reason, it is important to consider the resistance at first sliding.

Horizontal Shear Resistance at First Sliding

The calculation of the horizontal shear resistance at first sliding for a shear key with a smooth construction joint is based on the free-body diagram of the shear key as shown in Figure 11.2a, while that for a shear key with a rough joint is based on the free-body diagram shown in Figure 11.2b.

If the construction joint is smooth, then it is assumed that the shear forces are resisted by the vertical dowel bars developing the dowel force, F_d, and the cohesive force T and friction at the joint. If the construction joint surface is rough, the joint will open when the shear key starts to slide and ride over the rough surface. Thus, the vertical dowel bars will elongate and reach the yield strength f_y, introducing a clamping force F_s, which will increase the frictional resistance at the joint.

The friction coefficient is assumed to be zero on the inclined face of the shear key. Thus, the external load applied to the shear key has to be perpendicular to its inclined face and can be resolved into a horizontal component, denoted by V_{slid}, and a vertical component, denoted by P_{slid}, which are geometrically related as follows:

$$P_{slid} = V_{slid} \cdot \tan\beta \tag{11.5}$$

in which β is the angle of the inclined face of the shear key with respect to a vertical plane, as shown in Figure 11.2. It is recommended that the value of $\tan\beta$ be no less than 0.15 as explained in Section 11.2.1. The friction coefficient of the horizontal sliding surface of the shear key is denoted by μ_f.

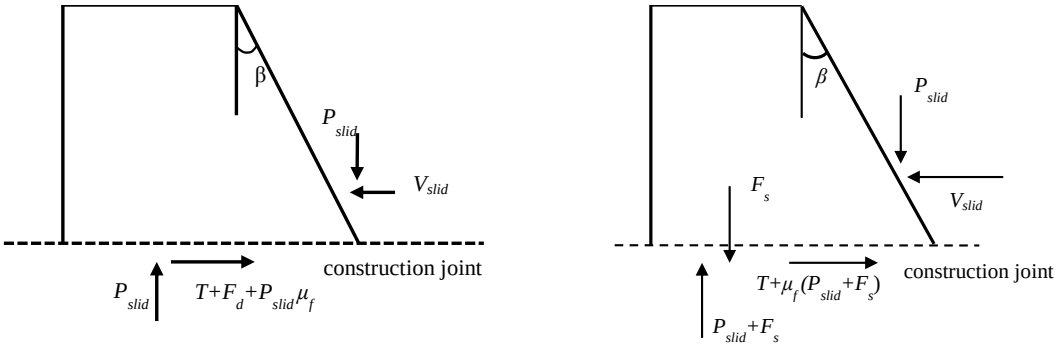

Figure 11.2 Free-body diagrams for the calculation of shear resistance at first sliding of a shear key with: a) a smooth construction joint; b) a rough construction joint

Based on the equilibrium of the horizontal and vertical forces in the free-body diagrams shown in Figure 11.2 and the relation given in Eq.(11.5), the shear resistance at first sliding, V_{slid} , can be calculated as follows:

$$V_{slid} = \frac{T + F_d}{(1 - \mu_f \cdot \tan\beta)} \quad \text{for a smooth joint} \tag{11.6}$$

and

$$V_{slid} = \frac{T + \mu_f F_s}{\left(1 - \mu_f \cdot \tan\beta\right)} \quad \text{for a rough joint} \tag{11.7}$$

In Equation (11.6) and (11.7), if bond breaker is applied on the construction joint, then T can be taken to be zero.

The shear resistance, F_d , due to the dowel action of a bar can be calculated with the following equation proposed in Chapter 3:

$$F_d = \sqrt{2M_{pl} \cdot f_{cb} \cdot d_b}$$
$$M_{pl} = \frac{f_y \cdot d_b^3}{6} \tag{11.8}$$

in which M_{pl} is the plastic moment capacity of the bar, and the strength of the confined concrete, f_{cb}, can be calculated as follows:

$$f_{cb} = a \cdot f_c'^{1.2}$$
$$a = 2.0 + \frac{0.5}{d_b} \tag{11.9}$$

in which f_c' is the uniaxial concrete compressive strength in ksi, d_b is the bar diameter in in. and f_{cb} is in ksi/in.

The cohesive strength, *c*, for concrete can be calculated by the formula proposed by Bazant and Pfeiffer (1986) as follows:

$$c = \frac{0.15 \cdot f_c'}{\sqrt{0.0099 \cdot X + 0.3659}} \tag{11.10}$$

in which, parameter *X* can be calculated as:

$$X = \frac{1.50 \cdot \alpha_c}{d_a} \tag{11.11}$$

in which d_a is the maximum aggregate size. Equation (13.10) was developed by the curve-fitting of data from a large number of Mode-II fracture tests. Thus, the cohesive force can be calculated as:

$$T = c \cdot \alpha_c \cdot d \tag{11.12}$$

in which α_c is the length of compression zone and *d* is the width of the shear key of the contact surface. From the experimental observation, the length of the compression zone, α_c, can be taken to be one quarter of the length of the shear key, i.e., $\alpha_c = 0.25l$.

Ultimate Shear Sliding Resistance

Regardless of the joint condition, the ultimate shear resistance of a shear key can be calculated by the method proposed by Borzogzadeh et al. (2006), as presented in Chapter 2. This method has been adopted by the Caltrans Seismic Design Criteria. It assumes that the vertical dowel bars have reached their ultimate tensile strength, f_{su}, when the ultimate shear resistance of the shear key, V_u, has been reached. Thus, the axial force in the vertical dowel bars is:

$$F_s = A_{vs} \cdot f_{su} \tag{11.13}$$

in which A_{vs} is the total area of the vertical dowel bars. In this method, it is also assumed that the dowel bars have been bent with an angle of inclination of a_k with respect to a vertical plane. It has been shown in an analytical study, as presented in Chapter 3, that the angle of kink is practically independent of the bar size and the concrete strength. In this study, the angle of kink is taken to be 37 degrees, which was measured by Borzogzadeh et al. (2006) in their shear key tests. Hence, the axial force, F_s, can be resolved into a horizontal component and a vertical component, F_{sx} and F_{sy}, as follows:

$$\begin{aligned} F_{sx} &= A_{vs} \cdot f_{su} \cdot \sin a_k \\ F_{sy} &= A_{vs} \cdot f_{su} \cdot \cos a_k \end{aligned} \tag{11.14}$$

To calculate the ultimate shear resistance of the shear key, the free-body diagram, shown in Figure 11.3, can be considered. Based on the equilibrium of the horizontal and vertical forces, the following equation is obtained:

$$V_u = \frac{\mu_f \cdot \cos a_k + \sin a_k}{1 - \mu_f \cdot \tan \beta} A_{vs} \cdot f_{su} \tag{11.15}$$

in which μ_f is the coefficient of friction of the construction joint.

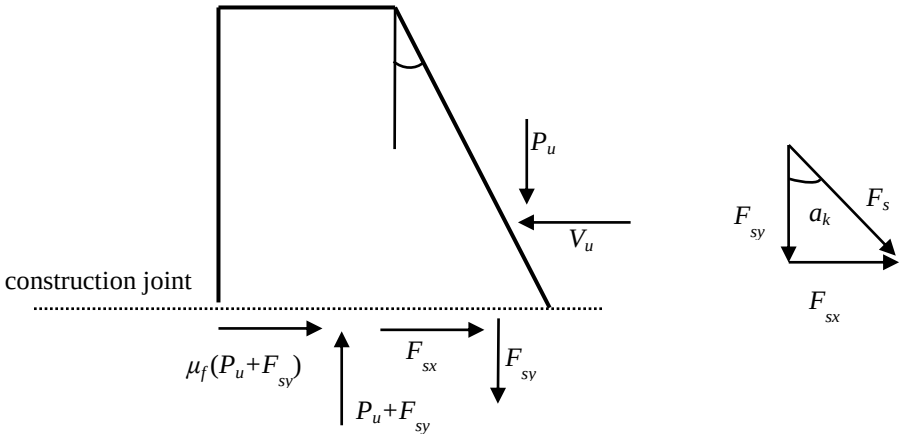

Figure 11.3 Free-body diagram of shear key for the calculation of ultimate shear resistance

Validation with Test Data

The above formulas have been validated with the experimental data from shear keys 5A and 5B tested by Borzogzadeh et al., and shear keys 7A and 7B tested in this study and presented in Chapter 5.

For the calculation of the resistance of shear keys 5A and 5B, the 28-day concrete compressive strength is used. This value was reported by Borzogzadeh et al. (2006) to be 4.90 ksi. In shear keys 7A and 7B, the concrete compressive strength used is 4.47 ksi. This is the average concrete strength of the stem wall and the shear keys, measured on the day of the test. The measured strengths of the reinforcing bars for shear keys 5A, 5B, 7A and 7B are shown in Table 11.4. The friction coefficient between the loaded face of the shear keys and the loading beam is assumed to be zero in all the cases.

For shear key 5A, in which part of the construction joint (8 in. x 8 in.) had a rough surface without bond breaker, the initial friction coefficient of the construction joint is

taken to be 1.0, and the final friction coefficient is assumed to be 0.7 when the ultimate shear resistance was reached. For shear key 5B, which had a smooth construction joint with oil-based bond breaker, the friction coefficient is assumed to be constant and equal to 0.36, as suggested by Borzogzadeh et al. The cohesive strength at the rough joint of shear key 5A is estimated to be 0.95 ksi, calculated with Eq. (11.10) proposed by Bazant and Pfeiffer (1986). For the calculation of the cohesive strength, the aggregate size is assumed to be ½ in., and the size of the contact area is 8 in. x 8 in. due to the special condition of the construction joint as explained in detail in Chapter 2. The cohesive strength at the construction joint of shear key 5B, which had oil-based bond breaker, is assumed to be zero.

Shear key 7B had a rough construction joint with several layers of water-based bond breaker applied. However, the effectiveness of the bond breaker is difficult to determine because the rough surface might not be able to keep the water-based bond breaker in place. The shear resistance of the shear key developed in the test indicates that limited cohesive resistance could have developed in the construction joint. For this reason, the load resistance of the shear key is calculated for two scenarios, one without cohesive force and the other with cohesive force. The initial friction coefficient is assumed to be 1.0 and the final is assumed to be 0.7, the same as those used for shear key 5A. For the case with cohesion, cohesive strength was calculated to be 0.87 ksi for the aggregate size of ⅜ in. using Eq.(11.10). For shear key 7A, which had a smooth construction joint, it is assumed that no cohesive force developed in the construction joint, and the friction coefficient is assumed to be 0.36, the same as that assumed for shear key 5B.

The calculated shear resistance at first sliding and the ultimate shear resistance before the failure of the shear keys are shown in Table 11.5 and Table 11.6. It can be observed that the calculated values are close to the measured. For shear key 7B, the measured shear resistance is close to the average of the two calculated values considering and without considering cohesion. The shear strengths of the stem walls calculated with the method presented in Section 13.2.1 are also shown in Table 11.5.

Table 11.4 Measured steel strengths for shear keys 5A and 5B (Borzogzadeh et al., 2006) and shear keys 7A and 7B

	Shear Keys 5A and 5B		Shear Key 7A	Shear Key 7B
	No. 3 bars	No. 4 bars	No. 5 bars	No. 4 bars
Yield strength (ksi)	63	66	70	70
Tensile strength (ksi)	104	104	93.6	94.5

Table 11.5 Calculated and measured horizontal resistance at first sliding and shear resistance of the stem wall for shear keys 5A, 5B, 7A and 7B

Shear Key	Calculated cohesive force T (kips)	Calculated dowel Force F_d (kips)	Calculated Shear Resistance at First Sliding (kips)	Measured Shear Resistance at First Sliding (kips)	Calculated Shear Resistance of Stem Wall (kips)
5A	61	-	155	165	259/262*
5B	0	22	25	21	259/262*
7A	0	31	34	37	286/299*
7B	0/87**	-	78/201**	132	278/288*

* Calculated without iteration

**Calculated assuming no bond breaker

Table 11.6 Calculated and measured ultimate sliding shear resistance for shear keys 5A, 5B, 7A and 7B

Tested Shear Key	Calculated Ultimate Sliding Shear Resistance (kips)	Measured Ultimate Sliding Shear Resistance (kips)
5A	119	123
5B	81	76
7A	128	142
7B	109	109

11.2.3 Horizontal Shear Resistance of Monolithic Shear Keys

Horizontal shear sliding failure was observed in the monolithic shear keys of Specimens 8 through 10, presented in Chapter 6. The shear keys in these specimens first rotated about the toe of the shear key at the free end of the specimen. After the peak resistance had been reached, a horizontal sliding plane was created right above the horizontal shear reinforcement in the stem wall, and the shear key started to slide.

The shear strength of a monolithic shear key with the aforementioned failure mechanism depends on the cohesive and frictional forces developed along the horizontal shear crack. For this reason, the sliding shear resistance of a monolithic shear key can be calculated with Eq. (11.7) based on the free-body diagram shown in Figure 11.2b. It should be mentioned that cohesive resistance should always be considered for monolithic shear keys, which can be calculated with Eqs. (11.10) through (11.12).

Validation with Test Data

This method has been validated with the experimental results from Specimens 8 through 10. Since the length of the shear keys was 24 in., the length of the compression zone length, α_c, is calculated to be 6 in. for all the shear keys. The friction coefficient is taken to be 1.4, as suggested in ACI-318 for concrete placed monolithically. The strengths of the vertical bars (No. 3 bars) and the concrete are shown in Table 11.7. The cohesive force *T*, the total vertical force F_s, and the calculated and measured horizontal shear strengths, V_s, are shown in Table 11.8. For the interest of assessing the margin of safety against the diagonal shear failure of the stem walls, the shear strengths of the stem

walls calculated with the method presented in Section 11.2.1 are also shown in the table. Shear keys 8B, 9B, and 10B had a vertical loaded face, while the loaded face of 8A, 9A, and 10A had an angle of inclination of 16 degrees with respect to a vertical plane. Specimens 8 and 10 had the same amount of vertical steel connecting the shear keys to the stem wall. Specimen 10 had a higher concrete strength than Specimens 8 and 9, while Specimen 9 had a higher amount of vertical steel.

It can be observed that the method predicts the strength of the shear keys reasonably well. For most shear keys, the difference between the calculated and measured shear strengths is less than 10% with respect to the measured values. However, for shear key 9B, the method under-predicts the shear strength by 19%. It is interesting to point out that the difference in the shear strengths of 9A and 9B obtained from the test is a lot smaller than that for Specimens 8 and 10. The horizontal resistances measured in shear keys 8B and 10B were 70% and 75% of the horizontal resistances of shear keys 8A and 10A, while the horizontal resistance of shear key 9B was measured to be 95% of that of shear key 9A.

Table 11.7 Strengths of steel and concrete for the monolithic shear keys

Shear Key	Yield strength/Amount of vertical bars (ksi)	Concrete strength (ksi)
8A	67.00/6 No.3	4.71
8B	67.00/6 No.3	4.71
9A	67.20/10 No. 3	5.10
9B	67.20/10 No. 3	5.10
10A	67.20/6 No.3	6.74
10B	67.20/6 No.3	6.74

Table 11.8 Horizontal shear resistances of monolithic shear keys

Shear Key	Cohesive force, T (kips)	Total force of vertical bars, F_s (kips)	Calculated horizontal shear strength (kips)	Measured horizontal shear strength (kips)	Calculated Shear Resistance of Stem Wall (kips)
8A	91.40	44.22	260	285	689/705*
8B	91.40	44.22	194	198	563/564*
9A	98.97	73.92	342	334	689/705*
9B	98.97	73.92	256	316	563/564*
10A	130.79	44.22	326	335	682/695*
10B	130.79	44.22	244	250	563/564*

*Calculated without iteration

11.3 Conclusions

In this chapter, analytical methods have been presented for the calculation of the load capacities of isolated and monolithic shear keys. These methods have been validated with experimental data from the past and present studies.

Three failure mechanisms have been identified. One is the diagonal shear failure of the stem wall. This mechanism can occur when the stem wall does not have sufficient horizontal shear reinforcement near the top to prohibit the propagation of diagonal shear cracks or when the resistance of the shear key to horizontal sliding on top of the stem wall is overly high. If diagonal shear cracks are prevented from propagating in the stem wall, the failure of the shear key will be governed by horizontal shear sliding. When a shear key is built monolithically with the stem wall, sliding is expected to develop on a horizontal crack plane right above the top shear reinforcement in the stem wall. When a shear key is isolated from the stem wall with a construction joint, sliding will occur at the construction joint.

An analytical method has been proposal for the calculation of the load capacity for each of the aforementioned mechanisms. These analytical methods can be used to design shear keys and stem walls to prevent diagonal shear failures and avoid the transmission of excessive seismic forces to piles supporting bridge abutments.

11.4 Acknowledgement of Publication

Part of this chapter is a reprint of the material that will appear in a technical report which will be submitted to the California Department of Transportation in 2016, Kottari, A., P. B. Shing, J. I. Restrepo, under the title "Design and Capacity Assessment of External Shear Keys in Bridge Abutments". The dissertation author will be the primary investigator and author of this report.

CHAPTER 12

SUMMARY AND CONCLUSIONS

12.1 Summary

An investigation of the strength and behavior of shear keys in bridge abutments has been presented in this dissertation. The investigation included experimental and numerical studies that have provided useful information regarding the behavior of shear keys with and without construction joints, with and without skew, and with different surface preparations of construction joints, different concrete strengths, and different amounts of vertical dowel reinforcement. The dowel behavior of steel reinforcing bars has also been investigated in detail. A simplified analytical model has been developed to calculate the dowel resistance in a reliable fashion, and a constitutive model has been proposed and implemented in an interface element for finite element analysis of shear key behavior. A cohesive crack interface model has been developed for 3D finite element analysis of concrete fracture. Simplified formulas that can be used to calculate the shear sliding resistance of shear keys and the diagonal shear strength of stem walls have also be developed for design practice.

An extensive experimental study of non-isolated and isolated shear keys was conducted. Six specimens were tested, each consisting of two shear keys. The experimental study was aimed at validating existing as well as newly proposed analytical

methods for the calculation of the resistance of shear keys and stem walls. Furthermore, reinforcing details that can have the failure of a non-isolated shear key governed by horizontal shear sliding were investigated and validated with tests. The influence of the angle of skew of the abutment in the resistance of a shear key was also evaluated with one of the test specimens. An innovative design utilizing post-tensioned rocking shear keys, which have ductile behavior, was also investigated.

For the calculation of the shear resistance provided by the dowel action of reinforcing bars, an existing constitutive law for dowel behavior has been adopted and extended to account for the cyclic behavior and for three-dimensional analysis. The material law has been implemented in an interface element and validated with past experimental data from dowel tests and the tests of reinforced masonry wall tests. To simulate concrete fracture in an accurate manner, a cohesive crack interface model suitable for 3D analysis has been developed. The proposed dowel action and cohesive crack interface models have been implemented for finite element analysis to investigate the behavior of isolated and non-isolated shear keys. The models have been validated with shear key test data obtained in this and previous studies.

12.2 Conclusions

The experimental study has shown that stem walls and shear keys in bridge abutments can be so designed and reinforced that the diagonal shear failure of a stem wall can be prevented even if the shear keys are not isolated from the stem wall with construction joints. The analytical formulas proposed in this study for the strength

calculations can be used to design shear keys and stem walls to achieve this purpose. It has been found that the concrete strength, amount of vertical dowel bars, surface roughness and bond breaker in the construction joint, vertical force exerted on the shear key, and the angle of skew can influence the resistance of the shear key significantly. The resistance of a shear key with a 60-degree skew can be significantly weaker than a shear key with zero-degree skew and the same amount of vertical dowel reinforcement.

Isolated shear keys with smooth construction joints tend to slide early under a relatively low lateral load as compared to their ultimate strengths. After sliding has started, the resistance of an isolated shear key continues to increase as sliding increases until the vertical dowel bars develop a significant kink and fracture. The angle of kink of the dowel bars with respect to a vertical axis when bar fracture would occur was found to be about 37 degrees in a previous study (Borzogzadeh et al, 2006). This finding is consistent with the observation from this study, in which the angles of kink varied between 32-43 degrees. Furthermore, the numerical parametric analysis performed in this study has found that the concrete strength and the bar size have little influence on the angle of kink. Non-isolated shear keys as well as isolated shear keys with rough construction joints can develop much higher resistance due to the higher coefficient of friction and cohesive force. They develop the peak resistance early before sliding becomes noticeable. Hence, from the damage mitigation standpoint, the latter type of shear keys appears to be more desirable. The tests on post-tensioned, rocking shear keys have shown that these shear keys can develop a ductile behavior with much higher displacement capacity than isolated shear keys. Minor concrete damage was observed in the shear keys and the stem wall in the tests.

12.3 Recommendations for Future Research

This study has shown that the resistance of a shear key depends on many parameters including the geometry of a shear key, the load application conditions, the preparation of the construction joint, the amount and arrangement of vertical reinforcing bars, and the degree of skew. While most of them have been addressed, the influence of the different degrees of skew on the shear key response remains to be quantified. The finite element modeling methods that have been presented in this dissertation can be readily used to identify the influence. From these analyses, simplified analytical methods can be derived for the design of skewed shear keys.

The feasibility of using post-tensioned shear keys and their ductile behavior have been demonstrated in this study. However, additional studies and development work are needed to improve the design details. Different configurations of post-tensioned shear keys should be investigated to identify the most practical design. Measures to secure the shear keys in place when the prestressing tendons fracture should be developed.

As discussed in Chapter 9, the dowel action model for three-dimensional analysis needs to be further improved so that the damage of the concrete around the dowel bar is more realistically represented. Furthermore, a more refined model should be developed to account for the interaction between the bond slip and the dowel action.

12.4 Acknowledgement of Publication

Part of this chapter is a reprint of the material that will appear in a technical report which will be submitted to the California Department of Transportation in 2016, Kottari,

A., P. B. Shing, J. I. Restrepo, under the title "Design and Capacity Assessment of External Shear Keys in Bridge Abutments". The dissertation author will be the primary investigator and author of this report.

REFERENCES

AASHTO LRFD Specifications, *American Association of State Highway and Transportation Officials, Washington*, USA, 2012.

Ahmadi, F., "Displacement-based Seismic Design and Tools for Reinforced Masonry", *Ph.D. Thesis*, Department of Civil Engineering, The University of Texas at Austin, 2012.

American Concrete Institute (ACI), Building Code Requirements for Structural Concrete and Commentary, *ACI Committee 318*, Farmington Hills, MI, 2012.

Bauer, L. H., "The Effects of Shear Key Properties on the Response of Overpass Bridges to Earthquakes", *Master Thesis*, UC San Diego, La Jolla, CA, 2006.

Bazant, Z. P., "Instability, Ductility, and Size Effect in Strain-Softening Concrete", *Journal of the Engineering Mechanics Division*, Vol. 102, No. 2, 1976, pp. 331-344.

Bazant, Z. P., B. H. Oh, "Crack band Theory for Fracture of Concrete", *Materiaux et Constructions*, Vol. 16, No. 3, 1983, pp. 155-177.

Bazant, Z. P., P. A. Pfeiffer, "Shear Fracture Tests of Concrete", Materiaux et Constructions, Vol. 19, No. 110, 1986, pp. 111-121.

Bennett, E. W., S. Banerjee, "Strength of Beam-Column Connections With Dowel Reinforcement", *The Structural Engineering*, 1976, pp. 133-139.

Borzogzadeh A., S. H. Megally, J. Restrepo, S. Ashford, "Seismic Response of Sacrificial Exterior Shear Keys in Bridge Abutments", *Journal of Bridge Engineering*, Vol. 11, No. 5, 2006, pp. 555-565.

Brenna, A., S. Dei Poli, M. Di Prisco, "Dowel Action: Some Experimental and Theoretical Results Regarding Special Concretes", *Studi e Ricerce*, 1990, pp. 321-380.

Carol, I., P. C. Prat, C. M. Lopez, "Normal/shear Cracking Model: Application to Discrete Crack Analysis", *Journal of Engineering Mechanics*, Vol. 123, No. 8, 1997, pp. 765-773.

Cervenka, J., "Discrete Crack Modeling in Concrete Structures", *Ph.D. Thesis*, Department of Civil, Environmental & Architectural Engineering, University of Colorado at Boulder, CO, 1994.

Dei Poli, S., M. Di Prisco, P. G. Gambarova, "Dowel Action as a Means of Shear Transmission in RC Elements: a State of the Art and New Test Results", *Studi e Ricerche* (School for the Design of R/C Structures, Milan University of Technology) 9-87, 1988, pp. 217-303.

Dei Poli, S., M. Di Prisco, P. G. Gambarova, "Shear Response, Deformationsm and Subgrade Stiffness of a Dowel Bar Embedded in Concrete", *ACI Structural Journal*, Vol. 89, No. 6, 1992, pp. 665-675.

Dodd, L. L., J. I., Restrepo-Posada, "Model for Predicting Cyclic Behavior of Reinforcing Steel", *Journal of Structural Engineering*, Vol. 121, No. 3, 1995, pp. 433-445.

Dulacska, H., "Dowel Action of Reinforcement Crossing Cracks in Concrete", *ACI Journal*, Vol. 69, 1972, pp. 754-757.

Fridberg, B. F., "Design of Dowels in Transverse Joints of Concrete Pavements", *Proceedings of ASCE*. 1938, pp. 1809-1828.

Hofbeck, J. A., I. O. Ibrahim, A. H. Mattock, "Shear Transfer in Reinforced Concrete", *ACI-Journal*, Vol. 66, 1969, pp. 119-128.

Koutromanos, I., P. B. Shing, "A Cohesive Crack Model to Simulate Cyclic Response of Concrete and Masonry Structures", *ACI Structural Journal*, Vol. 109, No. 3, 2011, pp. 349-358.

Lotfi, H. R., P. B. Shing, "An Appraisal of Smeared Crack Models for Masonry Shear Wall Analysis", *Journal of Computers and Structures*, Vol. 41, No. 3, 1991, 413-425.

Lotfi, H. R., P. B. Shing, "Interface Model Applied to Fracture of Masonry Structures," *Journal of Structural Engineering*, Vol. 120, No. 1, 1994, pp. 63–80.

Mavros, M., "Experimental and Numerical Investigation of the Seismic Performance of Reinforced Masonry Structures", *Ph.D. Thesis*, University of California, San Diego, La Jolla, CA, 2015.

McKenna, F., G. L. Fenves, M. H. Scott, B. Jeremic, "Open System for Earthquake Engineering Simulation (OpenSees)", *Pacific Earthquake Engineering Research Center*, University of California, Berkeley, 2000.

Mehrabi, A., P. B. Shing, "Finite Element Modeling of Masonry-Infilled RC Frames", *Journal of Structural Engineering*, Vol. 123, No. 5, 1997, pp. 604-613.

Millard, S. G., R. P. Johnson, "Shear Transfer Across Cracks in Reinforced Concrete due to Aggregate Interlock and Dowel Action", *Magazine of Concrete Research*, Vol. 36, No. 126, 1984, pp. 9-21.

Mills, G. M., "A Partial Kinking Yield Criterion for Reinforced Concrete Slabs", *Magazine of Concrete Research*, Vol. 27, No. 130, 1975, pp. 13-22.

Moharrami, M., I. Koutromanos, "Triaxial Constitutive Model for Concrete under Cyclic Loading", *Journal of Structural Engineering*, 2016 (Accepted for publication)

Murcia-Delso, J., P. B. Shing, "Bond-Slip Model for Detailed Finite-Element Analysis of Reinforced Concrete Structures", *Journal of Structural Engineering*, Vol. 141, No. 4, 2015, 04014125.

Paulay, T., R. Park, M. H. Philips, "Horizontal Construction Joints in Cast in Place Reinforced Concrete", *ACI Special Publication SP-42*, Vol. II, 1974, pp. 599-616.

Pruijssers, A. F., "Aggregate Interlock and Dowel Action Under Monotonic and Cyclic Loading", *Ph.D.Thesis*, Delft University of Technology, 1988, pp. 192.

Puntel, E., G. Bolzon, V. E. Saouma, "Fracture mechanics based model for joints under cyclic loading", *Journal of Engineering Mechanics*, Vol. 132, No. 11, 2006, pp. 1151-1159.

Rasmussen, B. H., "The Carrying Capacity of Transversely Loaded Bolts and Dowels Embedded in Concrete", *Bygningsstatiske Meddelser*, Vol. 34, No. 2, 1963, pp. 39-55.

Rots, J. G., J. Blaauwendraad, "Crack Models for Concrete: Discrete or Smeared? Fixed, Multi-Directional or Rotating?", Heron 34, *Delft University of Technology*, Delft, 1989, pp. 59.

Soroushian, P., K. Obaseki, M. C. Rojas, "Bearing Strength and Stiffness if Concrete Under Reinforcing Bars", *ACI Materials Journal*, 1987, pp. 179-184.

Stankowski, T., Runesson, K., and Sture, S., "Fracture and Slip of Interfaces in Cementitious Composites, I: Characteristics", *Journal of Engineering Mechanics*, Vol. 119, No. 2, 1993, pp. 292-314.

Tanaka, Y., J. Murakoshi, "Reexamination of Dowel Behavior of Steel Bars Embedded in Concrete", *ACI Structural Journal*, 2011, pp. 659-668.

Taylor, R. L., FEAP - Finite Element Analysis Program, 2014, University of California, Berkeley, http://www.ce.berkeley/feap.

Timoshenko, S, *In Strength of Materials, Part II: Advanced Theory and Problems*, Third Edition, New Jersey, D. Van Nostrand Co. Inc., 1956.

Vintzeleou, E. N., "Mechanisms of Load Transfer Along Reinforced Concrete Interfaces Under Monotonic and Cyclic Actions", *Ph.D. Thesis*, Department of Civil Engineering, National Technical University of Athens, Athens, Greece, 1984, 549 pp.

Vintzeleou, E., T. P. Tassios, "Behaviour of Dowels Under Cyclic Deformations", *ACI Structural Journal*, Vol. 84, 1987, pp. 18-30.

Vintzeleou, E., T. P. Tassios, "Behaviour of Dowels Under Cyclic Deformations", *ACI Structural Journal*, 1987, pp. 18-30.

Voon, K. C., "In-plane Seismic Design of Concrete Masonry Structures", *Ph.D. Thesis*, University of Auckland, New Zealand, 2007.